VIBRATION OF A NONLINEAR SHEAR DEFORMABLE BEAM BY NUMERICAL SIMULATION

by

Christopher Hagmann

Thesis submitted to the Faculty of the

Virginia Polytechnic Institute and State University

in partial fulfillment of the requirements for the degree of

MASTER OF SCIENCE

in

Engineering Mechanics

APPROVED:

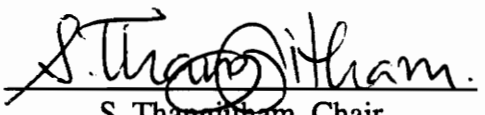

S. Thangjitham, Chair

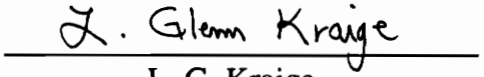

L. G. Kraige

R. A. Heller

June, 1996
Blacksburg, Virginia

Keywords: Beam, Vibration, Nonlinear, Shear-Deformable, Simulation

VIBRATION OF A NONLINEAR SHEAR DEFORMABLE BEAM BY NUMERICAL SIMULATION

by

Christopher Hagmann

Dr. Surot Thangjitham, Chairman

Engineering Mechanics

(ABSTRACT)

The vibration of a uniform geometrically nonlinear shear deformable beam subjected to a transverse harmonic excitation is investigated by the method of numerical simulation. Rotatory and axial inertia are included in the model. The beam is simply supported with supports a fixed distance apart. The nonlinear partial differential equations of motion are discretized in space by the Rayleigh-Ritz method, resulting in a set of nonlinear ordinary differential equations in time. The ordinary differential equations are integrated numerically to produce a time history of the solution of the equations.

Transverse displacement, axial displacement, and cross sectional rotation are approximated by series of the corresponding linear natural mode shapes of the beam. Solutions of the equations of motion are compared to corresponding solutions where shear deformation and rotatory inertia are neglected. The effect of slenderness on the difference between the shear deformable case and the non shear deformable case is investigated by considering two beam configurations.

In the simulations considered, the difference between the shear deformable model and the non shear deformable model increases as excitation frequency is increased and the length to thickness ratio of the beam is decreased.

ACKNOWLEDGMENTS

I would like to thank my advisor, Professor Surot Thangjitham, for his support and encouragement during my graduate studies at Virginia Tech. Thanks also go to Professor L. G. Kraige and Professor R. A. Heller for reviewing this thesis and suggesting improvements.

Special thanks are extended to my parents, Bill and Ellie Hagmann, for their love and support through my entire life, and to my grandmother, Viola Williams, whose support made my graduate studies possible.

I would also like to thank my friends Scot Goodman and Jay Warren, who were always there to guide me when the going seemed tough.

Table of Contents

List of Symbols

a	Amplitude of excitation function
A	Area of cross section
A_s	Shear area
E	Young's modulus
$f_A(x)$	Function representing distribution of area along the length of the beam
$f_r(x)$	Function representing distribution of radius of gyration along the length of the beam
G	Shear modulus
H	Height of cross section
i, j, k, l	Indices
I	Second moment of area
J	Mass moment of inertia per unit length
$(K_a^a)_{ij}$	Coefficients of axial displacement terms in discretized axial equations of motion of shear deformable beam
$(K_a^{tt})_{ijk}$	Coefficients of nonlinear axial-transverse coupling terms of discretized axial equations of motion of shear deformable beam
$(K_t^t)_{ij}$	Coefficients of linear transverse displacement terms of discretized transverse equations of motion of shear deformable beam
$(K_t^r)_{ij}$	Coefficients of linear transverse-rotational coupling terms of discretized transverse equations of motion of shear deformable beam
$(K_t^{at})_{ijk}$	Coefficients of nonlinear axial-transverse coupling terms of discretized transverse equations of motion of shear deformable beam
$(K_t^{ttt})_{ijkl}$	Coefficients of nonlinear transverse displacement terms of discretized transverse equations of motion of shear deformable beam
$(K_r^r)_{ij}$	Coefficients of linear rotational terms of discretized rotational equations of motion of shear deformable beam
$(K_r^t)_{ij}$	Coefficients of linear transverse-rotational coupling terms of discretized rotational equations of motion of shear deformable beam
$(K_a^a)'_{ij}$	Coefficients of axial displacement terms in discretized axial equations of motion of non shear deformable beam
$(K_a^{tt})'_{ijk}$	Coefficients of nonlinear axial-transverse coupling terms of discretized axial equations of motion of non shear deformable beam
$(K_t^t)'_{ij}$	Coefficients of linear transverse displacement terms of discretized transverse equations of motion of non shear deformable beam

$(K_t^{at})'_{ijk}$	Coefficients of nonlinear axial-transverse coupling terms of discretized transverse equations of motion of non shear deformable beam
$(K_t^{ttt})'_{ijkl}$	Coefficients of nonlinear transverse displacement terms of discretized transverse equations of motion of non shear deformable beam
L	Length of beam
$\mathcal{L}$	Lagrangian
m	Mass per unit length
$(M_a^a)_{ij}$	Coefficients of inertial terms of discretized axial equations of motion of shear deformable beam
$(M_t^t)_{ij}$	Coefficients of inertial terms of discretized transverse equations of motion of shear deformable beam
$(M_r^r)_{ij}$	Coefficients of inertial terms of discretized rotational equations of motion of shear deformable beam
$(M_a^a)'_{ij}$	Coefficients of inertial terms of discretized axial equations of motion of non shear deformable beam
$(M_t^t)'_{ij}$	Coefficients of inertial terms of discretized transverse equations of motion of non shear deformable beam
O	Point located on centroidal axis
$p(x,t)$	General excitation function
$\widehat{p}(x,t)$	Excitation function with variable amplitude
$\overline{p}(x,t)$	Excitation function with variable frequency
P	Point located off centroidal axis
r	Radius of gyration of cross section
t	Time
T	Kinetic energy
$u(x,t)$	Axial displacement of point O
$u_1(t),\ u_2(t), \ldots$	Axial generalized coordinates
U	Strain energy
$U_1(x),\ U_2(x),\ \ldots$	Axial shape functions
$\mathcal{U}(x,y,t)$	Axial displacement of point P
V	Total potential energy
$w(x,t)$	Transverse displacement of point O
$w_1(t),\ w_2(t),\ \ldots$	Transverse generalized coordinates
$w_c(t)$	Transverse displacement of midspan
$W_1(x),\ W_2(x),\ \ldots$	Transverse shape functions
$\mathcal{W}(x,y,t)$	Transverse displacement of point P
$x,\ y$	Rectangular coordinates
α	Slope of excitation amplitude
ϵ	Damping ratio
ϵ_{xx}	Normal strain

γ_{xy}	Shear strain
κ	Shear correction factor
ω_1^a, ω_2^a, ...	Linear natural frequencies of axial vibration
ω_1^t, ω_2^t, ...	Linear natural frequencies of transverse vibration
Ω	Excitation frequency
ϕ	Phase angle of excitation function
$\psi(x,t)$	Rotation of centroidal axis
σ_{xx}	Normal stress
τ_{xy}	Shear stress
$\theta(x,t)$	Rotation of cross section
$\theta_1(t)$, $\theta_2(t)$, ...	Rotational generalized coordinates
$\Theta_1(x)$, $\Theta_2(x)$, ...	Rotational shape functions

Chapter 1

INTRODUCTION

The vibration of a geometrically nonlinear shear deformable elastic beam with ends restrained against axial motion is considered. The equations of motion consist of a set of three nonlinear partial differential equations.

It is common to assume that when a beam deforms under a transverse load, plane cross sections of the beam remain plane and perpendicular to the neutral axis of the beam during bending. This assumption requires that the shear strain of the deformed beam be zero. Such a model is commonly referred to as Euler-Bernoulli beam theory.

A model which includes shear deformation is commonly called Timoshenko beam theory. In this model plane cross sections are assumed to remain plane, but they can rotate with respect to the neutral axis of the beam under deformation. This rotation is independent of the deflection of the neutral axis. Thus, another degree of freedom is introduced to the equations of motion. In addition to deflection, there is an inertial property associated with this extra degree of freedom. This is called *rotatory inertia*, and it comes from the mass moment of inertia of the cross section of the beam. Although this

quantity can be associated with the second time derivative of the slope of the neutral axis in the Euler-Bernoulli case, it is usually neglected in non shear deformable formulations.

Much research has been done analytically and experimentally to study the differences between Euler-Bernoulli beam theory and Timoshenko beam theory, for both the static case and the dynamic case. It has been found that for relatively slender beams composed of common materials, such as metals, there is very little difference in static deflection and vibratory motion between the two models. However, geometric and material properties of a beam can sometimes result in a significant difference between the two models.

Usually, most of the transverse deflection of a beam is associated with bending. Some shear deformation occurs with any transverse loading, but it usually results in a very small contribution to the transverse deflection. If the second moment of area of the cross section is very large compared to the area of the cross section, or the shear modulus of the material is very small compared to Young's modulus, as is the case with many composite materials and timber, a significant portion of the deformation of the beam can be caused by shear strain.

Geometric nonlinearities arise in the equations of motion for beams as a result of large deflections and some types of boundary conditions. If the ends of a beam are a fixed distance apart, the neutral axis of the beam must stretch under deformation, and an axial stress not associated with bending develops. This results in a nonlinear coupling between axial and transverse displacements that is not apparent unless geometric nonlinearities are considered.

The equations of motion for a geometrically nonlinear beam are generally not able to be solved analytically. Therefore the equations are usually solved by an approximate analytical method or a numerical method.

Analysis and experiment in the vibration of geometrically nonlinear beams has focused primarily on the case where transverse shear deformation and rotatory inertia are neglected. Some research has been done on the effects of neglecting the inertia associated with axial deformation.

An investigation of the effects of shear deformation and rotatory inertia on the motion of a geometrically nonlinear beam will be made. The partial differential equations of motion are discretized in space to yield a set of nonlinear ordinary differential equations in time governing the motion of the beam. These equations are integrated numerically to produce a time history of the motion of the beam.

The time histories of the response of the shear deformable beam will be compared to the corresponding time histories of the response of a beam in which shear deformation and rotatory inertia are neglected. One of the quantities compared is the maximum absolute value of the displacement of the beams at their midspan for various excitation functions.

In Chapter 2 a survey of previous research on the effects of specific physical quantities on the vibration of beams and columns is made. The formulation of the equations of motion is described in Chapter 3. Chapter 4 contains a description of the procedures used to produce time histories of the solutions to the equations of motion. The results of some simulations run for the case of uniform beams with pinned ends are presented in Chapter 5, and conclusions drawn from those results are given in Chapter 6.

Chapter 2

LITERATURE REVIEW

An investigation of the effects of including shear deformation and rotatory inertia in the vibration analysis of linear uniform beams with various radii of gyration of cross section and boundary conditions was made by Abramovich (1992), Abramovich and Elishakoff (1987), Abramovich and Elishakoff (1990). None of these studies included the coupling term between rotatory inertia and shear deformation in the equations of motion, but Abramovich and Elishakoff (1990) compared their solutions to previous solutions by other authors that included coupling between rotatory inertia and shear deformation, and found that they were close. Abramovich and Elishakoff (1987) applied Krein's method to compute natural frequencies of shear flexible multispan beams for different numbers of spans, and Abramovich (1992) computed natural frequencies of uniform symmetrically laminated composite beams for various fiber orientations.

Datta and Ganguli (1990) used the finite element method to analyze a straight cantilever beam rotating about an axis perpendicular to the beam. They modeled the effect of a damaged region as a reduction in the elastic properties in the material, and

investigated the effects of rotatory inertia, shear deformation and damage parameters on the natural frequencies of the beam.

Dawe and Roufaeil (1980) used series of products of Timoshenko beam mode shapes as interpolation functions in the Rayleigh-Ritz method applied to square isotropic Mindlin plates to obtain natural frequencies for a range of boundary conditions. They obtained the best results with supported edges, where the boundary conditions were satisfied better than with free edges.

Benouna and White (1984) and Benamar, Bennouna, White (1991) obtained amplitude dependent non-linear vibration mode shapes for geometrically nonlinear beams, neglecting shear deformation and rotatory inertia. Bennouna and White (1984) examined the fundamental mode shape of a slender clamped-clamped beam and large deflections experimentally and fit a polynomial to that shape. They also used the method of harmonic balance to reduce the equation of motion to a fourth-order ordinary differential equation and solve it for the spatial function. Benamar, Bennouna, White (1991) assumed harmonic motion and substituted an assumed displacement in the form of a finite series of linear mode shapes into the equation of motion. They applied Hamilton's principle and solved the resulting algebraic equations to obtain the first three non-linear frequencies and mode shapes for clamped-clamped and pinned-pinned beams.

The finite element method was applied by Busby and Weingarten (1973) to study the stability of a straight beam-column subjected to a transverse harmonic excitation and a longitudinal periodic excitation. They obtained an approximate solution to the resulting differential equation by the method of averaging, and also solved the equation on an analog computer. They included linear viscous damping and considered cases only where the external excitation was not near the longitudinal natural frequencies of the beam.

Morris (1965) studied the dynamic stability of a pinned-pinned beam-column with a constant axial load. He assumed the solution to be of the form of the first buckling mode shape and obtained an ordinary differential equation with a cubic nonlinearity. He used perturbation techniques to solve this equation for both the free vibration case and the case where the column is subjected to a harmonic transverse load. He found that dynamic instability can occur at axial thrusts below the static buckling load, and that stable vibration can occur at axial loads above the static buckling load.

Plaut (1971) used some inequalities and an energy functional to derive an upper bound on the displacement of initially curved beam columns subjected to time-varying axial and distributed loads.

Sevin (1960) investigated the elastic bending motion of initially slightly curved columns subjected to time-dependent axial forces. The equations of motion included axial inertia and axial displacement explicitly but did not include rotatory inertia or shear deformation. The finite difference method was used to solve the equations of motion, and the results were compared to previous works. The effects of axial inertia were shown to be very small.

Tseng and Dugundji (1970) investigated the motion of a straight, viscously damped clamped-clamped beam with ends a fixed distance apart subjected to harmonic excitation of its supports. The first linear mode shape was used to apply Galerkin's method to the equation of motion to obtain Duffing's equation. The method of harmonic balance was applied to investigate the solution of simple harmonic motion and branch solutions involving superharmonic motion and subharmonic motion. This analysis was shown to agree well with experimental results.

Pollai and Rao (1992) conducted a single mode analysis of large amplitude free vibration of a simply supported uniform beam with ends restrained against axial motion.

They solved the resulting Duffing equation by the simple harmonic oscillations assumption, Galerkin's method, and the harmonic balance method.

Rehfield (1974) used Hamilton's Principle and a perturbation procedure to obtain freqency-response curves for beams and plates for large amplitudes of vibration. He considered forcing functions which are harmonic in time and spatially distributed so as to excite only one mode.

Ray and Bert (1969), Eisley and Bennett (1970), Bennett and Eisley (1970), and Busby and Weingarten (1972) used partial series of linear mode shapes to study the forced vibration of beams with geometric nonlinearities. Ray and Bert (1969) obtained freqency-response plots of a nonlinear beam subjected to support excitation for the resonant frequency at different amplitudes of response. They compared solutions obtained by the assumed-space-mode method, the assumed-time-mode method, and the Ritz-Galerkin method to experimental results. Eisley and Bennett (1970) investigated the validity of a single mode analysis of a beam with ends a fixed distance apart by doing a multi-mode analysis with only one mode forced and examining the stability of the unforced modes. Bennett and Eisley (1970) studied the response of a harmonically excited beam with ends restrained against axial motion elastically, rather than rigidly, in order to relate theory to experiment, but no damping was included. The first three linear mode shapes were used to approximate displacement, and the method of harmonic balance was used to solve the resulting ordinary differential equations. Busby and Weingarten (1972) used the first and third linear mode shapes in the analysis of a viscously damped non-linear beam subjected to a spatially symmetric harmonic load. The method of averaging was used to solve the two resulting differential equations, and plots of amplitude vs. frequency for the first and third modes were made for the cases of clamped-clamped and pinned-pinned ends.

Fertis and Lee (1972) studied the free vibration of a beam with elastically supported ends, both vertically and horizontally, subjected to an initial axial compressive load. The model included shear deformation and rotatory inertia, but not damping. Galerkin's method was used to reduce the equations of motion to a set of ordinary differential equations in time, and an assumed solution was substituted to solve the resulting equations. They showed that there are regions of static and dynamic instability, depending on initial deflections of the supports.

Singh, Sharma, Rao (1990) and Singh, Rao, Iyengar (1990) studied the effect of including axial displacement in the vibration analysis of beams with ends restrained against axial motion. Singh, Sharma, Rao (1990) used the Rayleigh-Ritz method with one term approximations for axial and transverse displacements in the free vibration analysis of simply supported beams with ends restrained against axial motion. They concluded that neglecting axial displacement increases the non-linear stretching force by three halves. Singh, Rao, Iyengar (1990) used the finite element method and assumed harmonic oscillations to obtain non-linear mode shapes of non-linear beams with various boundary conditions. They applied the direct numerical integration method to obtain nonlinear frequencies and concluded that the frequencies obtained neglecting axial deflection are higher than those obtained while including axial deflection.

Hsieh (1984) examined the motion of a nonlinear shallow arch under multi-frequency excitation. He used Galerkin's method to obtain a set of ordinary differential equations governing the motion and integrated the equations numerically. Time histories and phase portraits were examined for certain excitations. Damping was included in the analysis.

Ueda (1980) obtained solutions to Duffing's equation with digital and analog computers. He defined steady motion as a physical state which continues infinitely after

transient aspects have vanished. He included damping and used the numerical solutions to survey the whole aspect of steady motions exhibited by Duffing's equation.

Chapter 3

FORMULATION

This chapter contains a description of the derivation of the equations of motion governing the vibration of a shear-deformable elastic beam with ends restrained against axial motion. The Lagrangian for the beam is obtained from the total potential energy and the kinetic energy of the beam. Hamilton's principle is applied to derive the partial differential equations of motion from the Lagrangian. The Rayleigh-Ritz method is used to obtain a set of ordinary differential equations in time governing the motion of the beam.

The beam being considered in this study is illustrated in Figure 3.1. In this figure, the beam is shown to have a rectangular profile, but the equations of motion are derived for a beam with a cross section which is not necessarily uniform over its length. The coordinate system used in this analysis is illustrated on the beam. The origin of the coordinate system is located at the left end of the beam. The x-axis is coincident with the centroid of the cross section of the beam, and the y-axis is perpendicular to x-axis, pointing up in the plane of the figure. The y-axis is coincident with one of the principal

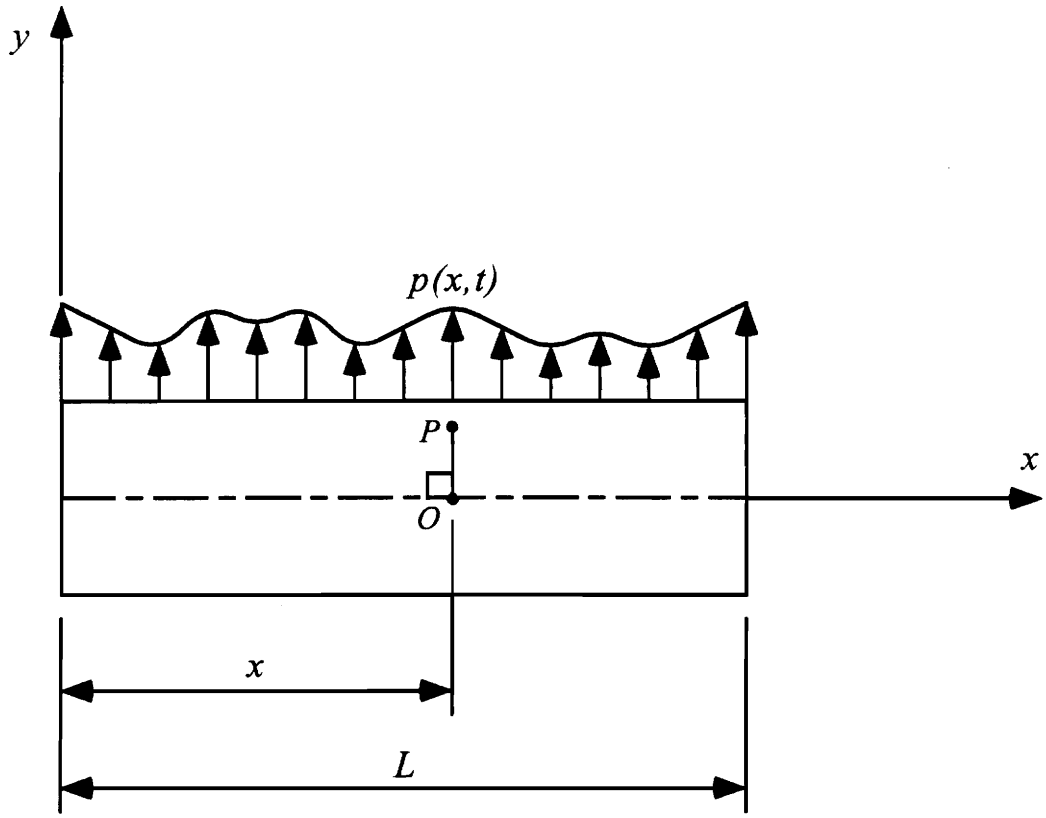

Figure 3.1: General beam with a distributed excitation.

axes of the cross section. A distributed vertical load, denoted by $p(x,t)$, is also illustrated in this figure.

A portion of the beam in the undeformed state and the deformed state is illustrated in Figure 3.2. In the undeformed state the centroidal axis of the beam, shown as a broken line, is initially straight and horizontal and the line segment OP is perpendicular to the centroidal axis. Point O is any arbitrary point on the centroidal axis of the beam, with position given by x. Point P is any point on the cross section which is perpendicular to the centroidal axis and contains point O. In the deformed state, the displacement of point O in the x-direction is given by $u(x,t)$, the displacement of point O in the y-direction is given by $w(x,t)$, and the angle between the y-axis and the plane containing points O and P is given by $\theta(x,t)$. The cross section can rotate only about the line perpendicular to the x and y axes, and it is assumed to be planar in the deformed state. The angle between the y-axis and the line perpendicular to the deformed centroidal axis at point O is given by $\psi(x,t)$. Angle ψ is also the angle between the centroidal axis and the x-axis at point O. For small rotations of the centroidal axis and the cross section, the following approximations are made.

$$\psi \approx \frac{\partial w}{\partial x} \tag{3.1}$$

$$sin\theta \approx \theta \tag{3.2}$$

$$cos\theta \approx 1 \tag{3.3}$$

The total displacement of point P in the deformed state is expressed in terms of the displacement of point O in the deformed state and the position of point P with respect

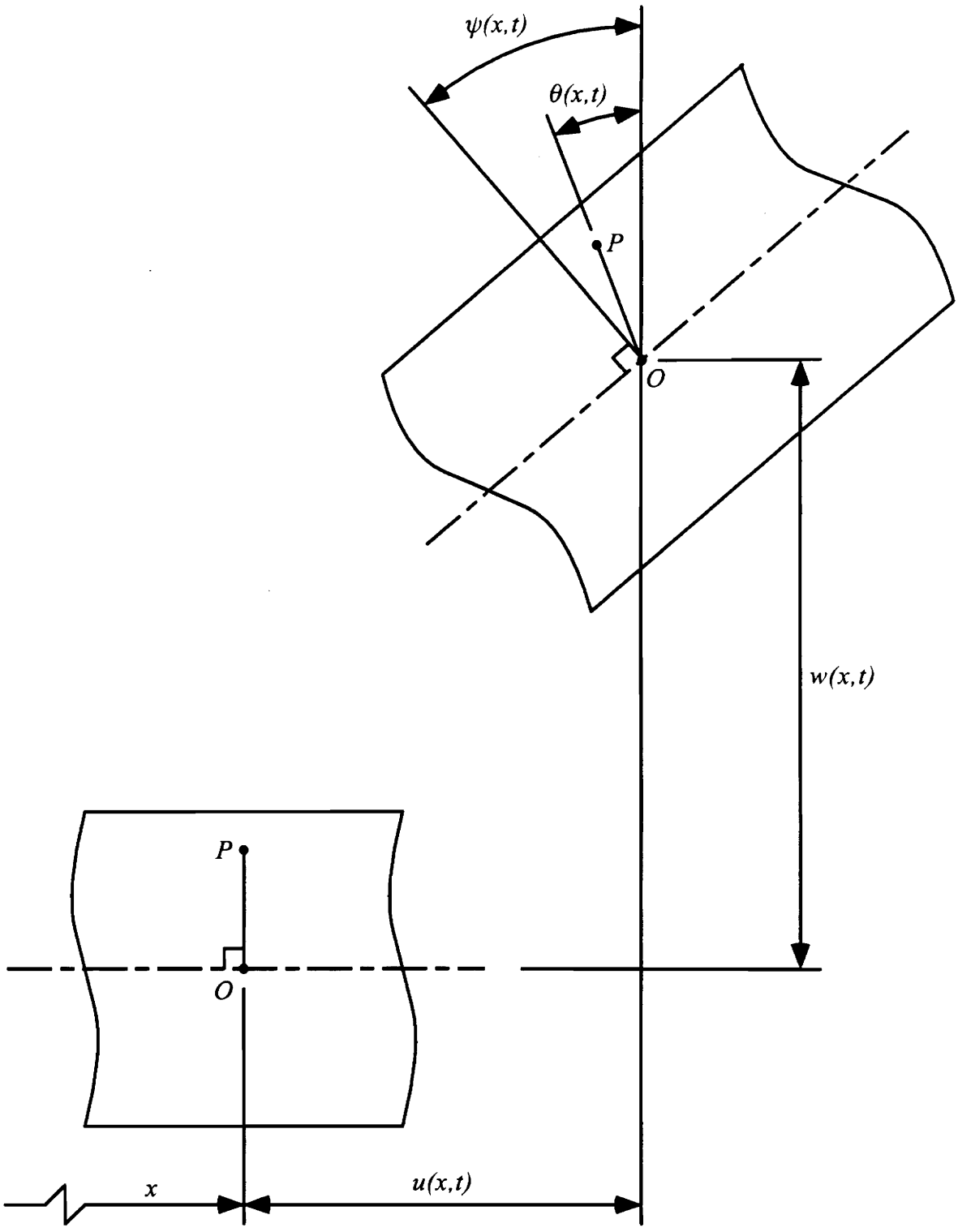

Figure 3.2: Kinematics of line segment OP.

to point O. These displacements are given by

$$\mathcal{U}(x,y,t) = u(x,t) - y\theta(x,t) \tag{3.4}$$

$$\mathcal{W}(x,y,t) = w(x,t) \tag{3.5}$$

where $\mathcal{U}(x,y,t)$ is the displacement of point P in the x-direction, and $\mathcal{W}(x,y,t)$ is the displacement of point P in the y-direction. It is assumed that there is no displacement in the out-of-plane direction, and the derivatives of the displacement functions with respect to the out-of-plane coordinate are assumed to be zero.

The state of strain at point P is defined by the following expressions:

$$\epsilon_{xx} = \frac{\partial \mathcal{U}}{\partial x} + \frac{1}{2}\left[\left(\frac{\partial \mathcal{U}}{\partial x}\right)^2 + \left(\frac{\partial \mathcal{W}}{\partial x}\right)^2\right] \tag{3.6}$$

$$\epsilon_{yy} = \frac{\partial \mathcal{W}}{\partial y} + \frac{1}{2}\left[\left(\frac{\partial \mathcal{U}}{\partial y}\right)^2 + \left(\frac{\partial \mathcal{W}}{\partial y}\right)^2\right] \tag{3.7}$$

$$\gamma_{xy} = \frac{\partial \mathcal{U}}{\partial y} + \frac{\partial \mathcal{W}}{\partial x} + \left(\frac{\partial \mathcal{U}}{\partial x}\right)\left(\frac{\partial \mathcal{U}}{\partial x}\right) + \left(\frac{\partial \mathcal{W}}{\partial x}\right)\left(\frac{\partial \mathcal{W}}{\partial y}\right) \tag{3.8}$$

Substituting the expressions for the total displacement into the expressions for strain and neglecting higher order terms not involving transverse displacement, w, yields two non-zero components of strain, ϵ_{xx} and γ_{xy}, given by the following expressions:

$$\epsilon_{xx} = \frac{\partial u}{\partial x} + \frac{1}{2}\left(\frac{\partial w}{\partial x}\right)^2 - y\frac{\partial \theta}{\partial x} \tag{3.9}$$

$$\gamma_{xy} = \frac{\partial w}{\partial x} - \theta \tag{3.10}$$

The strain ϵ_{xx} is called axial strain, and γ_{xy} is called shear strain.

Strain energy, U, is calculated by multiplying axial stress, σ_{xx}, by axial strain, multiplying shear stress, τ_{xy}, by shear strain, and integrating half of the sum of these two quantities over the entire volume of material.

$$U = \frac{1}{2}\int (\sigma_{xx}\epsilon_{xx} + \tau_{xy}\gamma_{xy}) dA dx \tag{3.11}$$

Stress and strain are related through Hooke's Law by the following expressions:

$$\sigma_{xx} = E\epsilon_{xx} \tag{3.12}$$

$$\tau_{xy} = G\gamma_{xy} \tag{3.13}$$

The quantity E is Young's modulus, and G is the shear modulus.

The total potential energy, V, of the beam is obtained by summing the strain energy and the potential energy due to loads applied to the structure. Only vertical transverse loads will be considered here. The potential energy of such a load is simply the negative of the product of the load and the vertical displacement of the beam integrated over the entire length.

The integrand in the expression for strain energy is integrated over the area of the cross section to yield strain energy per unit length of the beam. To this is added the potential energy of the applied load to yield the total potential energy per unit length. This is integrated over the length of the beam to produce the total potential energy.

The total potential energy of the beam, including the effects of shear deformation is given by

$$V = \int_0^L \left\{ \frac{1}{2} EA \left(\frac{\partial u}{\partial x} \right)^2 + \frac{1}{2} EA \left(\frac{\partial u}{\partial x} \right) \left(\frac{\partial w}{\partial x} \right)^2 + \frac{1}{8} EA \left(\frac{\partial w}{\partial x} \right)^4 \right.$$

$$+ \frac{1}{2} EI \left(\frac{\partial \theta}{\partial x} \right)^2 + \frac{1}{2} GA_s \left(\frac{\partial w}{\partial x} \right)^2 - GA_s \left(\frac{\partial w}{\partial x} \right) \theta$$

$$\left. + \frac{1}{2} GA_s \theta^2 - p(x,t)\, w \right\} dx \tag{3.14}$$

where A is the cross sectional area of the beam, and I is the second moment of area of the cross section about the horizontal centroidal axis in the plane of the cross section. The quantity A_s is the shear area of the beam. Shear area is related to the area of the cross section, A, by the relation

$$A_s = \kappa A \tag{3.15}$$

where κ is the shear correction factor. This correction is necessary because shear stress is not uniformly distributed over the area of the cross section.

The kinetic energy of the beam, including the effect of rotatory inertia, is

$$T = \int_0^L \left\{ \frac{1}{2} m \left(\frac{\partial u}{\partial t} \right)^2 + \frac{1}{2} m \left(\frac{\partial w}{\partial t} \right)^2 + \frac{1}{2} J \left(\frac{\partial \theta}{\partial t} \right)^2 \right\} dx \tag{3.16}$$

where m is the mass per unit length of the beam, and J is the mass moment of inertia of the cross section per unit length. The Lagrangian, $\mathcal{L}$, is defined as the difference of kinetic and potential energy.

$$\mathcal{L} = T - V \tag{3.17}$$

Applying Hamilton's principle, given by

$$\delta \int_{t_1}^{t_2} \mathcal{L}\, dt = 0 \tag{3.18}$$

yields the equations of motion and the associated boundary conditions, which are listed below.

The equations of motion are:

$$m\left(\frac{\partial^2 u}{\partial t^2}\right) - \frac{\partial}{\partial x}\left[EA\left(\frac{\partial u}{\partial x} + \frac{1}{2}\left(\frac{\partial w}{\partial x}\right)^2\right)\right] = 0 \tag{3.19}$$

$$m\left(\frac{\partial^2 w}{\partial t^2}\right) - \frac{\partial}{\partial x}\left[EA\left(\frac{\partial u}{\partial x} + \frac{1}{2}\left(\frac{\partial w}{\partial x}\right)^2\right)\frac{\partial w}{\partial x}\right]$$

$$- \frac{\partial}{\partial x}\left[GA_s\left(\frac{\partial w}{\partial x} - \theta\right)\right] = p \tag{3.20}$$

$$J\left(\frac{\partial^2 \theta}{\partial t^2}\right) - \frac{\partial}{\partial x}\left[EI\left(\frac{\partial \theta}{\partial x}\right)\right] - GA_s\left(\frac{\partial w}{\partial x} - \theta\right) = 0 \tag{3.21}$$

The boundary conditions are:

At $x = 0$ and $x = L$:

$$\text{either} \quad u = 0 \tag{3.22}$$

$$\text{or} \quad EA\left(\frac{\partial u}{\partial x}\right) + \frac{1}{2}EA\left(\frac{\partial w}{\partial x}\right)^2 = 0 \tag{3.23}$$

$$\text{either} \quad w = 0 \tag{3.24}$$

$$\text{or} \quad EA\left(\frac{\partial u}{\partial x}\right)\left(\frac{\partial w}{\partial x}\right) + \frac{1}{2}EA\left(\frac{\partial w}{\partial x}\right) + GA_s\left(\frac{\partial w}{\partial x}\right) - GA_s\theta = 0 \tag{3.25}$$

$$\text{either} \quad \theta = 0 \tag{3.26}$$

$$\text{or} \quad EI\left(\frac{\partial \theta}{\partial x}\right) = 0 \tag{3.27}$$

It is desired to reduce the partial differential equations of motion to a set of ordinary differential equations. The Rayleigh-Ritz method is used to accomplish this by discretizing the displacement functions in space. In this method the displacement functions are assumed to be series of products of specified functions of space and generalized coordinates, which are undetermined functions of time. The spacial functions, or shape functions, must satisfy any geometric boundary conditions which are imposed. Geometric boundary conditions are slope and deflection of the beam at the endpoints. The generalized coordinates are denoted by lowercase subscripted letters, and the shape

functions are denoted by uppercase letters.

$$u(x,t) = \sum_{i=1}^{N_a} u_i(t) U_i(x) \tag{3.28}$$

$$w(x,t) = \sum_{i=1}^{N_t} w_i(t) W_i(x) \tag{3.29}$$

$$\theta(x,t) = \sum_{i=1}^{N_r} \theta_i(t) \Theta_i(x) \tag{3.30}$$

These functions are substituted into the potential and kinetic energies, and Hamilton's principle is applied by taking the variation of the Lagrangian with respect to the generalized coordinates. The result of this is a set of nonlinear ordinary differential equations in time, with constant coefficients.

It will be convenient to nondimensionalize the equations of motion by substituting the following dimensionless variables, denoted by the superscript "*", into the energy functional.

$$x^* = \frac{x}{L}, \quad t^* = \sqrt{\frac{EI}{\rho A L^4}}\, t, \quad p^* = \frac{L}{EA} p$$

$$r^* = \sqrt{\frac{I}{AL^2}}, \quad U^* = \frac{U}{L}, \quad W^* = \frac{W}{L}$$

where r^* is the dimensionless radius of gyration of the cross section, and ρ is the density of the material which the beam is composed of.

The two quantities chosen to characterize the cross section of the beam as a function of position are radius of gyration, r^*, and area, A. These will be represented by

products of nondimensional functions of x and characteristic constant values of r^* and A.

$$r^*(x) = r^* f_r(x) \tag{3.31}$$

$$A(x) = A f_A(x) \tag{3.32}$$

Applying Hamilton's principle and dropping the asterisks from the nondimensional quantities yields

$$(M_a^a)_{ij}\ddot{u}_j + (K_a^a)_{ij}u_j + (K_a^{tt})_{ijk}w_j w_k = 0 \tag{3.33}$$

$$(M_t^t)_{ij}\ddot{w}_j + (K_t^t)_{ij}w_j - (K_t^r)_{ij}\theta_j + (K_t^{at})_{ijk}u_j w_k$$

$$+ (K_t^{ttt})_{ijkl}w_j w_k w_l = p_i(t) \tag{3.34}$$

$$(M_r^r)_{ij}\ddot{\theta}_j + (K_r^r)_{ij}\theta_j - (K_r^t)_{ij}w_j = 0 \tag{3.35}$$

Where

$$(M_a^a)_{ij} = r^2 \int_0^1 f_A(x) U_i U_j dx \tag{3.36}$$

$$(M_t^t)_{ij} = r^2 \int_0^1 f_A(x) W_i W_j dx \tag{3.37}$$

$$(M_r^r)_{ij} = r^4 \int_0^1 f_A(x) f_r^2(x) \Theta_i \Theta_j dx \tag{3.38}$$

$$(K_a^a)_{ij} = \int_0^1 f_A(x) \frac{dU_i}{dx}\frac{dU_j}{dx} dx \tag{3.39}$$

$$(K_t^t)_{ij} = \kappa \frac{G}{E} \int_0^1 f_A(x) \frac{dW_i}{dx}\frac{dW_j}{dx} dx \tag{3.40}$$

$$(K_r^r)_{ij} = \int_0^1 \left(r^2 f_A(x) f_r^2(x) \frac{d\Theta_i}{dx}\frac{d\Theta_j}{dx} + \kappa \frac{G}{E} f_A(x) \Theta_i \Theta_j \right) dx \tag{3.41}$$

$$(K_t^r)_{ij} = \kappa \frac{G}{E} \int_0^1 f_A(x) \frac{dW_i}{dx} \Theta_j dx \tag{3.42}$$

$$(K_r^t)_{ij} = \kappa \frac{G}{E} \int_0^1 f_A(x) \Theta_i \frac{dW_j}{dx} dx \tag{3.43}$$

$$(K_a^{tt})_{ijk} = \frac{1}{2} \int_0^1 f_A(x) \frac{dU_i}{dx} \frac{dW_j}{dx} \frac{dW_k}{dx} dx \tag{3.44}$$

$$(K_t^{at})_{ijk} = \int_0^1 f_A(x) \frac{dW_i}{dx} \frac{dU_j}{dx} \frac{dW_k}{dx} dx \tag{3.45}$$

$$(K_t^{ttt})_{ijkl} = \frac{1}{2} \int_0^1 f_A(x) \frac{dW_i}{dx} \frac{dW_j}{dx} \frac{dW_k}{dx} \frac{dW_l}{dx} dx \tag{3.46}$$

$$p_i(t) = \int_0^1 p(x,t) W_i dx \tag{3.47}$$

The subscripts and superscripts a, t, and r inside the parentheses stand for axial, transverse, and rotational, respectively. The subscripts pertain to the particular equation that the coefficients are associated with. The coefficients with the subscript a are in the equation with the axial inertia term, the coefficients with the subscript t are in the equation with the transverse inertia term, and the coefficients with the subscript r are in the equation with the rotational inertia term. For example, the coefficients $(K_t^{at})_{ijk}$ have the subscript t inside the parentheses, which indicates that these coefficients are in the equation containing the acceleration term for the transverse generalized coordinate, $\ddot{w}_j$.

The superscripts pertain to the quantities the coefficients are multiplied by in each equation. For example, the coefficients $(K_t^{at})_{ijk}$ have the superscript at inside the parentheses. This indicates that those coefficients are multiplied by the generalized coordinates in axial displacement, u_j, and the coordinates in transverse displacement, w_k.

The generalized coordinates which are the solution to the discretized equations of motion can be substituted into Equations (3.28) through (3.30) with their associated shape functions, producing three functions of time and space, which are approximate displacements of the beam.

The solution of the equations of motion for a beam including the effects of transverse shear deformation and rotatory inertia will be compared to the solution for the case where these effects are neglected. When rotatory inertia is neglected, the term in the expression for kinetic energy involving mass moment of inertia, J, becomes zero.

Neglecting shear deformation imposes the condition that cross sections initially perpendicular to the centroidal axis remain perpendicular to that axis in the deformed state. This requires that the quantities ψ and θ, illustrated in Figure 2.1, be equal. This leads to the conclusion that shear strain is zero, and all of the terms in the expression for potential energy involving the shear modulus sum to zero.

When these requirements are imposed, only the axial displacement, u, and transverse displacement, w, are necessary to describe the displacement of any point on the beam. The discretized equations of motion for this case are

$$(M_a^a)'_{ij}\ddot{u}_j + (K_a^a)'_{ij}u_j + (K_a^{tt})'_{ijk}w_j w_k = 0 \tag{3.48}$$

$$(M_t^t)'_{ij}\ddot{w}_j + (K_t^t)'_{ij}w_j + (K_t^{at})'_{ijk}u_j w_k + (K_t^{ttt})'_{ijkl}w_j w_k w_l = p_i'(t) \tag{3.49}$$

where all of the coefficients and the excitation function are identical to the unprimed quantities defined previously, with the exception of $(K_t^t)'_{ij}$, which is defined by the following expression.

$$(K_t^t)'_{ij} = r^2 \int_0^1 f_A(x) f_r(x) \frac{d^2W_i}{dx^2} \frac{d^2W_j}{dx^2} dx \tag{3.50}$$

Chapter 4

SIMULATION

The equations of motion of the discretized system are integrated numerically using the IMSL subroutine DIVPRK (1991), which uses the Runge-Kutta-Verner method, to produce a time history of the response to an excitation uniformly distributed in space and harmonic in time. This excitation has the form

$$p(x,t) = asin(\Omega t + \phi) \tag{4.1}$$

where a is a constant amplitude, Ω is a constant frequency, and ϕ is a constant phase angle.

It is desired to simulate an undamped system, but the time histories of such a system are strongly influenced by the initial conditions. Therefore, a method to eliminate or reduce the effects of initial conditions on the time history is needed.

It is assumed that for the system being considered, a periodic excitation should lead to a periodic response after a sufficiently long interval of time if light damping is present. Furthermore, for a harmonic excitation, the nature of the response should not depend on the phase angle of the excitation function after a long period of time, assuming

the system is started from rest at $t = 0$. However, for a completely undamped system, numerical integration yields results which are strongly dependent on the phase angle of excitation, and this appears to hold true for any length of time.

Figures 4.1 through 4.3 contain plots of time histories of the solution to the equations of motion with an excitation of the form of Equation (4.1). These were generated for a uniform beam, rigid in shear, with a value of nondimensional radius of $r = 0.01$. Both ends are supported by pins. The numerical simulation was carried out with the displacement functions approximated in the form of Equations (3.28) and (3.30), with only one function included in each series. Nayfeh and Mook (1979) suggest using the linear free vibration modes as shape functions. It was found that in the case of a uniform beam there is no coupling between the symmetric modes and the antisymmetric modes. Since the excitation is symmetric in space, none of the antisymmetric modes are excited. Therefore, only the symmetric modes are used in the simulation. The axial displacement was approximated by the second natural mode shape for a uniform bar in axial vibration, while the transverse displacement was approximated by the first natural mode for a uniform beam in transverse vibration. These functions are defined by the following expressions.

$$U_2(x) = sin(2\pi x) \tag{4.2}$$

$$W_1(x) = sin(\pi x) \tag{4.3}$$

The excitation function was of the form of Equation (4.1) with nondimensional amplitude $a = 0.0002$ and nondimensional frequency $\Omega = 8$.

Figure 4.1 contains two plots of transverse displacement at the midspan of the beam for two different phase angles, ϕ, both with the beam starting from rest. Both histories are plotted for a span of ten nondimensional time units. The upper plot is a time

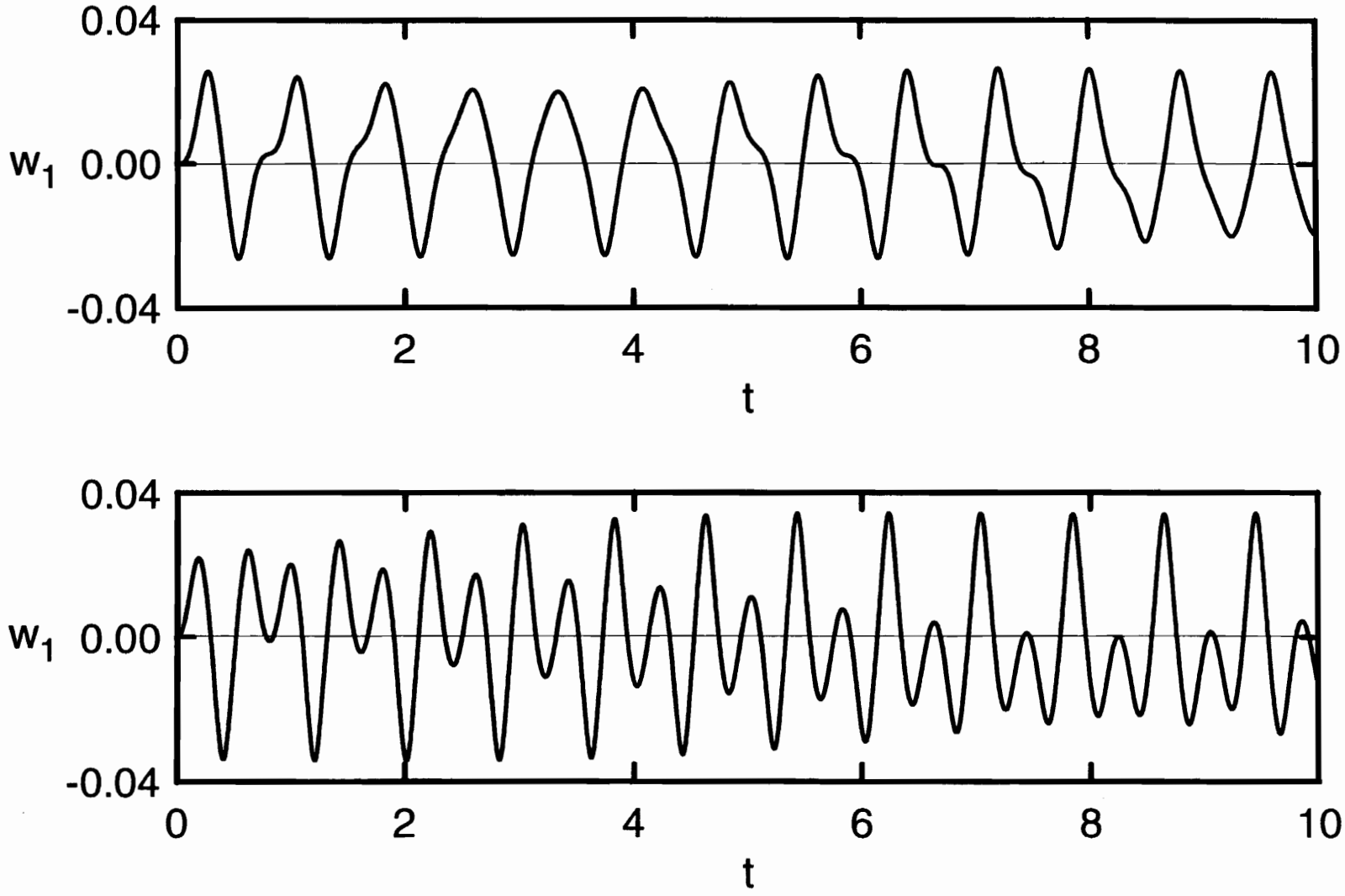

Figure 4.1: Transverse midspan displacement vs. time for $\phi = 0$ and $\phi = \pi/2$.
(zero initial conditions)

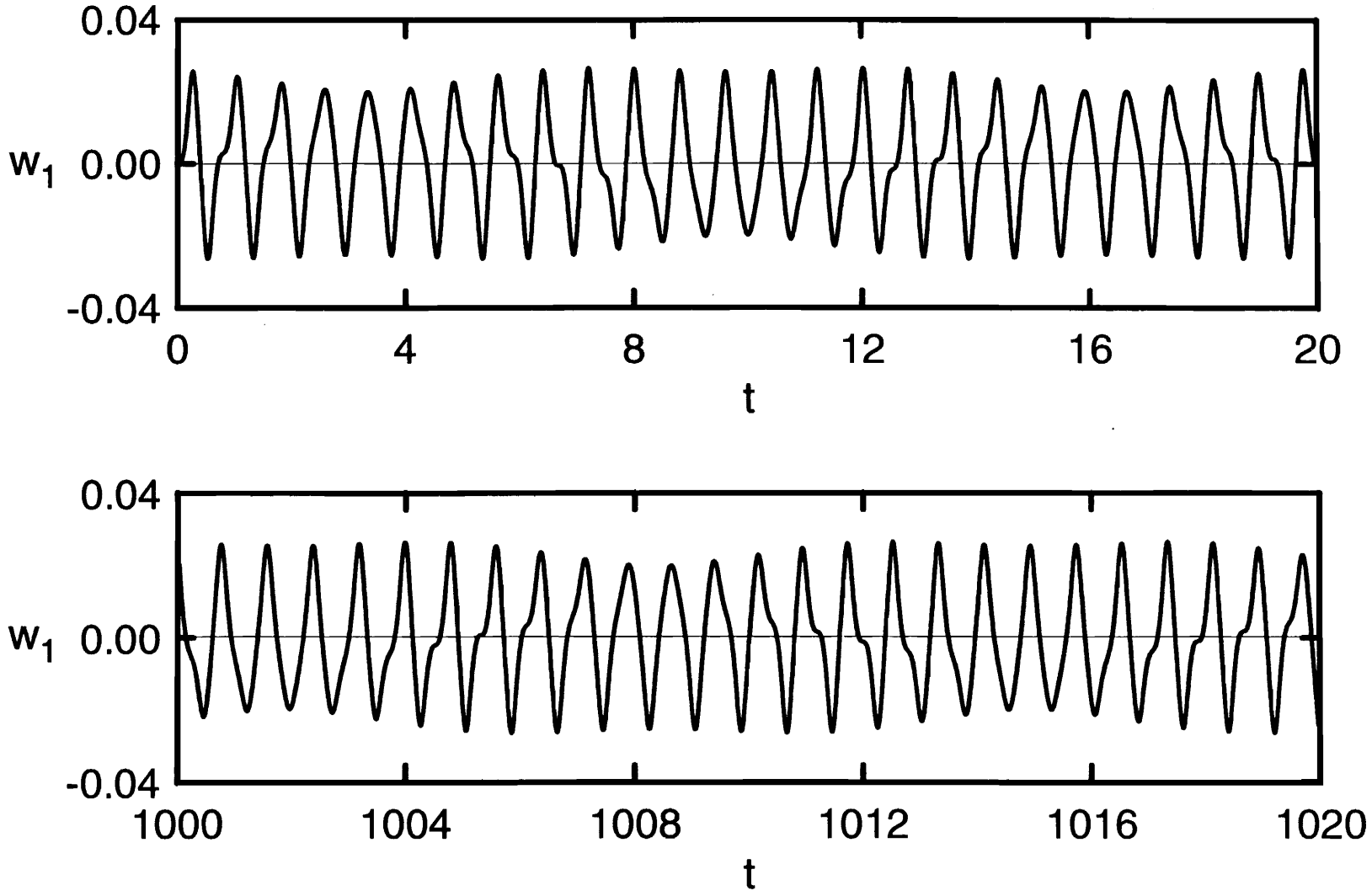

Figure 4.2: Transverse midspan displacement vs. time for $\phi = 0$.
(zero initial conditions)

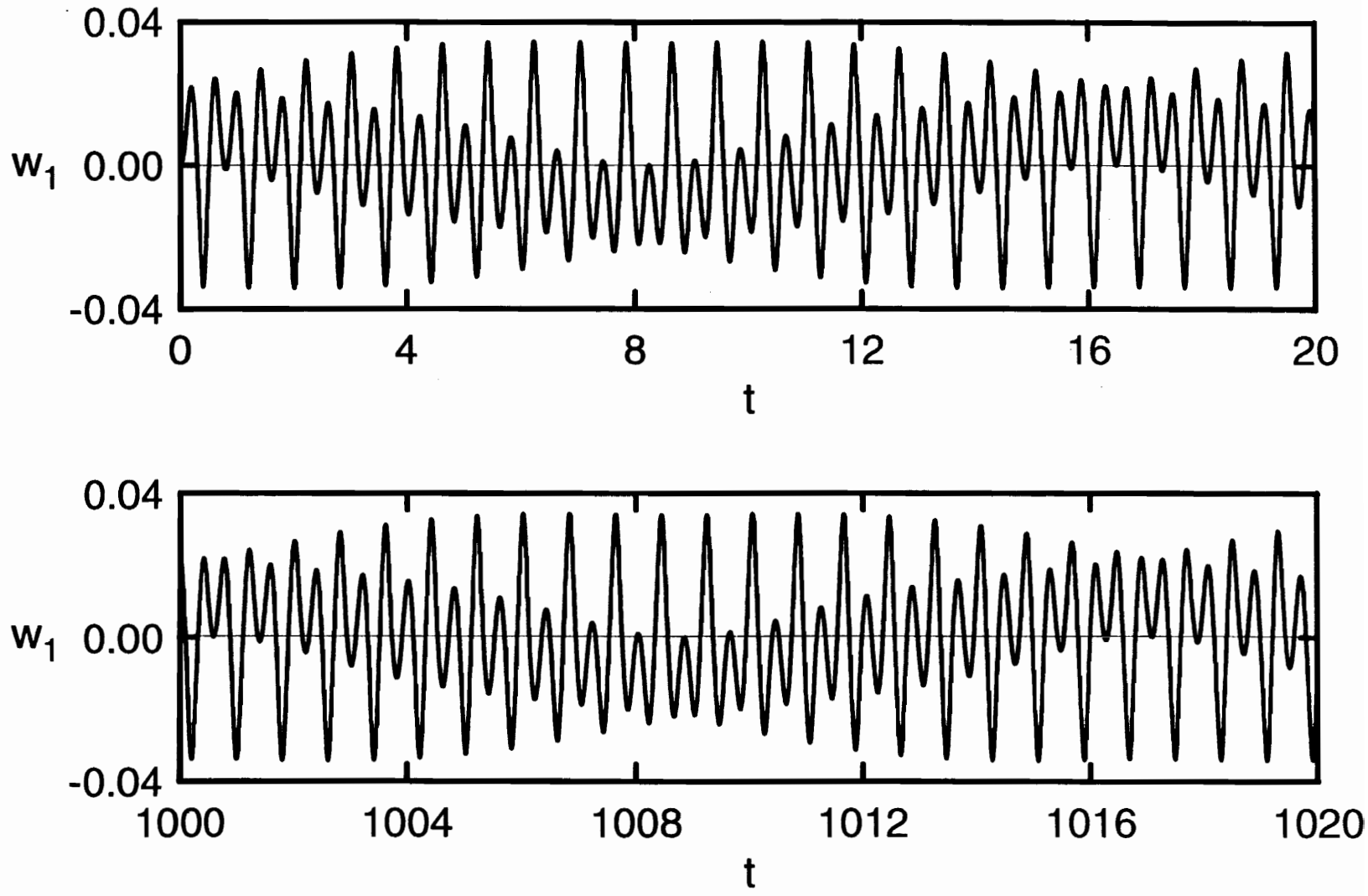

Figure 4.3: Transverse midspan displacement vs. time for $\phi = \pi/2$.
(zero initial conditions)

history of midspan displacement with a phase angle of excitation, $\phi = 0$. The lower plot is a time history of midspan displacement with a phase angle of excitation, $\phi = \pi/2$. It can be seen that the time histories of the response for the two cases differ in more than just phase angle.

Figure 4.2 contains two plots of transverse displacement at the midspan over 20 time units resulting from an excitation phase angle, $\phi = 0$. The upper plot is the displacement from $t = 0$ to $t = 20$. The lower plot is the displacement from $t = 1000$ to $t = 1020$. Comparing the two graphs suggests that the behavior of the solution to the equations of motion does not change after a long period of integration.

Figure 4.3 contains two plots as in Figure 4.2, but for an excitation phase angle, $\phi = \pi/2$. Again, the behavior of the solution appears not to change after a long period of integration.

One method of reducing the effect of phase angle is to slowly ramp the amplitude of the excitation from zero with the system at initially rest and hold the amplitude constant when the desired amplitude of excitation is reached. In this method, all of the initial conditions are zero, and the excitation function initially has the form

$$\widehat{p}(x,t) = \alpha t sin(\Omega t + \phi) \tag{4.4}$$

where α is a constant slope of excitation amplitude, Ω is frequency of excitation, and ϕ is a phase angle. When the quantity αt is equal to the desired amplitude of excitation, a, the form of the excitation amplitude is changed to Equation (4.1).

The two functions, p and $\widehat{p}$, are equal when $\alpha t = a$. However, the transition from the ramped portion of the excitation to the final portion with a constant amplitude is not smooth. This can be seen by considering the time derivatives of the two functions at the

instant the excitation amplitude reaches the desired value. The derivative of the ramped portion, $\widehat{p}$, is given by

$$\frac{\partial \widehat{p}}{\partial t} = \alpha sin(\Omega t + \phi) + \alpha t \Omega cos(\Omega t + \phi) \tag{4.5}$$

The derivative of the constant portion, p, is given by

$$\frac{\partial p}{\partial t} = a\Omega cos(\Omega t + \phi) \tag{4.6}$$

Equation (4.6) can be substituted into Equation (4.5) at the instant when $\alpha t = a$ to give the difference between the two functions. This difference can be expressed as follows:

$$\frac{\partial \widehat{p}}{\partial t} - \frac{\partial p}{\partial t} = \alpha sin(\Omega t + \phi) \tag{4.7}$$

The difference in the derivatives is proportional to the slope of the amplitude, α. This leads to the conclusion that while the transition to the constant amplitude portion of the excitation function is not smooth, the discontinuity in the slope can be made as small as desired by increasing the time interval over which the amplitude of the function is increased, thereby decreasing the slope, α.

If a sufficiently small value for α is chosen, plots of the time histories of the response for different values for ϕ appear to be identical visually, with the only apparent difference being the "phase" of the response. Figure 4.4 contains plots of the response of the same beam as in the previous examples excited by a force ramped to an amplitude of $a = 0.0002$ in the manner described above. In both cases the amplitude of the excitation function was increased with a slope of $\alpha = 10^{-7}$. The time history in the upper plot was obtained with a phase angle of $\phi = 0$ while the lower plot was obtained with a phase angle

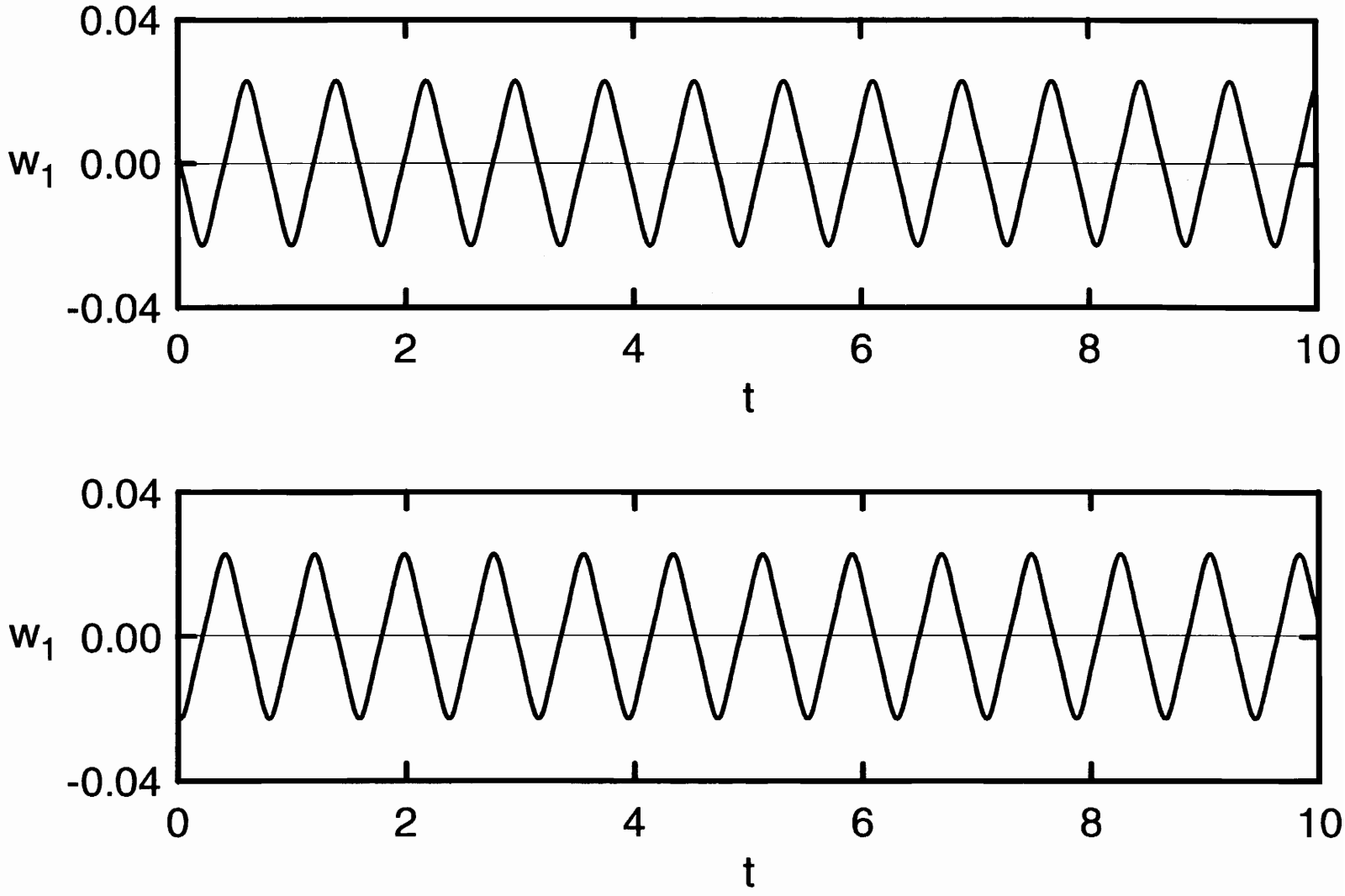

Figure 4.4: Transverse midspan displacement vs. time for $\phi = 0$ and $\phi = \pi/2$.
(ramped excitation)

of $\phi = \pi/2$. Time is defined as zero at the point where the excitation amplitude becomes constant. The two plots appear to be identical, aside from a difference in phase.

Figure 4.5 contains plots such as those in Figure 4.4, but for an interval of time later in the history. The behavior of the solution appears to remain the same after a long period of integration.

Figures 4.6 and 4.7 are time histories and phase portraits of the response of the beam for phase angles of $\phi = 0$ and $\phi = \pi/2$, respectively. Although the response for each case has a phase different from the other, their phase portraits appear the same. Moreover, the maximum values of the functions appear to be equal.

When the amplitude of excitation is increased from zero, the amplitude of the response can suddenly jump to a higher value when a certain amplitude of excitation is reached. When this happens, it is not possible to obtain a periodic response of the undamped system from that point on. The disturbance caused by the sudden change in response is preserved as a part of the time history throughout the integration process.

A method which was used to reduce the effect of uncontrollable disturbances to the time histories of the response involved the inclusion of linear proportional damping for a period of time and removing this damping to produce a time history of an undamped system. The equations of motion including damping terms are given below.

$$(M_a^a)_{ij}\ddot{u}_j + (K_a^a)_{ij}(u_j + \epsilon\dot{u}_j) + (K_a^{tt})_{ijk}w_j w_k = 0 \tag{4.8}$$

$$(M_t^t)_{ij}\ddot{w}_j + (K_t^t)_{ij}(w_j + \epsilon\dot{w}_j) - (K_t^r)_{ij}(\theta_j + \epsilon\dot{\theta}_j) + (K_t^{at})_{ijk}u_j w_k + (K_t^{ttt})_{ijkl}w_j w_k w_l = p_i(t) \tag{4.9}$$

$$(M_r^r)_{ij}\ddot{\theta}_j + (K_r^r)_{ij}(\theta_j + \epsilon\dot{\theta}_j) - (K_r^t)_{ij}(w_j + \epsilon\dot{w}_j) = 0 \tag{4.10}$$

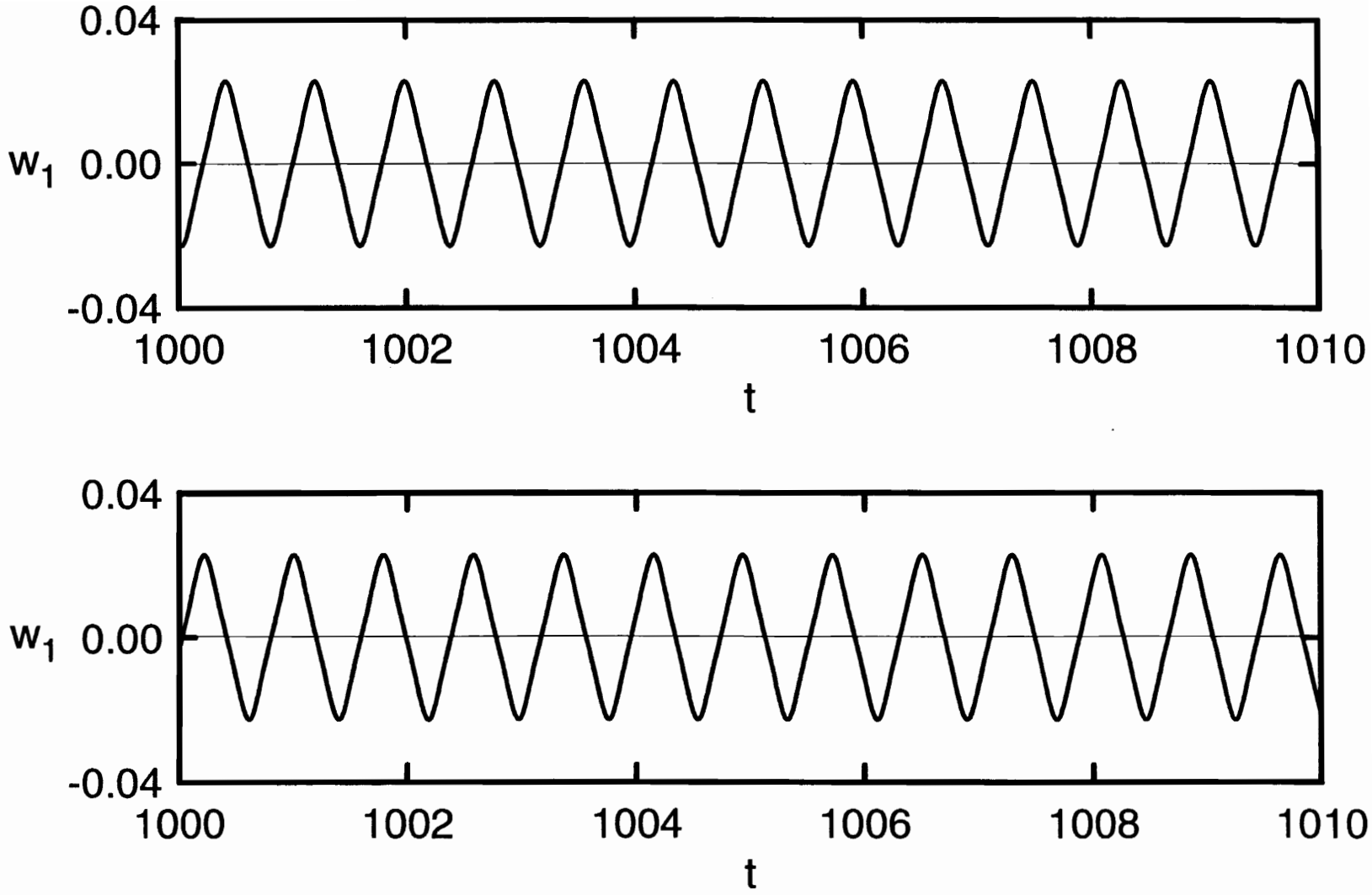

Figure 4.5: Transverse midspan displacement vs. time for $\phi = 0$ and $\phi = \pi/2$.
(ramped excitation)

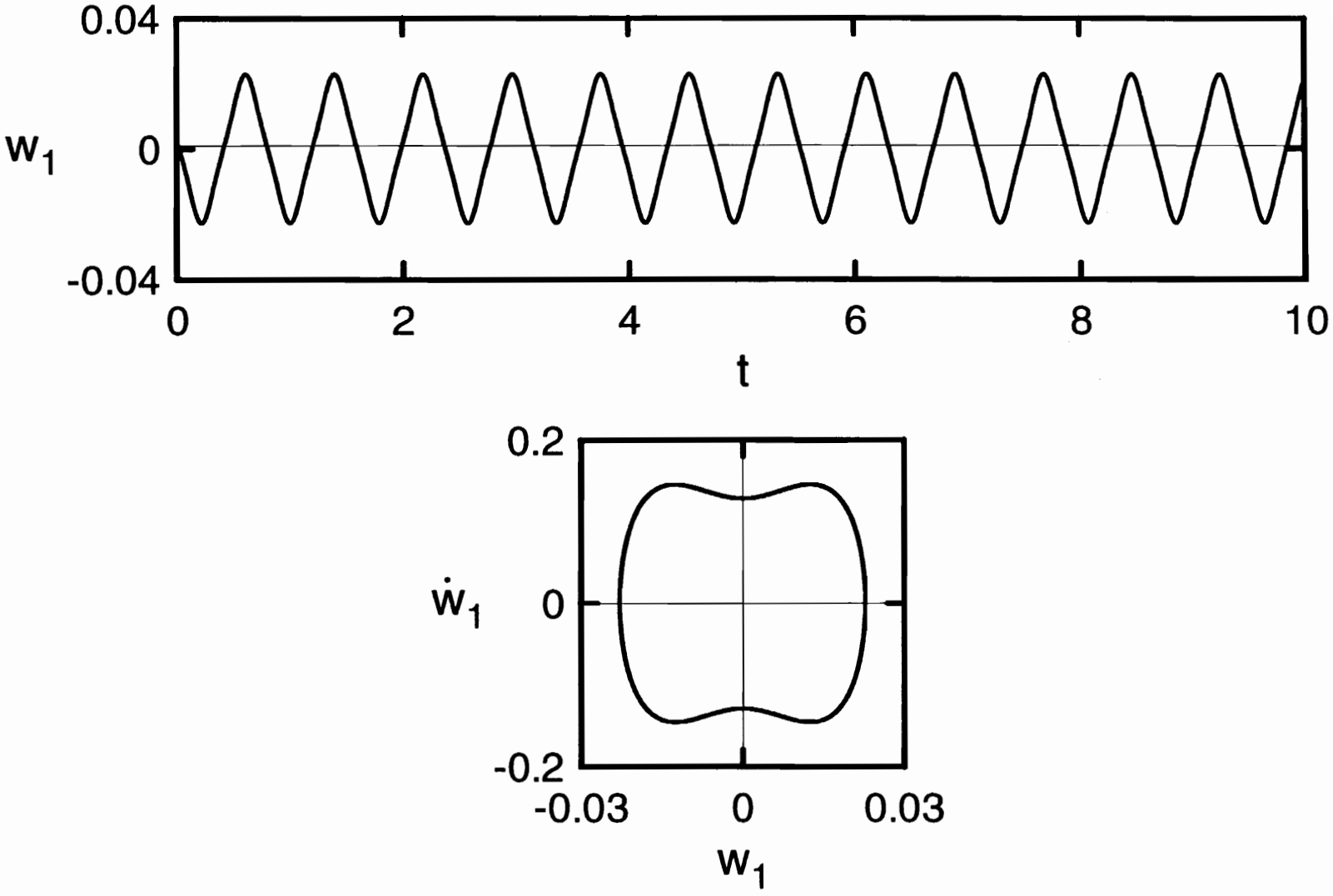

Figure 4.6: Time history and phase portrait of midspan displacement for $\phi = 0$.

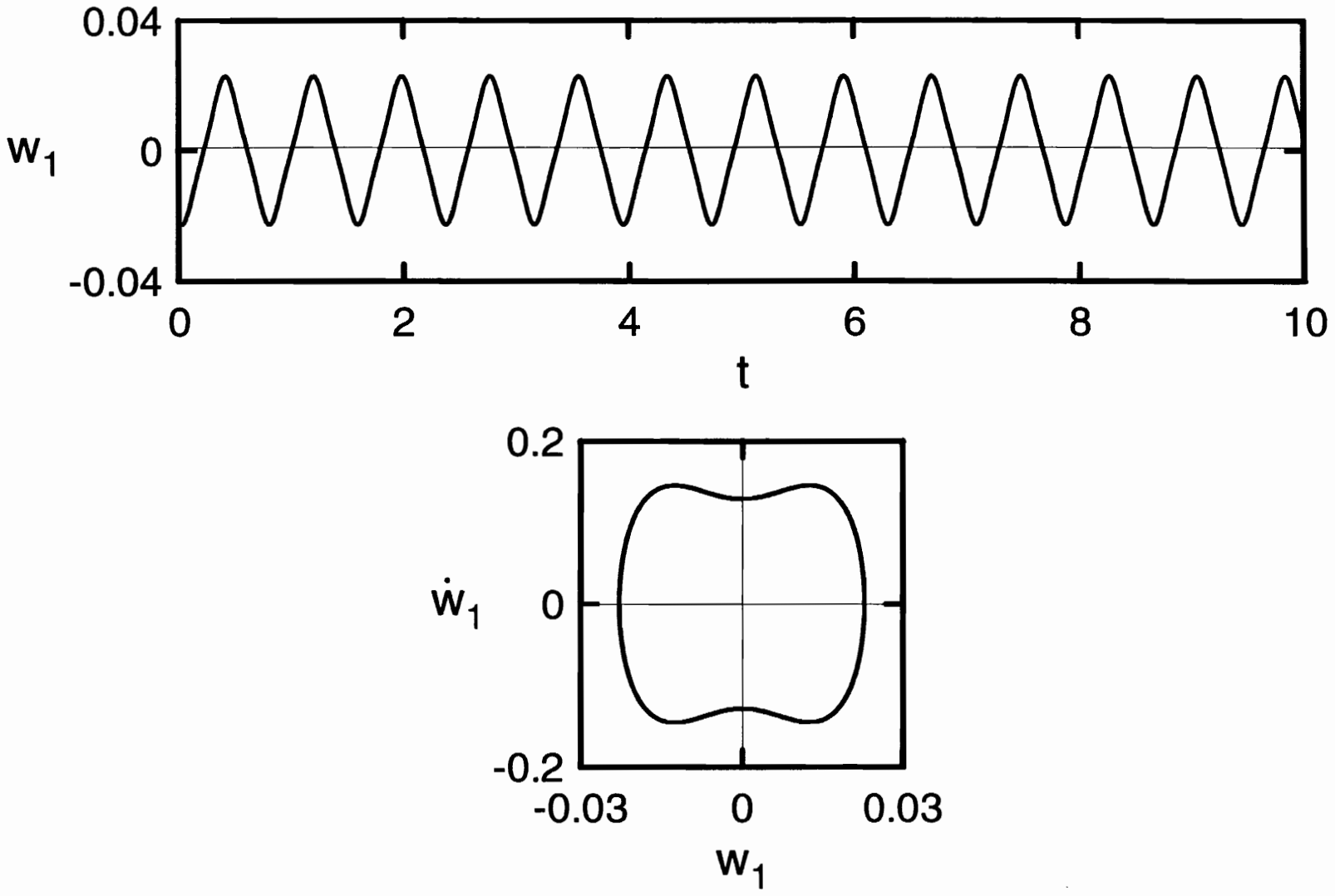

Figure 4.7: Time history and phase portrait of midspan displacement for $\phi = \pi/2$.

The damping coefficients are proportional to the coefficients of the linear displacement terms through the constant ϵ. Damping is similarly included in the equations of motion for the case where shear deformation and rotatory inertia are neglected.

The equations of motion are integrated with damping present for a period of time sufficient to produce a time history which is periodic to the eye. The damping coefficients in the equations of motion are then changed to linear functions of time which decay to zero. When a value of zero is reached by the damping coefficients, the integration is continued with damping coefficients which are exactly zero. If the damping coefficients are reduced at a sufficiently slow rate, the response of the undamped system appears to be periodic for any length of time.

Plots of the amplitudes of the generalized coordinates vs. excitation frequency show that the amplitude sometimes jumps suddenly to a lower value for a small increase in frequency. It was thought that this was due to multiple solutions existing for certain ranges of excitation frequency rather than a very steep slope of the frequency-amplitude curve. If two such curves overlap for a range of excitation frequency, the method just described will naturally yield points on the lower curve. This is due to the fact that the system is started from rest, and its amplitude gradually increases and stops when the desired excitation amplitude is reached. Therefore, it will always stop at the lowest amplitude of response for a given frequency of excitation.

In order to demonstrate the possibility of multiple solutions to the equations of motion for certain excitation frequencies, the equations of motion are integrated while subjected to an excitation function with a constant amplitude and a variable frequency function. The function used in this method is of the form

$$\overline{p}(x,t) = asin(\Omega(t)t + \phi) \tag{4.11}$$

This method is implemented by obtaining initial conditions from a selected time history. The function $\Omega(t)$ is defined such that it begins with the same value as the frequency for which the initial conditions were obtained and ends with the value for which a new time history is desired. At this point in the integration the excitation is changed to the form of Equation (4.1).

It was found that increasing the frequency of excitation linearly from one value to another did not yield satisfactory results. When the frequency function, $\Omega(t)$, reaches the desired value and the excitation function is changed to a function with constant frequency, the time history of the solution appears to be disturbed and loses its periodic appearance. This can be understood by considering the excitation function and its derivative. While the function itself has no discontinuities at any point, its derivative is discontinuous when the frequency changes from being linear in time to constant. The time derivative of $\overline{p}(x,t)$ is given by

$$\frac{\partial \overline{p}}{\partial t} = a\cos(\Omega(t)+\phi)\left[\frac{d\Omega}{dt}t+\Omega(t)\right] \tag{4.12}$$

Equation (4.6) can be substituted into Equation (4.12) when $\Omega(t)$ is equal to the desired value to give the difference in derivatives of the excitation functions. This difference is given by

$$\frac{\partial \overline{p}}{\partial t} - \frac{\partial p}{\partial t} = a\cos(\Omega t+\phi)\Delta\Omega \tag{4.13}$$

where $\Delta\Omega$ is the change in frequency. Since the difference is proportional to the change in frequency, for a given change in frequency the difference in the derivatives cannot be made arbitrarily small.

To make a smooth transition from a variable frequency to a constant frequency a frequency function is chosen such that its derivative is zero when it reaches the desired

value at the end of the time interval. This provides a function $\overline{p}(x,t)$ which has a value and first time derivative which match those of the function $p(x,t)$. The function chosen for this analysis has the form of a constant plus a quarter of a sine wave. This function is defined by the following expression:

$$\Omega(t) = \Omega_0 + \Delta\Omega sin\Big(\frac{\pi}{2\Delta t}(t - t_0)\Big) \tag{4.14}$$

where Ω_0 is the starting frequency, t_0 is the time when the frequency begins to change, and Δt is the time span over which the frequency is varied.

It is not possible to obtain a simple periodic response to a harmonic excitation with an arbitrary phase angle and initial conditions. However, by using a combination of the methods described in this chapter, it is possible to obtain time histories of the response which appear to be simple periodic functions when plotted.

Chapter 5

RESULTS

Computer simulations were run for a straight uniform elastic beam, with pinned ends fixed against axial motion, subjected to an excitation of the form of Equation (4.1). The simulations were run for the case where both shear strain and rotatory inertia are included in the Lagrangian and the case where both of these quantities are neglected. The methods described in the previous chapter were used to obtain time histories which do not appear to depend on the phase angle of the excitation function.

In order to observe the effects of including shear deformation and rotatory inertia in the Lagrangian, two beam configurations are considered. The two beams have different radii of gyration. It is expected that the effects of shear deformation and rotatory inertia will be smaller for the beam with the smaller radius of gyration.

The quantities required to define the properties of the beam are radius of gyration, r, shear correction factor, κ, and the ratio of shear modulus to Young's modulus, G/E. The functions which define the variation of area and radius of gyration over the length of the beam, $f_A(x)$ and $f_r(x)$ respectively, will be defined as unity for a uniform beam.

The shear correction factor depends on the shape of the cross section. A rectangle was selected as the shape, and a shear correction factor was obtained from Humar (1990). A ratio of shear modulus to Young's modulus was selected for an isotropic material with a Poisson's ratio of 0.3. Both of these quantities are listed below.

$$\kappa = \frac{5}{6}$$

$$\frac{G}{E} = \frac{1}{2.6}$$

The two radii of gyration selected are $r = 0.01$ and $r = 0.05$. For $r = 0.01$, the ratio of length, L, to height, H, of the beam is $L/H = 28.9$. This is a slender beam, and the radius of gyration was selected because it is expected that the effects of shear deformation and rotatory inertia will be very small for this case. For $r = 0.05$ the length to height ratio is $L/H = 5.8$. This is a very short thick beam, and this radius of gyration was selected because it is expected that the effects of shear deformation and rotatory inertia will be significant for this case.

The linear free vibration frequencies, ω, for both cases are obtained by neglecting the nonlinear terms in the equations of motion, assuming harmonic motion, and solving the resulting eigenvalue problem. Since the transverse displacement and axial displacement are coupled through nonlinear terms, the axial free vibration frequencies are independent of the transverse free vibration frequencies.

The first few linear natural frequencies computed for the shear deformable case and the non shear deformable case are listed below. All frequencies listed are nondimensional. The natural frequencies for transverse vibration are denoted by the superscript "t". The natural frequencies for axial vibration are denoted by the superscript "a".

Natural frequencies for a shear deformable beam

$r = 0.01$:

$$\omega_1^t = 9.85 \qquad \omega_1^a = 314$$
$$\omega_2^t = 39.2 \qquad \omega_2^a = 628$$
$$\omega_3^t = 87.3 \qquad \omega_3^a = 942$$

$r = 0.05$:

$$\omega_1^t = 9.41 \qquad \omega_1^a = 62.8$$
$$\omega_2^t = 33.5 \qquad \omega_2^a = 126$$
$$\omega_3^t = 65.6 \qquad \omega_3^a = 188$$

Natural frequencies for a non shear deformable beam

$r = 0.01$:

$$\omega_1^t = 9.87 \qquad \omega_1^a = 314$$
$$\omega_2^t = 39.5 \qquad \omega_2^a = 628$$
$$\omega_3^t = 88.8 \qquad \omega_3^a = 942$$

$r = 0.05$:

$$\omega_1^t = 9.87 \qquad \omega_1^a = 62.8$$
$$\omega_2^t = 39.5 \qquad \omega_2^a = 126$$
$$\omega_3^t = 88.8 \qquad \omega_3^a = 188$$

A comparison of the natural frequencies for transverse vibration indicates that there is a very small difference between the shear deformable case and the non shear deformable case for the first natural frequencies, even when the beam is very thick. However, the higher natural frequencies, in particular the third, show a much greater

difference between the two cases if the beam is thick. For the slender beam, the difference between the frequencies for the shear deformable beam the non shear deformable beam is still very small.

There is another difference between the slender and thick beams when the axial vibration modes are considered. In the case of the slender beam the first few linear axial frequencies are much higher than the first few transverse frequencies. But in the case of the thick beam the first axial frequencies are of the same order as the first transverse frequencies. This suggests that, for certain forms of excitation, axial inertia may have a significant effect on the response if the beam is very thick.

As suggested by Nayfeh and Mook (1979) the linear natural mode shapes are used as shape functions in the approximate displacement functions given by Equations (3.28) through (3.30). These shape functions are given by

$$U_n(x) = sin(n\pi x) \tag{5.1}$$

$$W_n(x) = sin(n\pi x) \tag{5.2}$$

$$\Theta_n(x) = cos(n\pi x) \tag{5.3}$$

These functions are linear mode shapes of the beam, and they satisfy the geometric boundary conditions of the problem. The geometric boundary conditions are that displacement be zero at the endpoints of the beam. For the case when shear deformation is not considered, only Equations (5.1) and (5.2) are used.

It was found that when the equations of motion are integrated for an excitation frequency near the first linear transverse frequency using these shape functions in the approximate displacement functions, the magnitude of the higher ranking generalized coordinates is very small compared to the first one. Therefore, only the first linear natural mode shapes, corresponding to a value of $n = 1$, are used to approximate the transverse

displacement and rotation of the beam for low excitation frequencies. The axial response was also found to be very small, but at least one term in the approximate function for the axial displacement must be included in order for the equations of motion to be complete. The second linear natural mode, corresponding to a value of $n = 2$, was used for this because it is the first symmetric mode shape in axial vibration. It was stated in the previous chapter that there is no coupling between symmetric and asymmetric modes when these shape functions are used, so no asymmetric shape functions are included.

Time histories of the generalized coordinates were produced using the methods described in the previous chapter for a range of excitation frequency ranging from $\Omega = 5$ to $\Omega = 25$. These were produced for several different excitation amplitudes for both the shear deformable and non shear deformable beams with two different cross sectional radii of gyration. The time increment in each case is 0.0005 with a tolerance for error control of 10^{-12} specified in parameter list of the IMSL numerical integrator, DIVPRK (1991). It was found that a much higher excitation amplitude was required for nonlinear effects to become obvious in the case of the thick beam than in the case of the slender one.

Phase portraits of the generalized coordinates were plotted and are illustrated in the figures of Appendix A. The maximum absolute value of the transverse generalized coordinates was found and plotted against excitation frequency for the range stated in the previous paragraph. Note that the maximum value of the generalized coordinate, $w_1(t)$, is the same as the maximum displacement of the beam for the approximation of the displacement functions considered here.

Figure 5.1 is a plot of the maximum absolute value of w_1 vs. excitation frequency, Ω, for a shear deformable beam with a radius of gyration $r = 0.01$. The excitation amplitude, a, is 0.0001. The data points are indicated by a dot and are connected by line segments. Two curves were plotted in order to demonstrate the multivalued nature of the

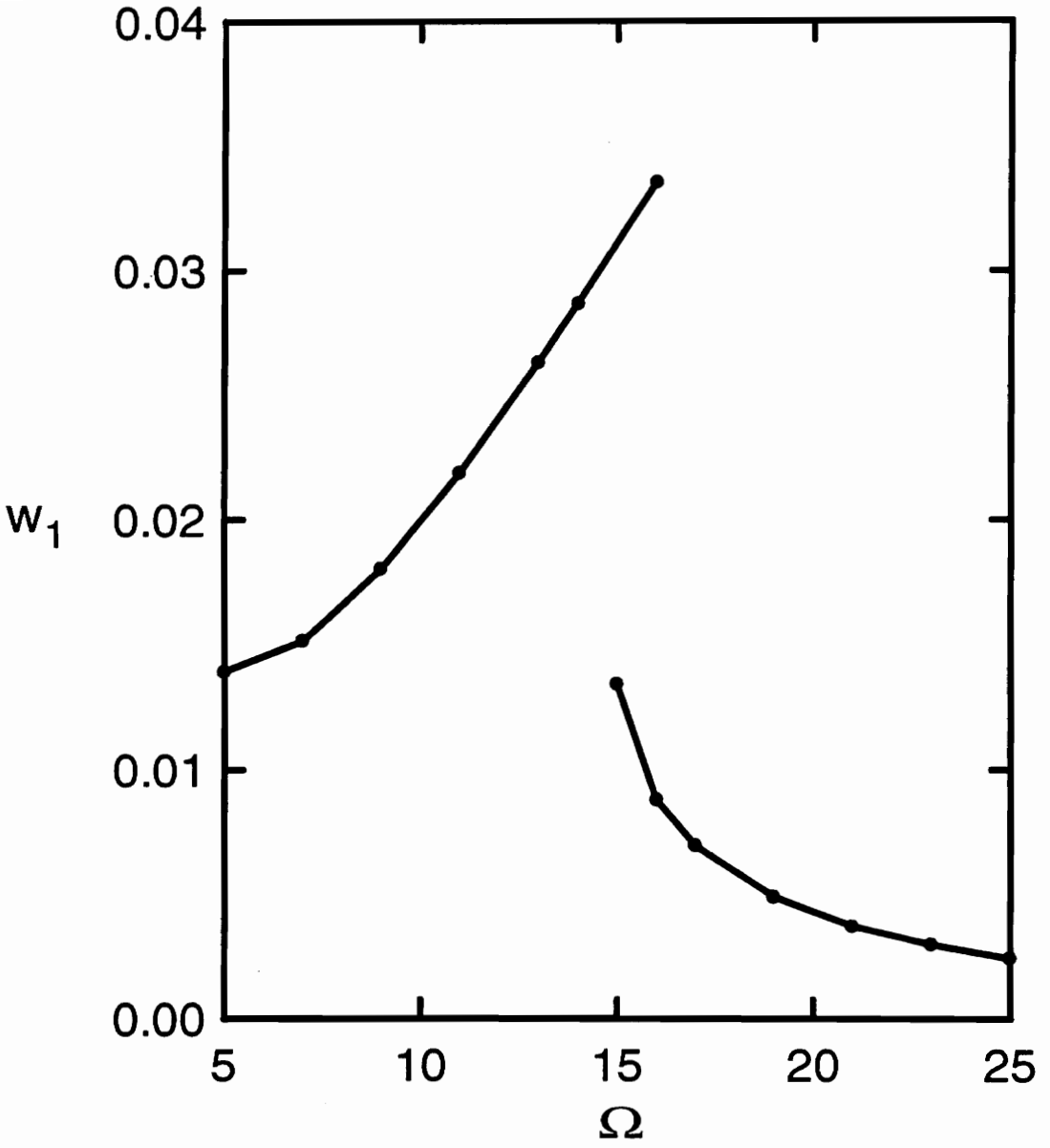

Figure 5.1: Maximum w_1 vs. frequency, Ω, for $a = 0.0001$.
(shear deformable beam, $r = 0.01$)

response. The points on the upper curve which overlap the lower curve were obtained by beginning at a point on the upper curve and increasing excitation frequency to a value higher than the lowest frequency of the lower curve.

The phase portraits associated with the data points of this plot are illustrated in Figures A.1 through A.8. This is not a complete set of phase portraits for this data set, but the points were selected to represent the general shapes that the phase portraits assume as frequency is varied. In most cases, a small change in frequency results only in a small change in size of the phase portraits, without a noticeable change in the shape of the phase portraits. An exception to this is when the generalized coordinate jumps from one curve to the other. Figures A.1 through A.4 correspond to the points on the upper curve, and Figures A.5 through A.8 correspond to points on the lower curve. Phase portraits of both the axial and transverse generalized coordinates are plotted in these figures.

Figure 5.2 is a plot of maximum absolute value of w_1 for the non shear deformable case with radius of gyration, $r = 0.01$, and excitation amplitude $a = 0.0001$. There is no noticeable difference between this and the plot for the shear deformable case. The phase portraits were very similar also, so they were not included in Appendix A.

Figure 5.3 is a plot of maximum absolute value of w_1 for a shear deformable beam with the same radius of gyration, but an excitation amplitude of 0.0003. The phase portraits associated with the data of this plot are illustrated in Figures A.9 through A.15. No points were plotted for an excitation frequency lower than $\Omega = 11$. For frequencies lower than this the maximum value of w_1 varies wildly with respect to frequency, and the phase portraits vary in shape substantially for small changes in frequency. Phase portraits associated with excitation frequencies of 5, 7, and 9 are plotted in Figures A.9, A.10, and A.11, respectively. Phase portraits associated with the upper curve of Figure 5.3 are plotted in Figures A.12 and A.13. These are for the data points at the ends of the curve.

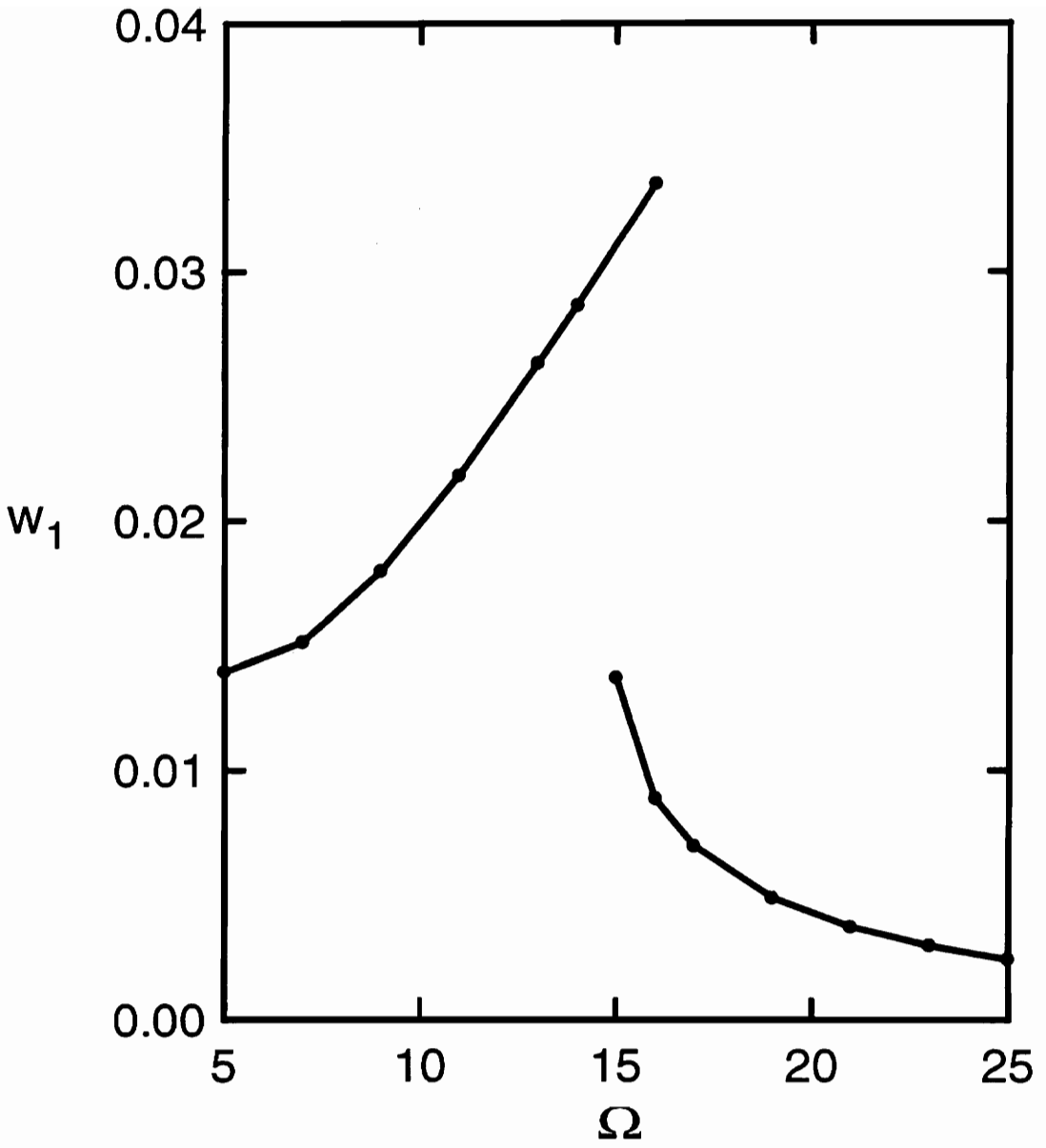

Figure 5.2: Maximum w_1 vs. frequency, Ω, for $a = 0.0001$.
(non shear deformable beam, $r = 0.01$)

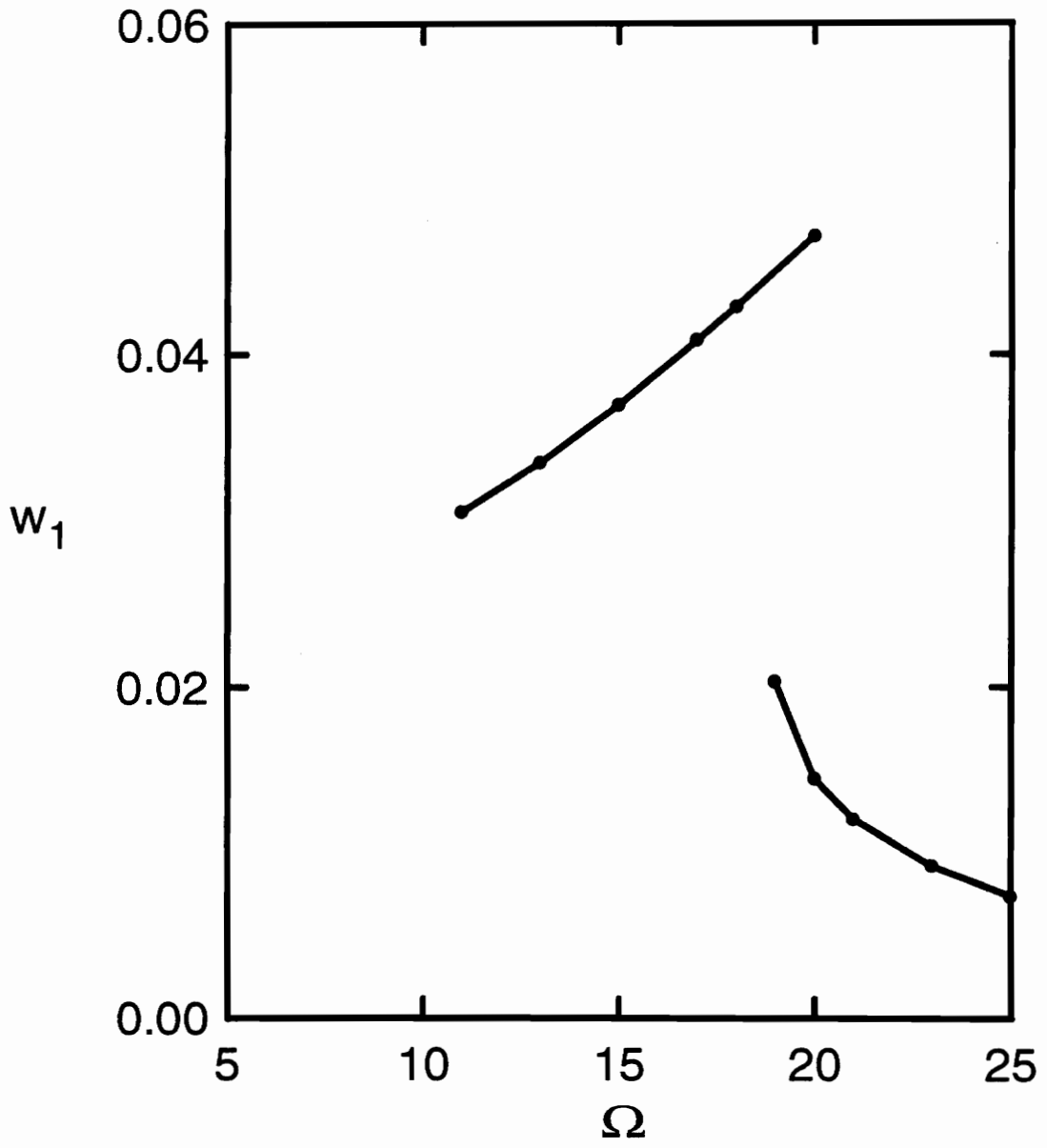

Figure 5.3: Maximum w_1 vs. frequency, Ω, for $a = 0.0003$.
(shear deformable beam, $r = 0.01$)

The phase portraits for the points between these differed primarily in size rather than shape. Phase portraits for the data points on the lower curve are plotted in Figures A.14 and A.15. Only plots associated with the endpoints of this curve are included, for the same reason.

Figure 5.4 is a plot of maximum w_1 for the non shear deformable case with the same radius of gyration and excitation amplitude as used in Figure 5.3. There is no noticeable difference between these plots. Also, there is no noticeable difference between the phase portraits associated with the data set, so these are not included in Appendix A.

Figures 5.5 and 5.6 are plots of maximum w_1 vs. frequency for a shear deformable beam and a non shear deformable beam, respectively, with radius of gyration of 0.01, as for the previous plots, but with an excitation amplitude of 0.0006. No points are plotted for excitation frequency of less than 13 because the nature of the response seemed to change drastically from one frequency to another. There is no noticeable difference between the curves in these two figures. Phase portraits for the shear deformable case are plotted in Figures A.16 through A.23. The phase portraits associated with excitation frequencies of $5, 7, 9,$ and 11 are plotted in Figures A.16 through A.19. Phase portraits for the data points on the upper curve are plotted in Figures A.20 and A.21. Phase portraits for the lower curve are plotted in Figures A.22 and A.23. The only excitation frequency for which there seemed to be a difference between the shear deformable case and the non shear deformable case is $\Omega = 5$. The phase portraits associated with this frequency for the non shear deformable case are plotted in Figure A.24.

Figure 5.7 is a plot of maximum w_1 vs. excitation frequency for the shear deformable beam with a radius of gyration of 0.05. The excitation amplitude is 0.01. Figures A.25 through A.30 are phase portraits for some of the data points of this plot. The first three pertain to the points on the upper curve. The last three are for points on

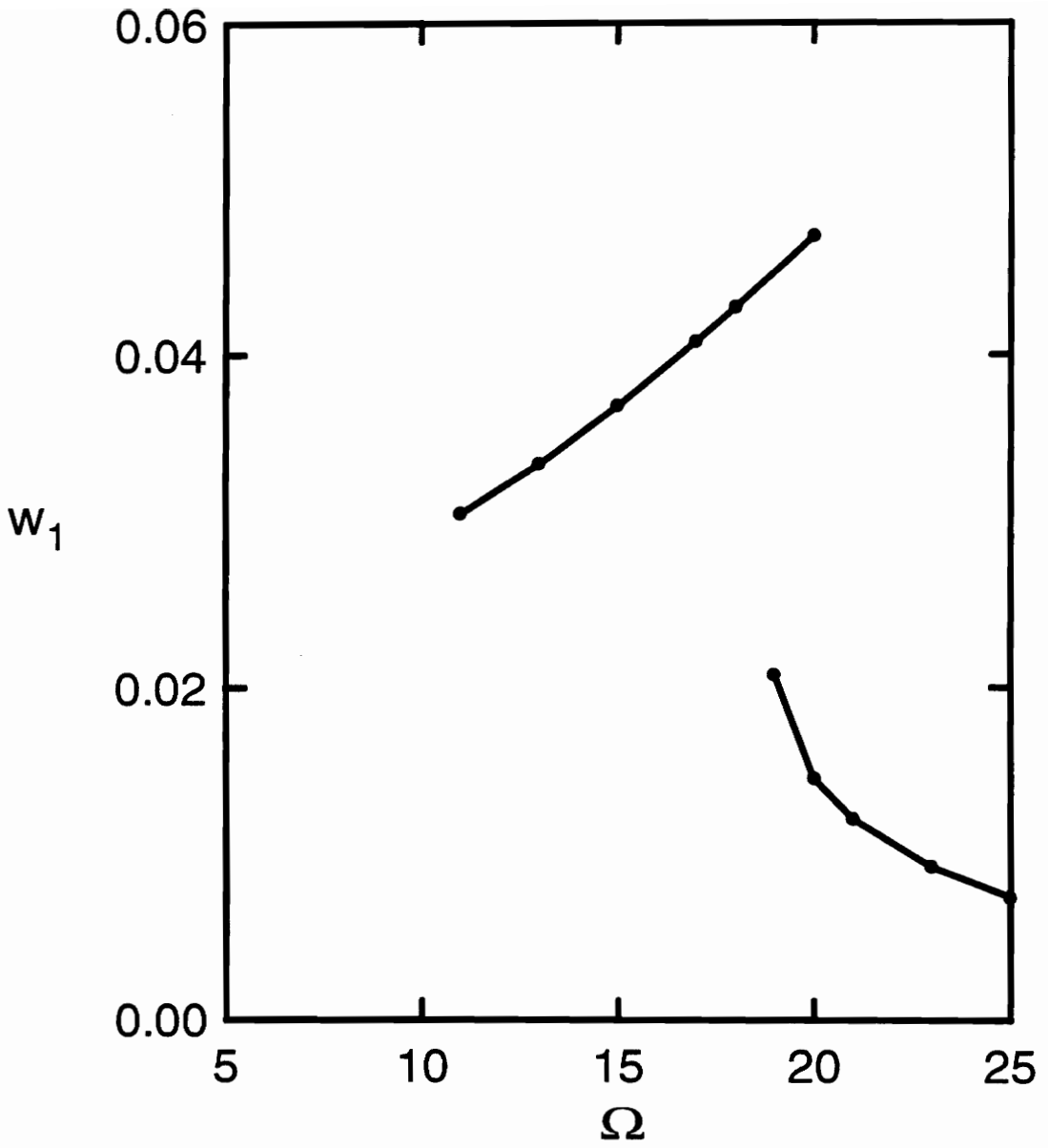

Figure 5.4: Maximum w_1 vs. frequency, Ω, for $a = 0.0003$.
(non shear deformable beam, $r = 0.01$)

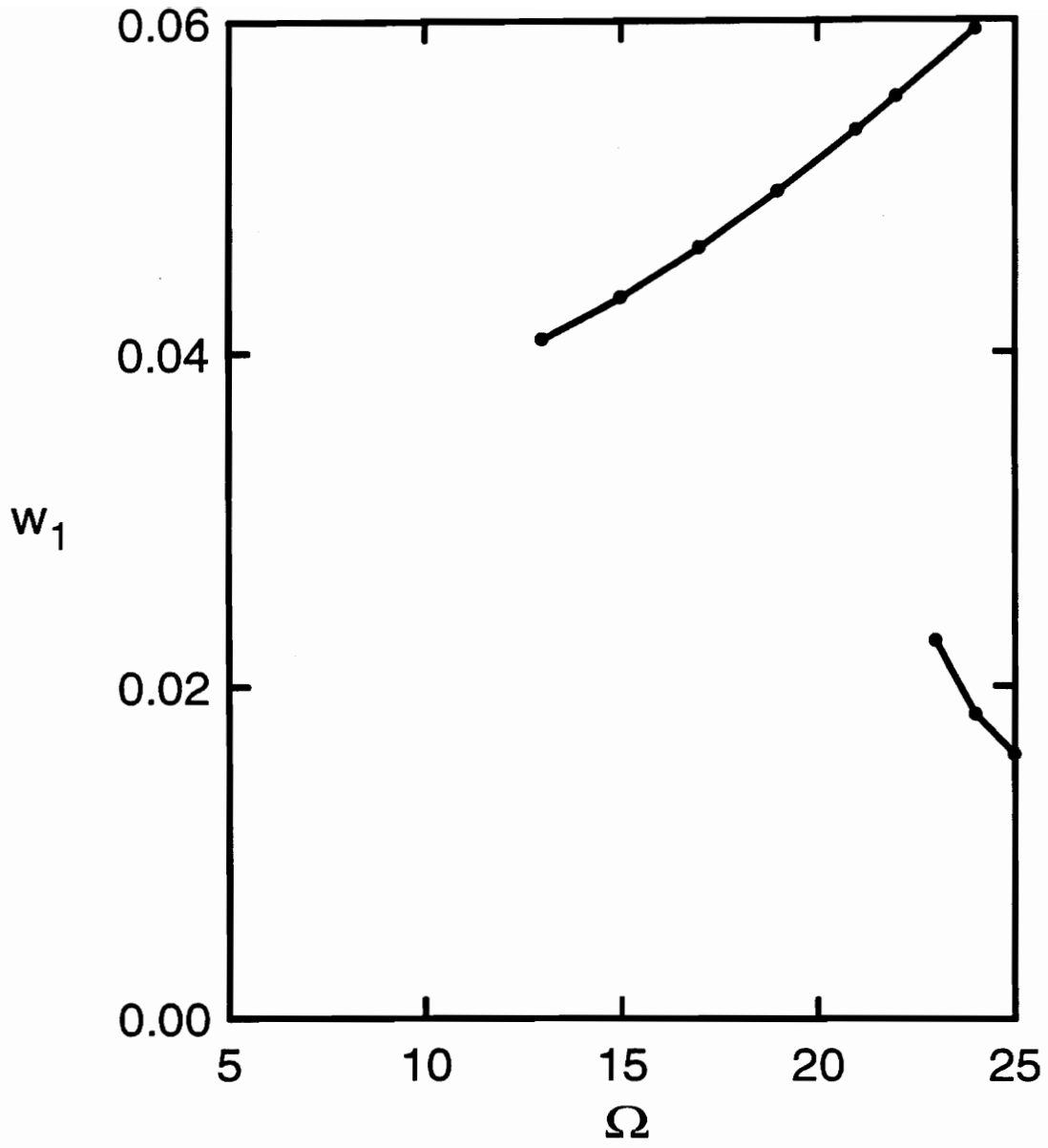

Figure 5.5: Maximum w_1 vs. frequency, Ω, for $a = 0.0006$.
(shear deformable beam, $r = 0.01$)

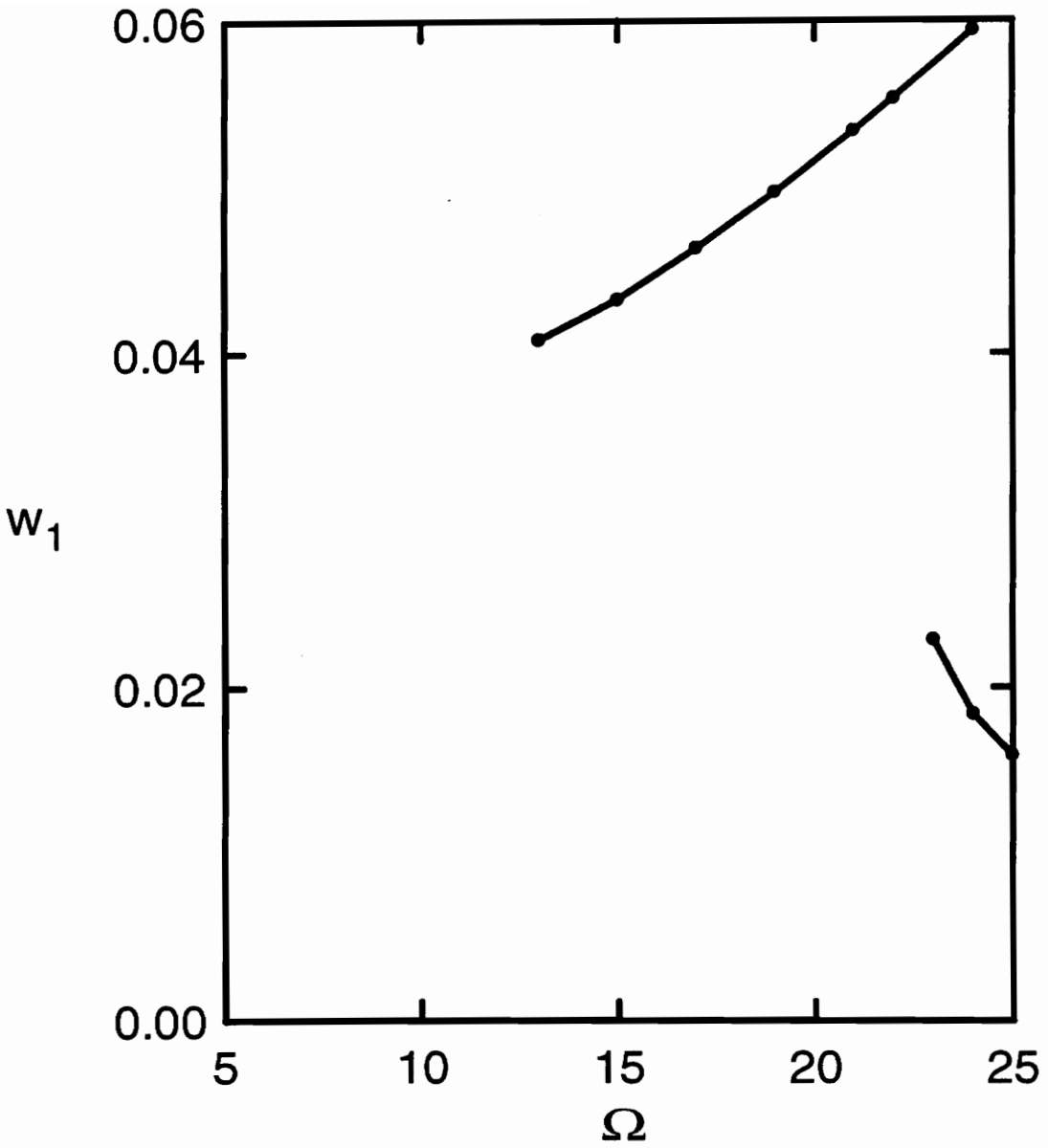

Figure 5.6: Maximum w_1 vs. frequency, Ω, for $a = 0.0006$.
(non shear deformable beam, $r = 0.01$)

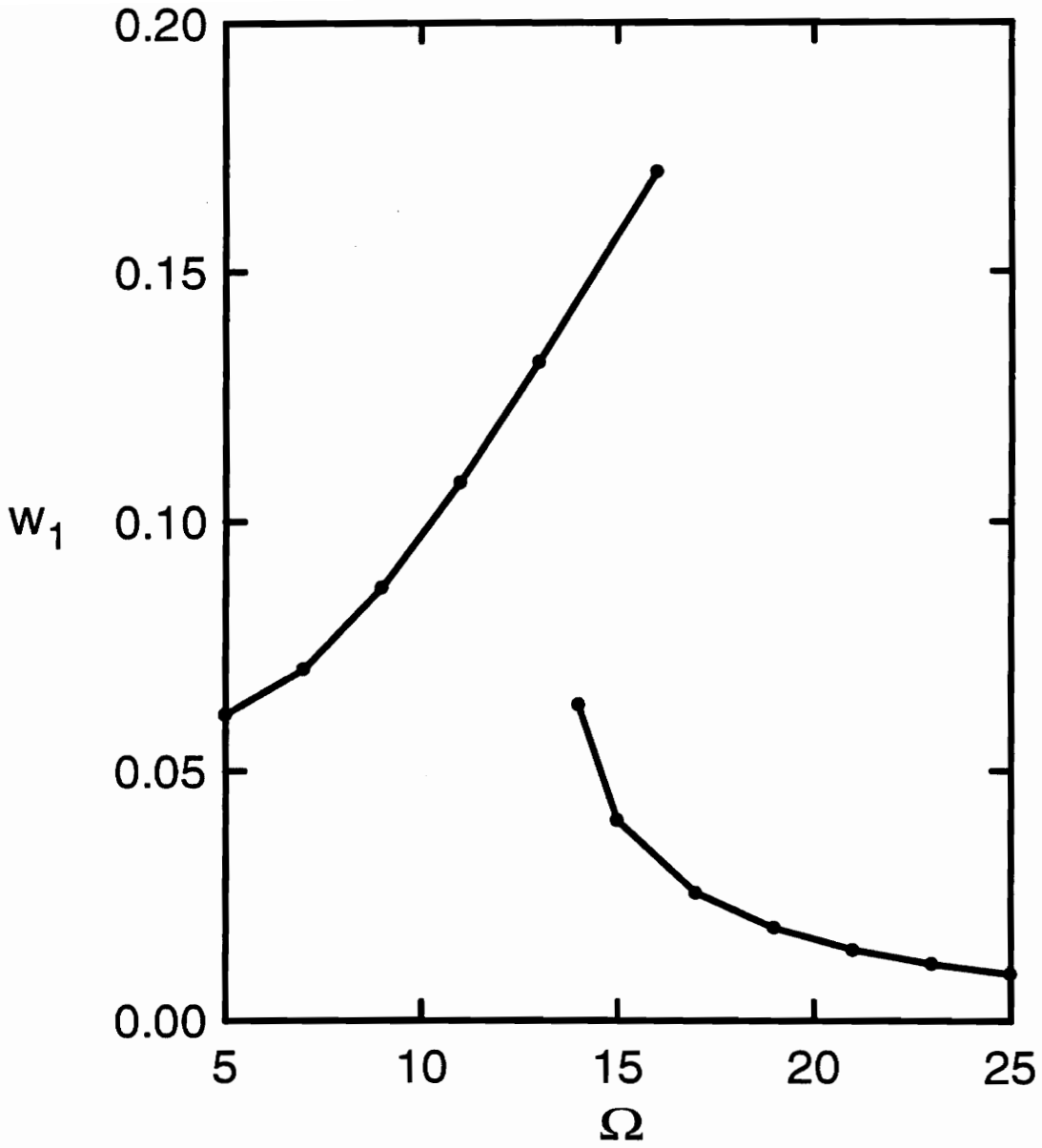

Figure 5.7: Maximum w_1 vs. frequency, Ω, for $a = 0.01$.
(shear deformable beam, $r = 0.05$)

the lower curve. Figure 5.8 is a plot of maximum w_1 for the non shear deformable case with the same radius of gyration and excitation amplitude. Phase portraits for the points in this graph are plotted in Figures A.31 through A.36. Figures A.31 through A.33 are associated with the upper plot. The remainder are associated with the lower curve.

Figure 5.9 is a plot of maximum w_1 for both the shear deformable and the non shear deformable beams. Data points for the shear deformable case are connected by solid lines, and data points for the non shear deformable beam are connected by dashed lines. The only differences between the two cases apparent from the plots of maximum w_1 are that the shear deformable case has a slightly larger maximum deflection for all frequencies on the upper curve and a slightly smaller maximum deflection on the lower curve. The phase portraits do not differ much from one case to the other except for their small difference in size.

Figures 5.10 and 5.11 are plots of maximum w_1 vs. excitation frequency for the shear deformable case and the non shear deformable case, respectively, with a radius of gyration of 0.05 and an excitation amplitude of 0.03. No points were plotted for excitation frequencies below $\Omega = 7$ because the path of the data points changed sharply below this frequency. Figures A.37 through A.43 are phase portraits for some of the cases plotted in Figure 5.10. Figures A.44 through A.50 are phase portraits for some of the points in the non shear deformable case. The phase portraits for the shear deformable case do not appear different from those of the non shear deformable case, aside from the slight differences in size.

Figure 5.12 is a plot of the data for both beams with radius of gyration of 0.05 and excitation amplitude of 0.03. Points for the shear deformable case are plotted with a solid line, and points for the non shear deformable case are plotted with a dashed line. The shear deformable case can be seen to have a larger maximum deflection for solutions

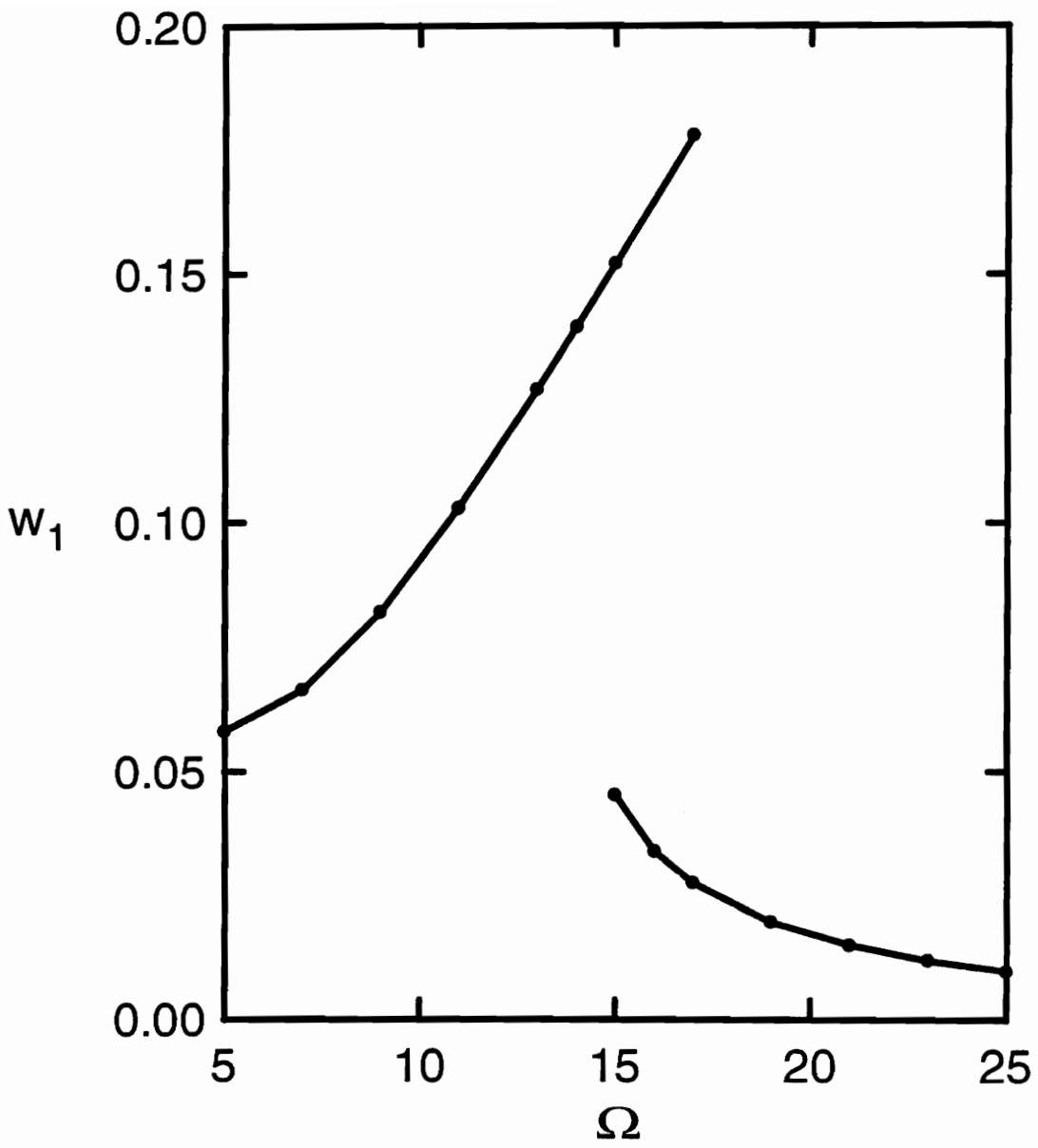

Figure 5.8: Maximum w_1 vs. frequency, Ω, for $a = 0.01$.
(non shear deformable beam, $r = 0.05$)

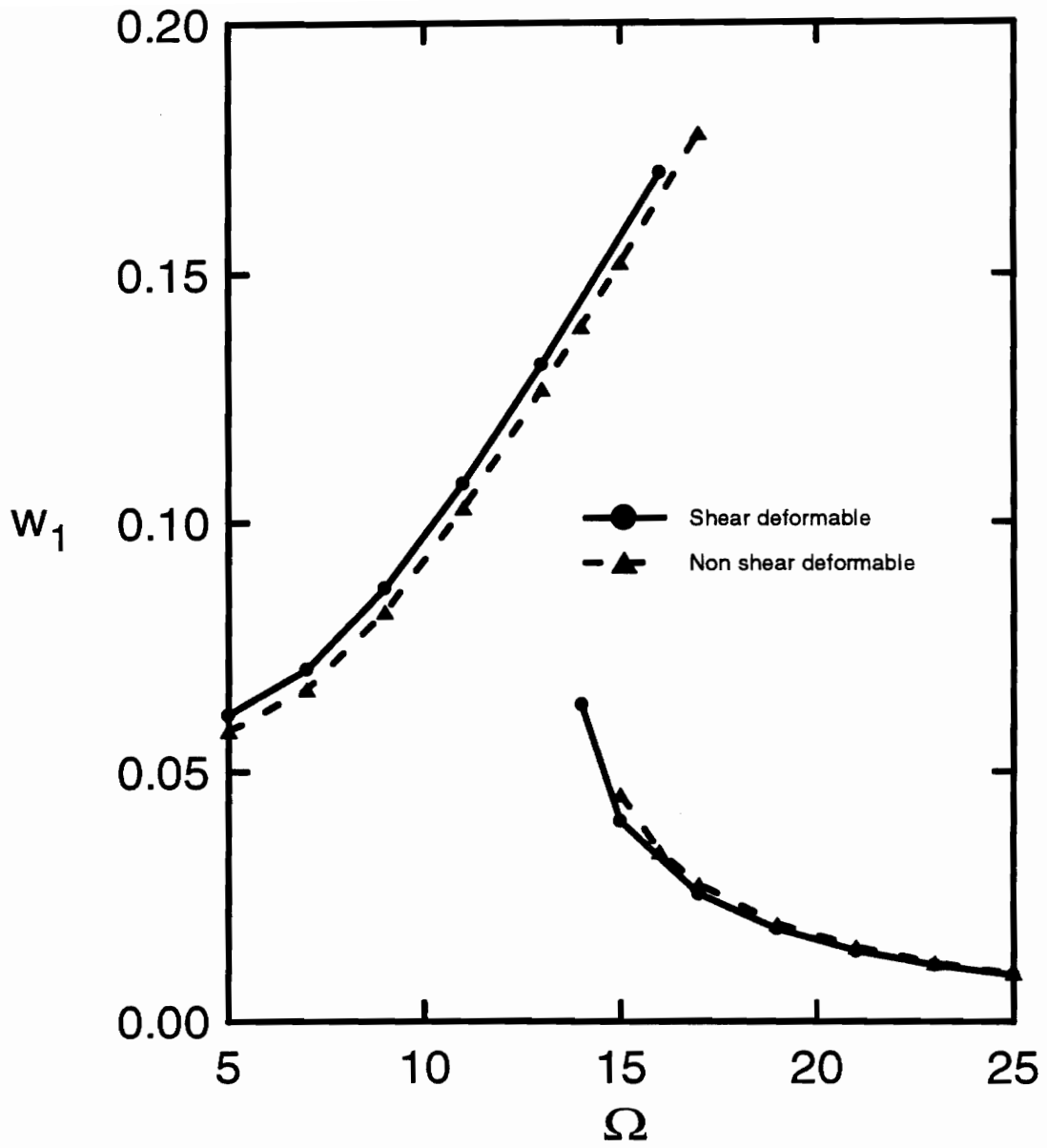

Figure 5.9: Maximum w_1 vs. frequency, Ω, for $a = 0.01$, $r = 0.05$.

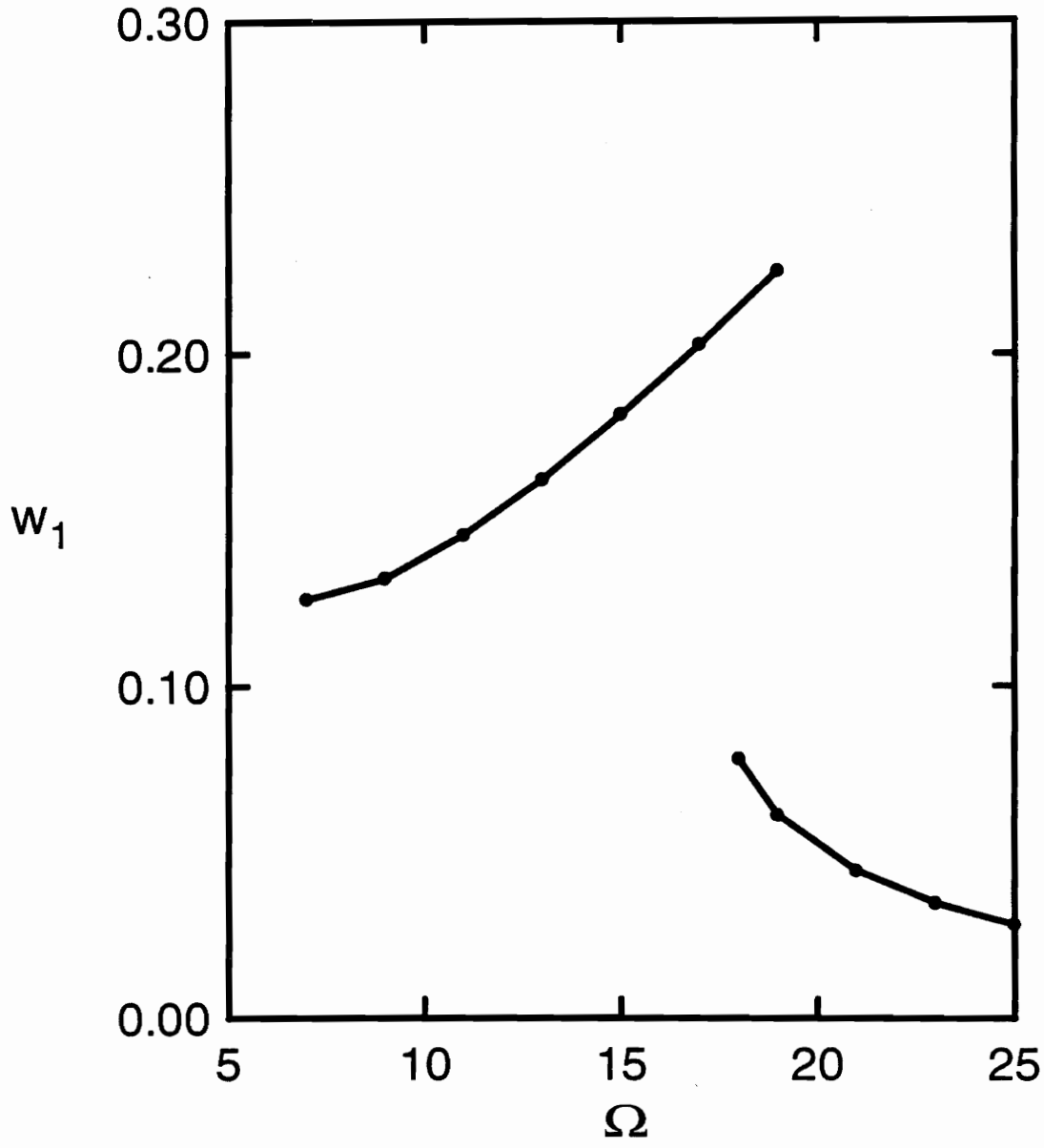

Figure 5.10: Maximum w_1 vs. frequency, Ω, for $a = 0.03$.
(shear deformable beam, $r = 0.05$)

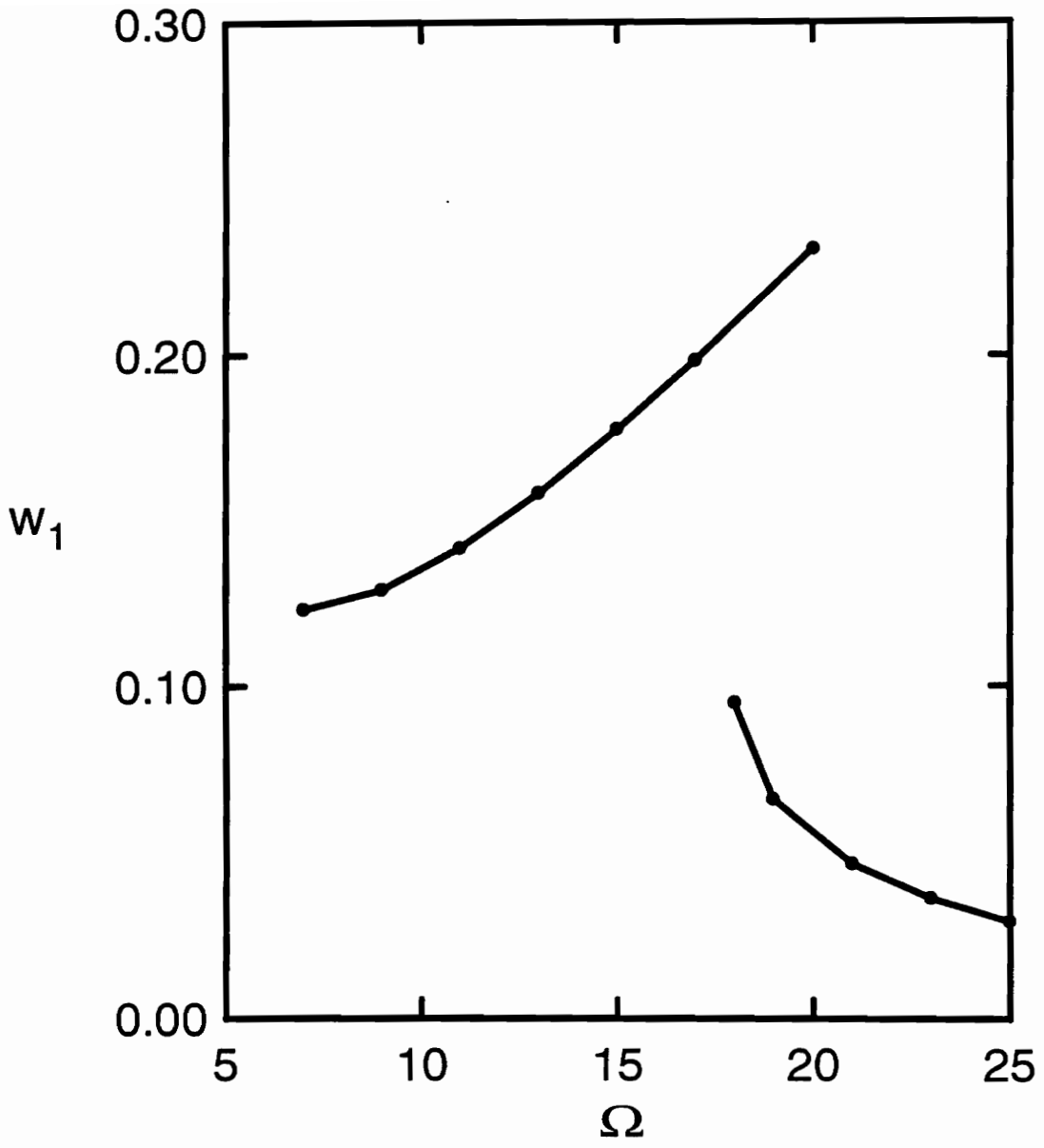

Figure 5.11: Maximum w_1 vs. frequency, Ω, for $a = 0.03$.
(non shear deformable beam, $r = 0.05$)

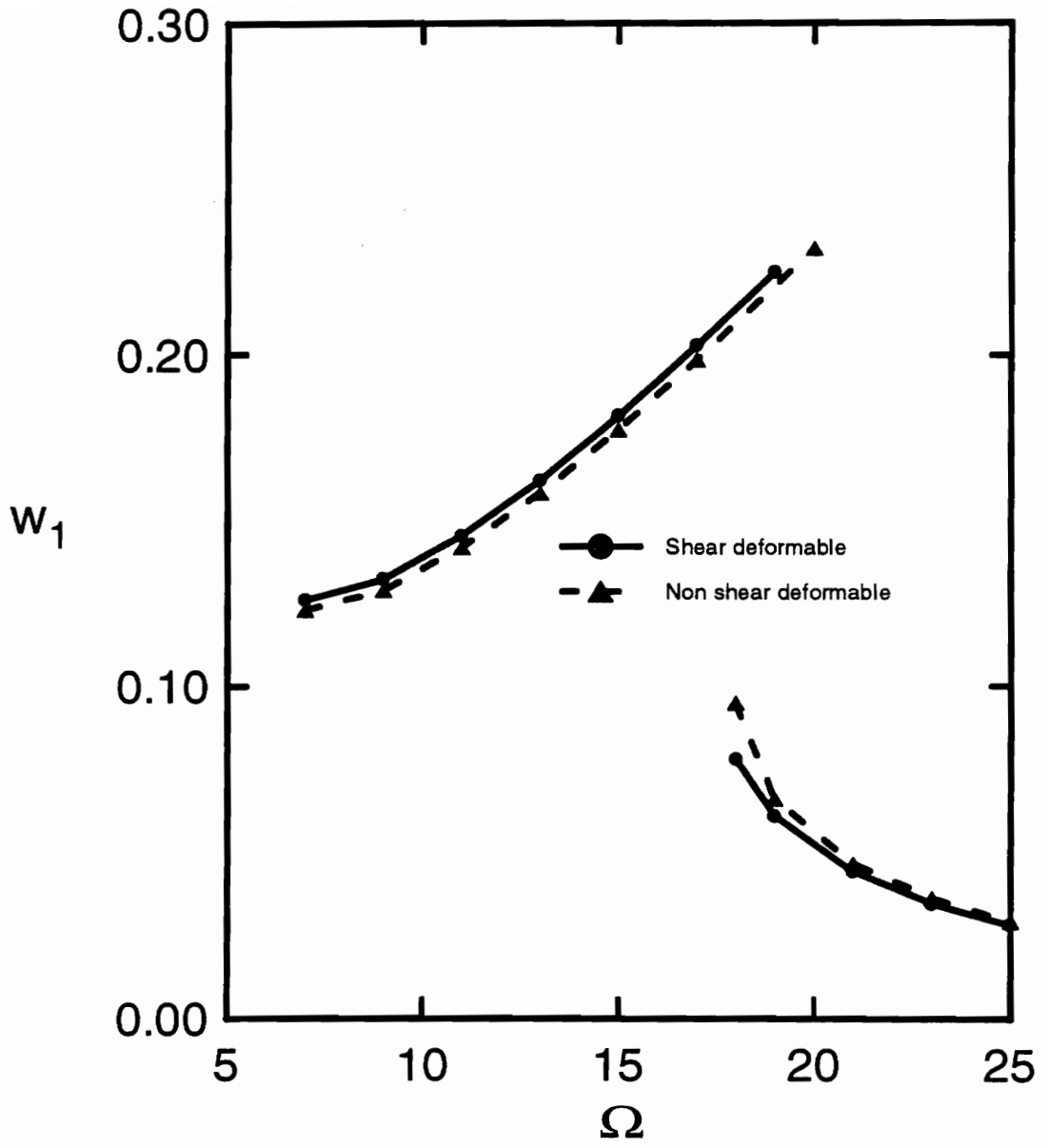

Figure 5.12: Maximum w_1 vs. frequency, Ω, for $a = 0.03$, $r = 0.05$.

associated with the upper curve and a smaller maximum deflection for solutions associated with the lower curve.

Figures 5.13 and 5.14 are plots of maximum w_1 for the shear deformable beam and the non shear deformable beam, respectively. The radius of gyration is 0.05 and the excitation amplitude is 0.06 in both cases. No points were plotted for excitation frequencies lower than $\Omega = 11$. Figures A.51 through A.57 are plots of phase portraits for the shear deformable case. Figures A.58 through A.66 are phase portraits for the non shear deformable case. The most significant differences between the two cases appear in the phase portraits for the points which were not plotted in Figures 5.13 and 5.14. The phase portraits for the shear deformable and the non shear deformable cases are similar for an excitation frequency of 5, which can be seen by comparing Figure A.51 to A.58. However, for frequencies of 7 and 9 the solutions appear very dissimilar. This can be seen by comparing Figures A.52 and A.53 to Figures A.59 and A.60.

Maximum w_1 vs. excitation frequency for both the shear deformable and non shear deformable beam are plotted in Figure 5.15. The shear deformable solution yields larger maximum deflections for points on the upper curve and smaller maximum deflections for points on the lower curve.

It was found that for excitation frequencies closer to the third linear natural frequency, the third generalized coordinate associated with transverse displacement and rotation becomes significant. Higher order terms in the axial displacement function, however, are still very small.

Time histories of the generalized coordinates were produced for excitation frequencies ranging from $\Omega = 60$ to $\Omega = 120$. This range of frequencies includes the third linear natural frequency of both the shear deformable beam and the non shear deformable beam with a radius of gyration of either $r = 0.01$ or $r = 0.05$. The approximate

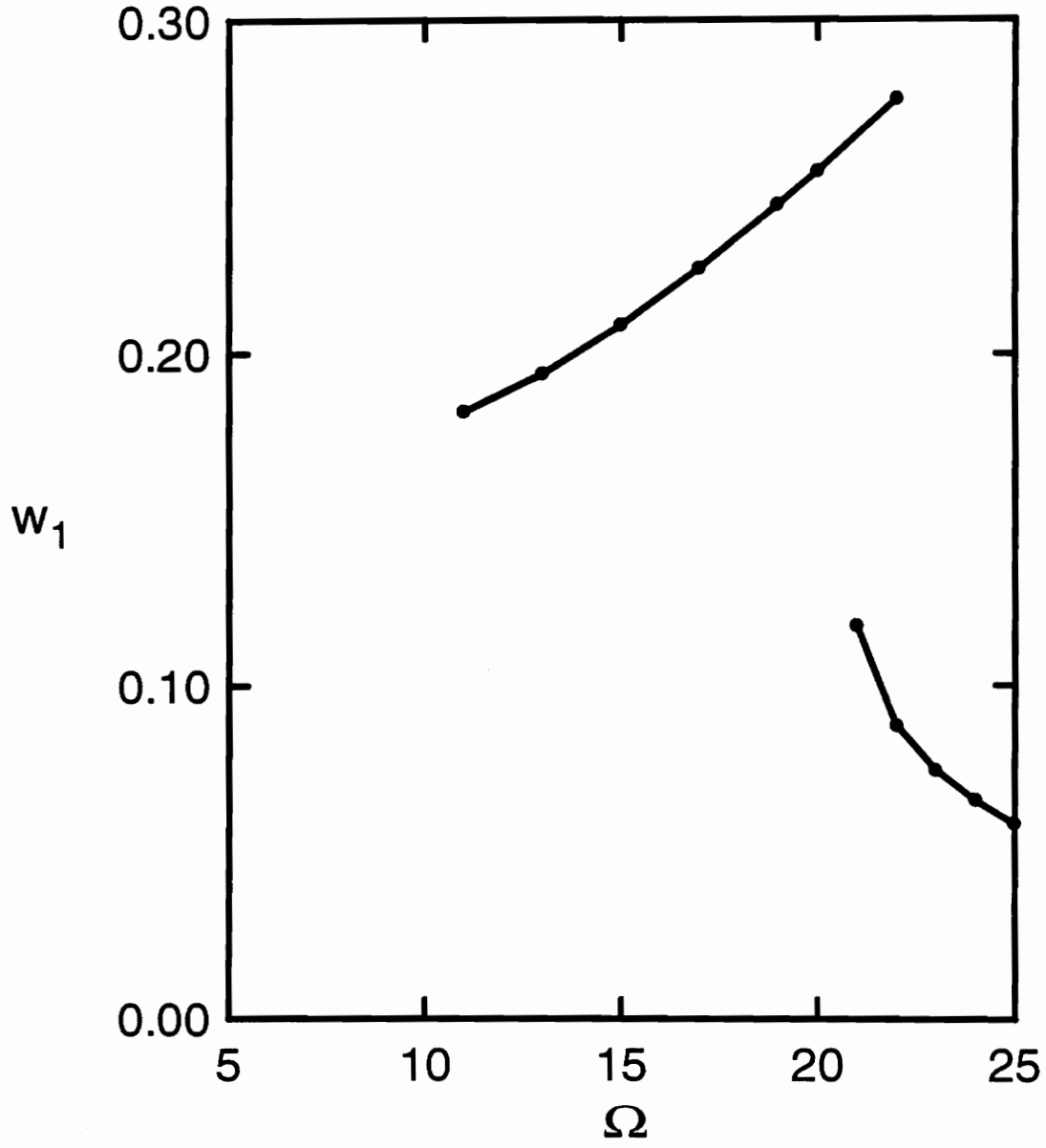

Figure 5.13: Maximum w_1 vs. frequency, Ω, for $a = 0.06$.
(shear deformable beam, $r = 0.05$)

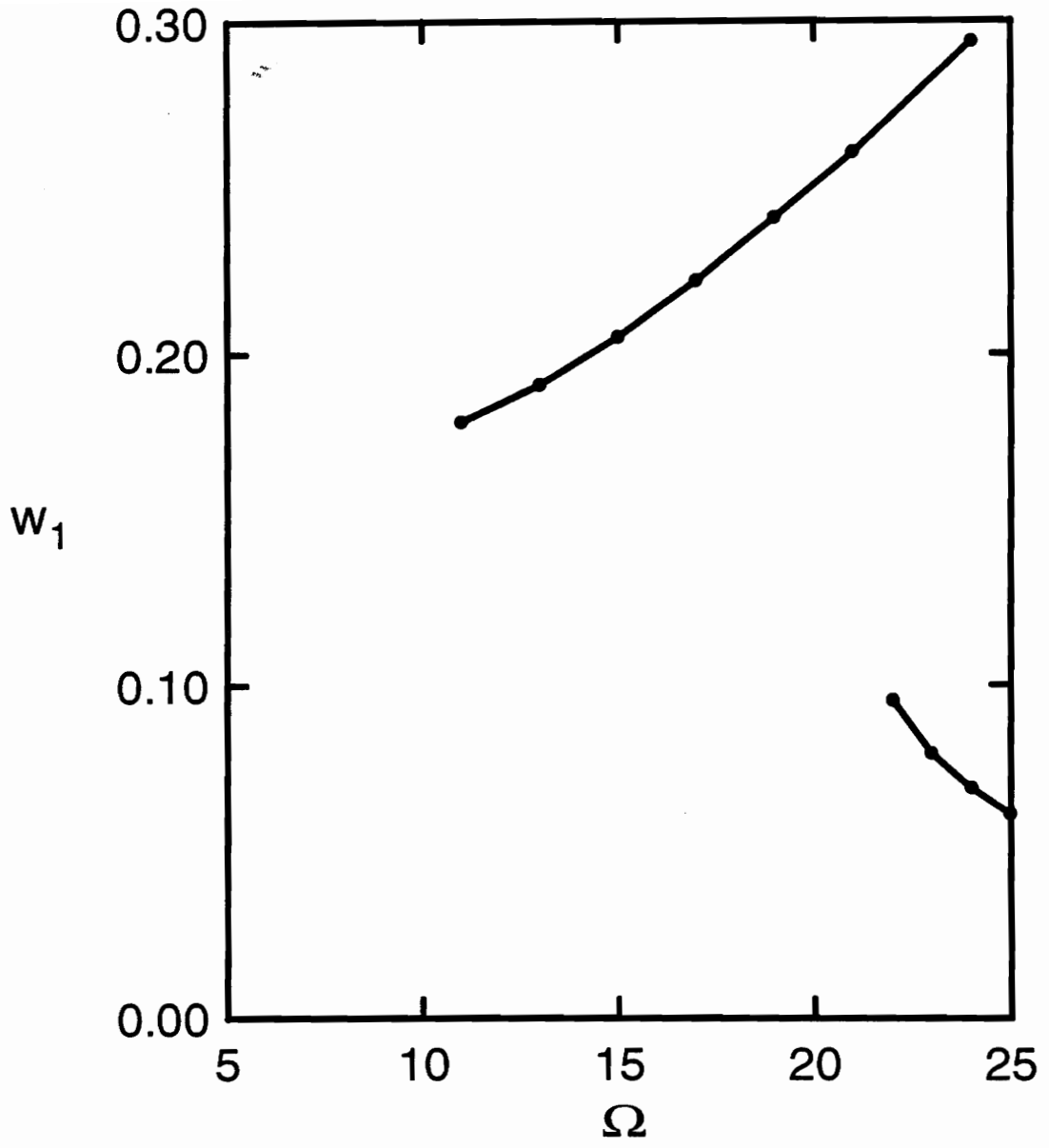

Figure 5.14: Maximum w_1 vs. frequency, Ω, for $a = 0.06$.
(non shear deformable beam, $r = 0.05$)

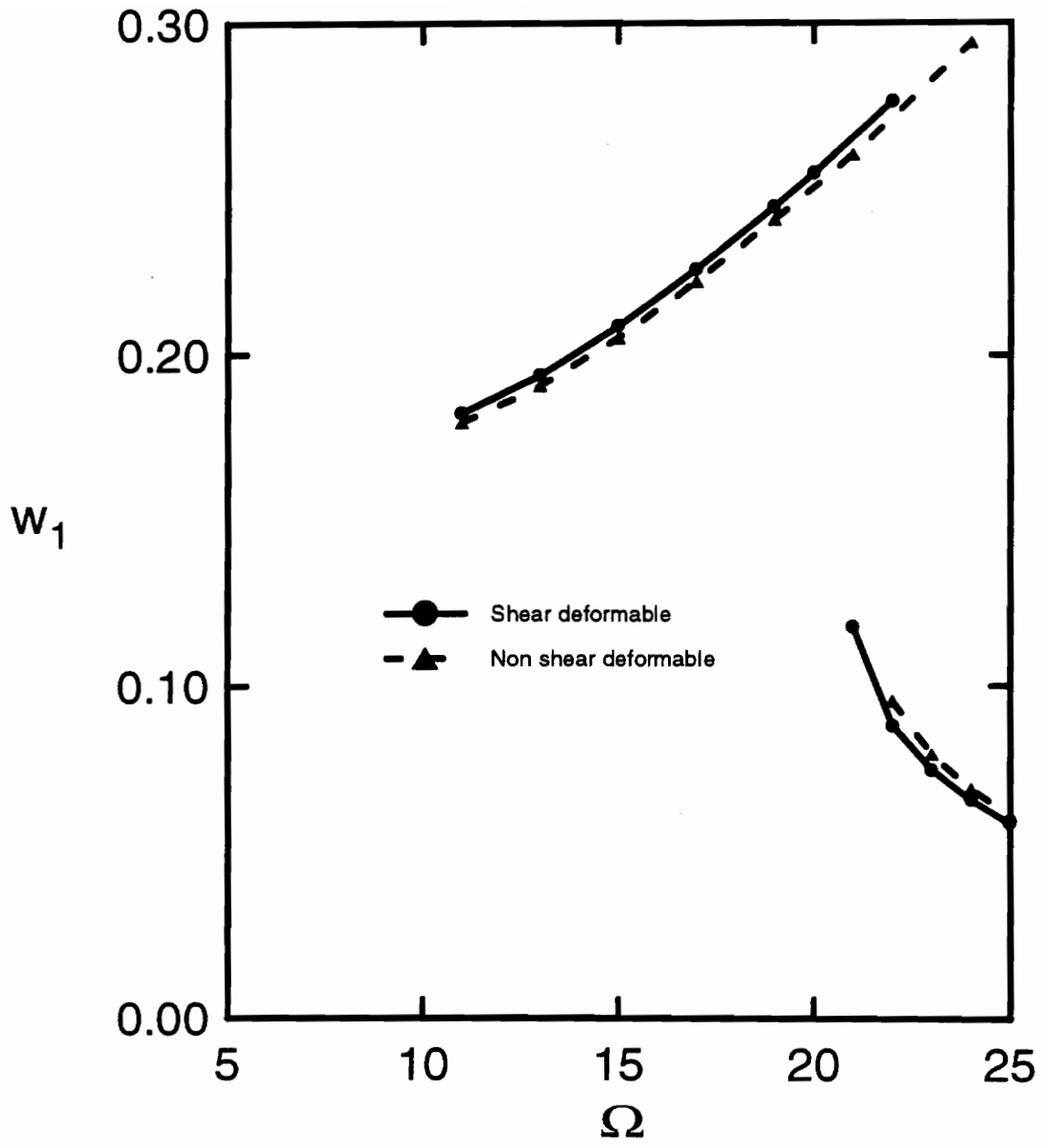

Figure 5.15: Maximum w_1 vs. frequency, Ω, for $a = 0.06$, $r = 0.05$.

displacement functions (3.28) through (3.30) included the terms associated with $n = 1$ and $n = 3$ for transverse displacement and rotation, and the term associated with $n = 2$ was used to approximate axial displacement. The time increment in each case is 0.0001 with a tolerance for error control of 10^{-12} specified in the parameter list of the IMSL numerical integrator, DIVPRK (1991).

The displacement of the midspan, denoted by w_c, is used to compare the displacement of the beam subjected to different frequencies and amplitudes of excitation. While this quantity is not necessarily representative of the deformed beam, and it is not even necessarily the maximum displacement of all points on the beam, it is computationally inexpensive to calculate. The quantity w_c is simply the difference between the first and third generalized coordinates.

$$w_c(t) = w_1(t) - w_3(t)$$

Figures 5.16, 5.17, and 5.18 are plots of maximum w_1, w_3, and w_c, respectively, for a shear deformable beam with a radius of gyration of 0.01 subjected to an excitation with an amplitude of 0.005. The generalized coordinates have multiple values beginning with an excitation frequency of 109. The first coordinate, w_1, has two curves which are very close together where they begin to overlap. The third coordinate, w_3, has a much larger difference from one curve to the other. The displacement of the midspan of the beam, w_c, also has a very substantial difference between the upper curve and the lower curve where they begin to overlap. Phase portraits for some of the points on these graphs are plotted in Figures A.67 through A.81. Figures A.67 through A.78 pertain to the points on the upper curves, and the remainder pertain to points on the lower curves.

Figures 5.19 through 5.21 are plots of maximum w_1, w_3, and w_c for a non shear deformable beam with the same cross sectional geometry subjected to the same excitation

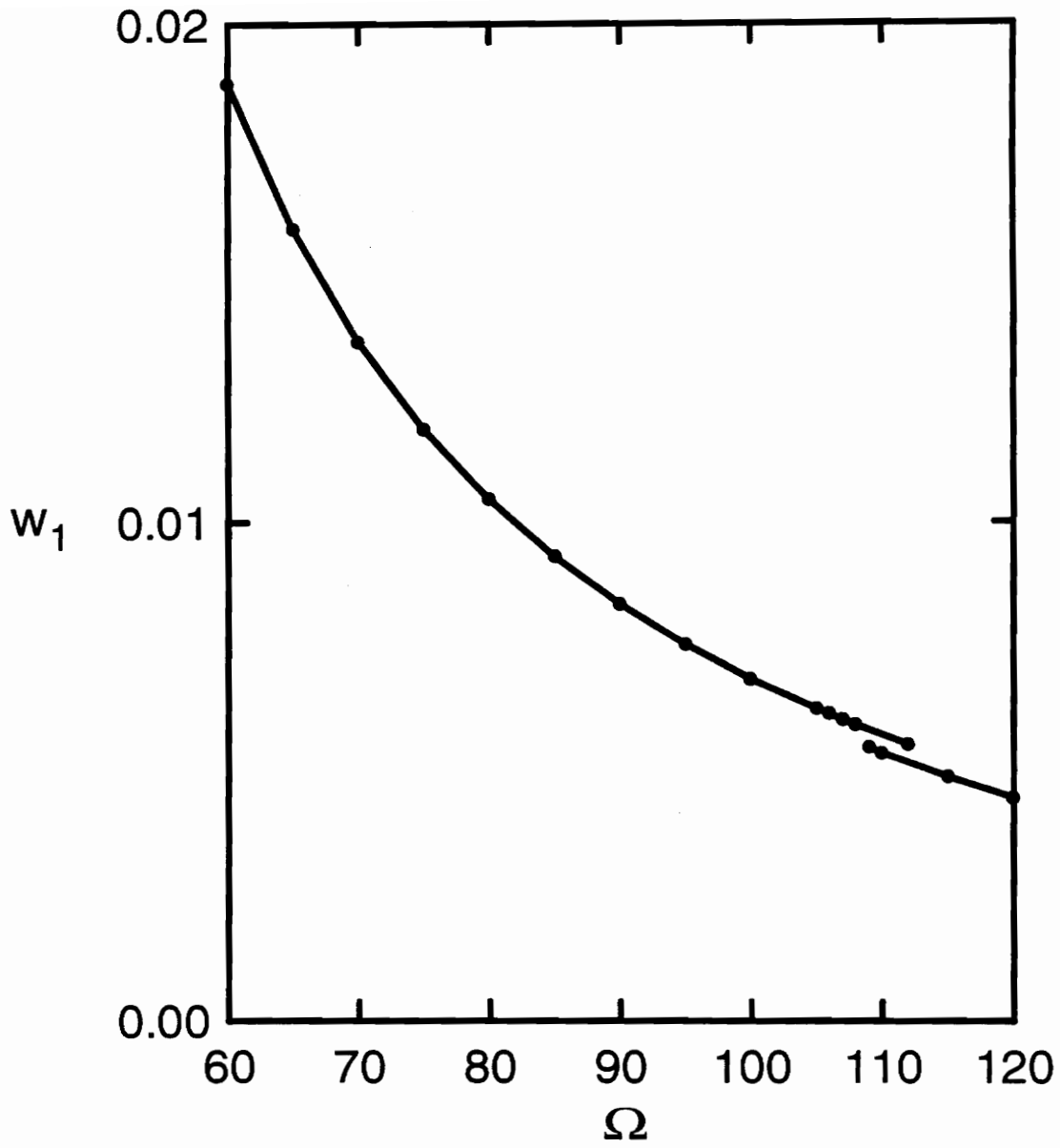

Figure 5.16: Maximum w_1 vs. frequency, Ω, for $a = 0.005$.
(shear deformable beam, $r = 0.01$)

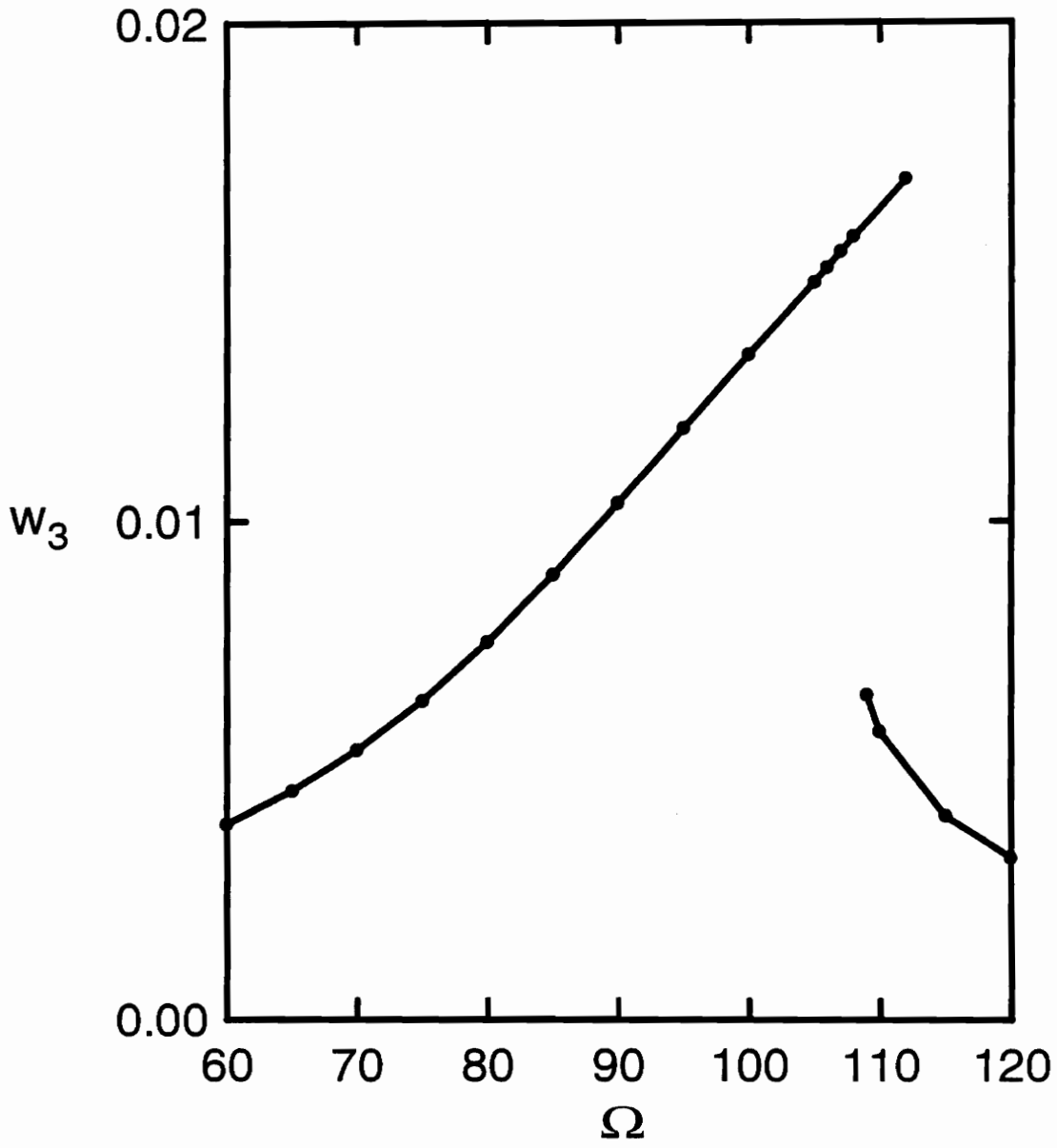

Figure 5.17: Maximum w_3 vs. frequency, Ω, for $a = 0.005$.
(shear deformable beam, $r = 0.01$)

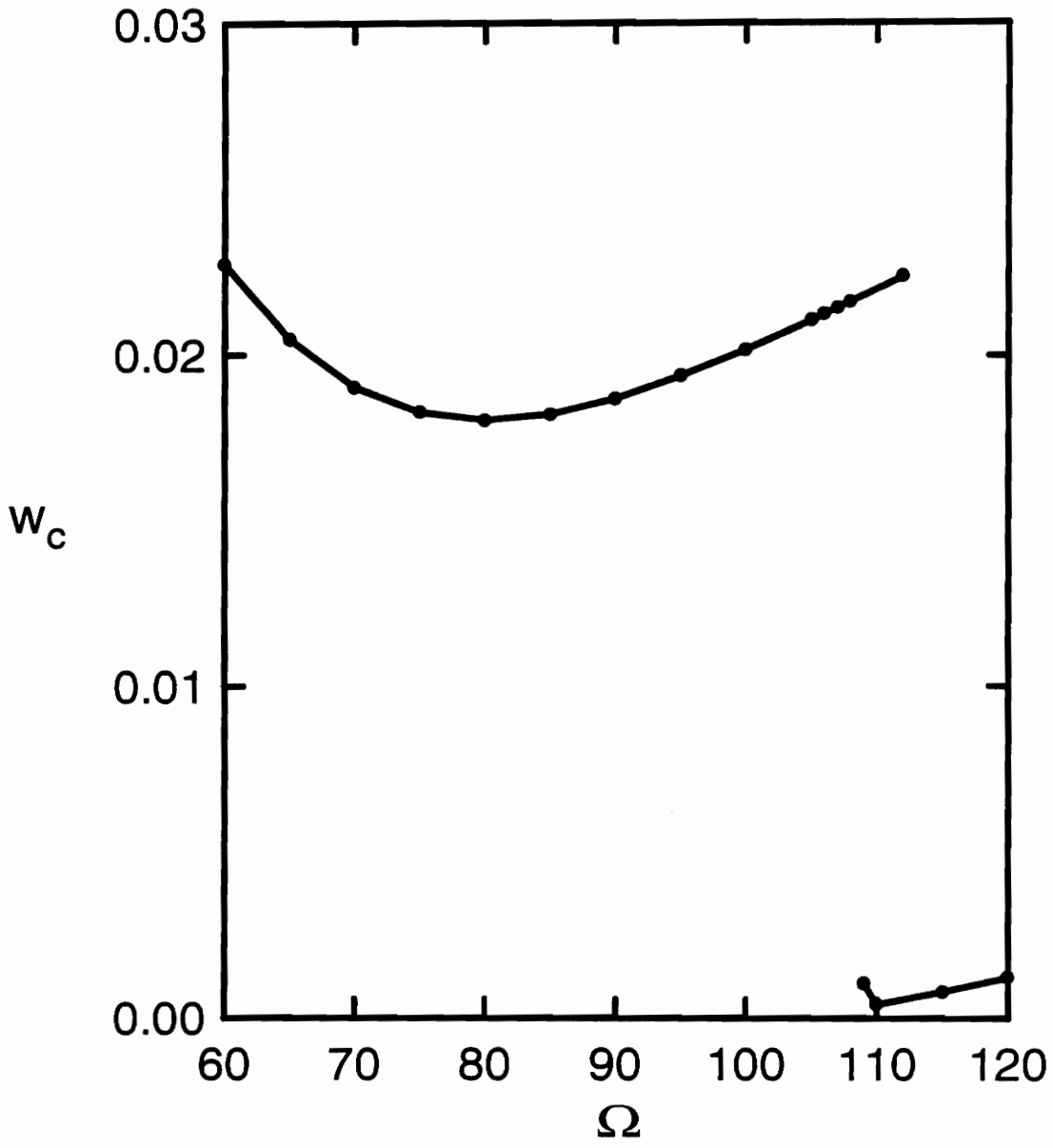

Figure 5.18: Maximum w_c vs. frequency, Ω, for $a = 0.005$.
(shear deformable beam, $r = 0.01$)

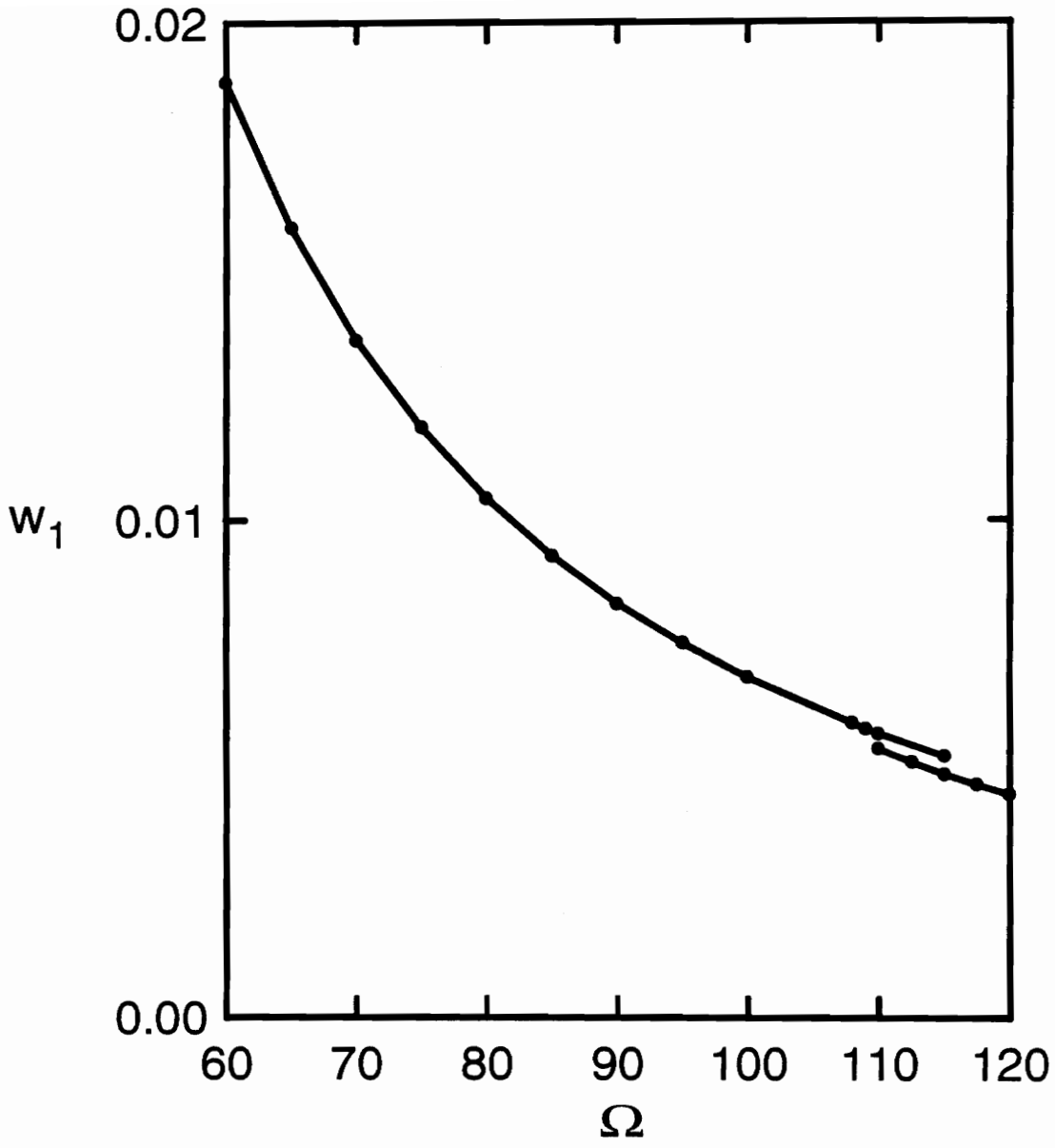

Figure 5.19: Maximum w_1 vs. frequency, Ω, for $a = 0.005$.
(non shear deformable beam, $r = 0.01$)

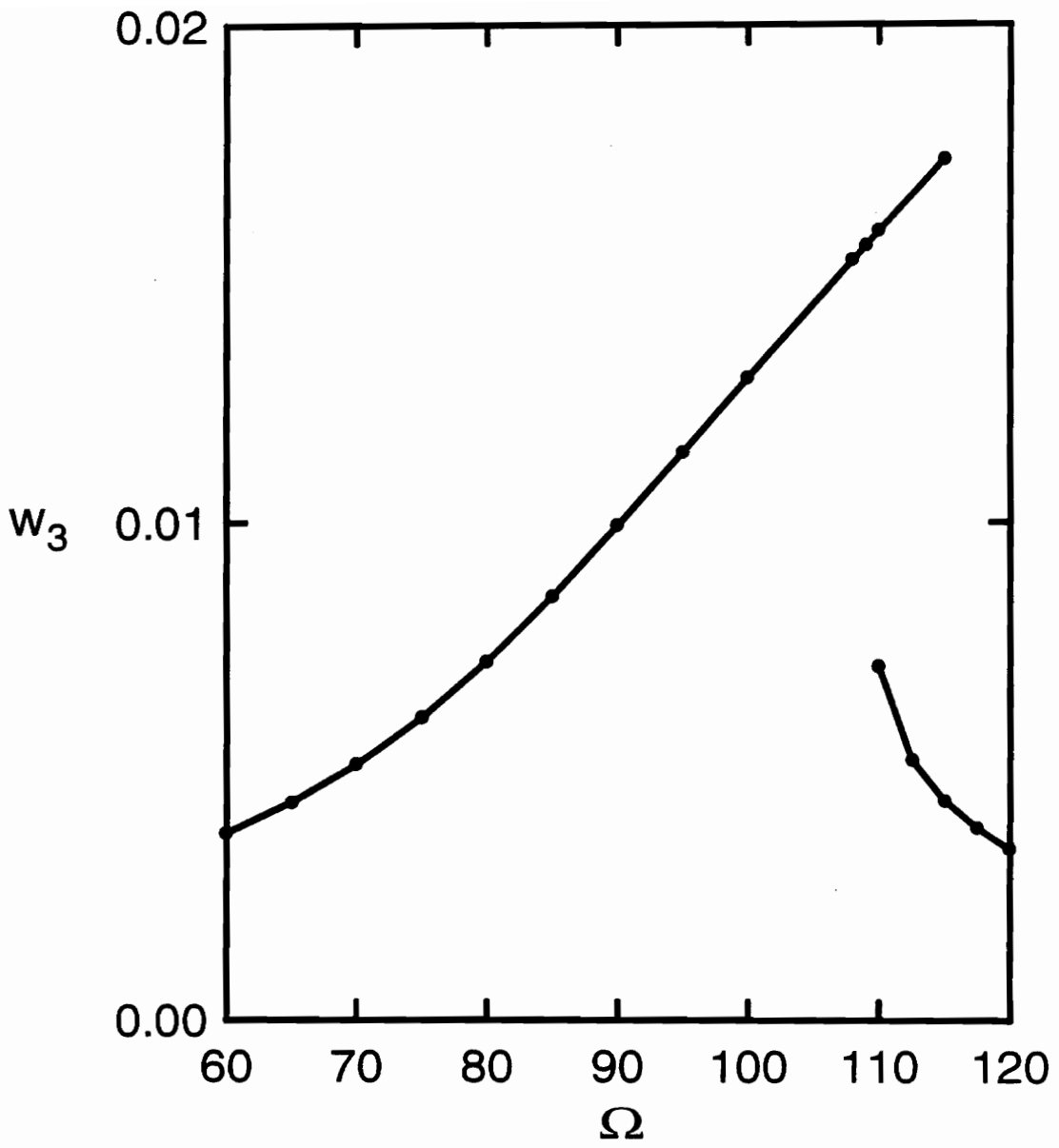

Figure 5.20: Maximum w_3 vs. frequency, Ω, for $a = 0.005$.
(non shear deformable beam, $r = 0.01$)

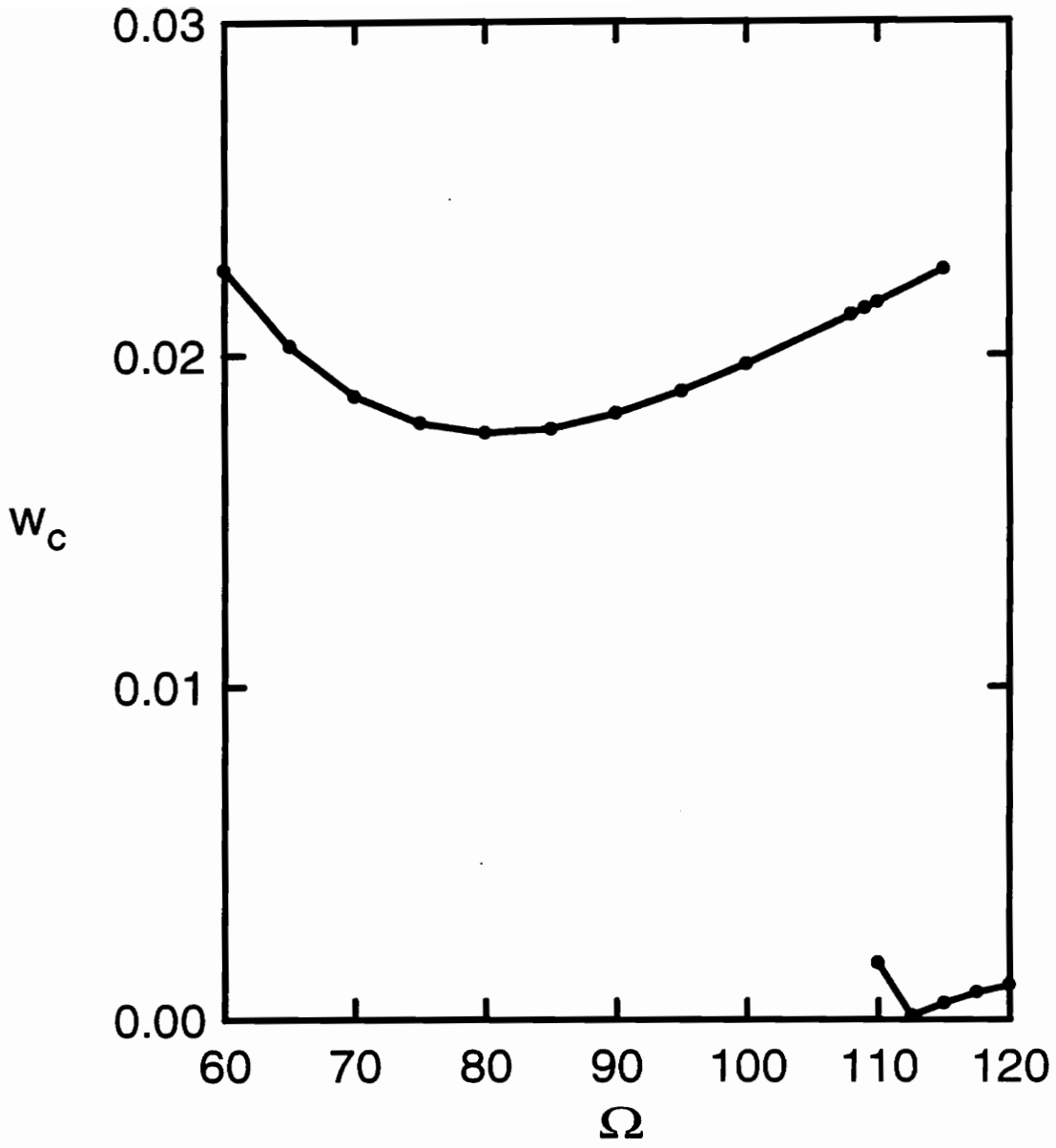

Figure 5.21: Maximum w_c vs. frequency, Ω, for $a = 0.005$.
(non shear deformable beam, $r = 0.01$)

function. The phase portraits for the non shear deformable case are very similar to those of the shear deformable case and have not been included in the appendix.

There is no noticeable difference between the plots of the first generalized coordinate for the two cases. But for the third generalized coordinate the upper curve is slightly higher for the shear deformable case, and the lower curve is slightly higher for the non shear deformable case. Figure 5.22 is maximum w_3 for both cases plotted together. The solid curve is for the shear deformable case, and the dashed curve is for the non shear deformable case. The maximum midspan displacement for both cases is plotted in Figure 5.23.

Figures 5.24, 5.25, and 5.26 are plots of maximum w_1, w_3, and w_c for the shear deformable beam with a radius of gyration of 0.01 subjected to an excitation function with an amplitude of 0.01. No points were plotted for excitation frequencies of less than 70 because the methods employed did not yield a simple periodic response for an excitation frequency of 65. Only one curve is plotted in each of these figures, but two points are plotted for an excitation frequency of 120, indicating that the response has multiple solutions here, and that a second curve possibly begins at that point. Phase portraits of the generalized coordinates and midspan displacement for the points which are not included in the data set are plotted in Figures A.82 and A.83. Phase portraits for the points which are plotted in Figures 5.24 through 5.26 are plotted in Figures A.84 through A.95.

Maximum values of w_1, w_3, and w_c for the non shear deformable beam with the same radius of gyration and excitation amplitude are plotted in Figures 5.27, 5.28, and 5.29. The phase portraits are very similar to those for the non shear deformable case, so they have not been included. However, only one solution was obtained for an excitation frequency of 120.

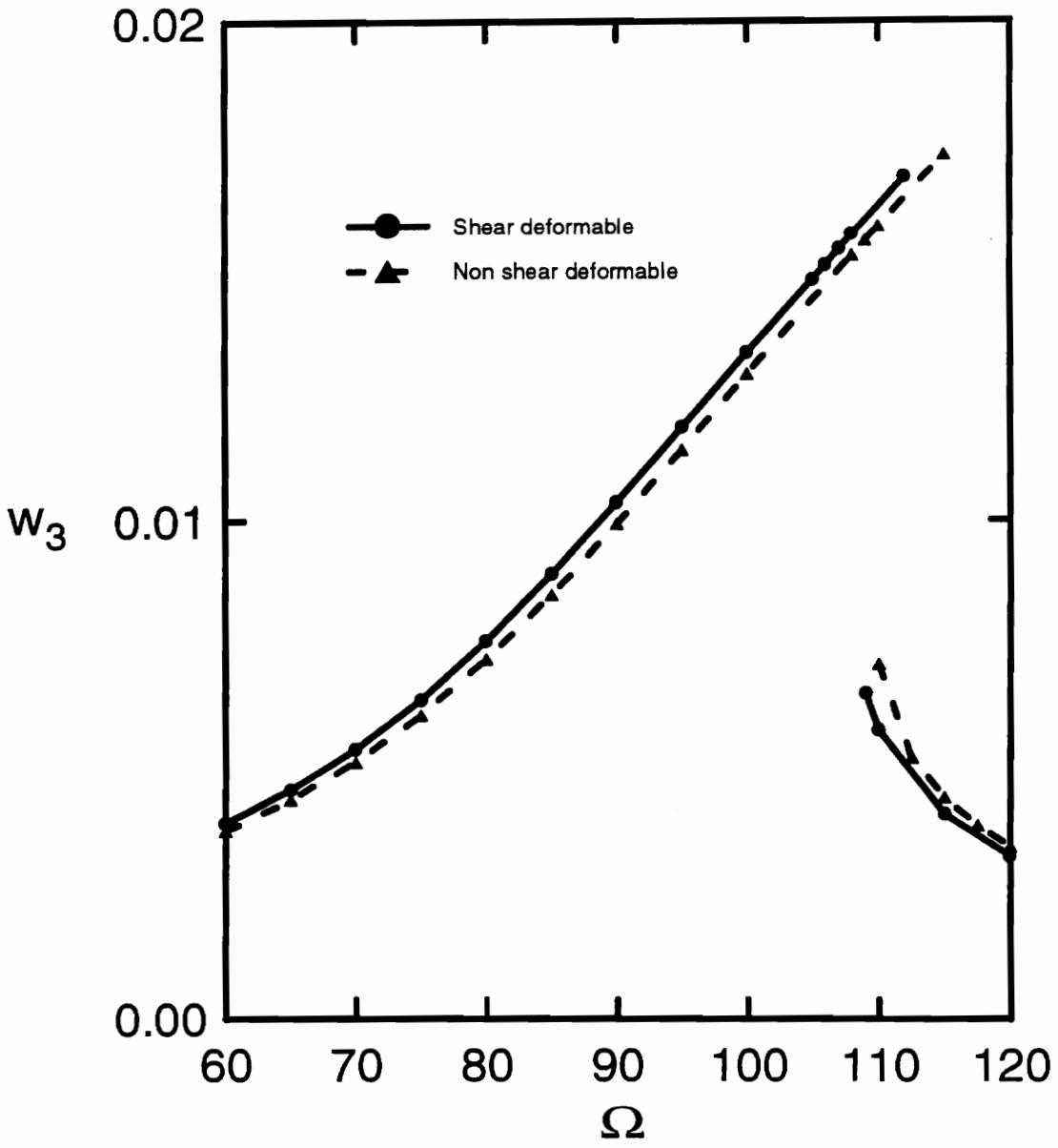

Figure 5.22: Maximum w_3 vs. frequency, Ω, for $a = 0.005$, $r = 0.01$.

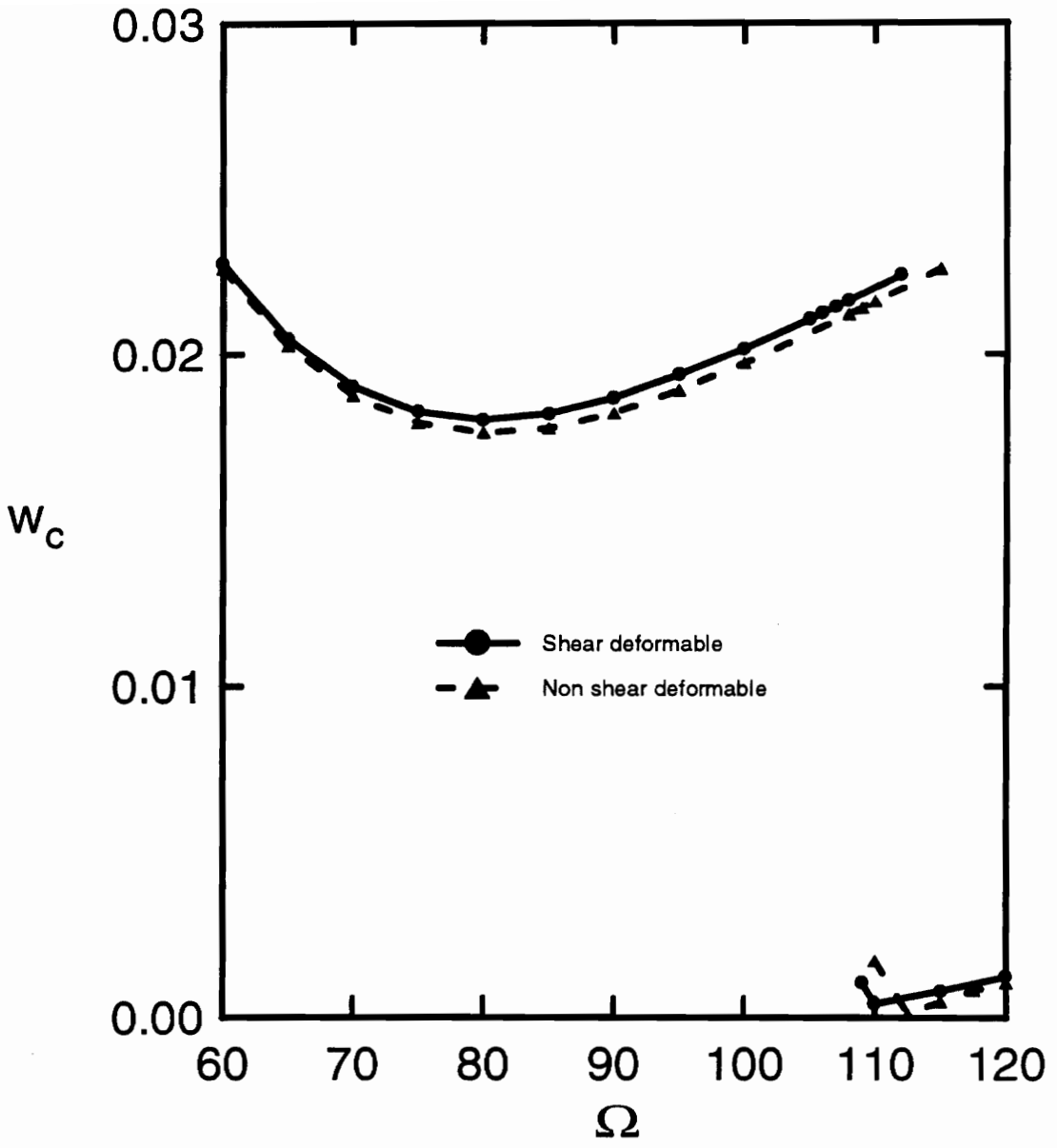

Figure 5.23: Maximum w_c vs. frequency, Ω, for $a = 0.005$, $r = 0.01$.

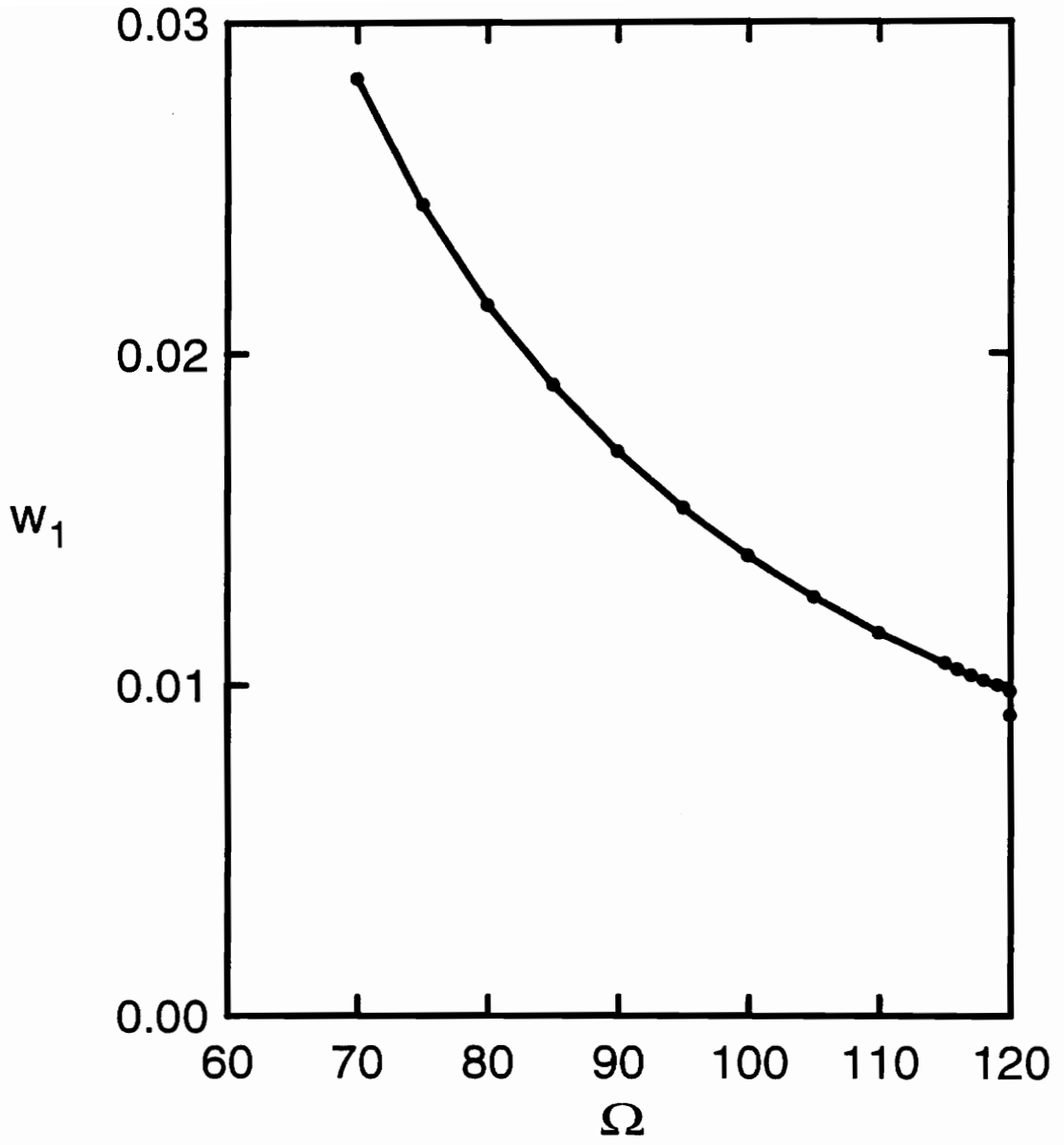

Figure 5.24: Maximum w_1 vs. frequency, Ω, for $a = 0.01$.
(shear deformable beam, $r = 0.01$)

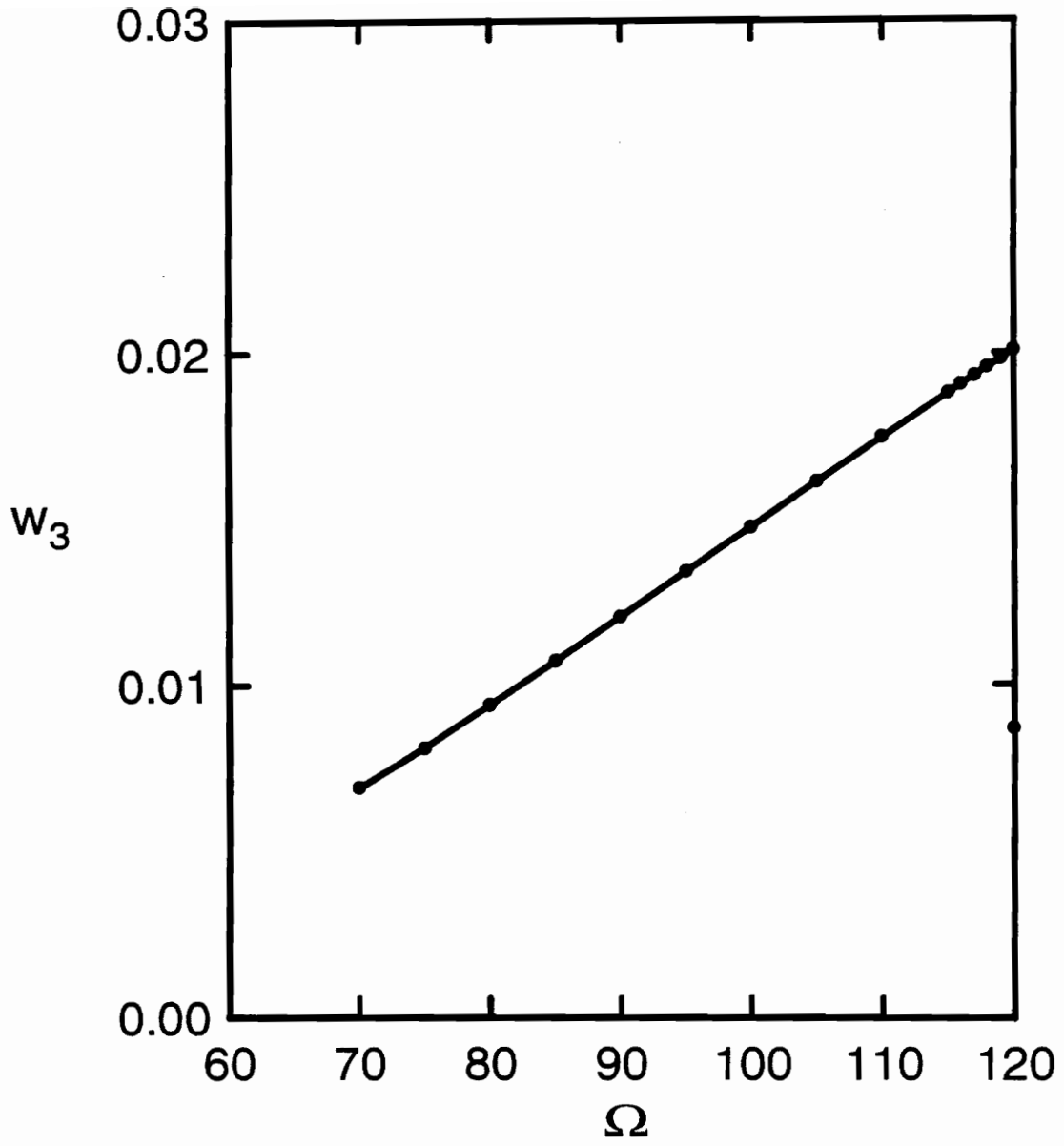

Figure 5.25: Maximum w_3 vs. frequency, Ω, for $a = 0.01$.
(shear deformable beam, $r = 0.01$)

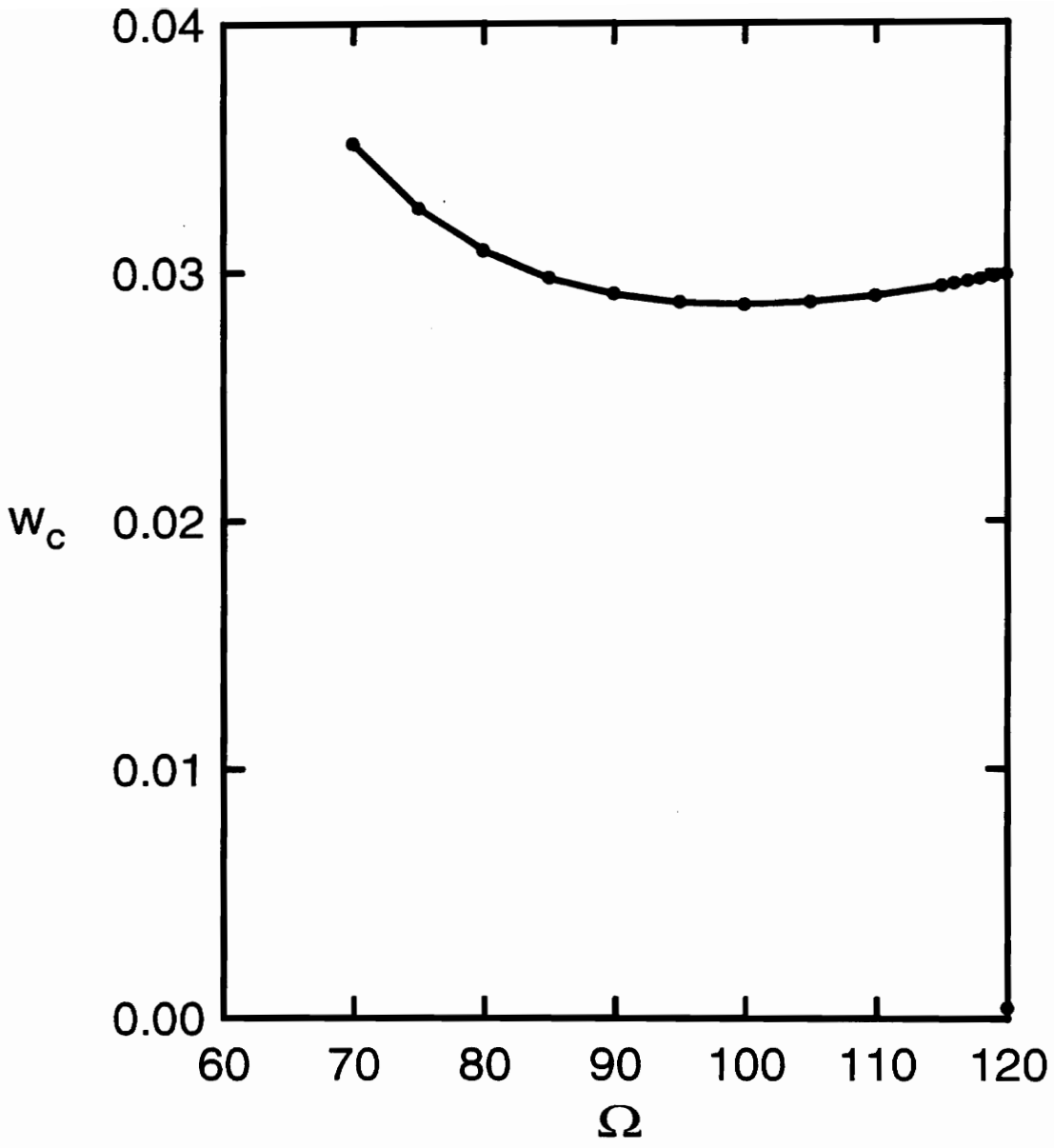

Figure 5.26: Maximum w_c vs. frequency, Ω, for $a = 0.01$.
(shear deformable beam, $r = 0.01$)

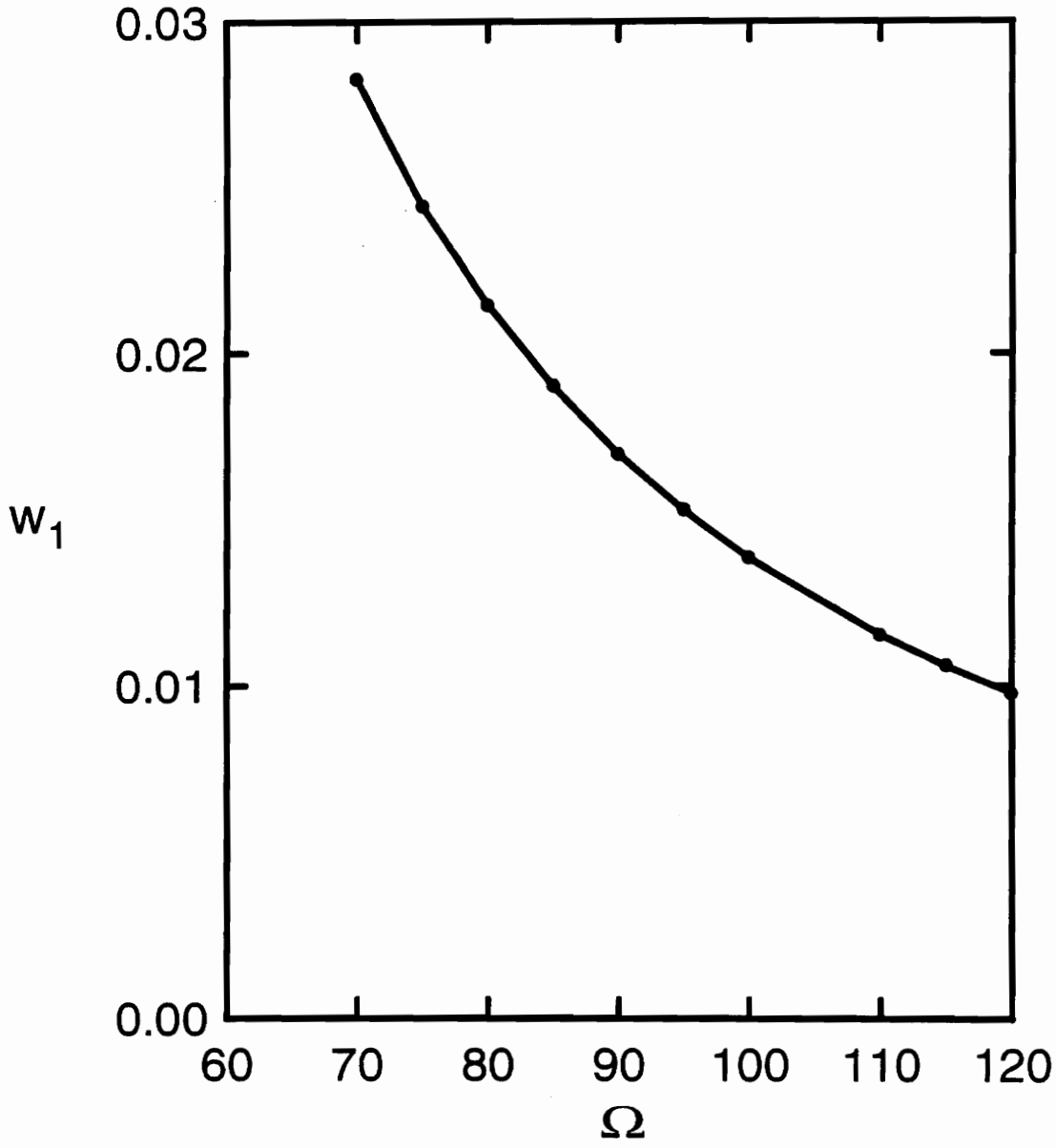

Figure 5.27: Maximum w_1 vs. frequency, Ω, for $a = 0.01$.
(non shear deformable beam, $r = 0.01$)

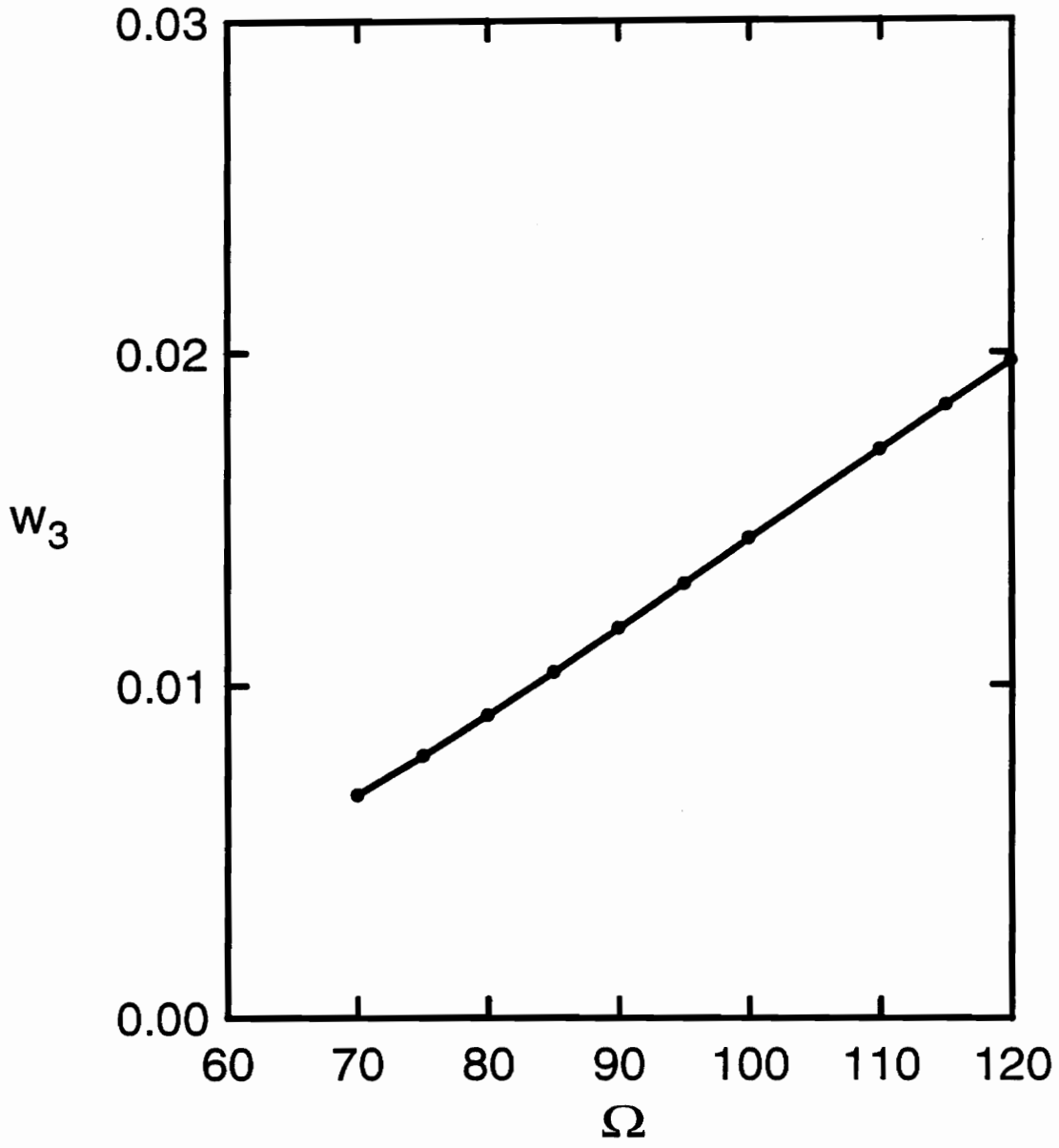

Figure 5.28: Maximum w_3 vs. frequency, Ω, for $a = 0.01$.
(non shear deformable beam, $r = 0.01$)

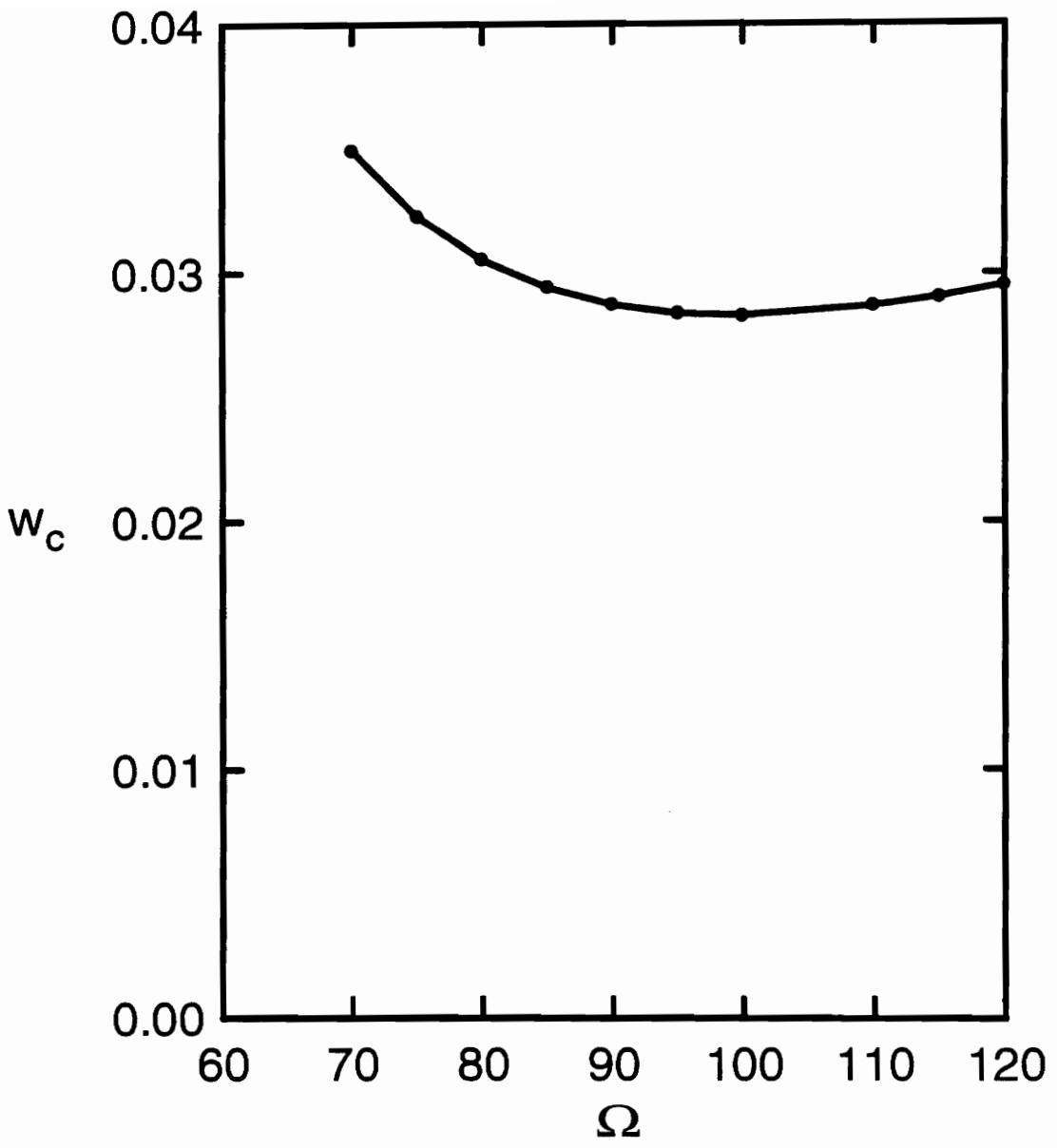

Figure 5.29: Maximum w_c vs. frequency, Ω, for $a = 0.01$.
(non shear deformable beam, $r = 0.01$)

The maximum values of w_1 do not differ noticeably between the two cases, but the maximum values of w_3 and midspan displacement are slightly higher for the shear deformable beam. Maximum values of w_3 and midspan displacement for both beams are plotted together in Figures 5.30 and 5.31.

Figures 5.32, 5.33, and 5.34 are plots of maximum w_1, w_3, and w_c for a shear deformable beam with a radius of gyration of 0.01 subjected to an excitation amplitude of 0.02. Periodic solutions were obtained for every frequency considered. For this case the response is dominated by the first term in the displacement functions. The maximum values of w_1 are much greater than the maximum values of w_3, and the plot of maximum midspan displacement appears to be very similar to the plot of maximum w_1. Phase portraits for the points in these graphs are plotted in Figures A.96 through A.111. Figures A.100 through A.102 pertain to the range in frequencies where maximum w_3 has a sudden change in slope beginning at an excitation frequency of 77. Here, the plot of w_3 with respect to $\dot{w}_3$ clearly loses symmetry with respect to the axes, and the maximum value of w_3 changes rapidly with respect to excitation frequency. Also, the plot of u_2 with respect to $\dot{u}_2$ loses symmetry with respect to the horizontal axis for frequencies in this portion of the plot.

Maximum values of w_1, w_3, and w_c for the non shear deformable beam subjected to the same excitation function are plotted in Figures 5.35 through 5.37. The phase portraits for the points on these curves were also very similar to those of the non shear deformable case and have not been included in the appendix.

Plots of the first generalized coordinate and midspan displacement indicate almost no difference between the shear deformable and the non shear deformable cases. However, the third generalized coordinate has a slightly higher value for the shear

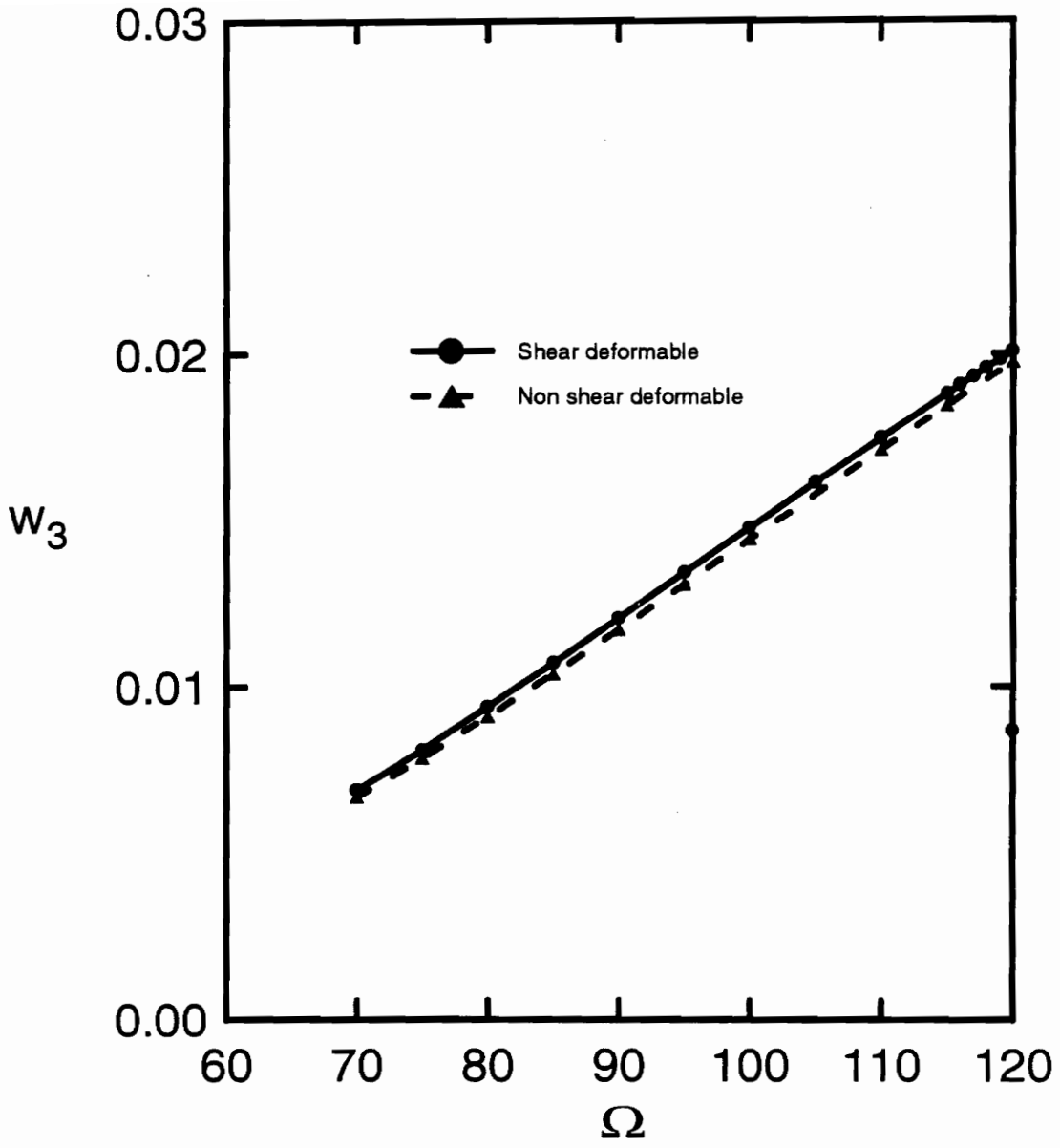

Figure 5.30: Maximum w_3 vs. frequency, Ω, for $a = 0.01$, $r = 0.01$.

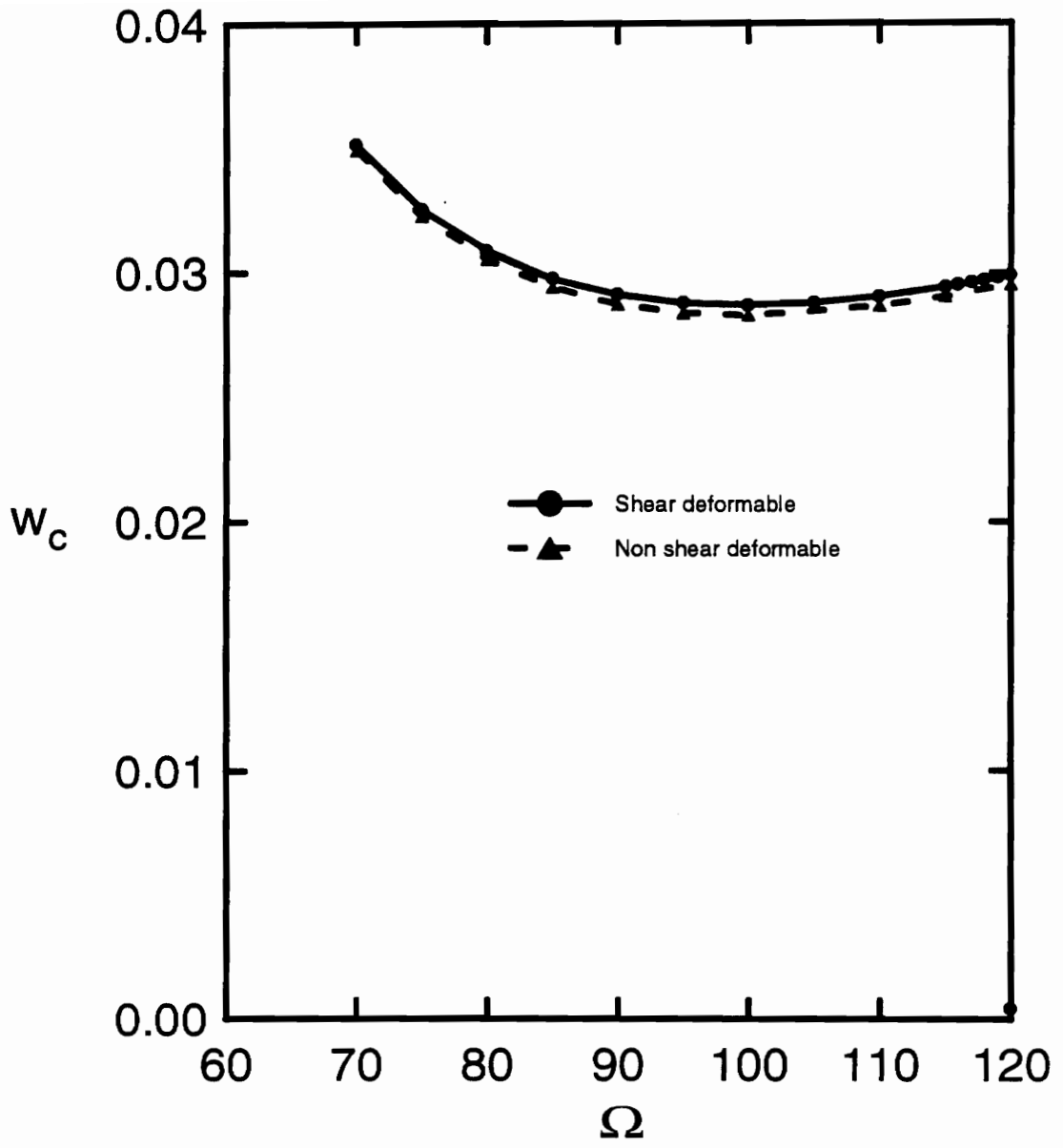

Figure 5.31: Maximum w_c vs. frequency, Ω, for $a = 0.01$, $r = 0.01$.

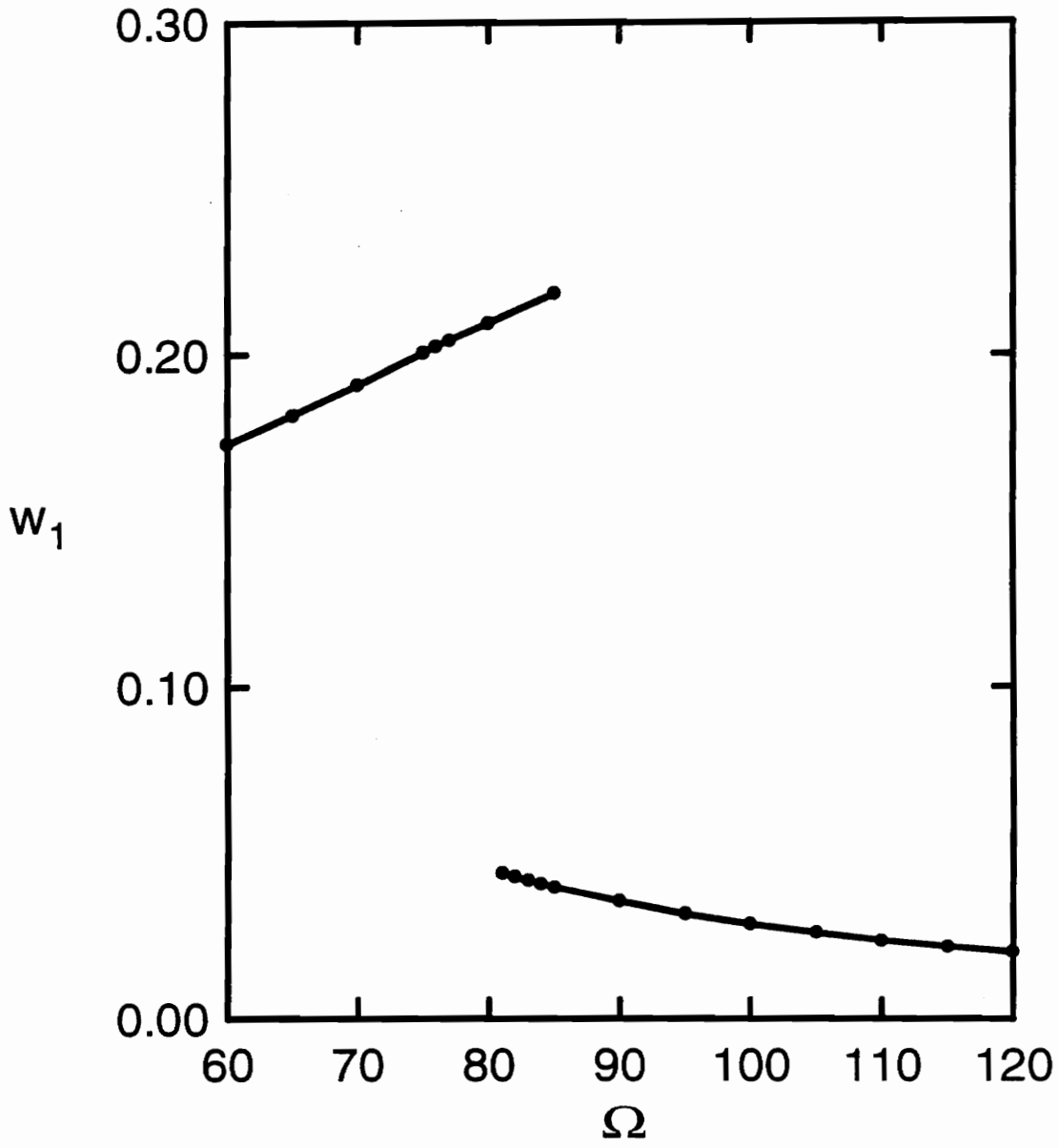

Figure 5.32: Maximum w_1 vs. frequency, Ω, for $a = 0.02$.
(shear deformable beam, $r = 0.01$)

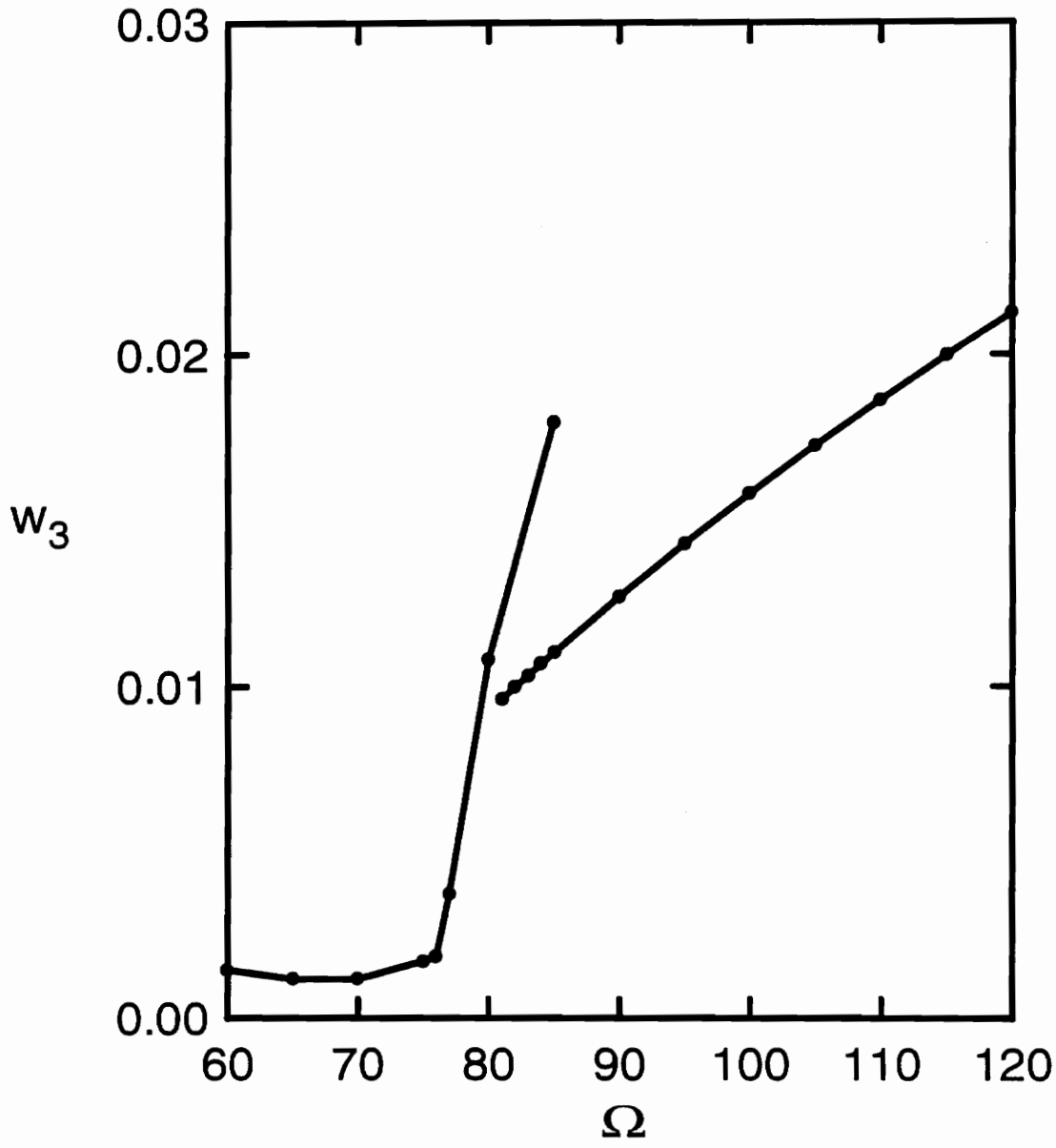

Figure 5.33: Maximum w_3 vs. frequency, Ω, for $a = 0.02$.
(shear deformable beam, $r = 0.01$)

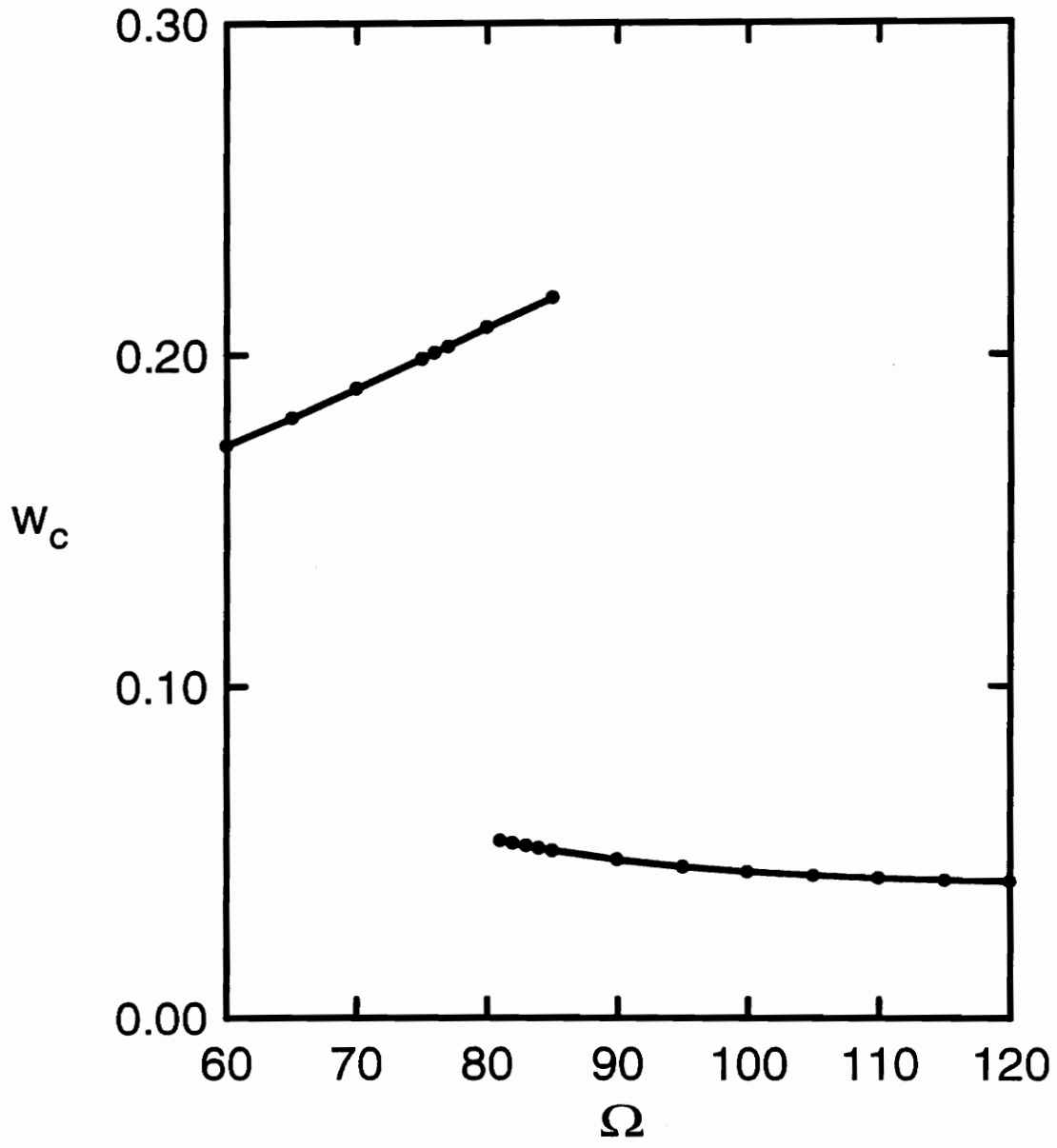

Figure 5.34: Maximum w_c vs. frequency, Ω, for $a = 0.02$.
(shear deformable beam, $r = 0.01$)

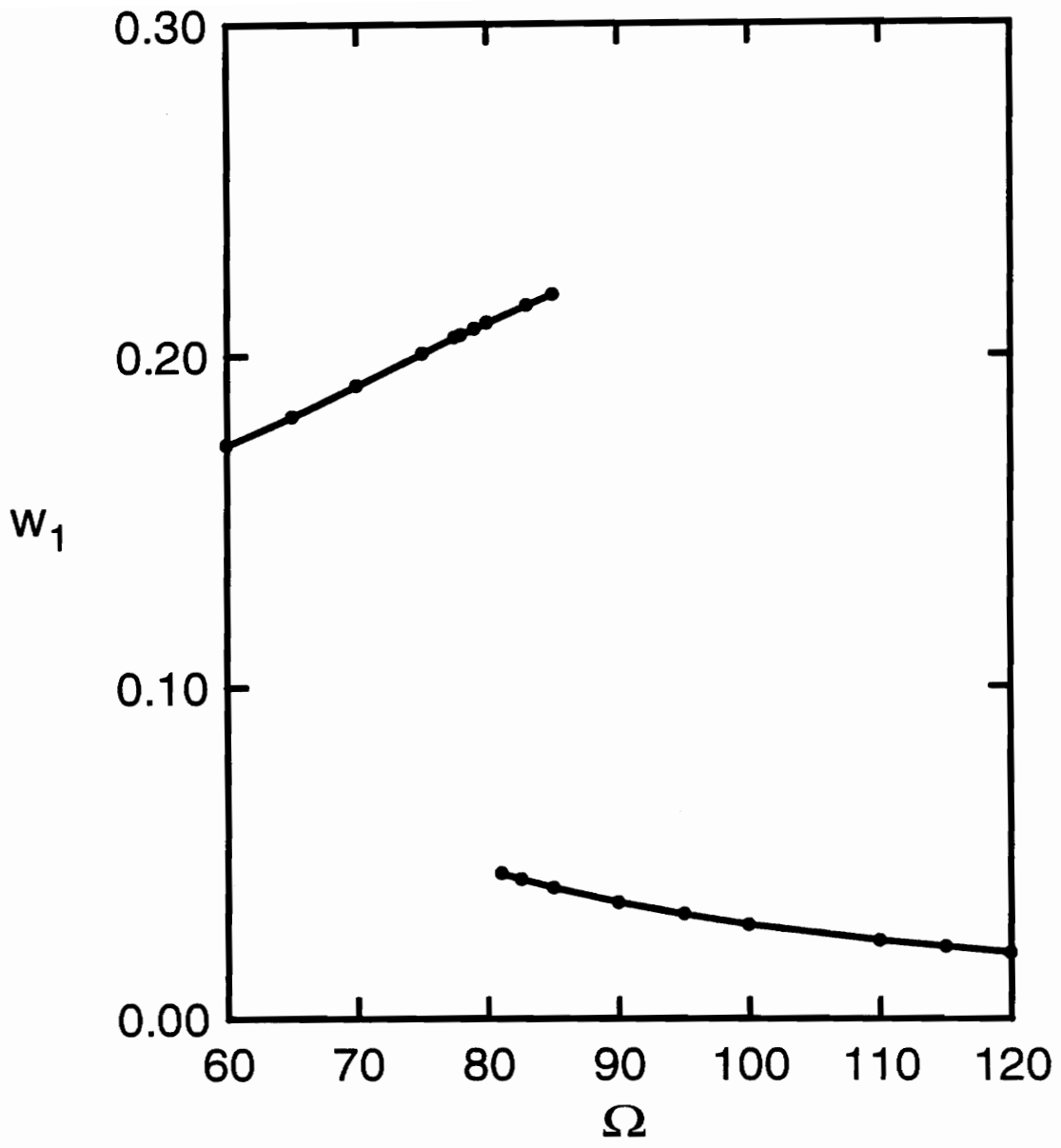

Figure 5.35: Maximum w_1 vs. frequency, Ω, for $a = 0.02$.
(non shear deformable beam, $r = 0.01$)

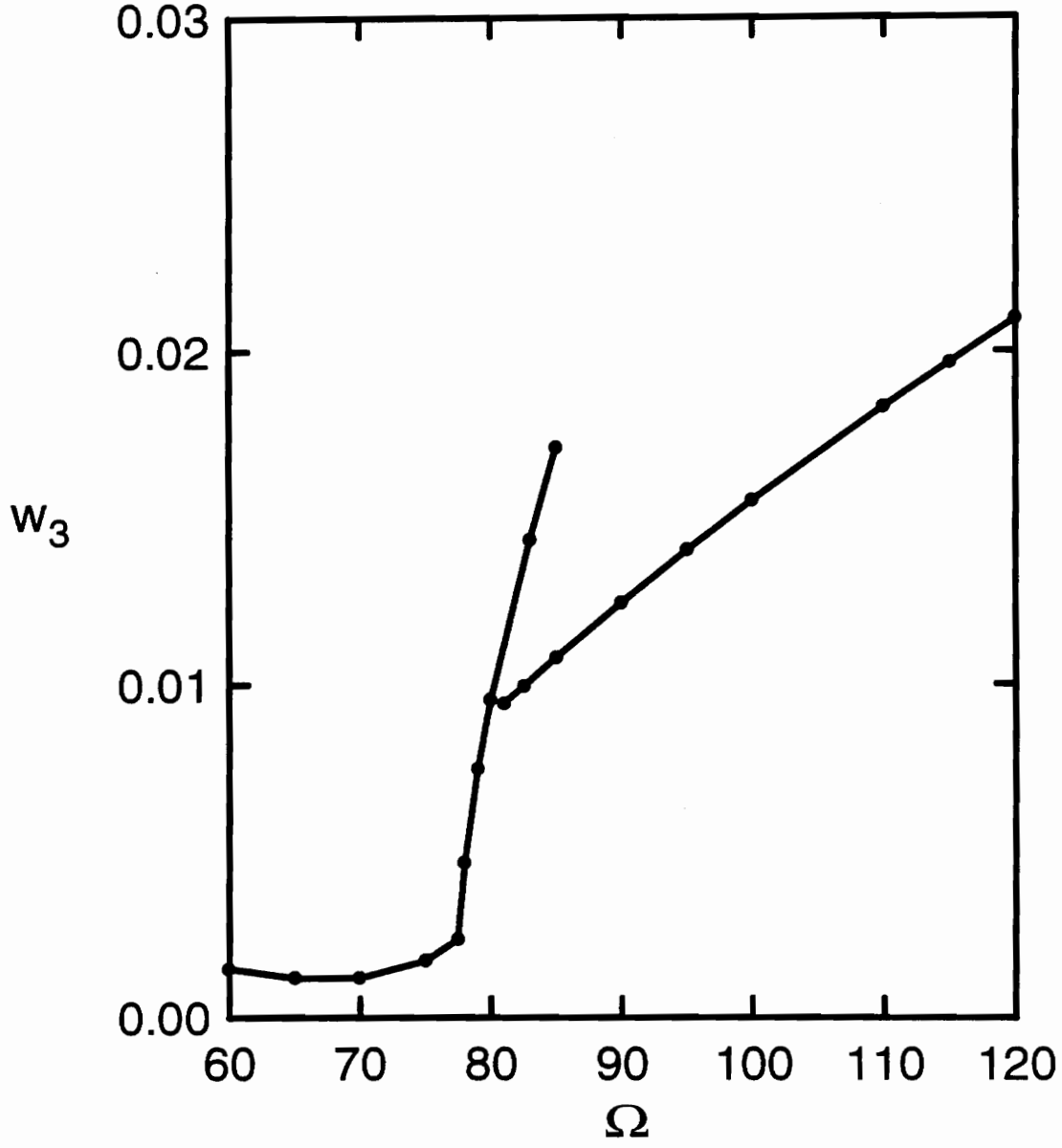

Figure 5.36: Maximum w_3 vs. frequency, Ω, for $a = 0.02$.
(non shear deformable beam, $r = 0.01$)

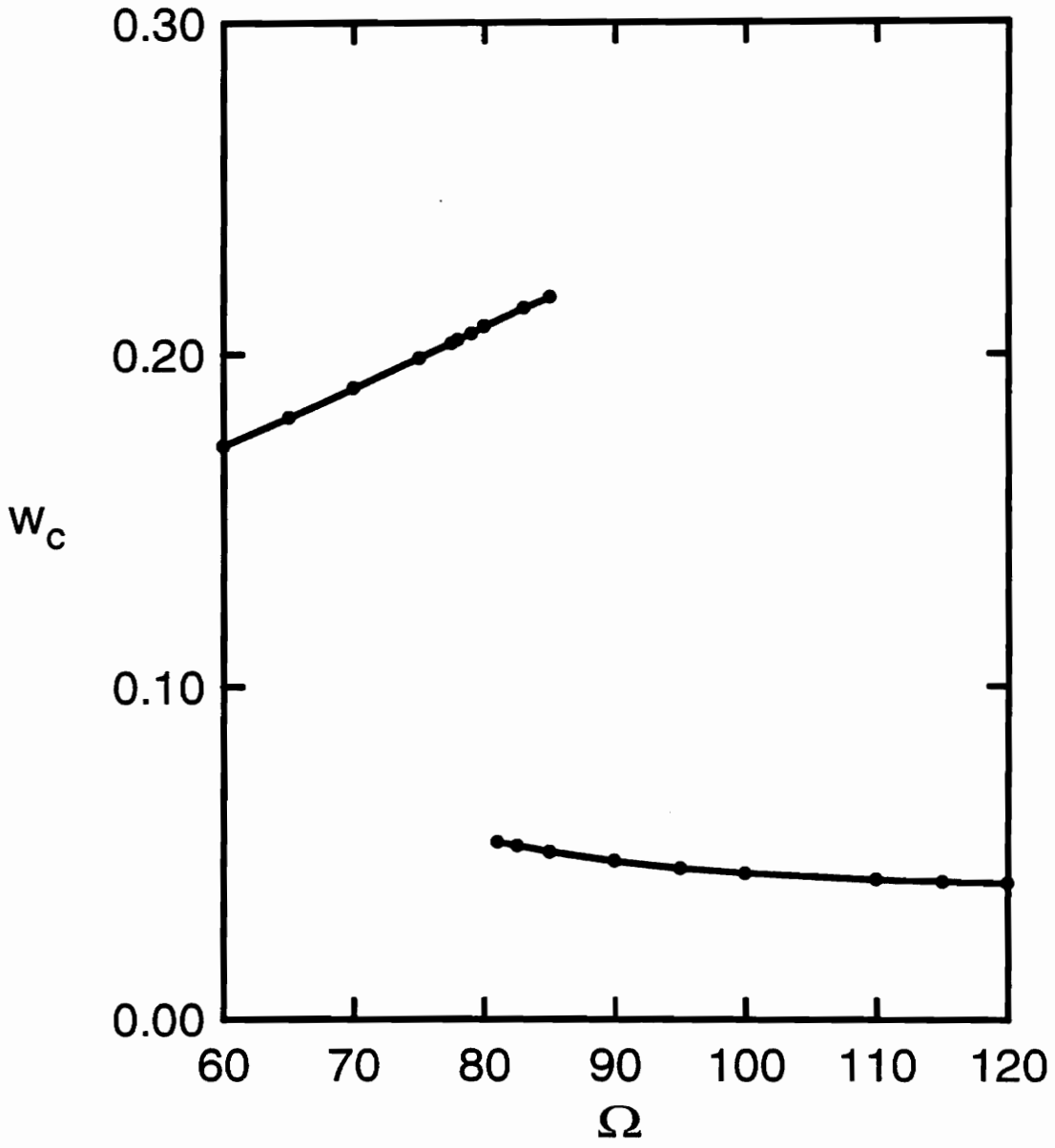

Figure 5.37: Maximum w_c vs. frequency, Ω, for $a = 0.02$.
(non shear deformable beam, $r = 0.01$)

deformable case for most frequencies in the range plotted. Figure 5.38 is a plot of maximum w_3 for both beams. The solid curve corresponds to the shear deformable case.

Figures 5.39, 5.40, and 5.41 are plots of maximum values of w_1, w_3, and w_c for a shear deformable beam with a radius of gyration of 0.05 subjected to an excitation amplitude of 0.5. No points for excitation frequencies of less than 75 are included in these plots because the maximum values of the generalized coordinates did not seem to lie on a reasonably smooth curve, and a periodic response was not even obtained for a frequency of 70. Figures A.112 through A.116 are phase portraits for the cases which have not been included in Figures 5.31 through 5.33. Figures A.117 through A.120 are phase portraits for points on the upper curve. Phase portraits for points on the lower curve are plotted in Figures A.121 through A.127.

Figures 5.42, 5.43, and 5.44 are plots of maximum w_1, w_3, and w_c for a non shear deformable beam with a radius of gyration of 0.05 subjected to an excitation function with an amplitude of 0.5. A periodic response was produced for every frequency considered between 60 and 120. Phase portraits associated with data points on the upper curves in these figures are plotted in Figures A.128 through A.138. Phase portraits for points on the lower curves are plotted in Figures A.139 through A.145.

A very sudden change in the slope of the lower curve in the plot of the maximum value of w_1 vs. excitation frequency occurs when the excitation frequency reaches a value of 115. Drift becomes very obvious in the phase portraits of w_1 when the excitation frequency is higher than 115. The phase portraits for this coordinate become asymmetric with respect to the displacement axis for these frequencies. The time history of w_1 clearly has a nonzero mean even though the excitation has a zero mean. Furthermore, the displacement of the midspan of the beam lies completely to one side of the undeformed state. It oscillates completely on one side of the original centerline without crossing zero.

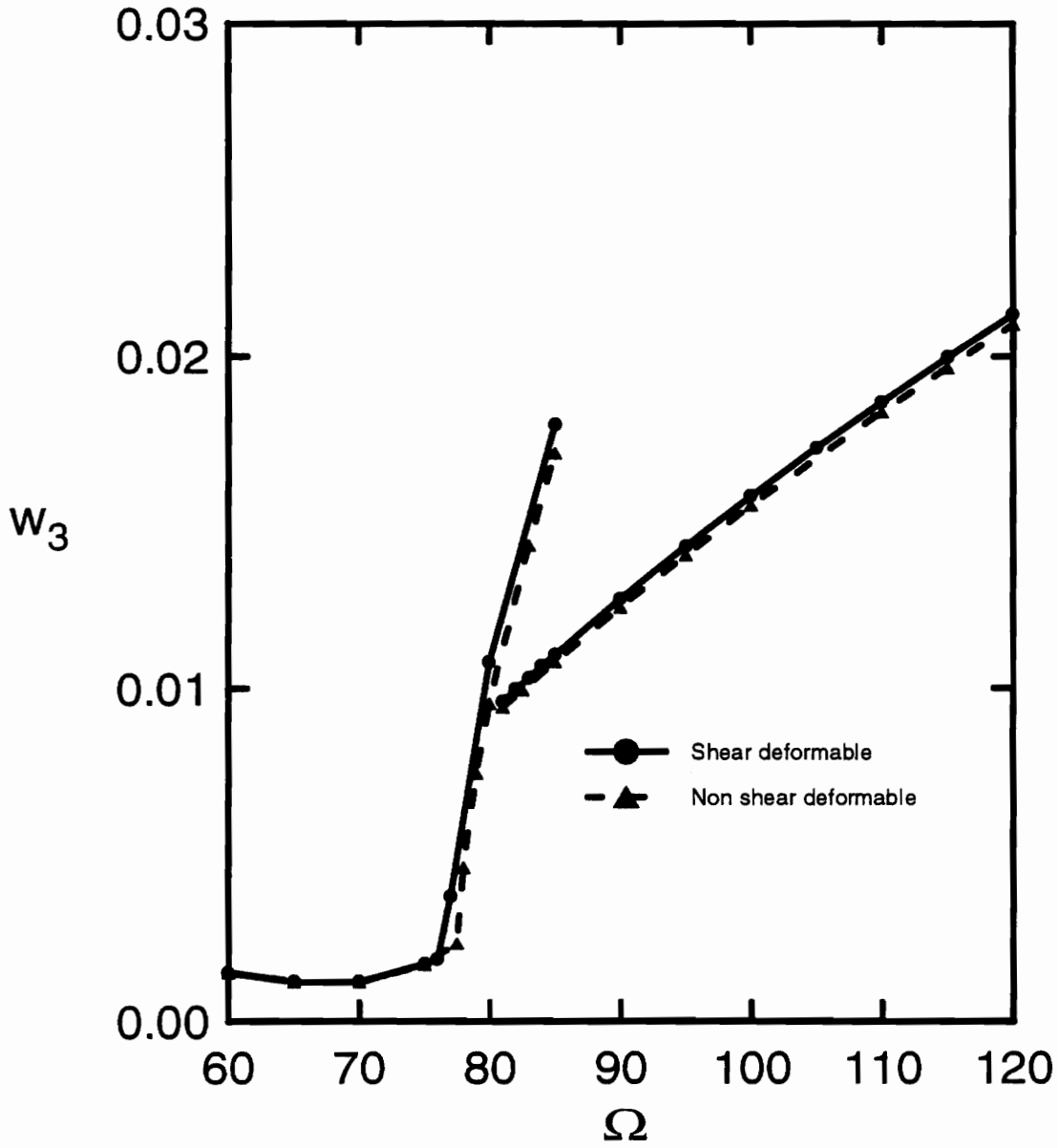

Figure 5.38: Maximum w_3 vs. frequency, Ω, for $a = 0.02$, $r = 0.01$.

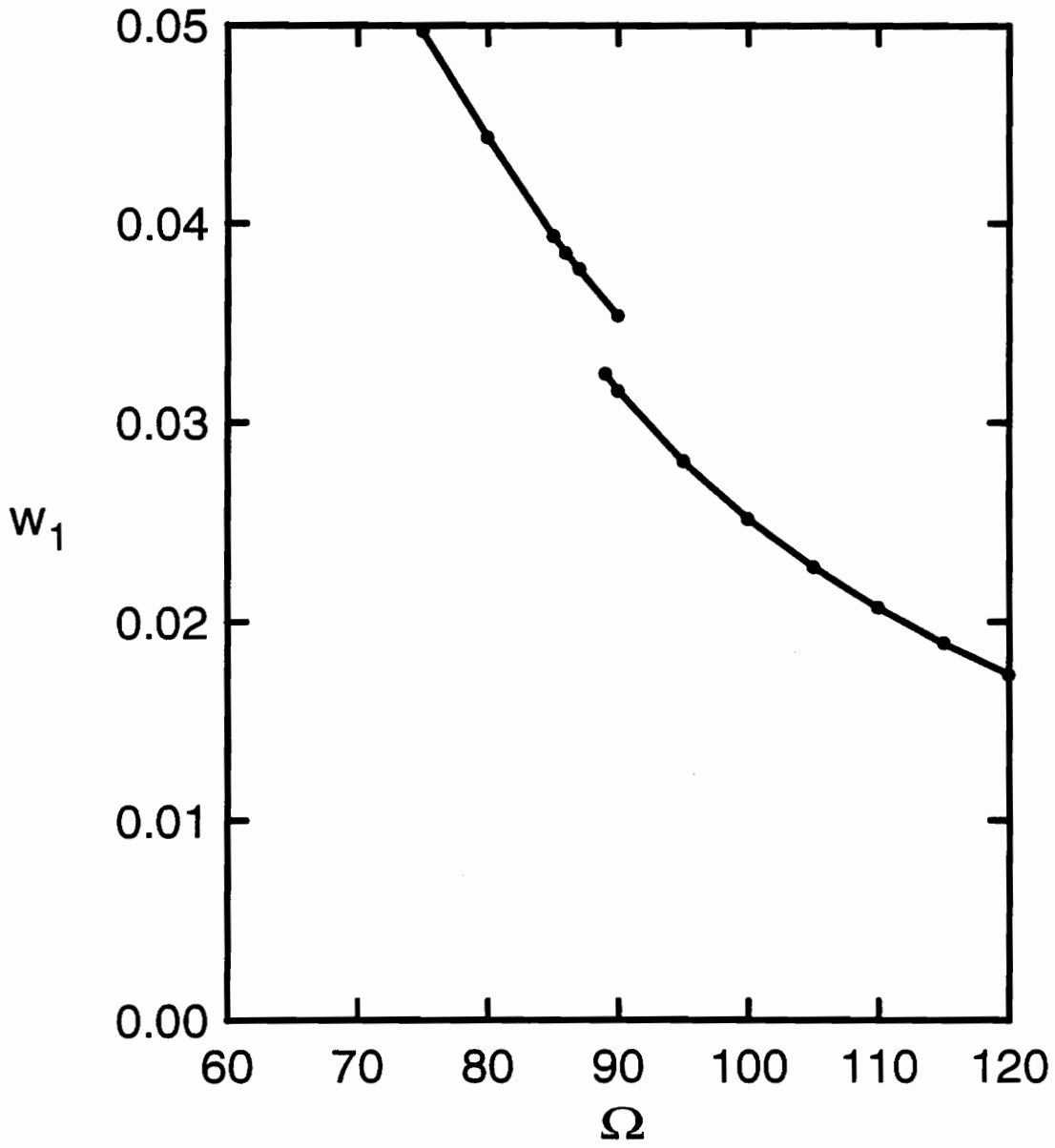

Figure 5.39: Maximum w_1 vs. frequency, Ω, for $a = 0.5$.
(shear deformable beam, $r = 0.05$)

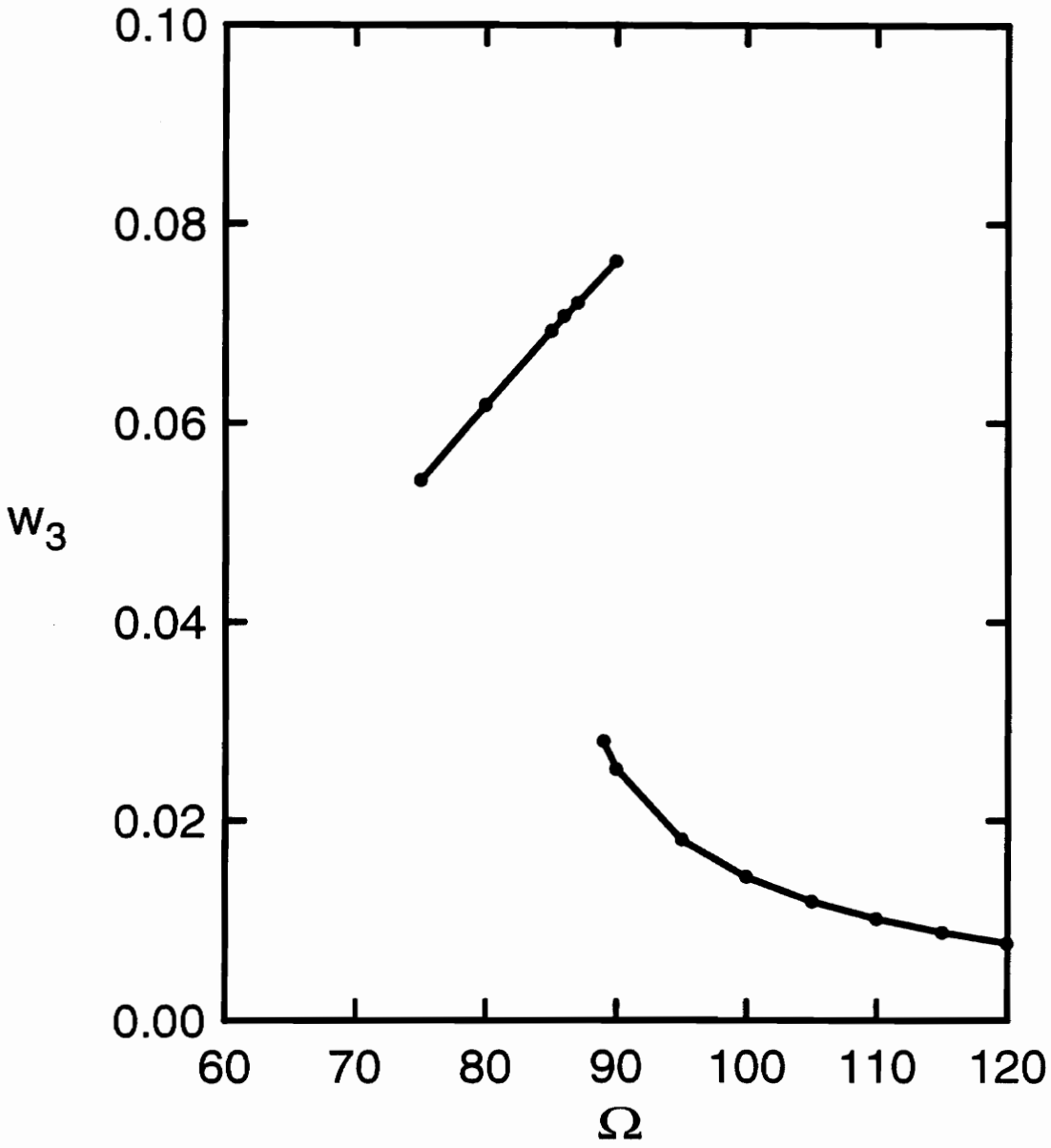

Figure 5.40: Maximum w_3 vs. frequency, Ω, for $a = 0.5$.
(shear deformable beam, $r = 0.05$)

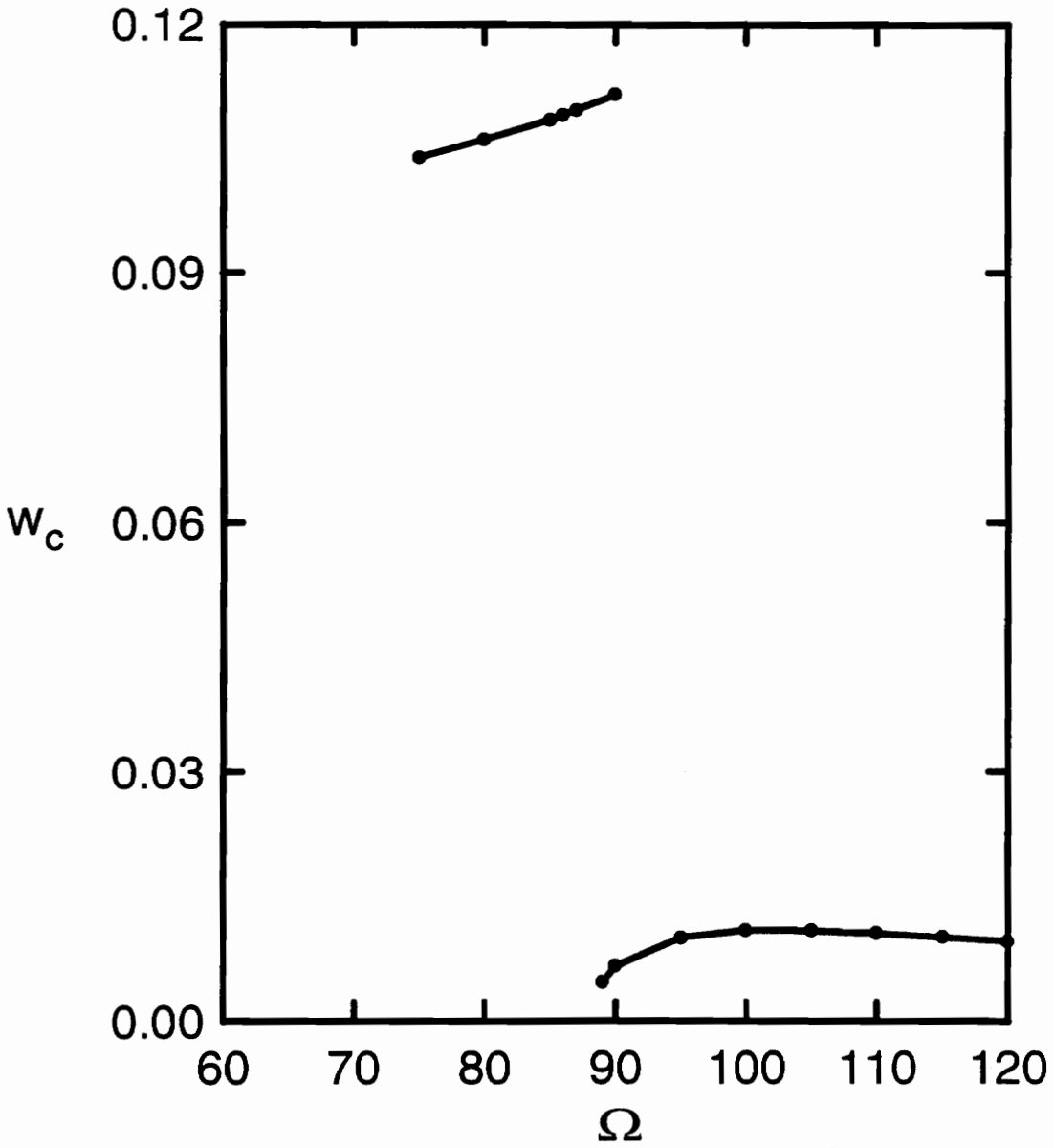

Figure 5.41: Maximum w_c vs. frequency, Ω, for $a = 0.5$.
(shear deformable beam, $r = 0.05$)

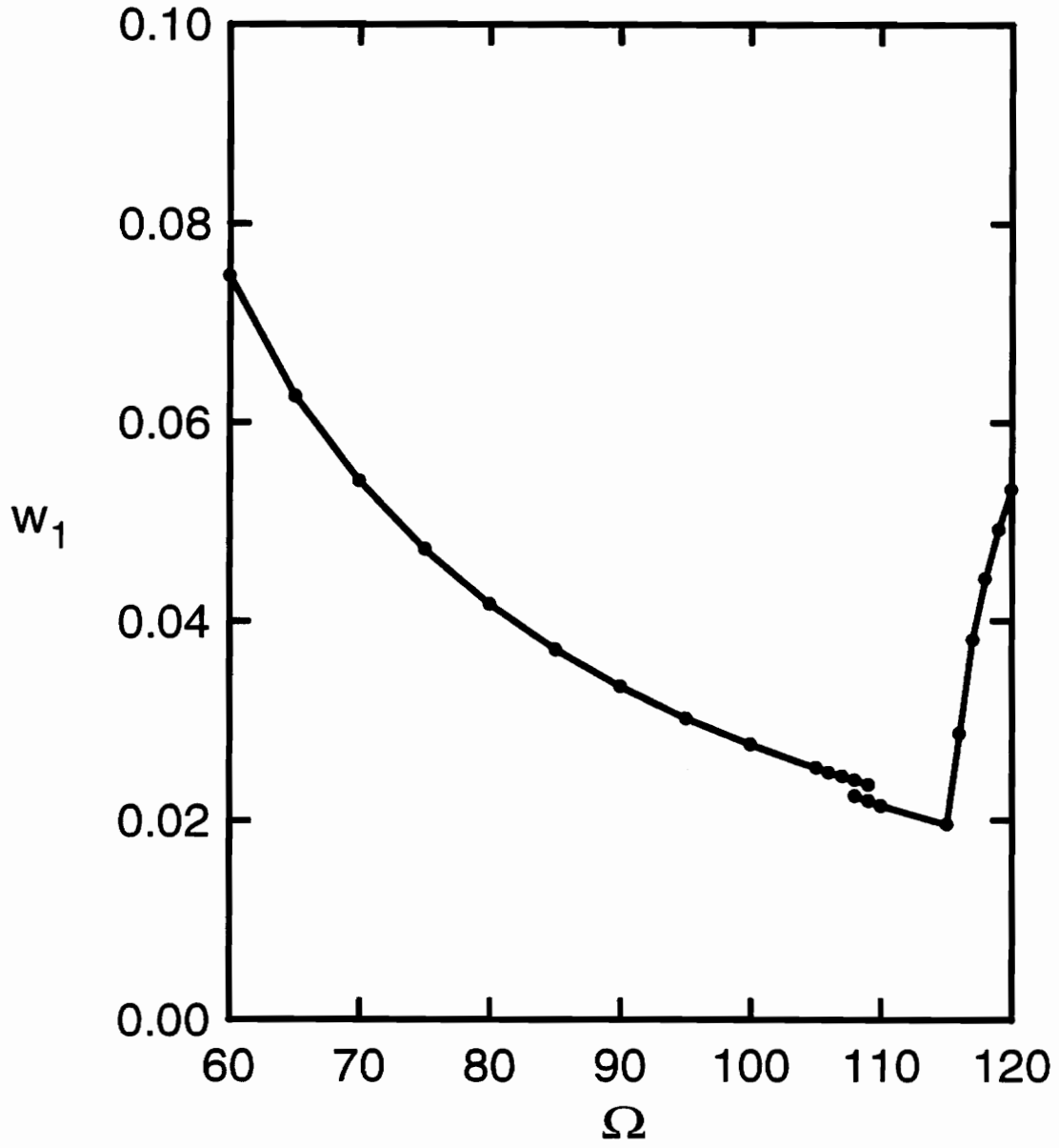

Figure 5.42: Maximum w_1 vs. frequency, Ω, for $a = 0.5$.
(non shear deformable beam, $r = 0.05$)

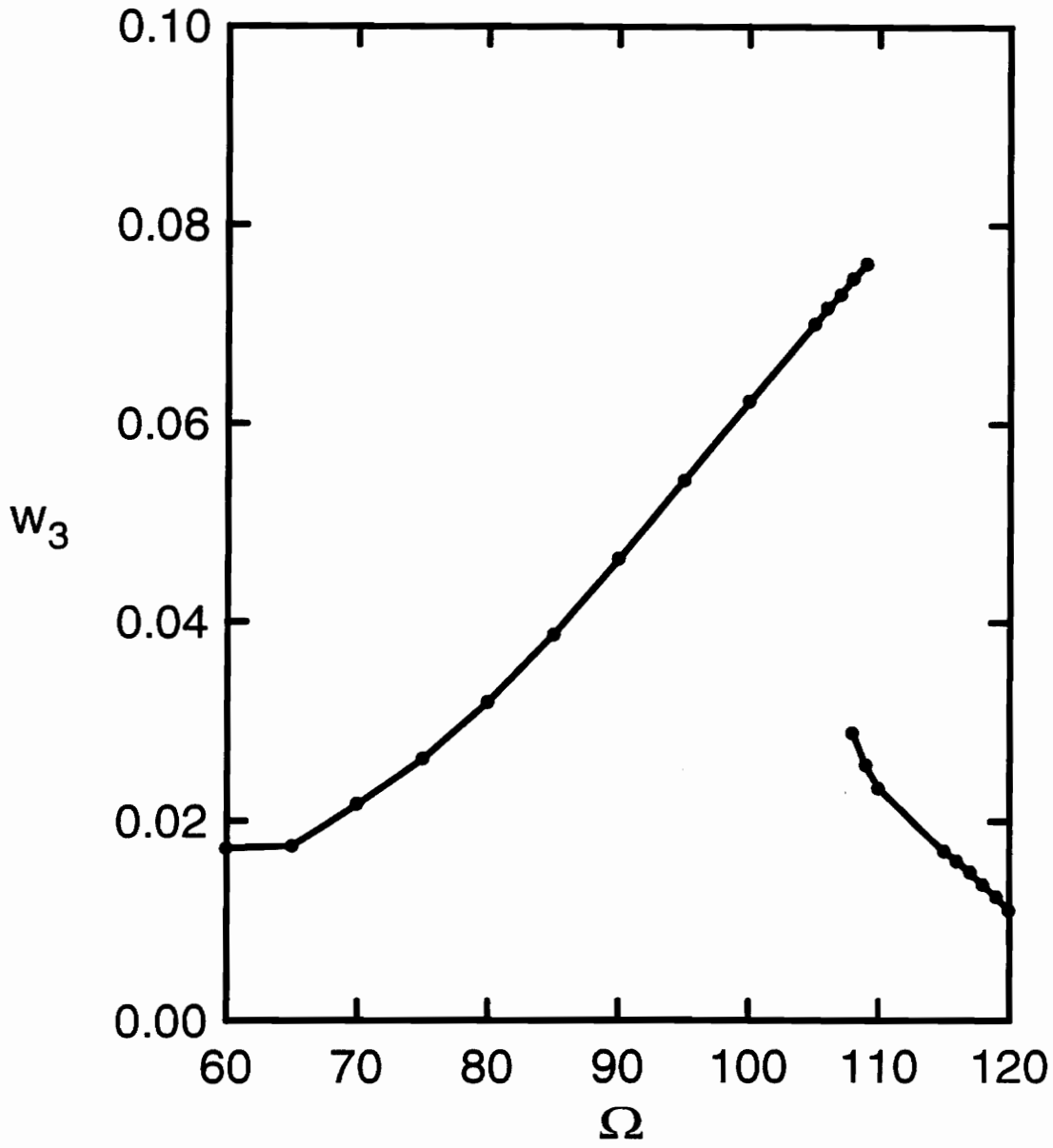

Figure 5.43: Maximum w_3 vs. frequency, Ω, for $a = 0.5$.
(non shear deformable beam, $r = 0.05$)

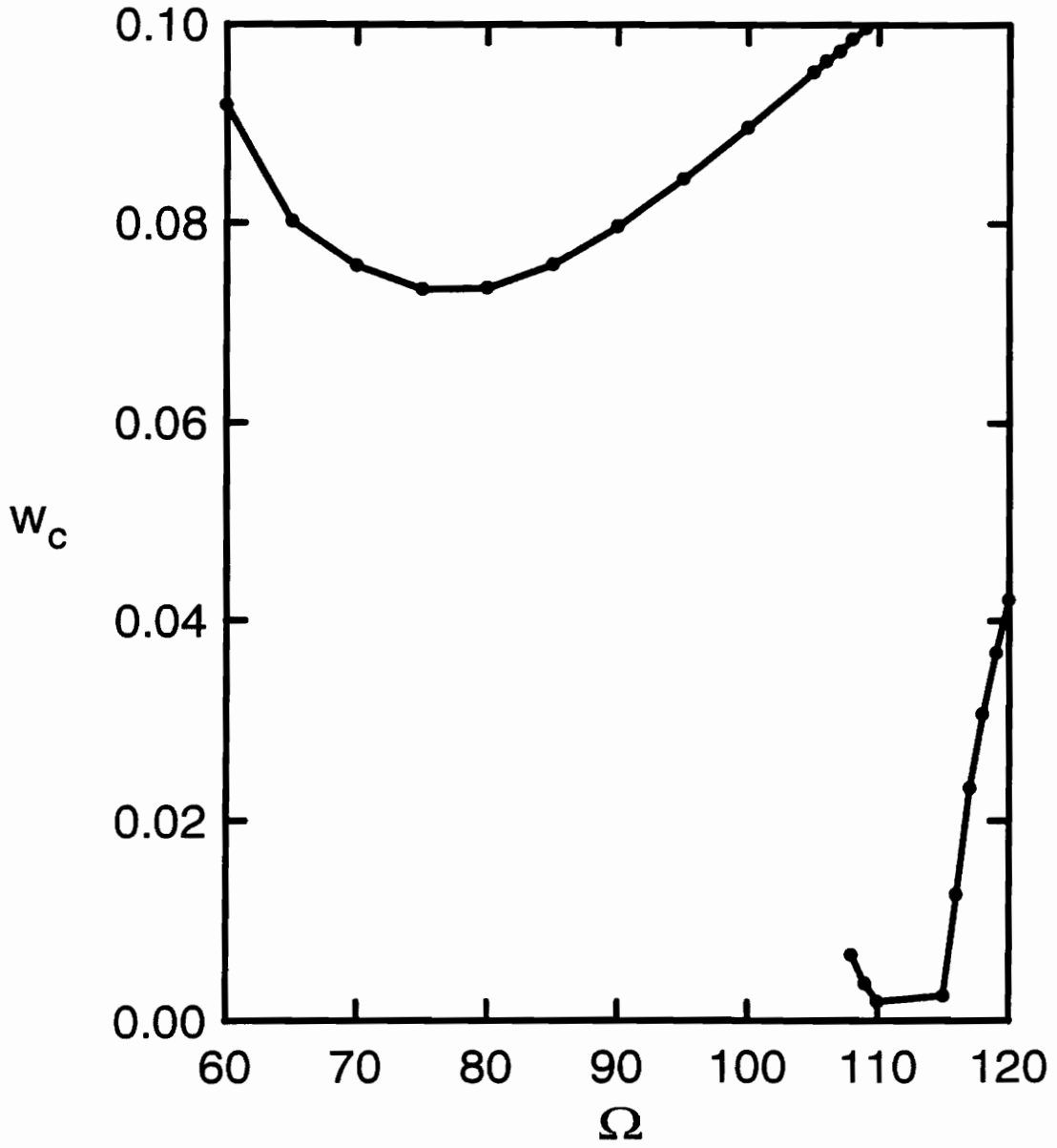

Figure 5.44: Maximum w_c vs. frequency, Ω, for $a = 0.5$.
(non shear deformable beam, $r = 0.05$)

Figures A.142, A.143, A.144, and A.145 are the phase portraits of the coordinates for excitation amplitudes of 116, 117, 119, and 120, respectively. For excitation frequencies of 116, 117, and 120 the displacement of the midspan is always positive. For a frequency of 119 this displacement is always negative, suggesting that the solution does not favor either side for excitation frequencies in this range. The side of the phase plane in which these portraits lie may only depend on the initial conditions and the time history of the excitation.

Figures 5.45, 5.46, and 5.47 are plots of maximum w_1, w_3, and w_c for a shear deformable beam with a radius of gyration of 0.05 subjected to an excitation with an amplitude of 1.0. No data points have been included for excitation frequencies lower than 80, because periodic responses were not obtained for all frequencies below this value, and the responses which were periodic had maximum values which jumped substantially for small changes in frequency. These points did not seem to lie on a smooth curve. Figures A.146, A.147, A.148, and A.149 are phase portraits for excitation frequencies of 60, 65, 70, and 75, respectively. The response for an excitation frequency of 60 not only was not periodic, but yielded axial and transverse displacements which are of the same order as the length of the beam. Figures A.150 through A.154 are phase portraits for points on the upper curve. Figures A.155 through A.166 are phase portraits for points on the lower curve.

The lower curves of Figures 5.46 and 5.47 show what looks like a discontinuity in the plots of w_3 and w_c vs. frequency at a frequency of 102. However, the integration procedure yielded only one point for each frequency considered. The phase portraits for w_3 and w_c for a frequency of 102 are shaped differently from those of the adjacent points.

The lower curve of Figures 5.46 and 5.47 have a sudden change in slope beginning with a frequency of 105. Phase portraits for points with excitation frequencies greater

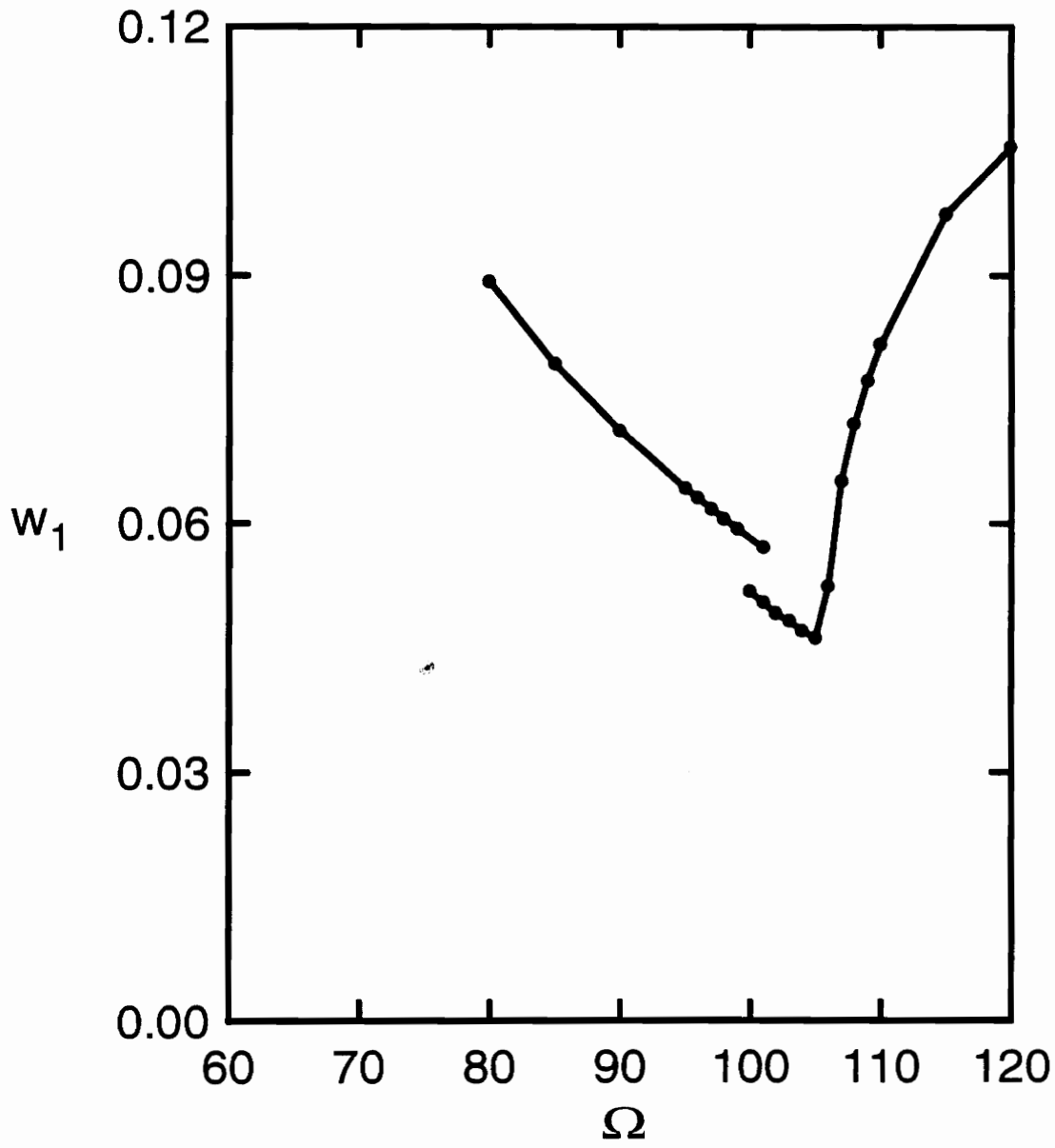

Figure 5.45: Maximum w_1 vs. frequency, Ω, for $a = 1.0$.
(shear deformable beam, $r = 0.05$)

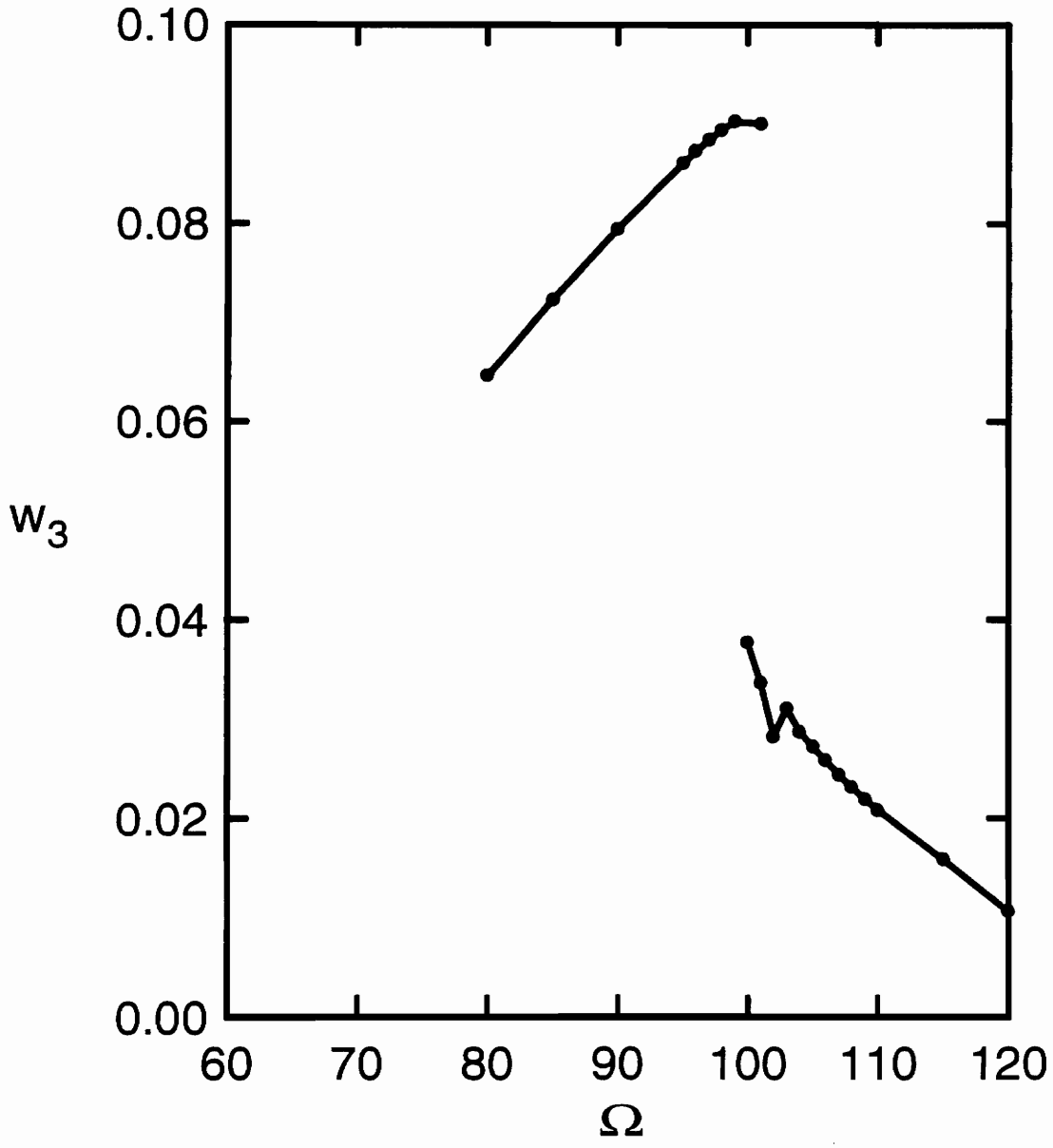

Figure 5.46: Maximum w_3 vs. frequency, Ω, for $a = 1.0$.
(shear deformable beam, $r = 0.05$)

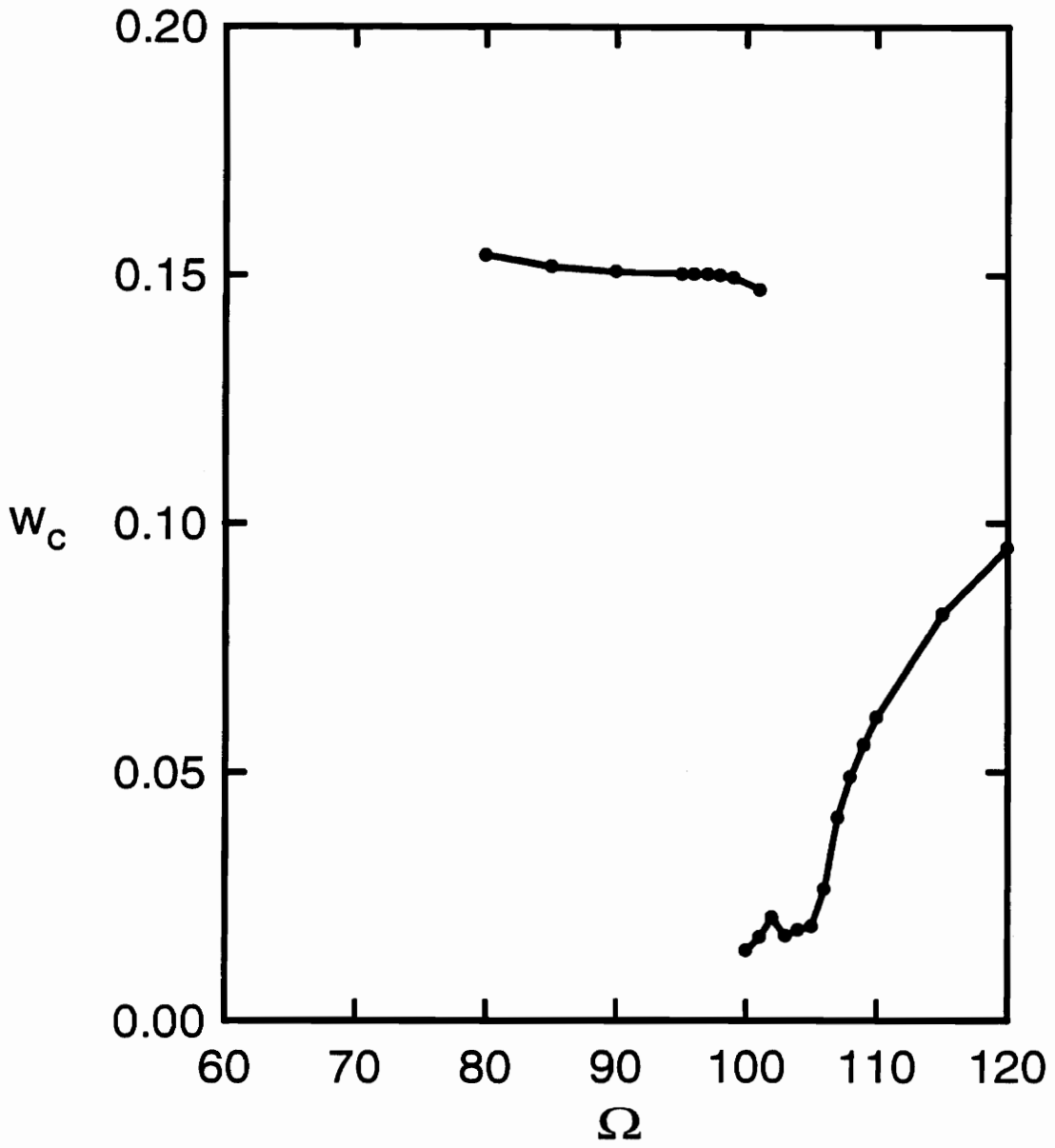

Figure 5.47: Maximum w_c vs. frequency, Ω, for $a = 1.0$.
(shear deformable beam, $r = 0.05$)

than 105 are plotted in Figures A.160 through A.166. The phenomenon of drift is very apparent in the phase portraits for the first transverse generalized coordinate, w_1, and the midspan displacement, w_c.

Figures 5.48, 5.49, and 5.50 are plots of the maximum values of w_1, w_3, and w_c for a non shear deformable beam with a radius of gyration of 0.05 subjected to an excitation with an amplitude of 1.0. No points were plotted for frequencies lower than 65. The phase portraits for the solution of the equations of motion with an excitation frequency of 60 are plotted in Figure A.167. The solution is aperiodic and very large. Phase portraits for the upper curve are plotted in Figures A168 through A.171, and phase portraits for the lower curve are plotted in Figures A.172 through A.180.

Points were not plotted for excitation frequencies greater than 110. Beyond this frequency the integration procedure produced solutions which were aperiodic and resulted in very large displacements, similar to those for an excitation frequency of 60. Phase portraits for excitation frequencies of 115 and 120 are plotted in Figures A.181 and A.182.

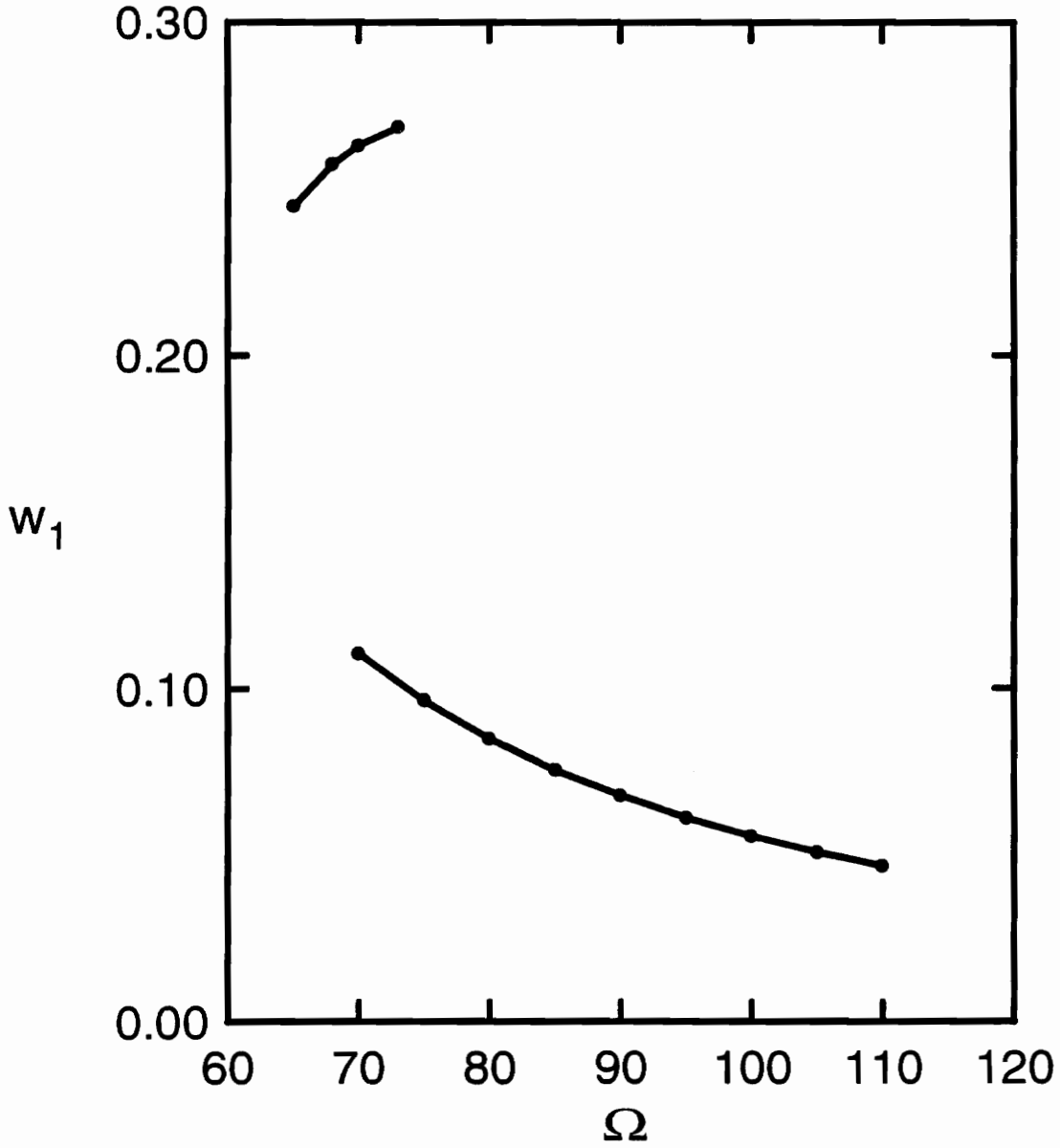

Figure 5.48: Maximum w_1 vs. frequency, Ω, for $a = 1.0$.
(non shear deformable beam, $r = 0.05$)

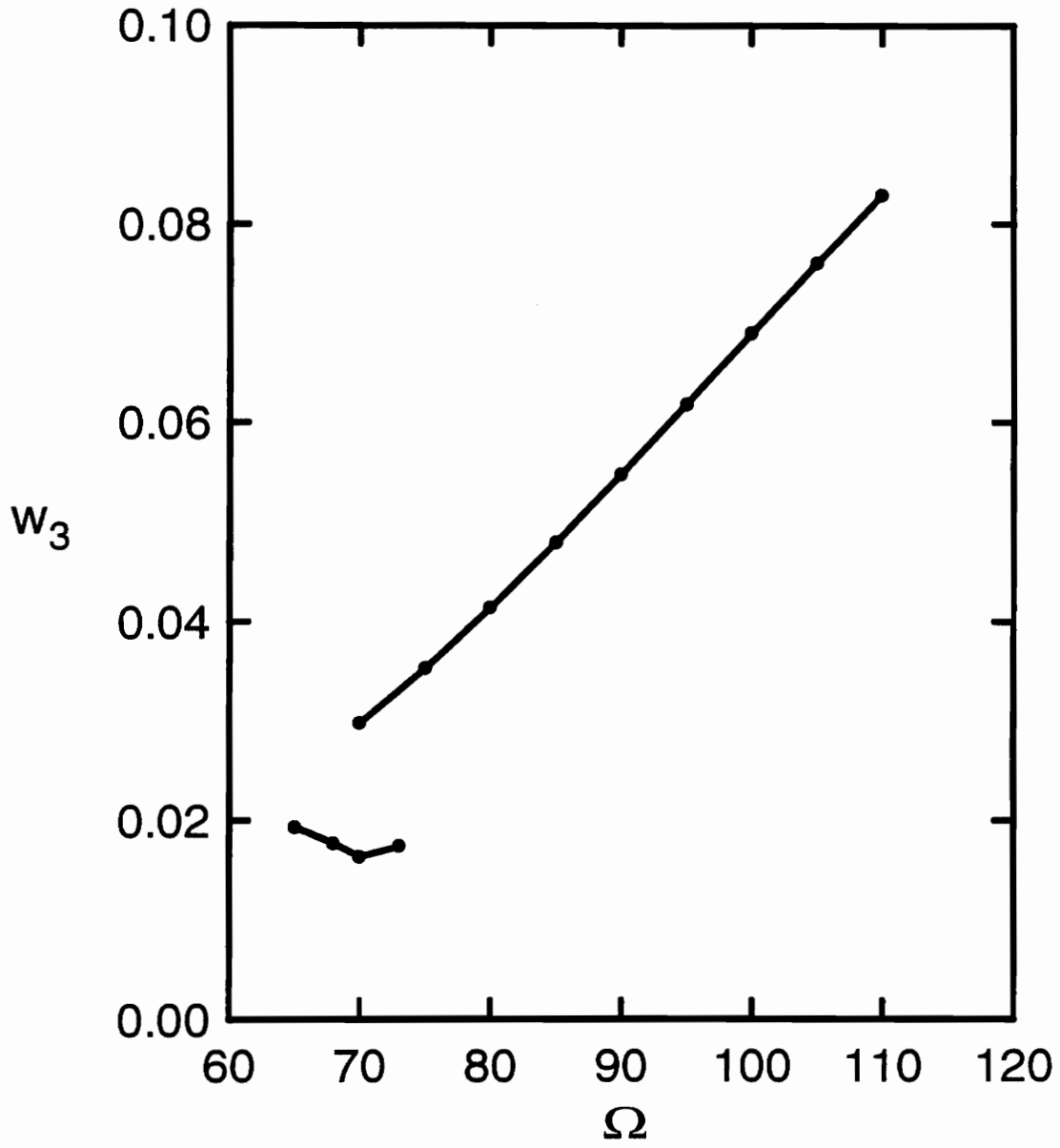

Figure 5.49: Maximum w_3 vs. frequency, Ω, for $a = 1.0$.
(non shear deformable beam, $r = 0.05$)

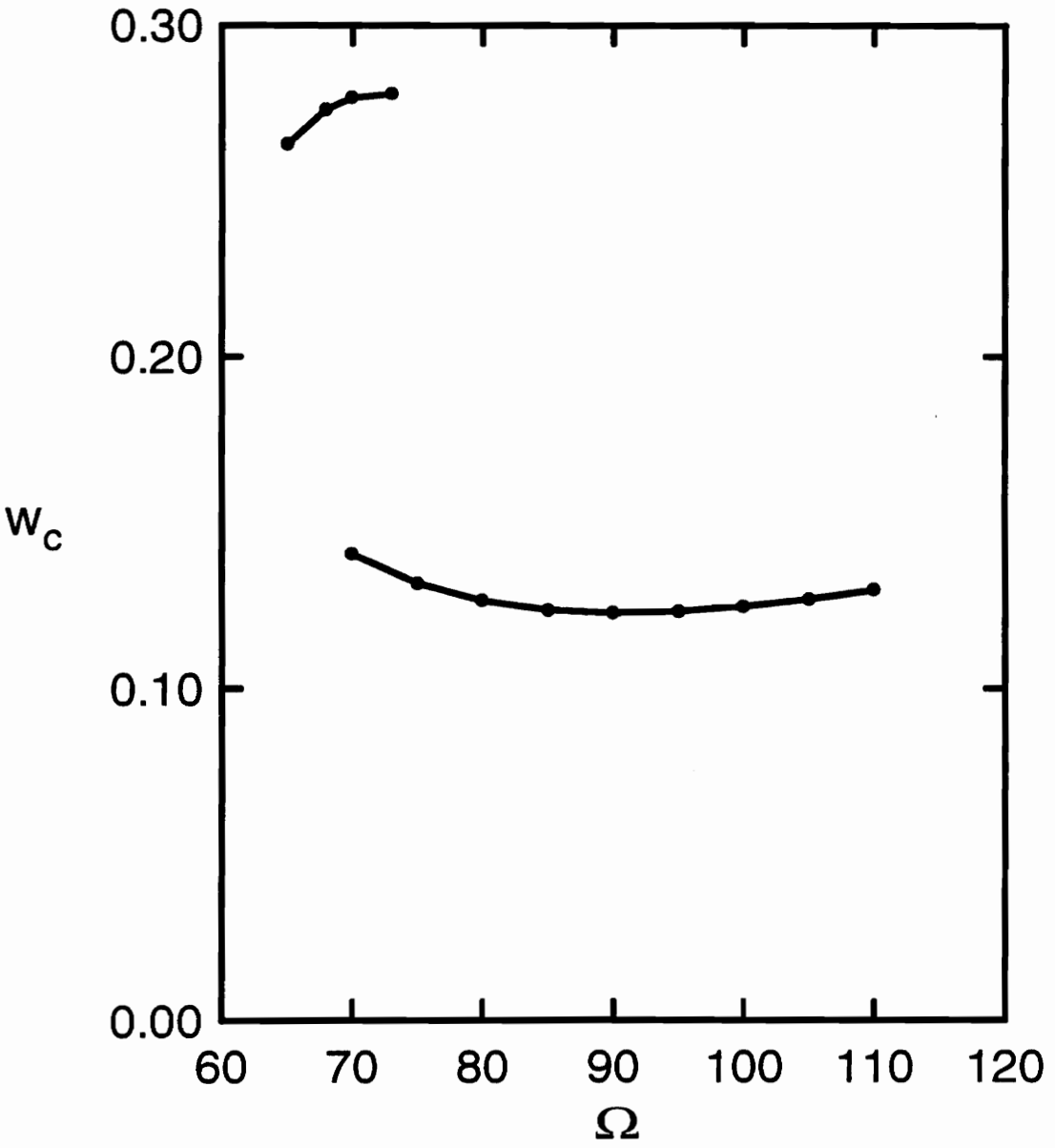

Figure 5.50: Maximum w_c vs. frequency, Ω, for a = 1.0.
(non shear deformable beam, r = 0.05)

Chapter 6

CONCLUSIONS

A procedure for simulating the vibration of a shear deformable beam with ends restrained against axial motion was developed. The Rayleigh-Ritz method was used to discretize the continuous system in space and yield a set of nonlinear ordinary differential equations governing the motion of the beam. The displacement was approximated by a finite series, and the resulting equations of motion were solved by numerical integration.

Damping was not included in the equations of motion, but it was recognized that there is some damping present in real systems. If damping is ignored entirely, all effects of initial conditions and loading history remain present in the simulated time history for any length of simulation. Several techniques were employed to reduce the appearance of the transient aspects of the solutions.

The techniques included controlling the rate at which the excitation function was applied and incorporating damping temporarily in the equations of motion. These techniques made it possible to obtain periodic responses with a harmonic excitation

function. Moreover, the general nature of the response does not appear to be affected by small differences in the excitation history.

Simulations were conducted for beams with two different cross section configurations subjected to harmonic excitation functions with various amplitudes and frequencies. The resulting time histories for all cases were compared to the corresponding time histories produced by neglecting shear deformation and rotatory inertia. Some trends in the response due to the differences in beam configuration and the strain model became apparent through the comparison.

The maximum absolute value of the generalized coordinates and maximum absolute value of the midspan displacement were plotted against excitation frequency for various excitation amplitudes. Only time histories which appeared to be periodic were considered for these plots. For certain ranges of excitation frequency it was possible to produce periodic time histories with two distinct maximum values, depending upon the way the exact excitation frequency and amplitude were approached.

For excitation frequencies near the first linear natural frequencies one term approximations were used for all displacement functions. The displacements were approximated by linear mode shapes.

The differences in the strain and kinetic energies between the shear deformable and non shear deformable cases did not result in any apparent differences in response for the slender beam. The maximum displacement seemed to be almost exactly the same for each excitation frequency and amplitude.

In the case of the thick beam the plots of the maximum displacement appeared very similar to those of the slender beam. However there was a small difference in the magnitudes of maximum displacement for the shear deformable and non shear deformable cases. Whether the shear deformable beam has a larger deflection than the non shear

deformable beam seems to depend on the frequency of the excitation function and, in the case of frequencies for which there is more than one maximum displacement, the history of the excitation function.

For excitation frequencies near the third linear natural frequency, the third linear mode shape was added to the approximate functions for transverse displacement and rotation. The approximate function for axial displacement still contained only one natural mode shape.

For the slender beam, the plots of the maximum values of the generalized coordinates and midspan displacement against excitation frequency were very similar for the shear deformable and non shear deformable cases. There were, however, small differences in the magnitude of the third generalized coordinate.

The simulations for the thick beam subjected to an excitation with a frequency near the third natural frequency produced substantially different results for the shear deformable and non shear deformable cases. The plots of the maximum values of the generalized coordinates for a range of frequencies from 60 to 120 were very dissimilar both in magnitude and appearance.

The results of these simulations suggest that the effects of shear deformation and rotatory inertia are smallest for long slender beams and low vibration frequencies. In the case of the slender beam subjected to a low frequency of excitation there was almost no noticeable difference in the response. In the cases of the thick beam subjected to a low frequency of excitation and the slender beam subjected to a high frequency of excitation there were small, but noticeable, differences in the response of the shear deformable and non shear deformable beams. In the case of the thick beam subjected to a high excitation frequency there were very substantial differences in the response of the shear deformable and non shear deformable beams.

Studying the response of a beam by numerical simulation is fairly simple and convenient. The method permits the application of nearly any form of excitation function which can be defined in a program subroutine. Increasing the number of terms in the approximate displacement functions is also not difficult. It requires no further analysis, and the increased burden falls primarily on the computer.

This method does, however, have important limitations. Perhaps one of the most obvious limitations appears in the cases for which the simulations did not yield a periodic solution or the simulation yielded displacements as large as the length of the beam. The failure of the method to produce a periodic response to a given excitation does not imply the lack of a periodic response for that excitation, but only that these cases should be investigated by other techniques. It is only when a simple periodic response is obtained that it can be said with reasonable certainty that a stable periodic solution exists.

It is also not possible to say that there are not more stable solutions than were obtained by varying the amplitude and frequency of excitation. It can be concluded that there are at least two solutions for certain ranges of excitation frequency and amplitude, but there could be more which were not arrived at by the methods employed.

It is probably necessary to apply an approximate analytical technique to study the solution in detail. This would not have the disadvantage of having to begin a simulation at a certain point in the phase plane and waiting to see what type of motion develops. All aspects of the solution, both stable and unstable, could be considered.

The usefulness of the simulation approach is limited without some knowledge of the nature of the solution to start with. However, it could be used in conjunction with approximate analytical techniques to confirm, or possibly to refute, solutions obtained by such techniques.

REFERENCES

Abramovich, H., (1992), "Shear deformation and rotary inertia effects of vibrating composite beams", *Composite Structures*, Vol. 20, pp. 165-173

Abramovich, H. and Eilishakoff, I., (1987), "Application of the Krein's Method for Determination of Natural Frequencies of Periodically Supported Beam Based on Simplified Bresse-Timoshenko Equations", *Acta Mechanica*, Vol. 66, pp. 39-59

Abramovich, H. and Elishakoff, I., (1990), "Influence of Shear Deformation and Rotary Inertia on Vibration Frequencies Via Love's Equations", *Journal of Sound and Vibration,* Vol. 137, No. 3, pp. 516-522

Benamar, R., Bennouna, M. M. K., White, R. G., (1991), "The Effects of Large Vibration Amplitudes on the Mode Shapes and Natural Frequencies of Thin Elastic Structures Part I: Simply Supported and Clamped-Clamped Beams", *Journal of Sound and Vibration*, Vol. 149, No. 2, pp. 179-195

Bennett, J. A. and Eisley, J. G., (1970), "A Multiple Degree-of-Freedom Approach to Nonlinear Beam Vibrations", *AIAA Journal*, Vol. 8, No. 4, pp. 734-739

Bennouna, M. M. and White, R. G., (1984), "The Effects of Large Vibration Amplitudes on the Fundamental Mode Shape of a Clamped-Clamped Uniform Beam", *Journal of Sound and Vibration*, Vol. 96, No. 3, pp. 309-331

Busby, H. R. Jr. and Weingarten, V. I., (1972), "Non-Linear Response of a Beam to Periodic Loading", *International Journal of Non-Linear Mechanics*, Vol. 7, pp. 289-303

Busby, H. R. Jr. and Weingarten, V. I., (1973), "Dynamic Stability of a Nonlinear Beam Subjected to Both Longitudinal and Transverse Excitation", *Developments in Mechanics, Proceedings of the 13th Midwestern Mechanics Conference*, Vol. 7, pp. 367-382

Datta, P. K. and Ganguli, R. (1990), "Vibration Characteristics of a Rotating Blade with Localized Damage Including the Effects of Shear Deformation and Rotary Inertia", *Computers & Structures*, Vol. 36, No. 6, pp. 1129-1133

Dawe, D. J. and Roufaeil, O. L., (1980), "Rayleigh-Ritz Vibration Analysis of Mindlin Plates", *Journal of Sound and Vibration*, Vol. 69, No. 3, pp. 345-359

Eisley, J. G. and Bennett J. A., (1970), "Stability of Large Amplitude Forced Motion of a Simply Supported Beam", *International Journal of Non-Linear Mechanics*, Vol. 5, pp. 645-657

Fertis, D. G. and Lee, C. T., (1992), "Nonlinear Vibration of Axially Restraint Elastically Supported Beams", *Dynamics and Vibrations*, ASME, PD-Vol. 44, pp. 13-19

Hsieh, J., (1984), "Nonlinear Oscillations of a Shallow Arch Under Multifrequency Excitation", VPI & SU Masters Thesis

Humar, J. L., (1990), *Dynamics of Structures*, Prentice Hall, Englewood Cliffs, NJ

IMSL, (1991), *User's Manual, FORTRAN subroutines for mathematical applications*, IMSL, Inc.

Morris, N. F., (1965), "The Dynamic Stability of Beam-Columns with a Fixed Distance Between Supports", *Journal of the Franklin Institute*, Vol. 280, pp. 163-173

Nayfeh, A. H. and Mook, D. T., (1979), *Nonlinear Oscillations*, John Wiley & Sons, New York, NY

Pillai, S. R. R. and Rao, B. N., (1992), "On Nonlinear Free Vibrations of Simply Supported Uniform Beams", *Journal of Sound and Vibration*, Vol. 159, No. 3, pp. 527-531

Plaut, R. H., (1971), "Displacement Bounds for Beam-Columns with Initial Curvature Subjected to Transient Loads", *International Journal of Solids and Structures*, Vol. 7, pp. 1229-1235

Ray, J. D. and Bert, C. W., (1969), "Nonlinear Vibrations of a Beam With Pinned Ends", *Journal of Engineering for Industry*, ASME, Vol. 91, pp. 997-1004

Rehfield, L. W., (1974), "Large Amplitude Forced Vibrations of Elastic Structures", *AIAA Journal*, Vol. 12, No. 3, pp. 388-390

Sevin, E., (1960), "On the Elastic Bending of Columns Due to Dynamic Axial Forces Including Effects of Axial Inertia", *Journal of Applied Mechanics*, ASME, Vol. 27, pp. 125-131

Singh, G., Sharma, A. K., Rao, G. V., (1990), "Large-Amplitude Free Vibrations of Beams - A Discussion on Various Formulations and Assumptions", *Journal of Sound and Vibration*, Vol. 142, No. 1, pp. 77-85

Singh, G., Rao, G. V., Iyengar, N. G. R., (1990), "Re-Investigation of Large-Amplitude Free Vibrations of Beams Using Finite Elements", *Journal of Sound and Vibration*, Vol. 143, No. 2, pp. 351-355

Tseng, W. Y. and Dugundji, J., (1970), "Nonlinear Vibrations of a Beam Under Harmonic Excitation", *Journal of Applied Mechanics*, ASME, Vol. 37, pp. 292-297

Ueda, Y., (1980), "Steady Motions Exhibited by Duffing's Equation: A Picture Book of Regular and Chaotic Motions", *New Approaches to Nonlinear Problems in Dynamics*, edited by Holmes, P. J., Siam, Philadelphia

Appendix A

PHASE PORTRAITS

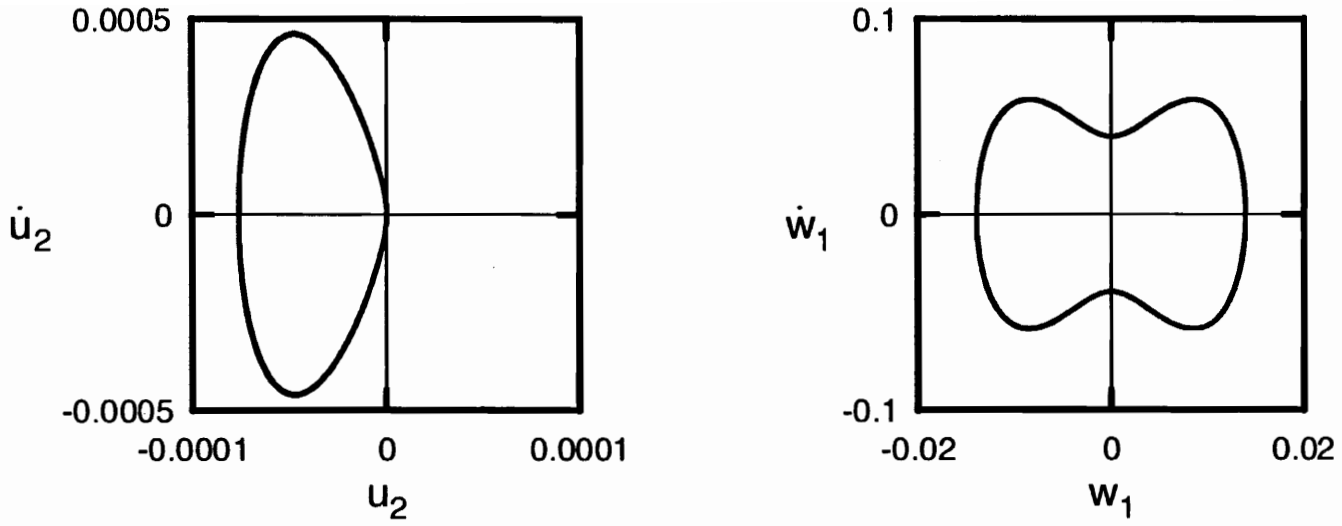

Figure A.1: Phase portraits for shear deformable beam with $r = 0.01$, $\Omega = 5.0$, $a = 0.0001$.

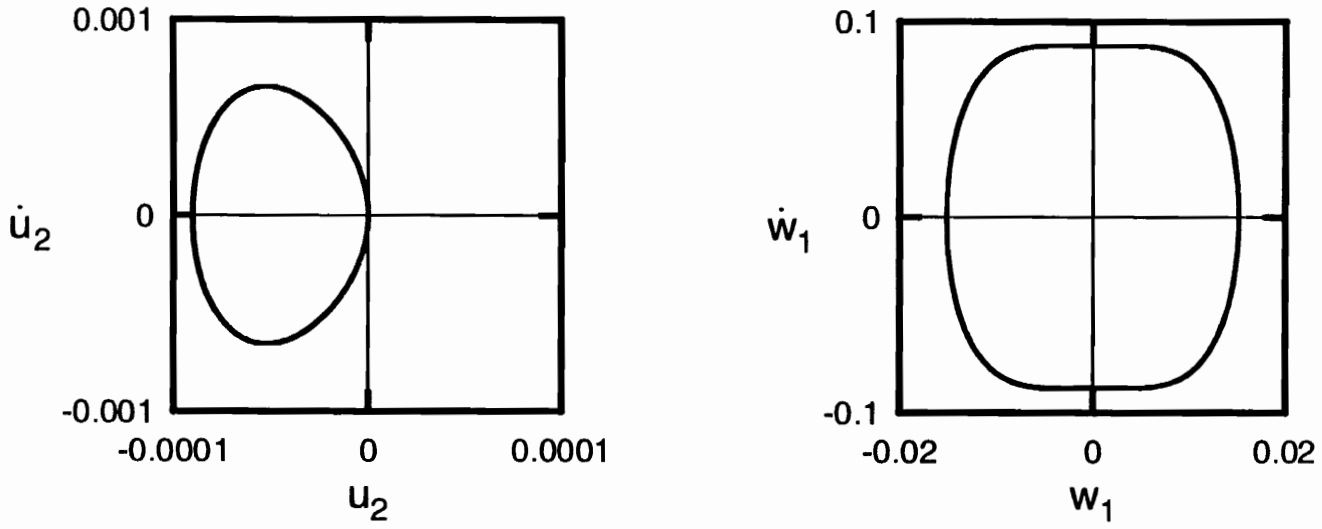

Figure A.2: Phase portraits for shear deformable beam with $r = 0.01$, $\Omega = 7.0$, $a = 0.0001$.

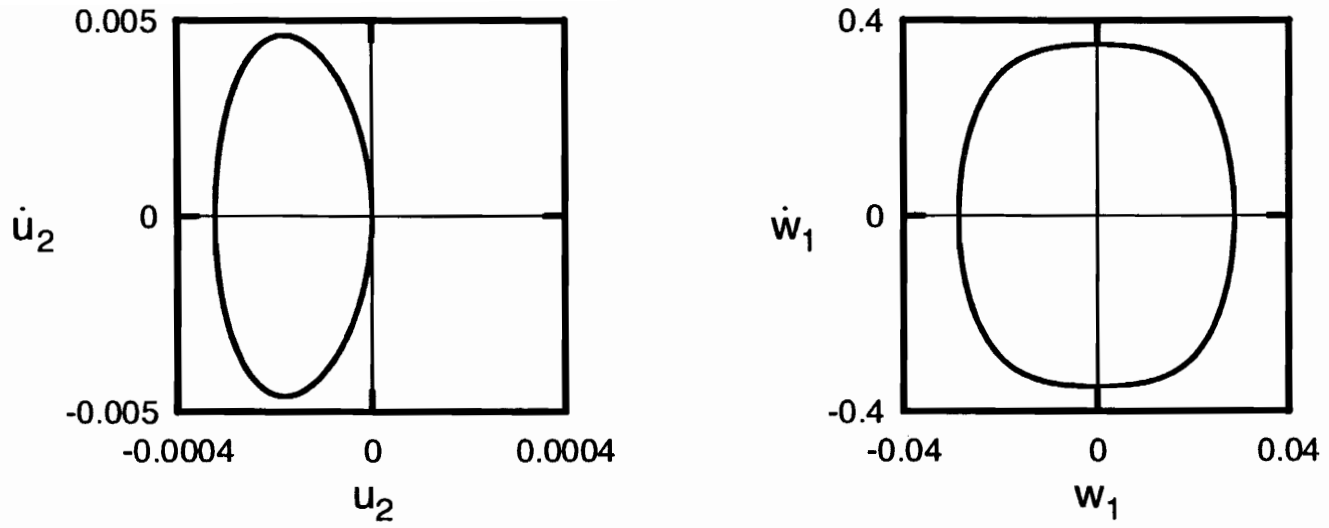

Figure A.3: Phase portraits for shear deformable beam with $r = 0.01$, $\Omega = 14.0$, $a = 0.0001$.

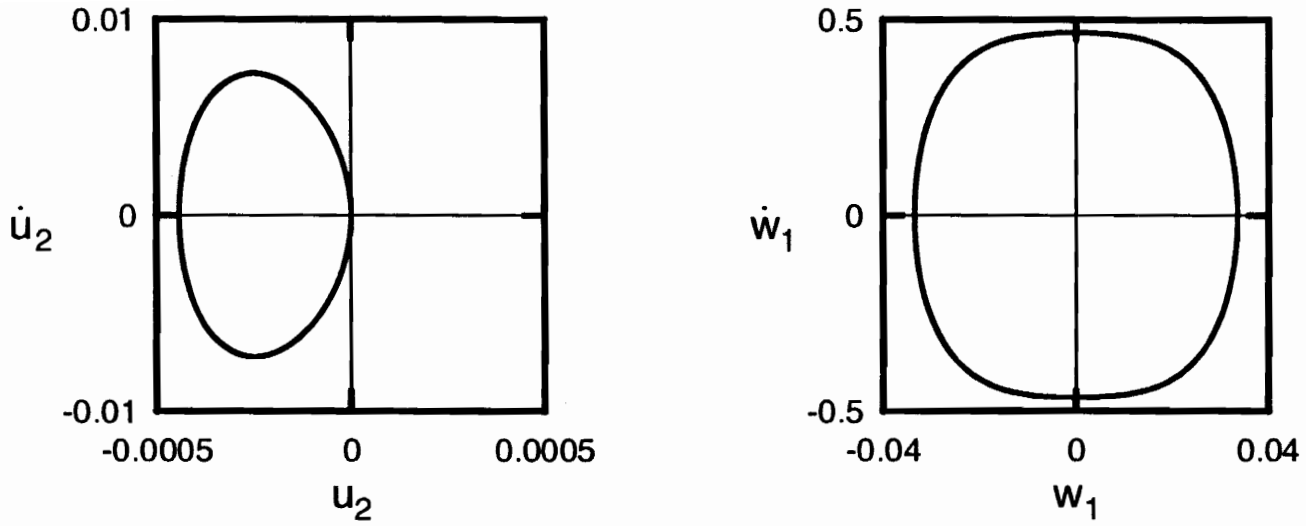

Figure A.4: Phase portraits for shear deformable beam with $r = 0.01$, $\Omega = 16.0$, $a = 0.0001$.

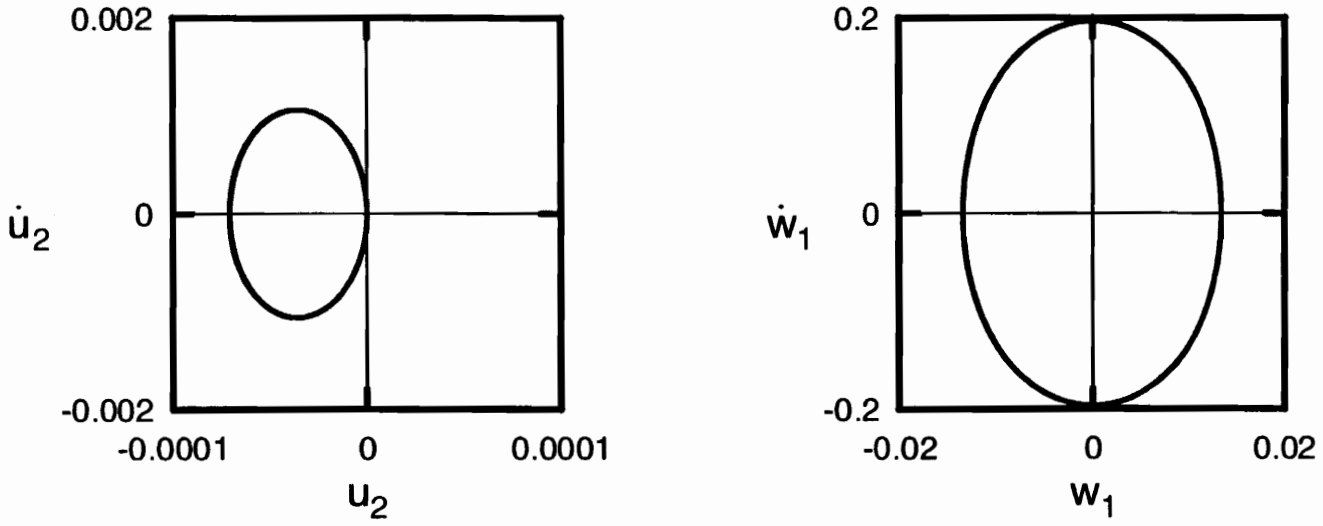

Figure A.5: Phase portraits for shear deformable beam with $r = 0.01$, $\Omega = 15.0$, $a = 0.0001$.

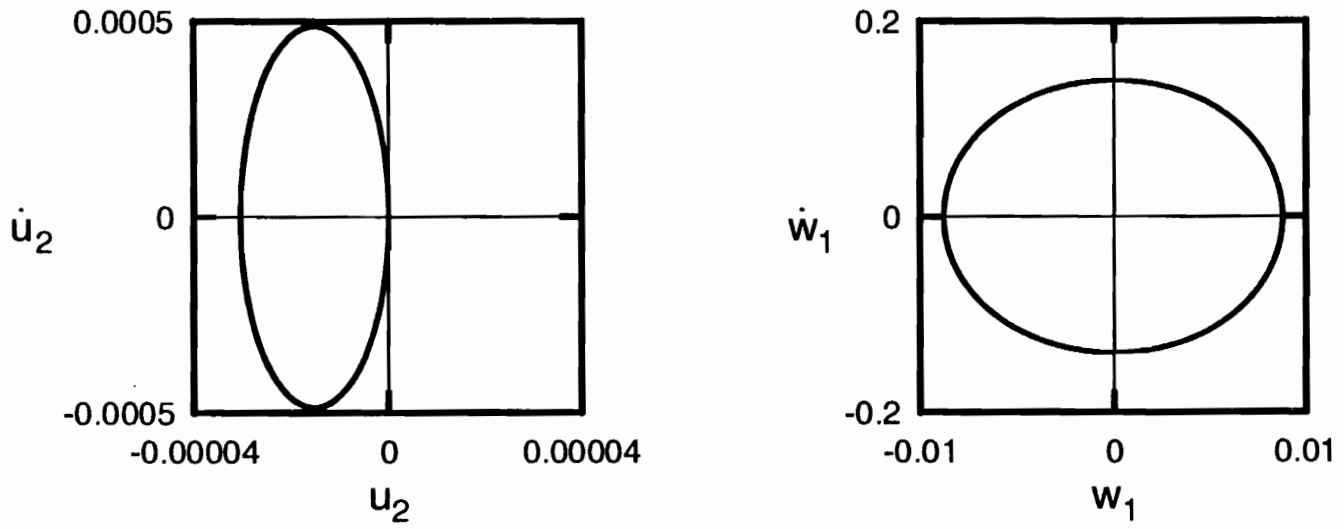

Figure A.6: Phase portraits for shear deformable beam with $r = 0.01$, $\Omega = 16.0$, $a = 0.0001$.

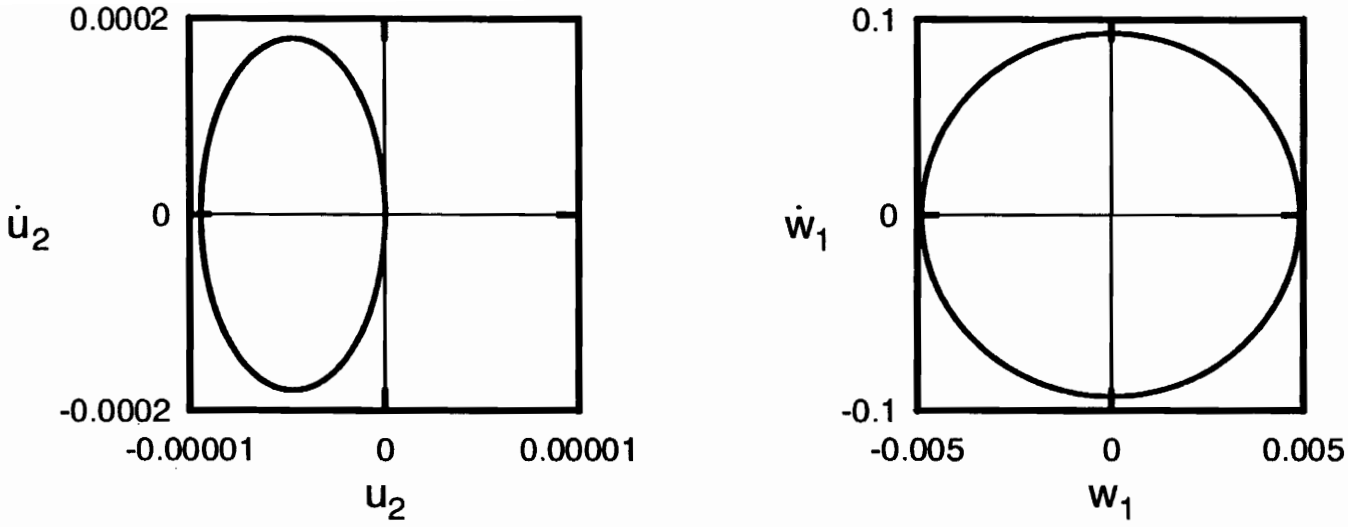

Figure A.7: Phase portraits for shear deformable beam with $r = 0.01$, $\Omega = 19.0$, $a = 0.0001$.

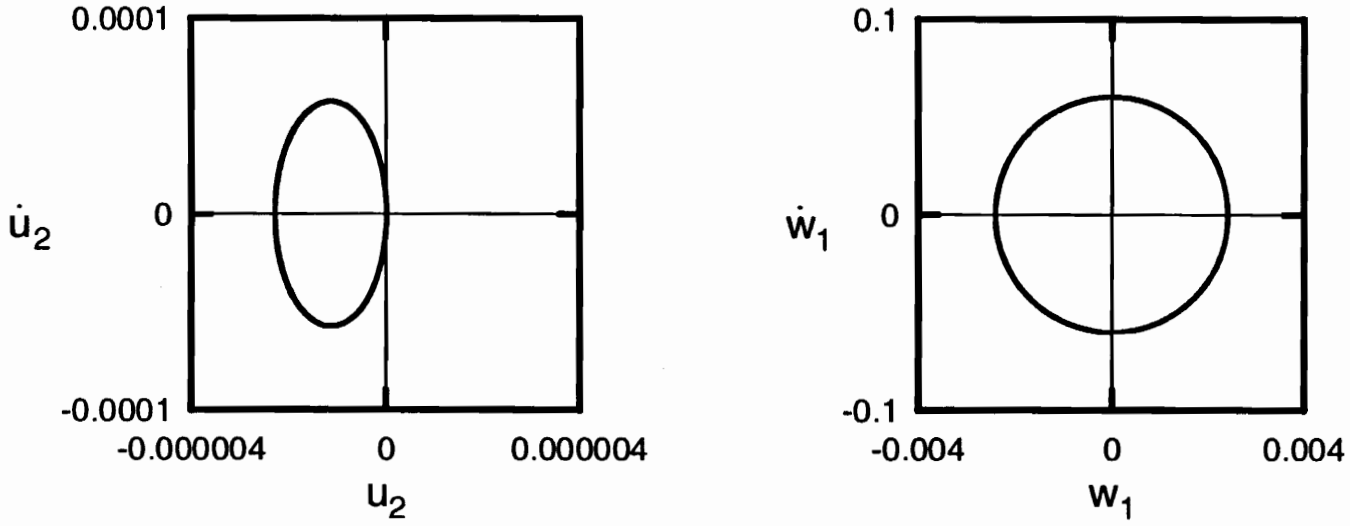

Figure A.8: Phase portraits for shear deformable beam with $r = 0.01$, $\Omega = 25.0$, $a = 0.0001$.

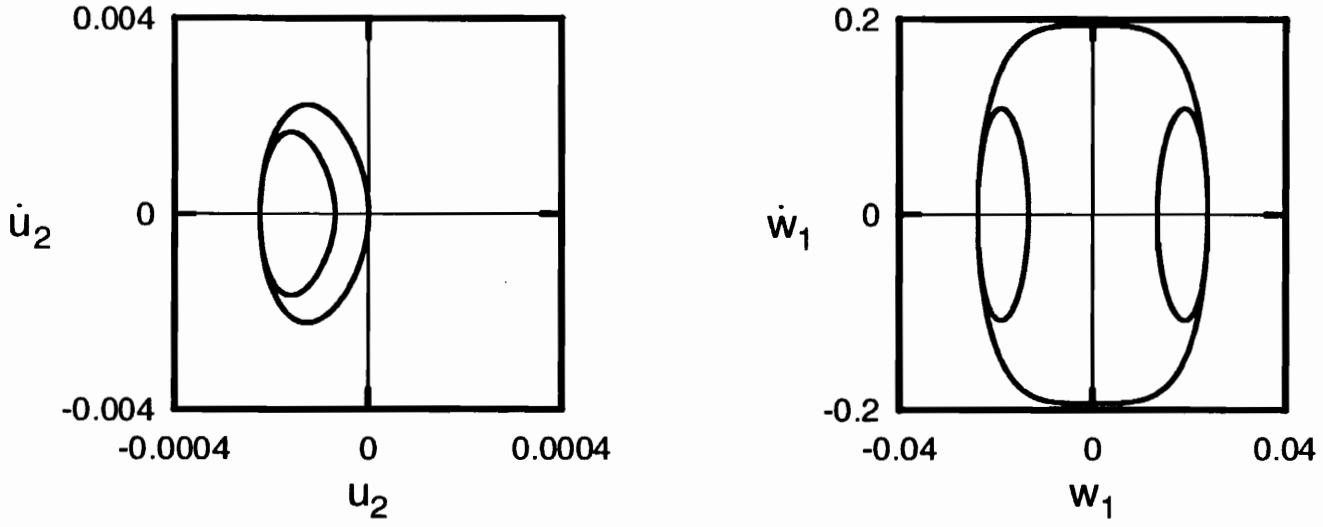

Figure A.9: Phase portraits for shear deformable beam with $r = 0.01$, $\Omega = 5.0$, $a = 0.0003$.

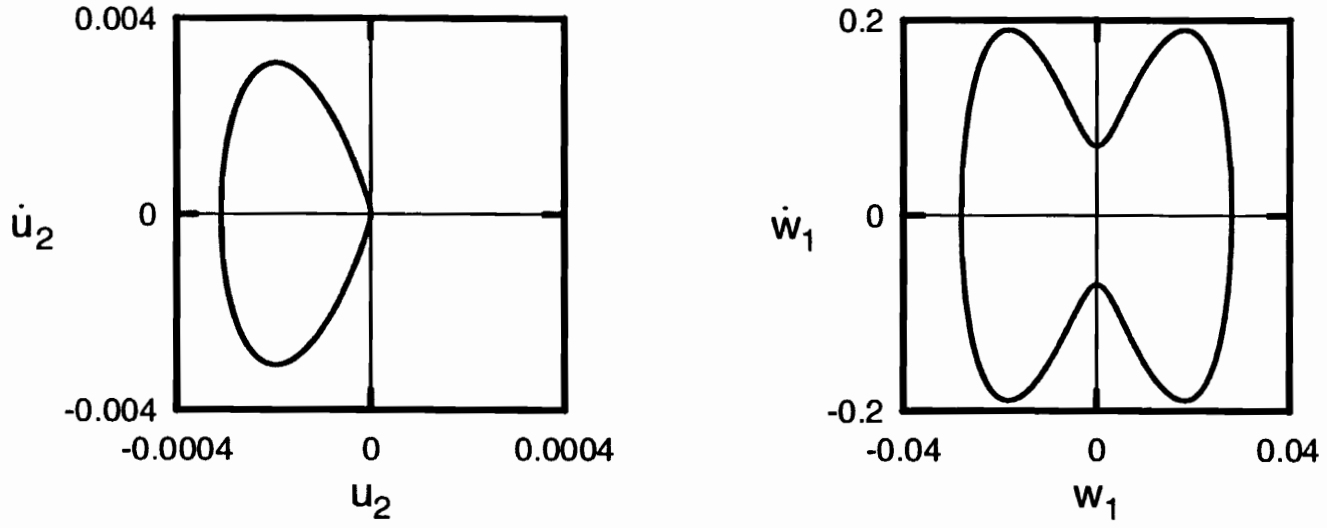

Figure A.10: Phase portraits for shear deformable beam with $r = 0.01$, $\Omega = 7.0$, $a = 0.0003$.

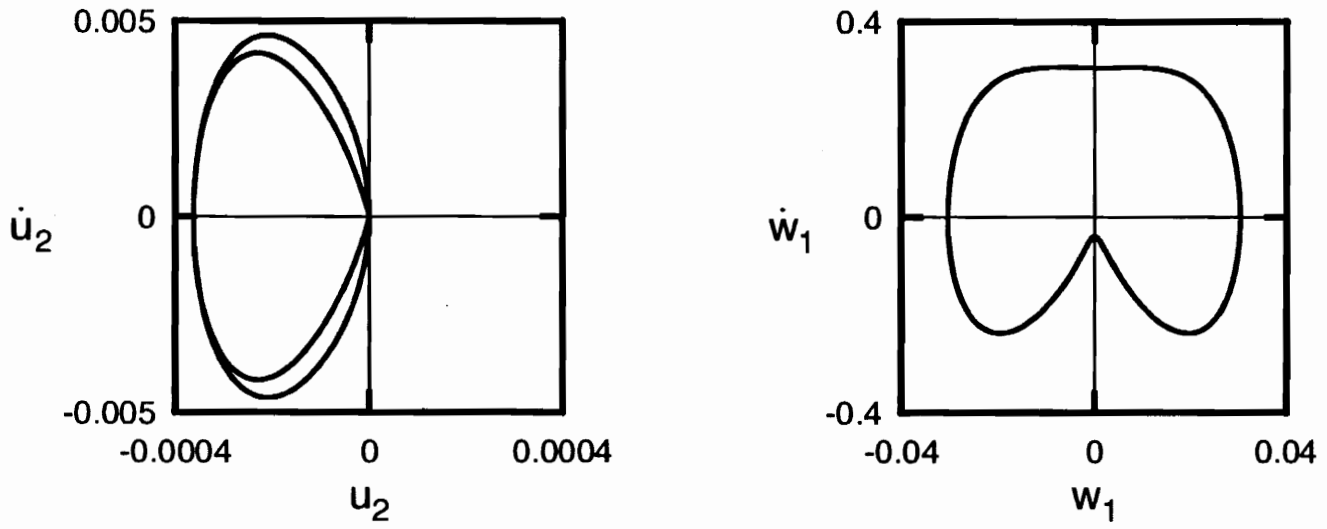

Figure A.11: Phase portraits for shear deformable beam with $r = 0.01,\ \Omega = 9.0,\ a = 0.0003$.

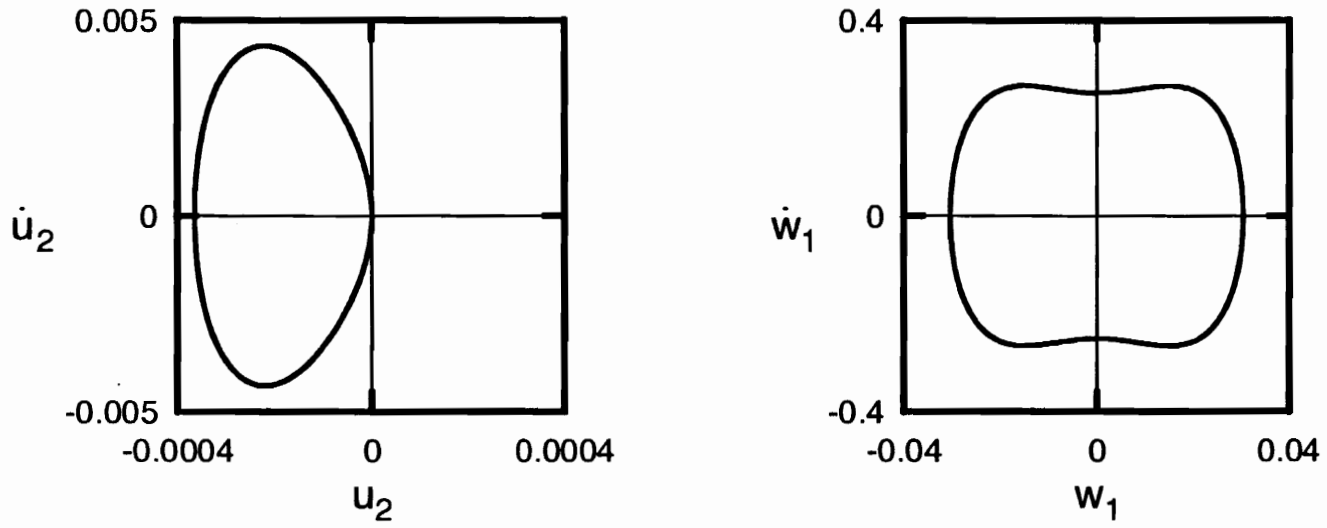

Figure A.12: Phase portraits for shear deformable beam with $r = 0.01$, $\Omega = 11.0$, $a = 0.0003$.

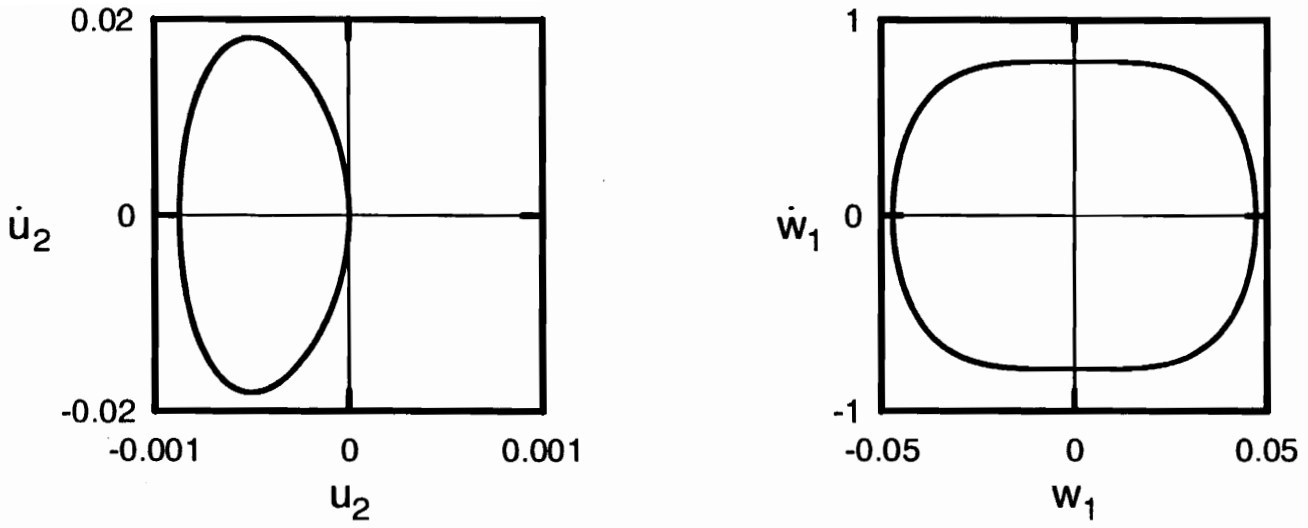

Figure A.13: Phase portraits for shear deformable beam with $r = 0.01$, $\Omega = 20.0$, $a = 0.0003$.

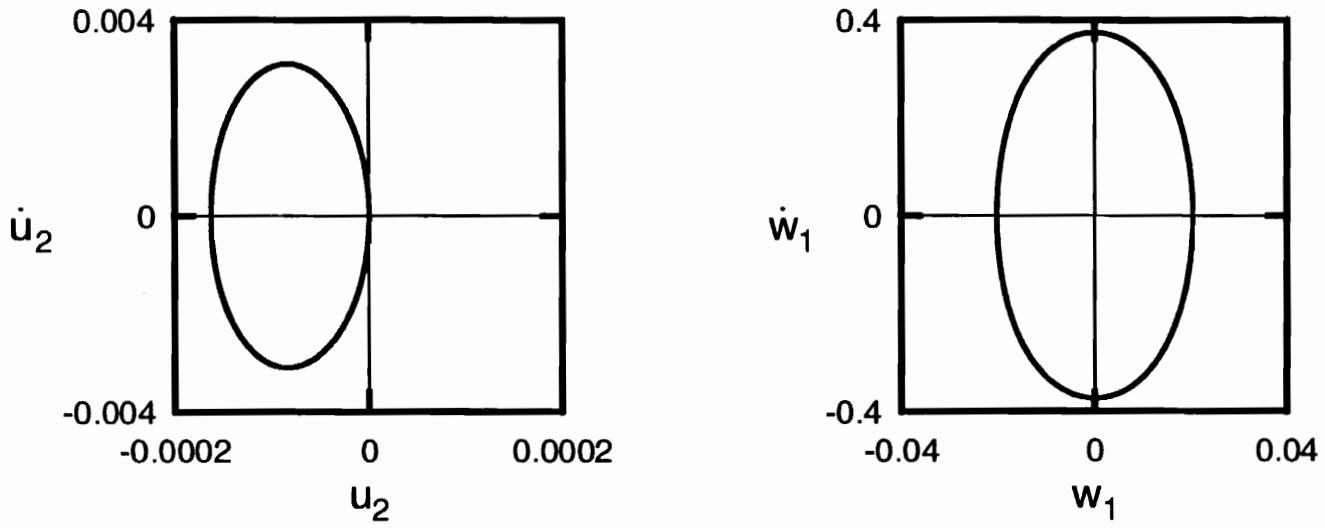

Figure A.14: Phase portraits for shear deformable beam with $r = 0.01$, $\Omega = 19.0$, $a = 0.0003$.

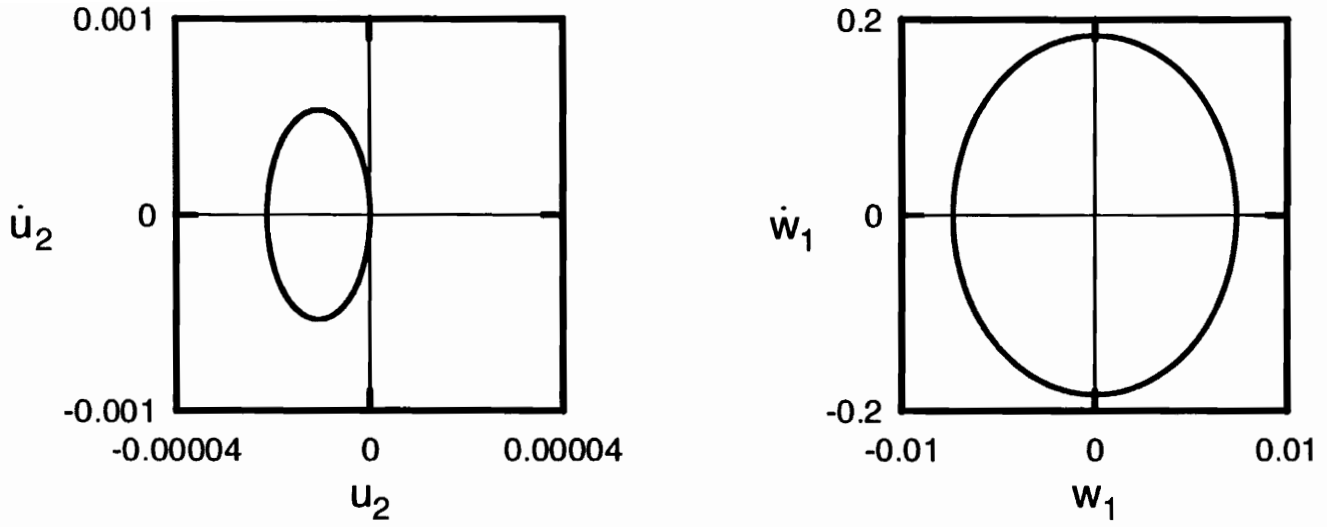

Figure A.15: Phase portraits for shear deformable beam with $r = 0.01$, $\Omega = 25.0$, $a = 0.0003$.

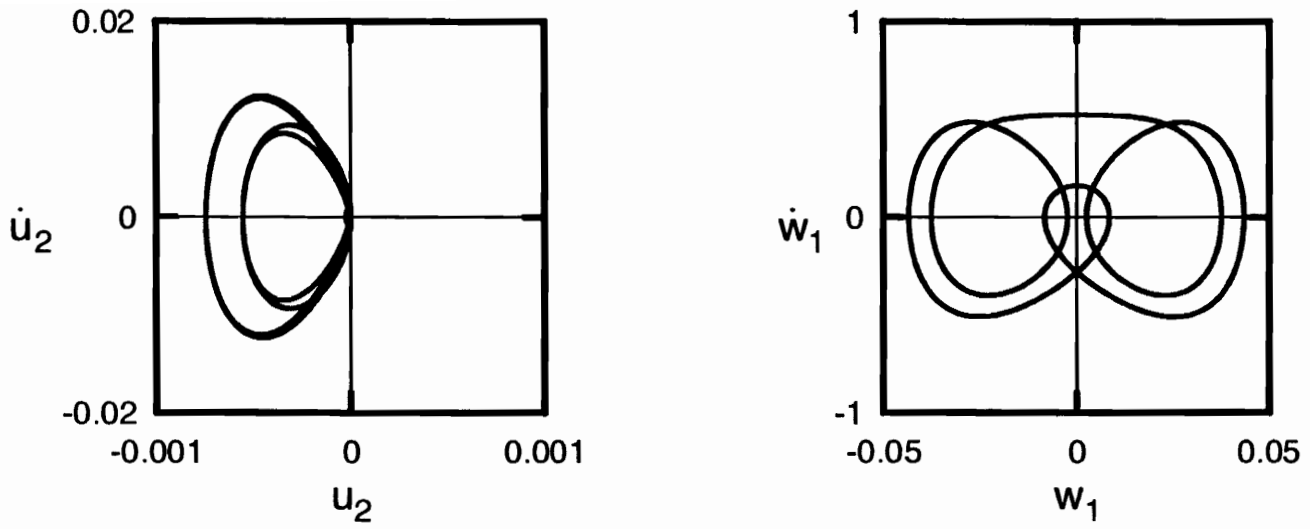

Figure A.16: Phase portraits for shear deformable beam with $r = 0.01,\ \Omega = 5.0,\ a = 0.0006$.

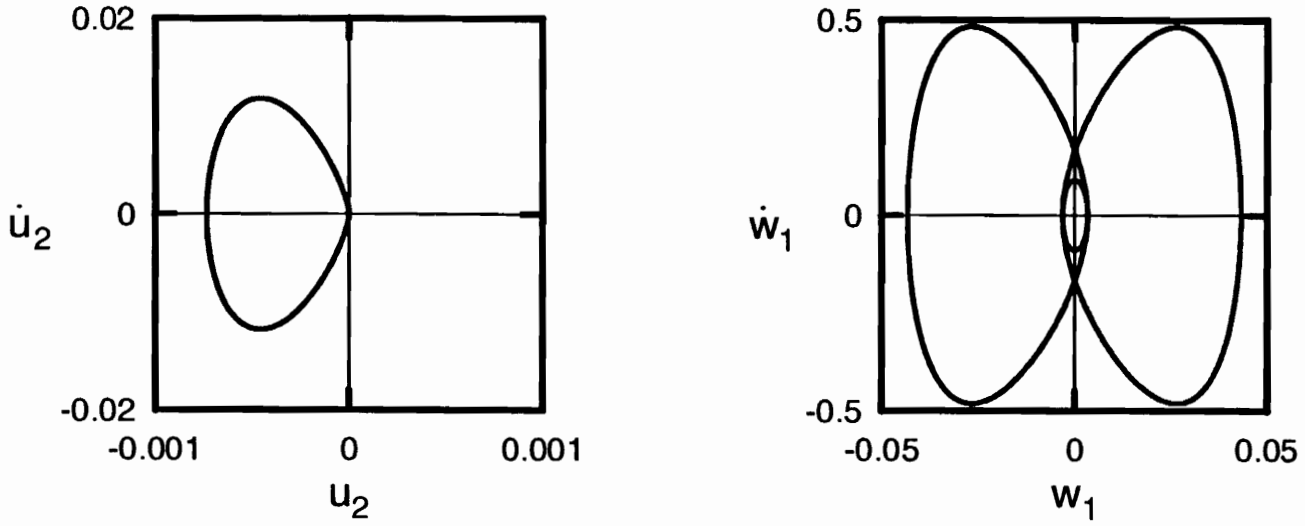

Figure A.17: Phase portraits for shear deformable beam with $r = 0.01,\ \Omega = 7.0,\ a = 0.0006$.

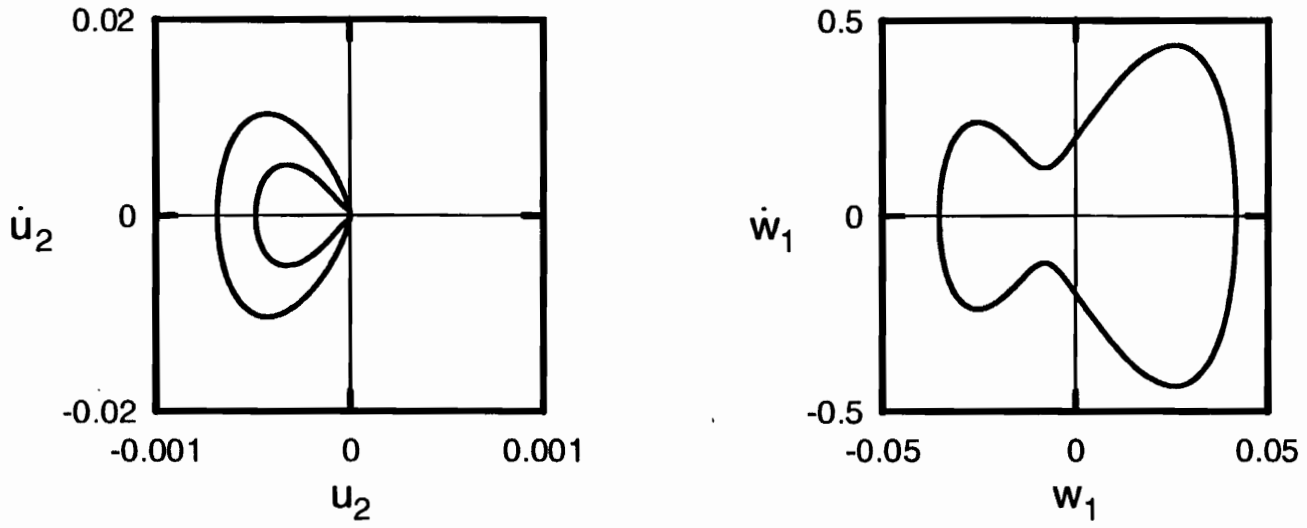

Figure A.18: Phase portraits for shear deformable beam with $r = 0.01,\ \Omega = 9.0,\ a = 0.0006$.

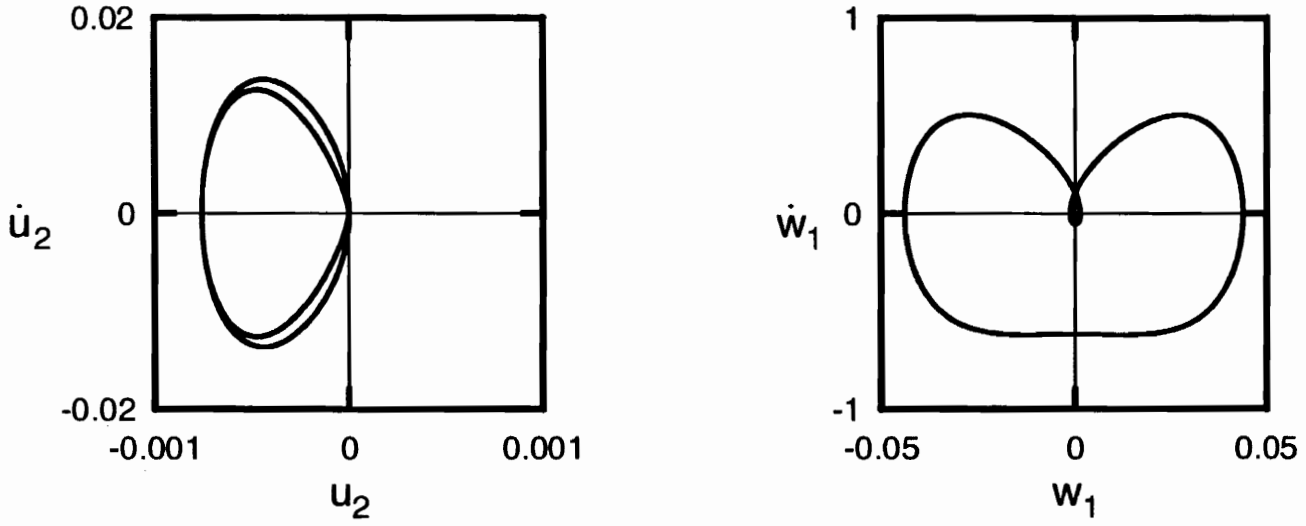

Figure A.19: Phase portraits for shear deformable beam with $r = 0.01$, $\Omega = 11.0$, $a = 0.0006$.

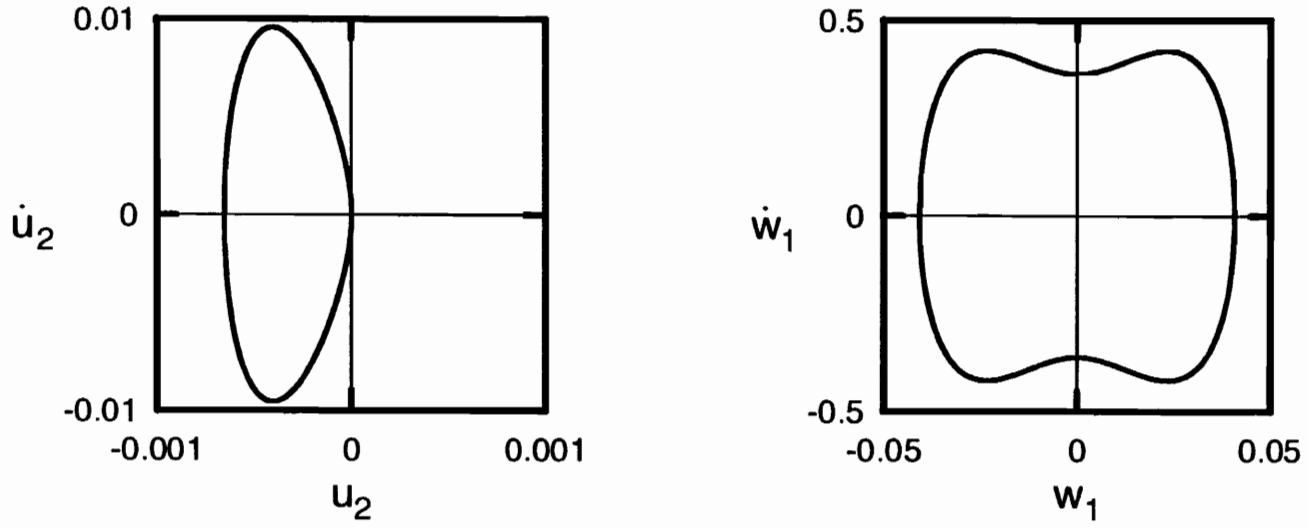

Figure A.20: Phase portraits for shear deformable beam with $r = 0.01$, $\Omega = 13.0$, $a = 0.0006$.

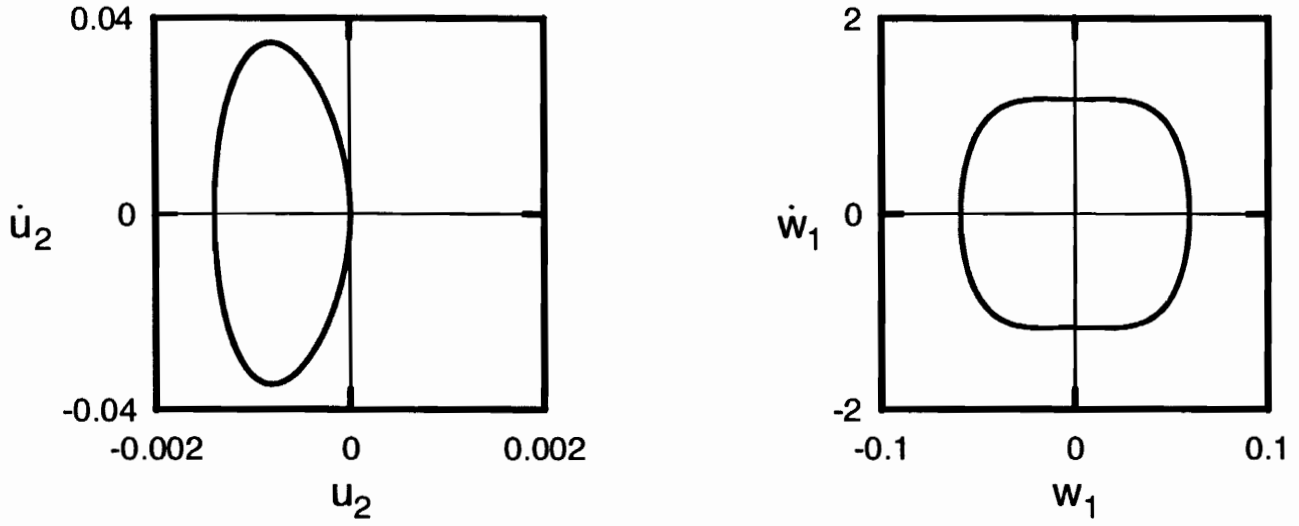

Figure A.21: Phase portraits for shear deformable beam with $r = 0.01$, $\Omega = 24.0$, $a = 0.0006$.

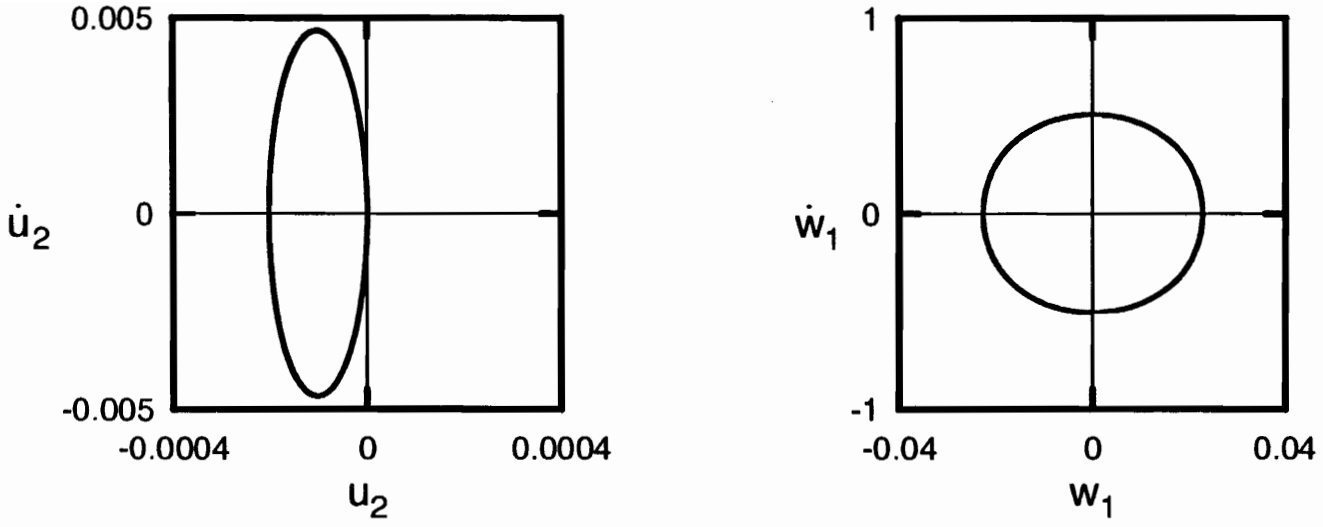

Figure A.22: Phase portraits for shear deformable beam with $r = 0.01$, $\Omega = 23.0$, $a = 0.0006$.

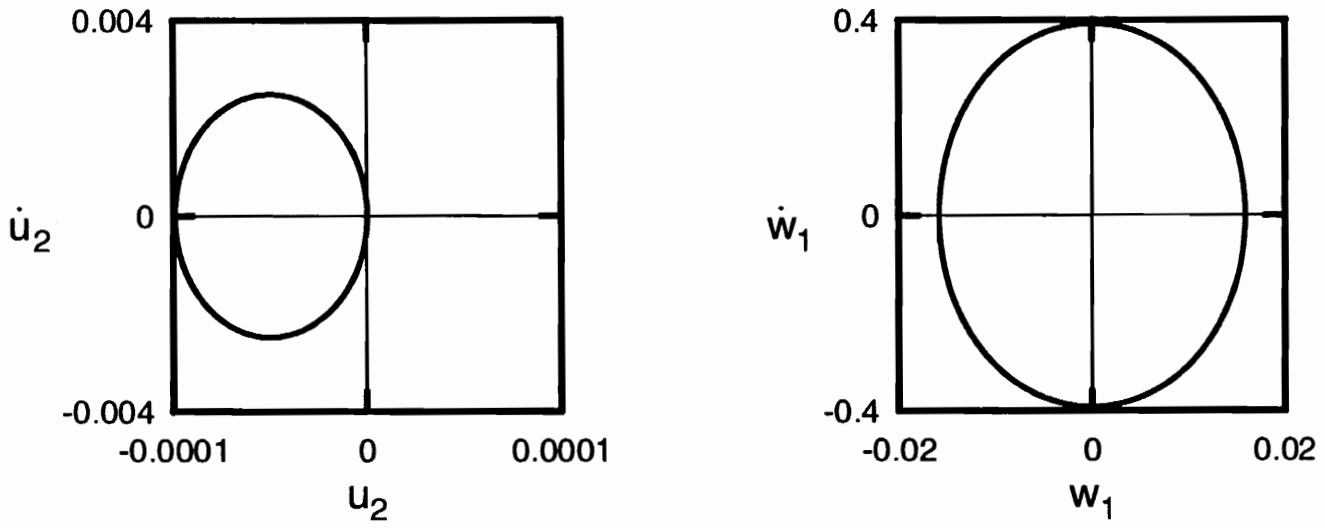

Figure A.23: Phase portraits for shear deformable beam with $r = 0.01$, $\Omega = 25.0$, $a = 0.0006$.

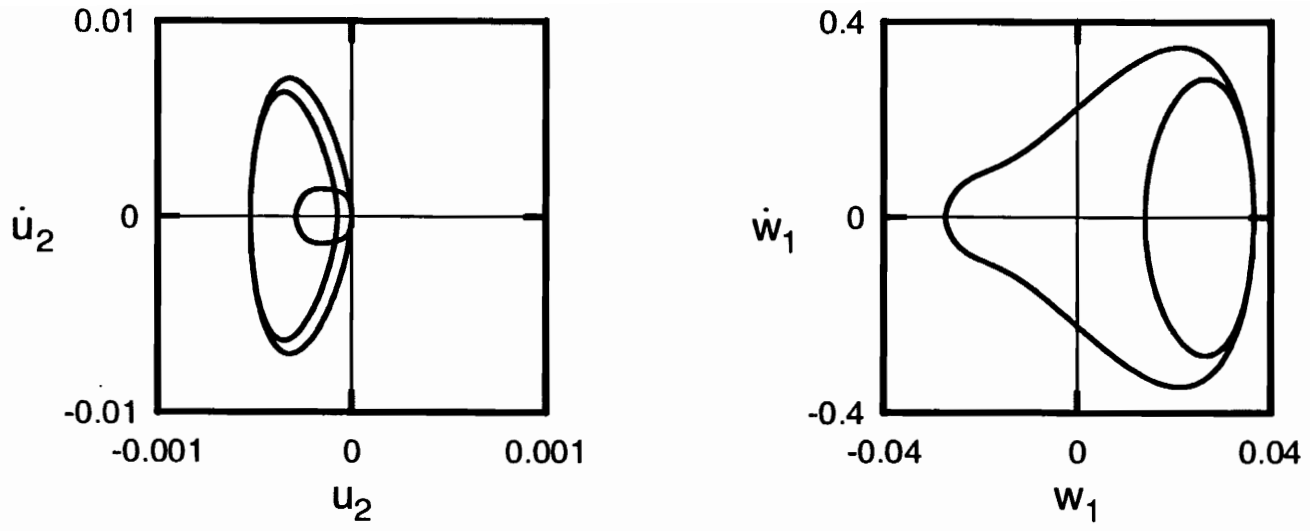

Figure A.24: Phase portraits for non shear deformable beam with $r = 0.01$, $\Omega = 5.0$, $a = 0.0006$.

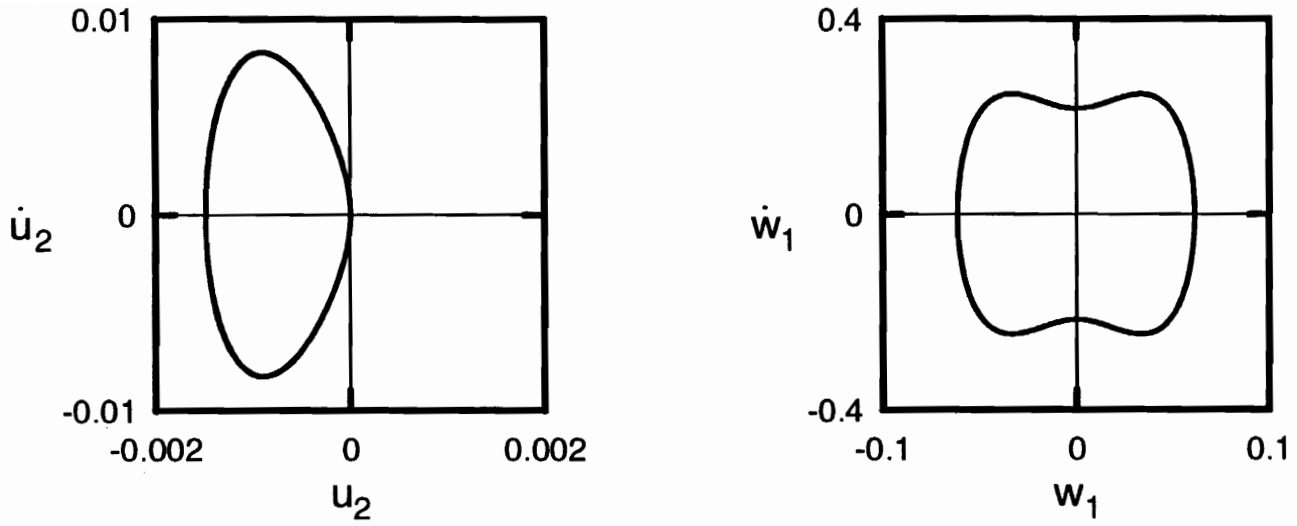

Figure A.25: Phase portraits for shear deformable beam with $r = 0.05$, $\Omega = 5.0$, $a = 0.01$.

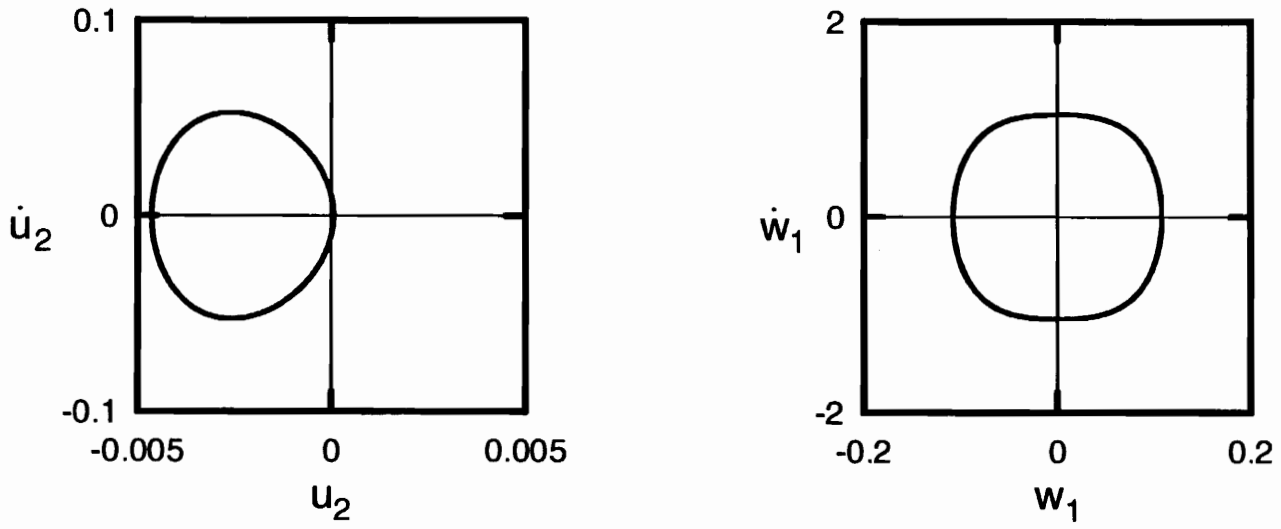

Figure A.26: Phase portraits for shear deformable beam with $r = 0.05$, $\Omega = 11.0$, $a = 0.01$.

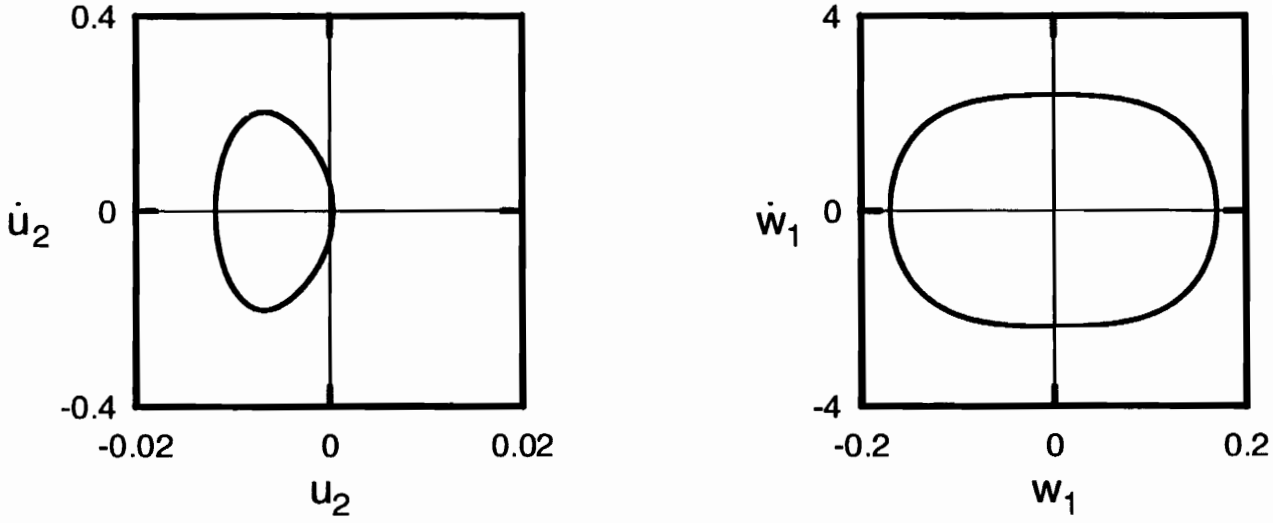

Figure A.27: Phase portraits for shear deformable beam with $r = 0.05$, $\Omega = 16.0$, $a = 0.01$.

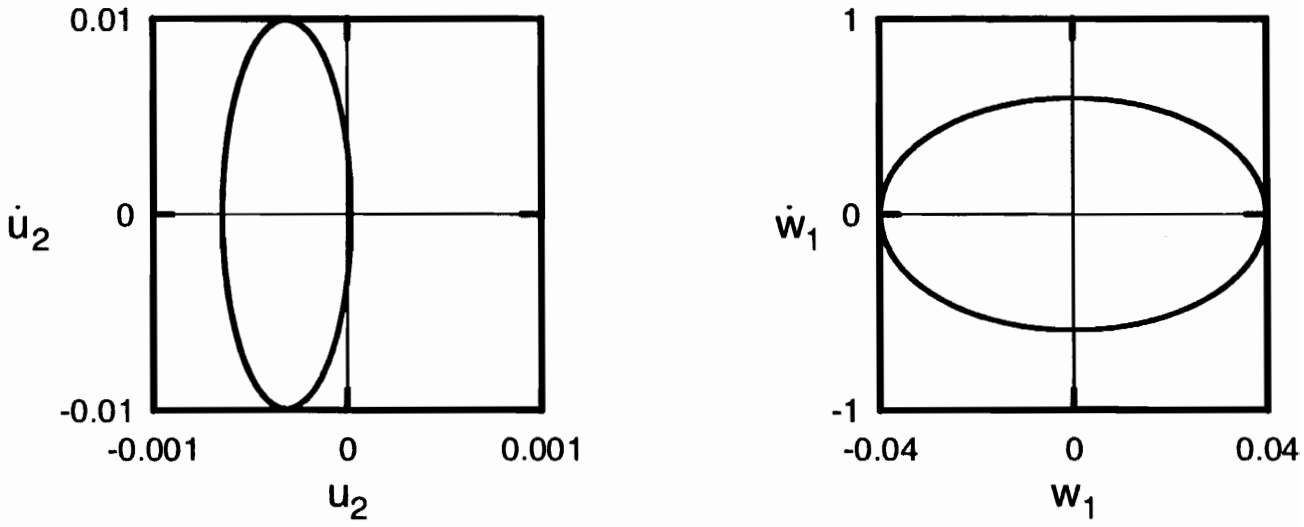

Figure A.28: Phase portraits for shear deformable beam with $r = 0.05$, $\Omega = 15.0$, $a = 0.01$.

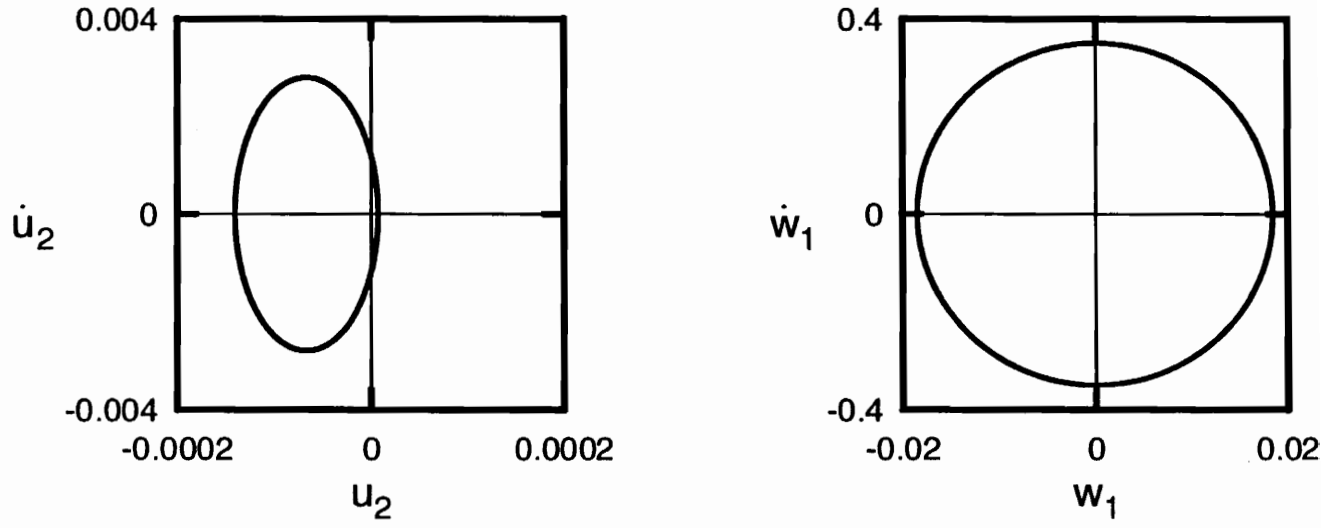

Figure A.29: Phase portraits for shear deformable beam with $r = 0.05$, $\Omega = 19.0$, $a = 0.01$.

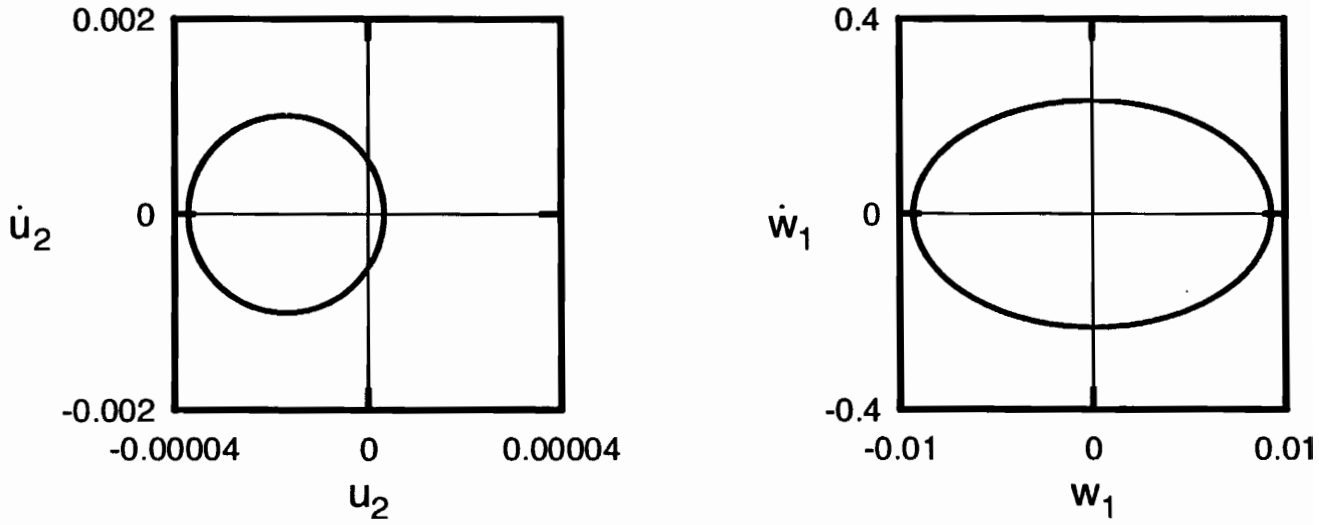

Figure A.30: Phase portraits for shear deformable beam with $r = 0.05$, $\Omega = 25.0$, $a = 0.01$.

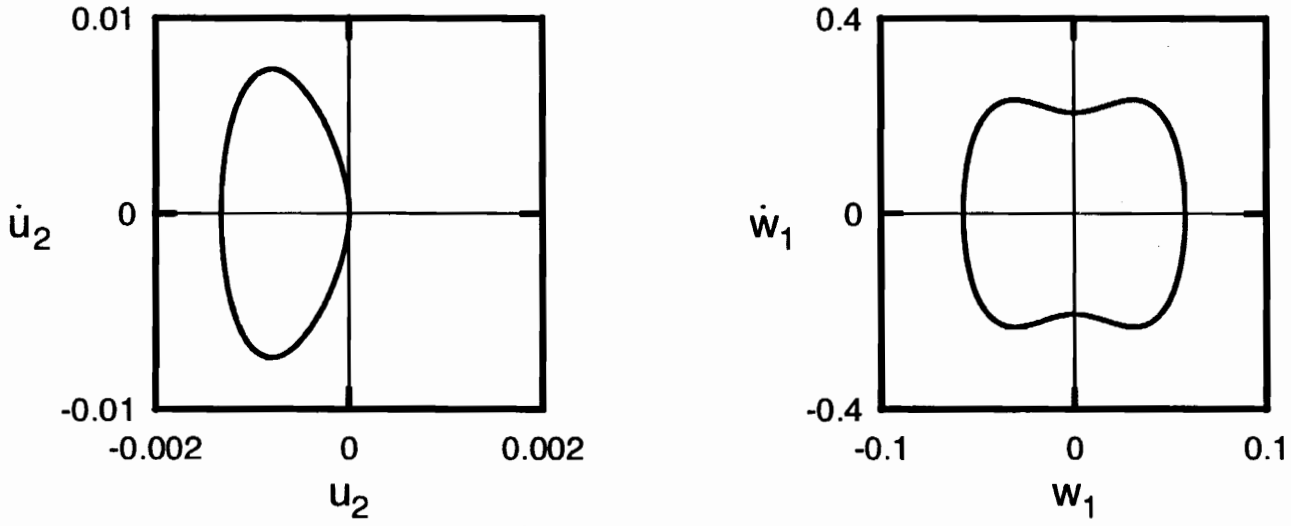

Figure A.31: Phase portraits for non shear deformable beam with $r = 0.05$, $\Omega = 5.0$, $a = 0.01$.

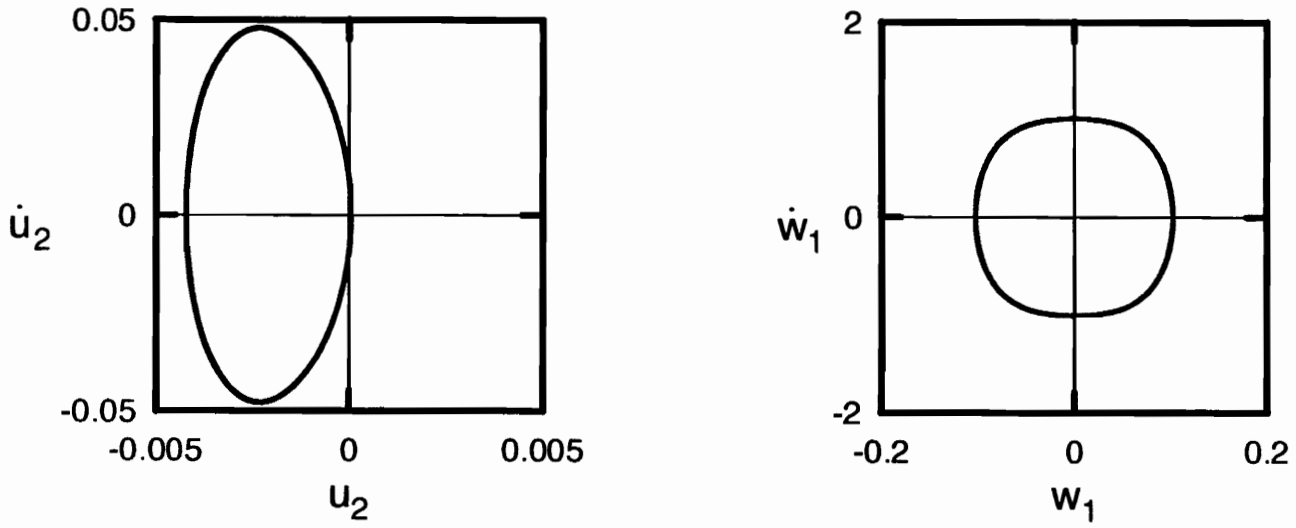

Figure A.32: Phase portraits for non shear deformable beam with $r = 0.05$, $\Omega = 11.0$, $a = 0.01$.

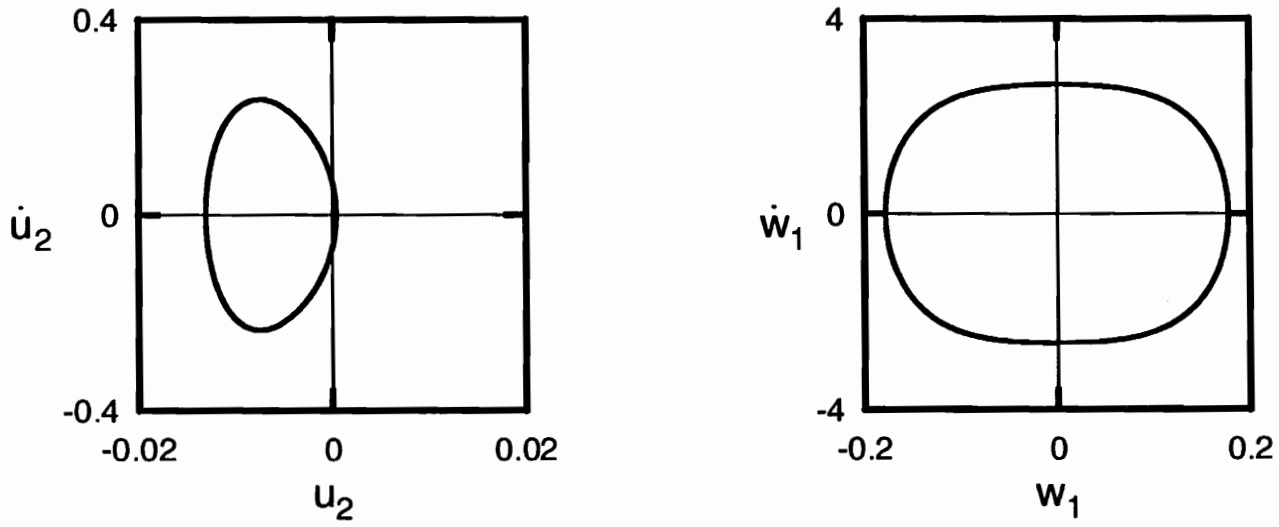

Figure A.33: Phase portraits for non shear deformable beam with $r = 0.05$, $\Omega = 17.0$, $a = 0.01$.

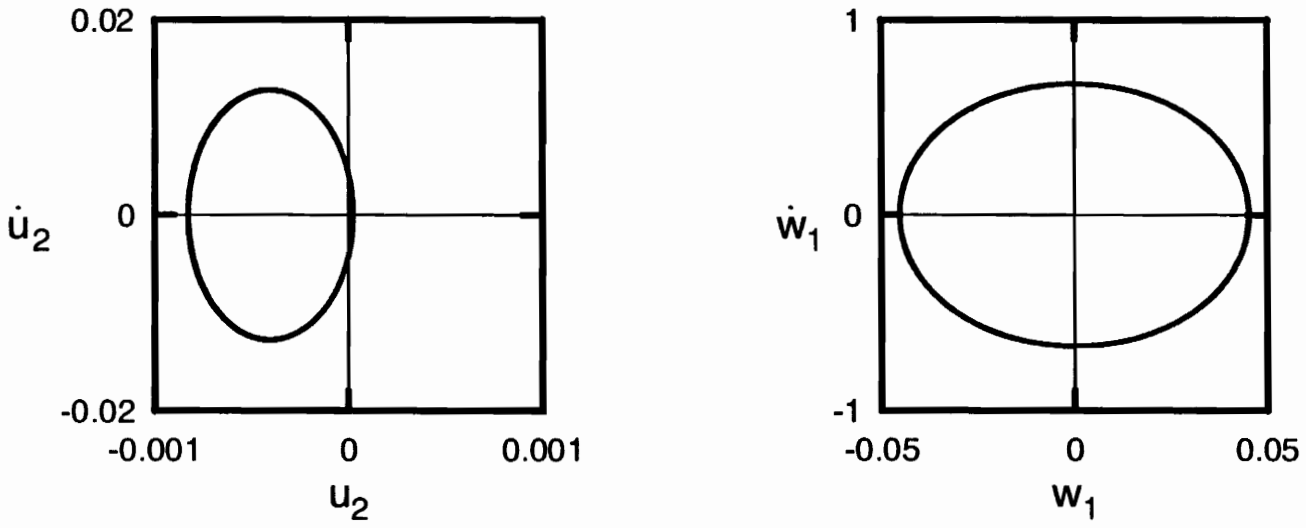

Figure A.34: Phase portraits for non shear deformable beam with $r = 0.05$, $\Omega = 15.0$, $a = 0.01$.

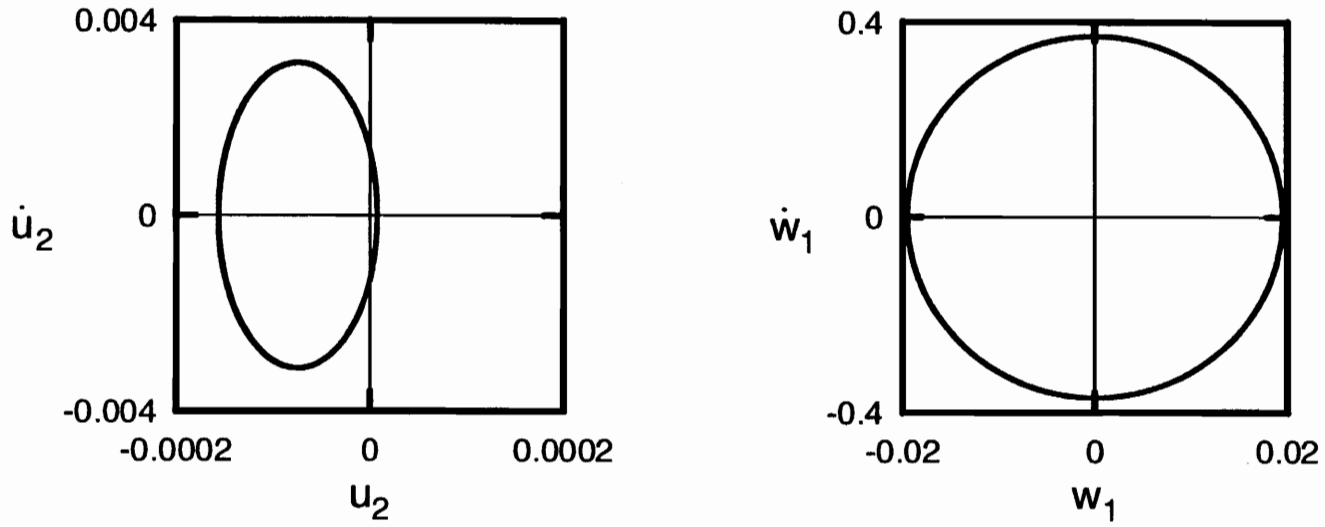

Figure A.35: Phase portraits for non shear deformable beam with $r = 0.05$, $\Omega = 19.0$, $a = 0.01$.

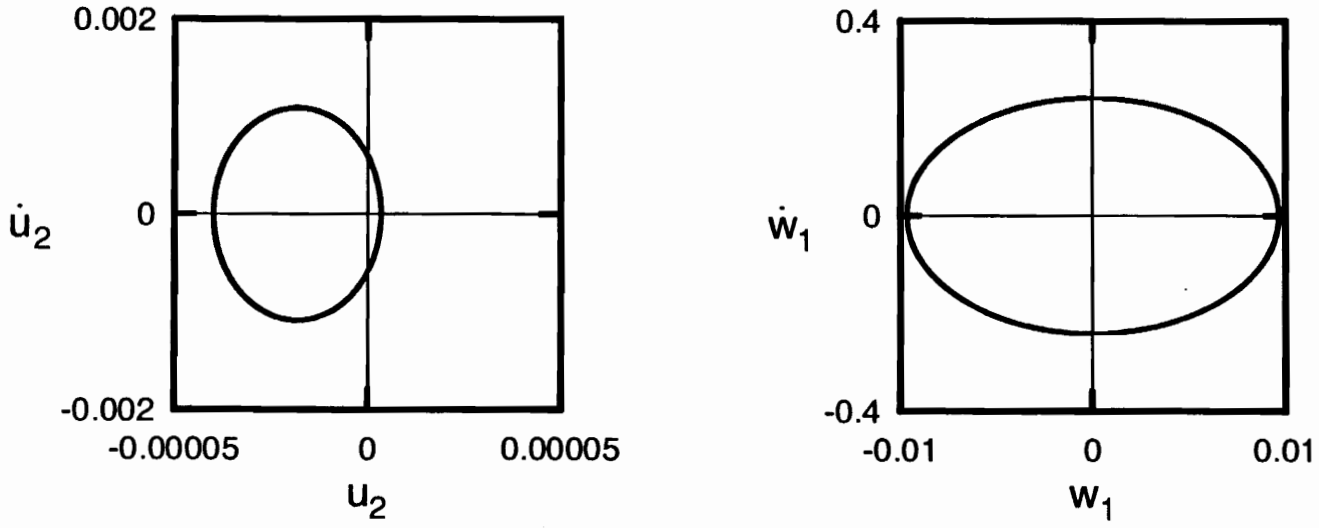

Figure A.36: Phase portraits for non shear deformable beam with $r = 0.05$, $\Omega = 25.0$, $a = 0.01$.

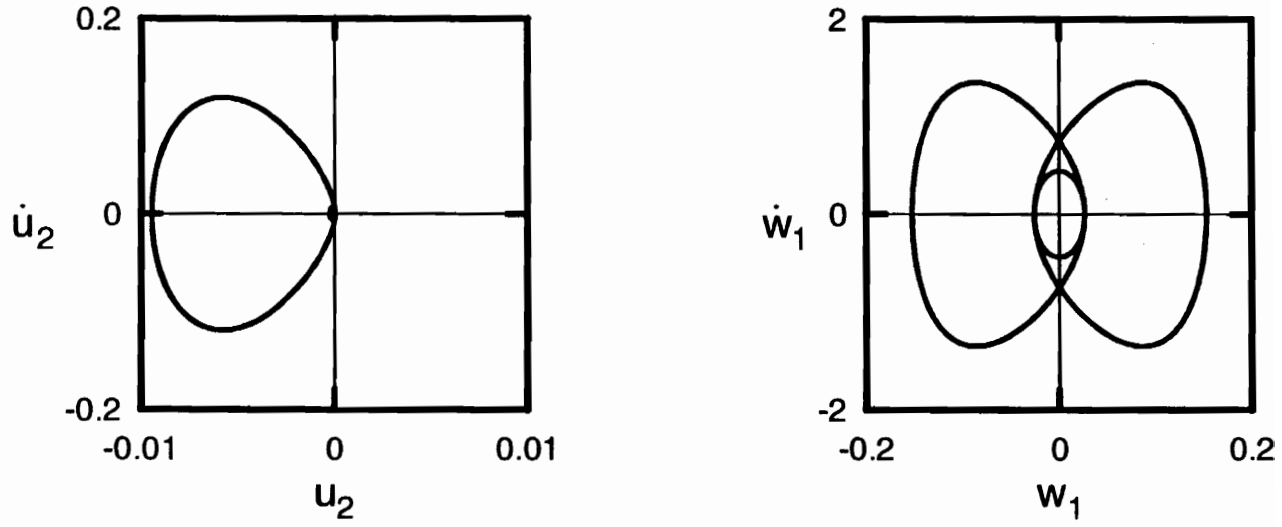

Figure A.37: Phase portraits for shear deformable beam with $r = 0.05$, $\Omega = 5.0$, $a = 0.03$.

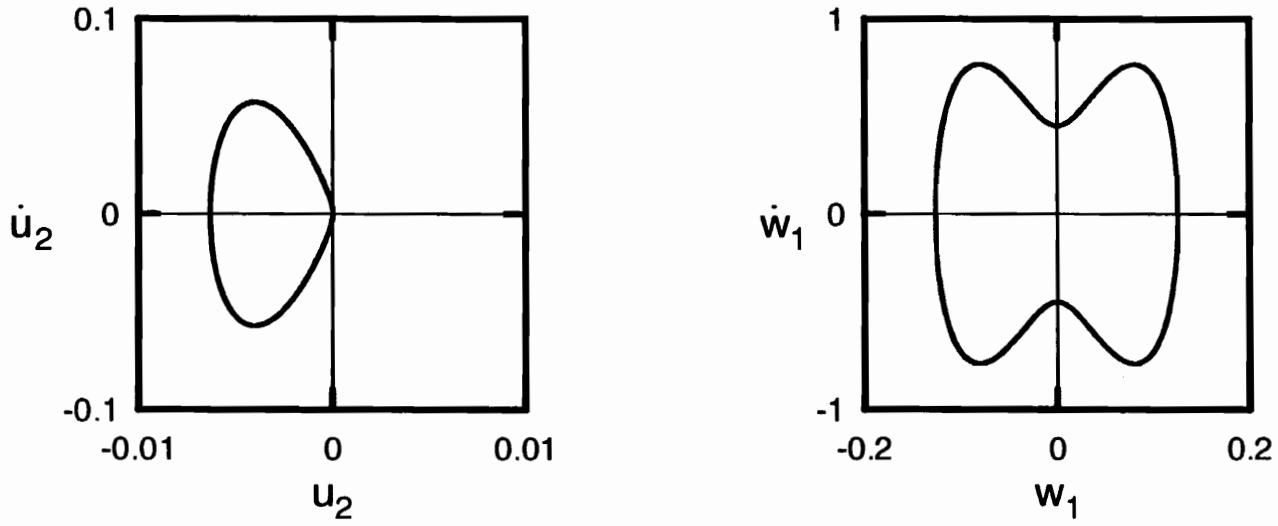

Figure A.38: Phase portraits for shear deformable beam with $r = 0.05$, $\Omega = 7.0$, $a = 0.03$.

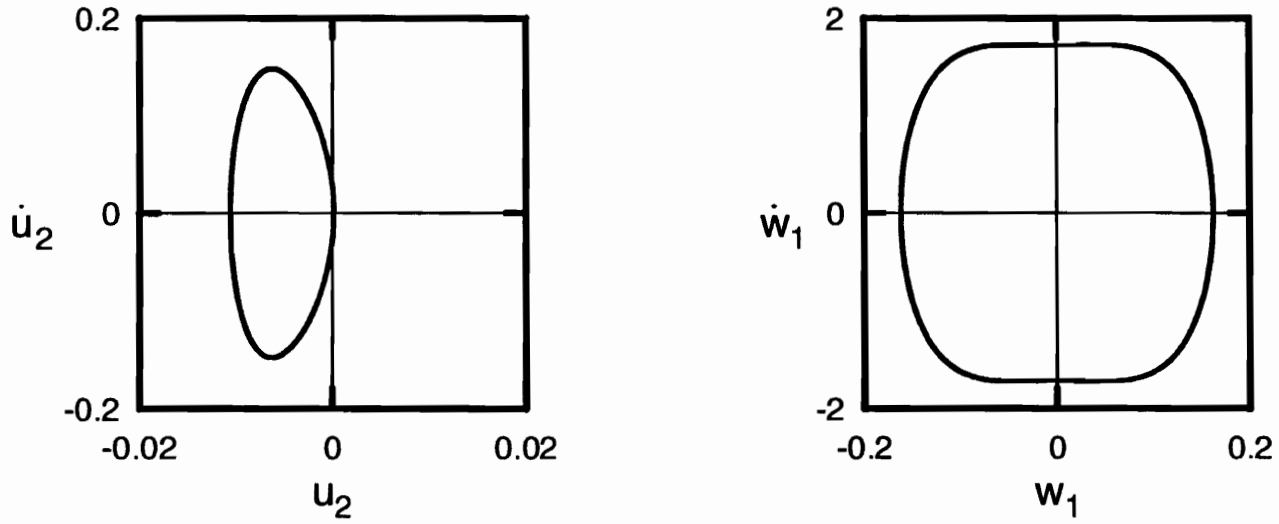

Figure A.39: Phase portraits for shear deformable beam with $r = 0.05$, $\Omega = 13.0$, $a = 0.03$.

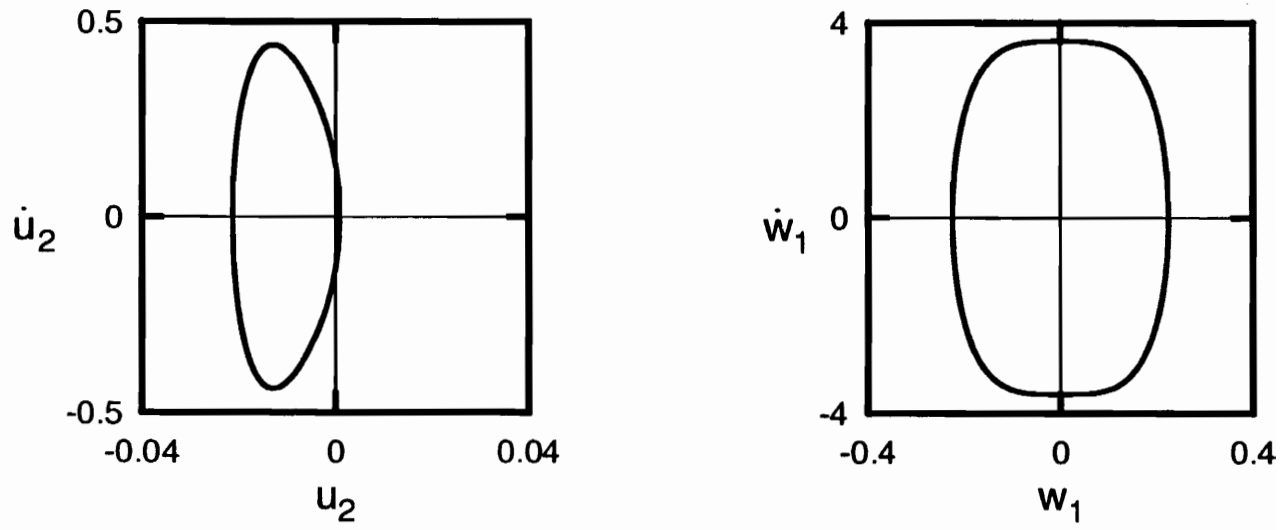

Figure A.40: Phase portraits for shear deformable beam with $r = 0.05$, $\Omega = 19.0$, $a = 0.03$.

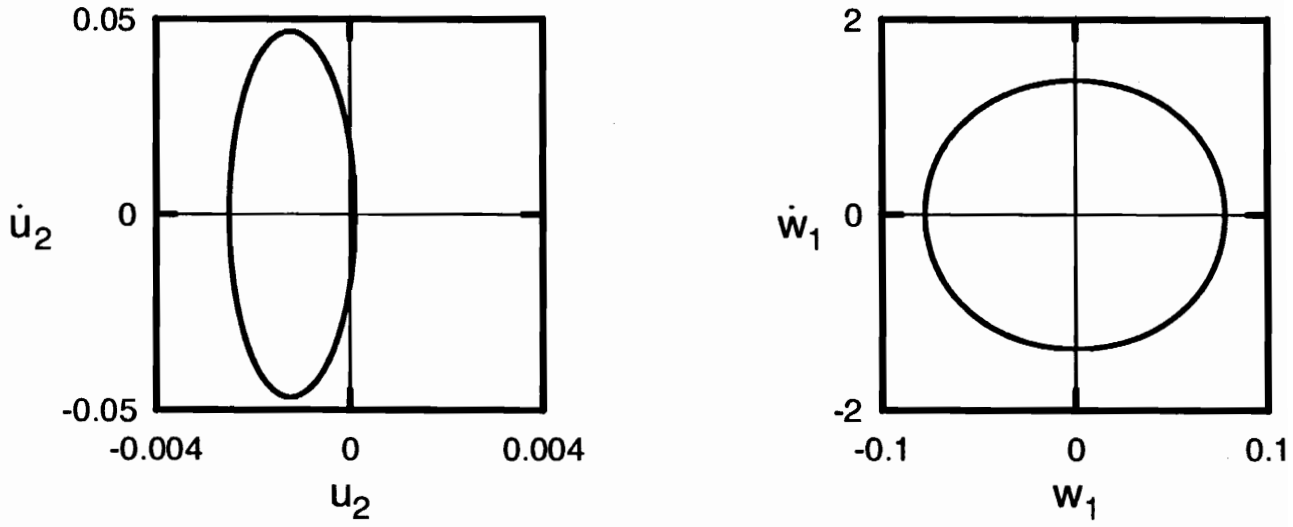

Figure A.41: Phase portraits for shear deformable beam with $r = 0.05$, $\Omega = 18.0$, $a = 0.03$.

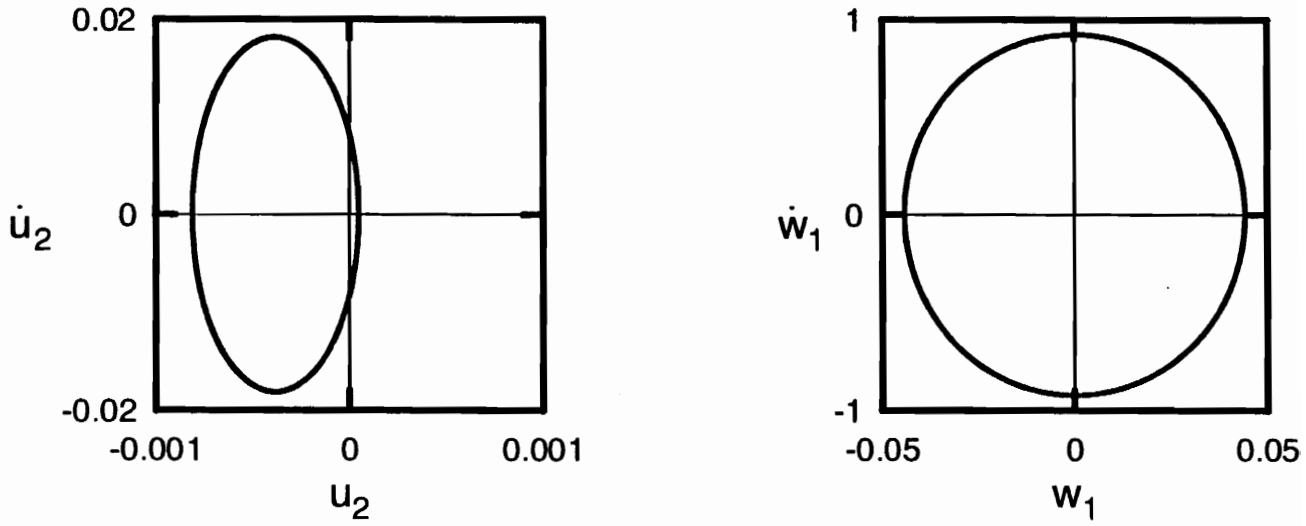

Figure A.42: Phase portraits for shear deformable beam with $r = 0.05$, $\Omega = 21.0$, $a = 0.03$.

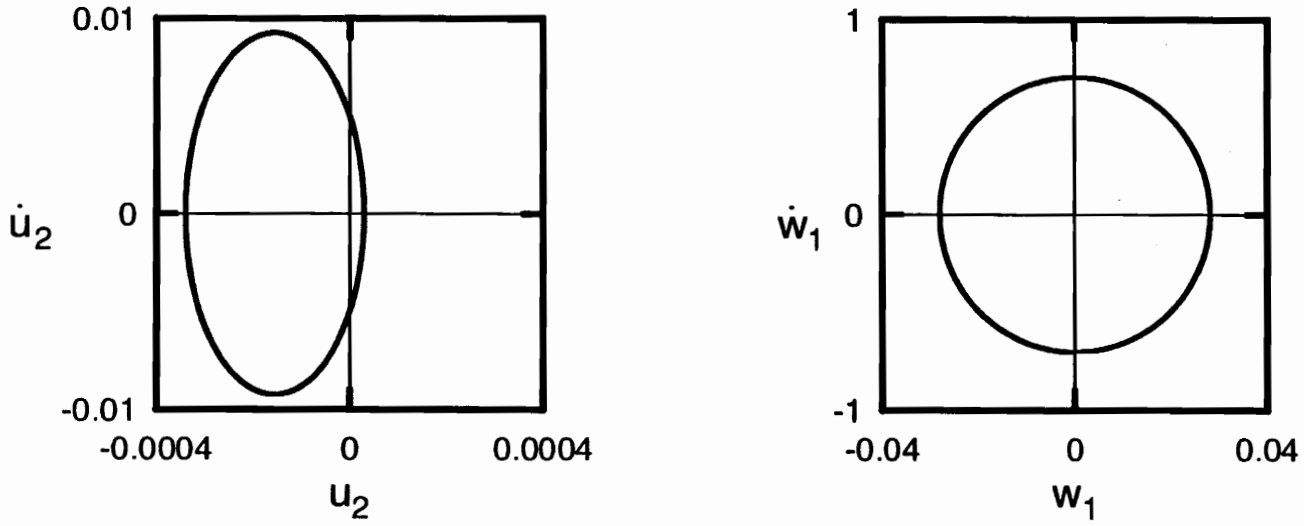

Figure A.43: Phase portraits for shear deformable beam with $r = 0.05$, $\Omega = 25.0$, $a = 0.03$.

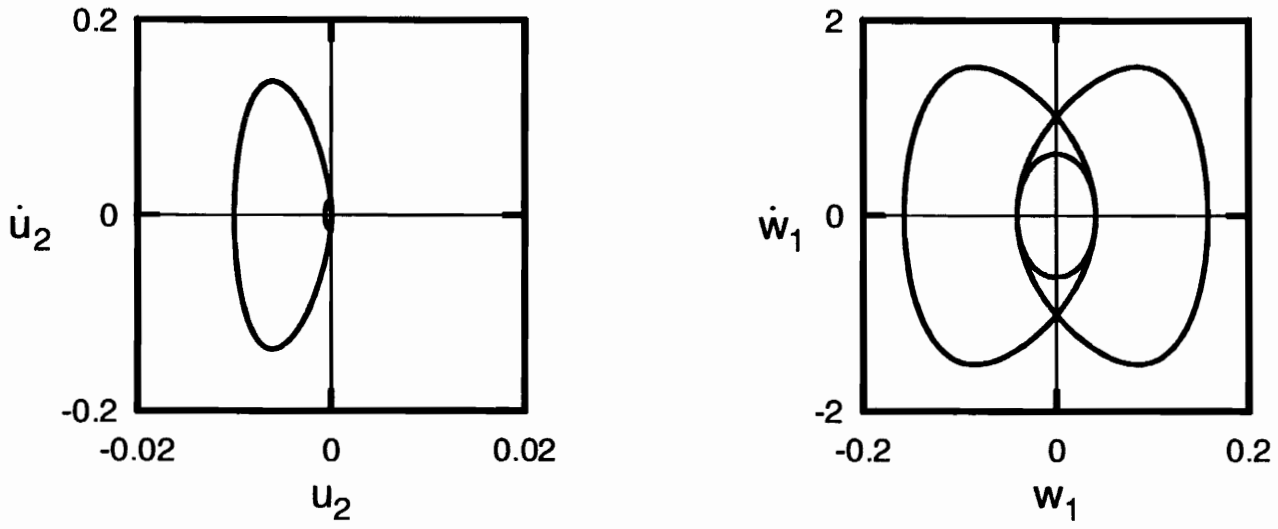

Figure A.44: Phase portraits for non shear deformable beam with $r = 0.05$, $\Omega = 5.0$, $a = 0.03$.

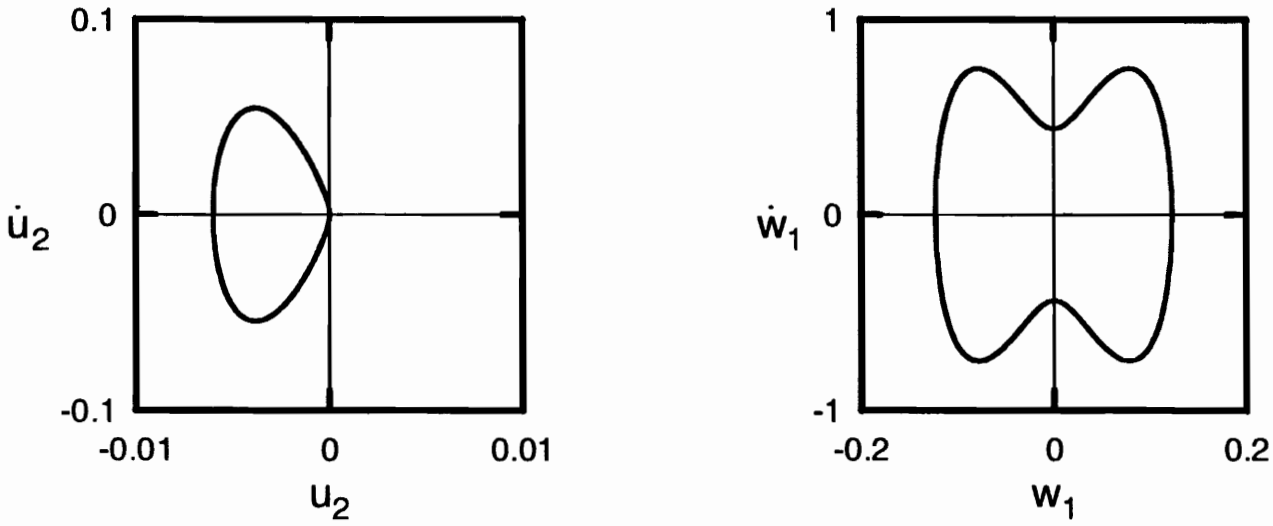

Figure A.45: Phase portraits for non shear deformable beam with $r = 0.05$, $\Omega = 7.0$, $a = 0.03$.

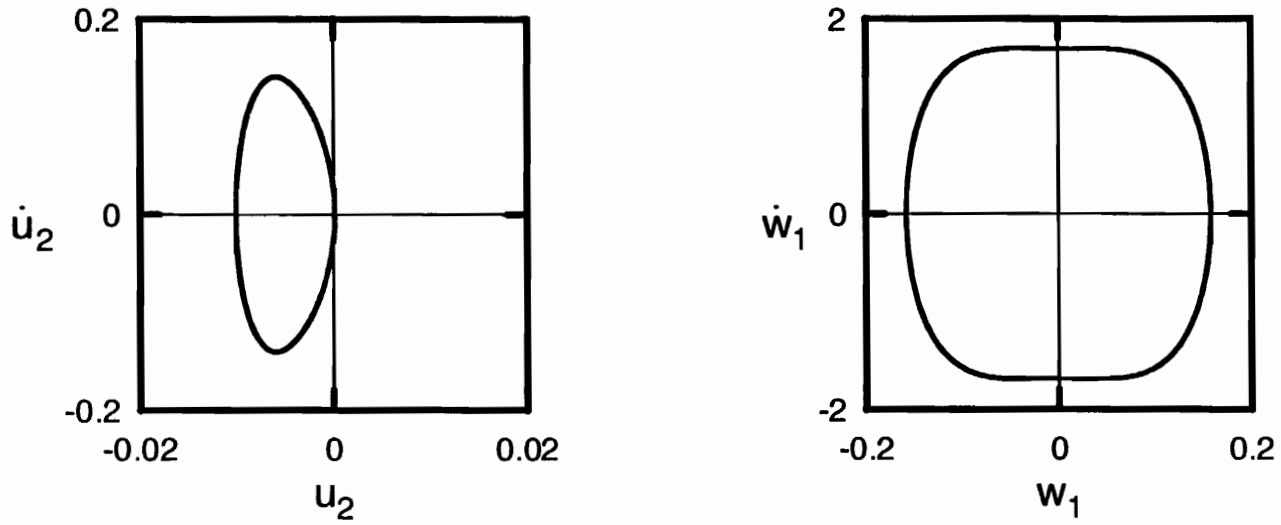

Figure A.46: Phase portraits for non shear deformable beam with $r = 0.05$, $\Omega = 13.0$, $a = 0.03$.

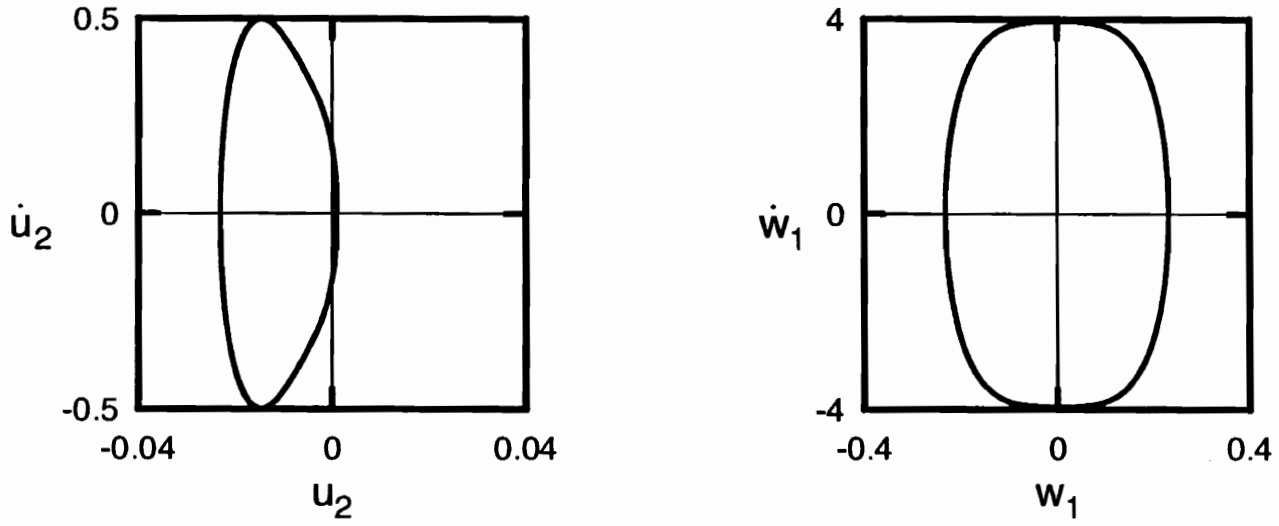

Figure A.47: Phase portraits for non shear deformable beam with $r = 0.05$, $\Omega = 20.0$, $a = 0.03$.

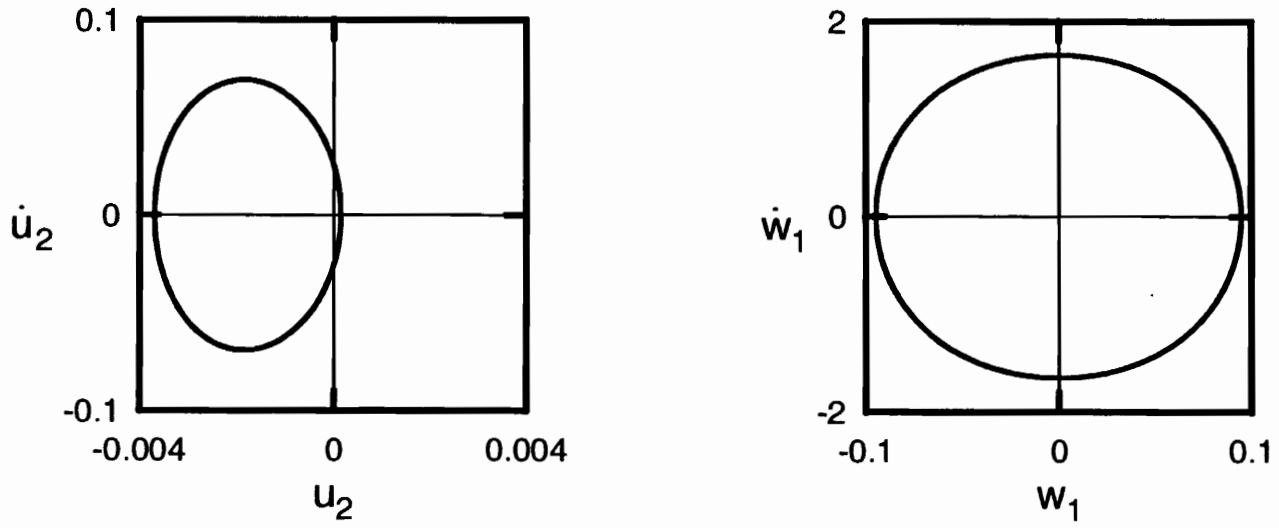

Figure A.48: Phase portraits for non shear deformable beam with $r = 0.05$, $\Omega = 18.0$, $a = 0.03$.

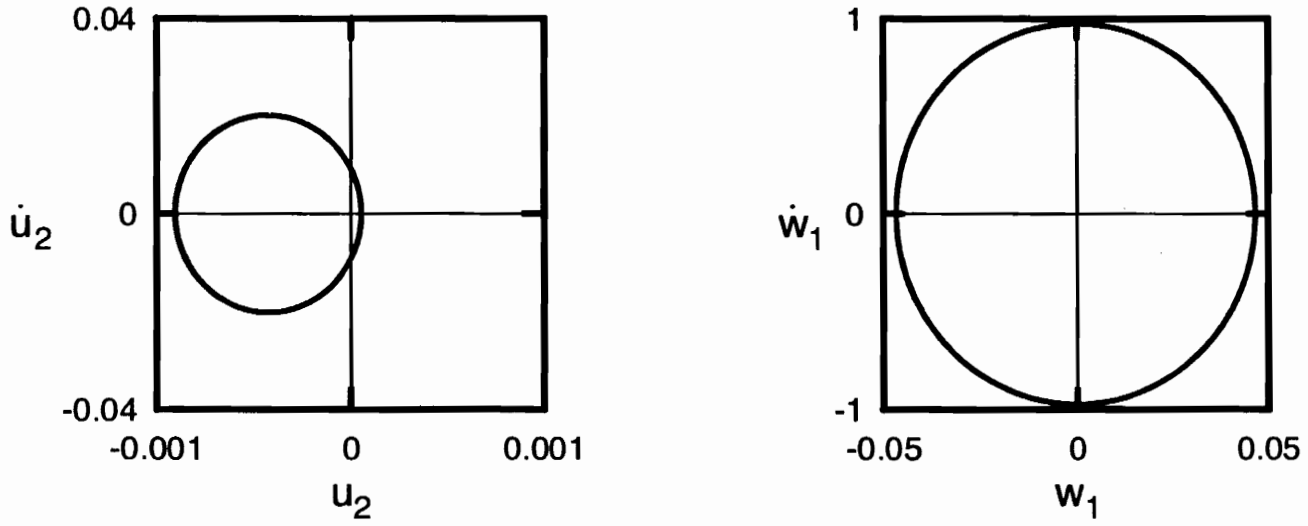

Figure A.49: Phase portraits for non shear deformable beam with $r = 0.05$, $\Omega = 21.0$, $a = 0.03$.

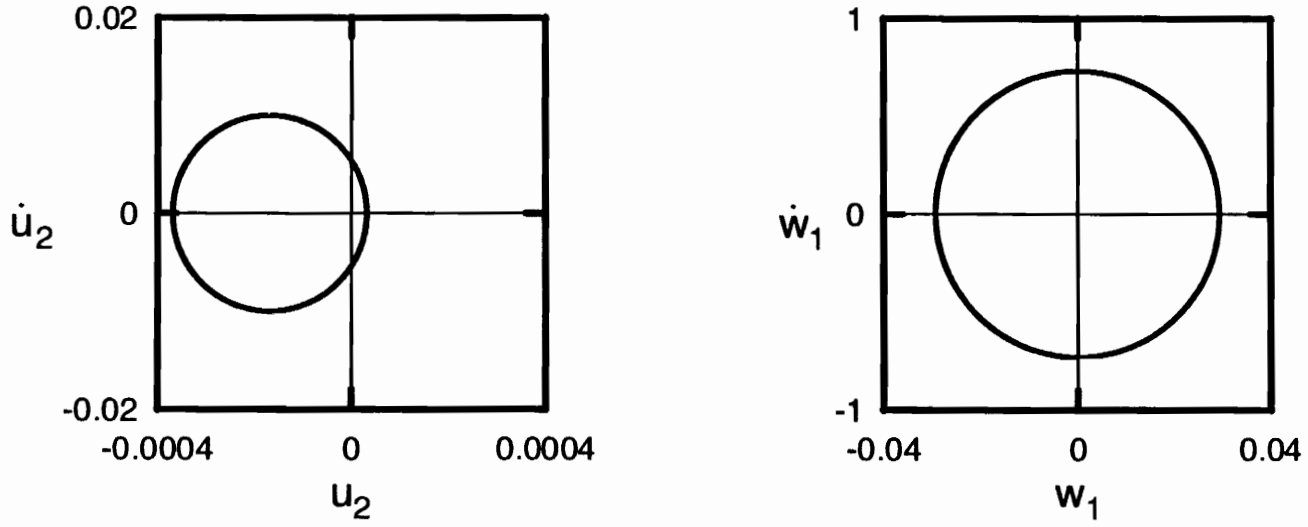

Figure A.50: Phase portraits for non shear deformable beam with $r = 0.05$, $\Omega = 25.0$, $a = 0.03$.

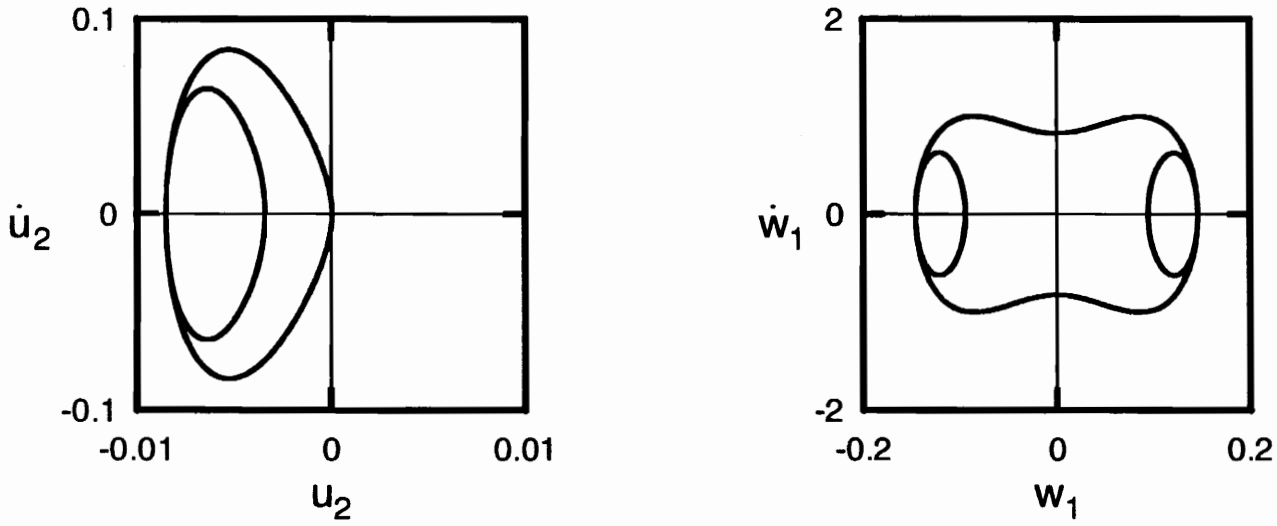

Figure A.51: Phase portraits for shear deformable beam with $r = 0.05$, $\Omega = 5.0$, $a = 0.06$.

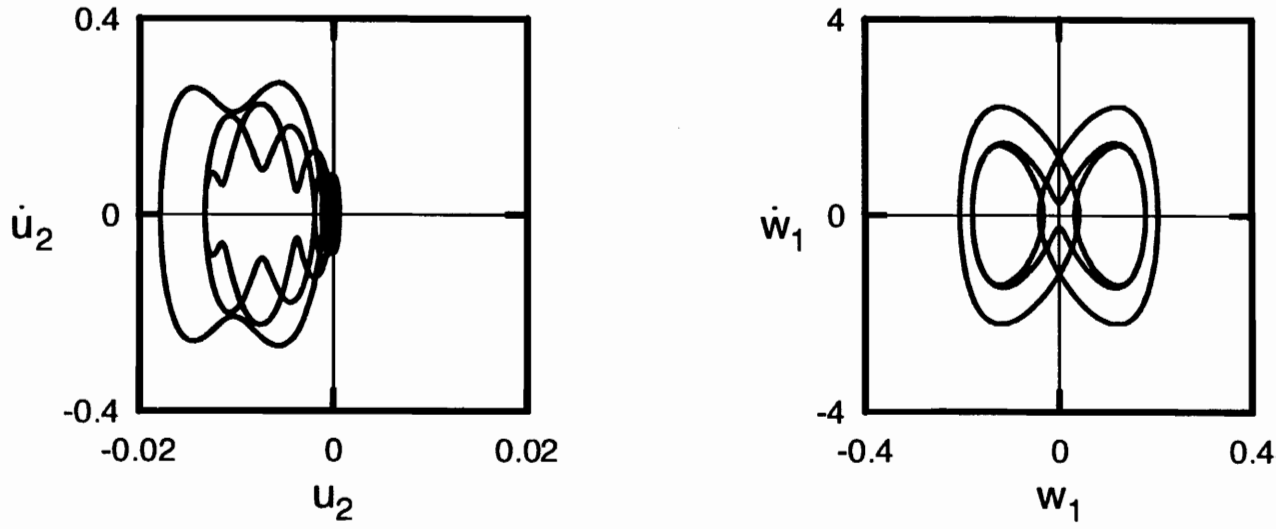

Figure A.52: Phase portraits for shear deformable beam with $r = 0.05$, $\Omega = 7.0$, $a = 0.06$.

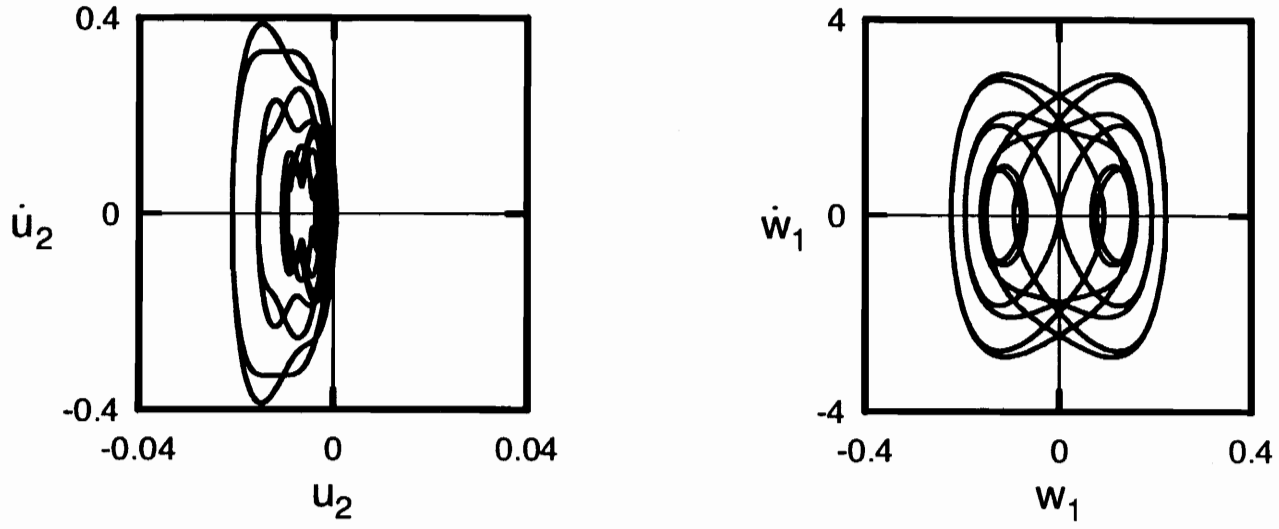

Figure A.53: Phase portraits for shear deformable beam with $r = 0.05$, $\Omega = 9.0$, $a = 0.06$.

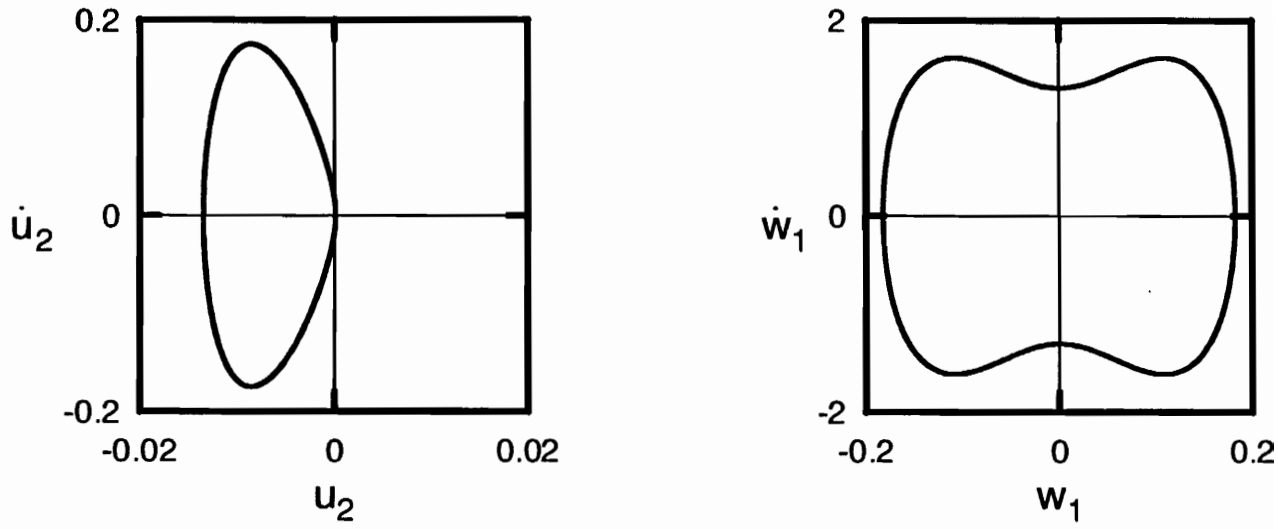

Figure A.54: Phase portraits for shear deformable beam with $r = 0.05$, $\Omega = 11.0$, $a = 0.06$.

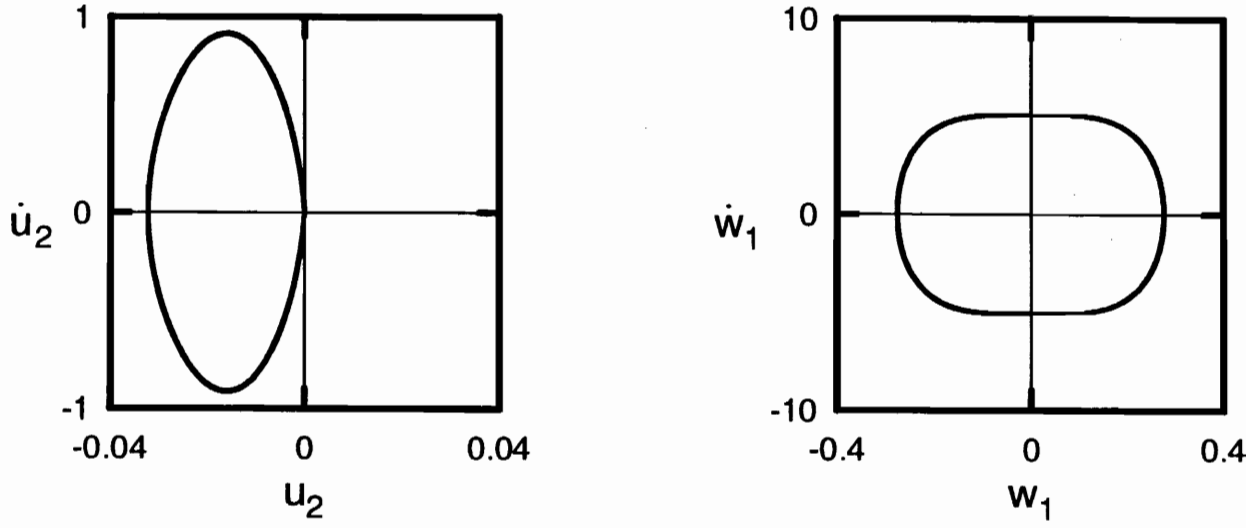

Figure A.55: Phase portraits for shear deformable beam with $r = 0.05$, $\Omega = 22.0$, $a = 0.06$.

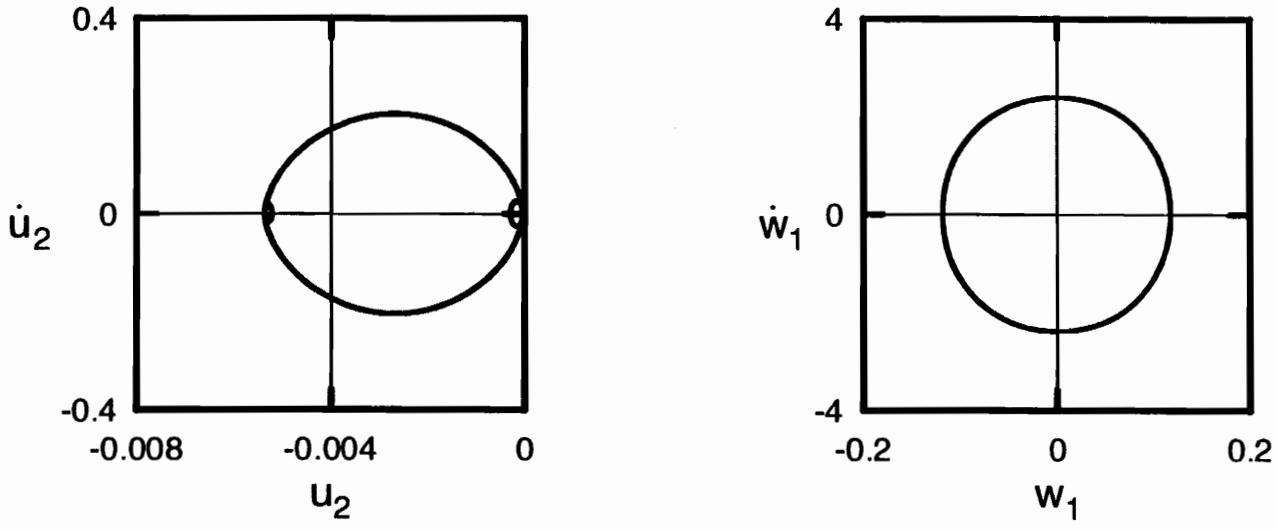

Figure A.56: Phase portraits for shear deformable beam with $r = 0.05$, $\Omega = 21.0$, $a = 0.06$.

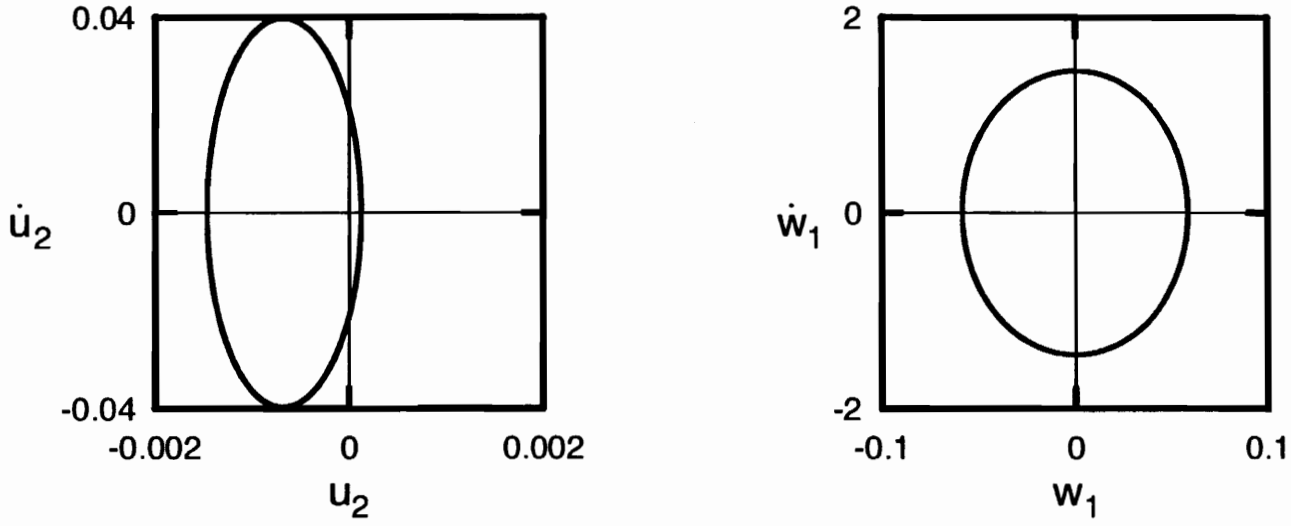

Figure A.57: Phase portraits for shear deformable beam with $r = 0.05$, $\Omega = 25.0$, $a = 0.06$.

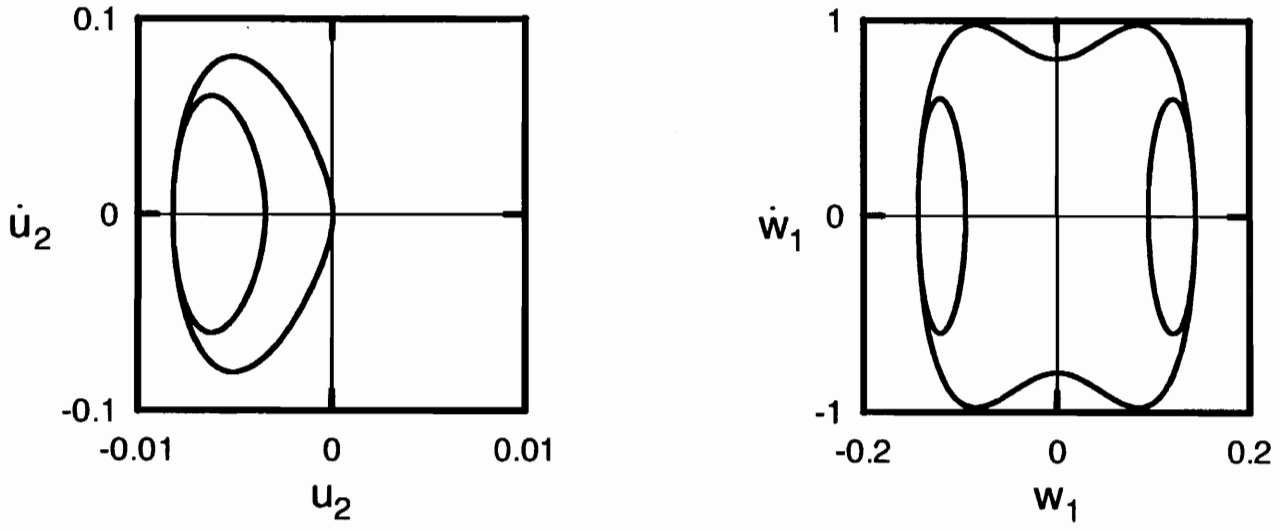

Figure A.58: Phase portraits for non shear deformable beam with $r = 0.05$, $\Omega = 5.0$, $a = 0.06$.

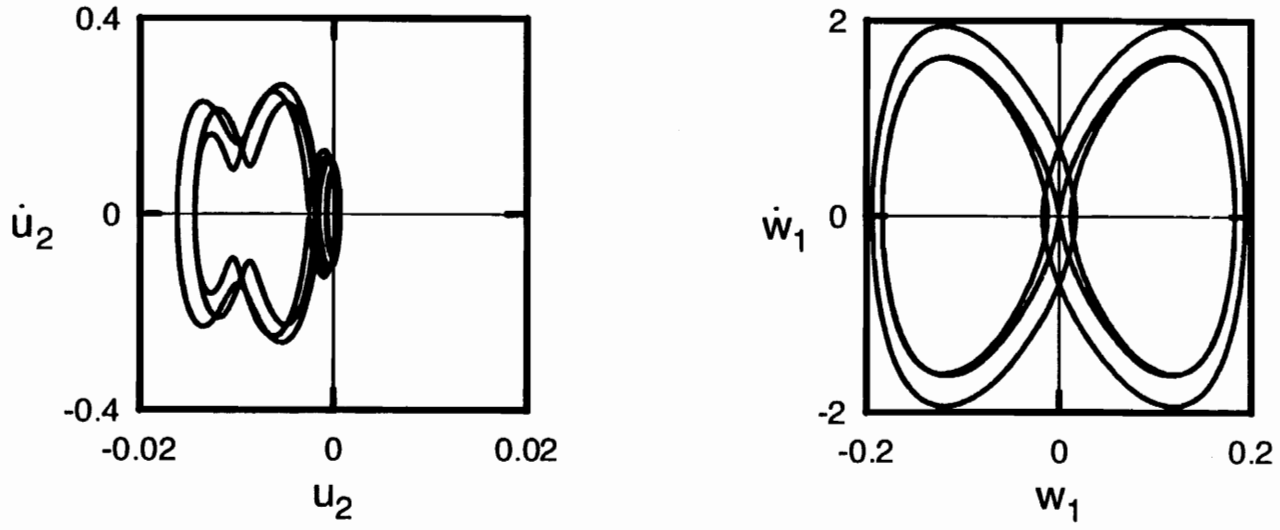

Figure A.59: Phase portraits for non shear deformable beam with $r = 0.05$, $\Omega = 7.0$, $a = 0.06$.

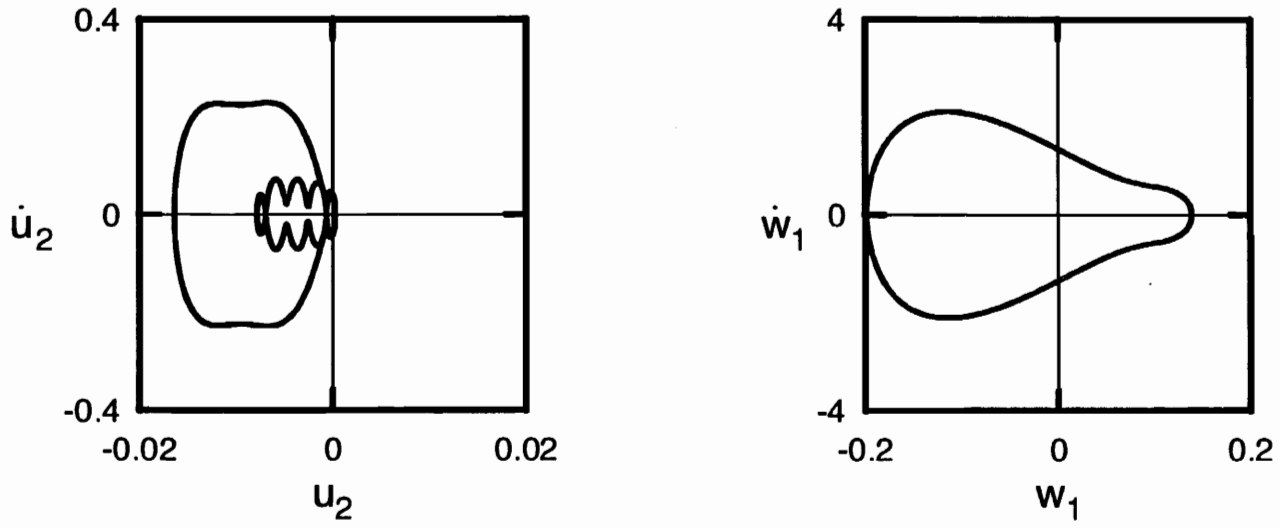

Figure A.60: Phase portraits for non shear deformable beam with $r = 0.05$, $\Omega = 9.0$, $a = 0.06$.

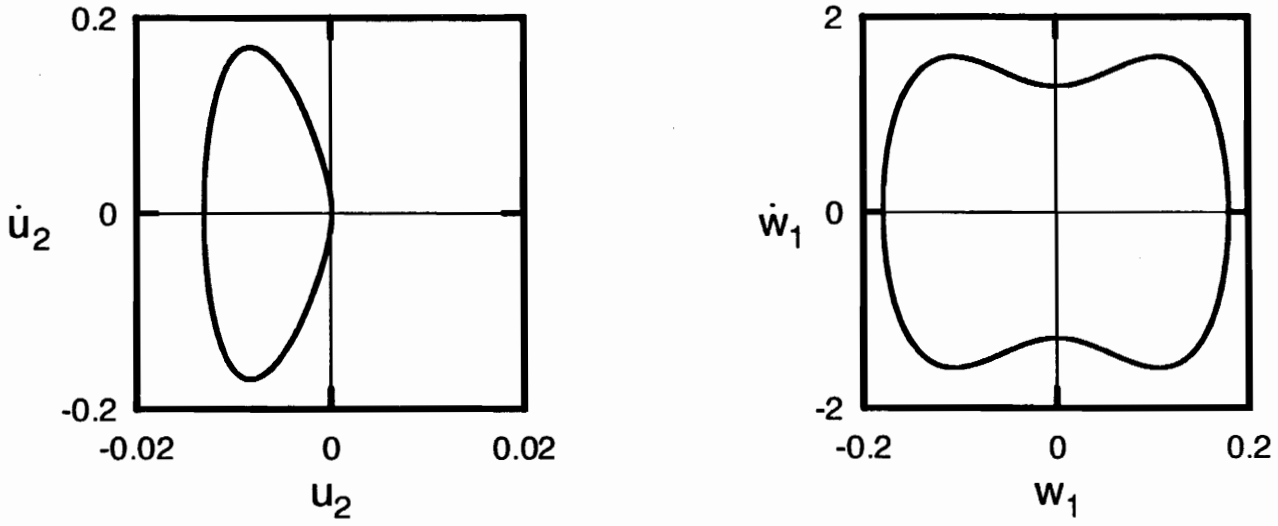

Figure A.61: Phase portraits for non shear deformable beam with $r = 0.05$, $\Omega = 11.0$, $a = 0.06$.

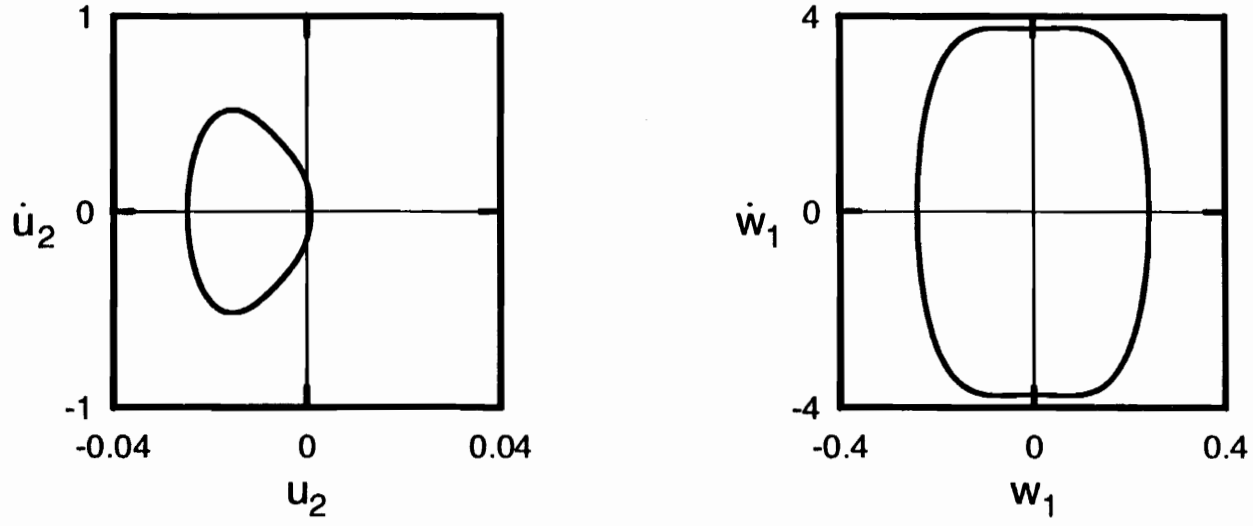

Figure A.62: Phase portraits for non shear deformable beam with $r = 0.05$, $\Omega = 19.0$, $a = 0.06$.

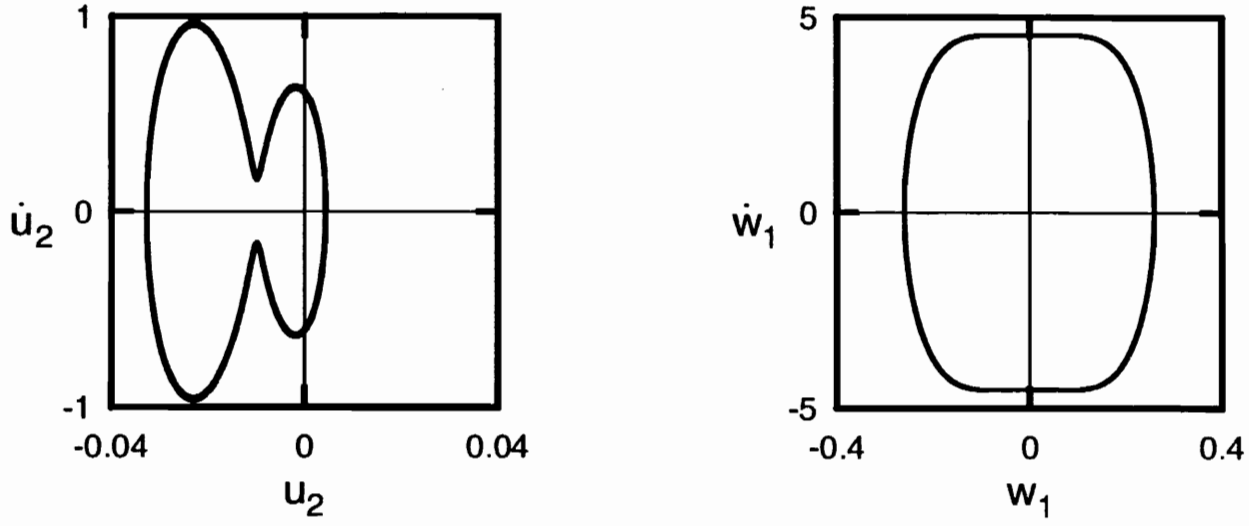

Figure A.63: Phase portraits for non shear deformable beam with $r = 0.05$, $\Omega = 21.0$, $a = 0.06$.

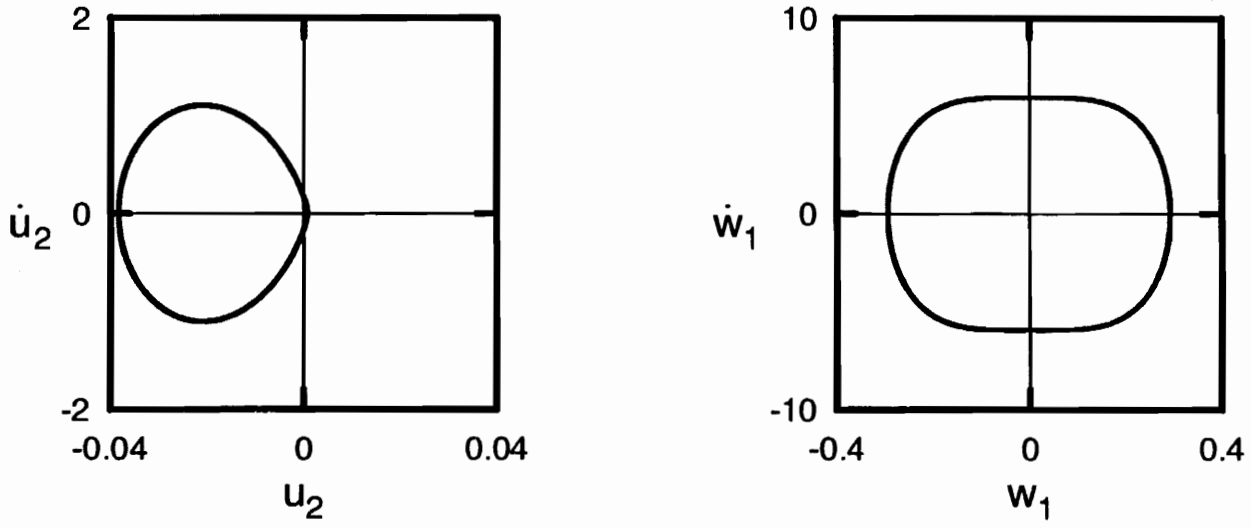

Figure A.64: Phase portraits for non shear deformable beam with $r = 0.05$, $\Omega = 24.0$, $a = 0.06$.

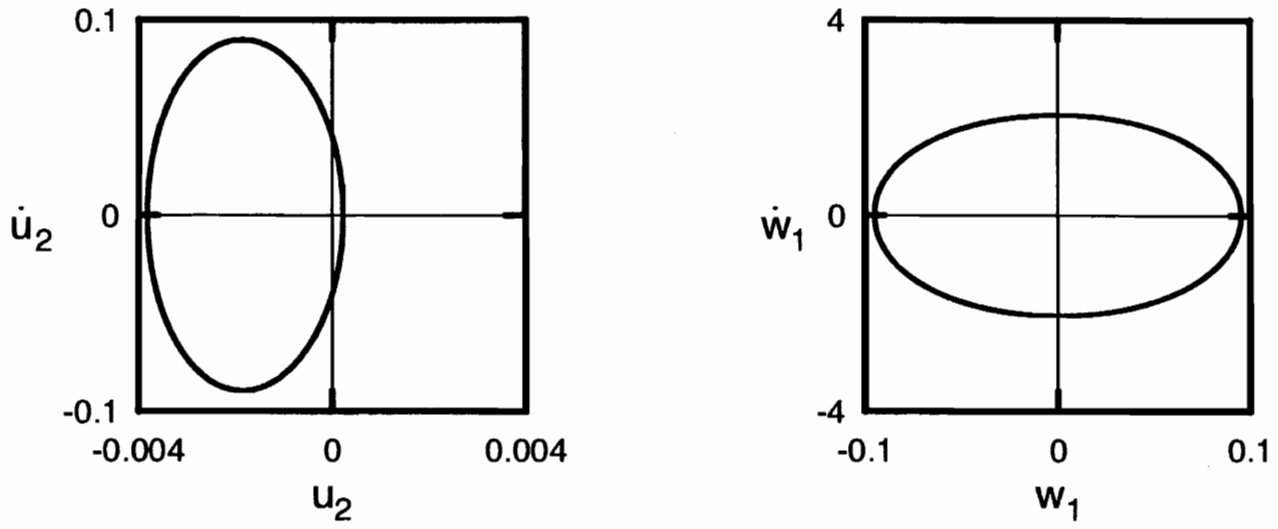

Figure A.65: Phase portraits for non shear deformable beam with $r = 0.05$, $\Omega = 22.0$, $a = 0.06$.

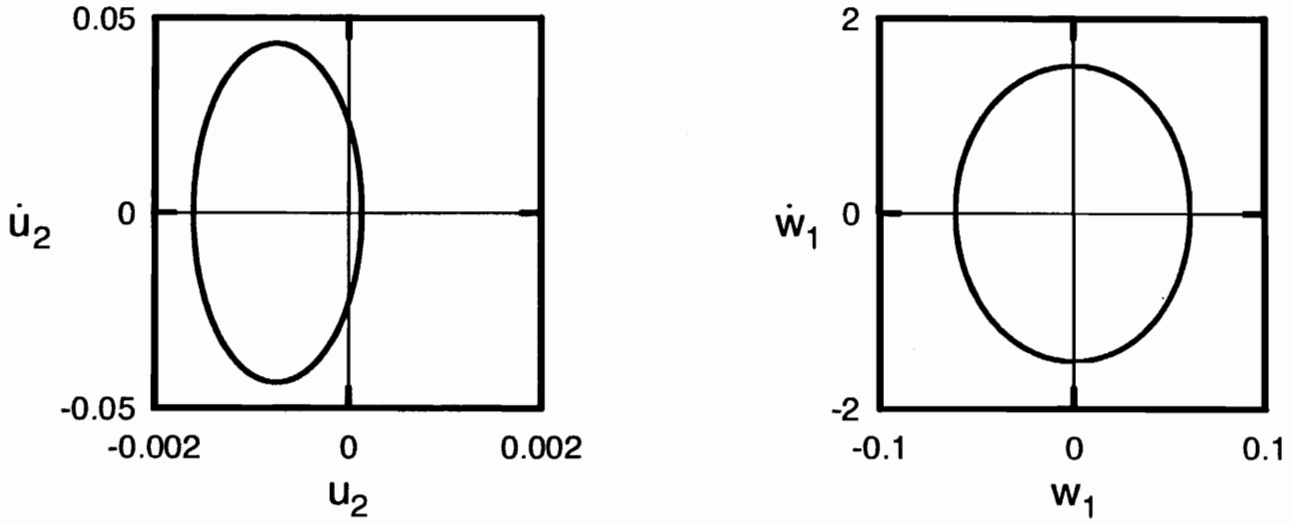

Figure A.66: Phase portraits for non shear deformable beam with $r = 0.05$, $\Omega = 25.0$, $a = 0.06$.

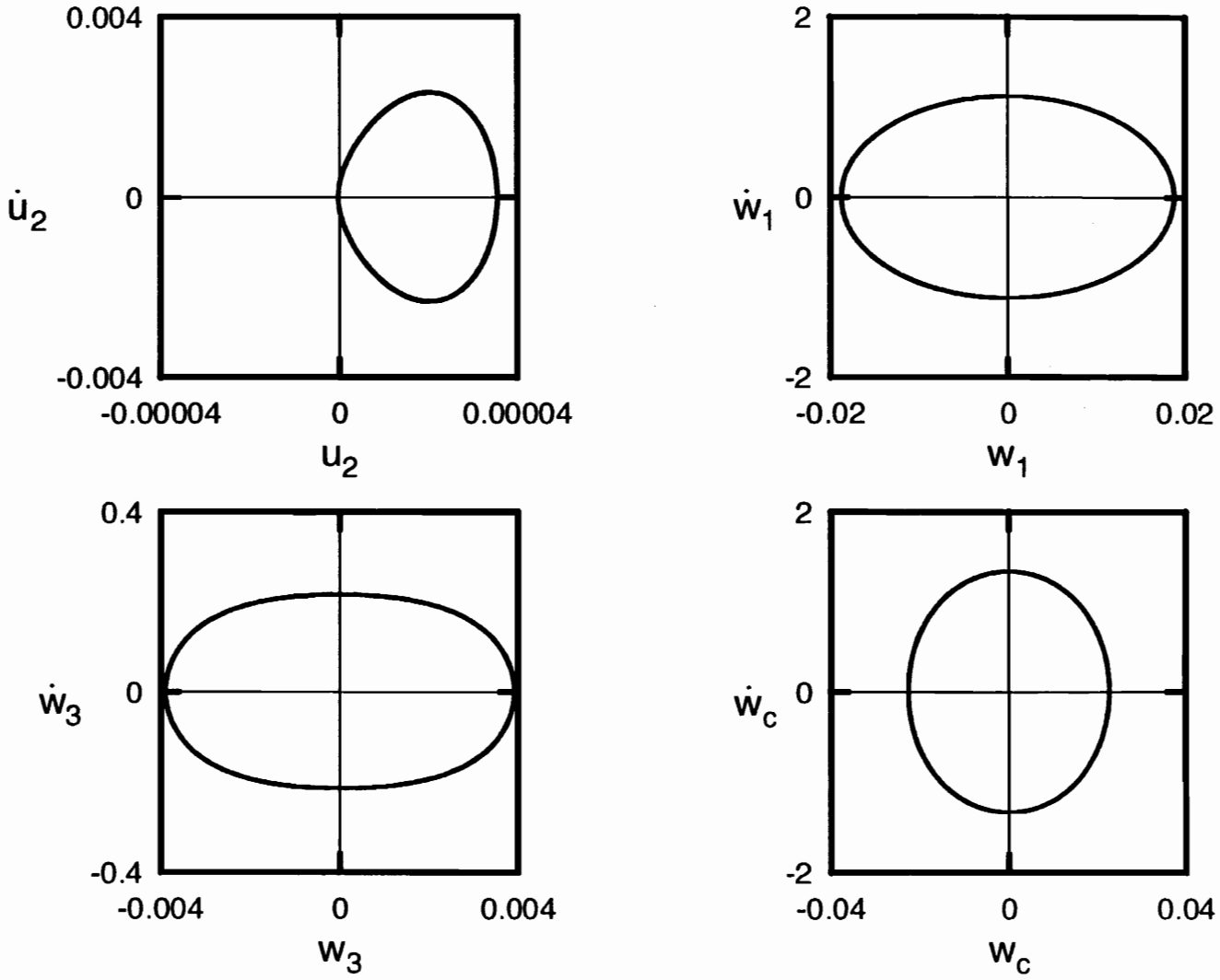

Figure A.67: Phase portraits for shear deformable beam with $r = 0.01$, $\Omega = 60.0$, $a = 0.005$.

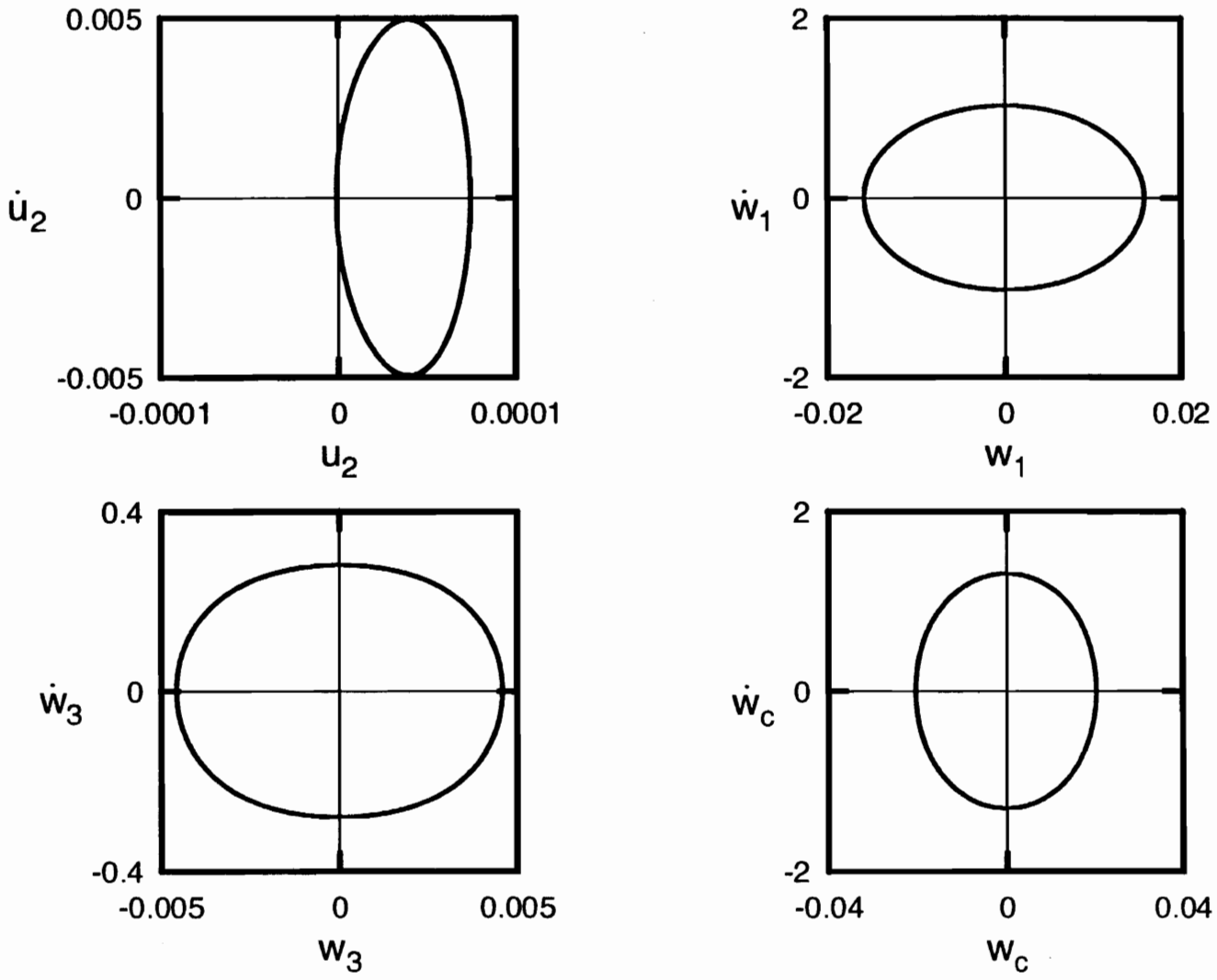

Figure A.68: Phase portraits for shear deformable beam with $r = 0.01$, $\Omega = 65.0$, $a = 0.005$.

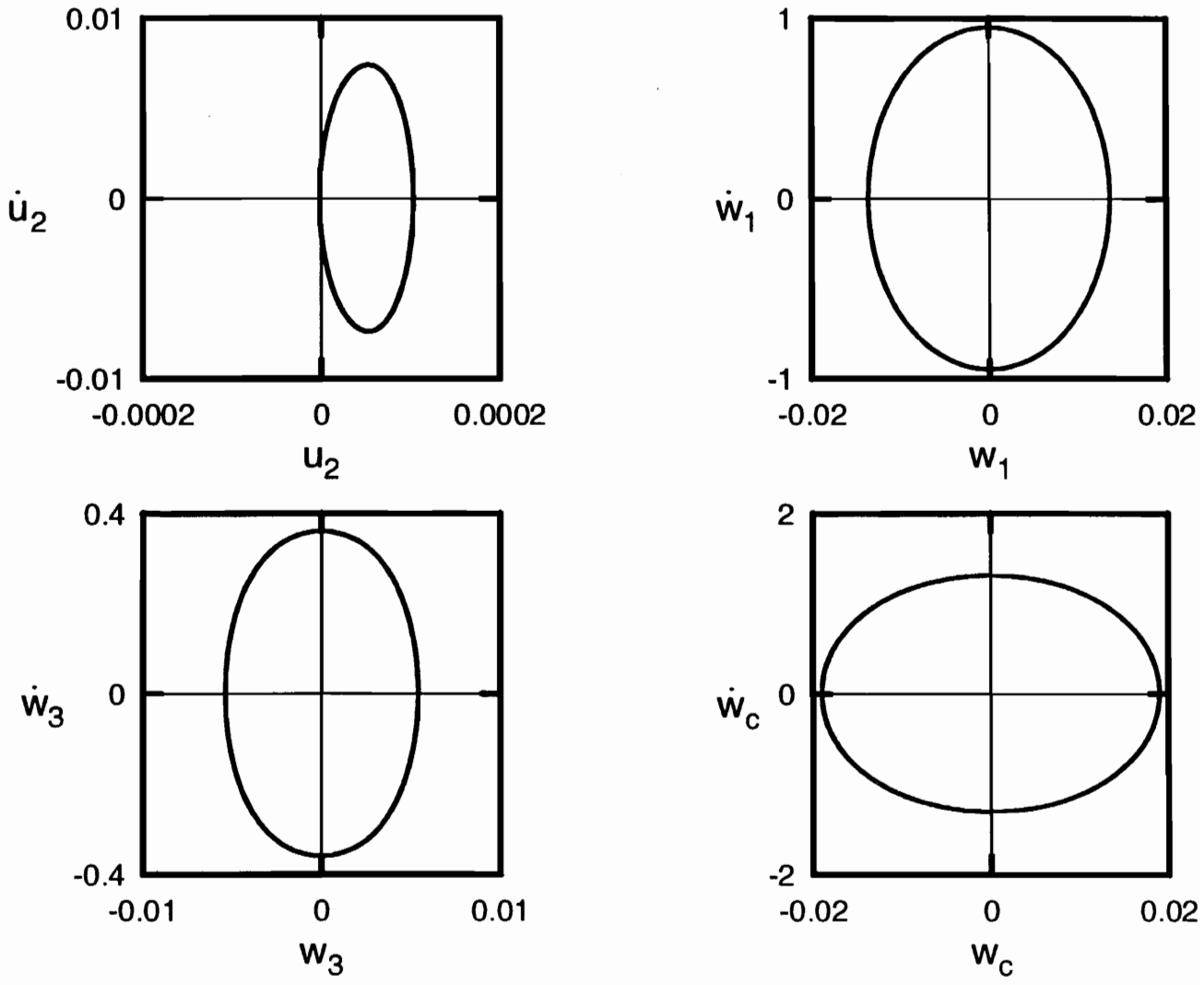

Figure A.69: Phase portraits for shear deformable beam with $r = 0.01$, $\Omega = 70.0$, $a = 0.005$.

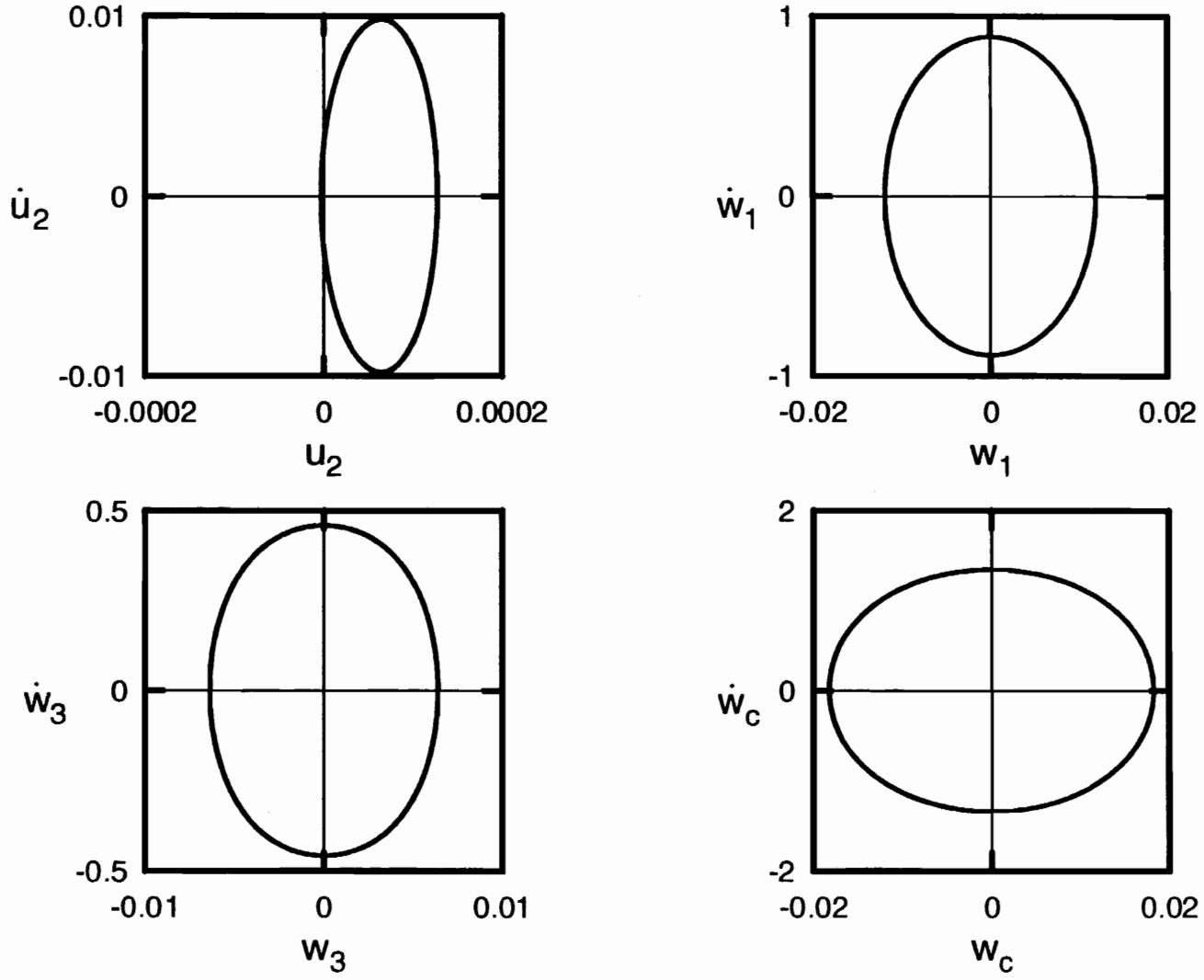

Figure A.70: Phase portraits for shear deformable beam with $r = 0.01$, $\Omega = 75.0$, $a = 0.005$.

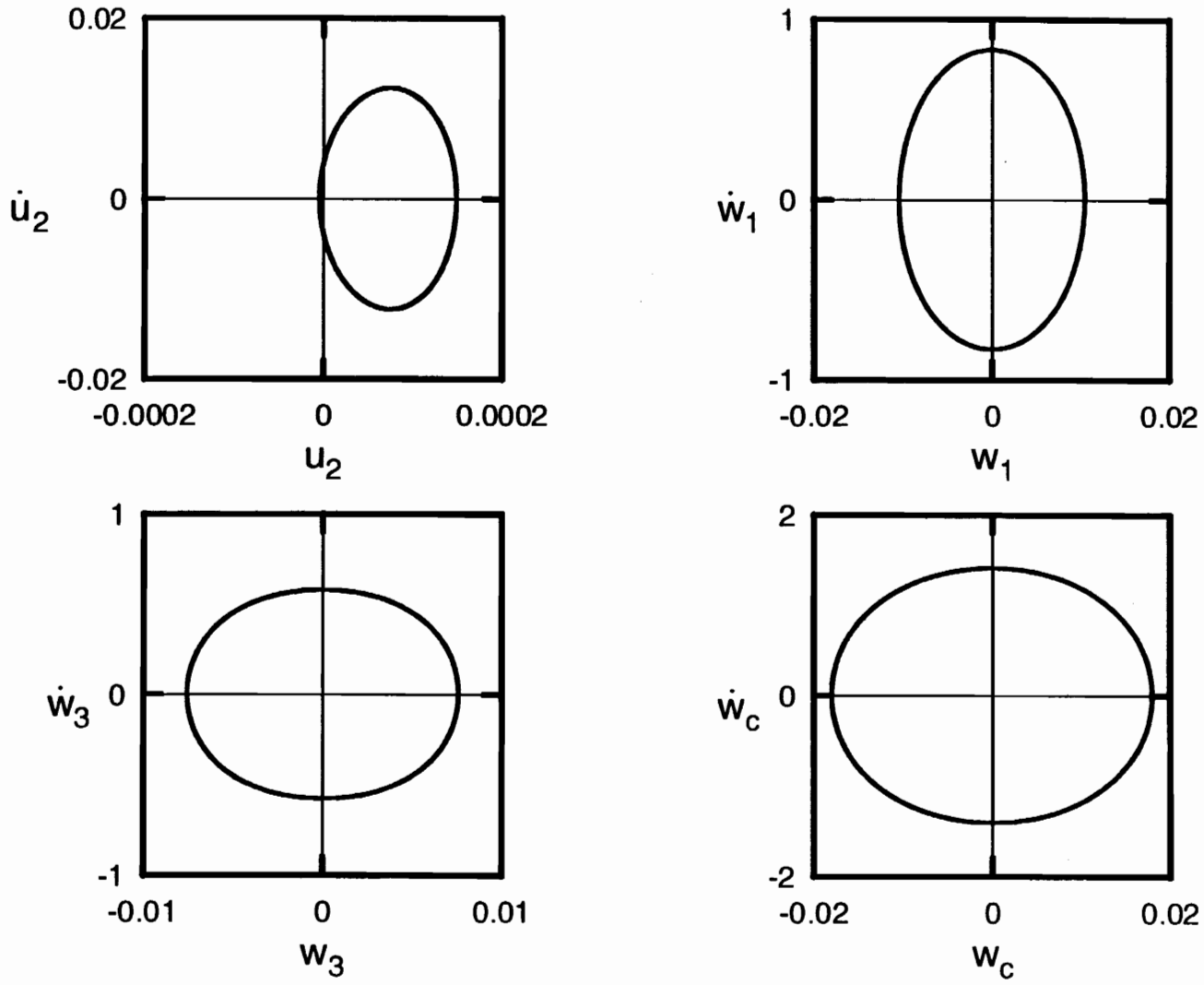

Figure A.71: Phase portraits for shear deformable beam with $r = 0.01$, $\Omega = 80.0$, $a = 0.005$.

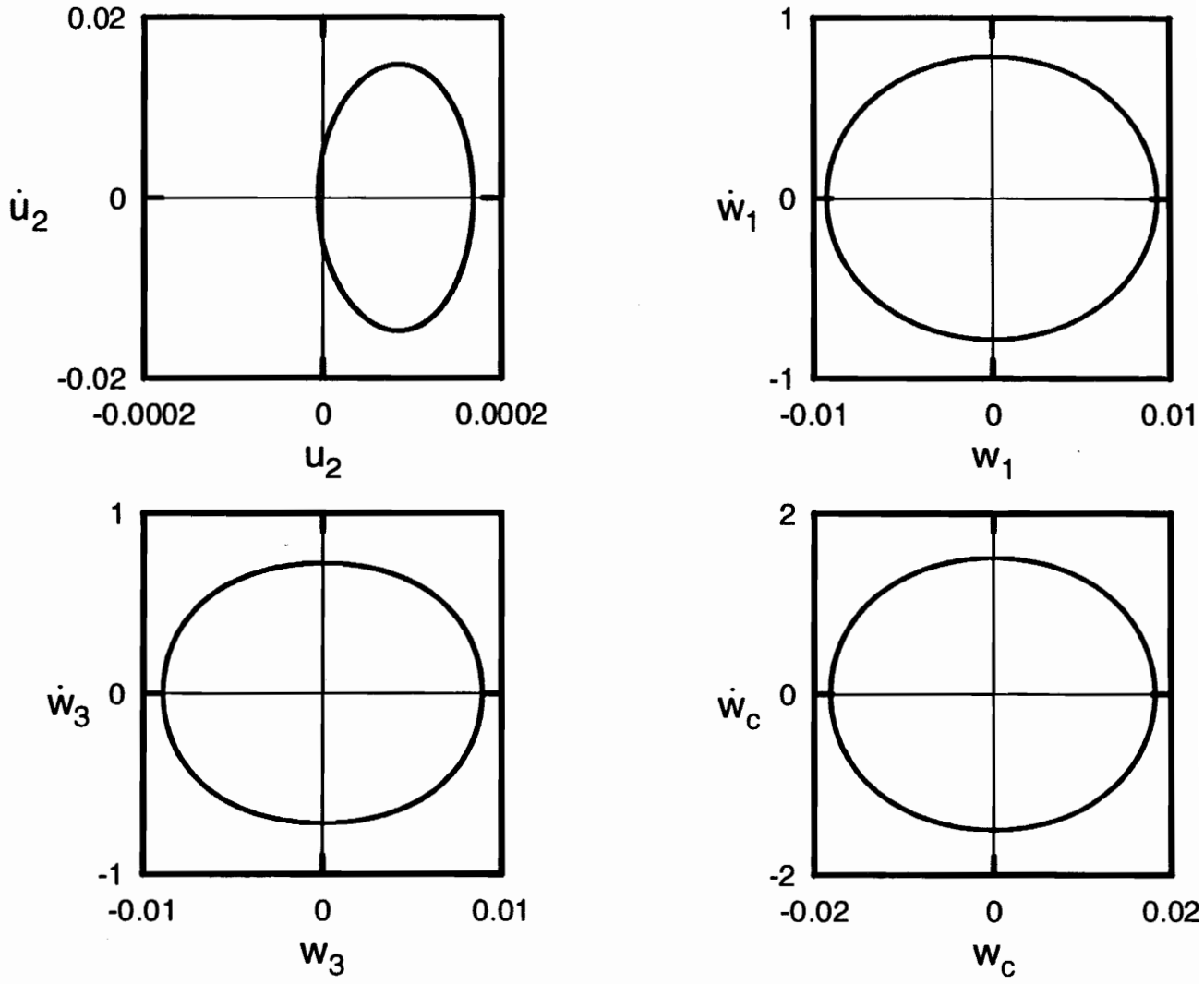

Figure A.72: Phase portraits for shear deformable beam with $r = 0.01$, $\Omega = 85.0$, $a = 0.005$.

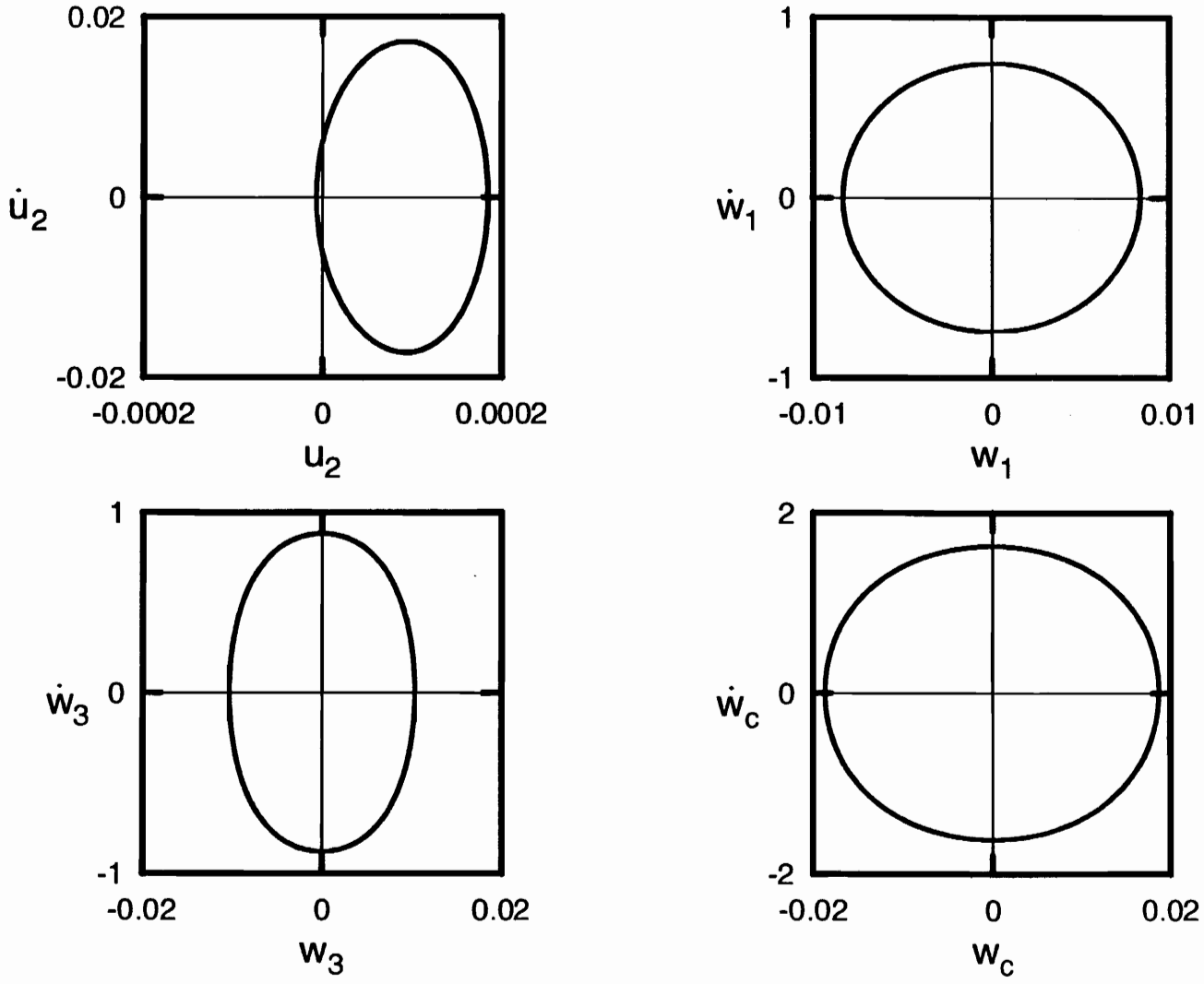

Figure A.73: Phase portraits for shear deformable beam with $r = 0.01$, $\Omega = 90.0$, $a = 0.005$.

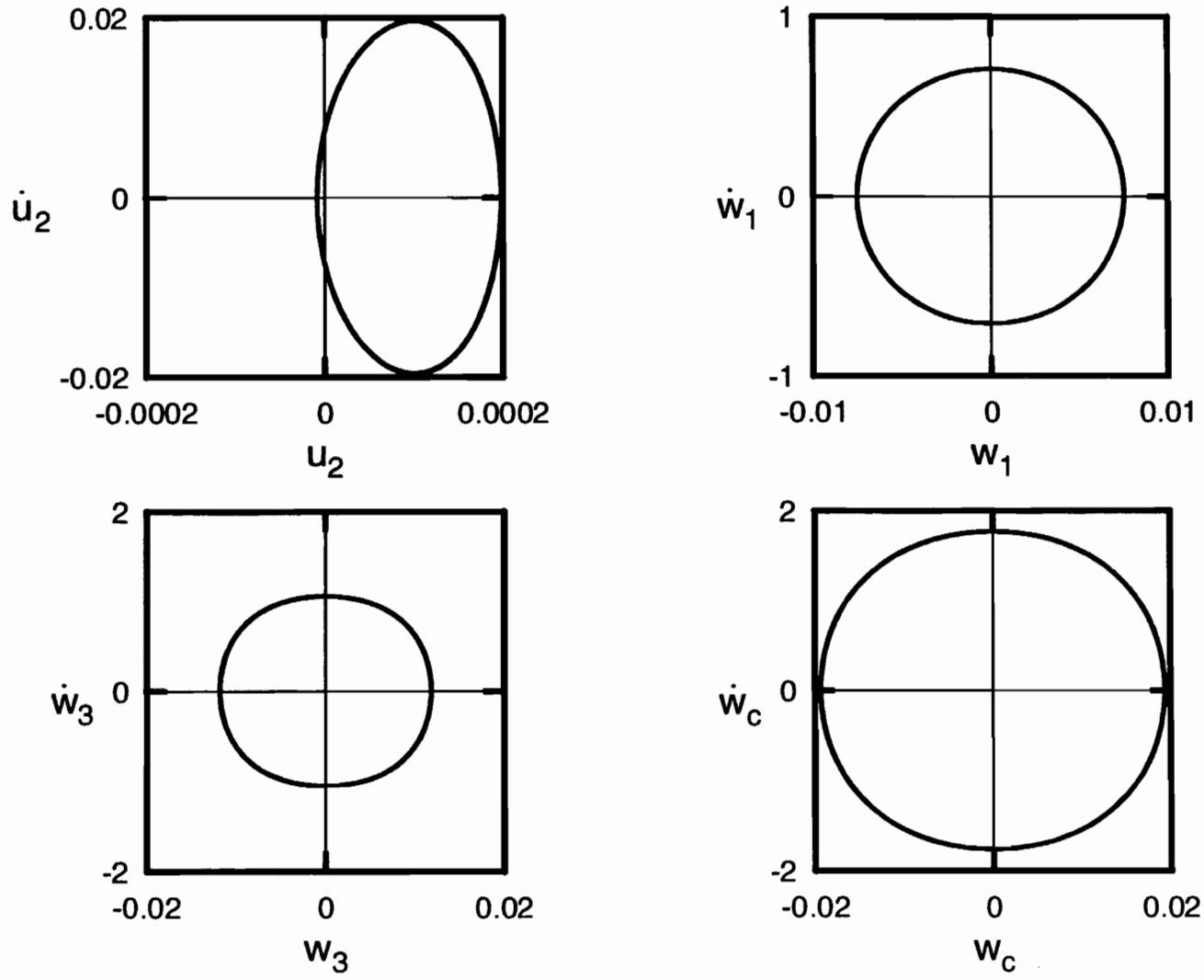

Figure A.74: Phase portraits for shear deformable beam with $r = 0.01$, $\Omega = 95.0$, $a = 0.005$.

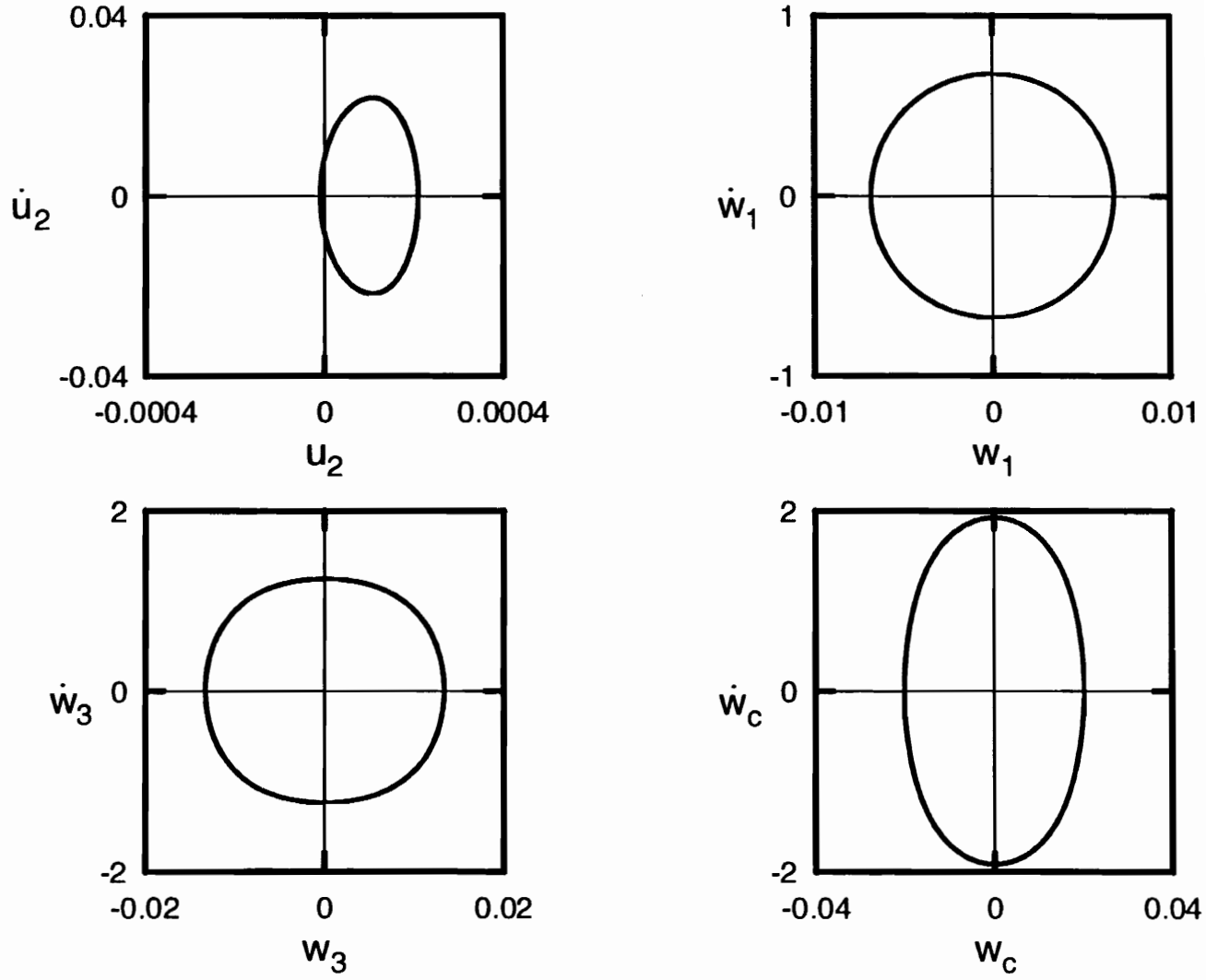

Figure A.75: Phase portraits for shear deformable beam with $r = 0.01$, $\Omega = 100.0$, $a = 0.005$.

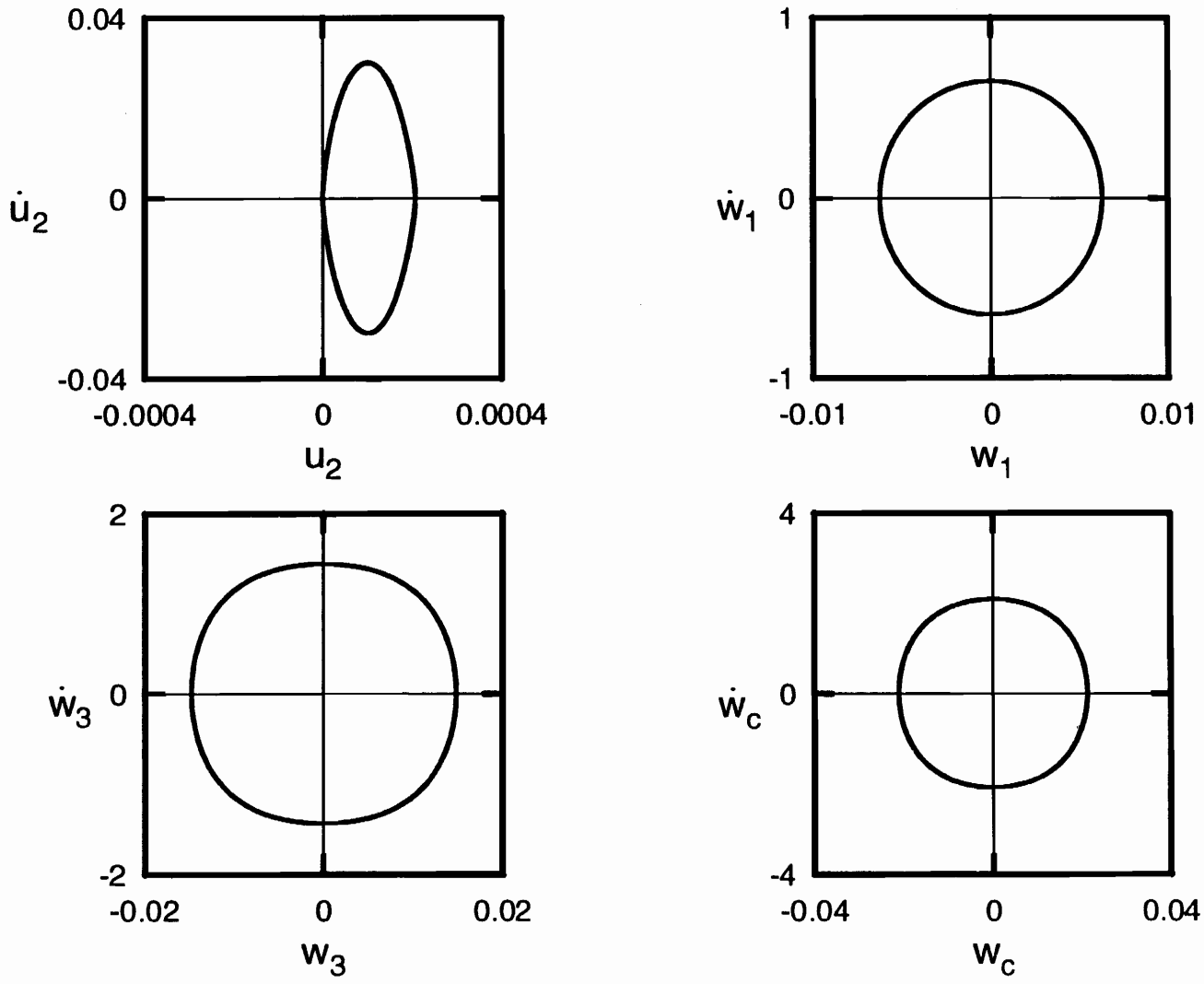

Figure A.76: Phase portraits for shear deformable beam with $r = 0.01$, $\Omega = 105.0$, $a = 0.005$.

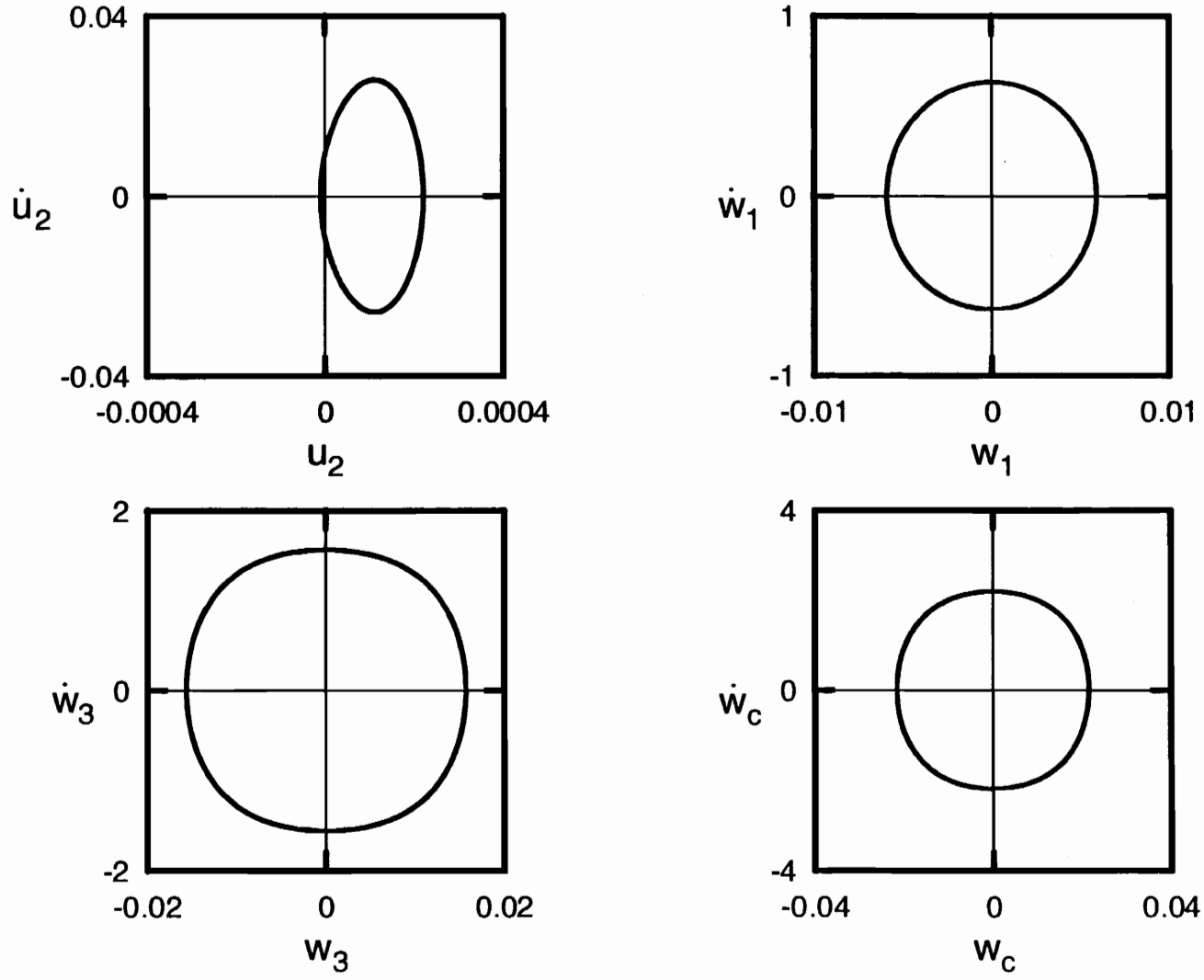

Figure A.77: Phase portraits for shear deformable beam with $r = 0.01$, $\Omega = 108.0$, $a = 0.005$.

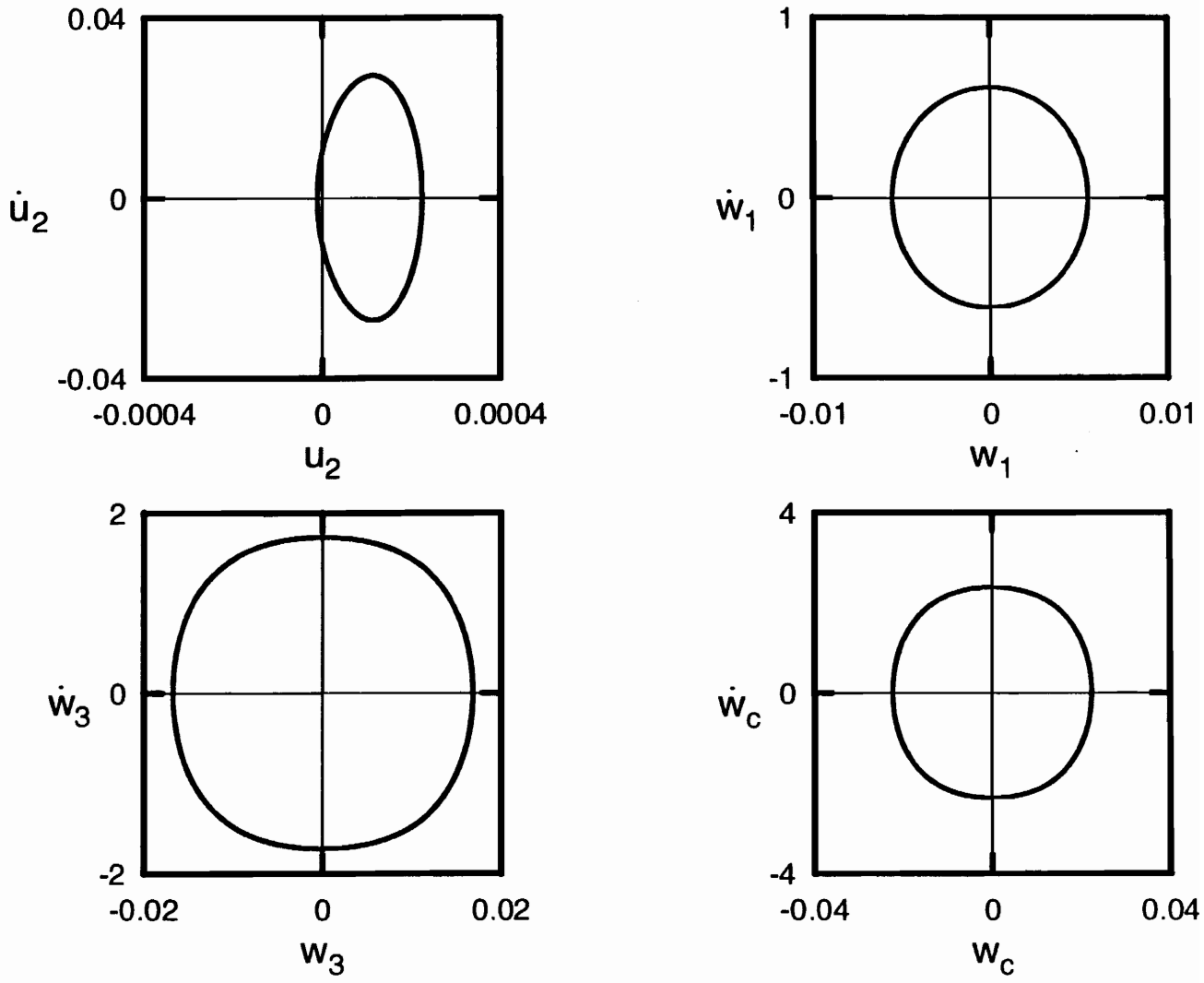

Figure A.78: Phase portraits for shear deformable beam with $r = 0.01$, $\Omega = 112.0$, $a = 0.005$.

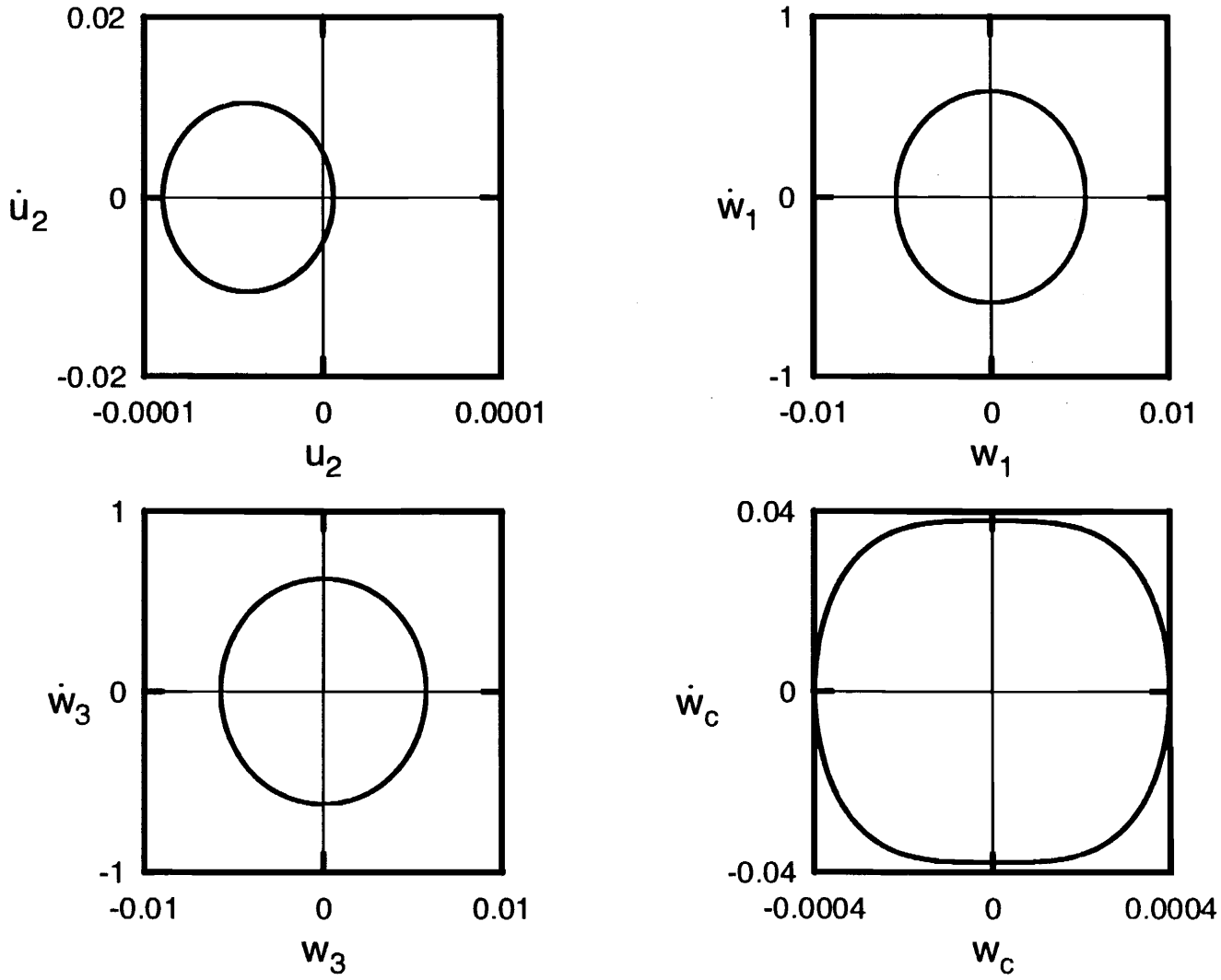

Figure A.79: Phase portraits for shear deformable beam with $r = 0.01$, $\Omega = 110.0$, $a = 0.005$.

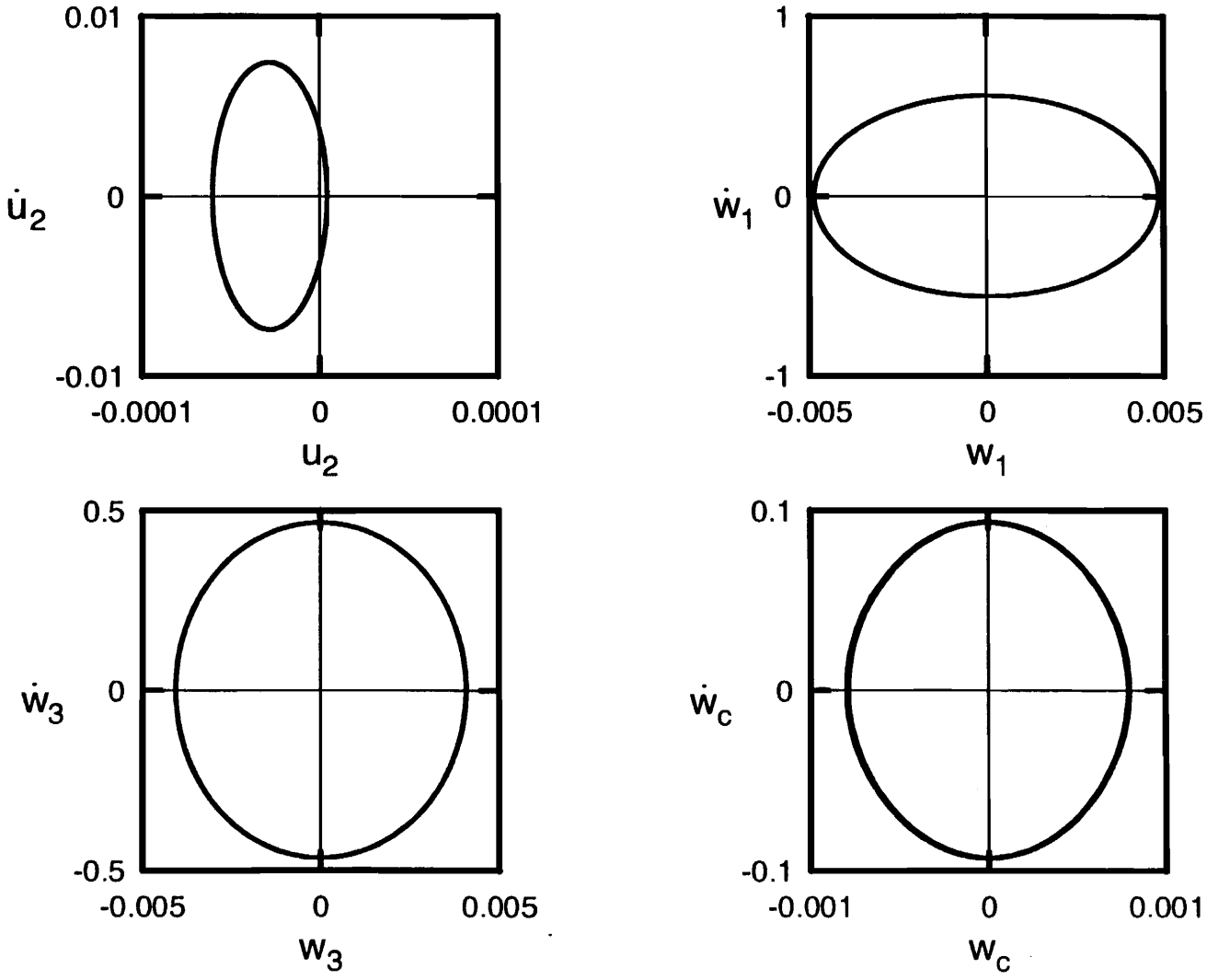

Figure A.80: Phase portraits for shear deformable beam with $r = 0.01$, $\Omega = 115.0$, $a = 0.005$.

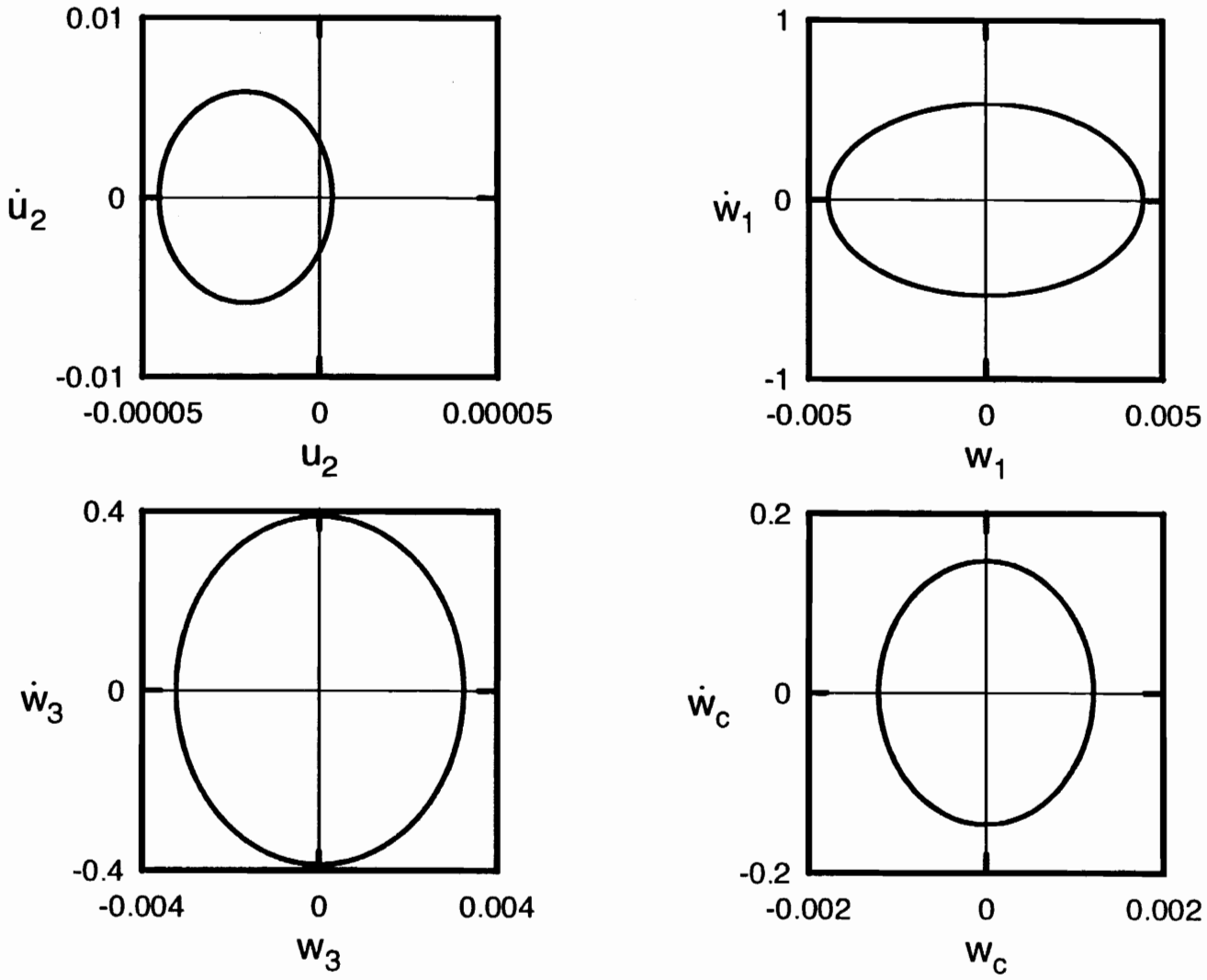

Figure A.81: Phase portraits for shear deformable beam with $r = 0.01$, $\Omega = 120.0$, $a = 0.005$.

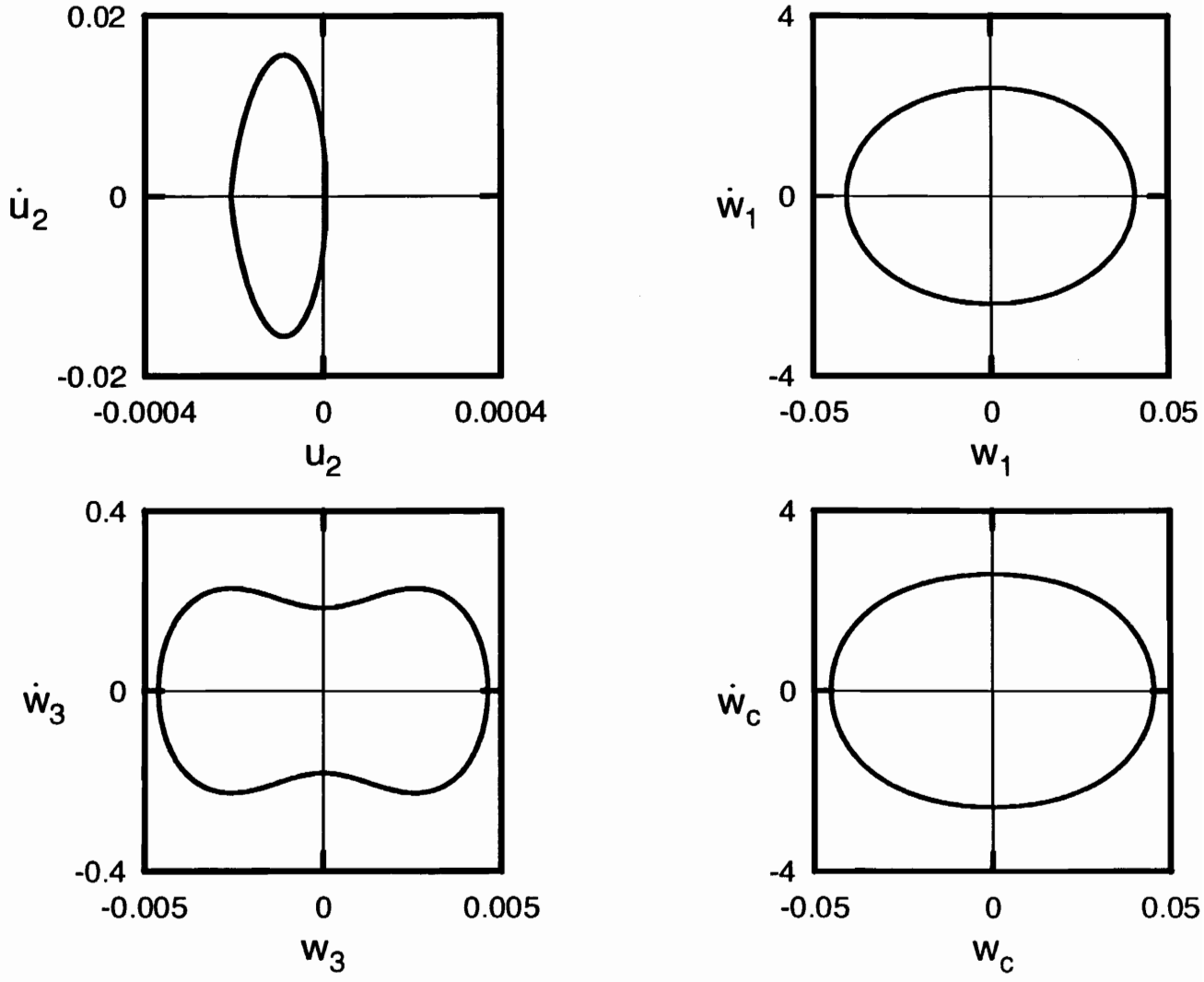

Figure A.82: Phase portraits for shear deformable beam with $r = 0.01$, $\Omega = 60.0$, $a = 0.01$.

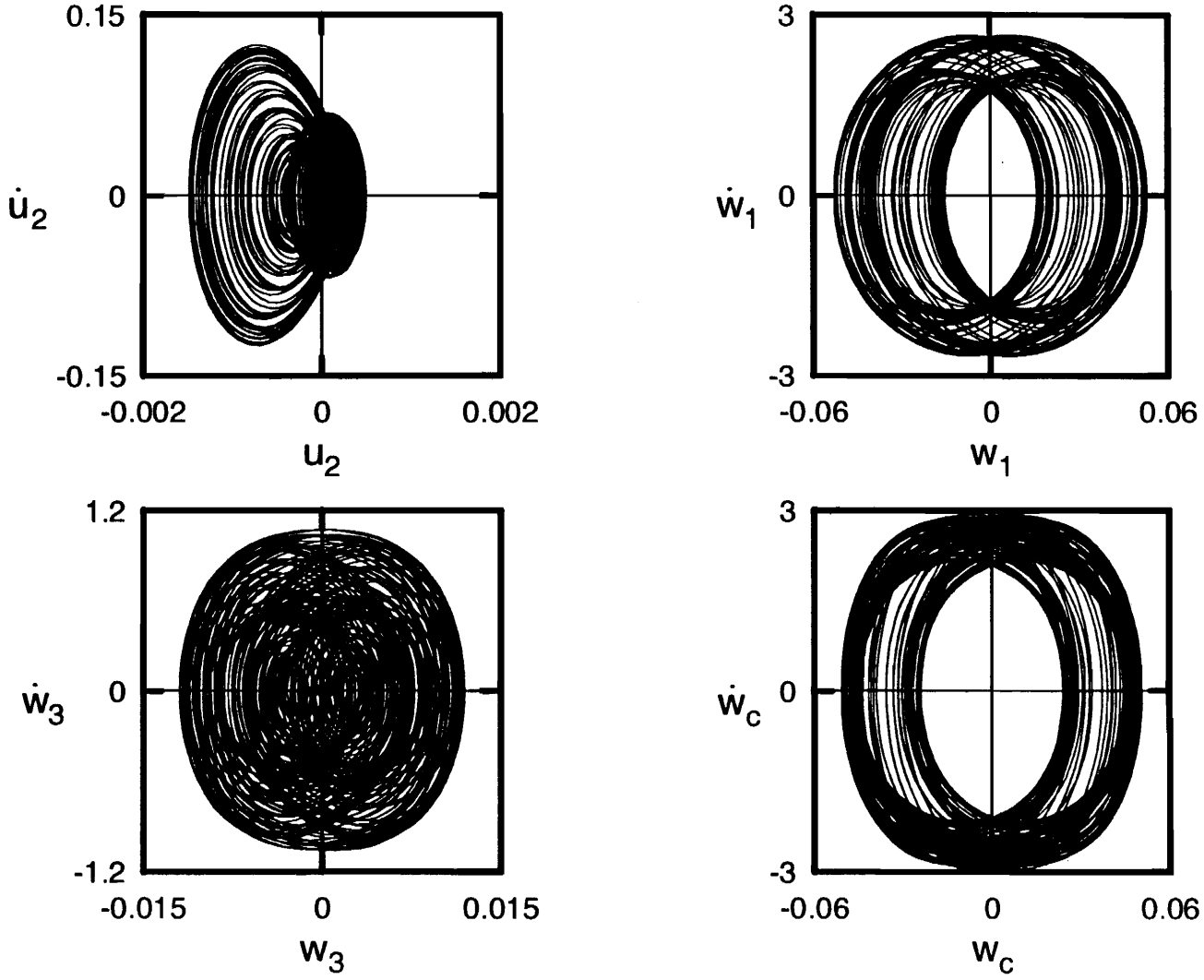

Figure A.83: Phase portraits for shear deformable beam with $r = 0.01$, $\Omega = 65.0$, $a = 0.01$.

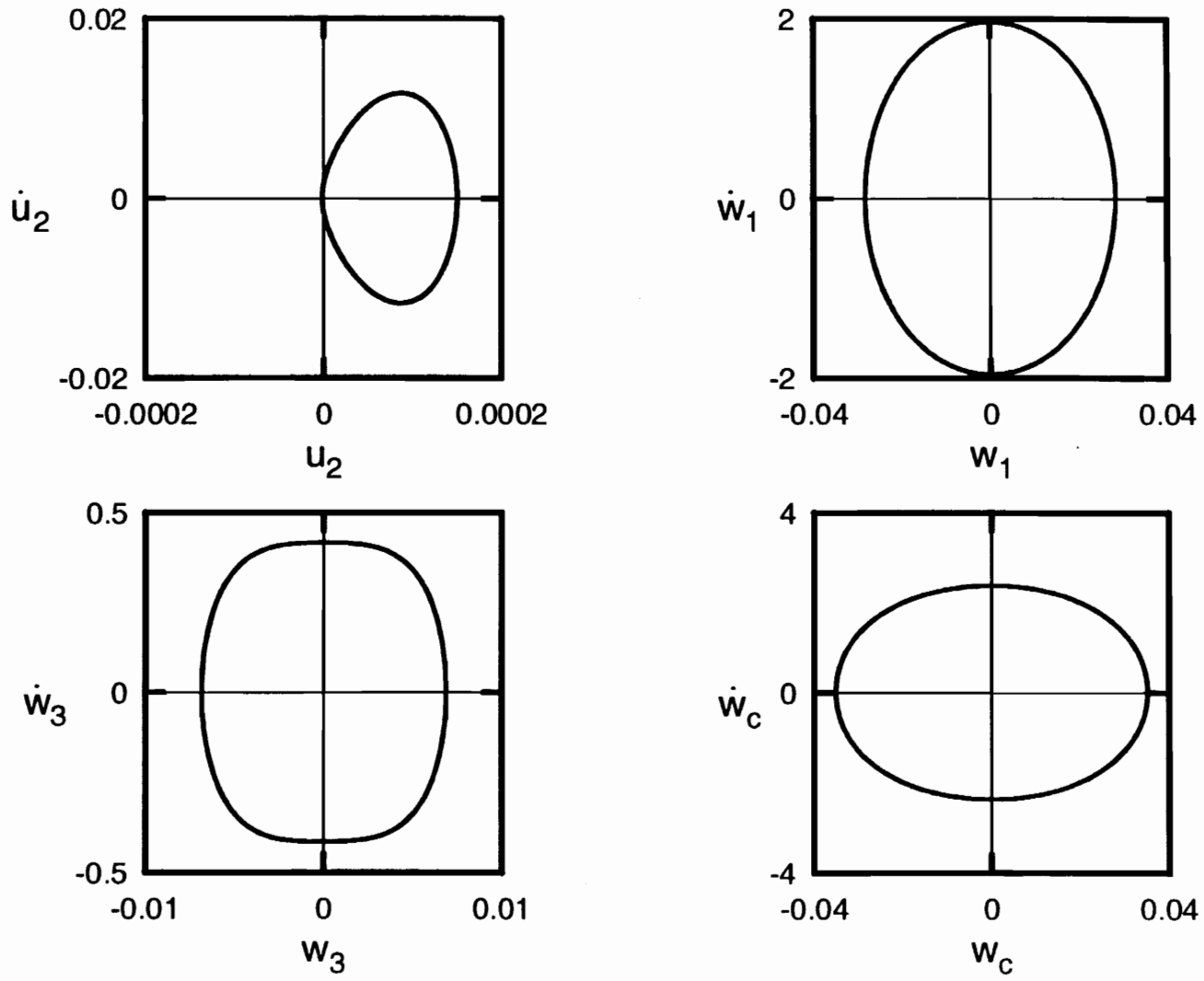

Figure A.84: Phase portraits for shear deformable beam with $r = 0.01$, $\Omega = 70.0$, $a = 0.01$.

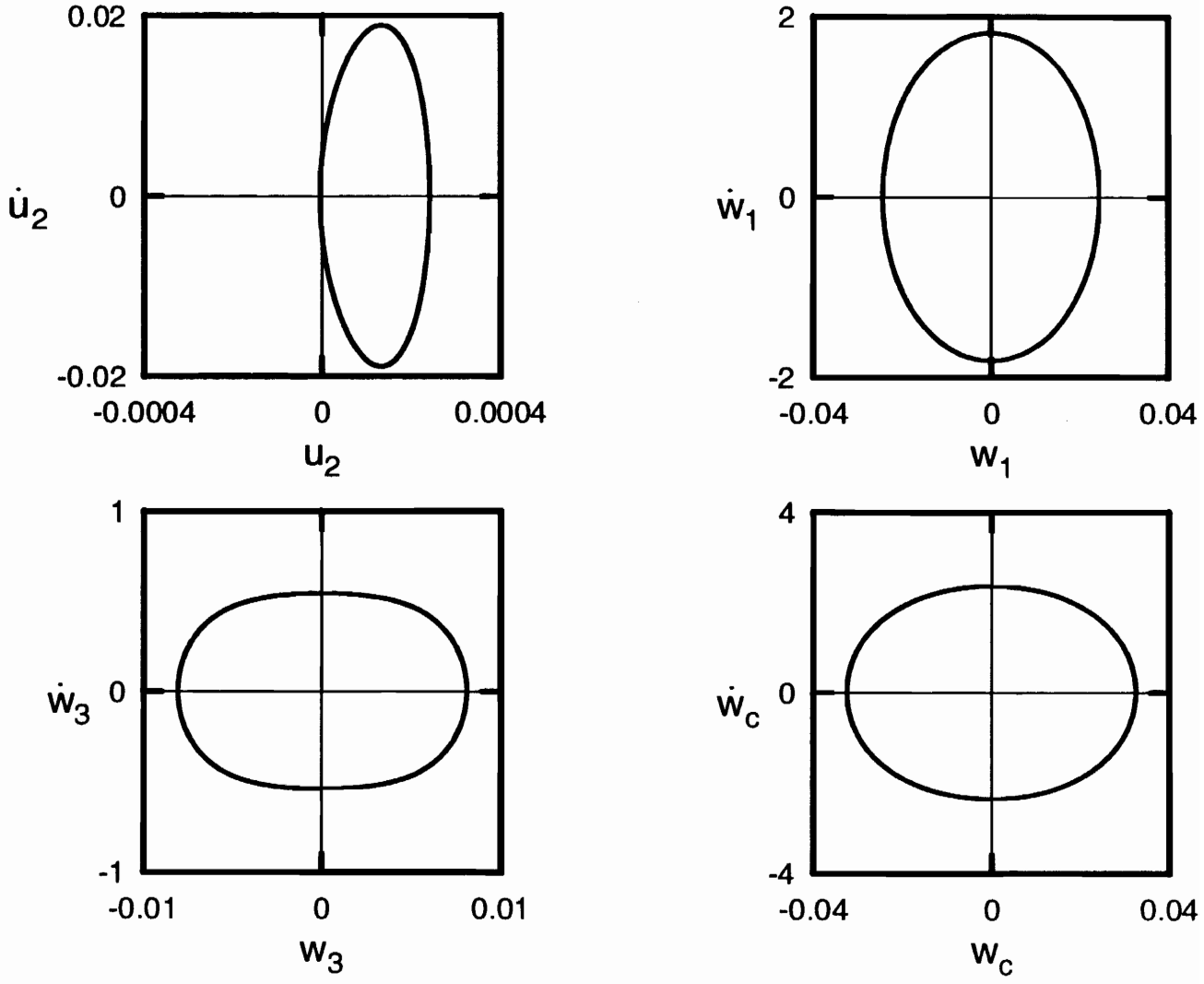

Figure A.85: Phase portraits for shear deformable beam with $r = 0.01$, $\Omega = 75.0$, $a = 0.01$.

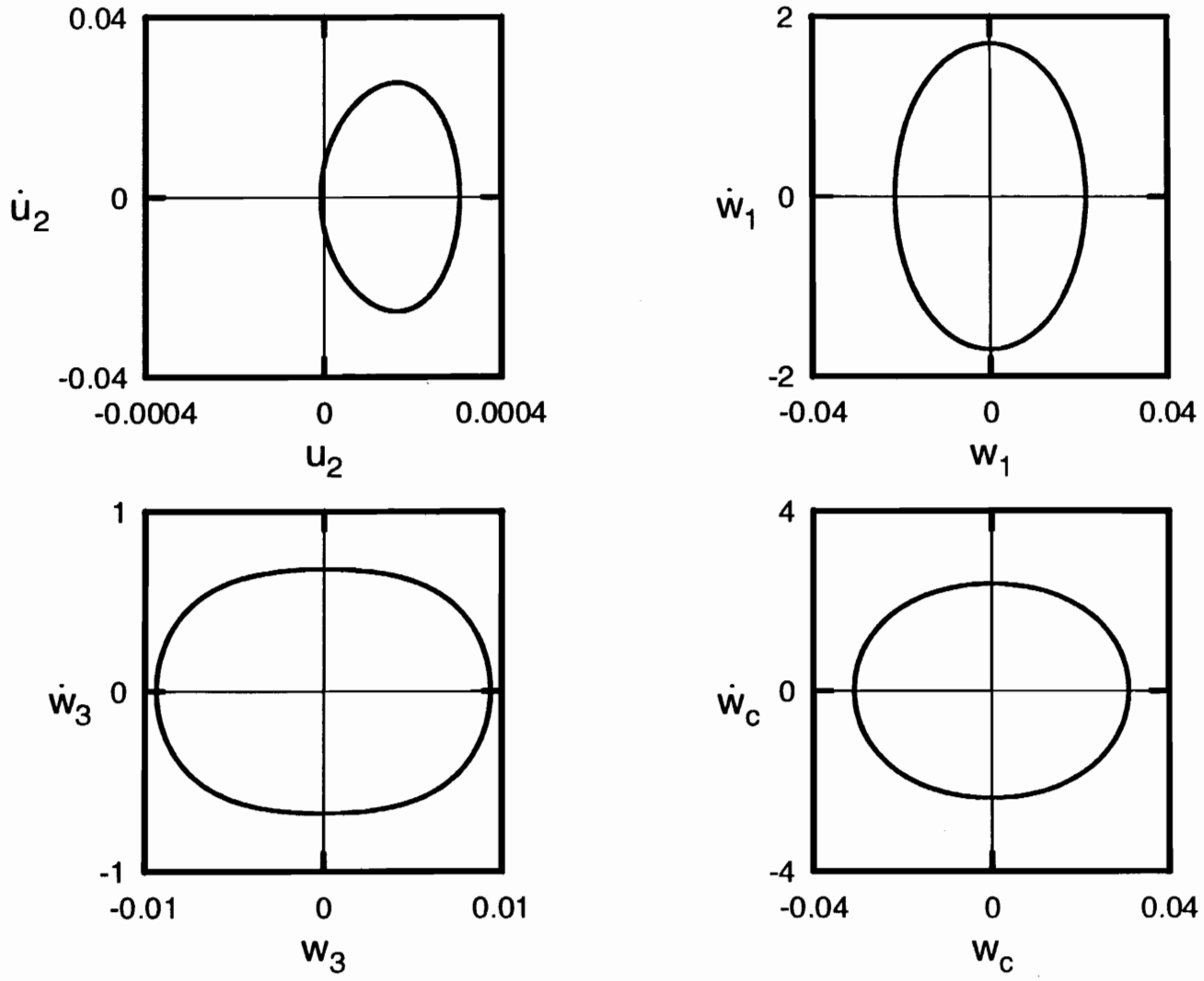

Figure A.86: Phase portraits for shear deformable beam with $r = 0.01$, $\Omega = 80.0$, $a = 0.01$.

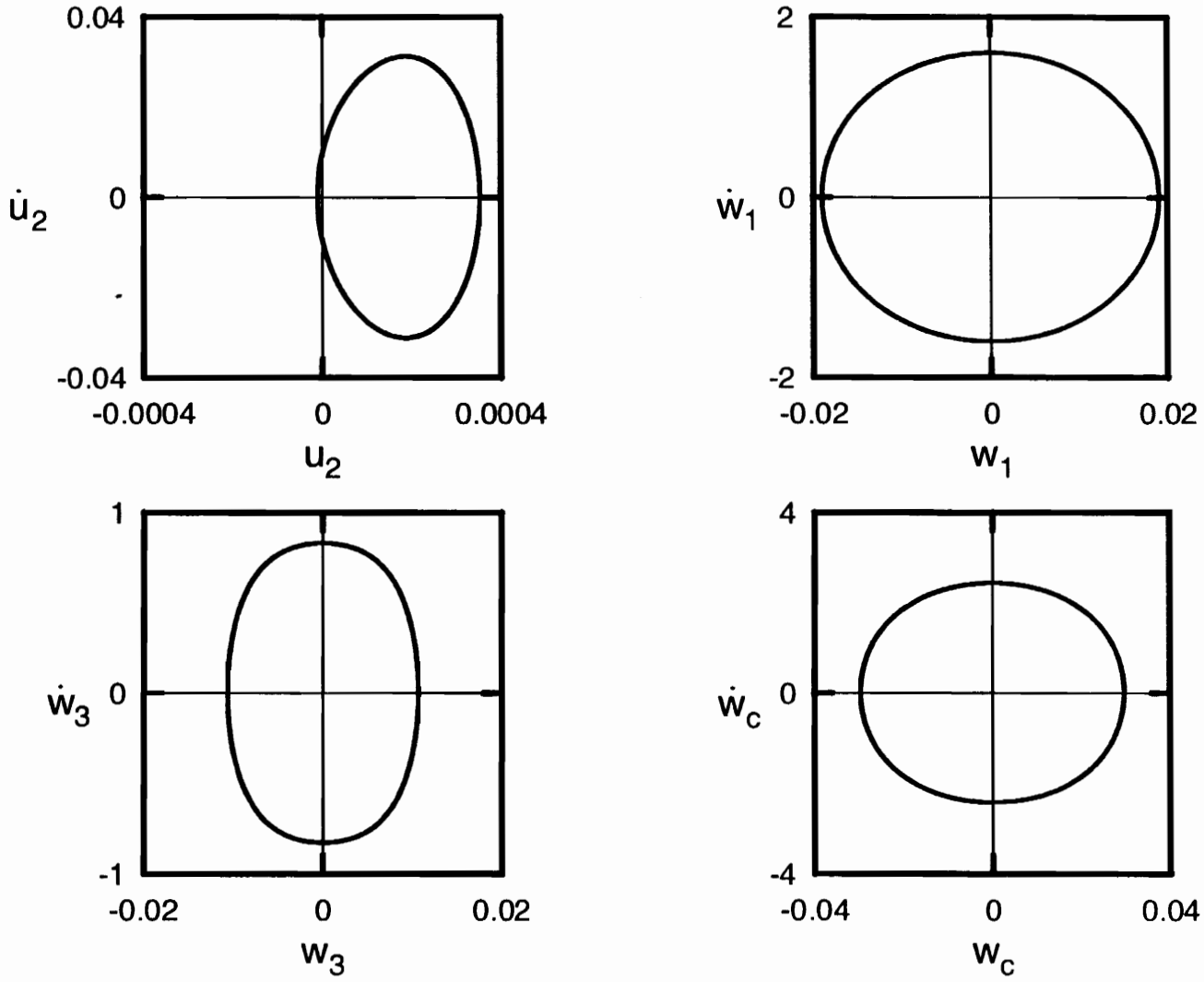

Figure A.87: Phase portraits for shear deformable beam with $r = 0.01$, $\Omega = 85.0$, $a = 0.01$.

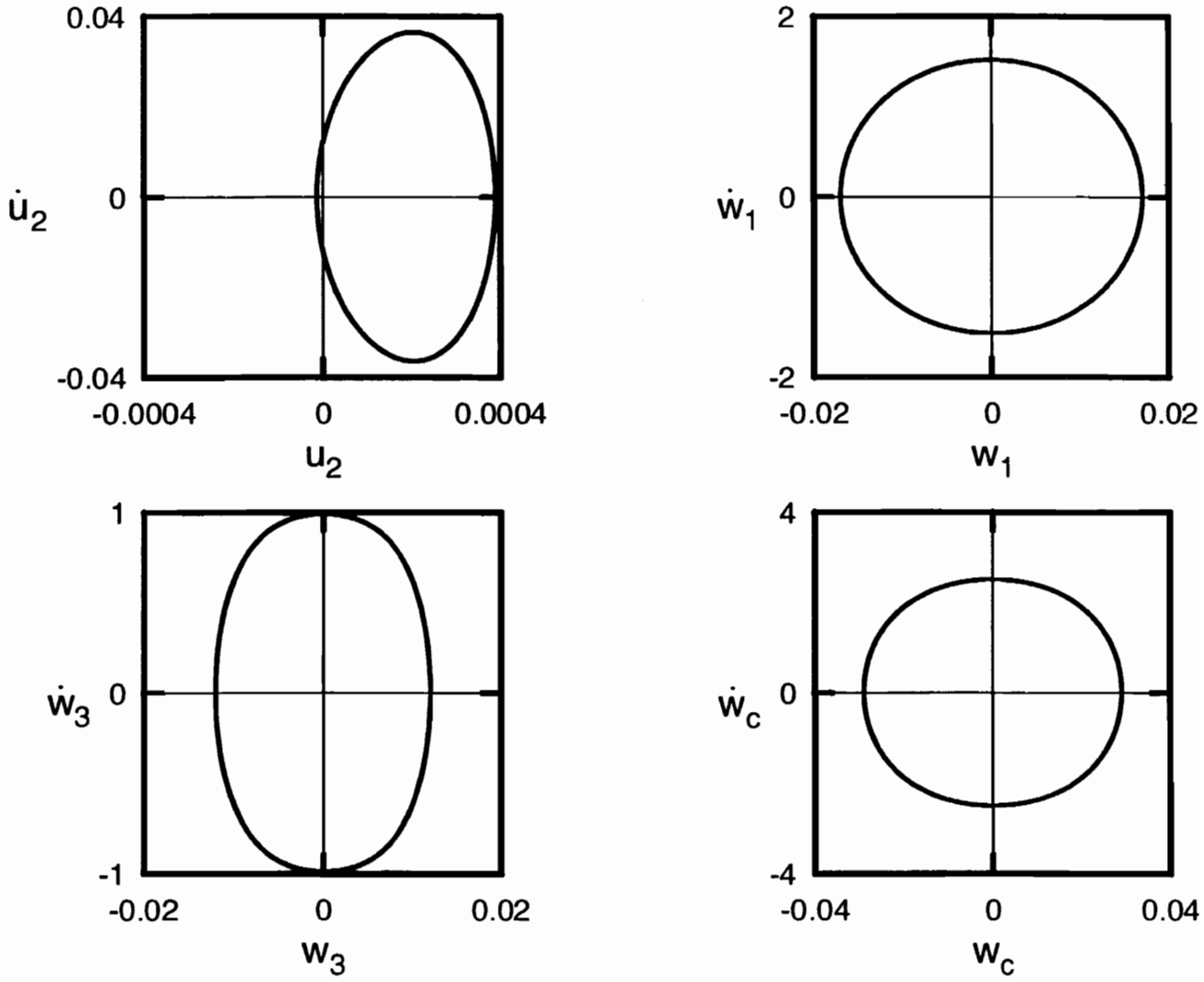

Figure A.88: Phase portraits for shear deformable beam with $r = 0.01$, $\Omega = 90.0$, $a = 0.01$.

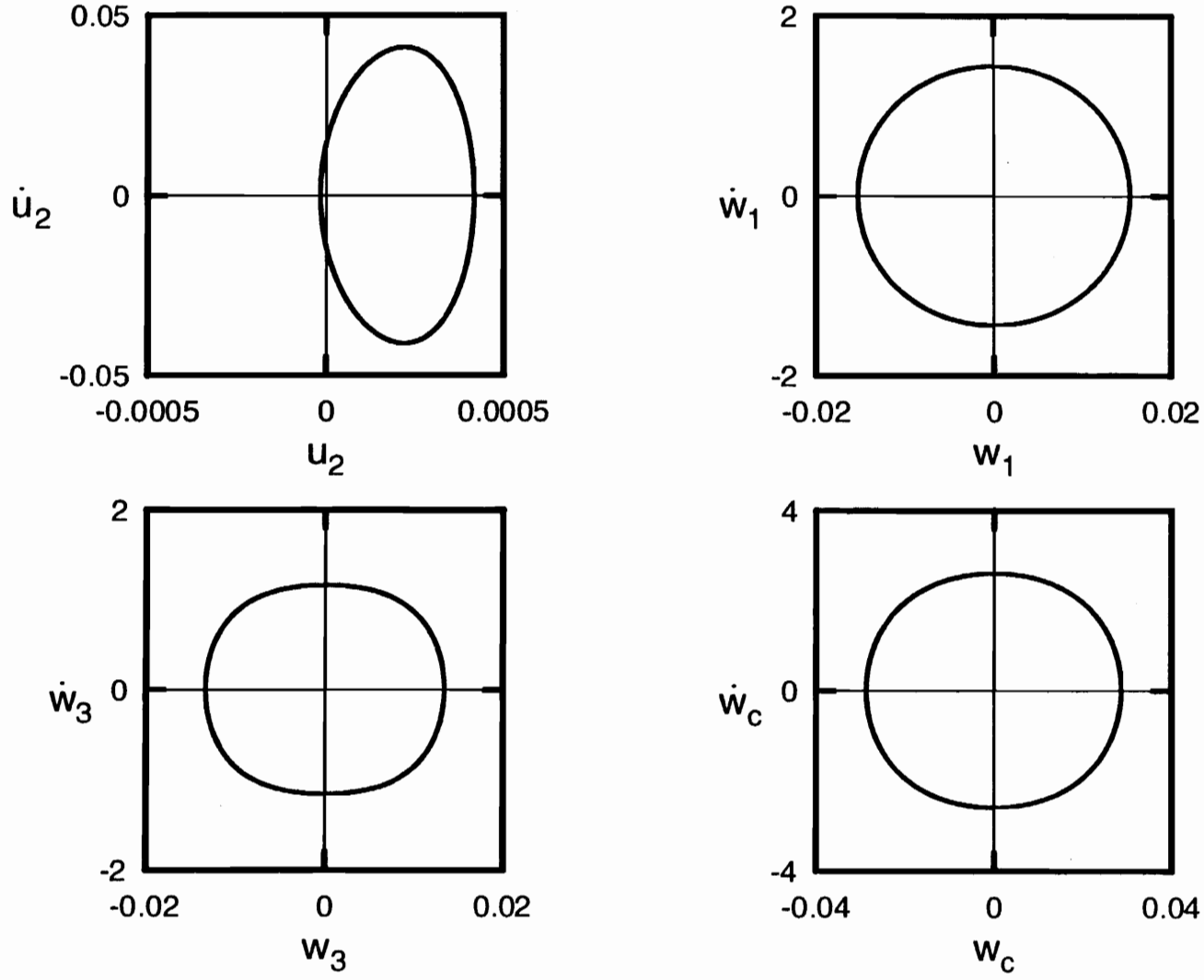

Figure A.89: Phase portraits for shear deformable beam with $r = 0.01$, $\Omega = 95.0$, $a = 0.01$.

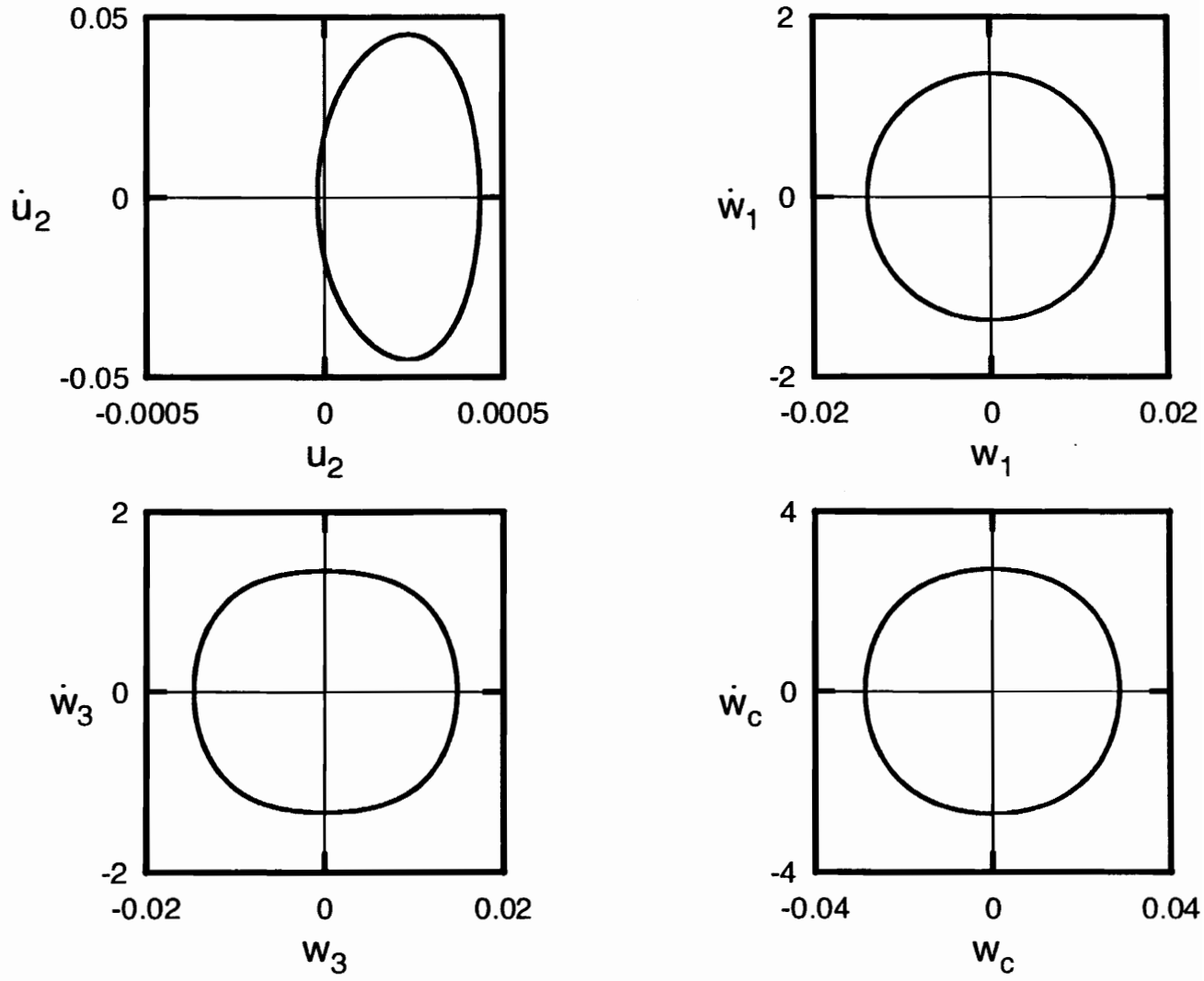

Figure A.90: Phase portraits for shear deformable beam with $r = 0.01$, $\Omega = 100.0$, $a = 0.01$.

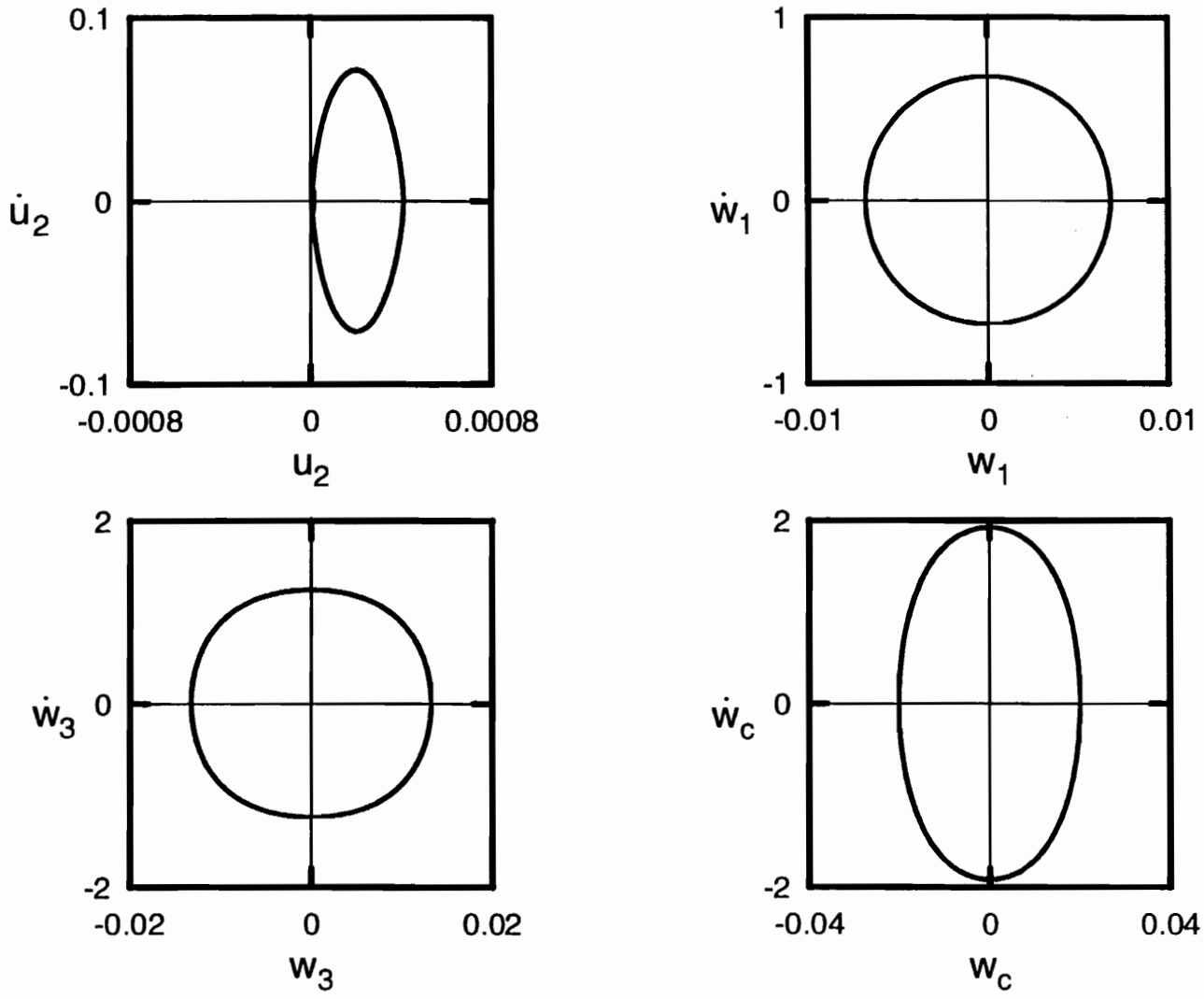

Figure A.91: Phase portraits for shear deformable beam with $r = 0.01$, $\Omega = 105.0$, $a = 0.02$.

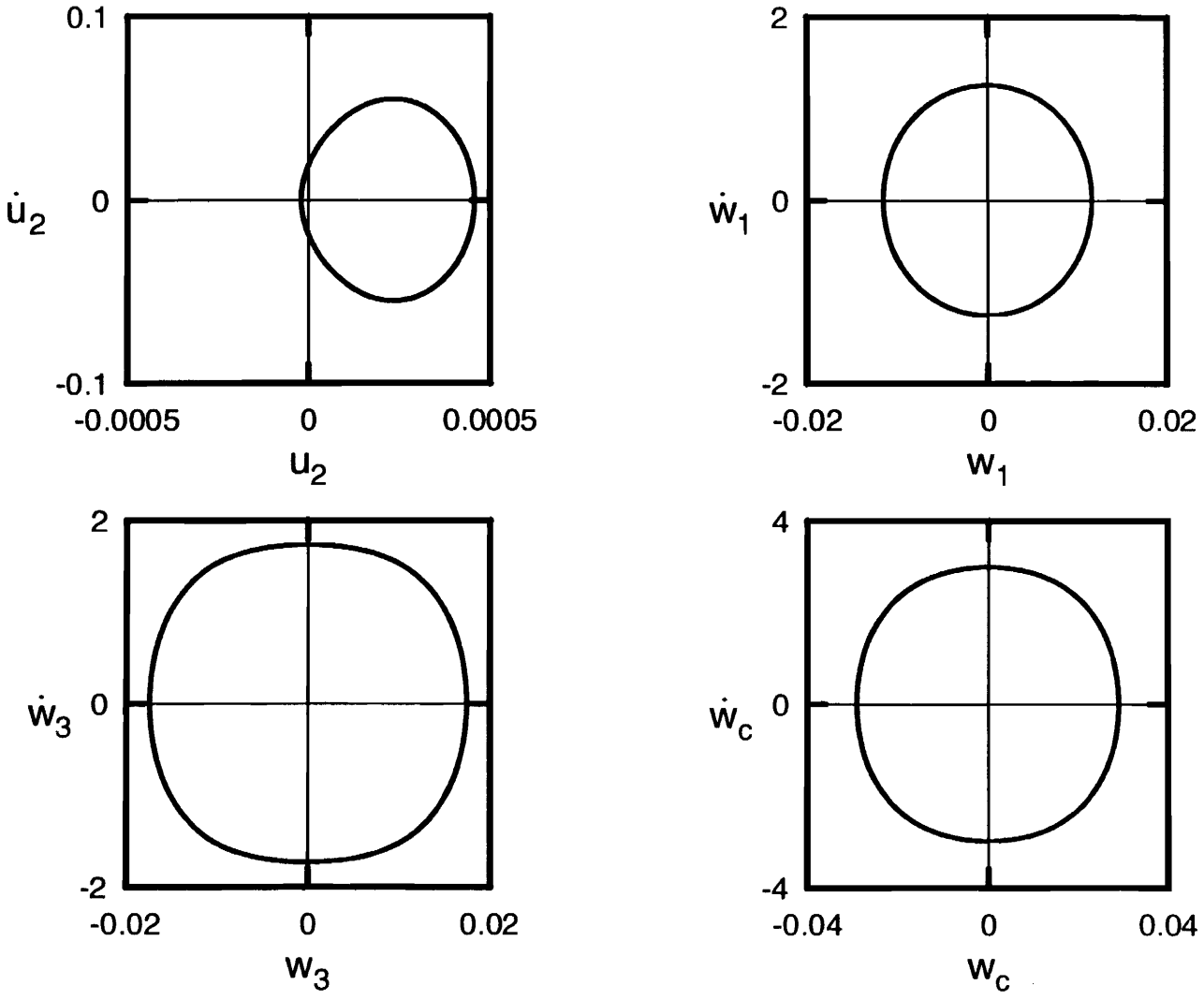

Figure A.92: Phase portraits for shear deformable beam with $r = 0.01$, $\Omega = 110.0$, $a = 0.01$.

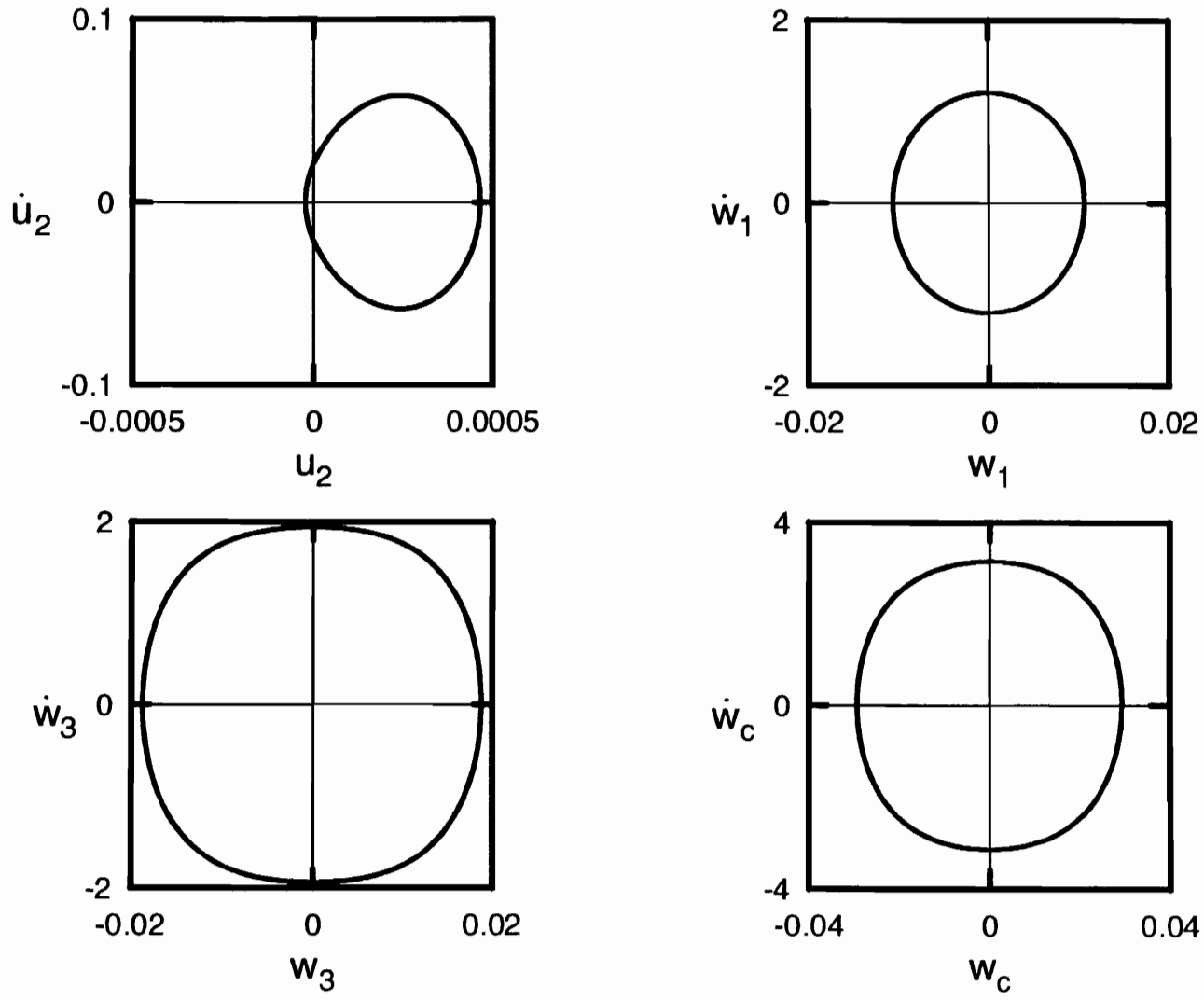

Figure A.93: Phase portraits for shear deformable beam with $r = 0.01$, $\Omega = 115.0$, $a = 0.01$.

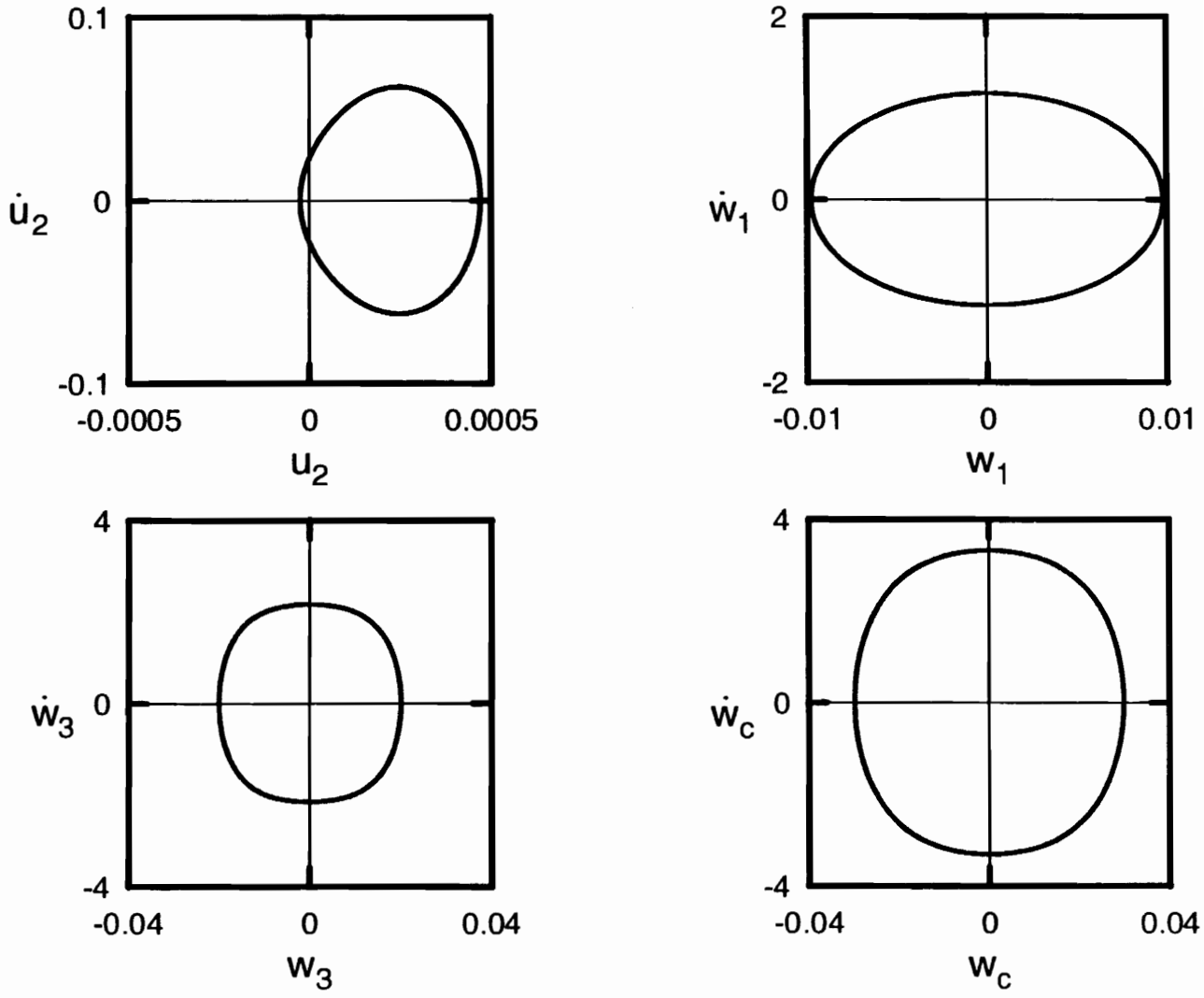

Figure A.94: Phase portraits for shear deformable beam with $r = 0.01$, $\Omega = 120.0$, $a = 0.01$.

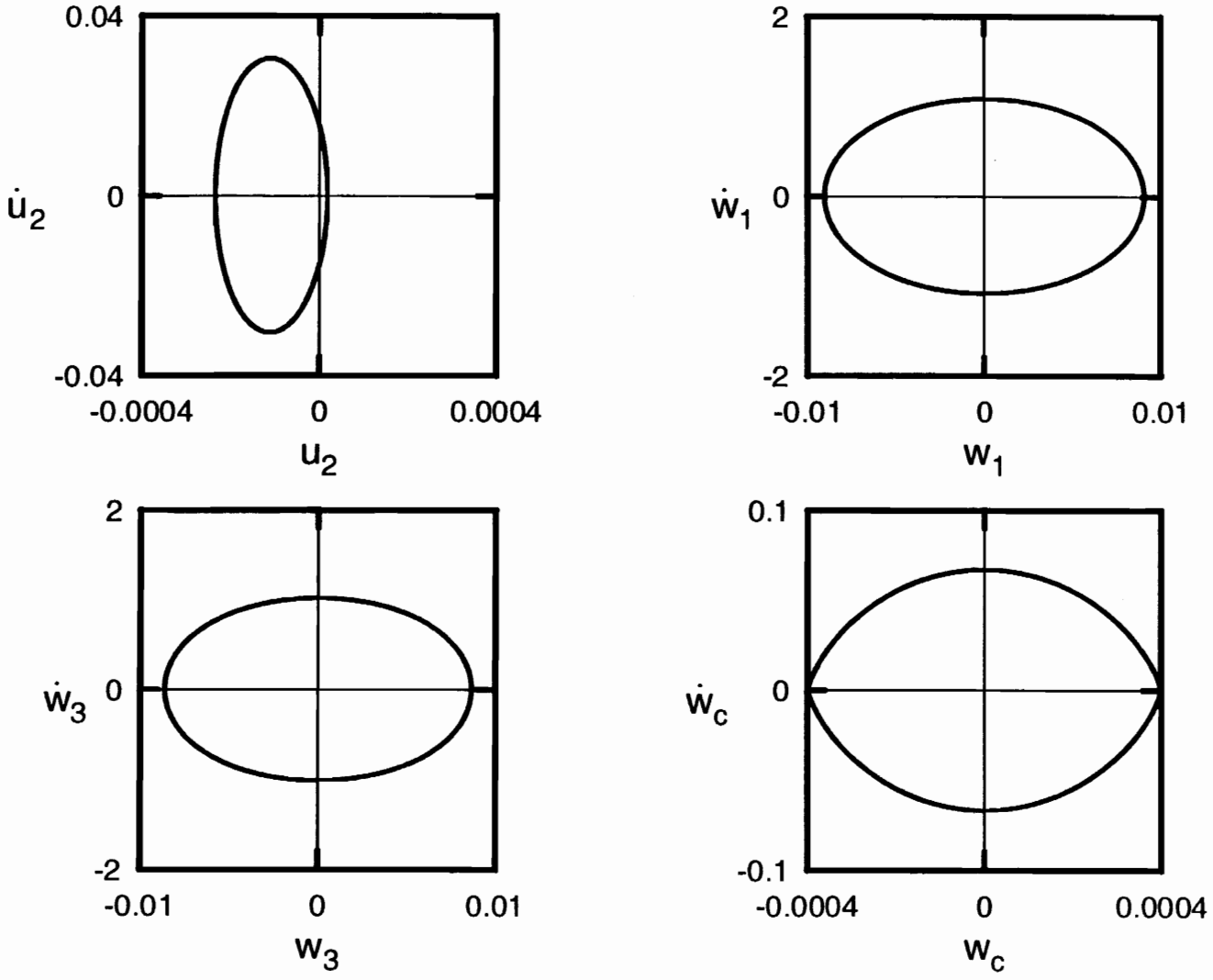

Figure A.95: Phase portraits for shear deformable beam with $r = 0.01$, $\Omega = 120.0$, $a = 0.01$.

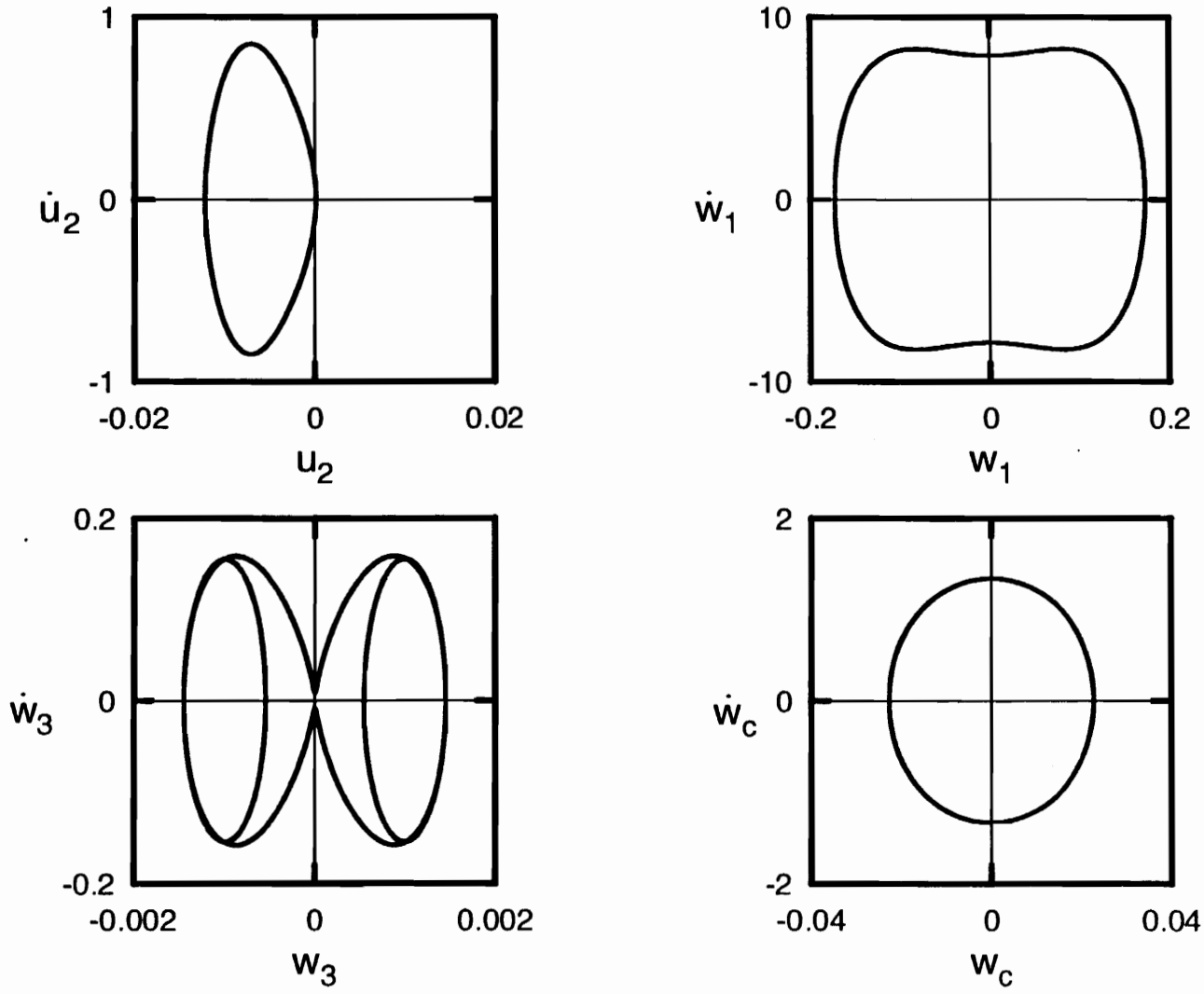

Figure A.96: Phase portraits for shear deformable beam with $r = 0.01$, $\Omega = 60.0$, $a = 0.02$.

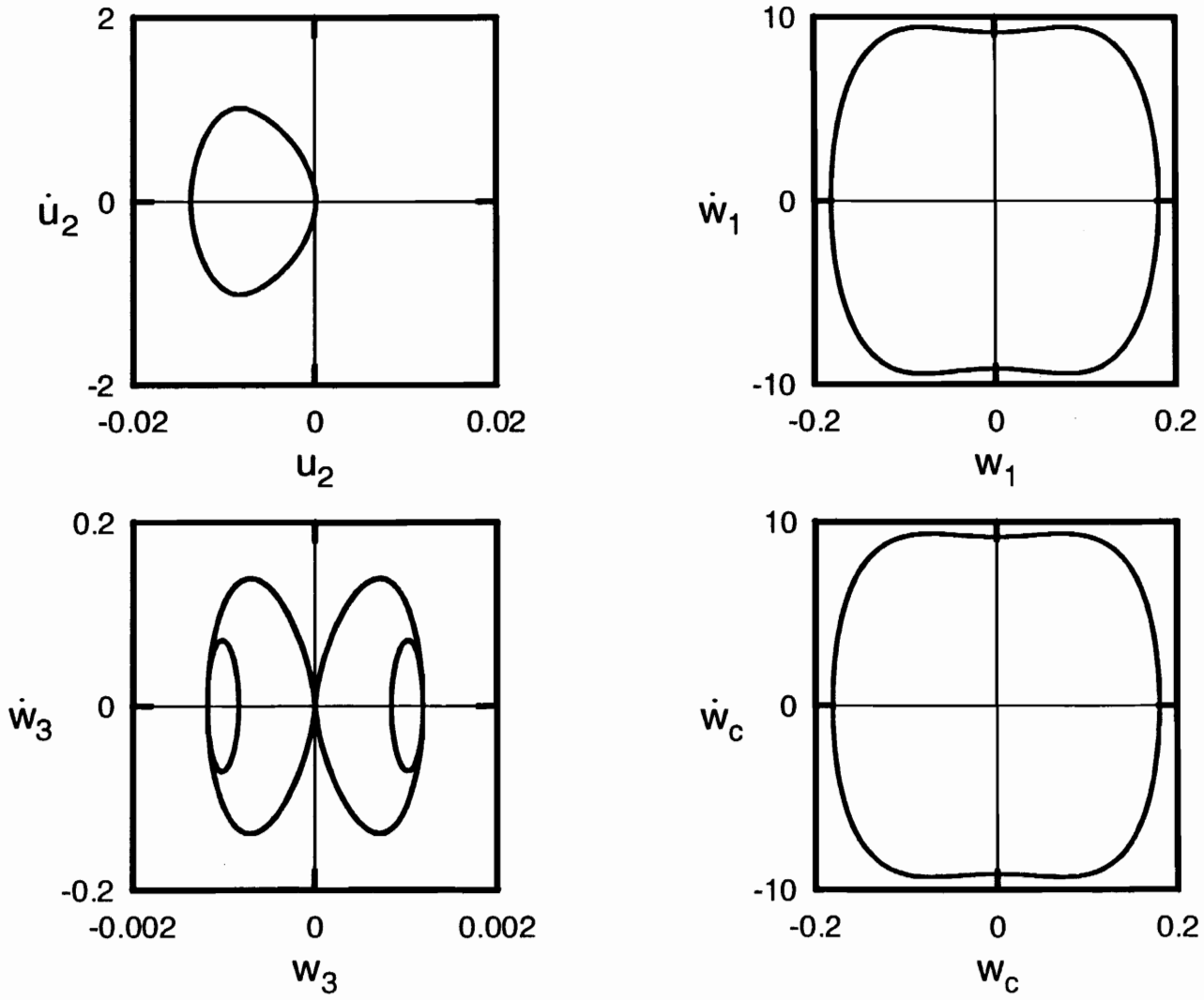

Figure A.97: Phase portraits for shear deformable beam with $r = 0.01$, $\Omega = 65.0$, $a = 0.02$.

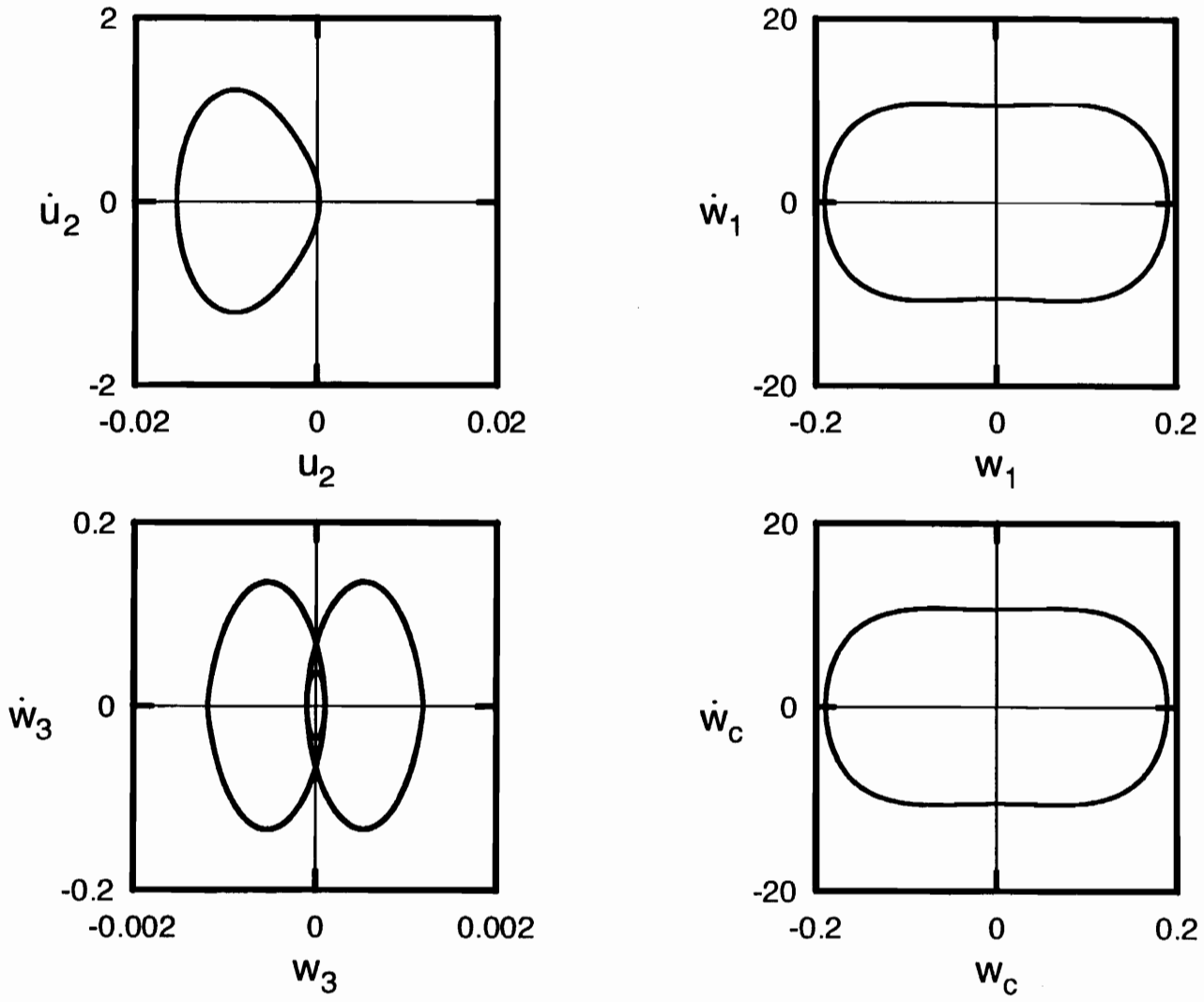

Figure A.98: Phase portraits for shear deformable beam with $r = 0.01$, $\Omega = 70.0$, $a = 0.02$.

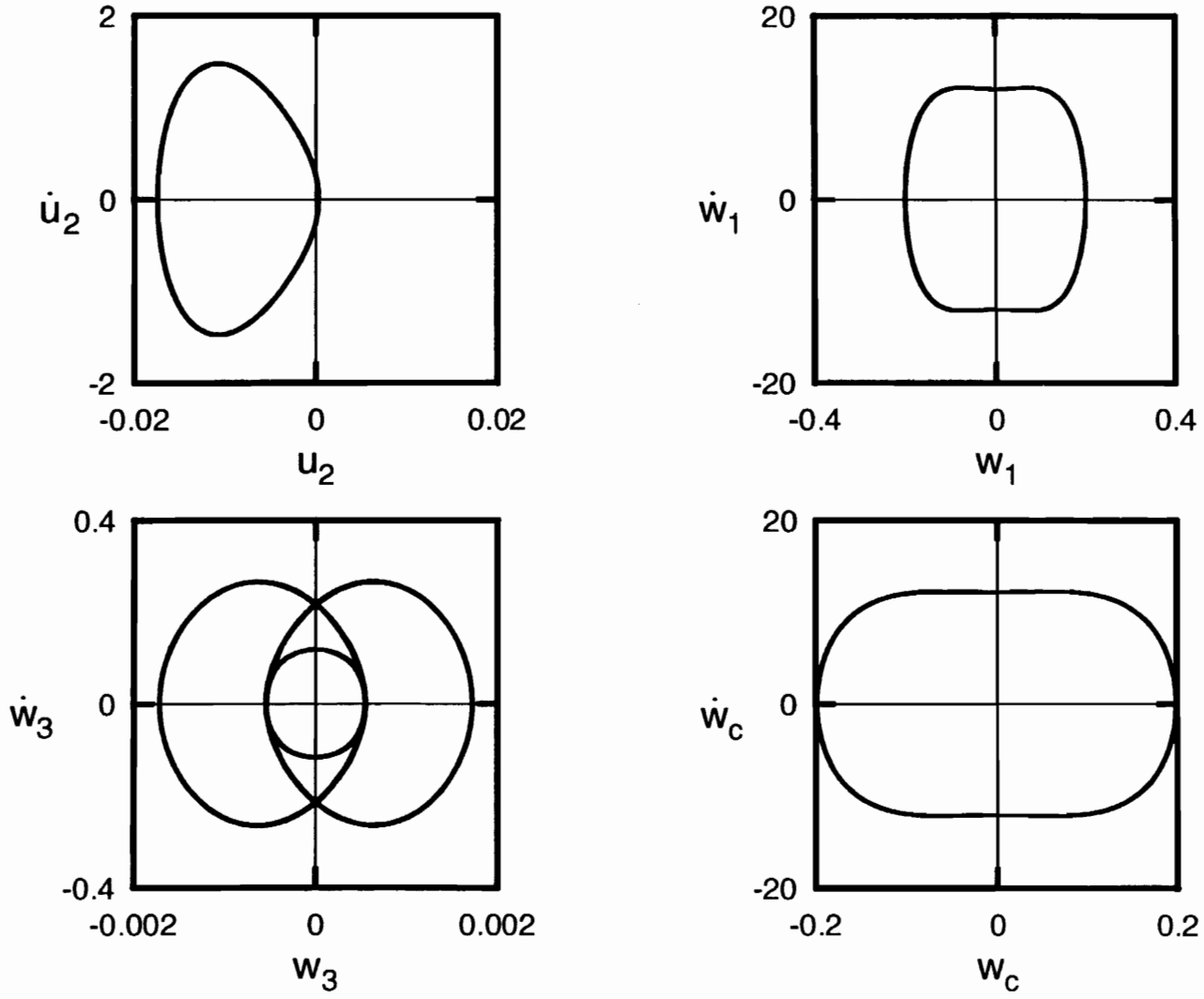

Figure A.99: Phase portraits for shear deformable beam with $r = 0.01$, $\Omega = 75.0$, $a = 0.02$.

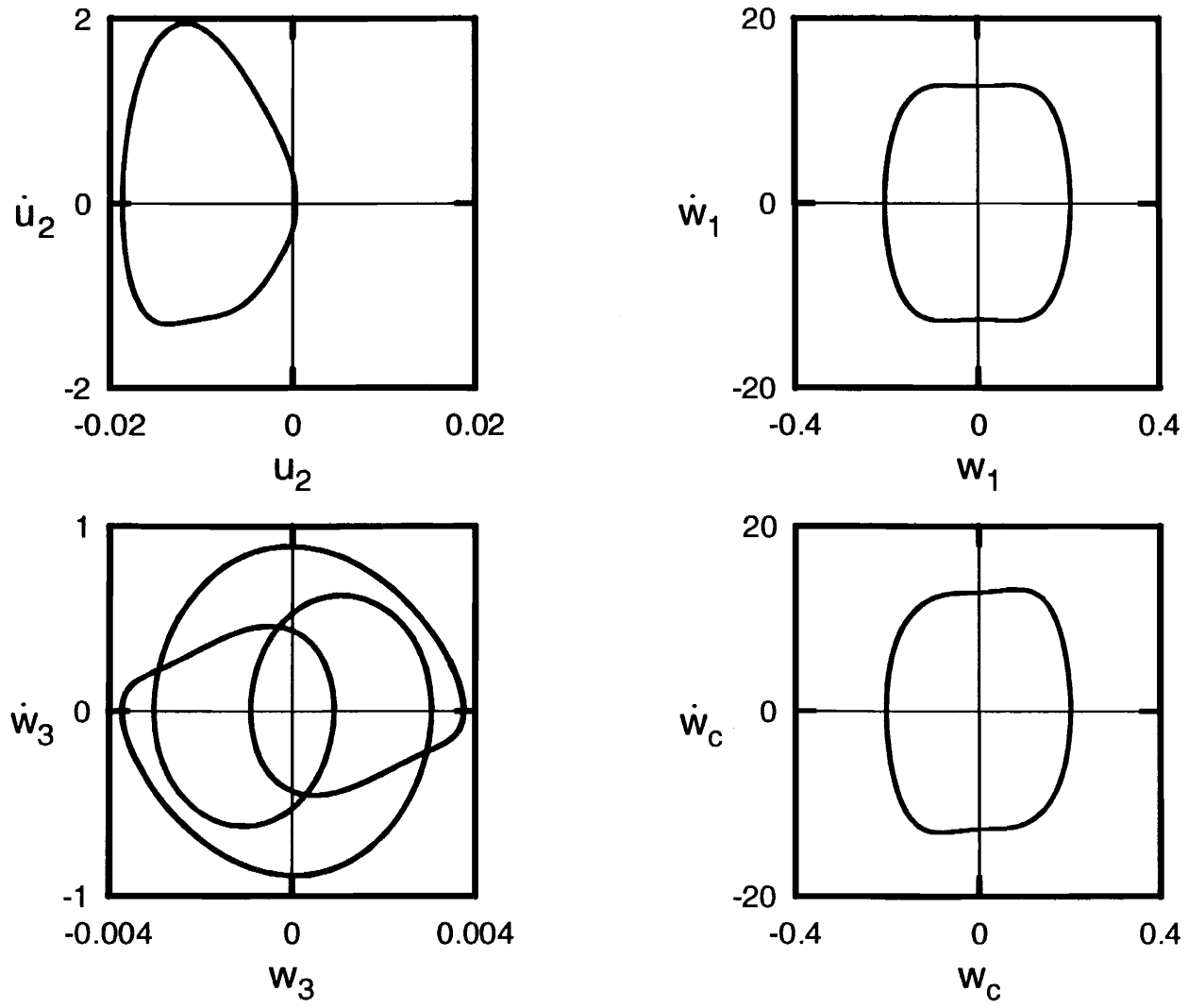

Figure A.100: Phase portraits for shear deformable beam with $r = 0.01$, $\Omega = 77.0$, $a = 0.02$.

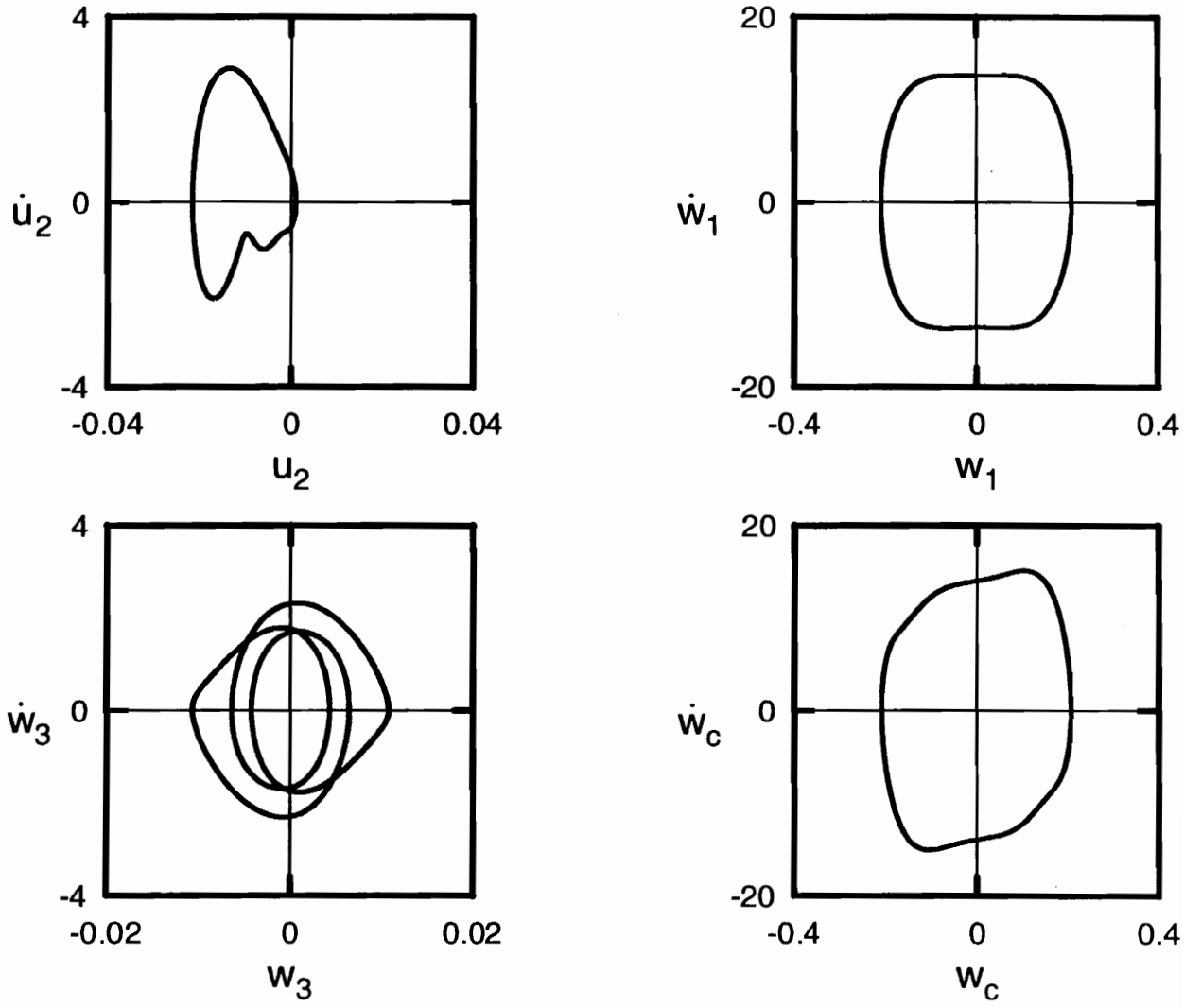

Figure A.101: Phase portraits for shear deformable beam with $r = 0.01$, $\Omega = 80.0$, $a = 0.02$.

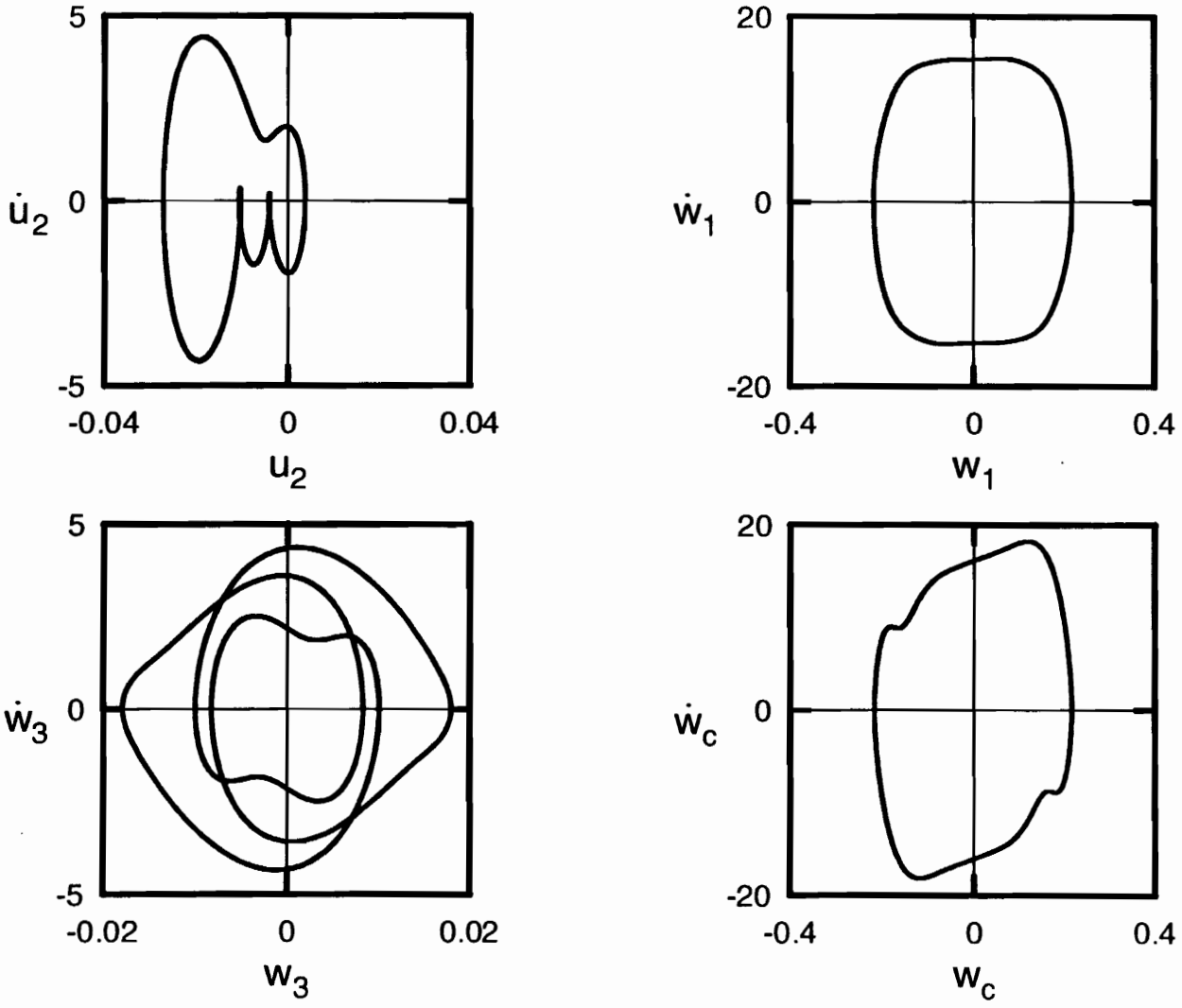

Figure A.102: Phase portraits for shear deformable beam with $r = 0.01$, $\Omega = 85.0$, $a = 0.02$.

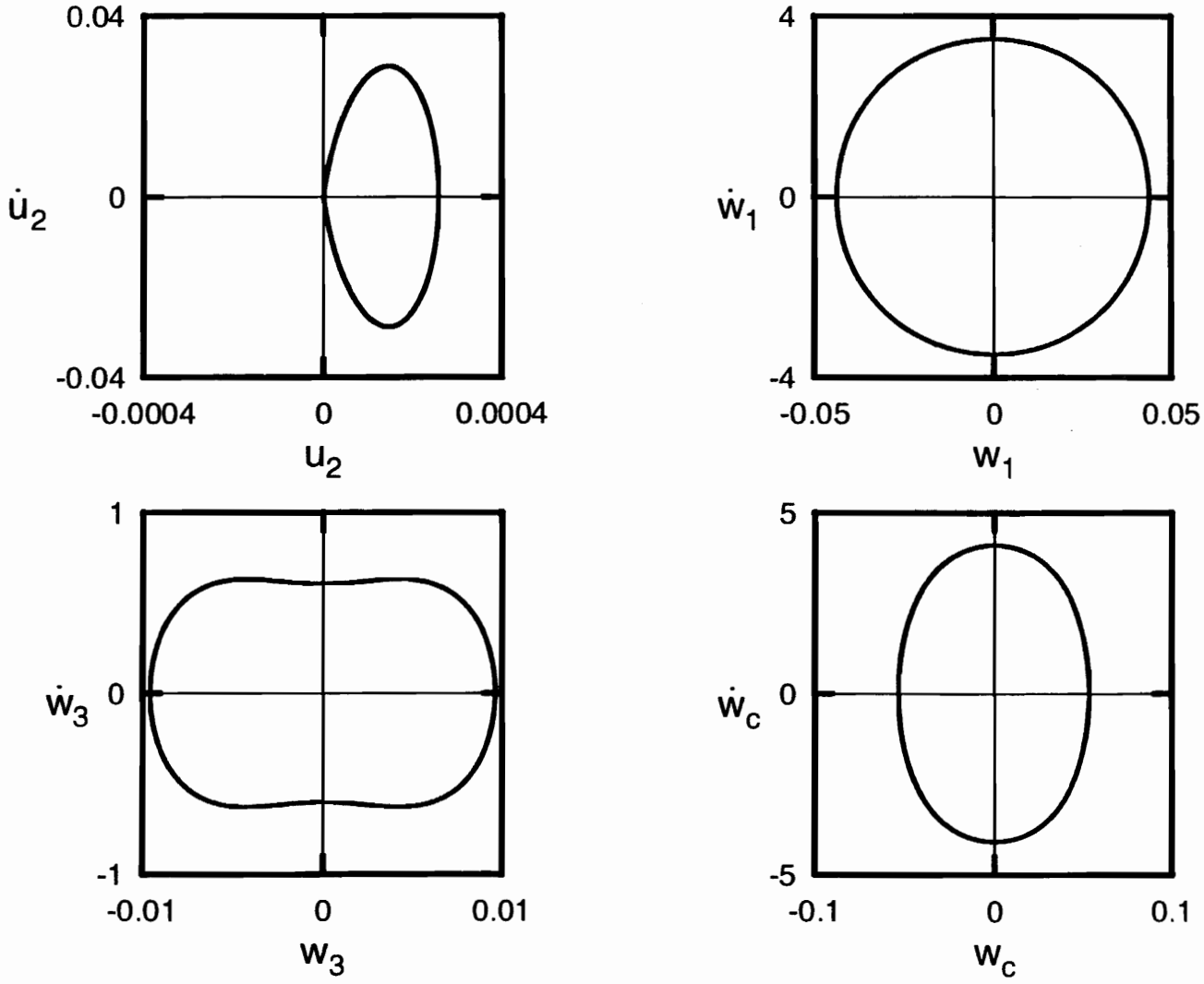

Figure A.103: Phase portraits for shear deformable beam with $r = 0.01$, $\Omega = 81.0$, $a = 0.02$.

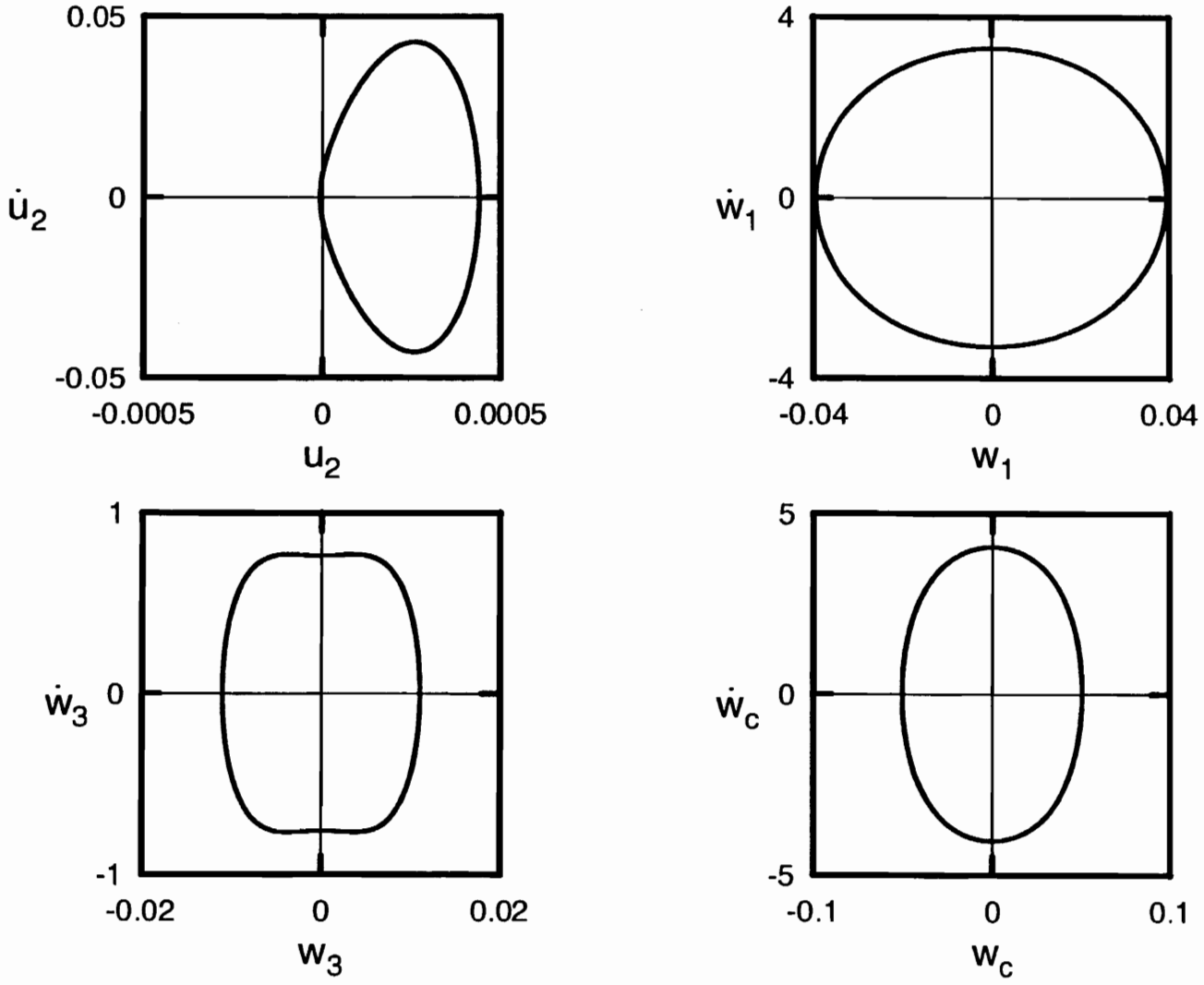

Figure A.104: Phase portraits for shear deformable beam with $r = 0.01$, $\Omega = 85.0$, $a = 0.02$.

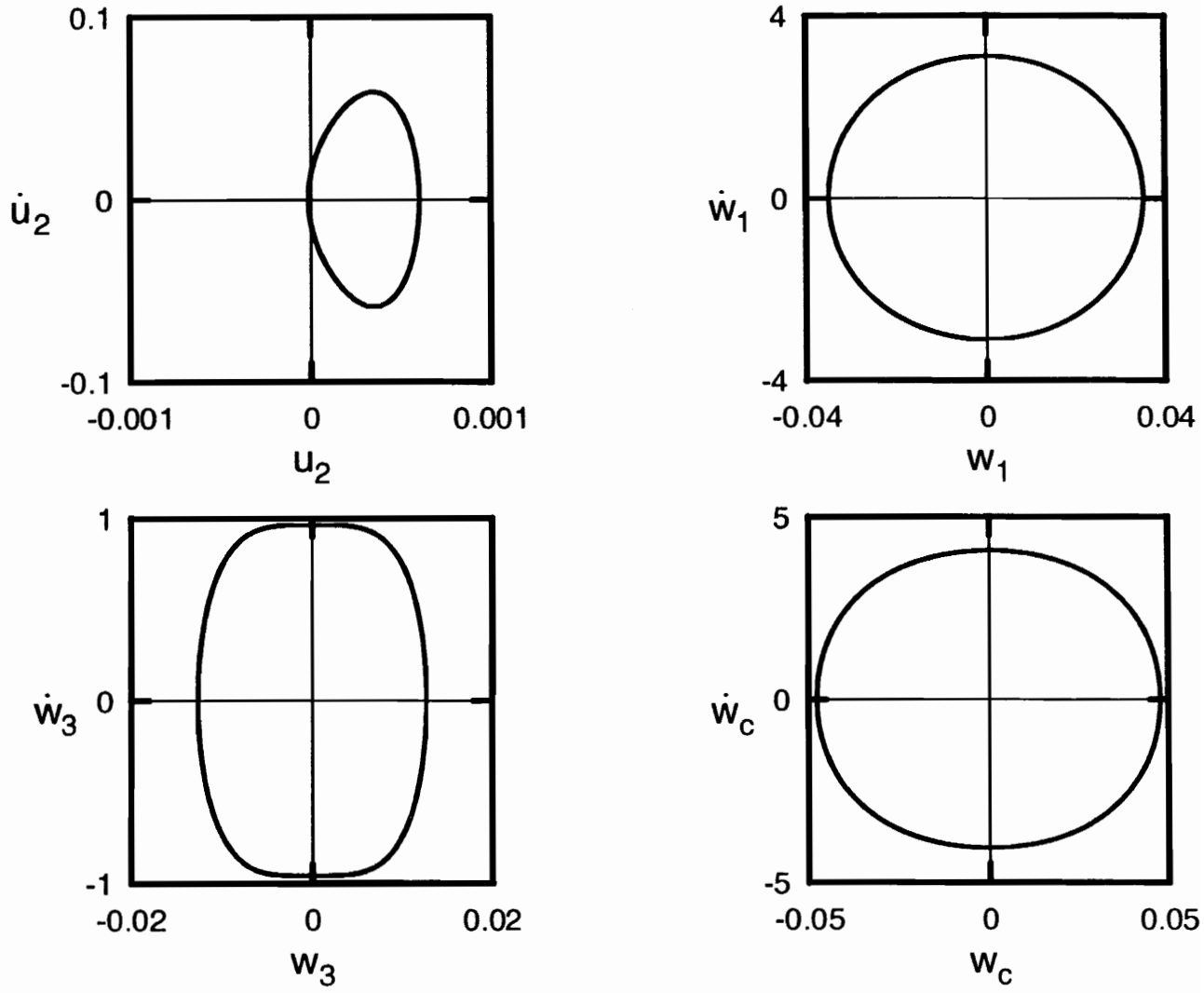

Figure A.105: Phase portraits for shear deformable beam with $r = 0.01$, $\Omega = 90.0$, $a = 0.02$.

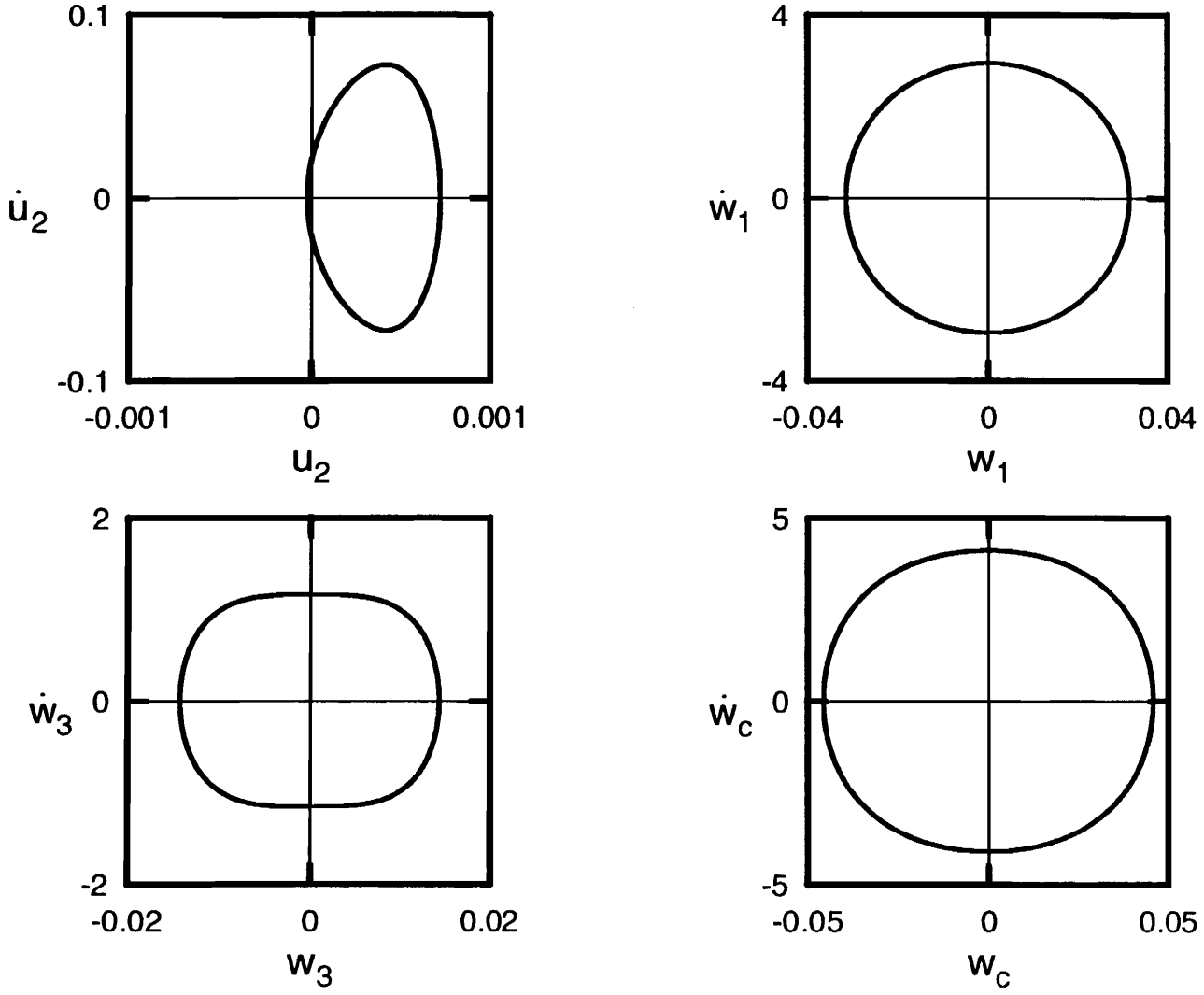

Figure A.106: Phase portraits for shear deformable beam with $r = 0.01$, $\Omega = 95.0$, $a = 0.02$.

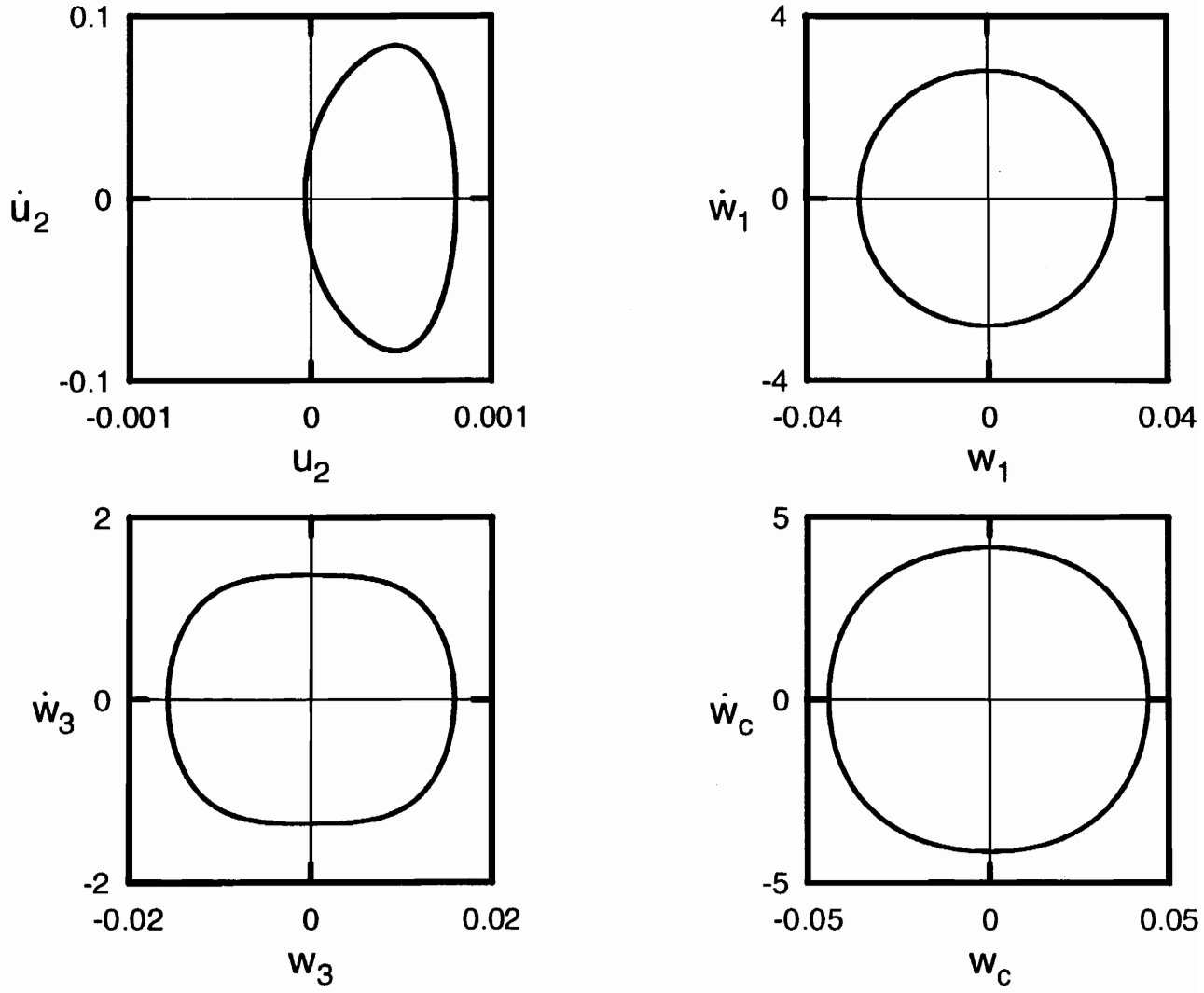

Figure A.107: Phase portraits for shear deformable beam with $r = 0.01$, $\Omega = 100.0$, $a = 0.02$.

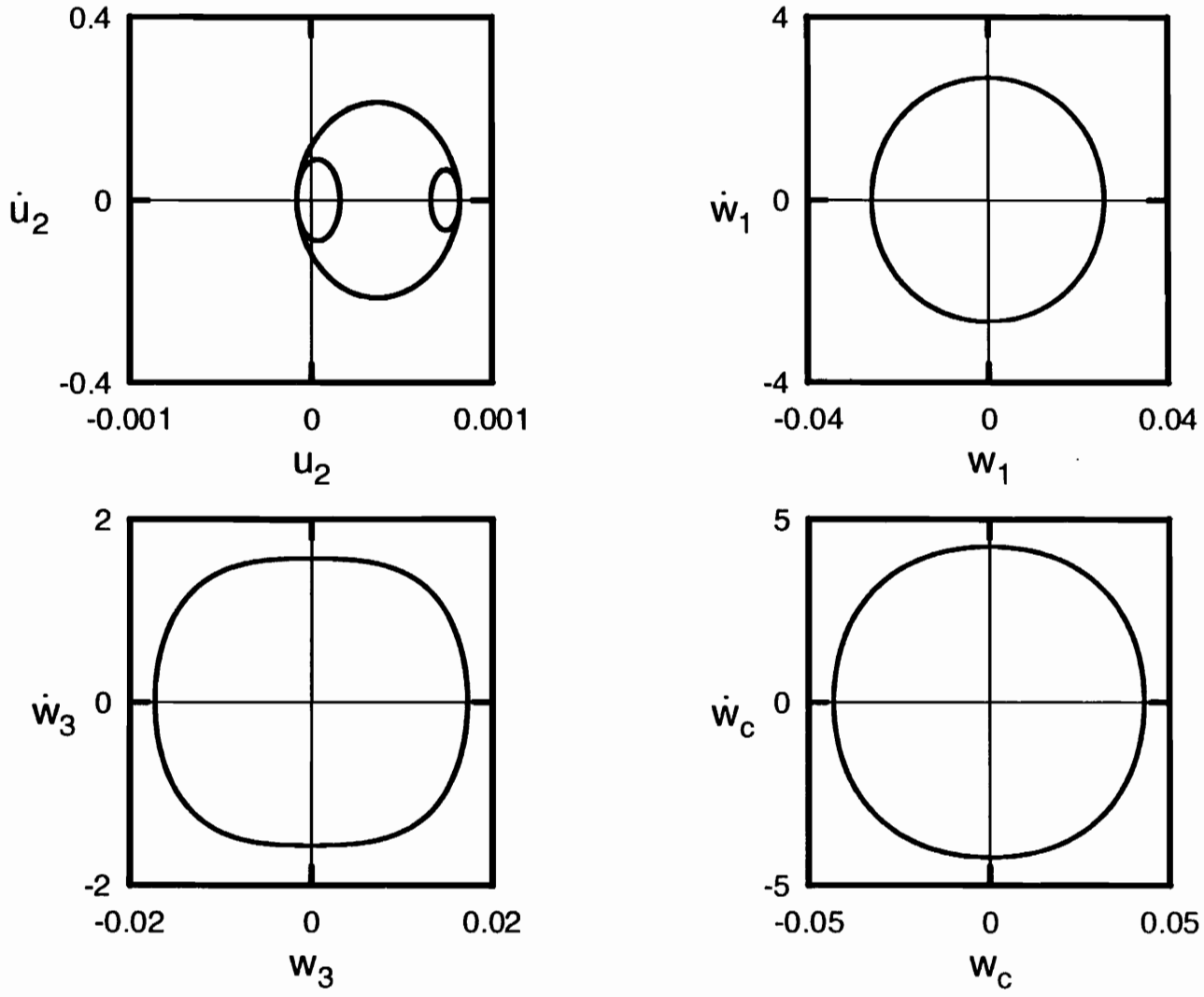

Figure A.108: Phase portraits for shear deformable beam with $r = 0.01$, $\Omega = 105.0$, $a = 0.02$.

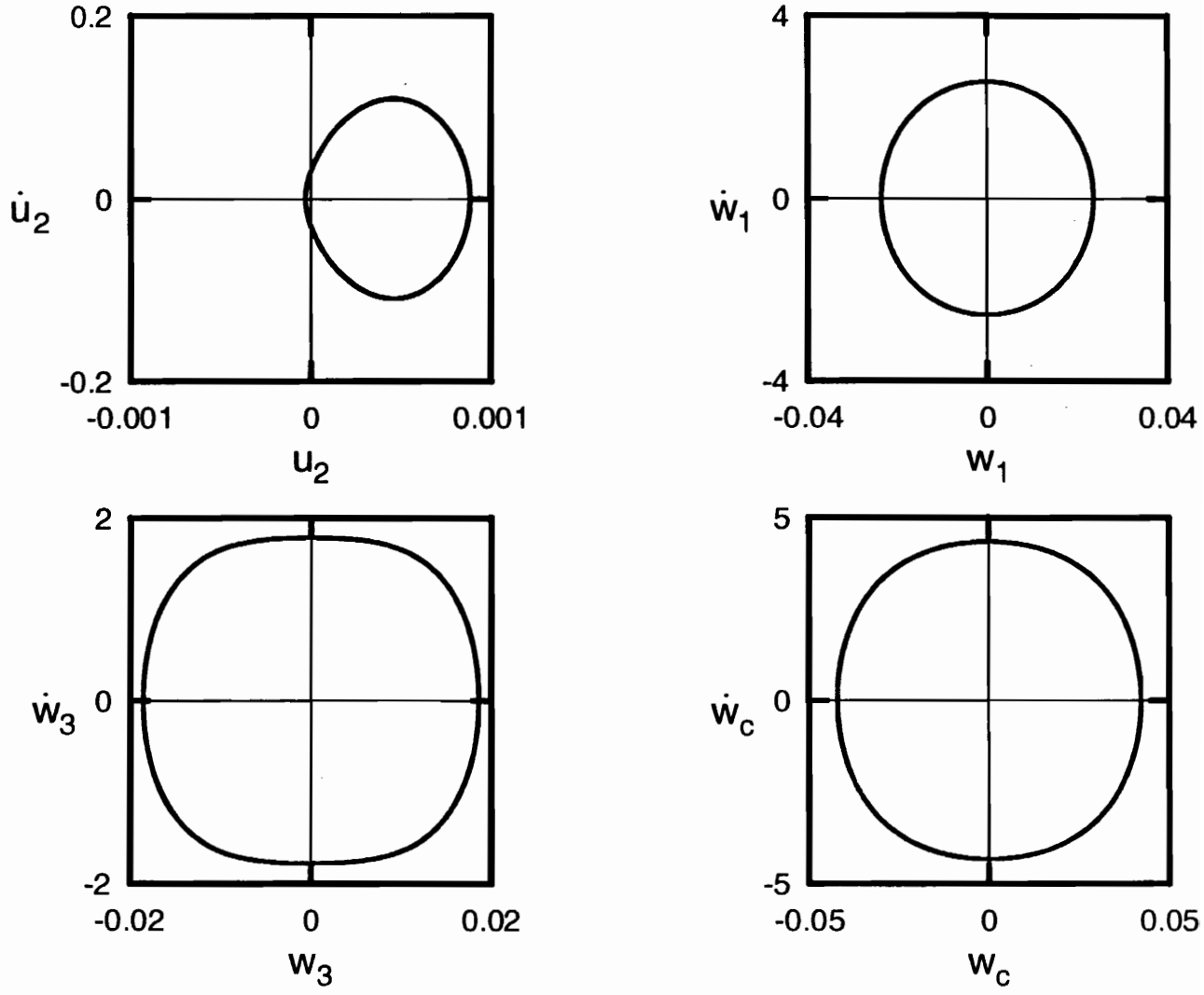

Figure A.109: Phase portraits for shear deformable beam with $r = 0.01$, $\Omega = 110.0$, $a = 0.02$.

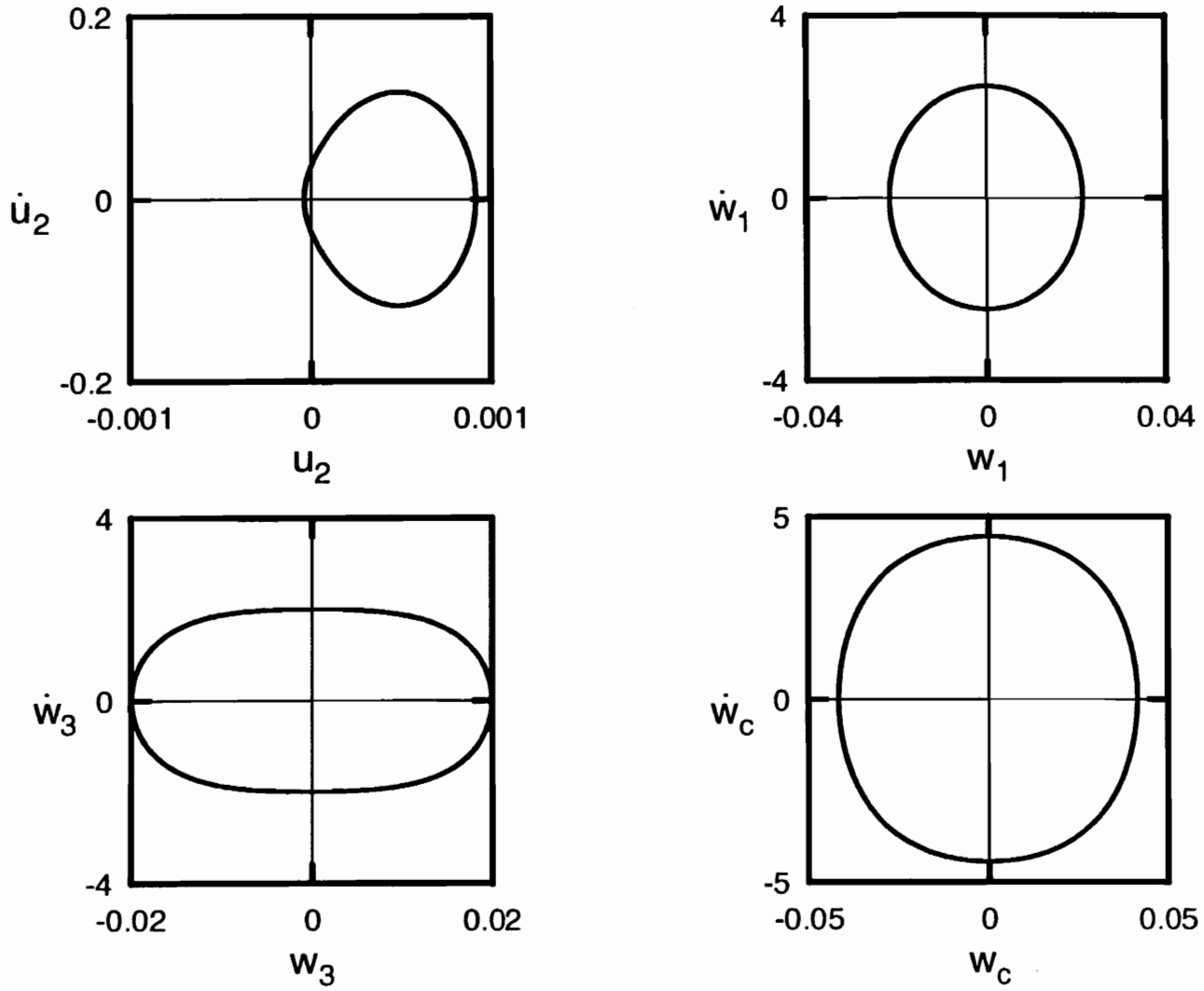

Figure A.110: Phase portraits for shear deformable beam with $r = 0.01$, $\Omega = 115.0$, $a = 0.02$.

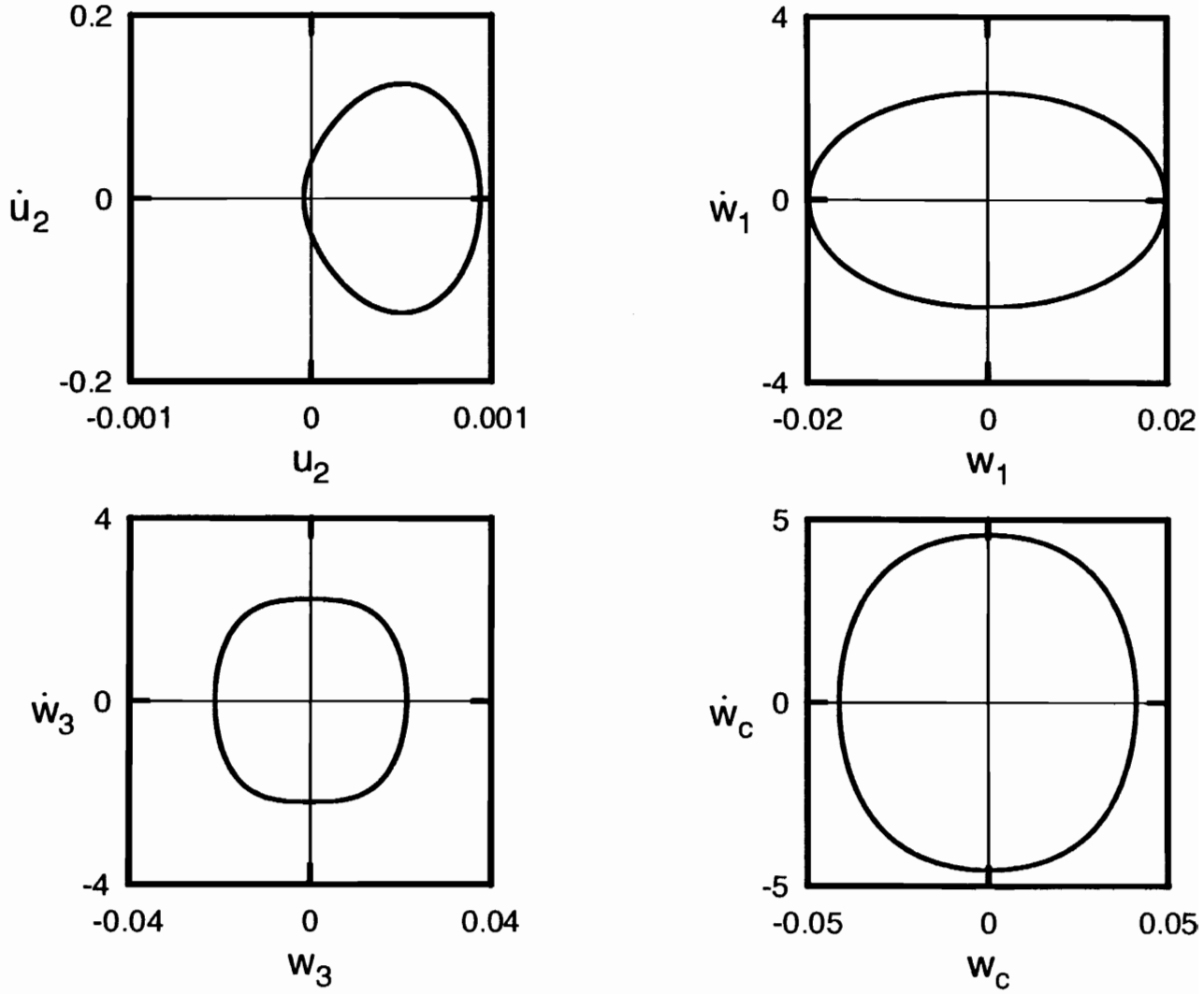

Figure A.111: Phase portraits for shear deformable beam with $r = 0.01$, $\Omega = 120.0$, $a = 0.02$.

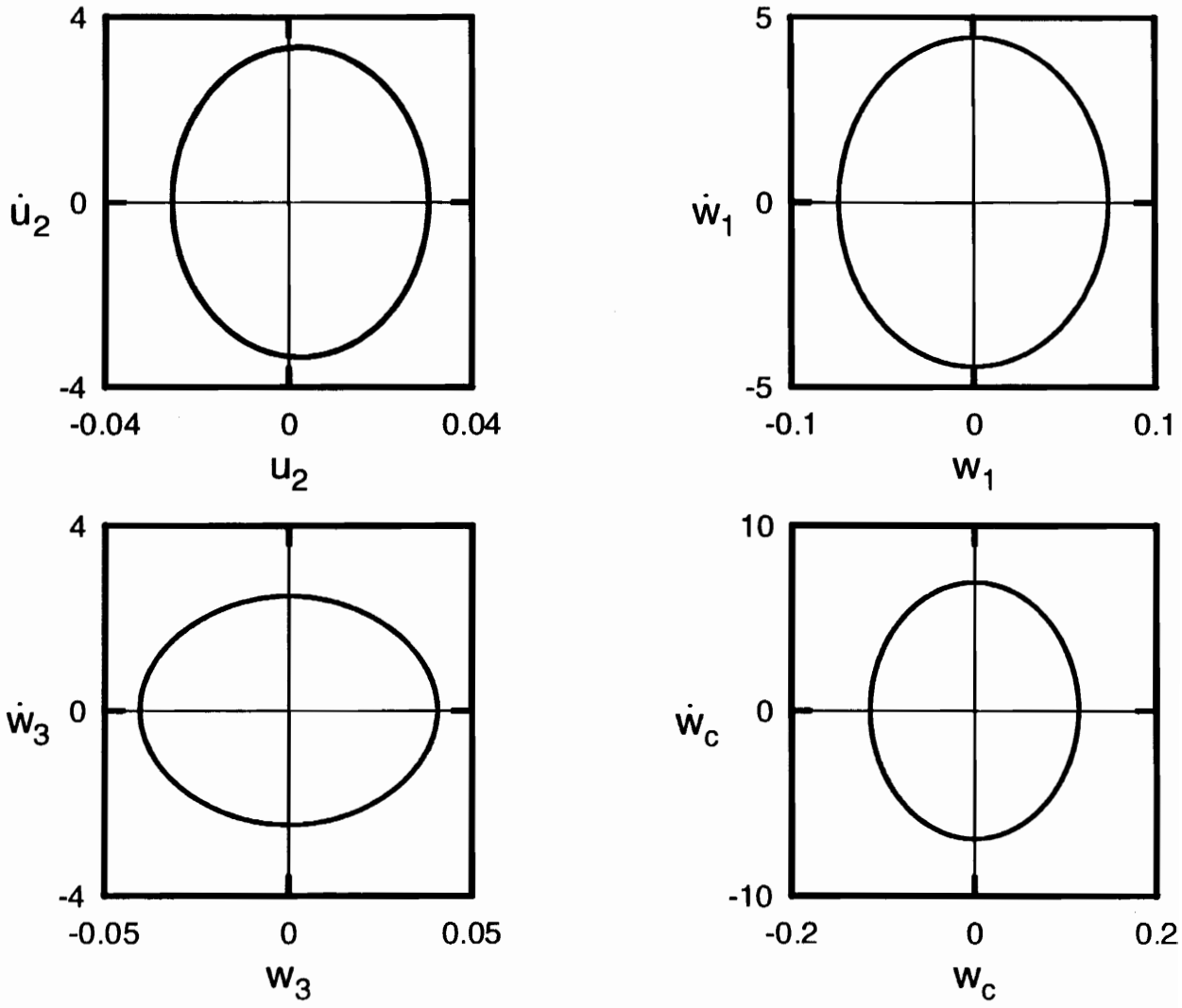

Figure A.112: Phase portraits for shear deformable beam with $r = 0.05$, $\Omega = 60.0$, $a = 0.5$.

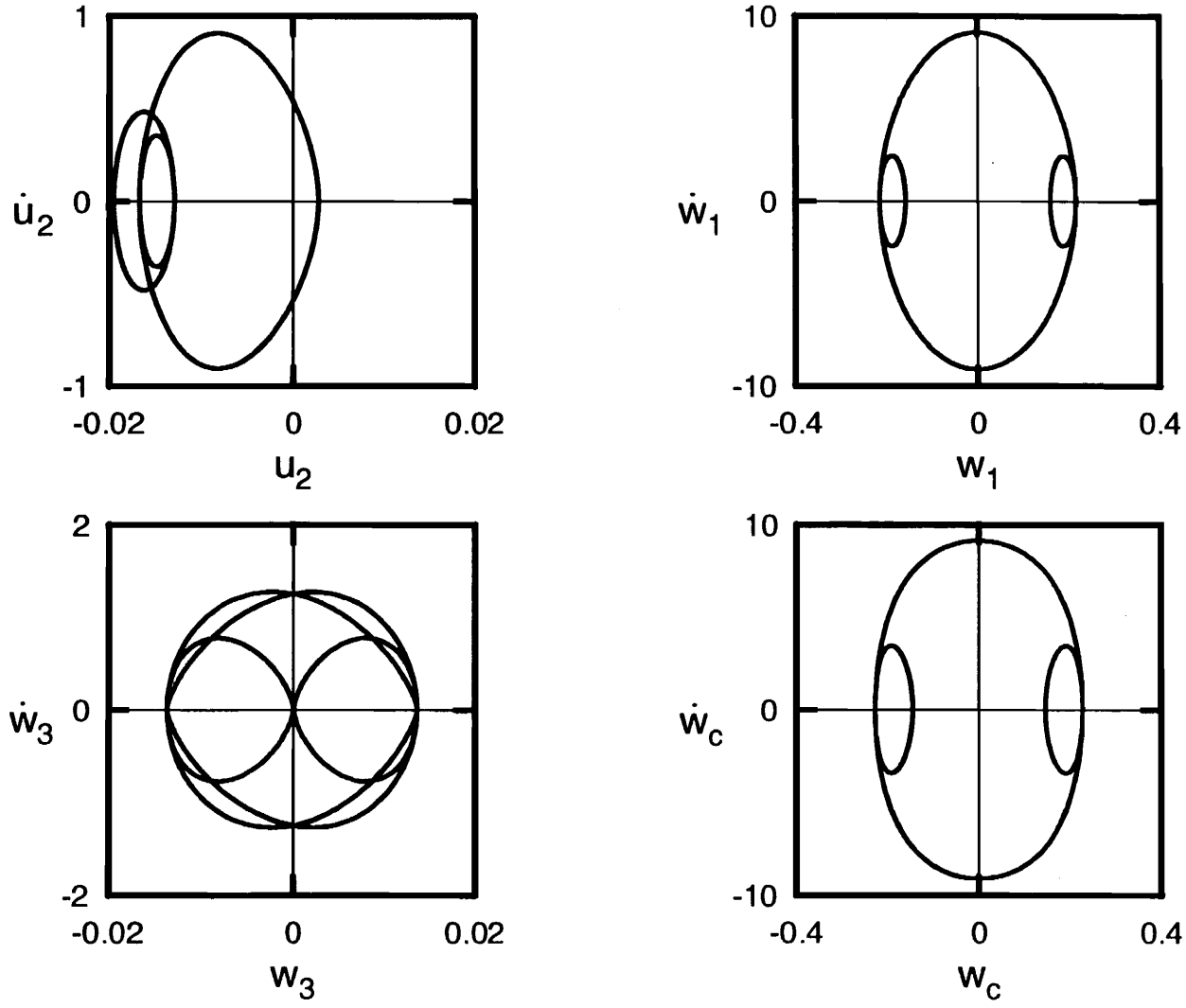

Figure A.113: Phase portraits for shear deformable beam with $r = 0.05$, $\Omega = 63.0$, $a = 0.5$.

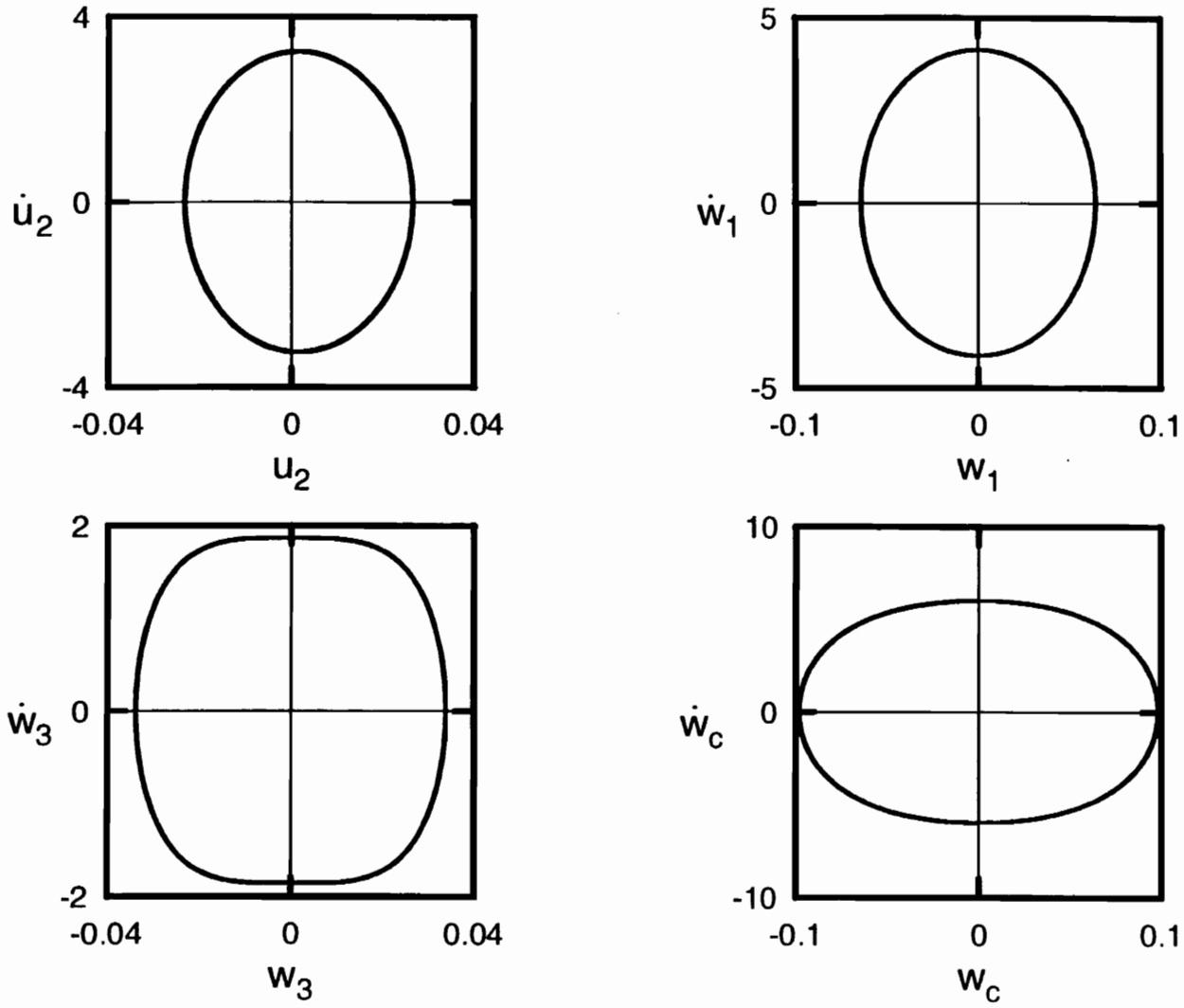

Figure A.114: Phase portraits for shear deformable beam with $r = 0.05$, $\Omega = 65.0$, $a = 0.5$.

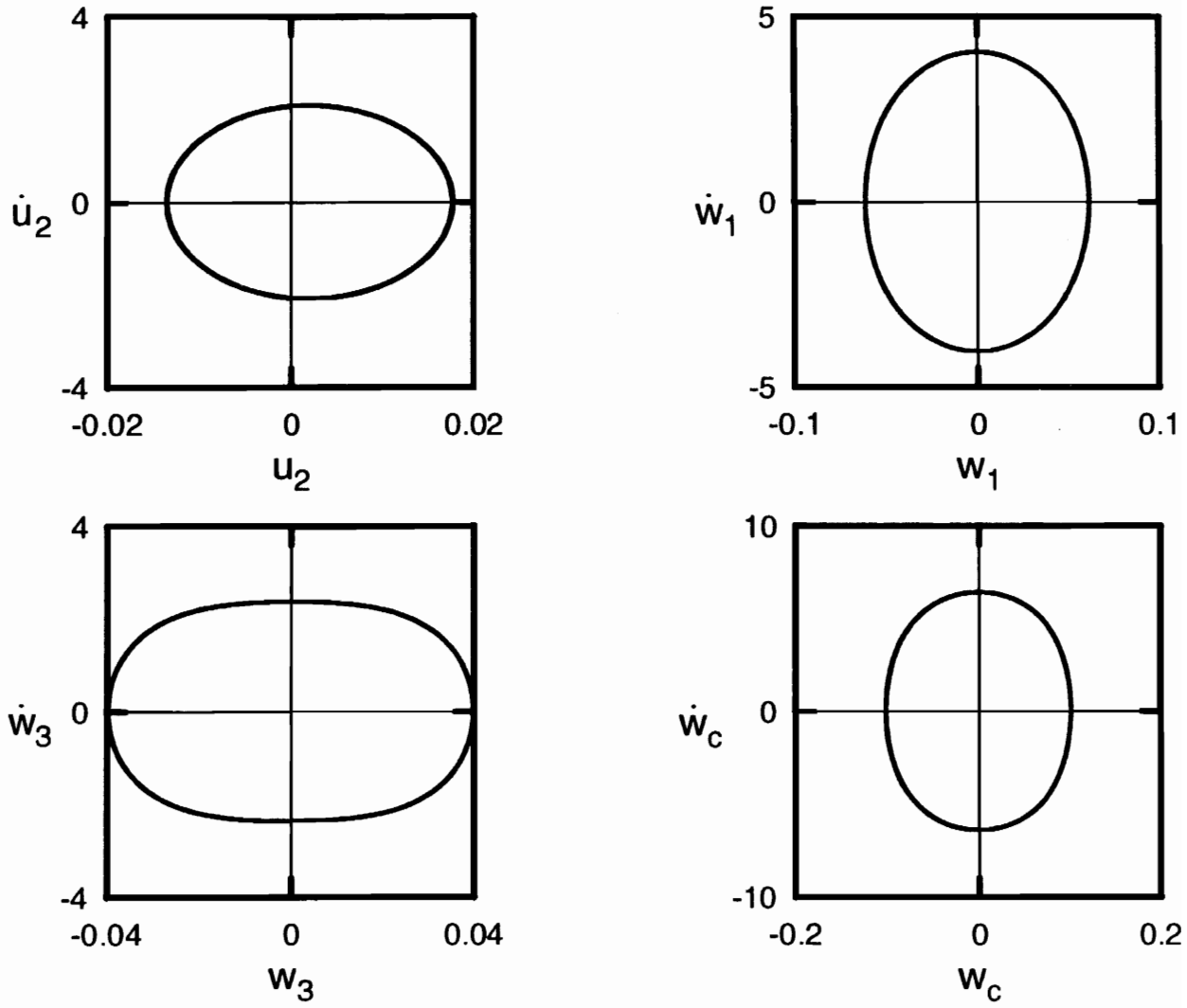

Figure A.115: Phase portraits for shear deformable beam with $r = 0.05$, $\Omega = 67.0$, $a = 0.5$.

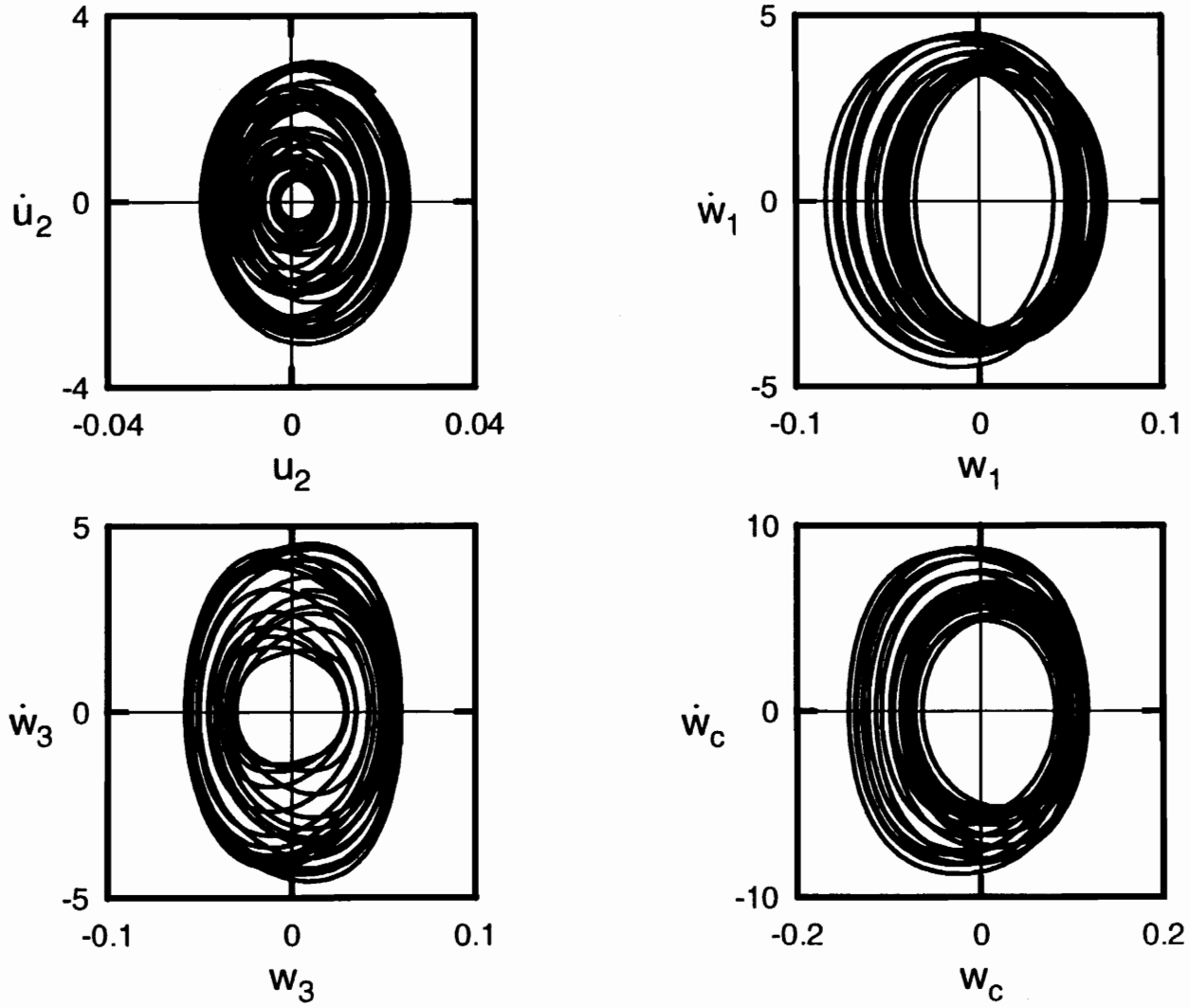

Figure A.116: Phase portraits for shear deformable beam with $r = 0.05$, $\Omega = 70.0$, $a = 0.5$.

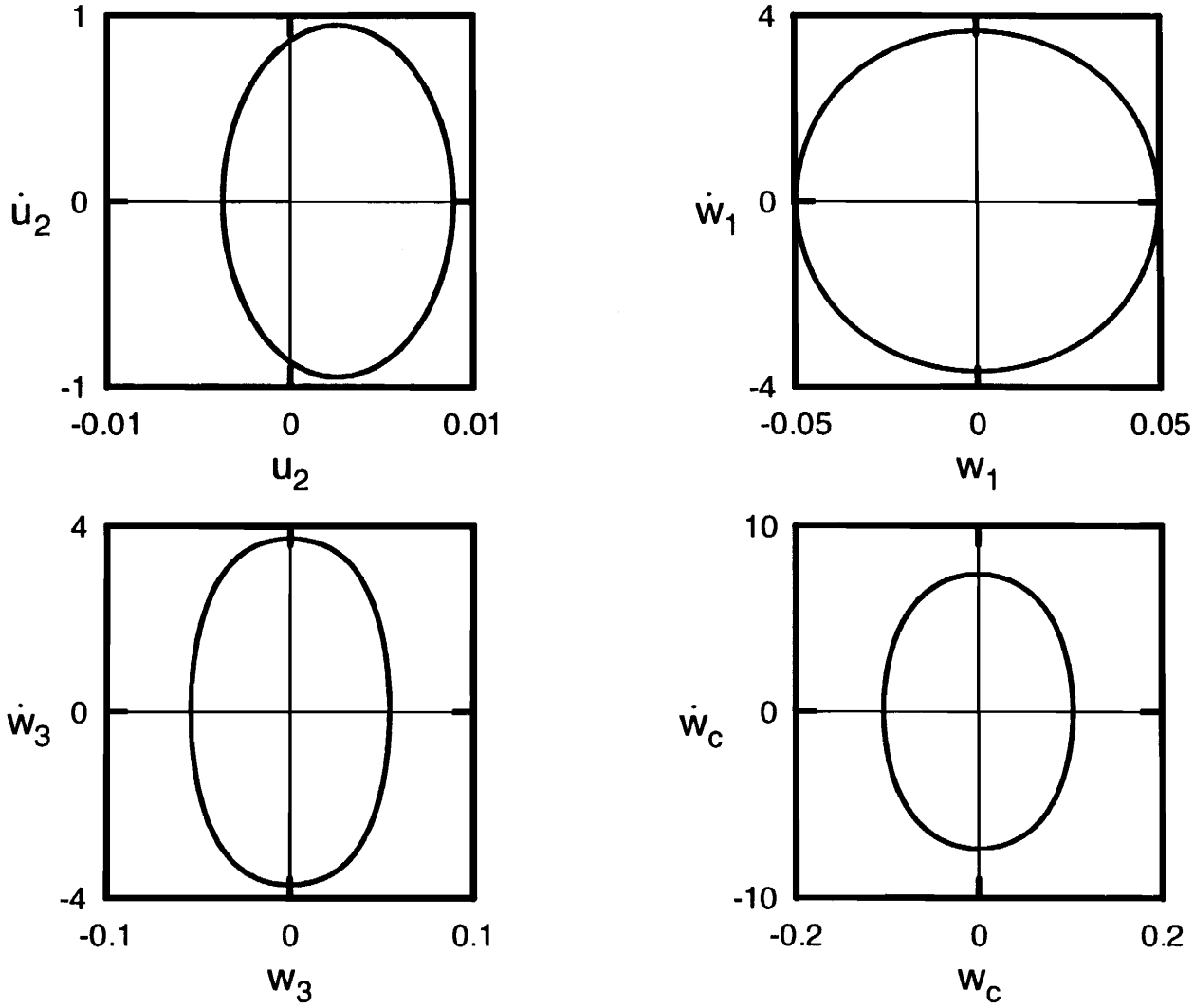

Figure A.117: Phase portraits for shear deformable beam with $r = 0.05$, $\Omega = 75.0$, $a = 0.5$.

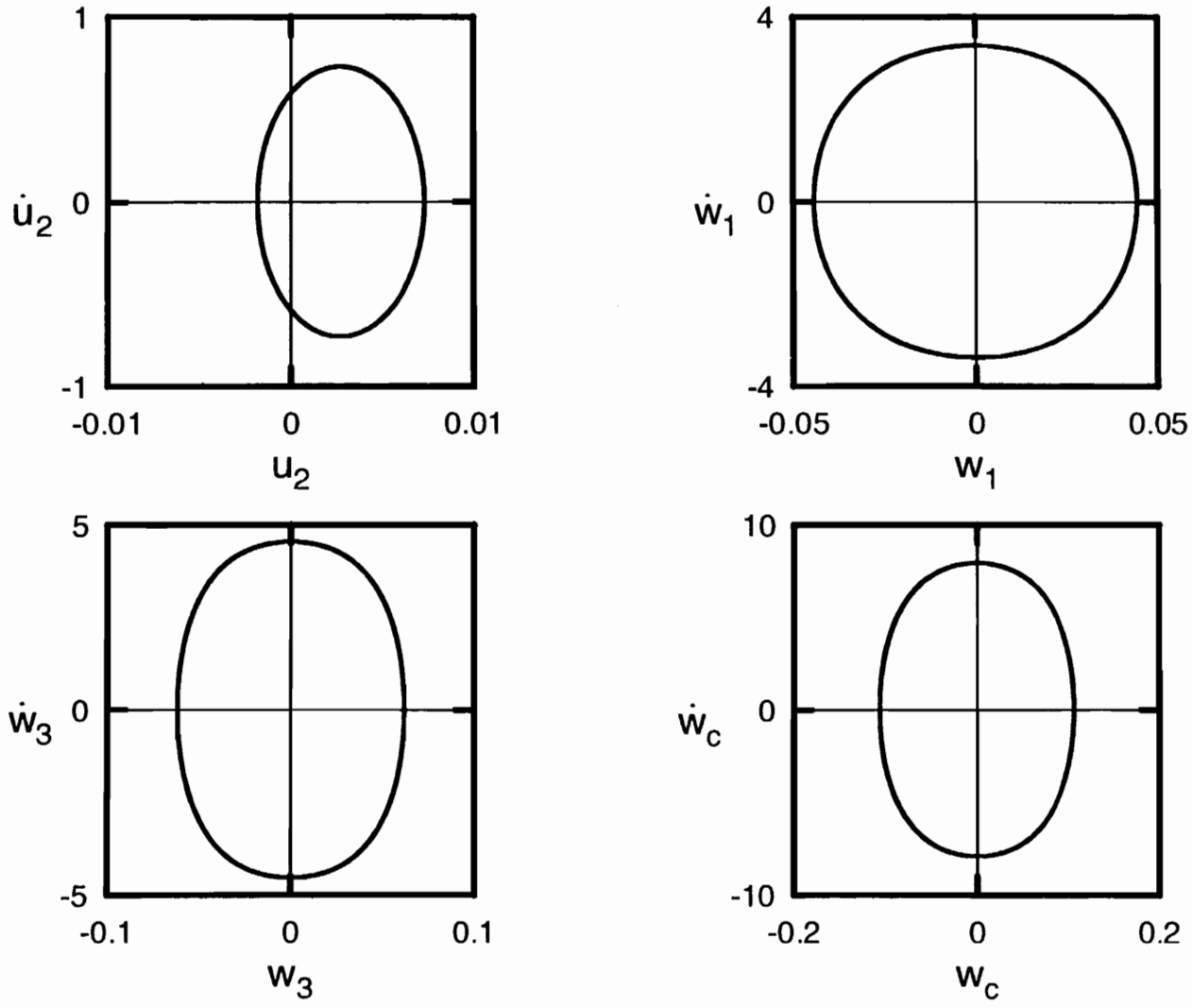

Figure A.118: Phase portraits for shear deformable beam with $r = 0.05$, $\Omega = 80.0$, $a = 0.5$.

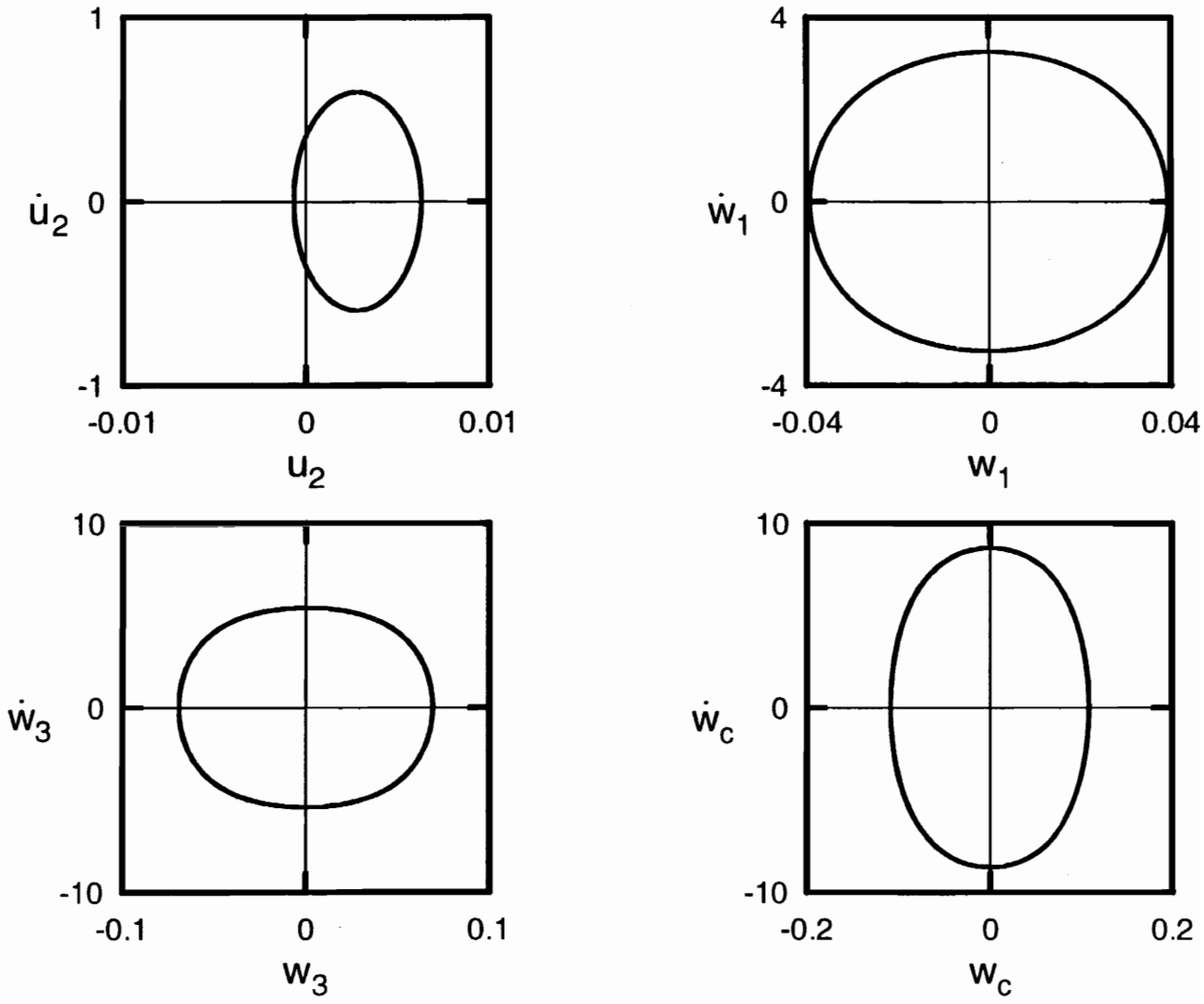

Figure A.119: Phase portraits for shear deformable beam with $r = 0.05$, $\Omega = 85.0$, $a = 0.5$.

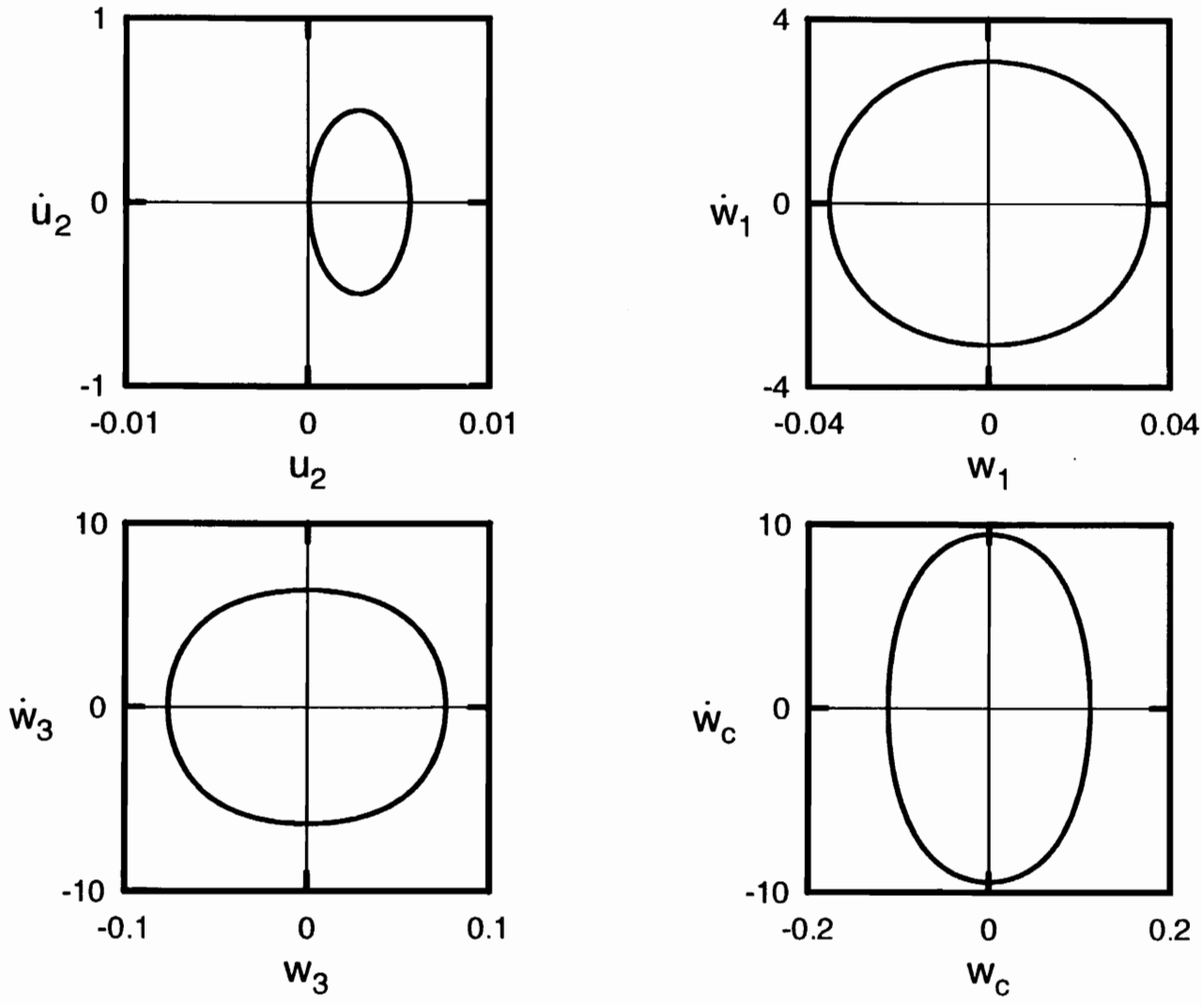

Figure A.120: Phase portraits for shear deformable beam with $r = 0.05$, $\Omega = 90.0$, $a = 0.5$.

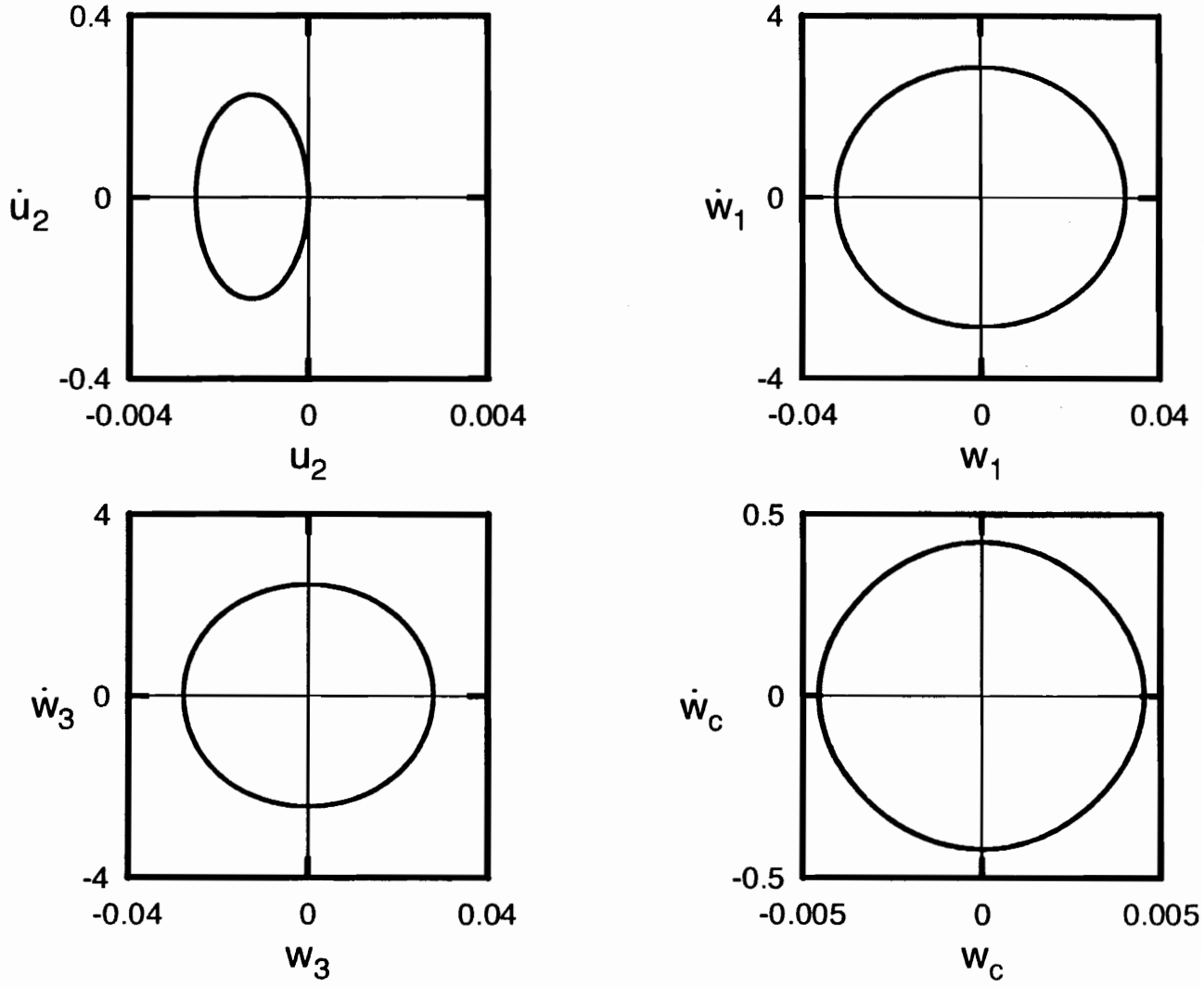

Figure A.121: Phase portraits for shear deformable beam with $r = 0.05$, $\Omega = 89.0$, $a = 0.5$.

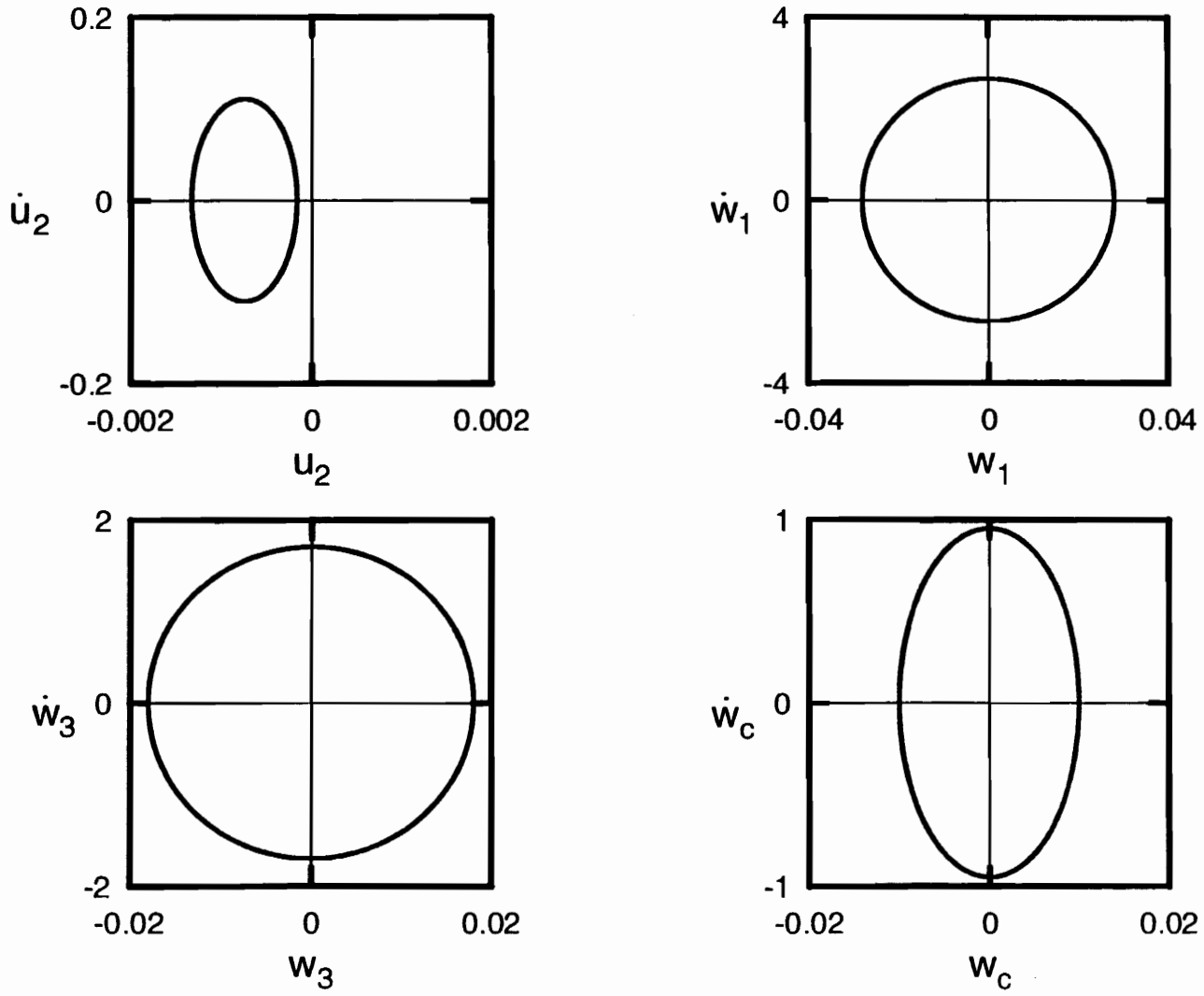

Figure A.122: Phase portraits for shear deformable beam with $r = 0.05$, $\Omega = 95.0$, $a = 0.5$.

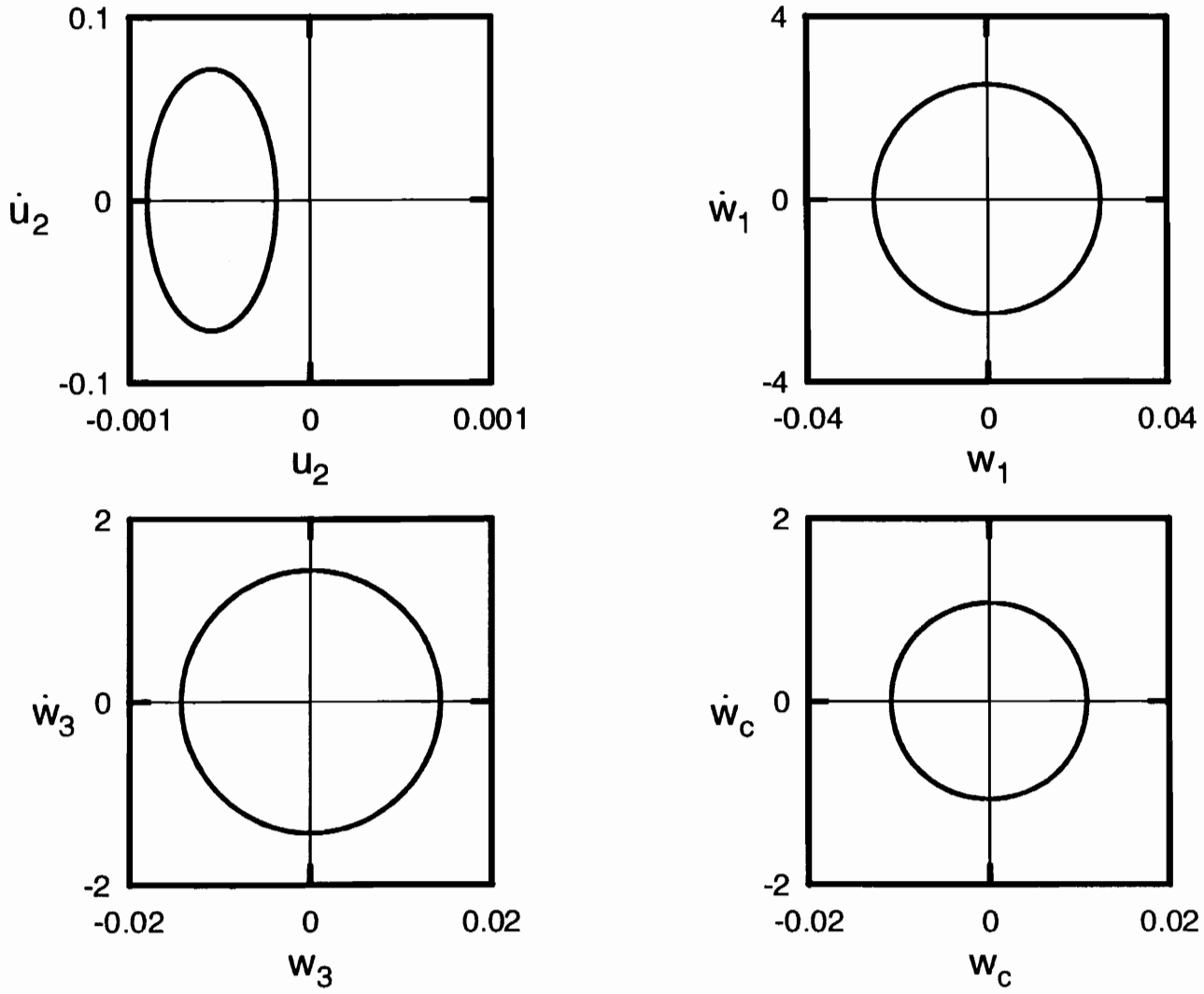

Figure A.123: Phase portraits for shear deformable beam with $r = 0.05$, $\Omega = 100.0$, $a = 0.5$.

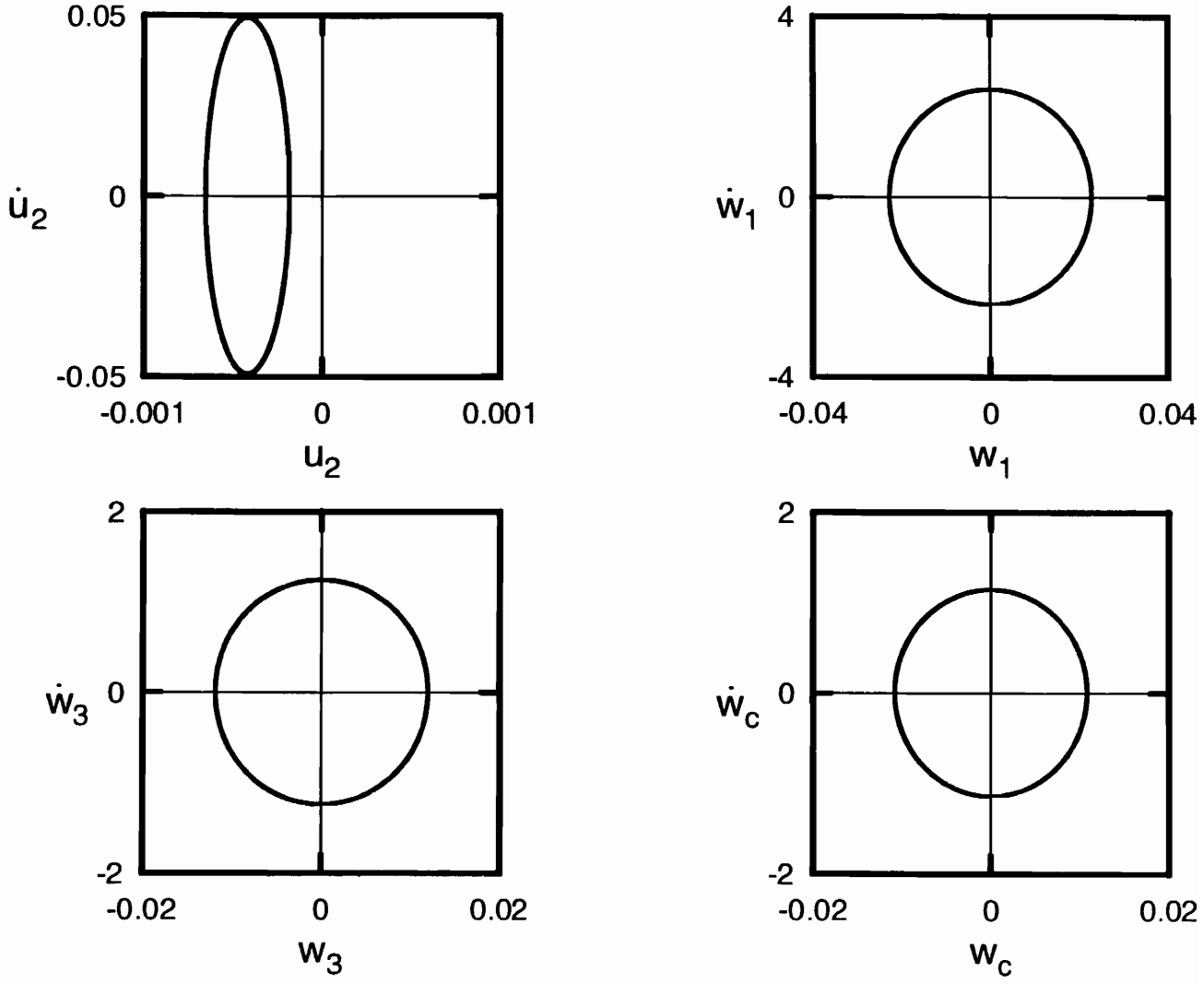

Figure A.124: Phase portraits for shear deformable beam with $r = 0.05$, $\Omega = 105.0$, $a = 0.5$.

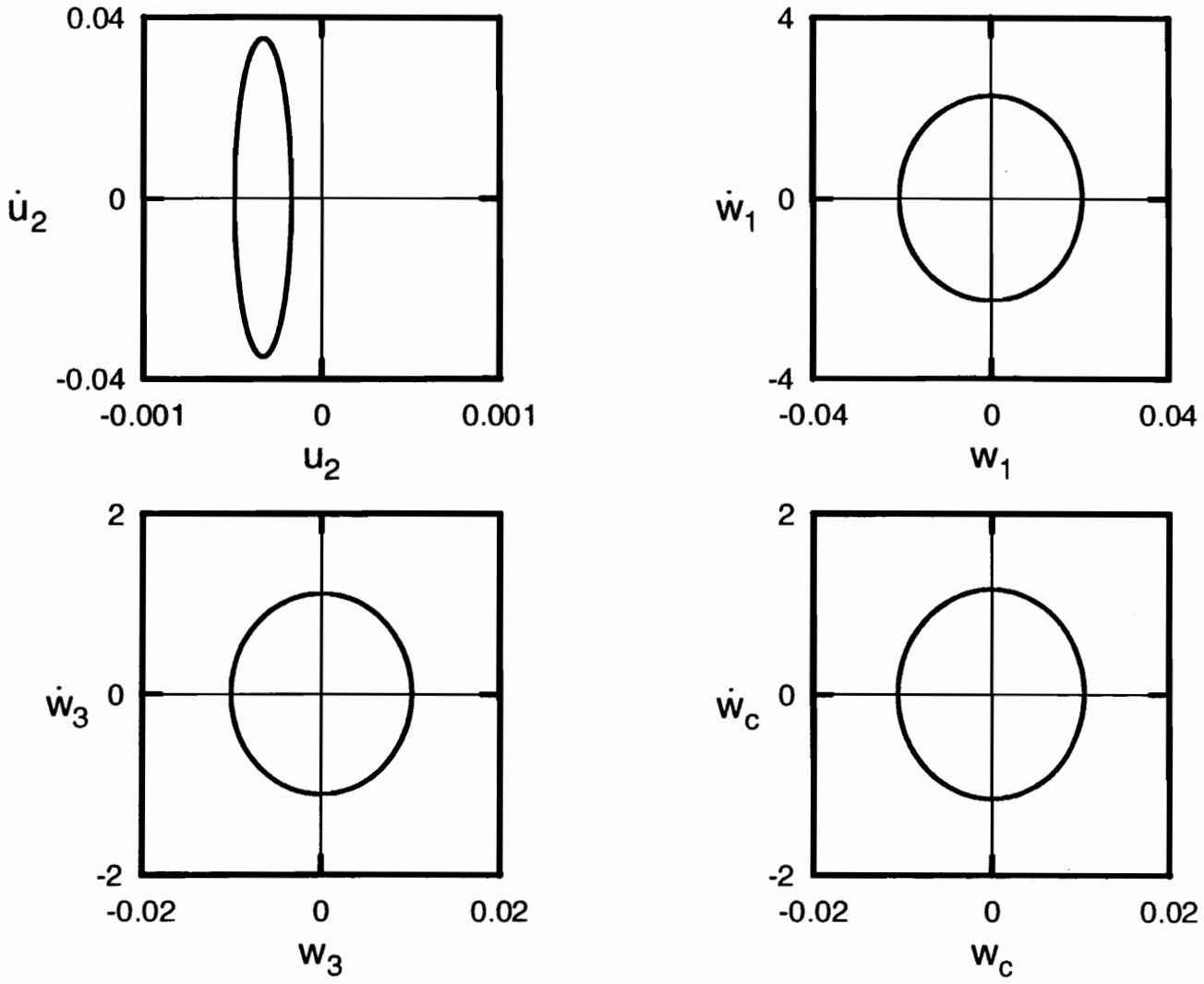

Figure A.125: Phase portraits for shear deformable beam with $r = 0.05$, $\Omega = 110.0$, $a = 0.5$.

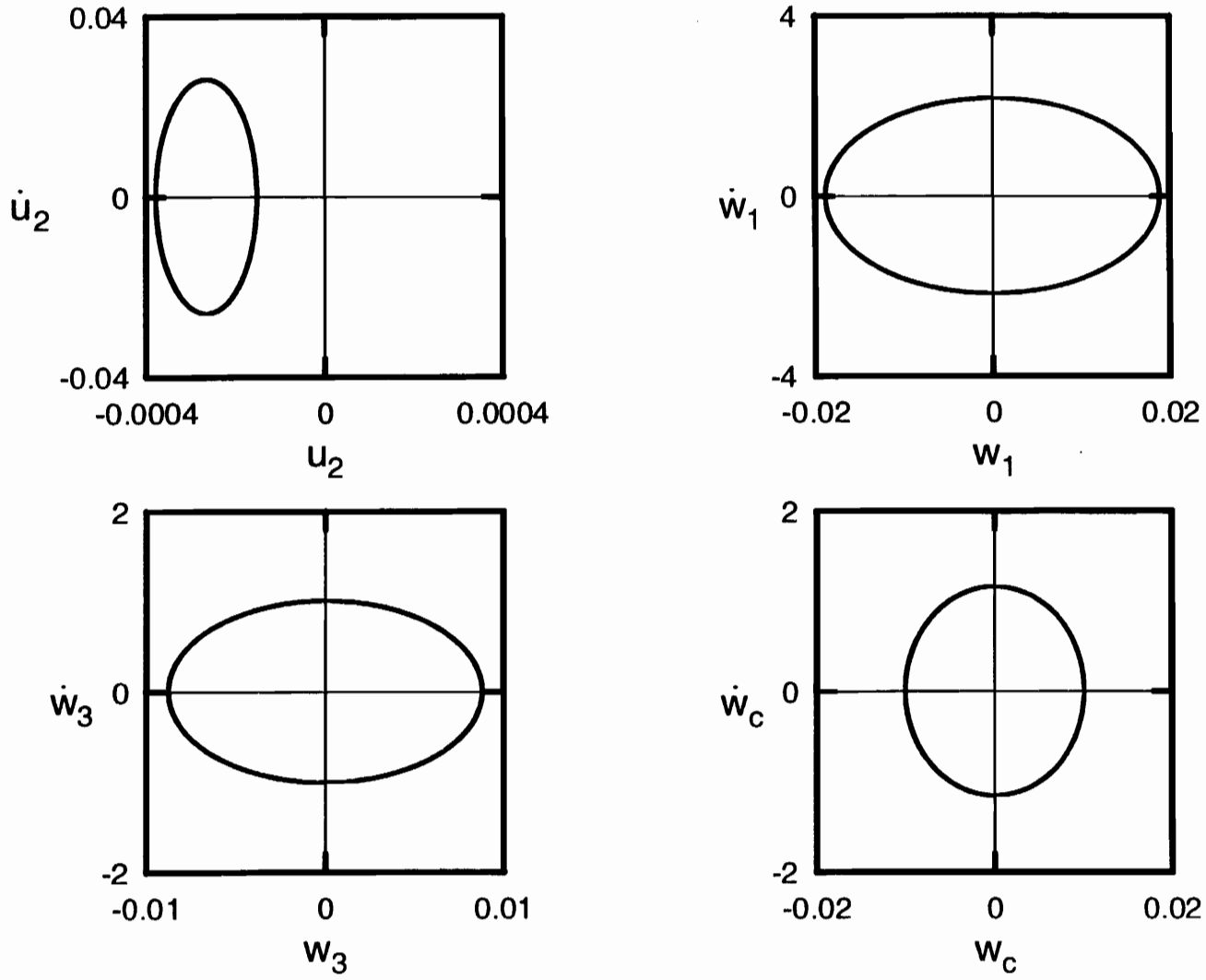

Figure A.126: Phase portraits for shear deformable beam with $r = 0.05$, $\Omega = 115.0$, $a = 0.5$.

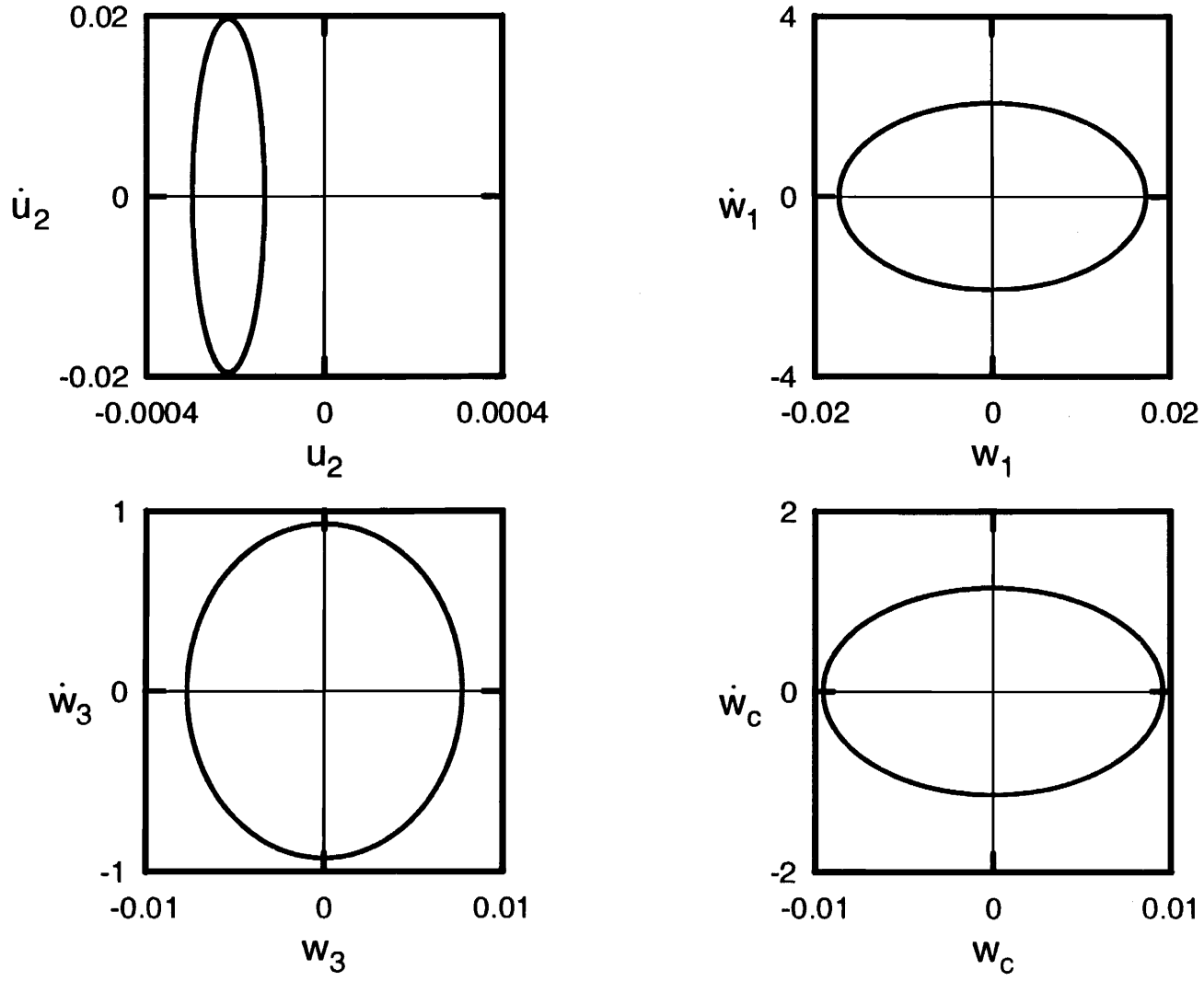

Figure A.127: Phase portraits for shear deformable beam with $r = 0.05$, $\Omega = 120.0$, $a = 0.5$.

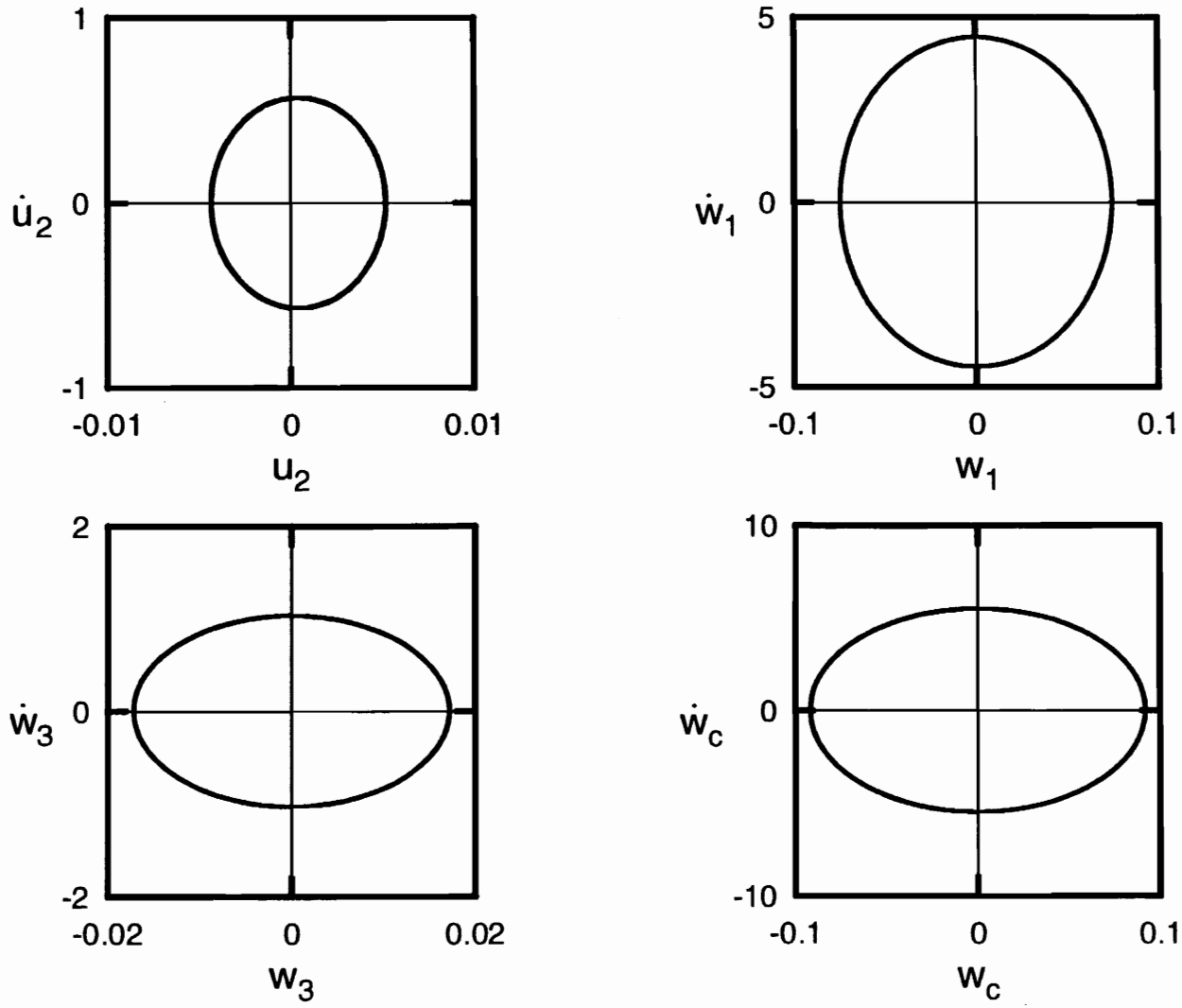

Figure A.128: Phase portraits for non shear deformable beam with $r = 0.05$, $\Omega = 60.0$, $a = 0.5$.

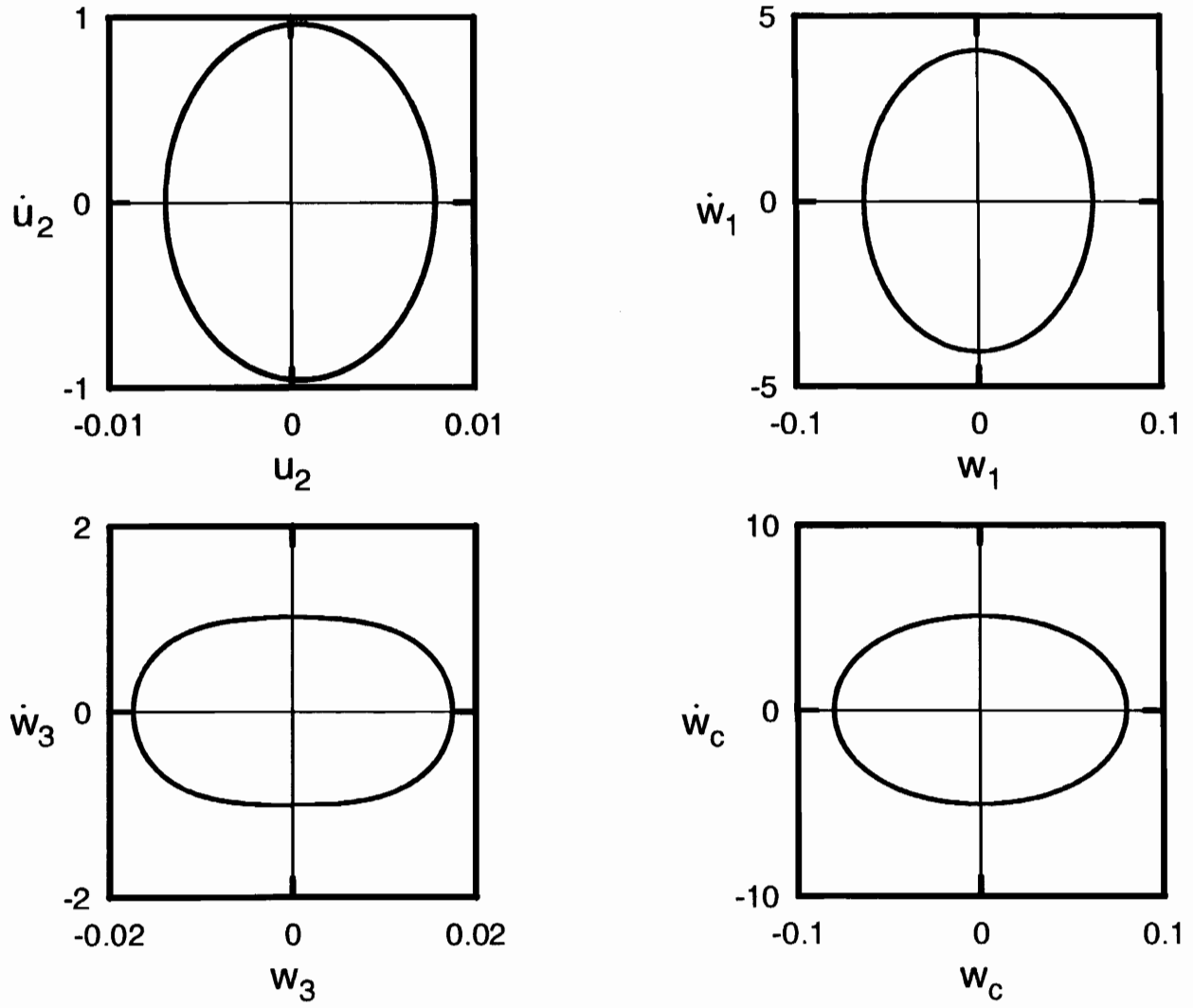

Figure A.129: Phase portraits for non shear deformable beam with $r = 0.05$, $\Omega = 65.0$, $a = 0.5$.

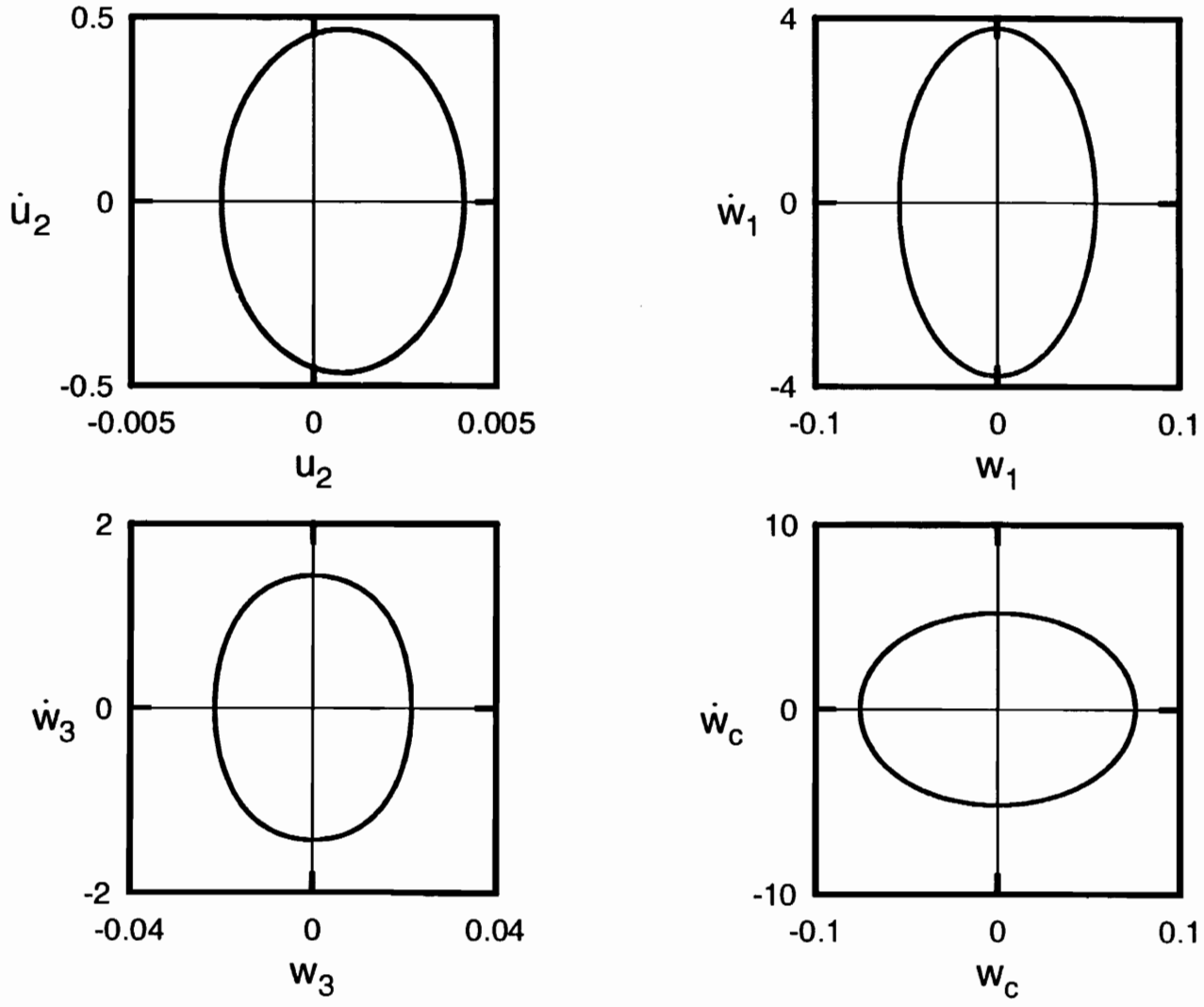

Figure A.130: Phase portraits for non shear deformable beam with $r = 0.05$, $\Omega = 70.0$, $a = 0.5$.

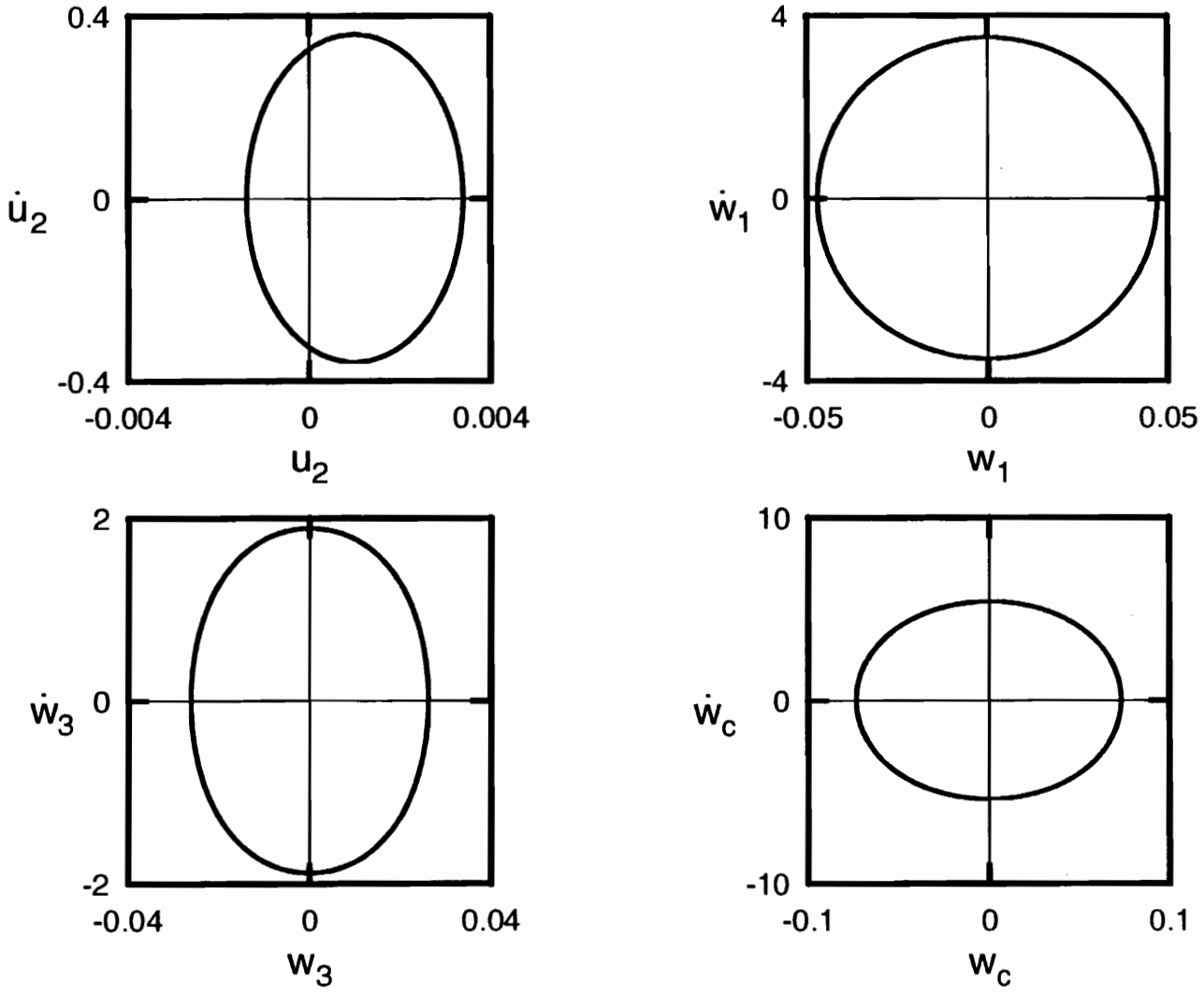

Figure A.131: Phase portraits for non shear deformable beam with $r = 0.05$, $\Omega = 75.0$, $a = 0.5$.

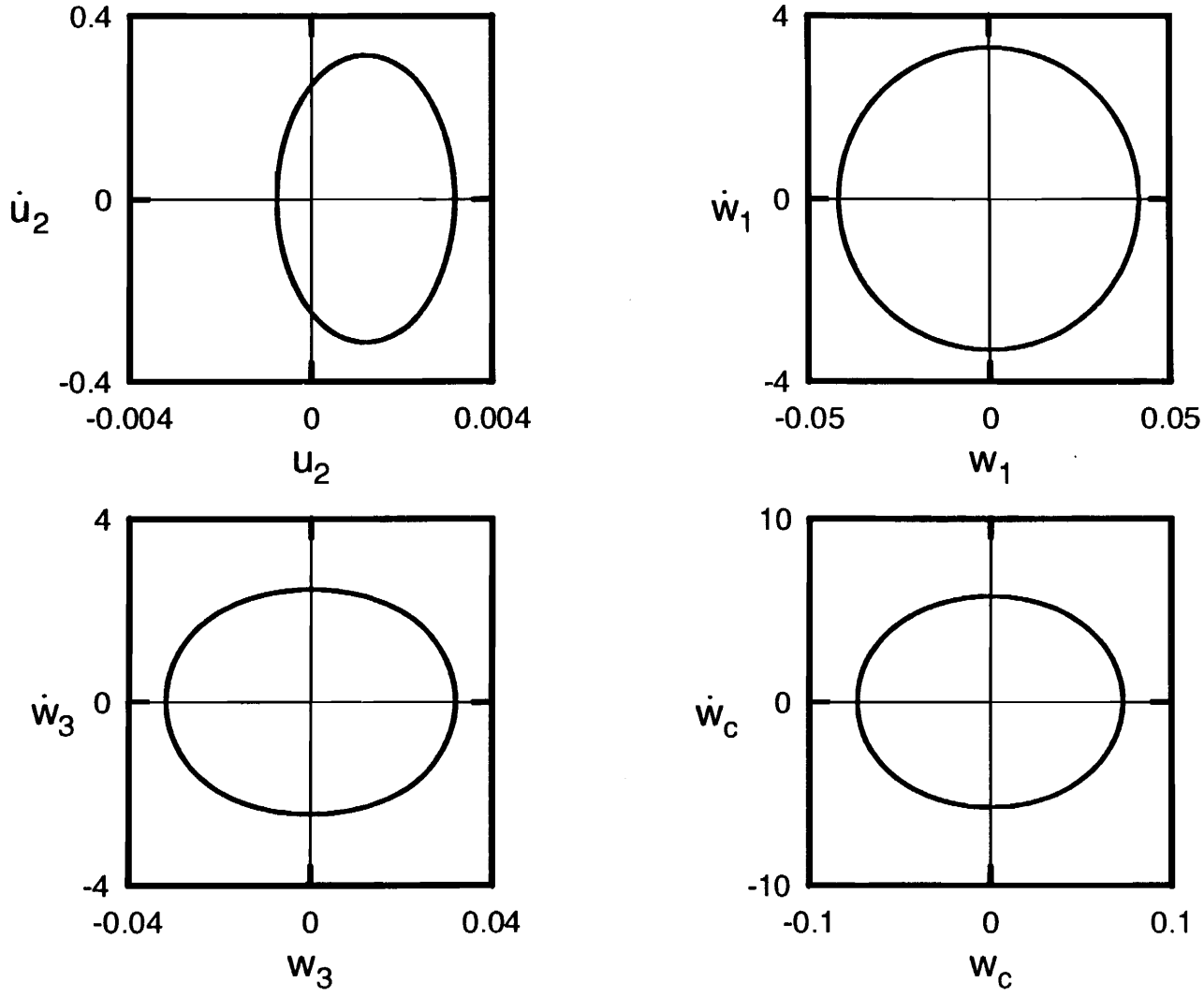

Figure A.132: Phase portraits for non shear deformable beam with $r = 0.05$, $\Omega = 80.0$, $a = 0.5$.

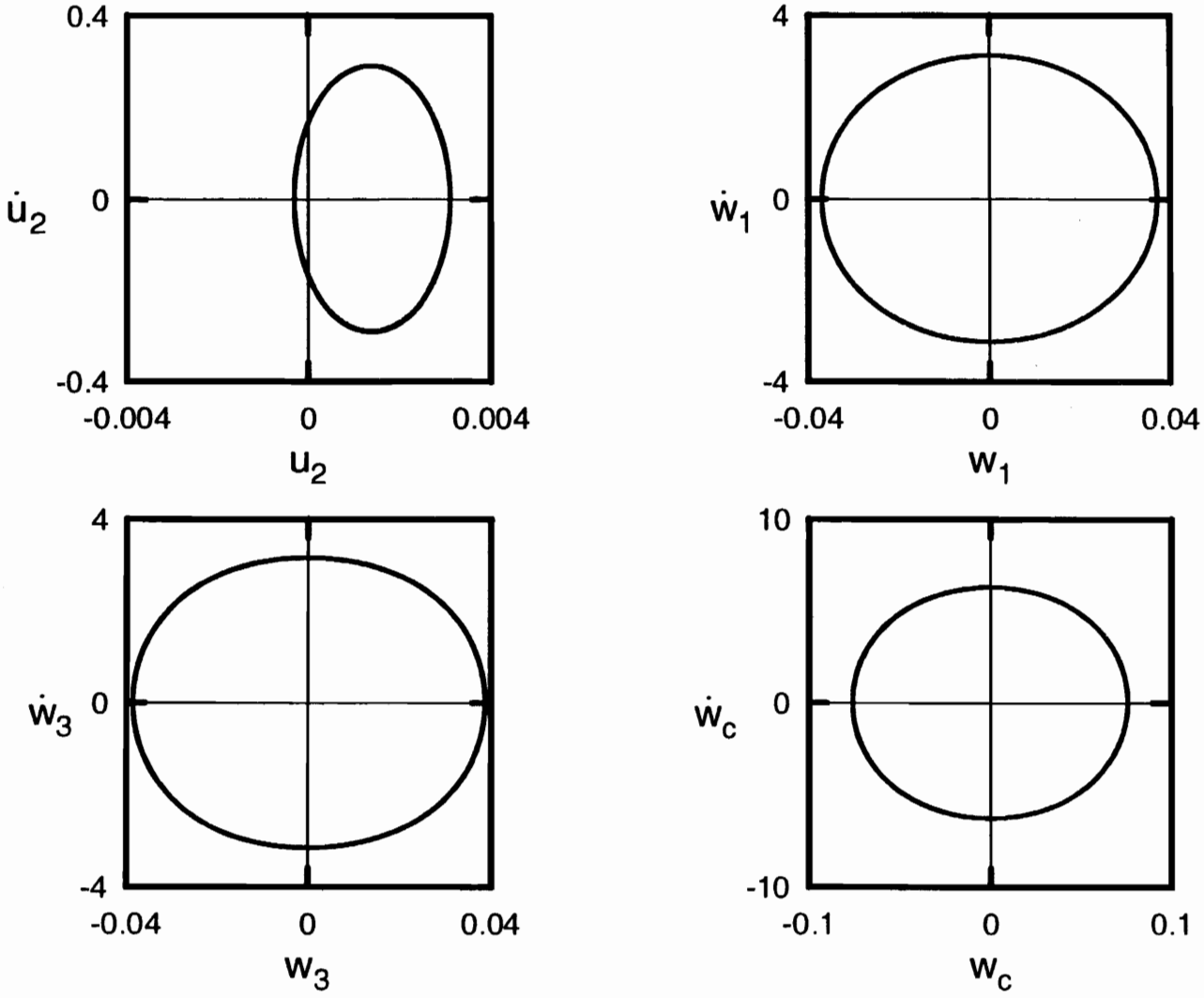

Figure A.133: Phase portraits for non shear deformable beam with $r = 0.05$, $\Omega = 85.0$, $a = 0.5$.

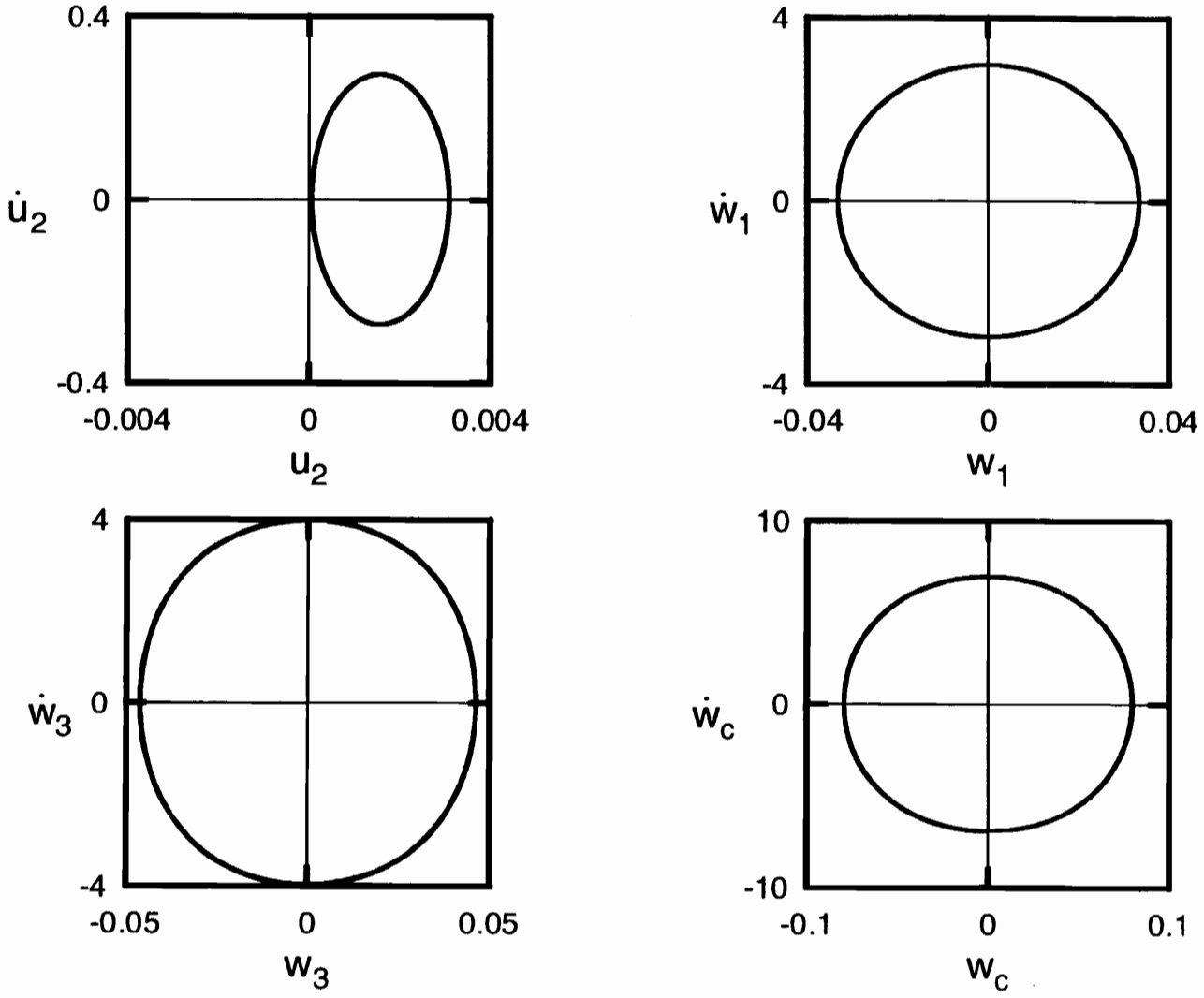

Figure A.134: Phase portraits for non shear deformable beam with $r = 0.05$, $\Omega = 90.0$, $a = 0.5$.

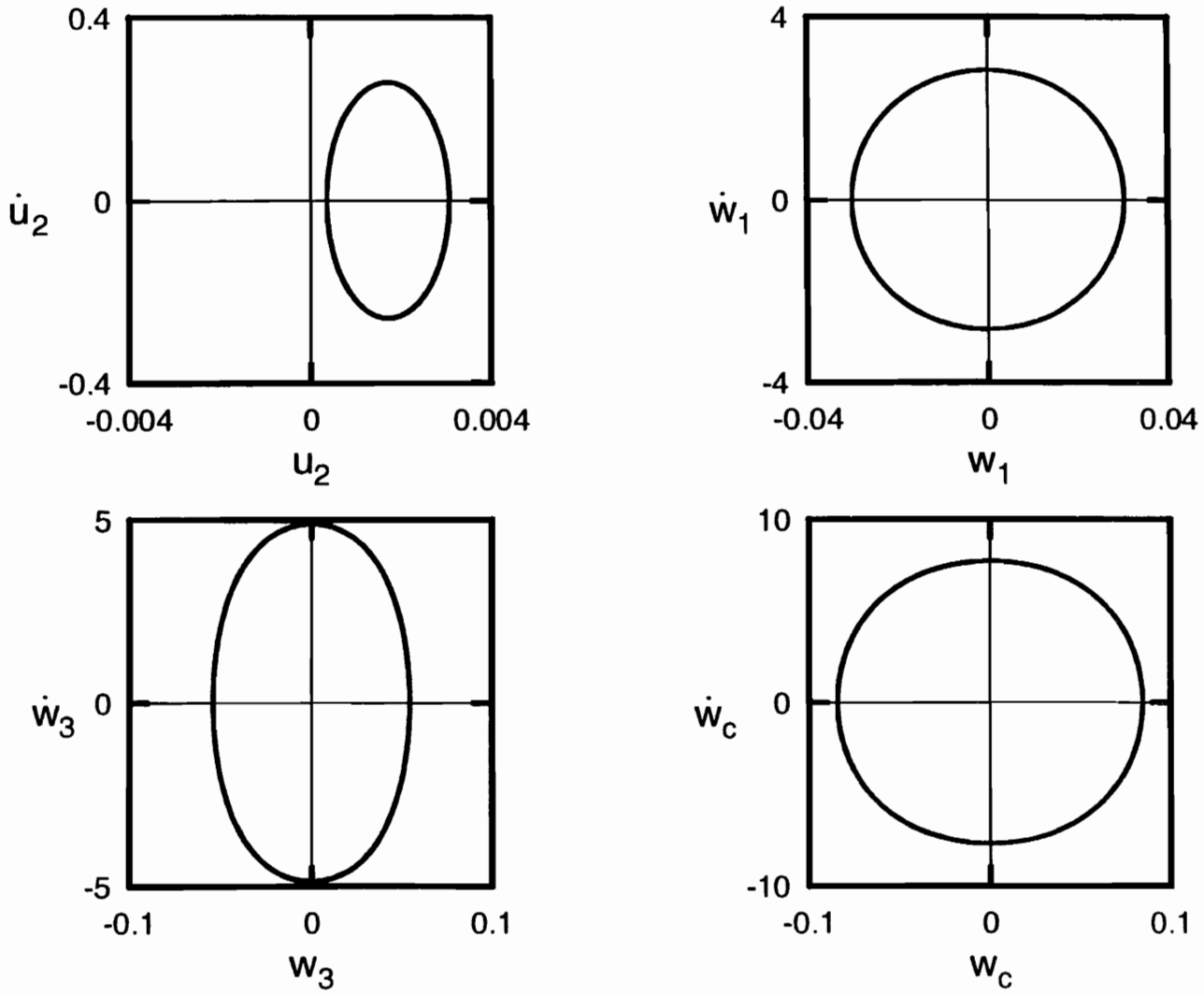

Figure A.135: Phase portraits for non shear deformable beam with $r = 0.05$, $\Omega = 95.0$, $a = 0.5$.

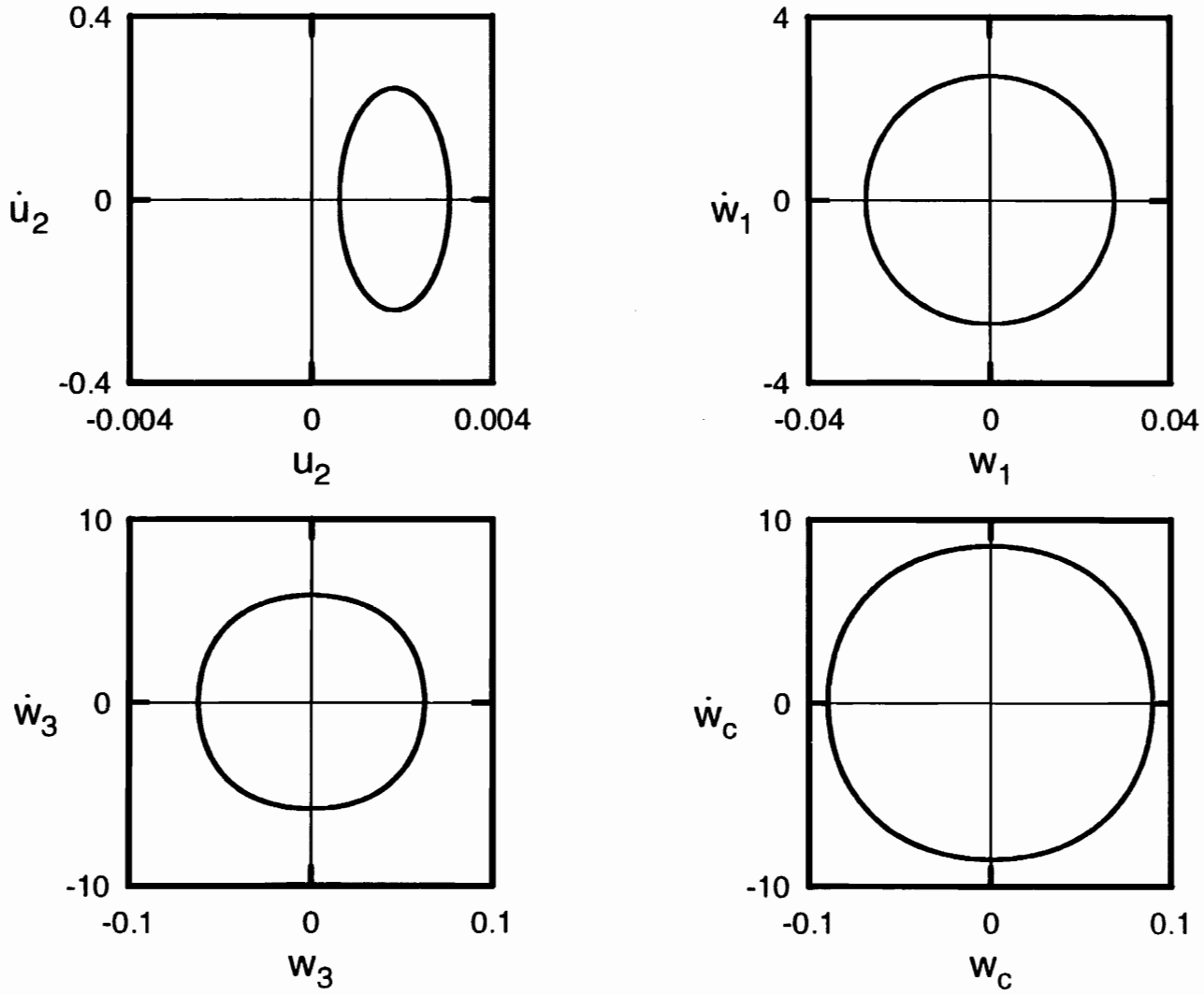

Figure A.136: Phase portraits for non shear deformable beam with $r = 0.05$, $\Omega = 100.0$, $a = 0.5$

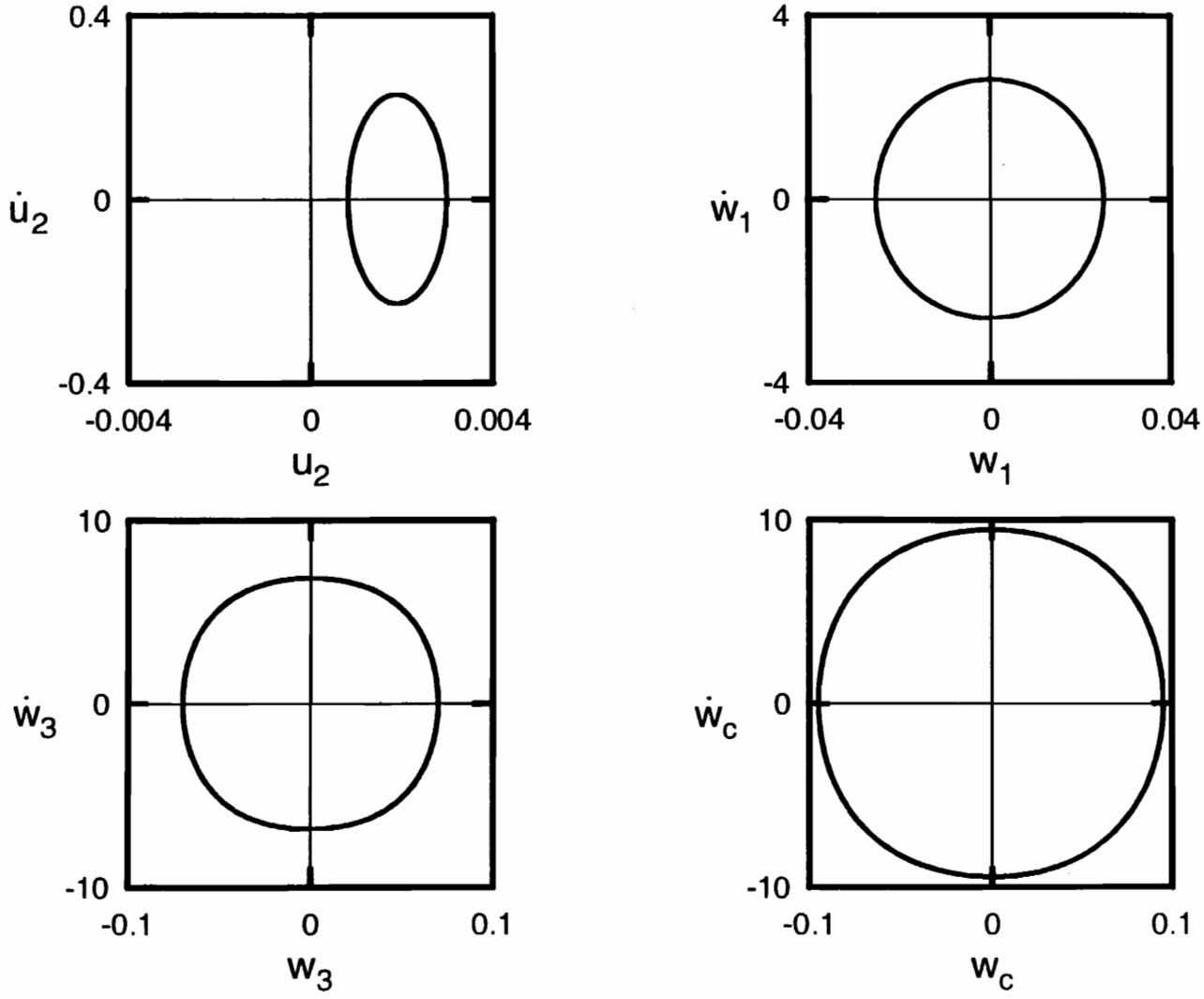

Figure A.137: Phase portraits for non shear deformable beam with $r = 0.05$, $\Omega = 105.0$, $a = 0.5$

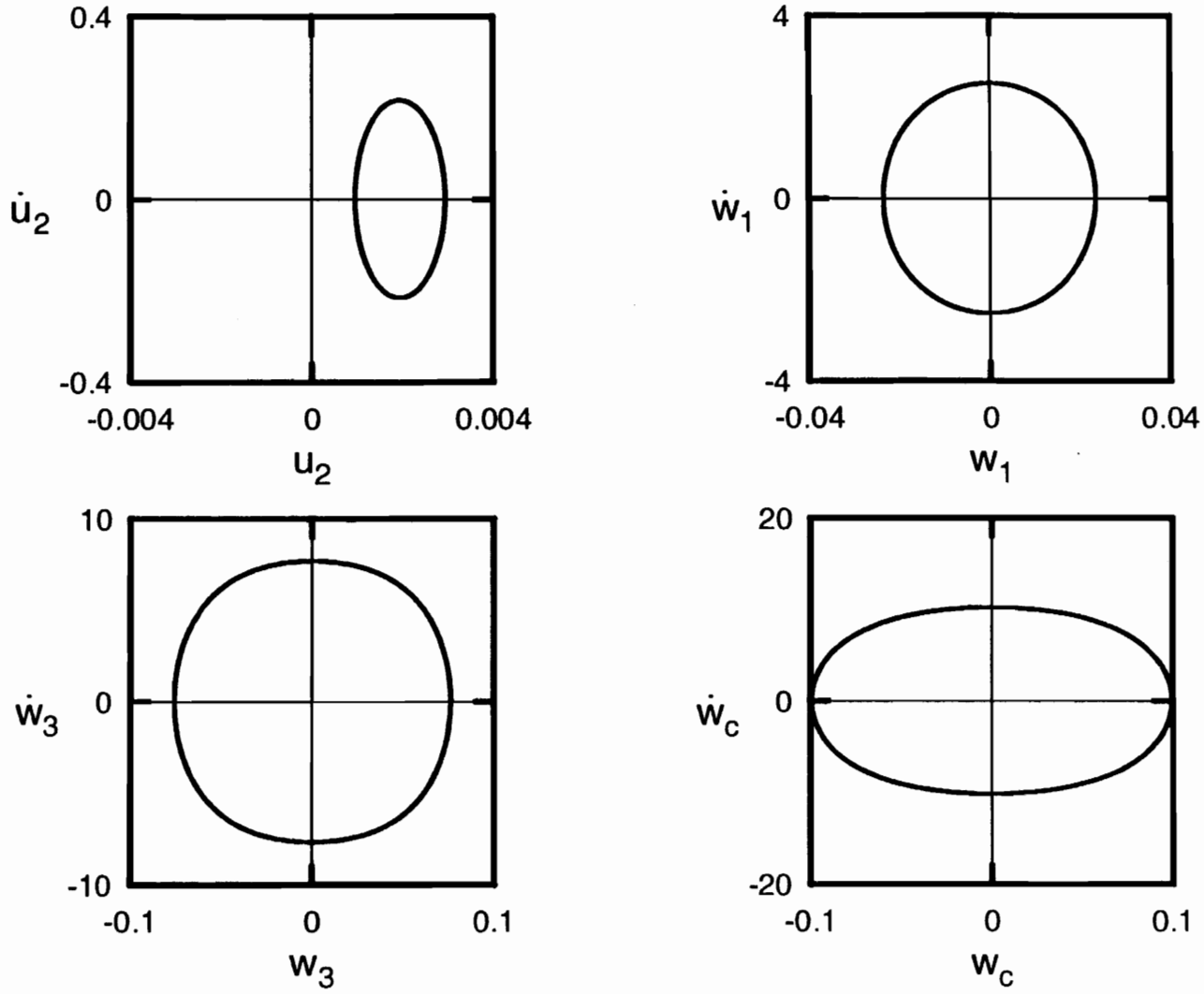

Figure A.138: Phase portraits for non shear deformable beam with $r = 0.05$, $\Omega = 109.0$, $a = 0.5$

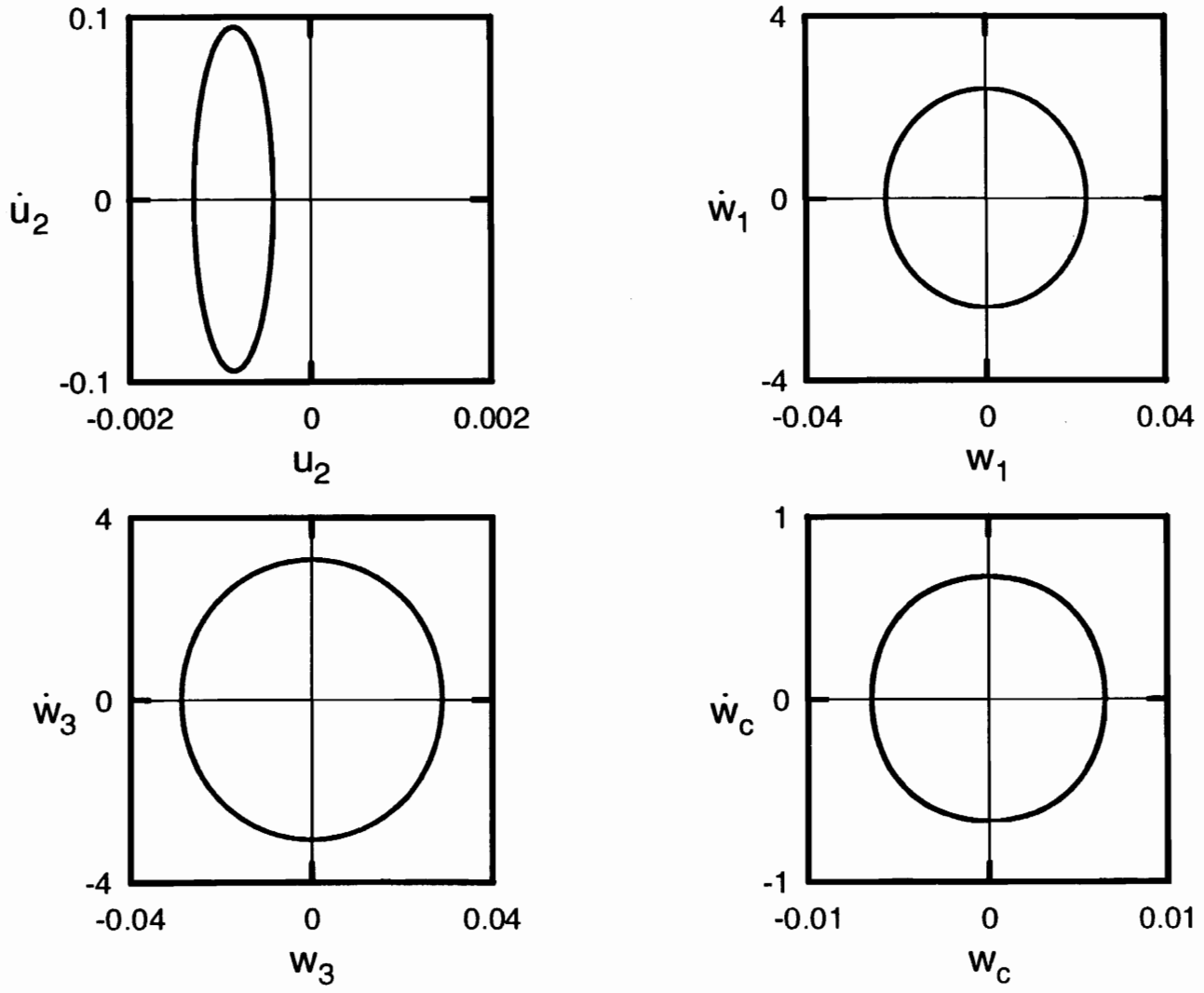

Figure A.139: Phase portraits for non shear deformable beam with $r = 0.05$, $\Omega = 108.0$, $a = 0.5$

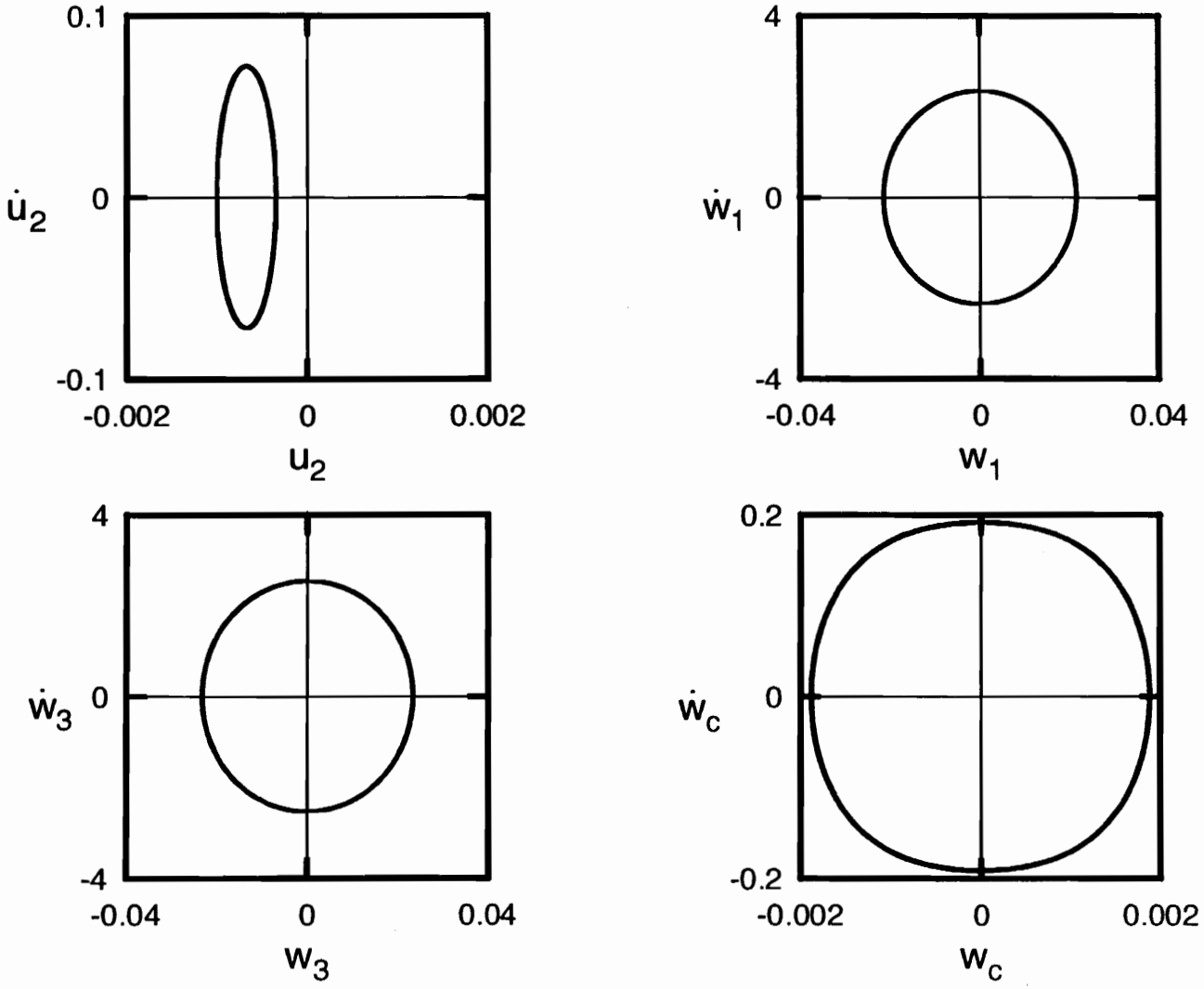

Figure A.140: Phase portraits for non shear deformable beam with $r = 0.05$, $\Omega = 110.0$, $a = 0.5$

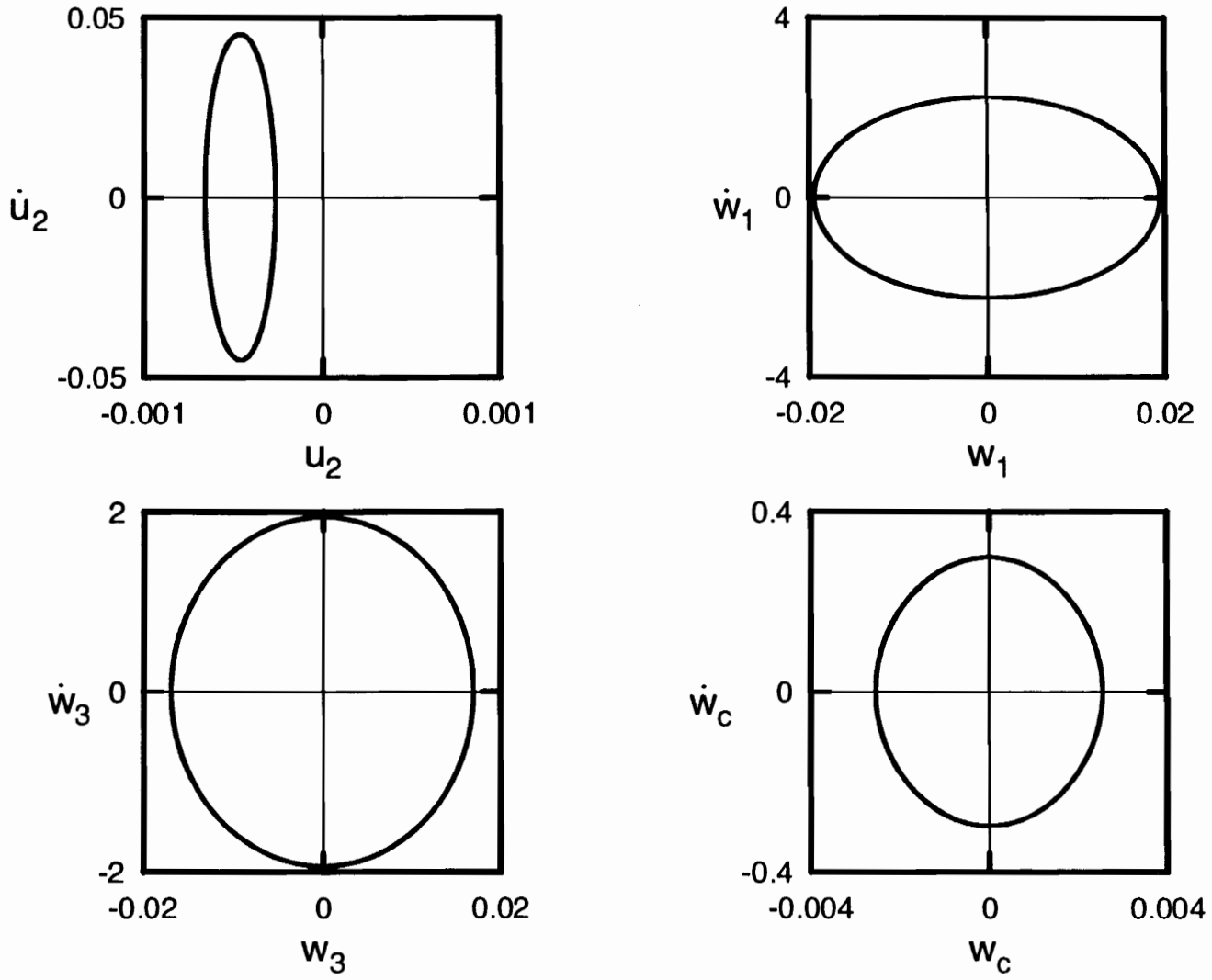

Figure A.141: Phase portraits for non shear deformable beam with $r = 0.05$, $\Omega = 115.0$, $a = 0.5$

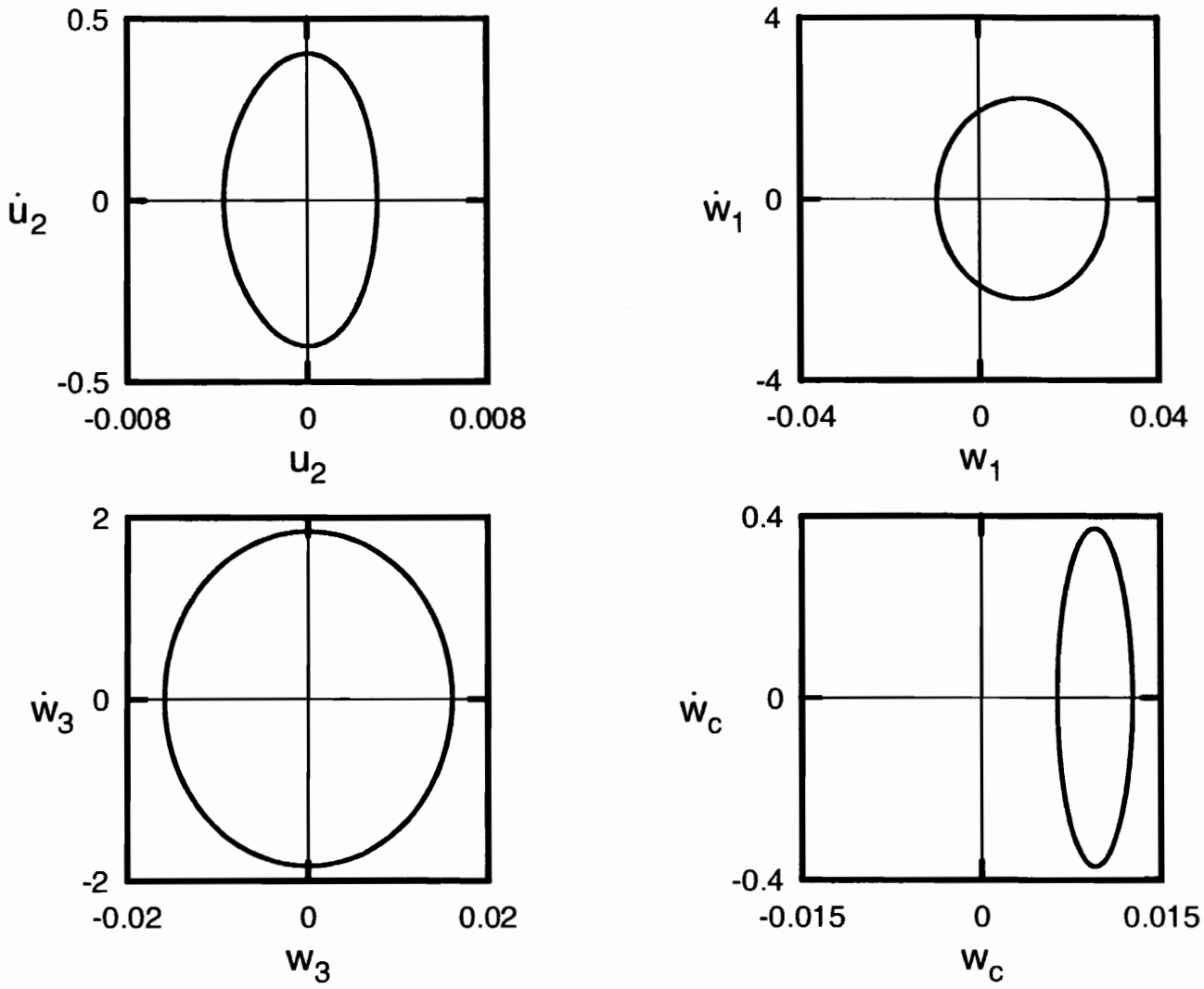

Figure A.142: Phase portraits for non shear deformable beam with $r = 0.05$, $\Omega = 116.0$, $a = 0.5$

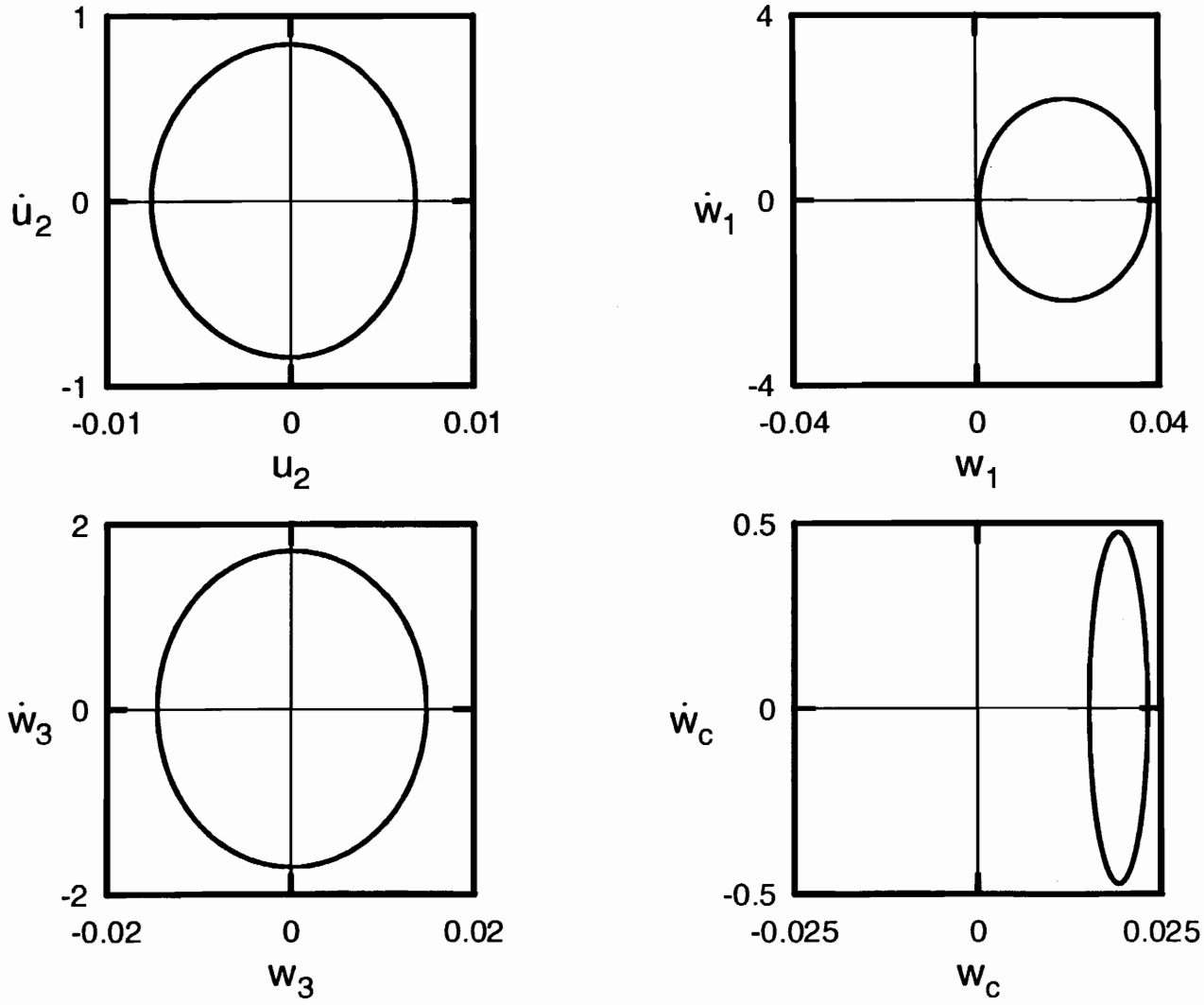

Figure A.143: Phase portraits for non shear deformable beam with $r = 0.05$, $\Omega = 117.0$, $a = 0.5$.

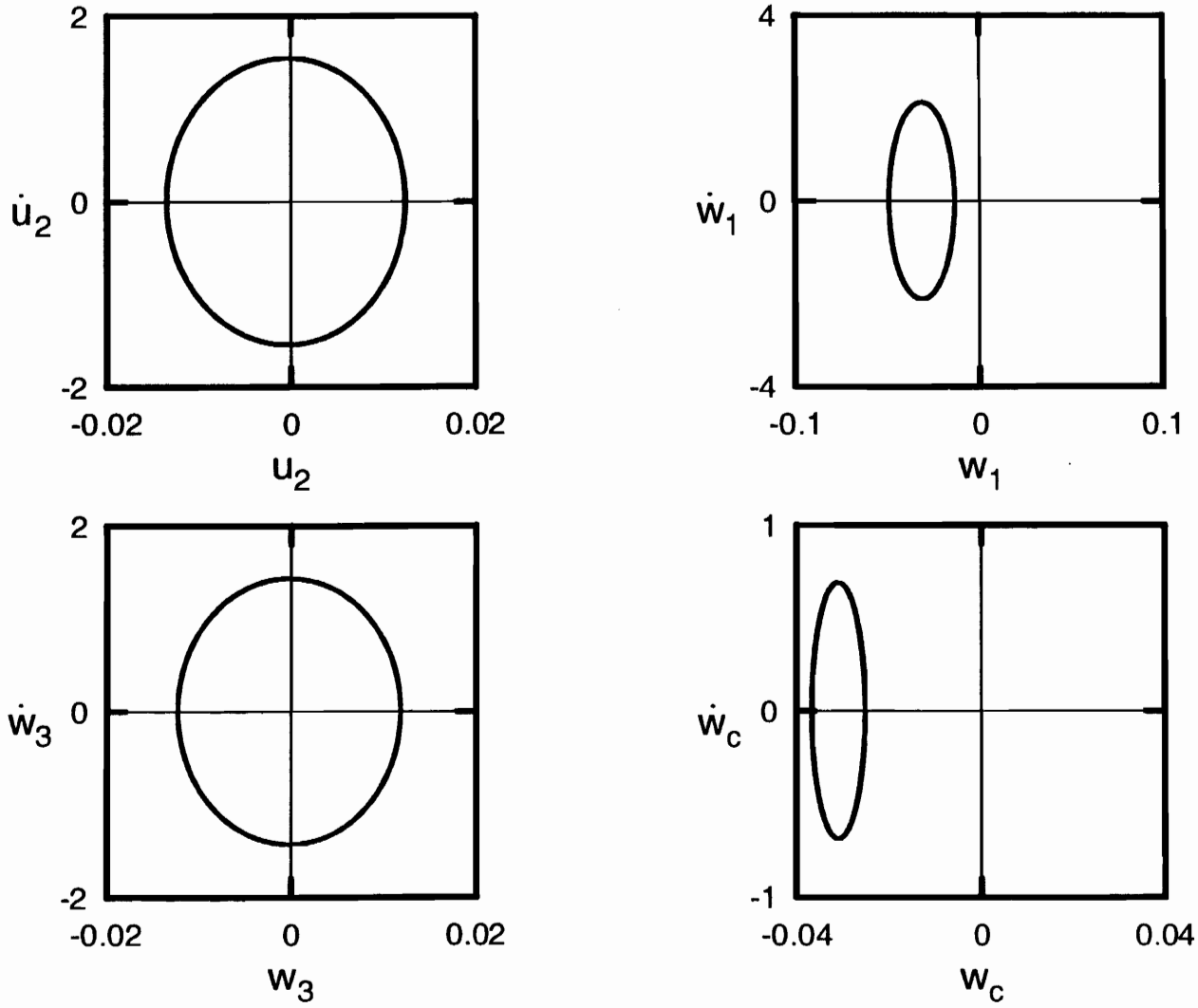

Figure A.144: Phase portraits for non shear deformable beam with $r = 0.05$, $\Omega = 119.0$, $a = 0.5$.

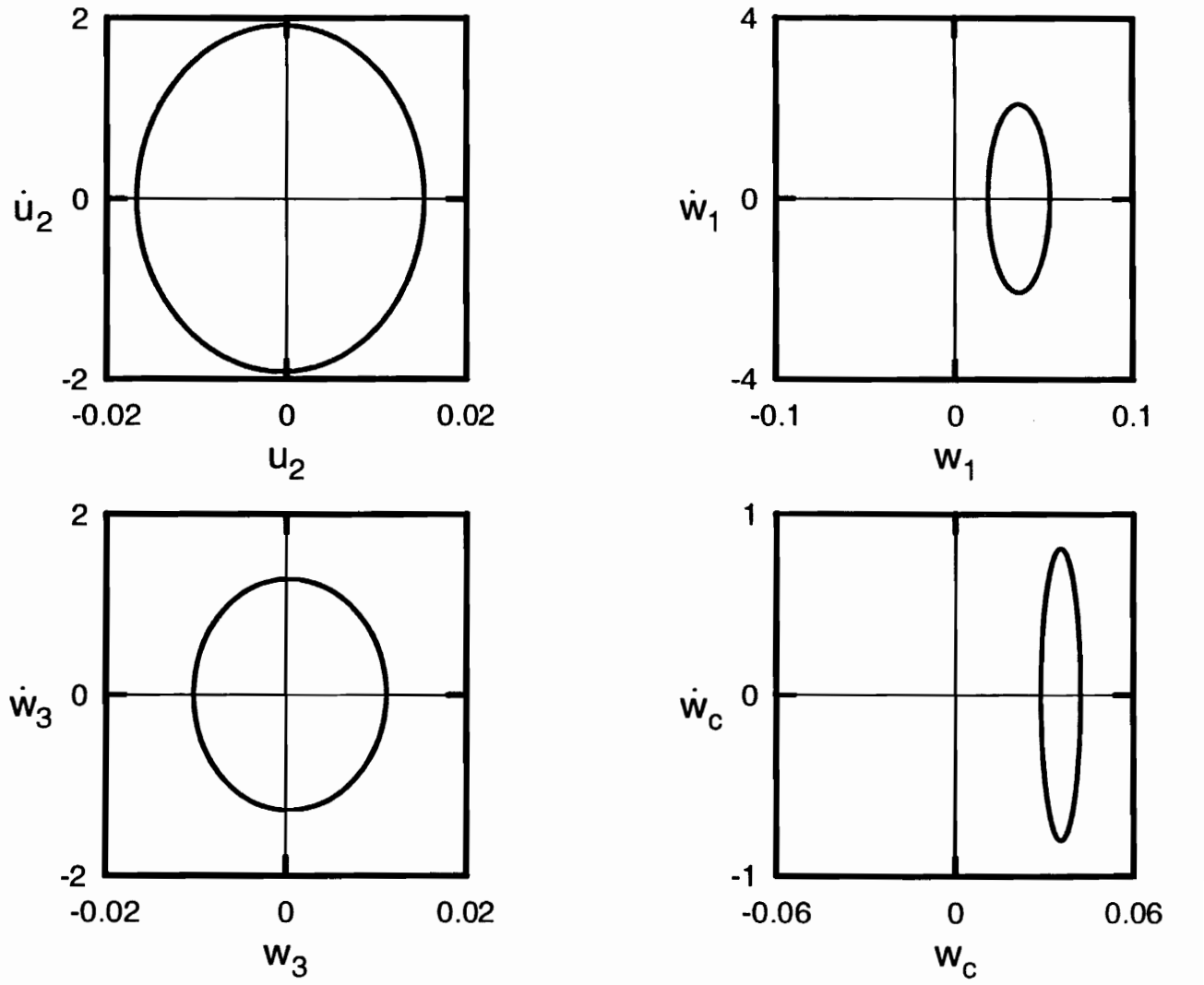

Figure A.145: Phase portraits for non shear deformable beam with $r = 0.05$, $\Omega = 120.0$, $a = 0.5$.

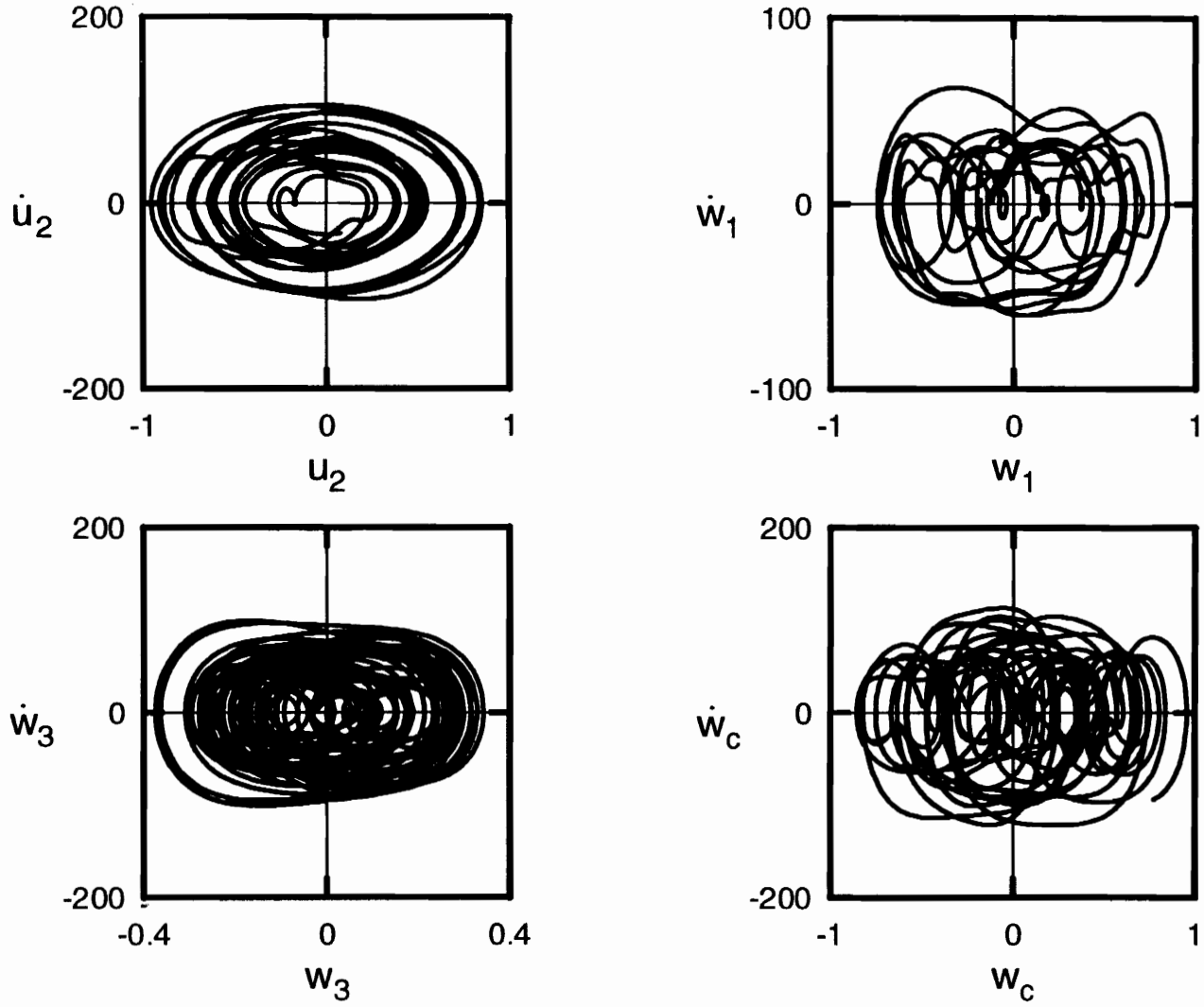

Figure A.146: Phase portraits for shear deformable beam with $r = 0.05$, $\Omega = 60.0$, $a = 1.0$.

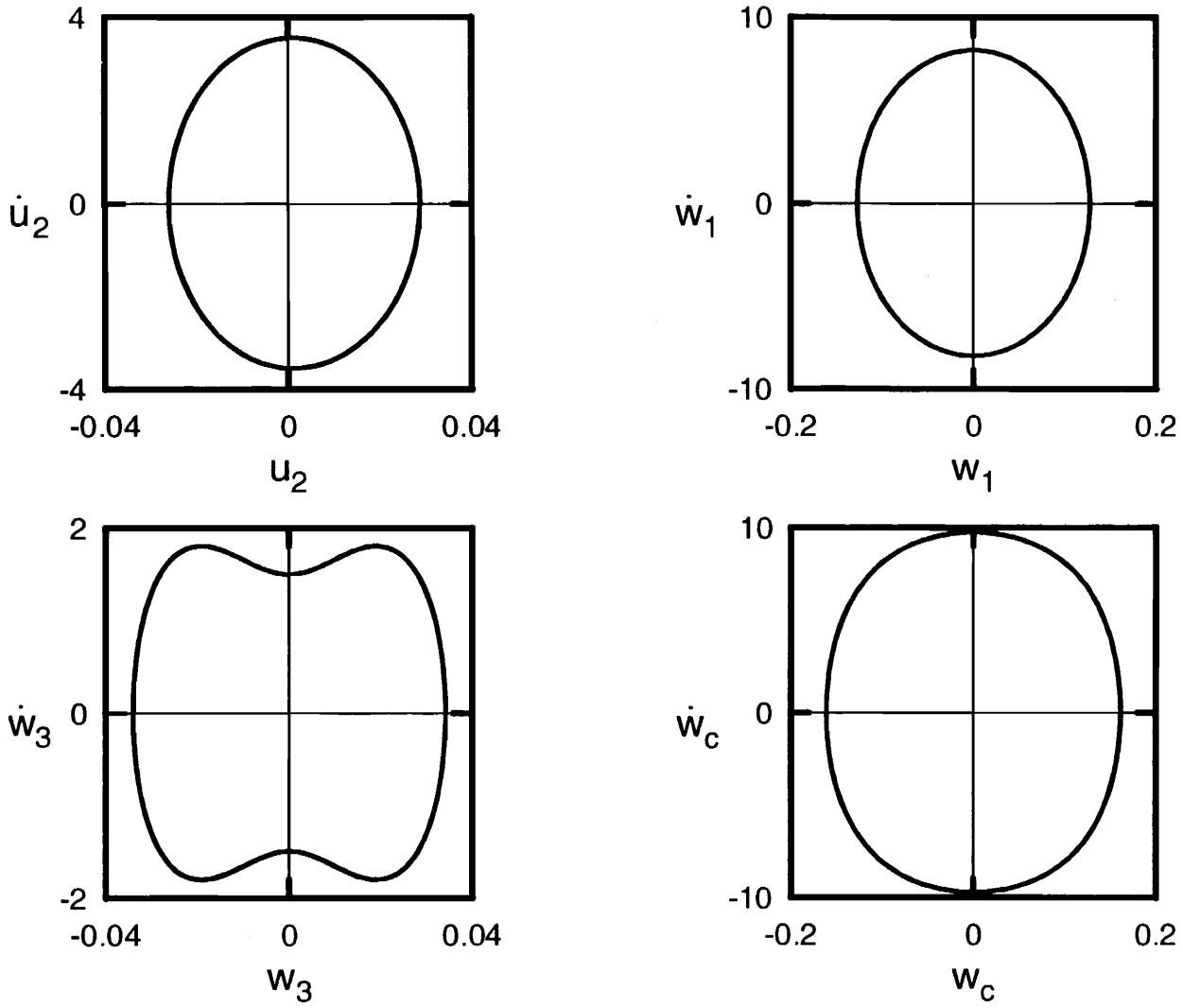

Figure A.147: Phase portraits for shear deformable beam with $r = 0.05$, $\Omega = 65.0$, $a = 1.0$.

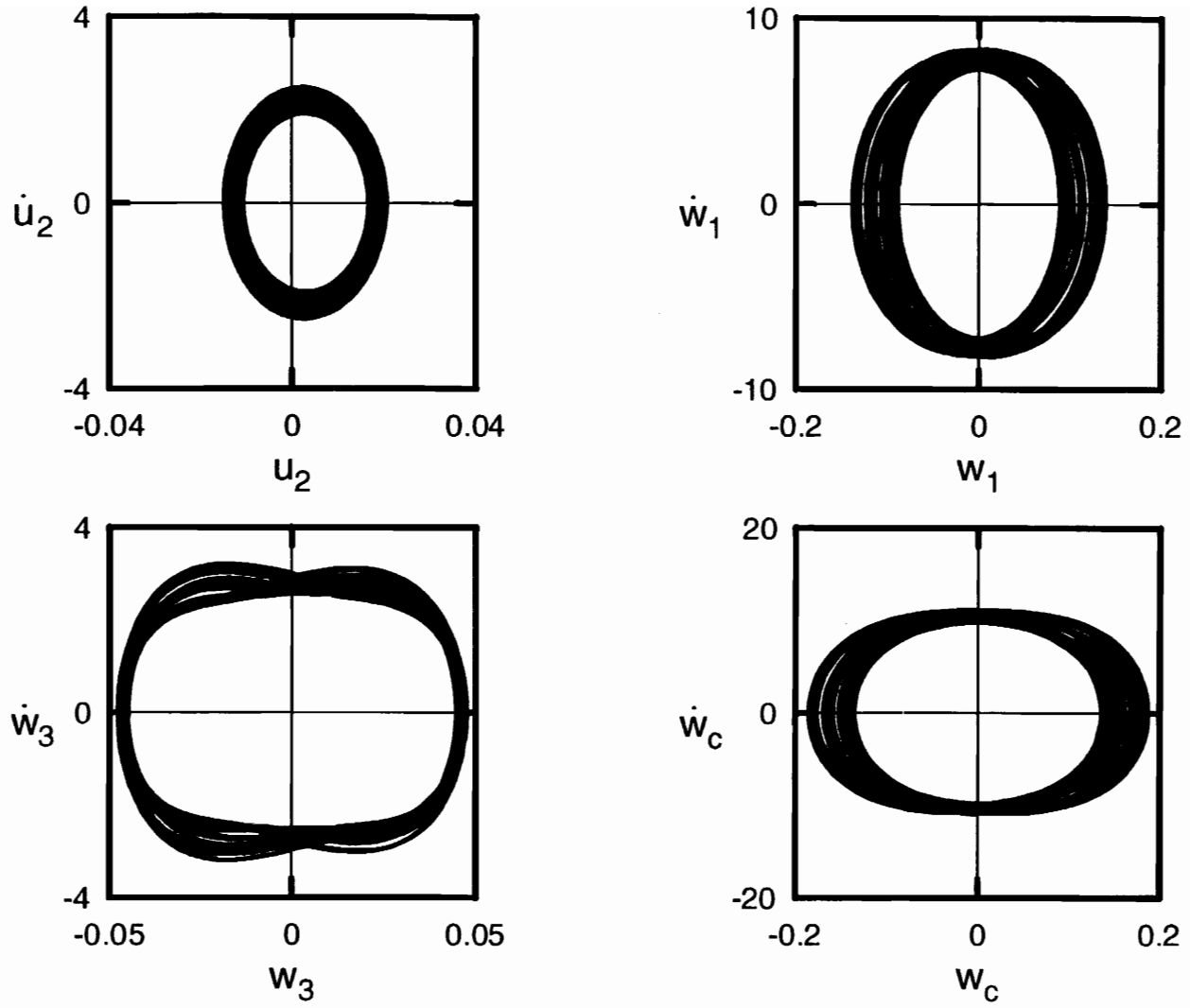

Figure A.148: Phase portraits for shear deformable beam with $r = 0.05$, $\Omega = 70.0$, $a = 1.0$.

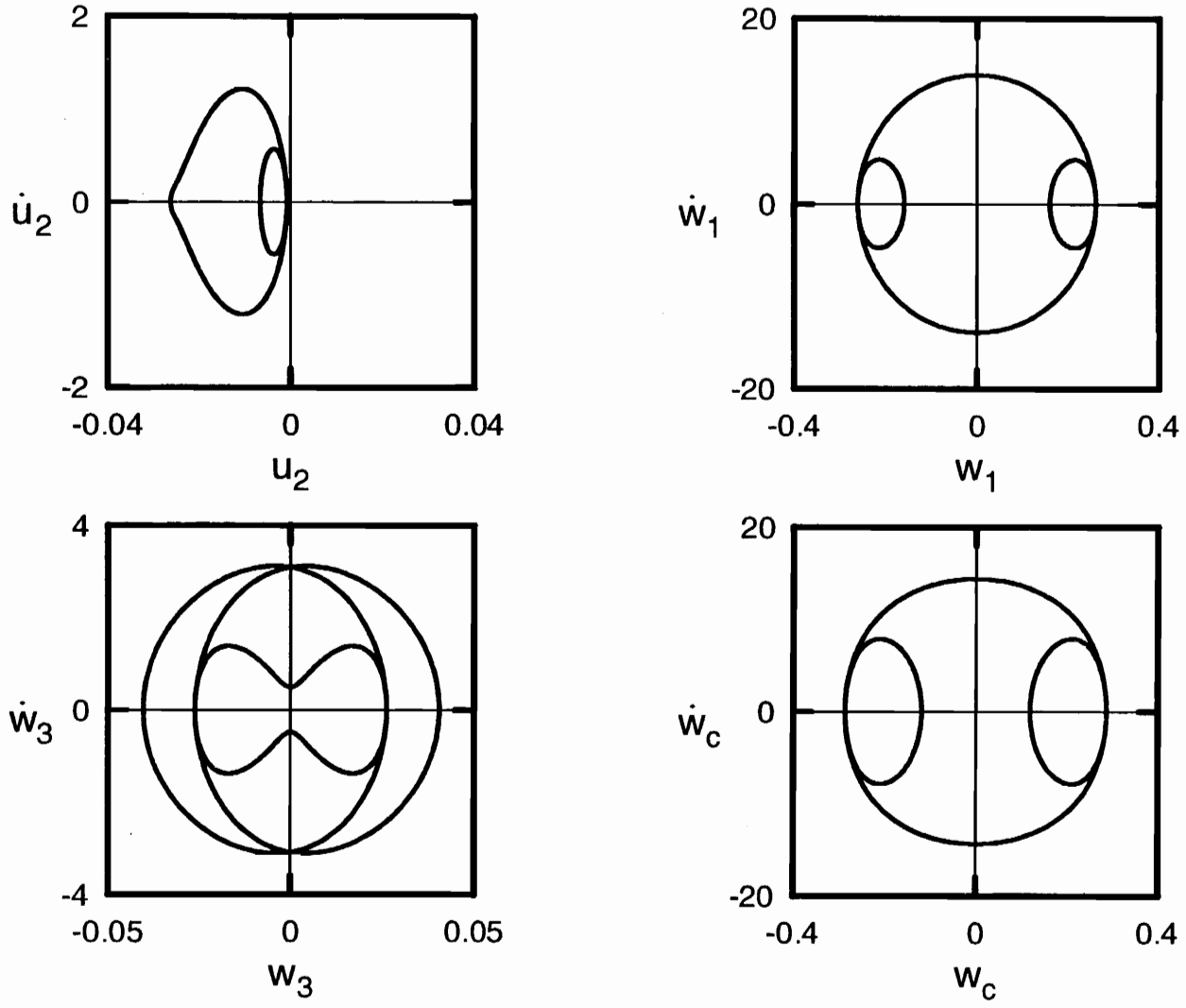

Figure A.149: Phase portraits for shear deformable beam with $r = 0.05$, $\Omega = 75.0$, $a = 1.0$.

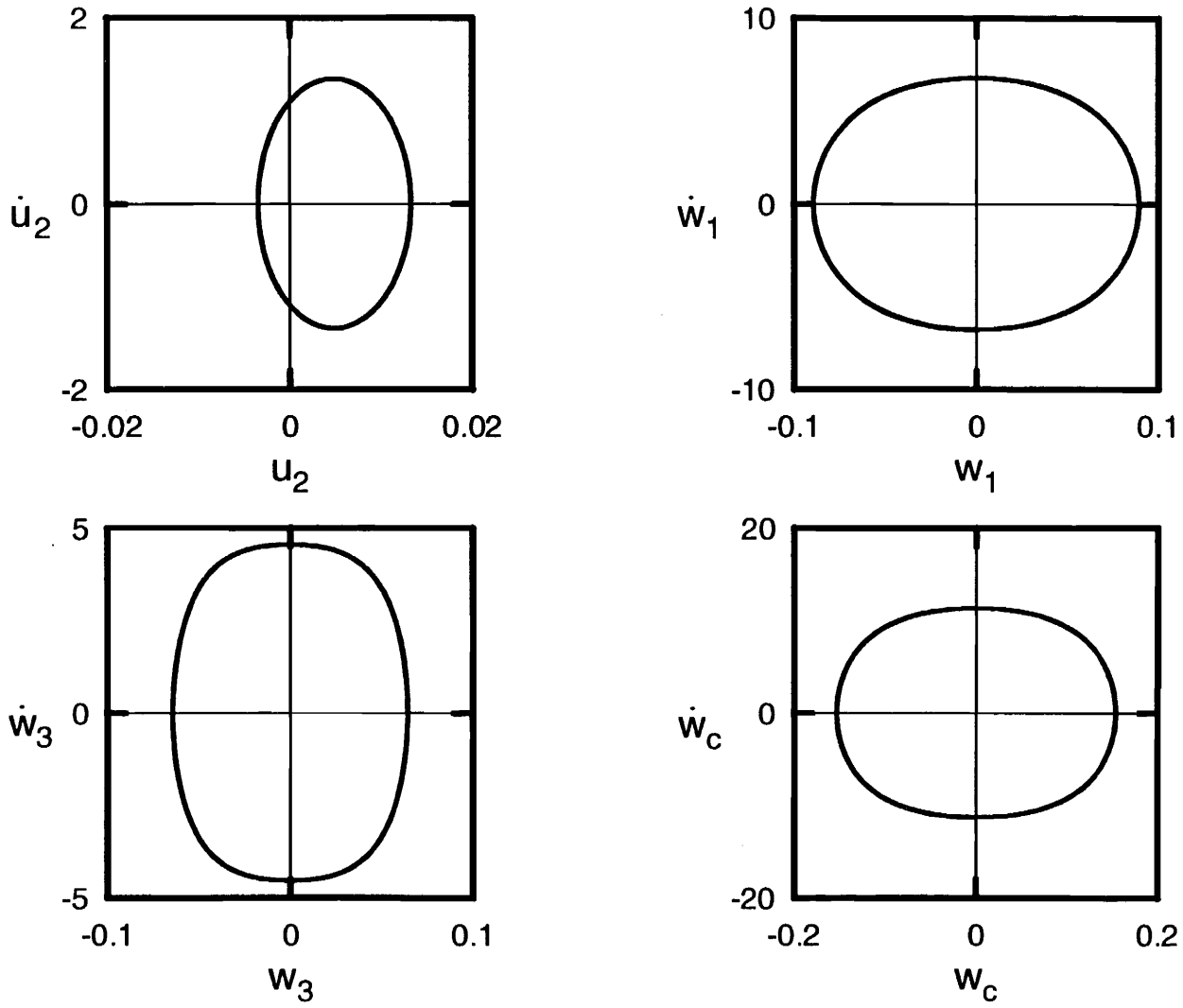

Figure A.150: Phase portraits for shear deformable beam with $r = 0.05$, $\Omega = 80.0$, $a = 1.0$.

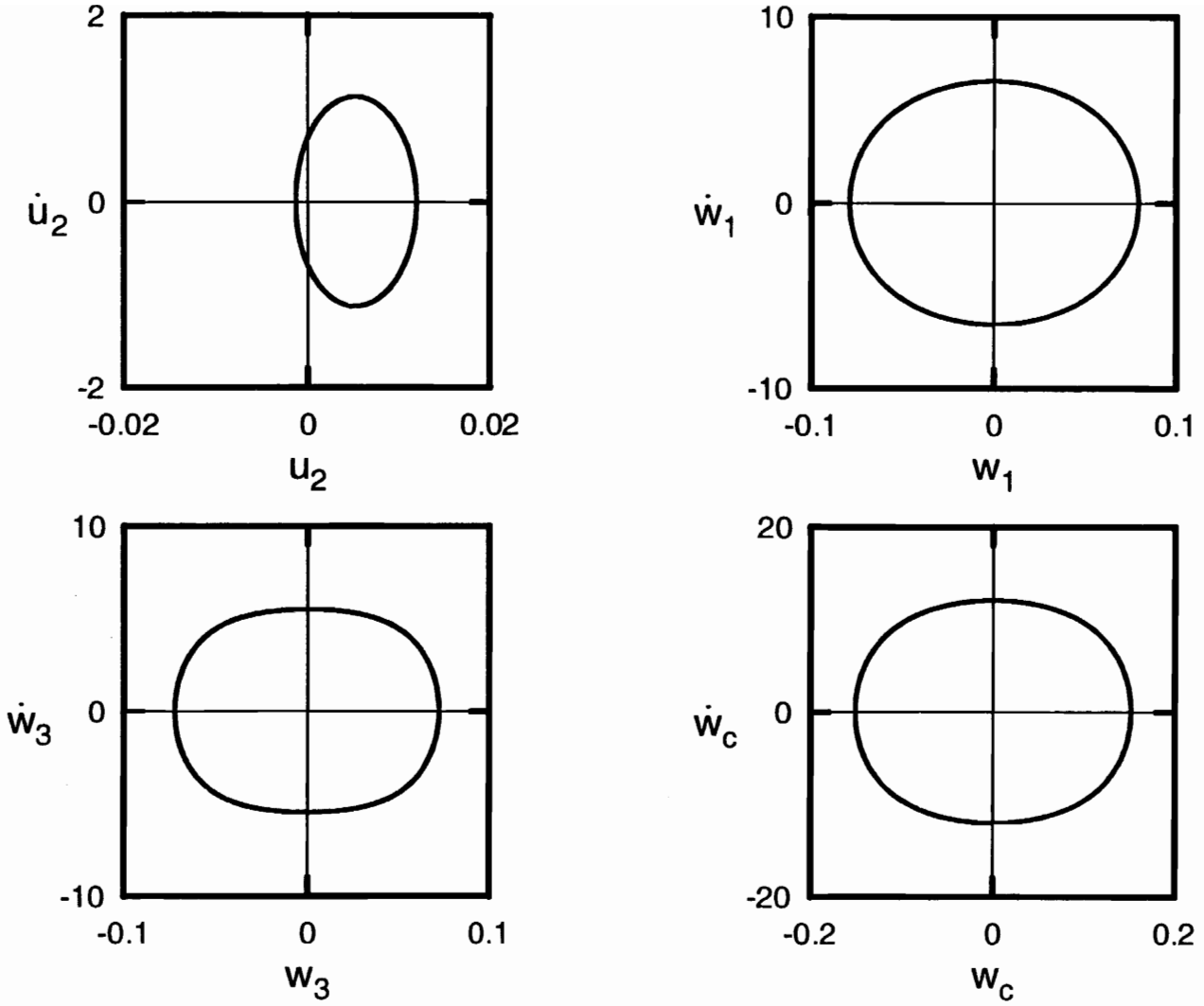

Figure A.151: Phase portraits for shear deformable beam with $r = 0.05$, $\Omega = 85.0$, $a = 1.0$.

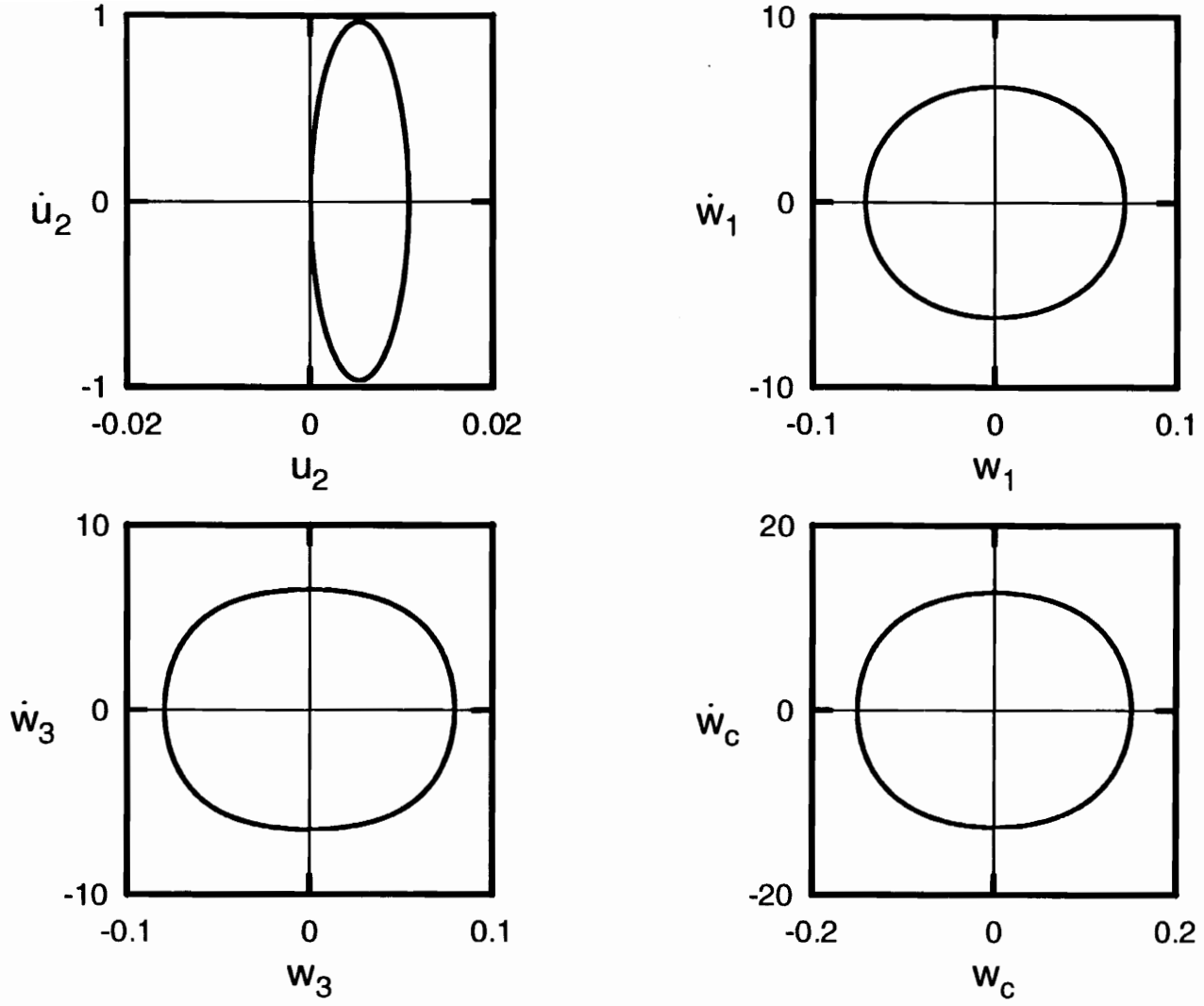

Figure A.152: Phase portraits for shear deformable beam with $r = 0.05$, $\Omega = 90.0$, $a = 1.0$.

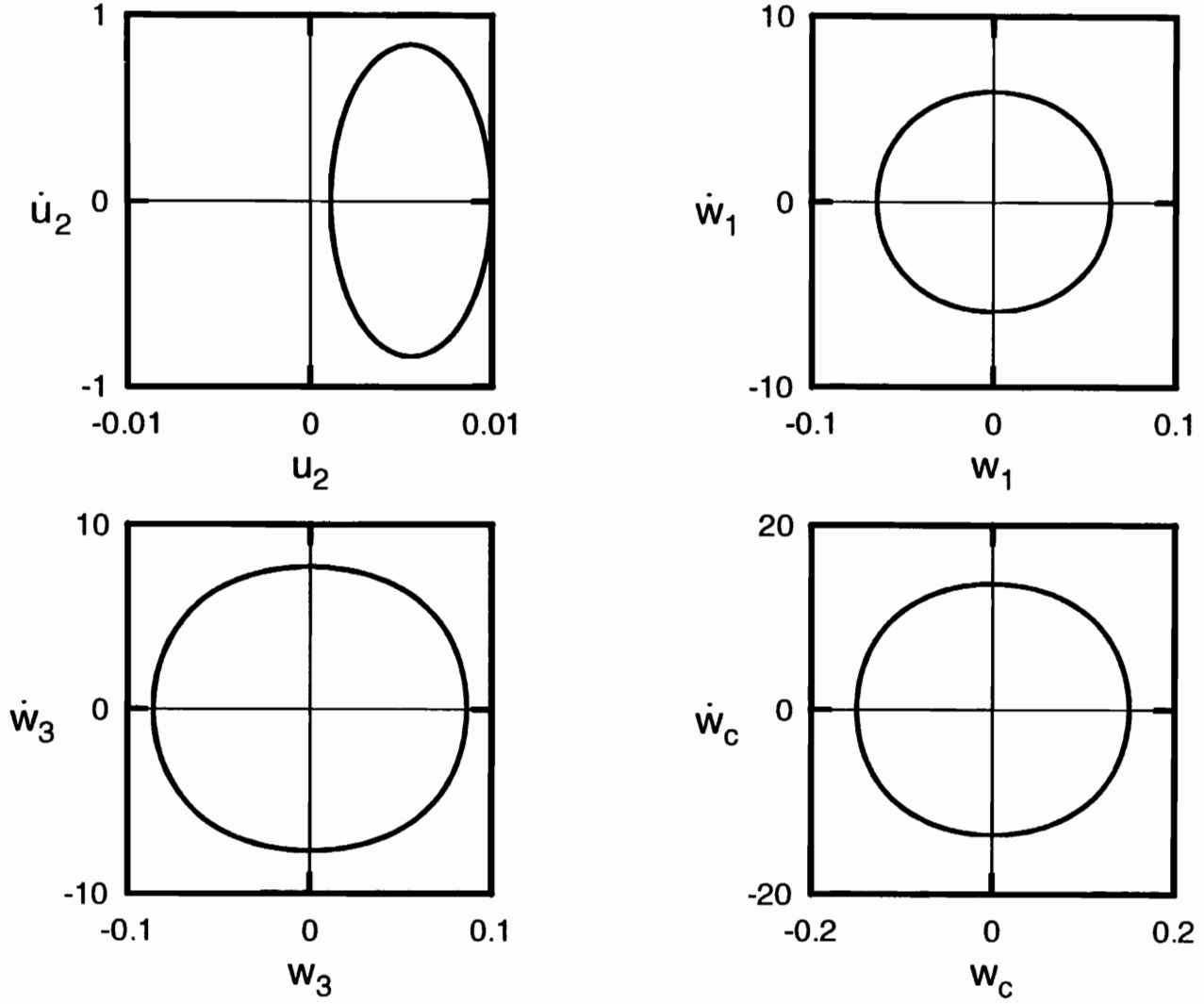

Figure A.153: Phase portraits for shear deformable beam with $r = 0.05$, $\Omega = 95.0$, $a = 1.0$.

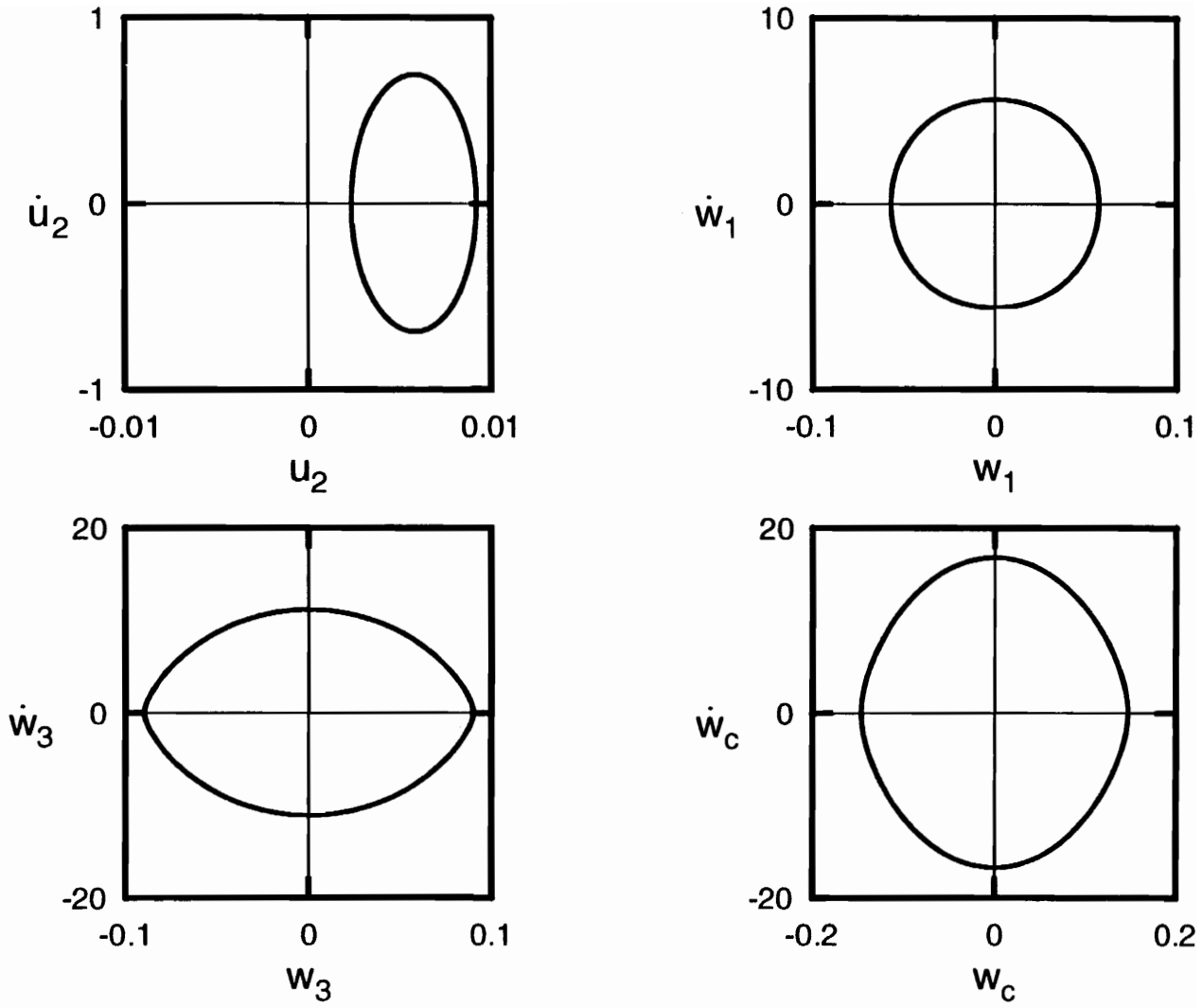

Figure A.154: Phase portraits for shear deformable beam with $r = 0.05$, $\Omega = 101.0$, $a = 1.0$.

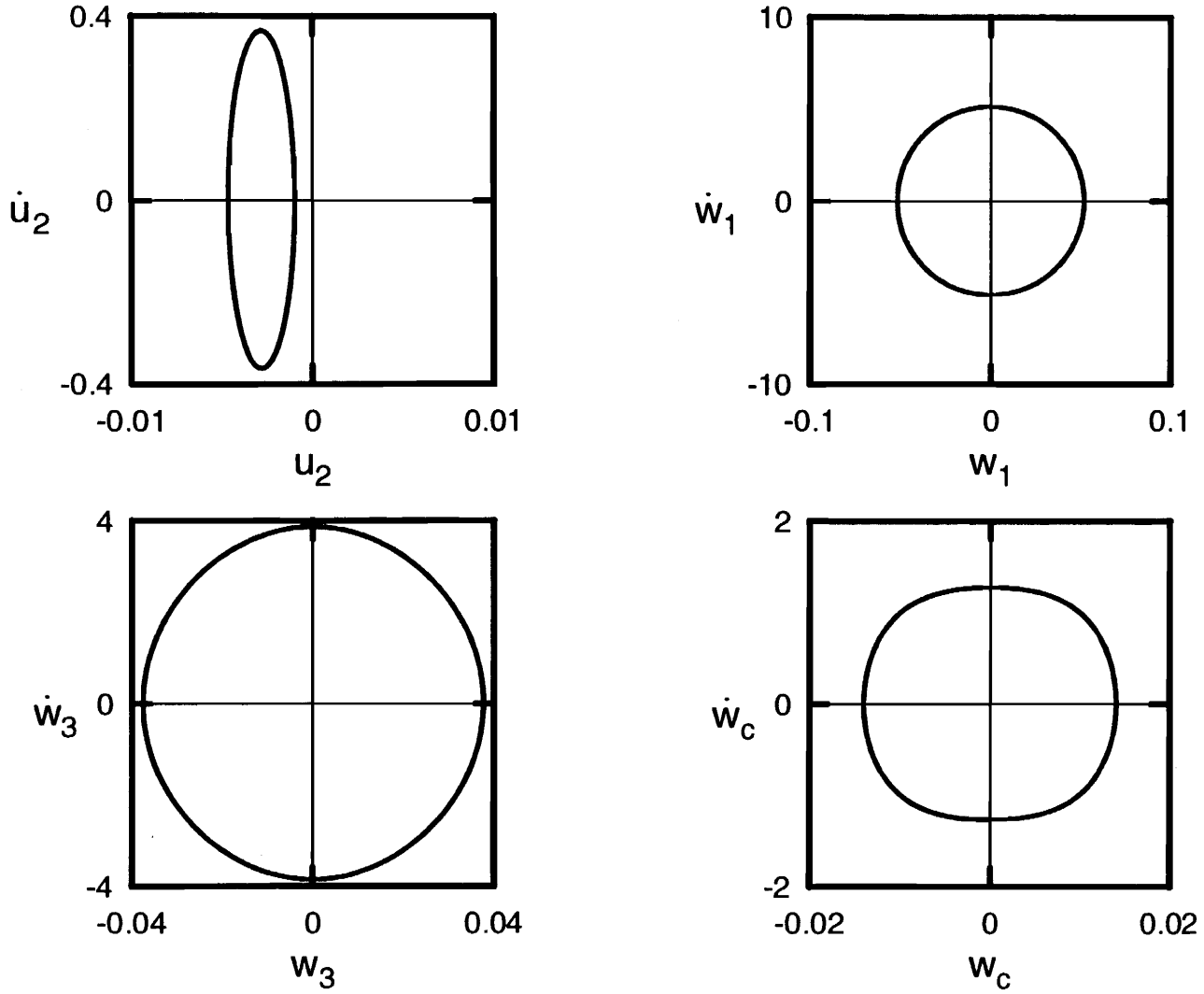

Figure A.155: Phase portraits for shear deformable beam with $r = 0.05$, $\Omega = 100.0$, $a = 1.0$.

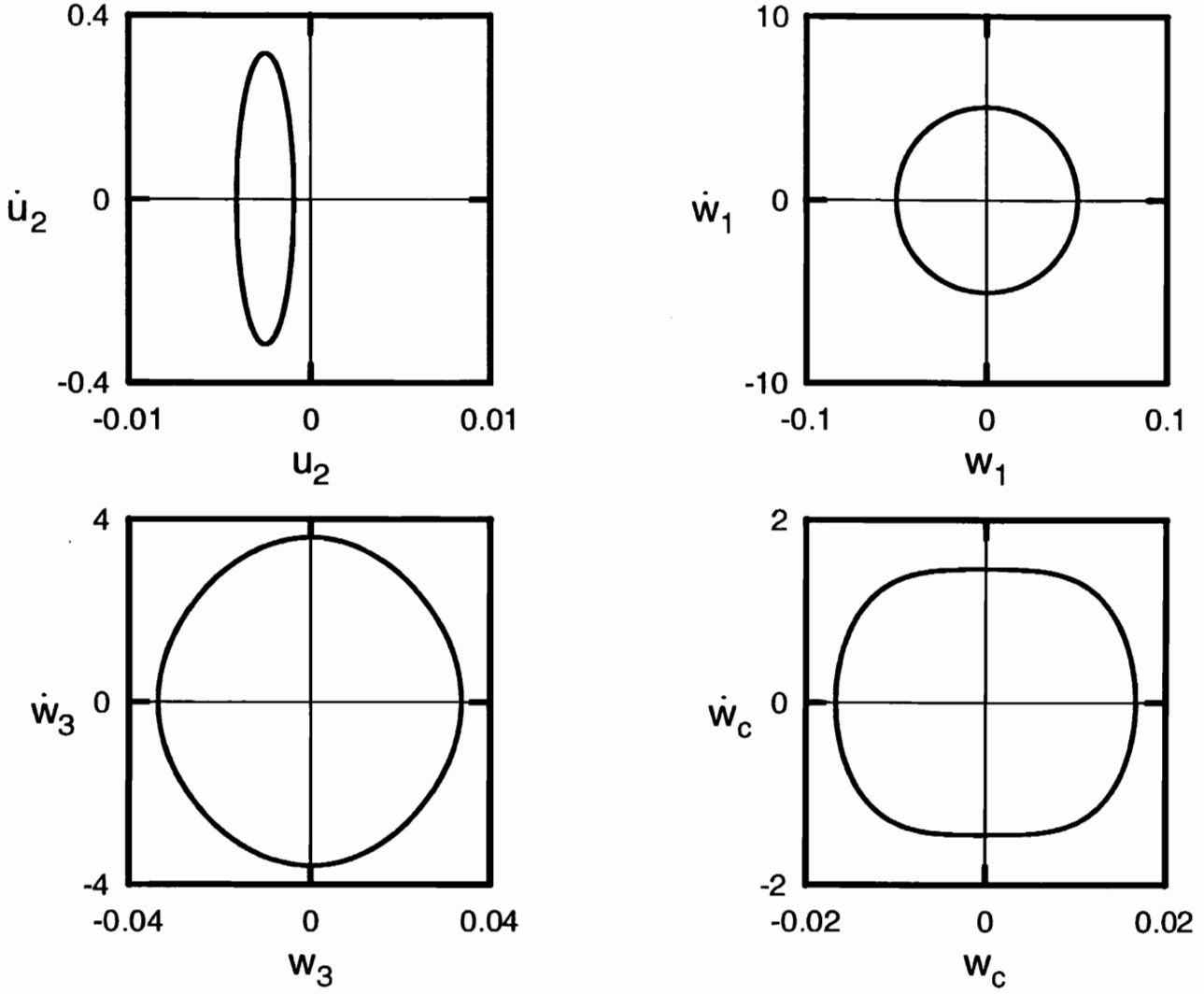

Figure A.156: Phase portraits for shear deformable beam with $r = 0.05$, $\Omega = 101.0$, $a = 1.0$.

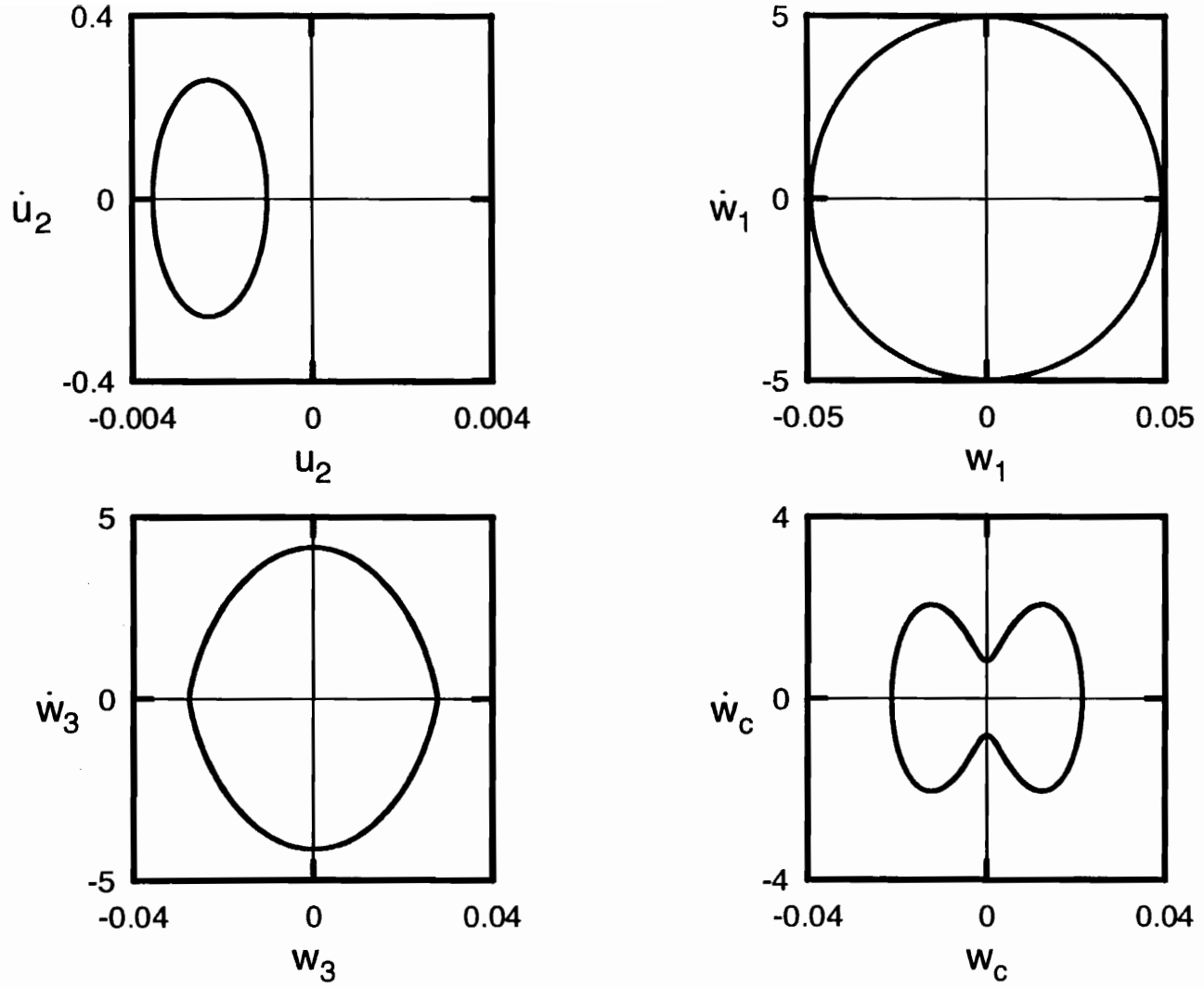

Figure A.157: Phase portraits for shear deformable beam with $r = 0.05$, $\Omega = 102.0$, $a = 1.0$.

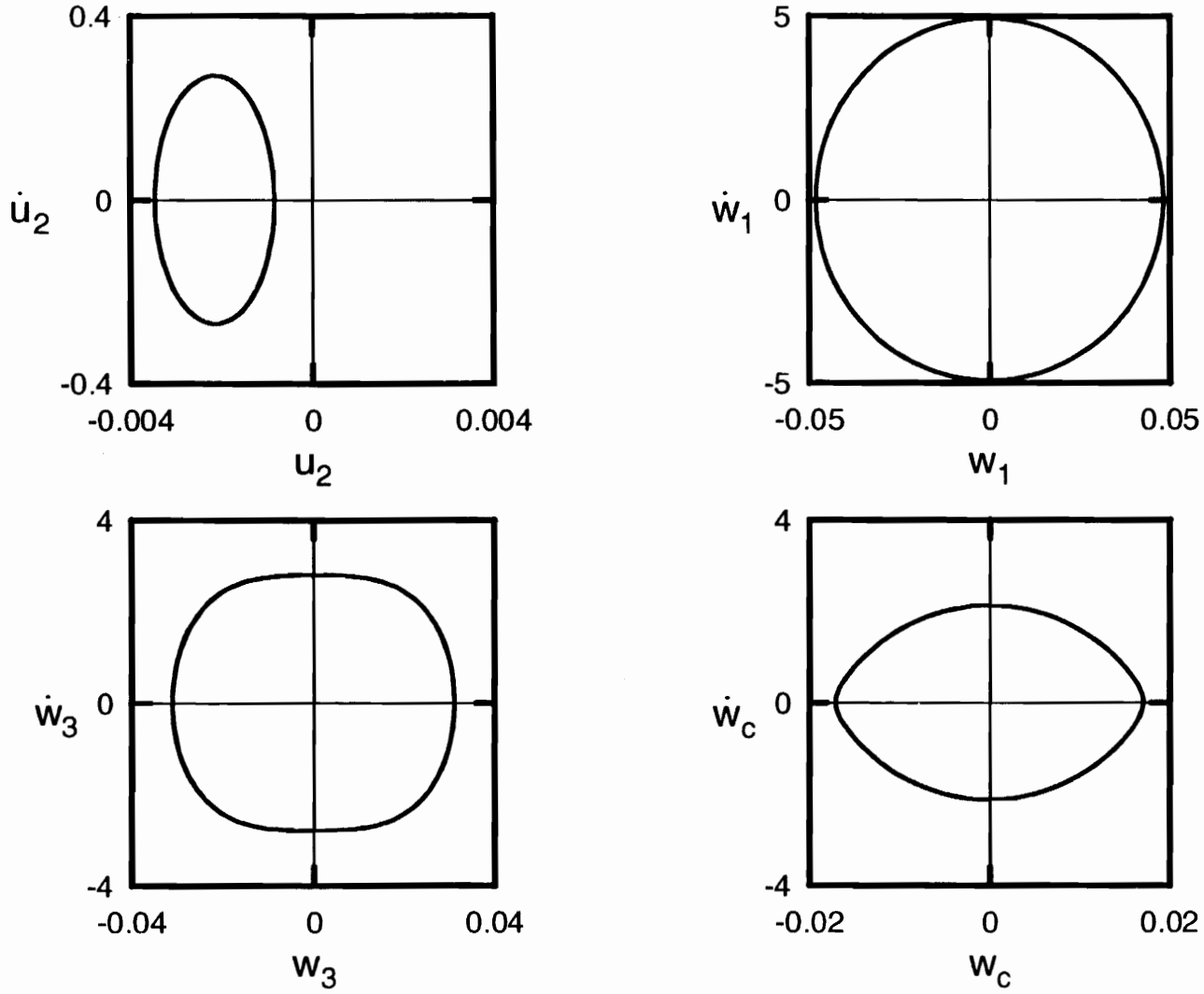

Figure A.158: Phase portraits for shear deformable beam with $r = 0.05$, $\Omega = 103.0$, $a = 1.0$.

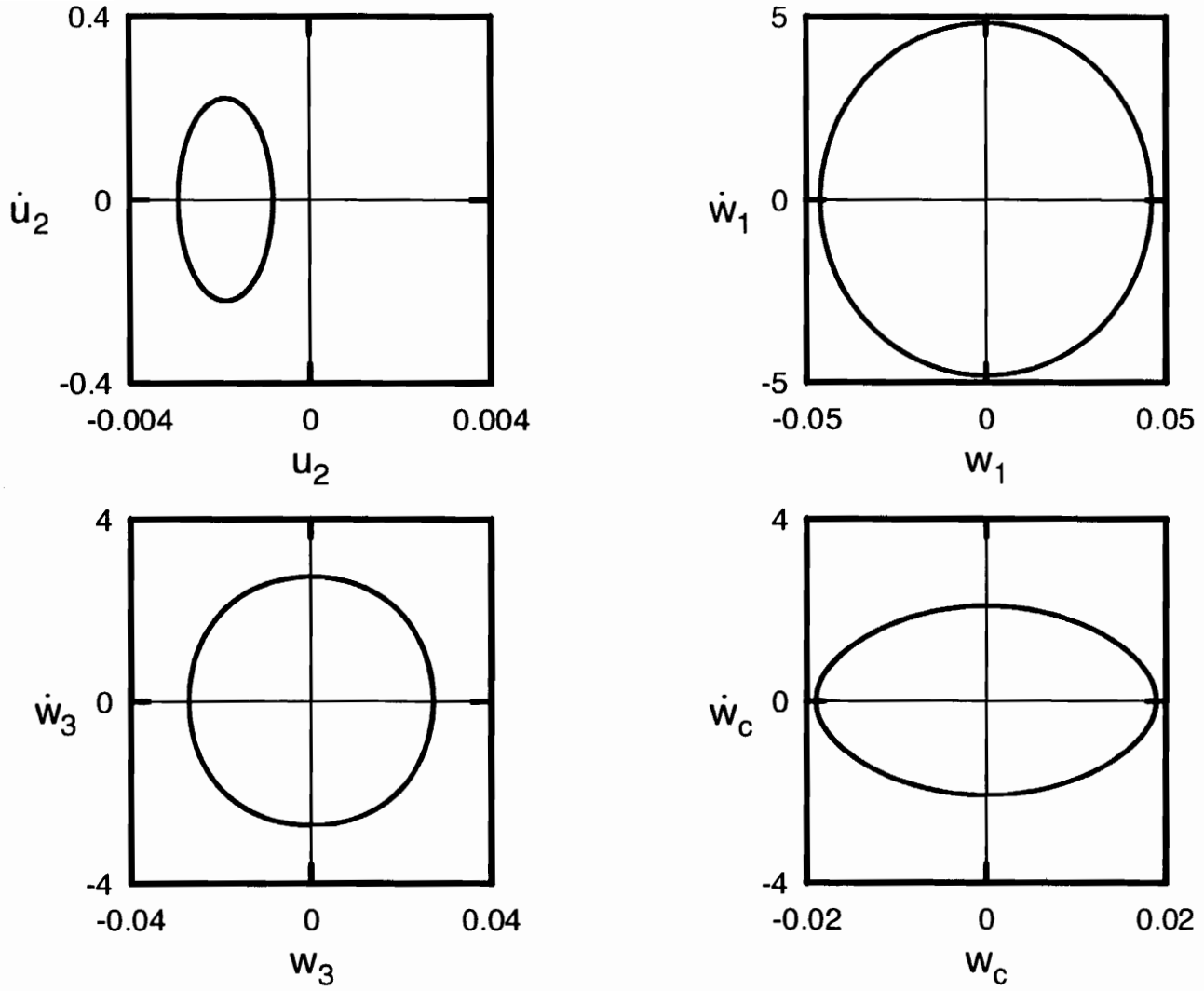

Figure A.159: Phase portraits for shear deformable beam with $r = 0.05$, $\Omega = 105.0$, $a = 1.0$.

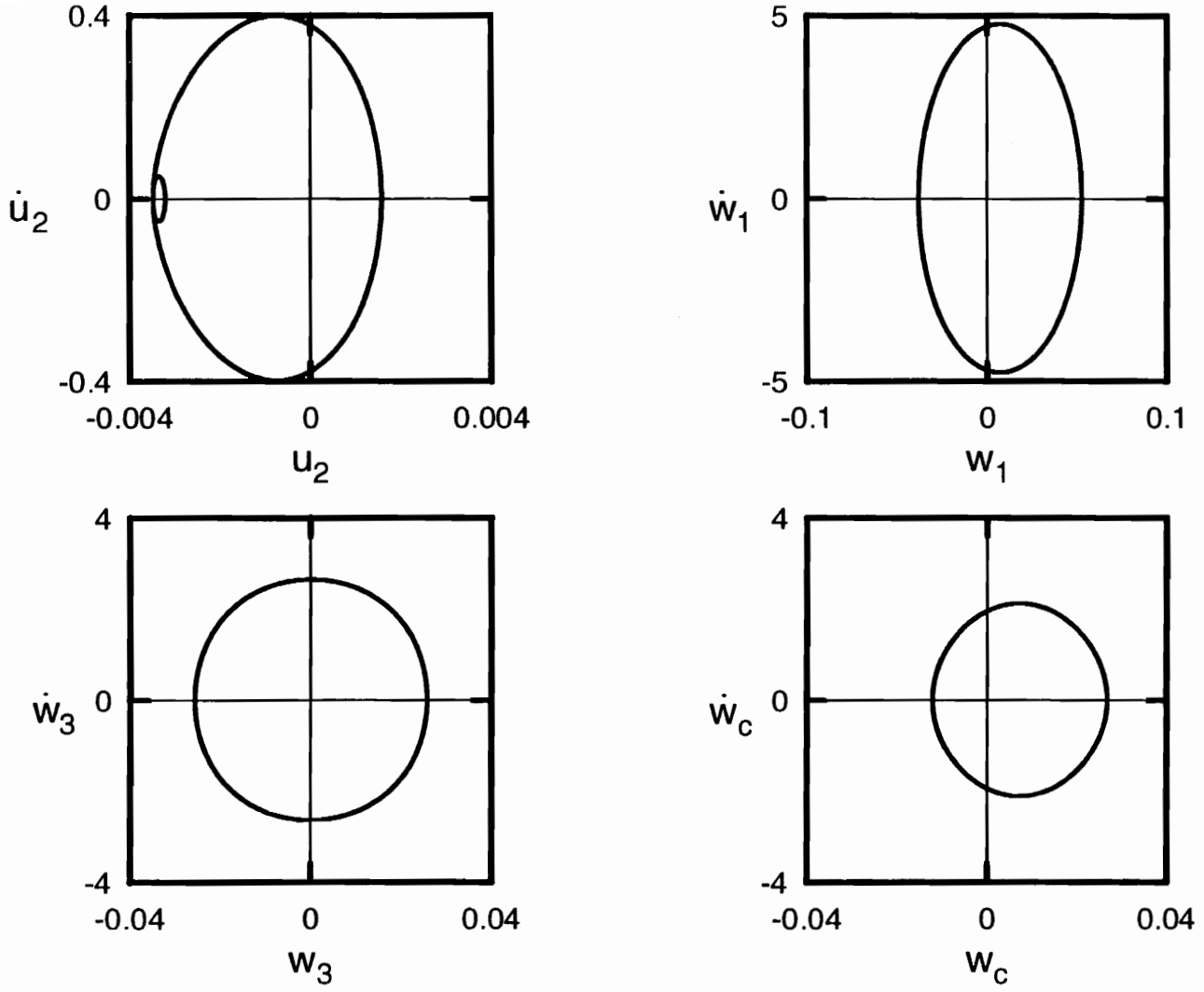

Figure A.160: Phase portraits for shear deformable beam with $r = 0.05$, $\Omega = 106.0$, $a = 1.0$.

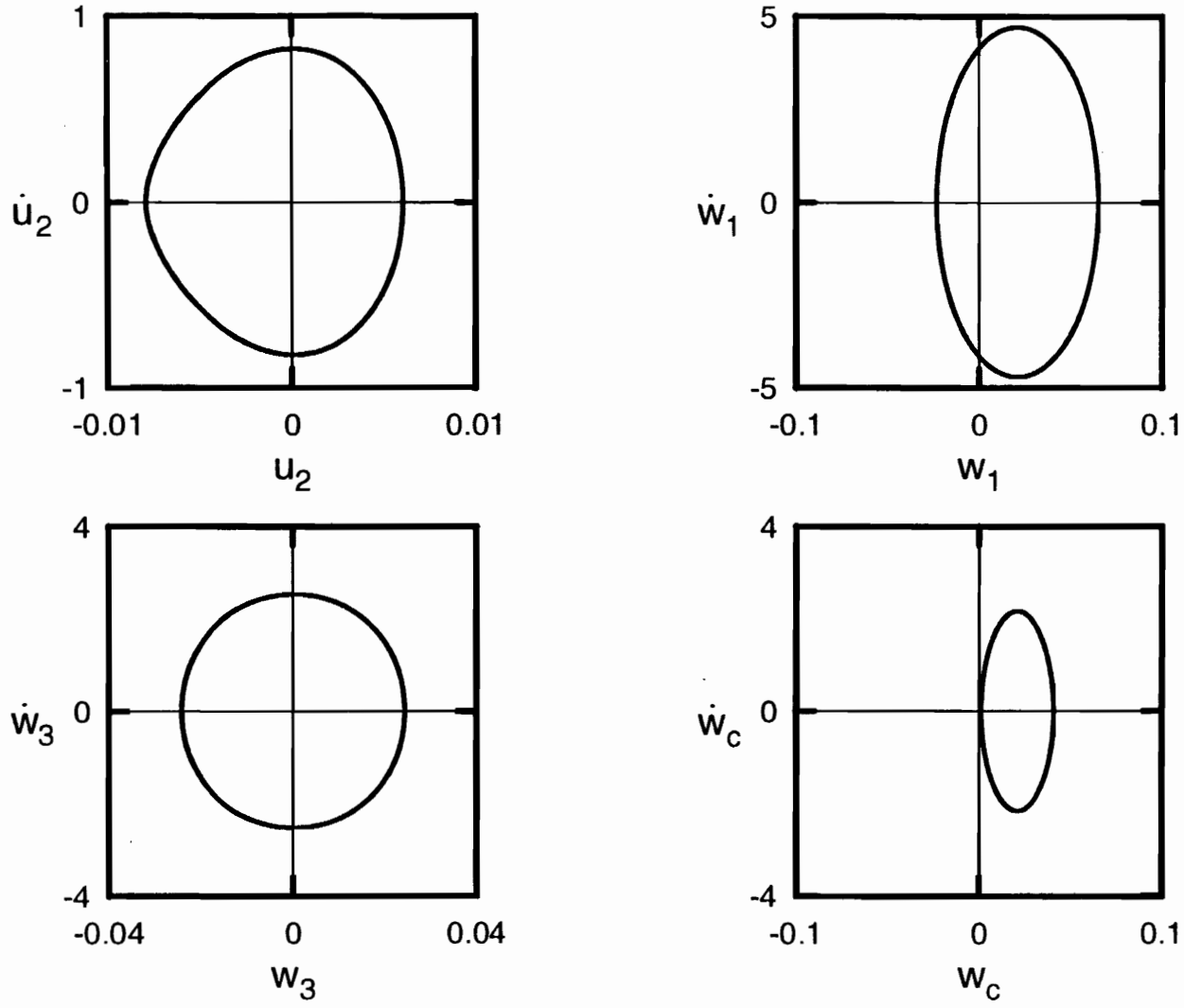

Figure A.161: Phase portraits for shear deformable beam with $r = 0.05$, $\Omega = 107.0$, $a = 1.0$.

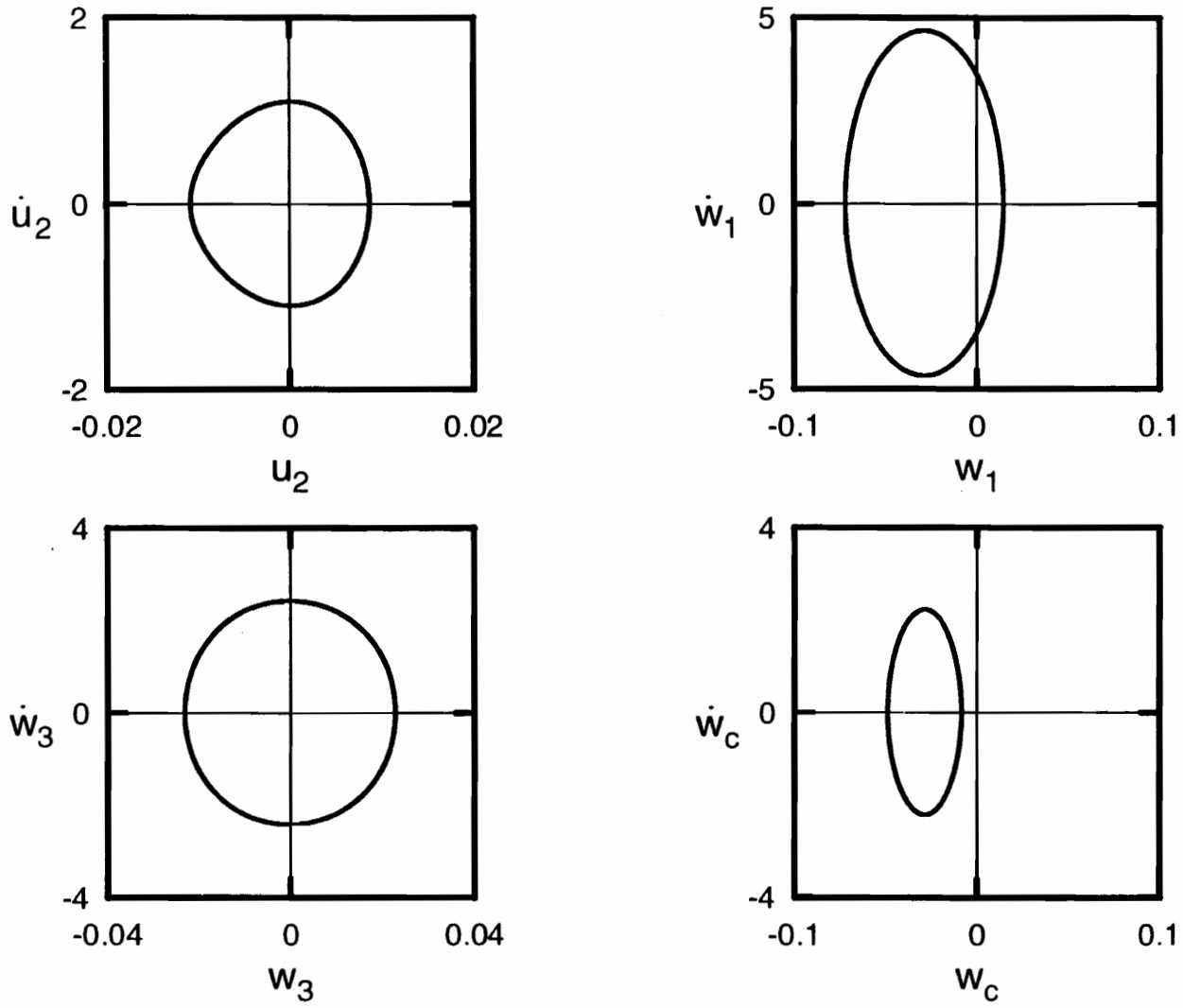

Figure A.162: Phase portraits for shear deformable beam with $r = 0.05$, $\Omega = 108.0$, $a = 1.0$.

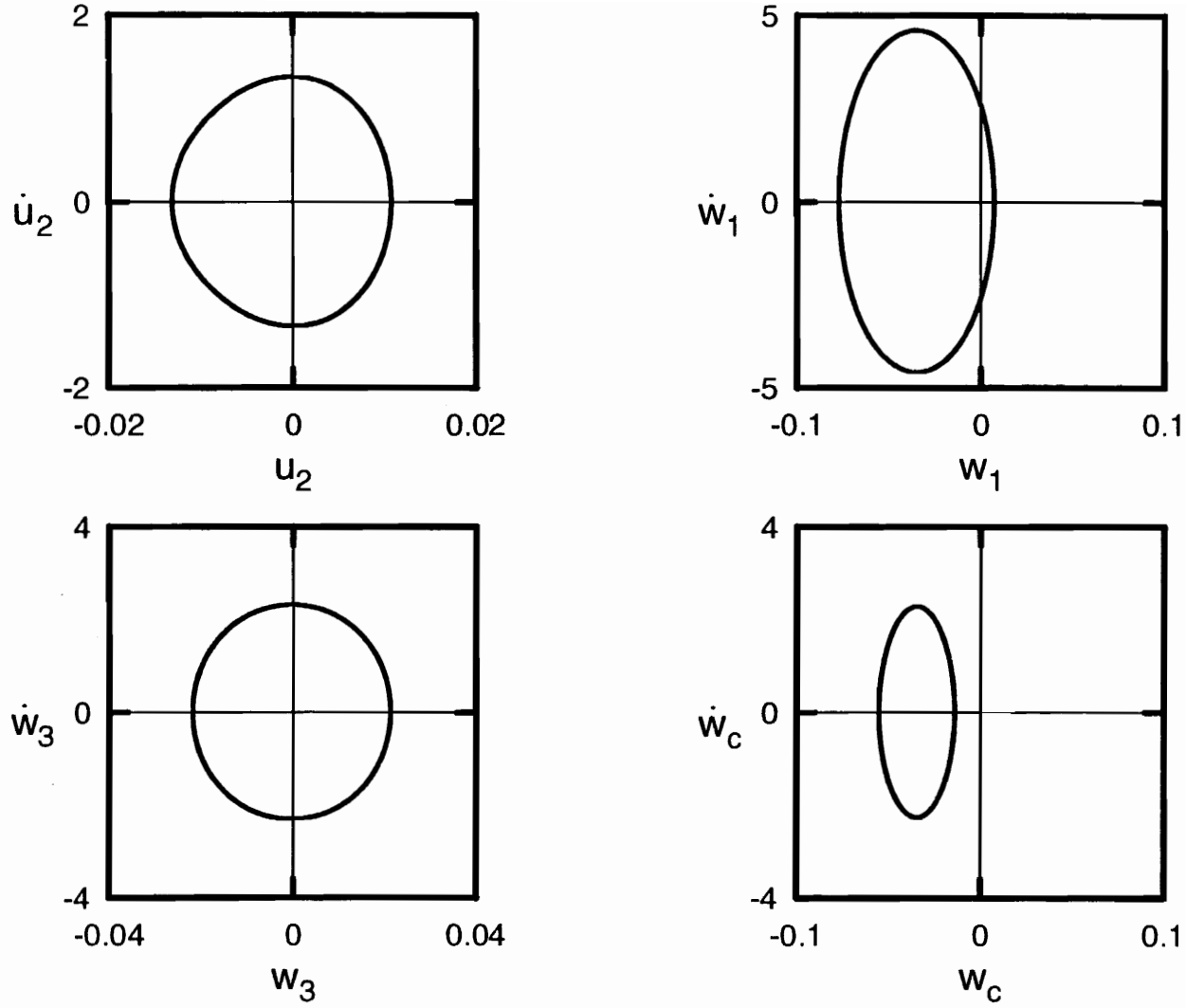

Figure A.163: Phase portraits for shear deformable beam with $r = 0.05$, $\Omega = 109.0$, $a = 1.0$.

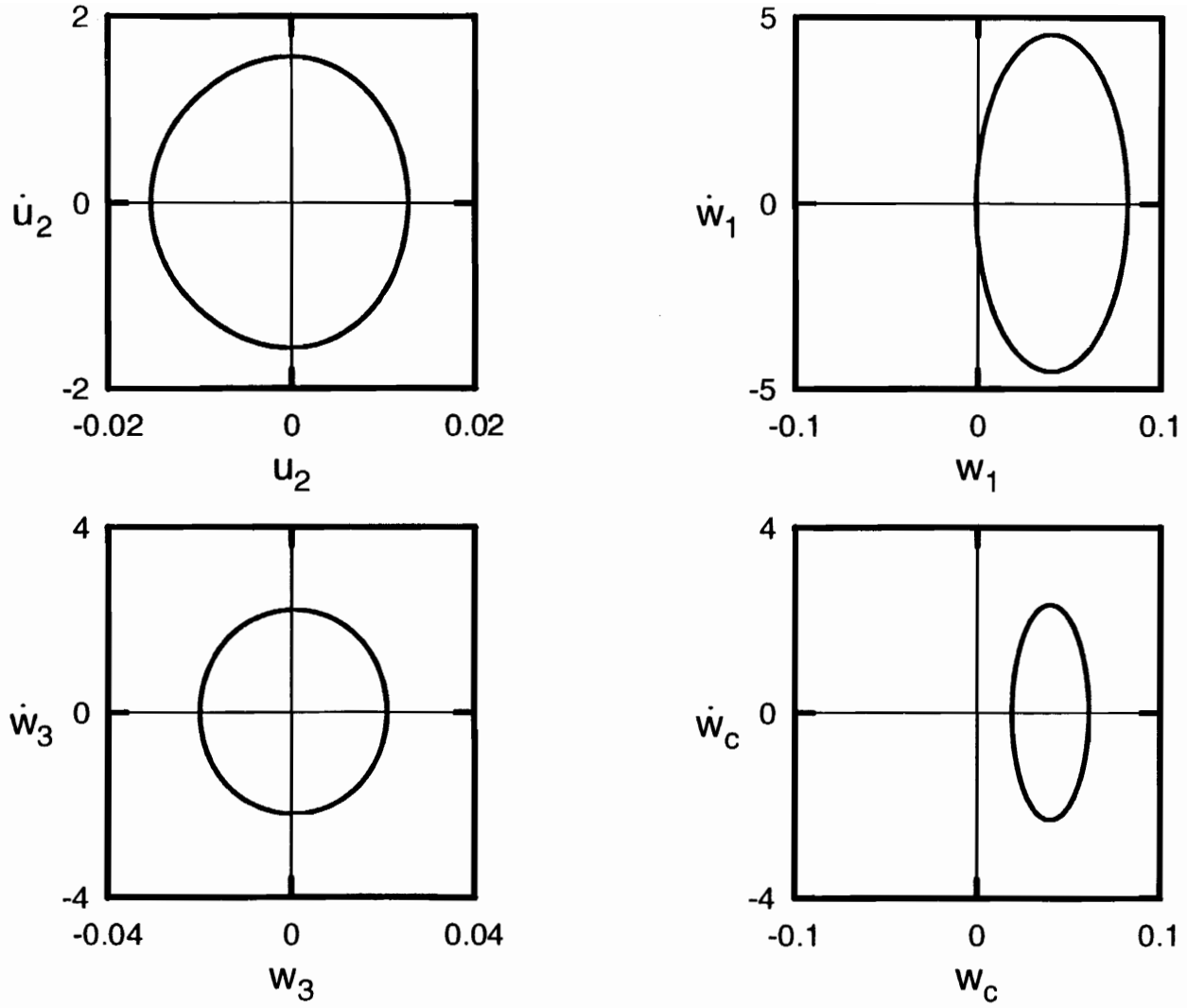

Figure A.164: Phase portraits for shear deformable beam with $r = 0.05$, $\Omega = 110.0$, $a = 1.0$.

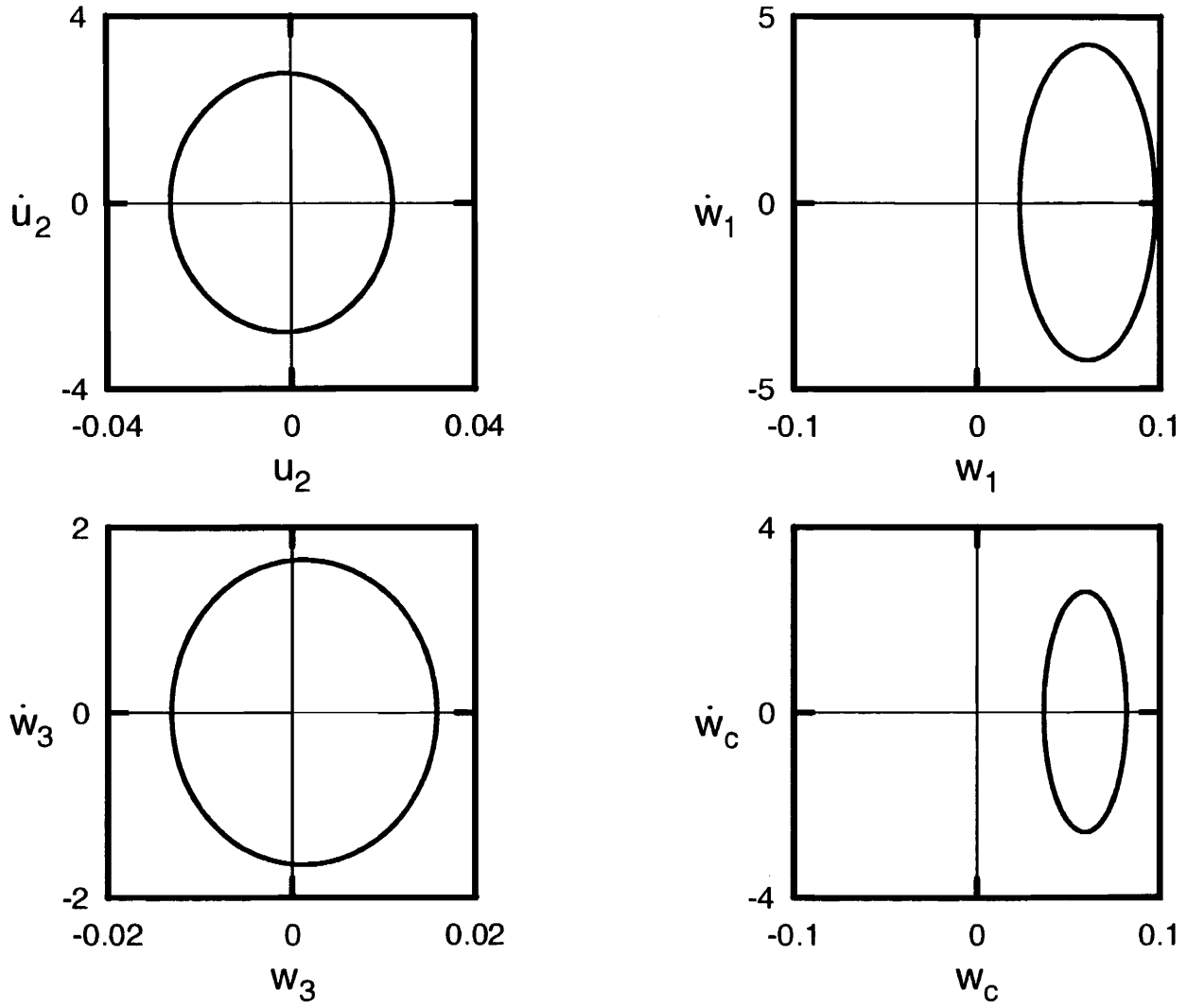

Figure A.165: Phase portraits for shear deformable beam with $r = 0.05$, $\Omega = 115.0$, $a = 1.0$.

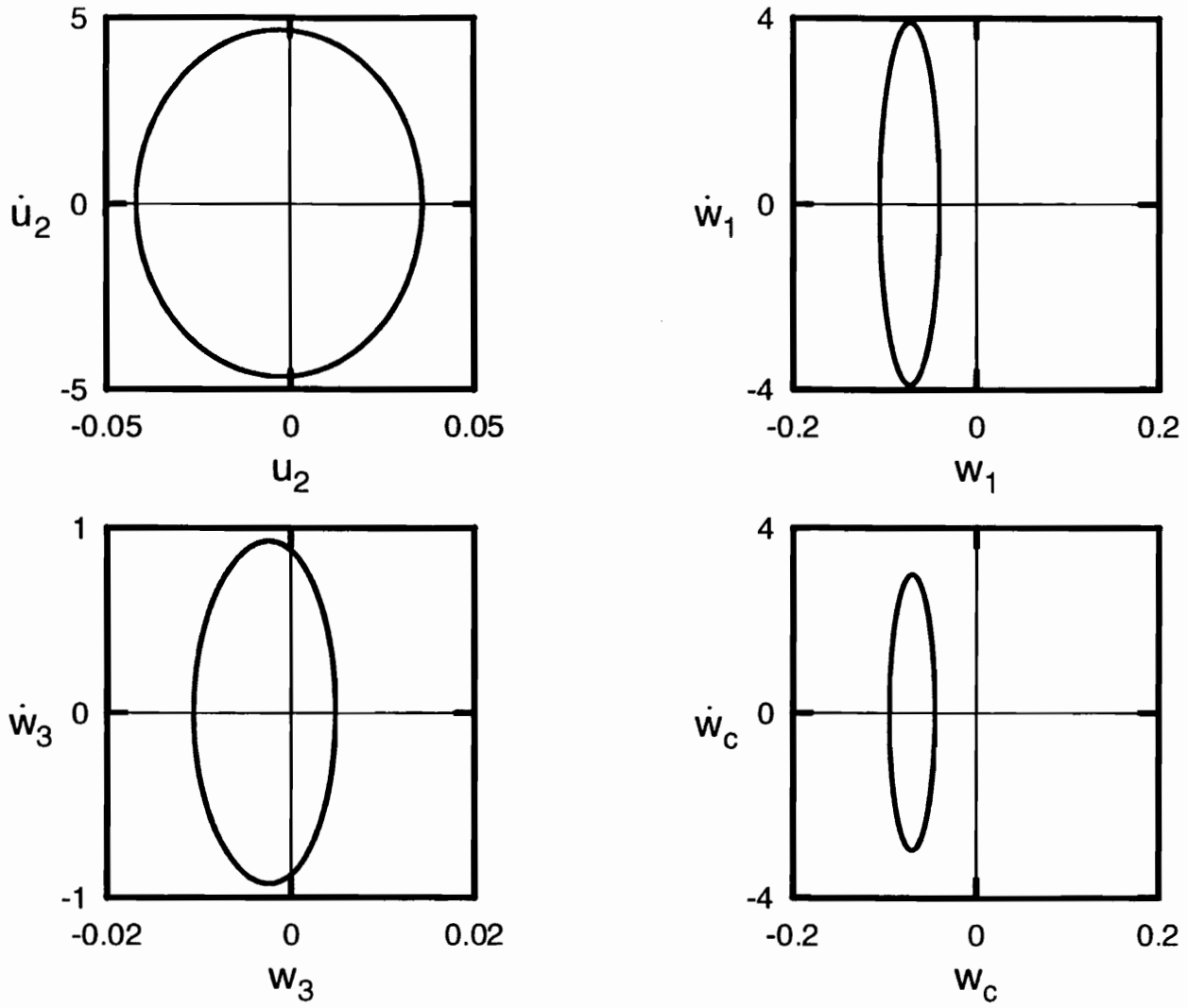

Figure A.166: Phase portraits for shear deformable beam with $r = 0.05$, $\Omega = 120.0$, $a = 1.0$.

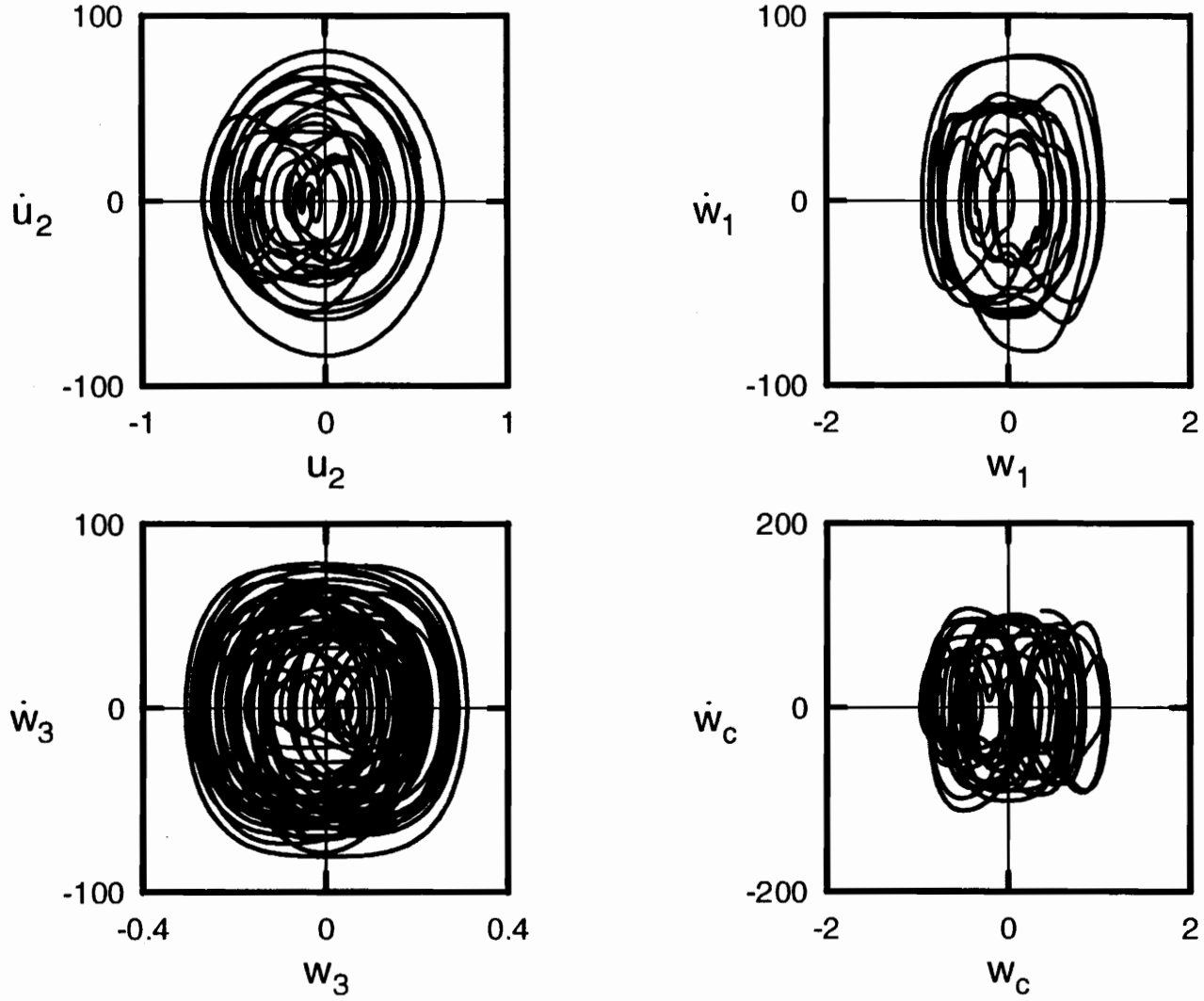

Figure A.167: Phase portraits for non shear deformable beam with $r = 0.05$, $\Omega = 60.0$, $a = 1.0$.

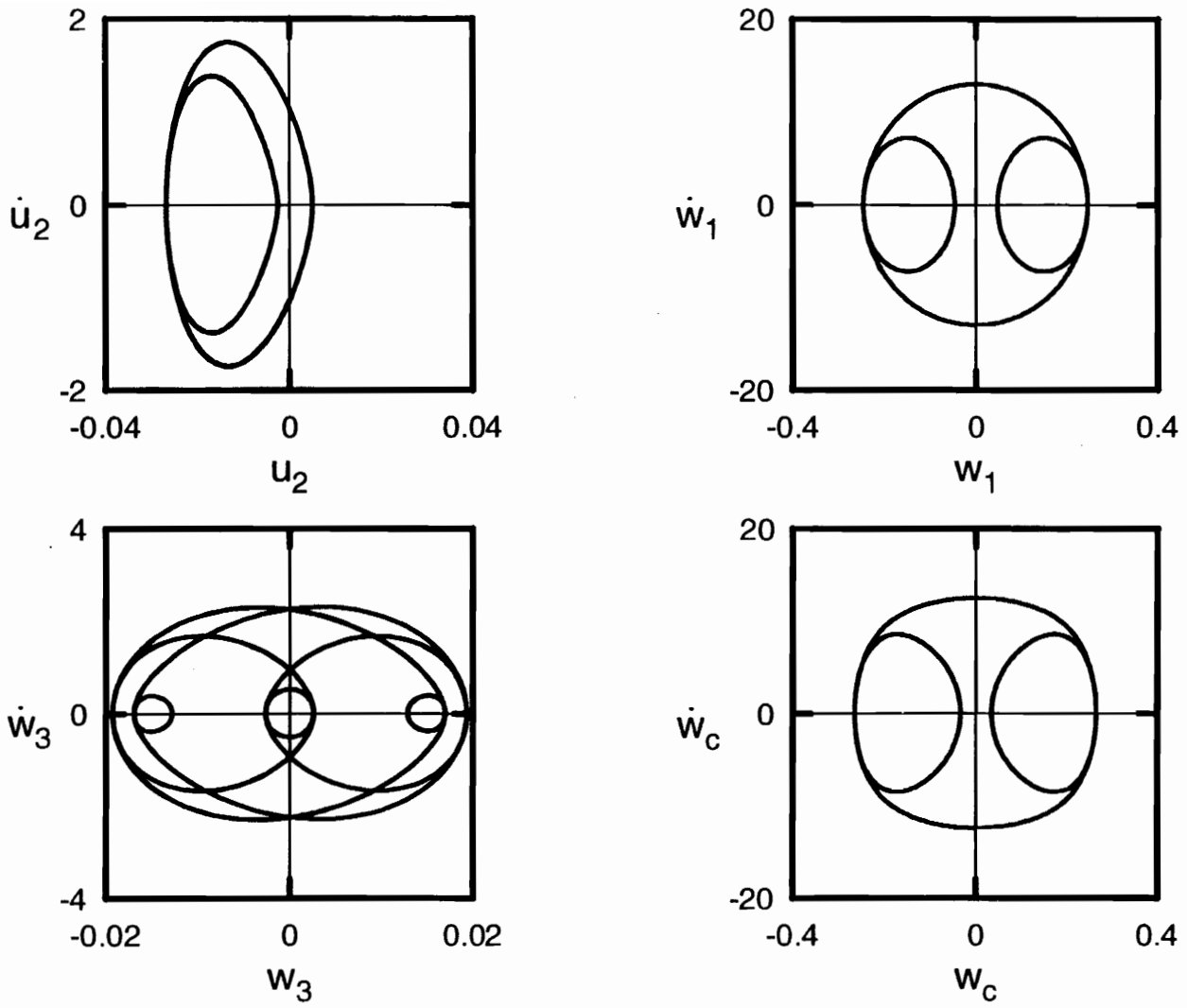

Figure A.168: Phase portraits for non shear deformable beam with $r = 0.05$, $\Omega = 65.0$, $a = 1.0$.

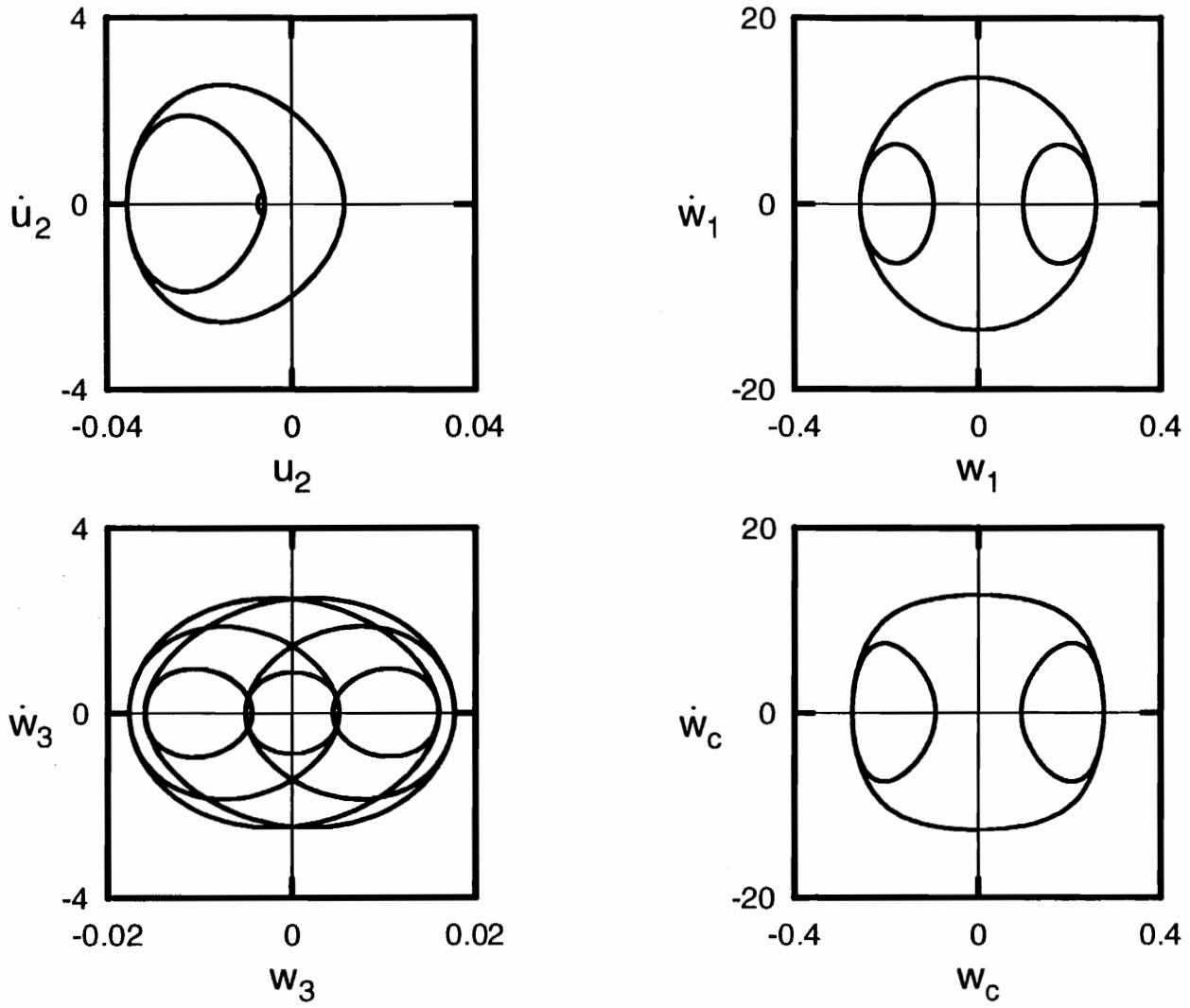

Figure A.169: Phase portraits for non shear deformable beam with $r = 0.05$, $\Omega = 68.0$, $a = 1.0$.

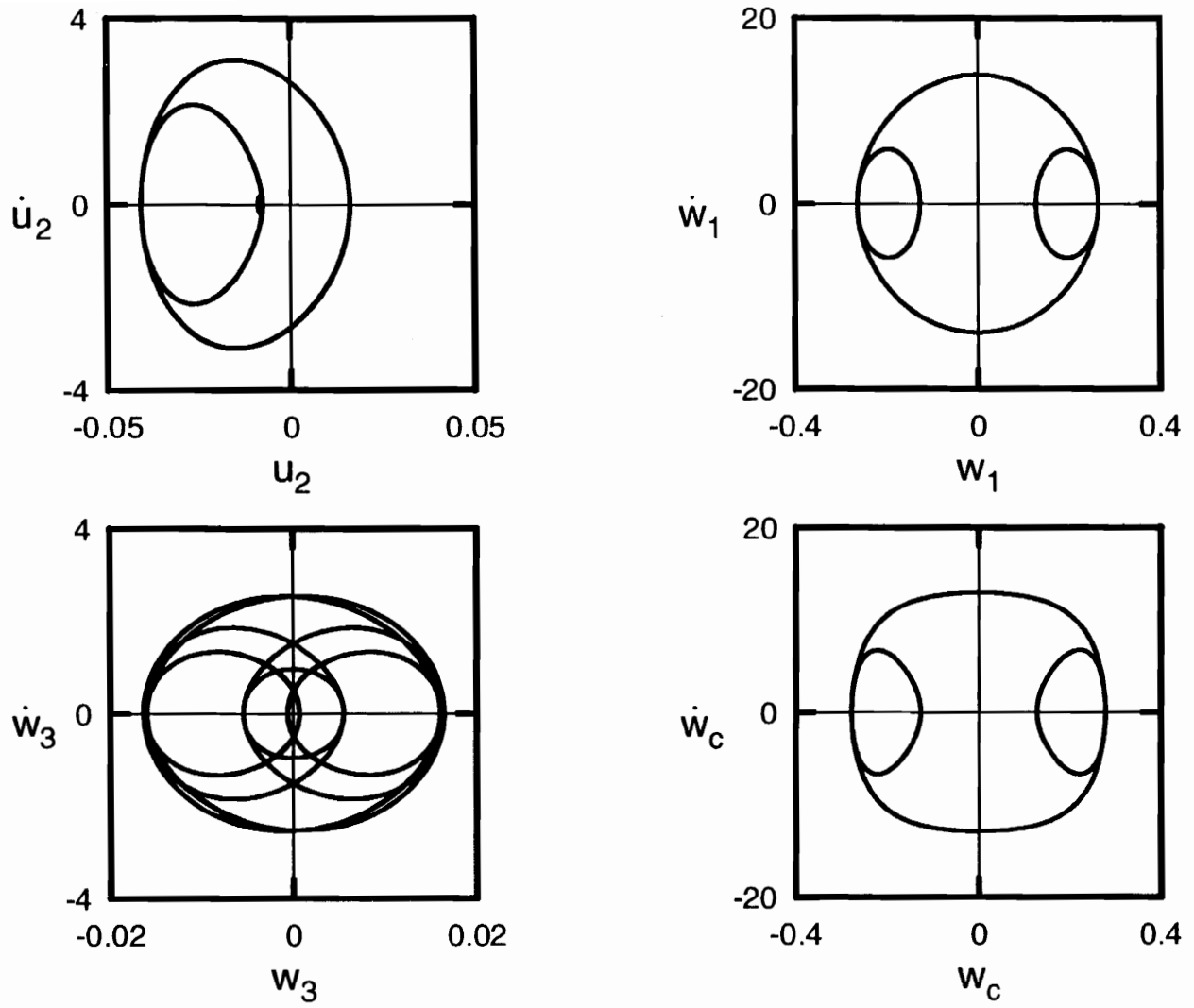

Figure A.170: Phase portraits for non shear deformable beam with $r = 0.05$, $\Omega = 70.0$, $a = 1.0$.

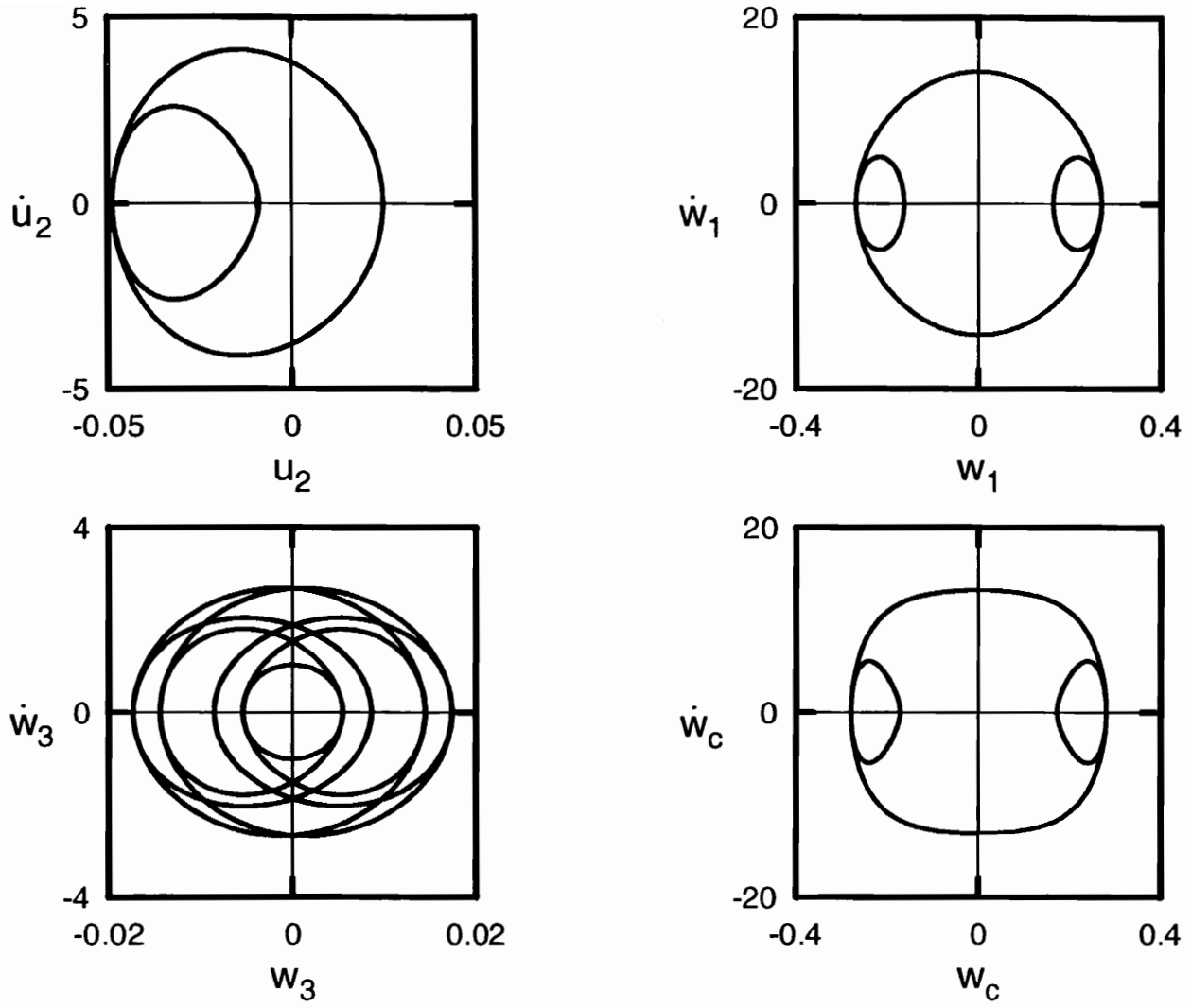

Figure A.171: Phase portraits for non shear deformable beam with $r = 0.05$, $\Omega = 73.0$, $a = 1.0$.

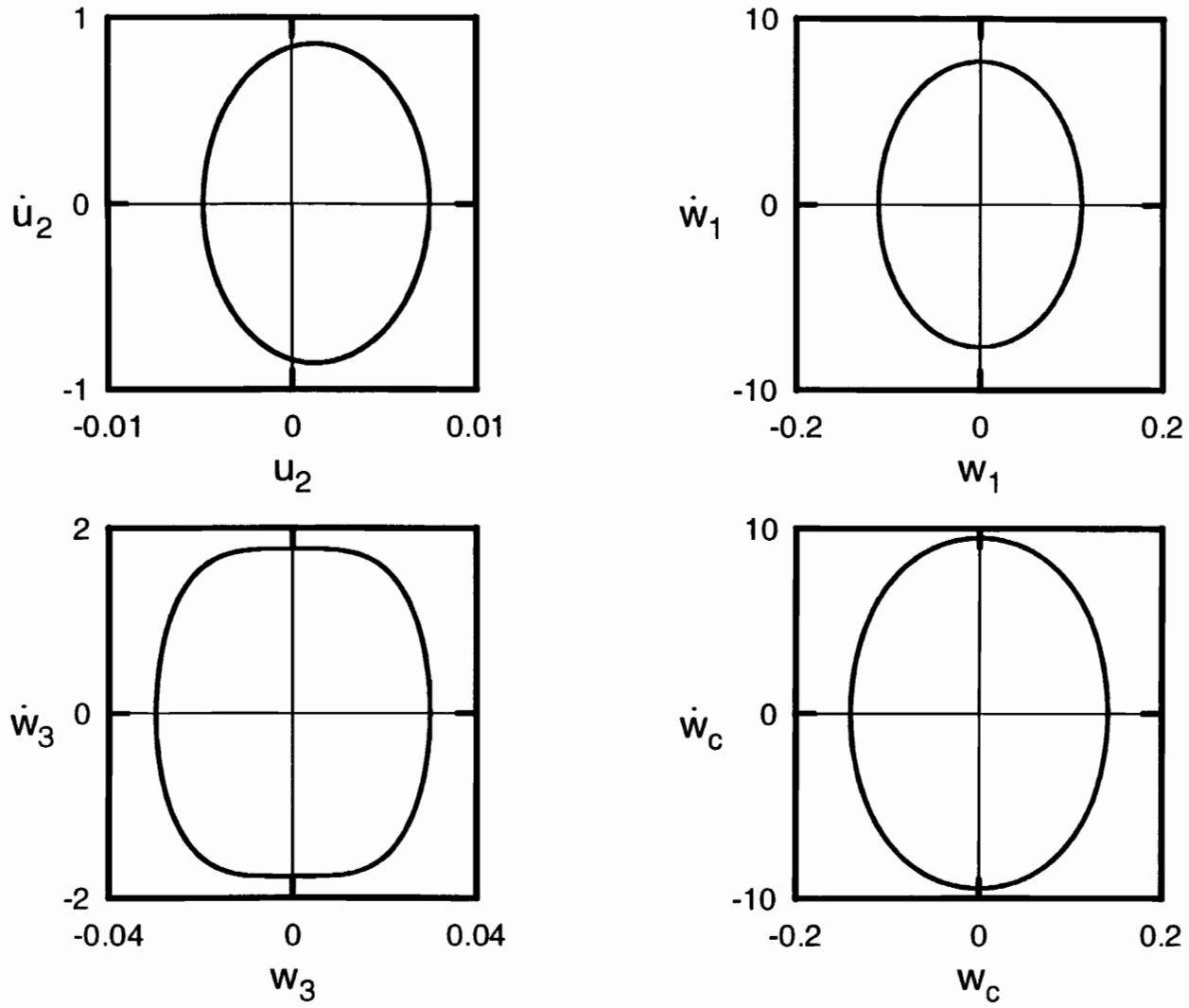

Figure A.172: Phase portraits for non shear deformable beam with $r = 0.05$, $\Omega = 70.0$, $a = 1.0$.

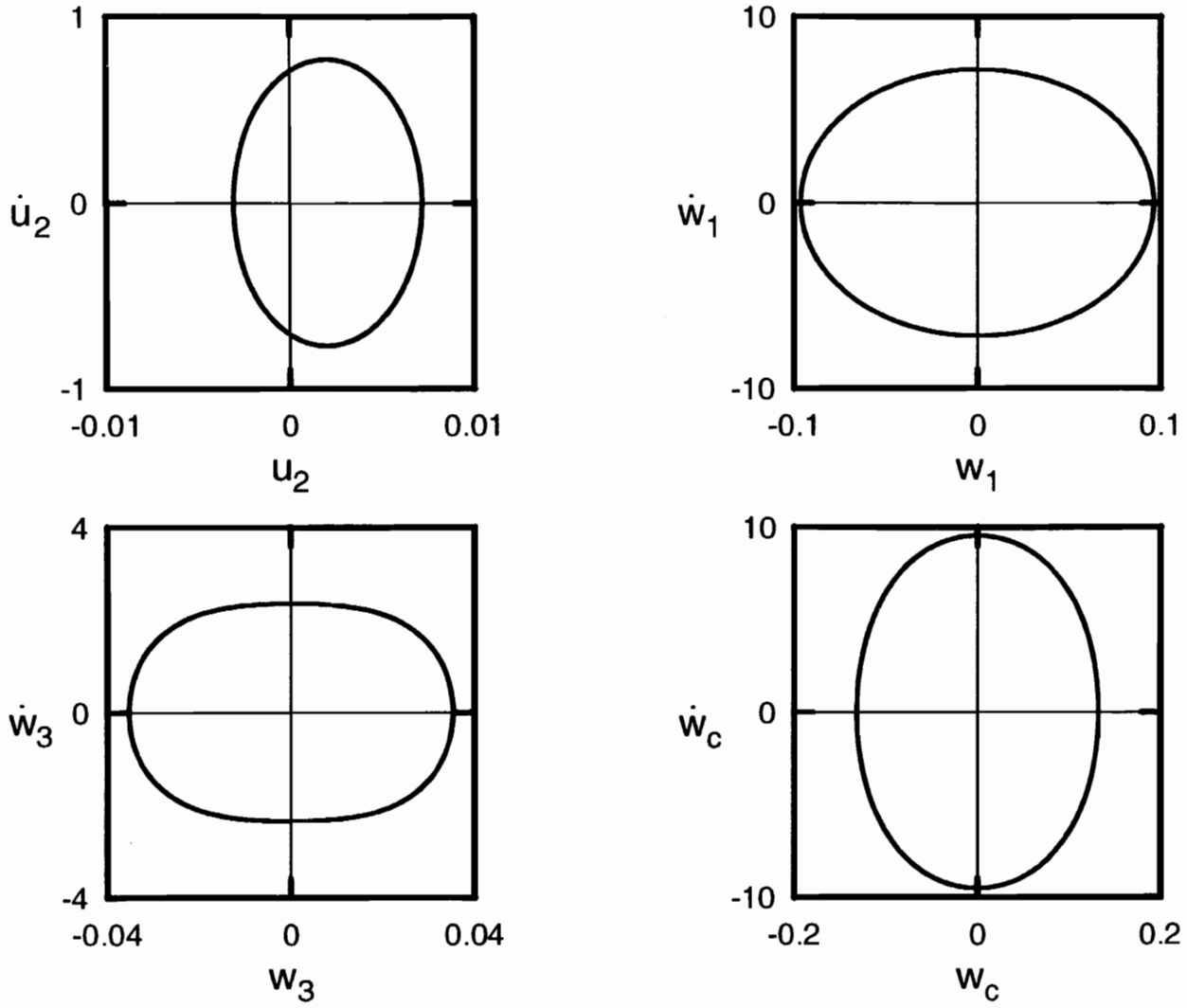

Figure A.173: Phase portraits for non shear deformable beam with $r = 0.05$, $\Omega = 75.0$, $a = 1.0$.

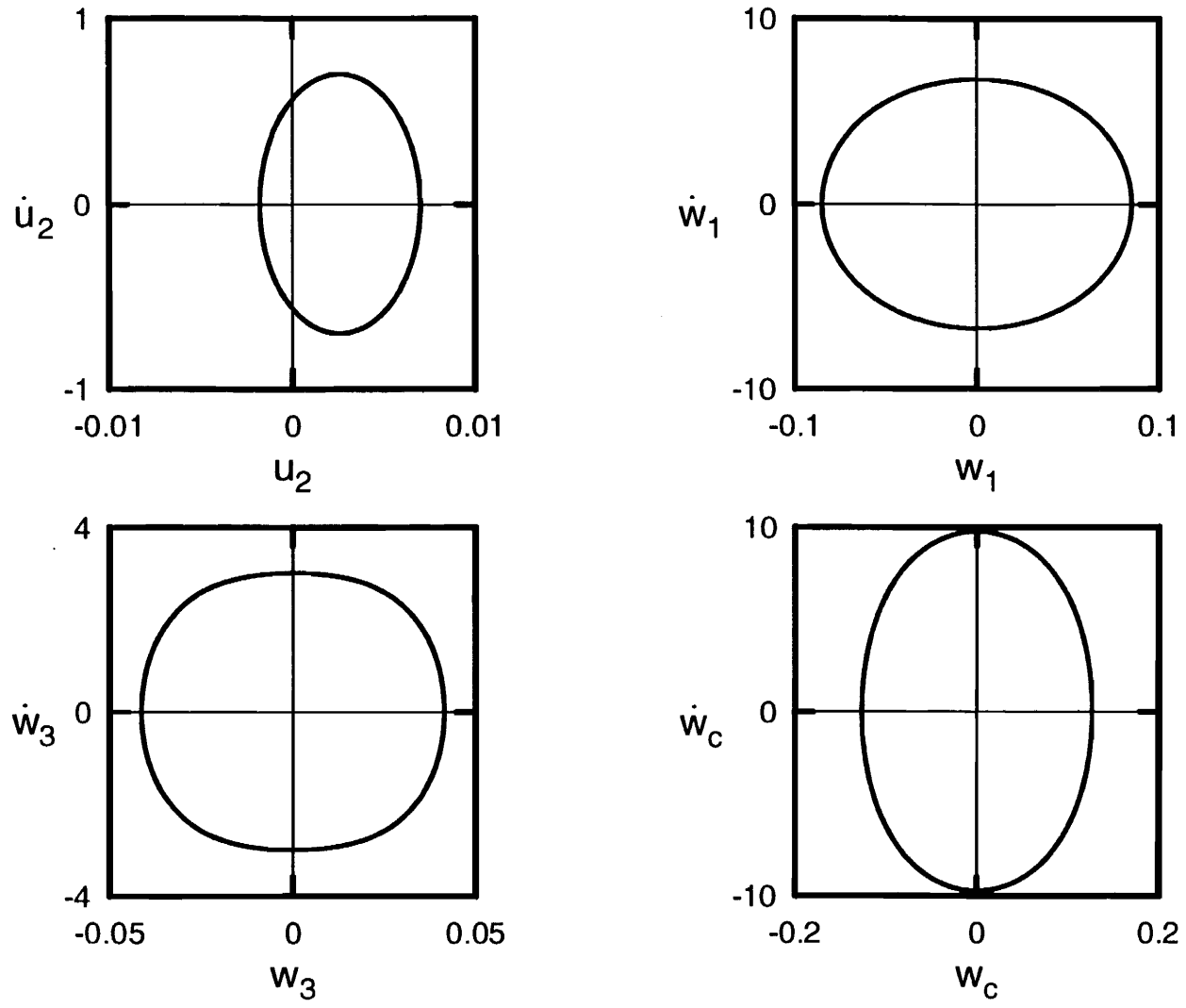

Figure A.174: Phase portraits for non shear deformable beam with $r = 0.05$, $\Omega = 80.0$, $a = 1.0$.

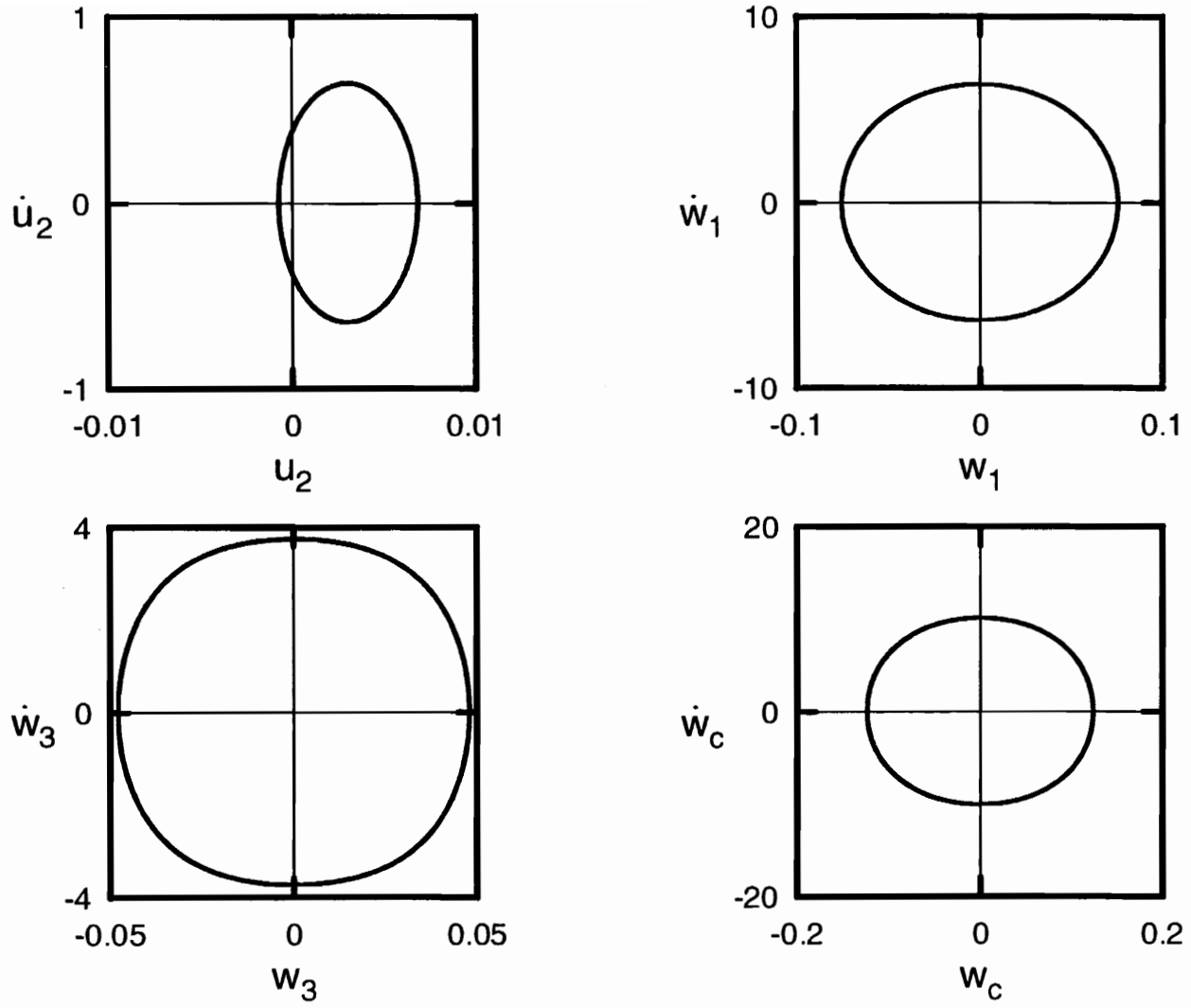

Figure A.175: Phase portraits for non shear deformable beam with $r = 0.05,\ \Omega = 85.0,\ a = 1.0.$

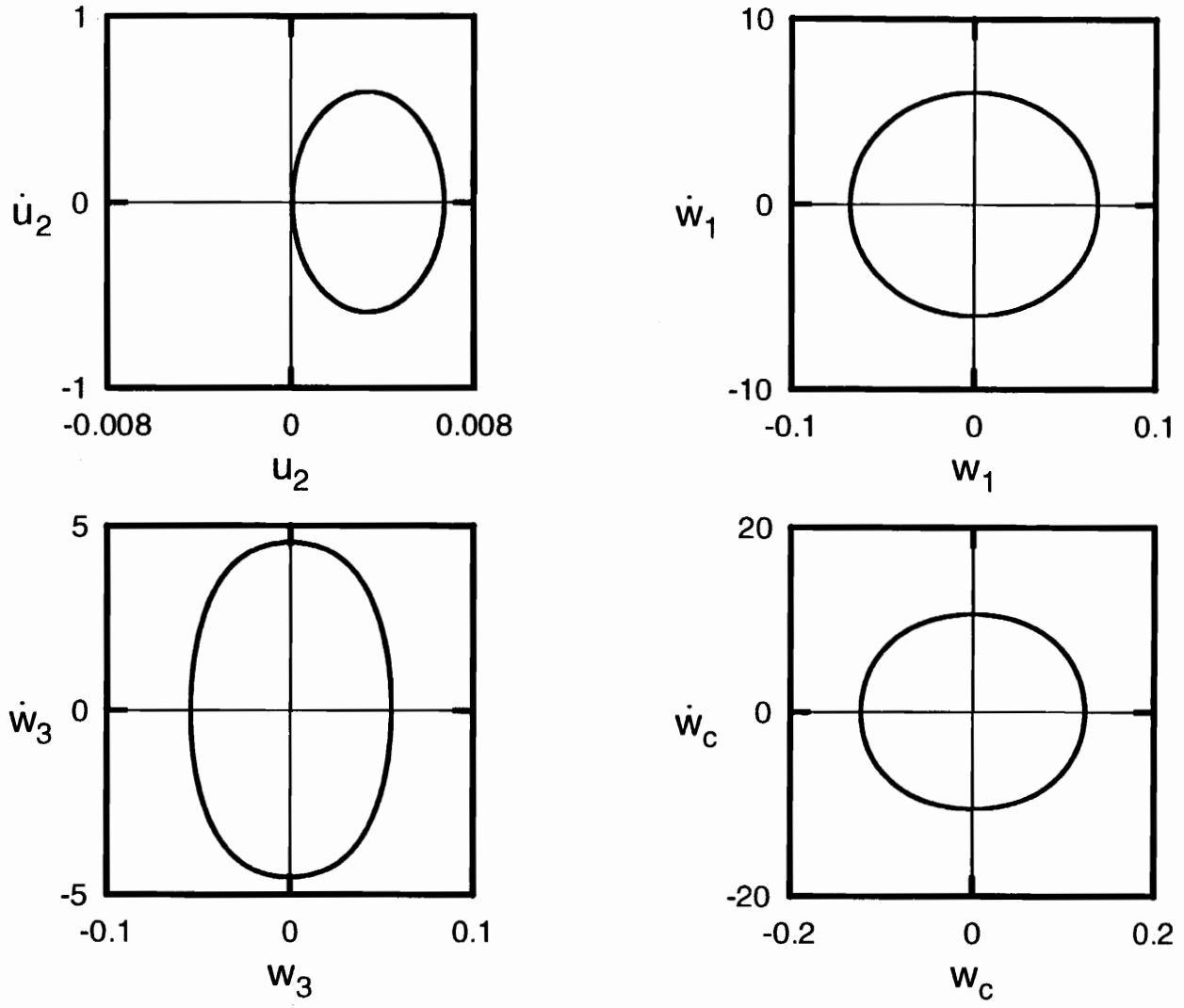

Figure A.176: Phase portraits for non shear deformable beam with $r = 0.05$, $\Omega = 90.0$, $a = 1.0$.

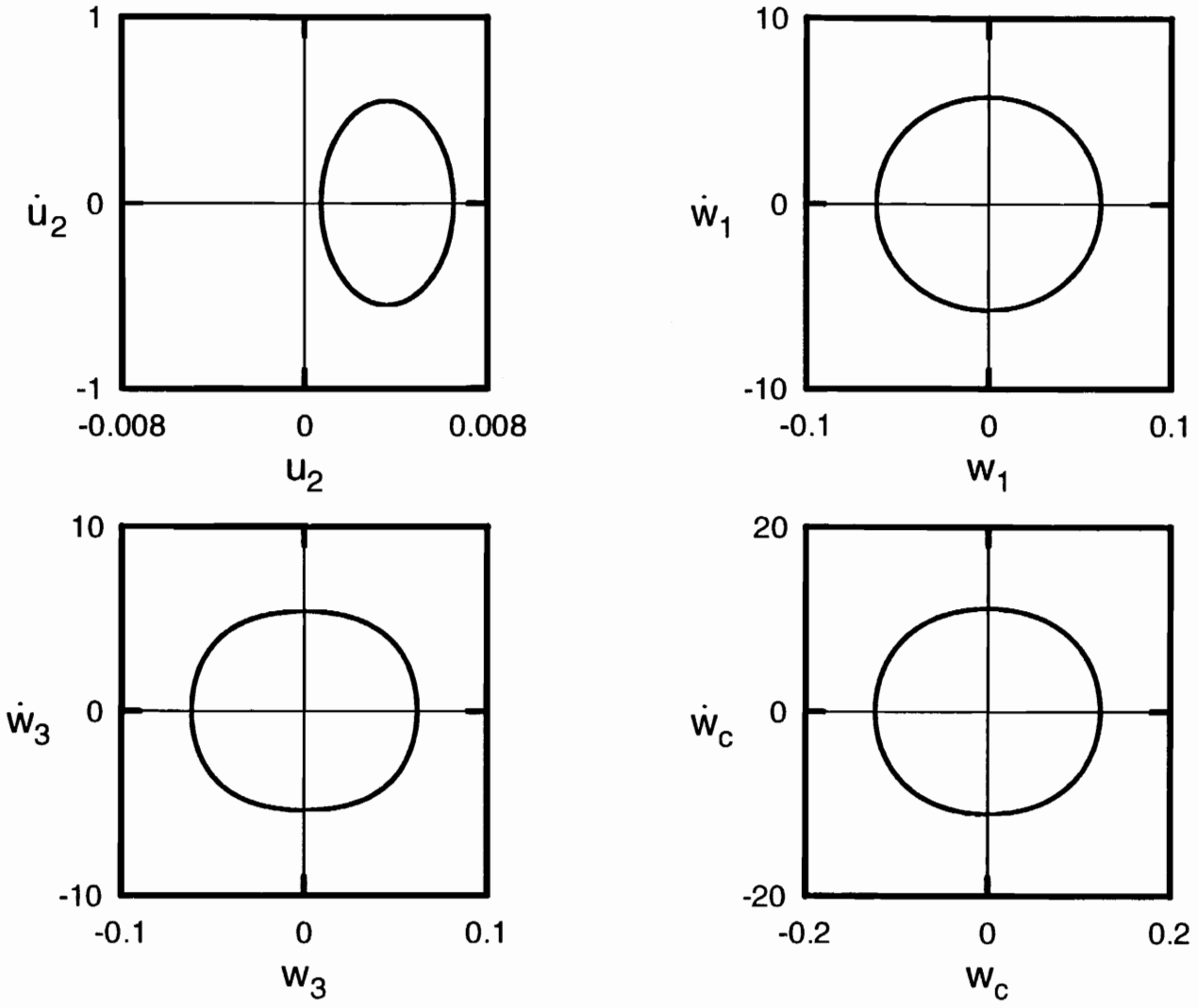

Figure A.177: Phase portraits for non shear deformable beam with $r = 0.05$, $\Omega = 95.0$, $a = 1.0$.

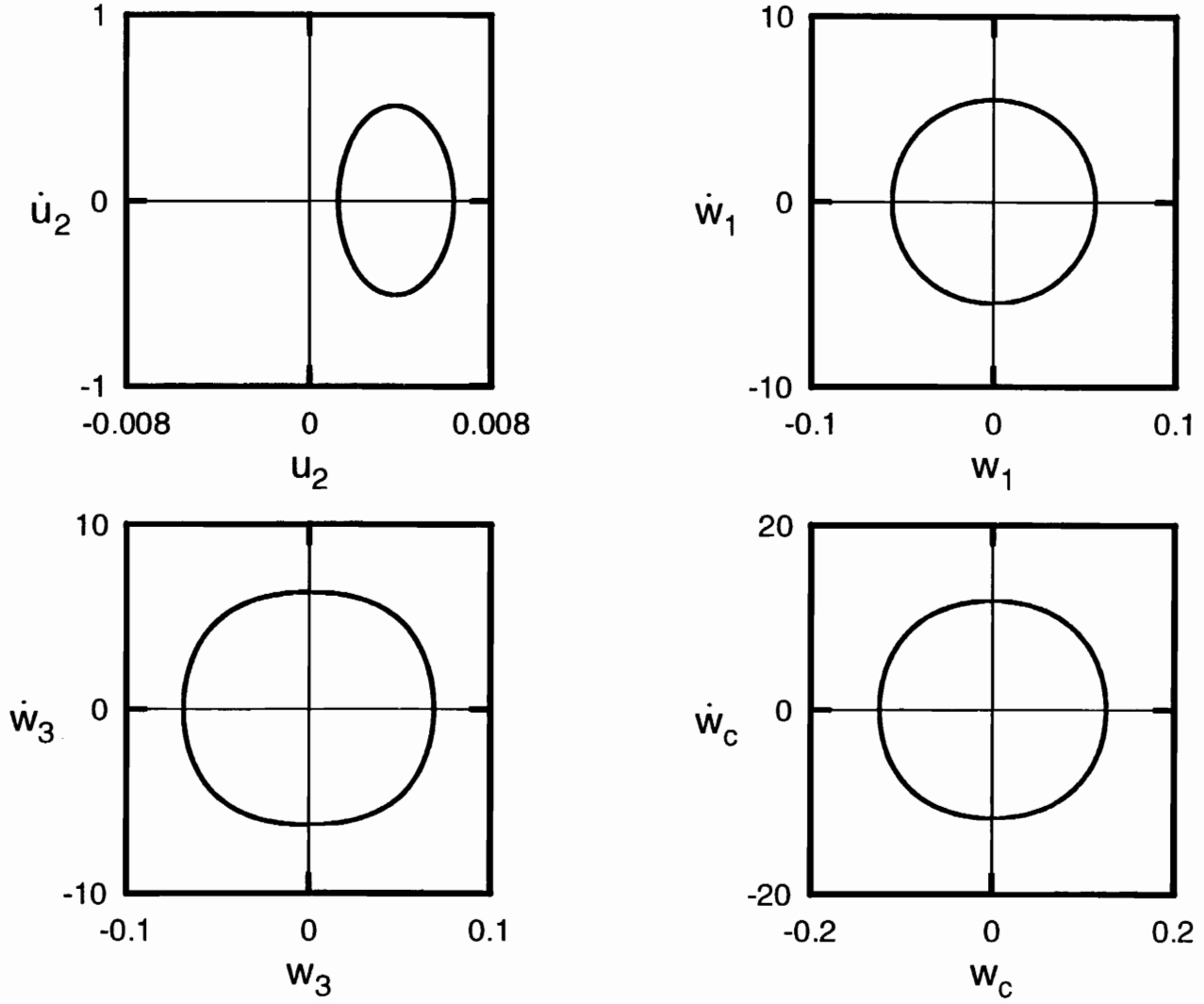

Figure A.178: Phase portraits for non shear deformable beam with $r = 0.05$, $\Omega = 100.0$, $a = 1.0$

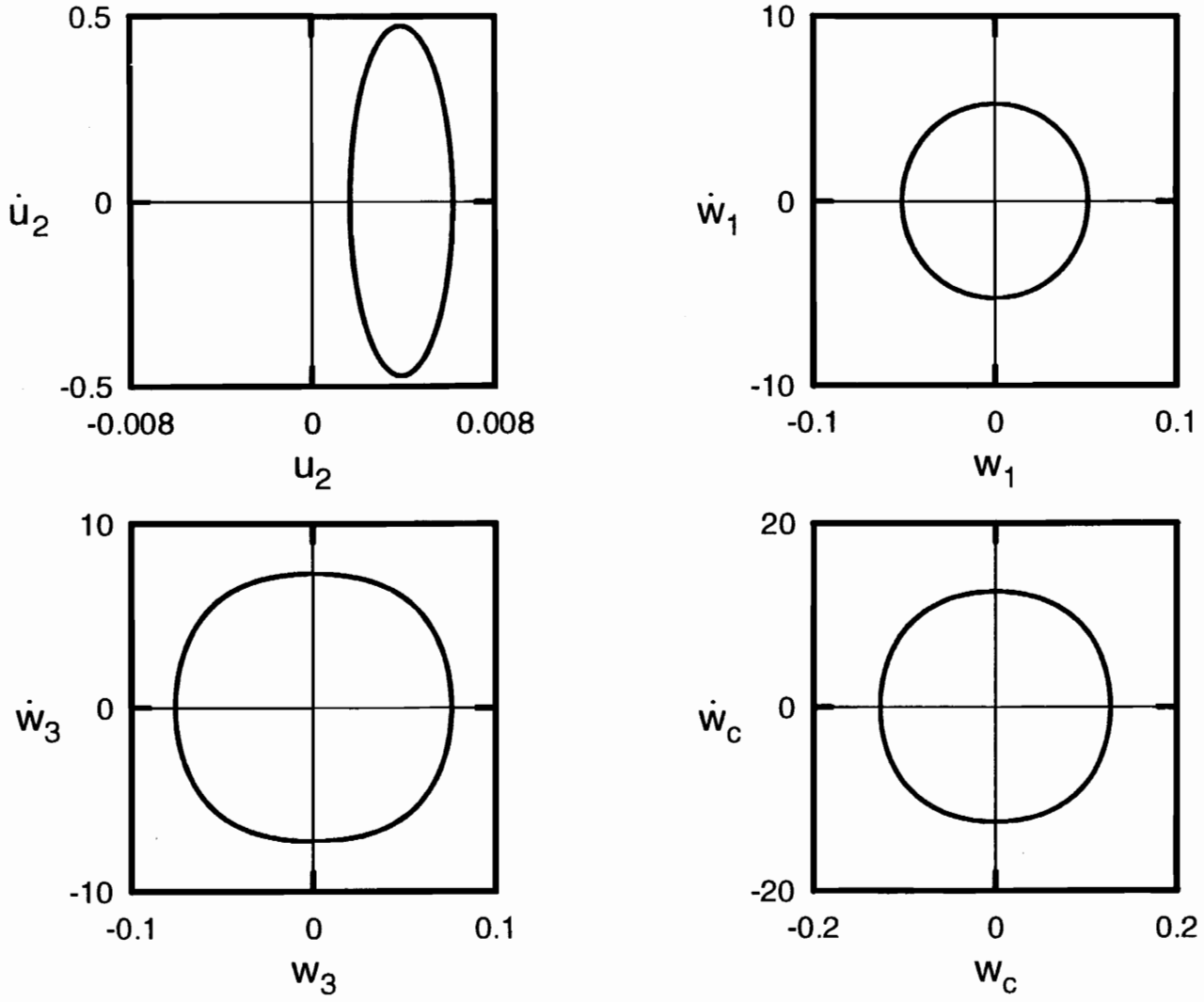

Figure A.179: Phase portraits for non shear deformable beam with $r = 0.05$, $\Omega = 105.0$, $a = 1.0$

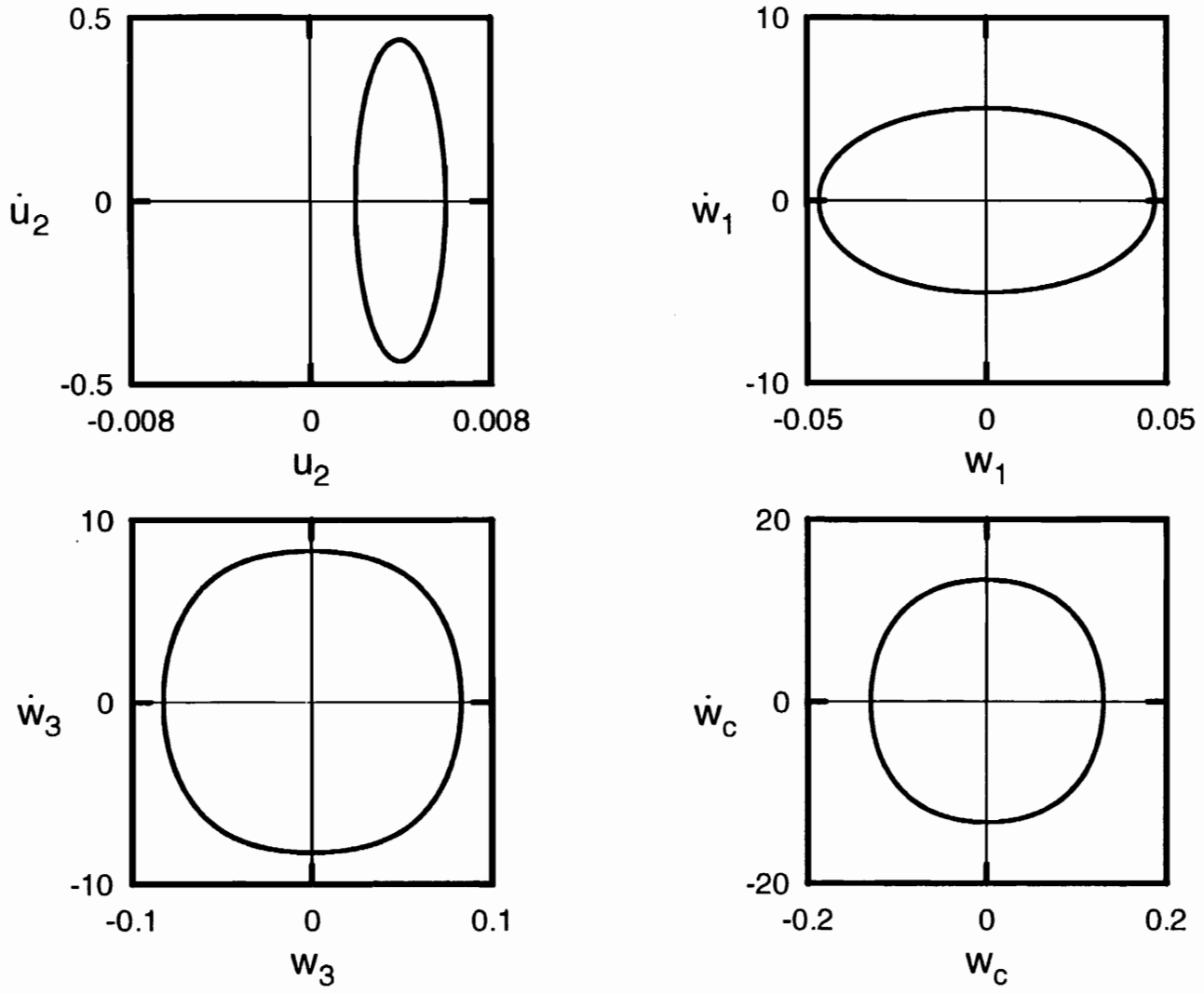

Figure A.180: Phase portraits for non shear deformable beam with $r = 0.05$, $\Omega = 110.0$, $a = 1.0$

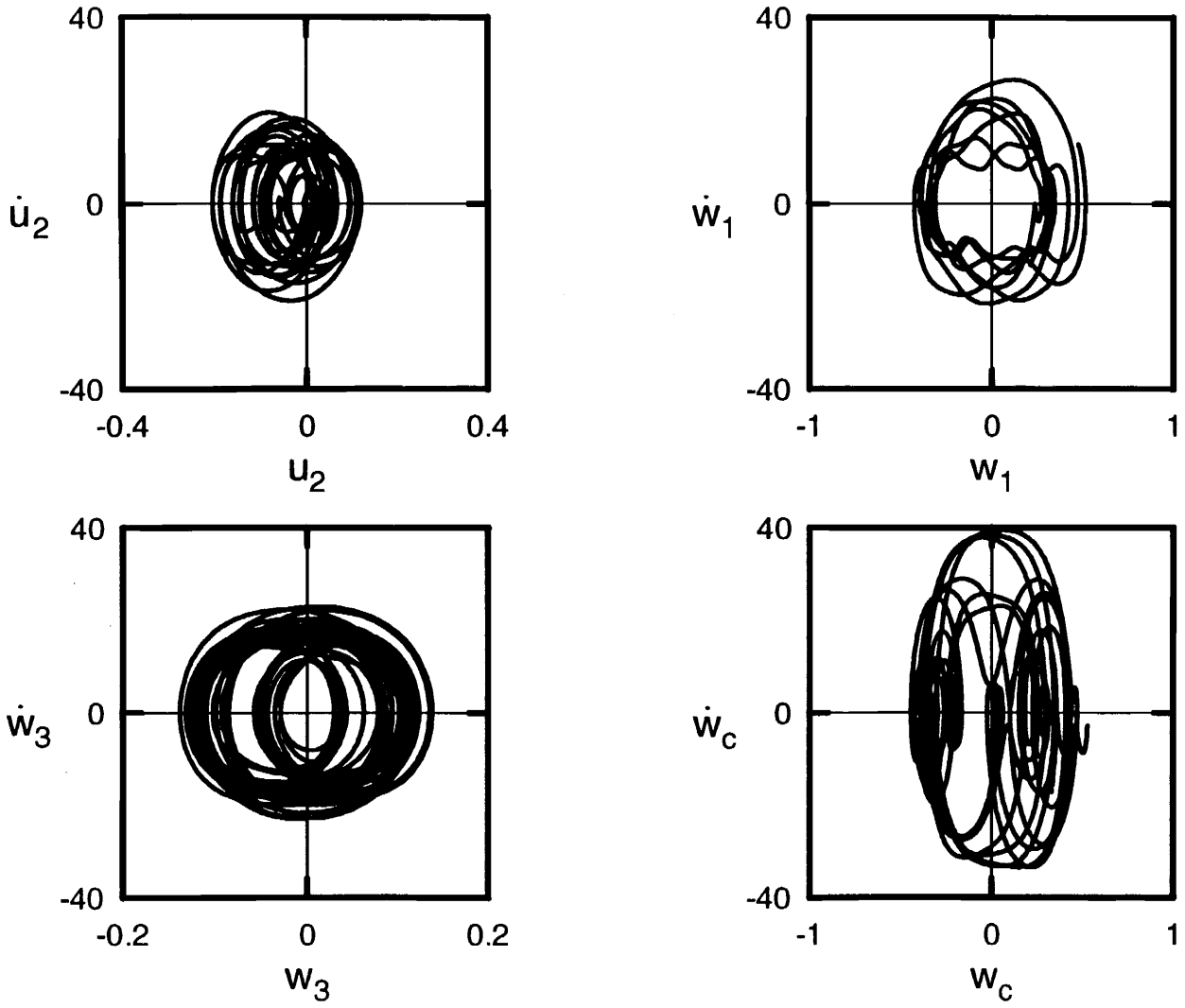

Figure A.181: Phase portraits for non shear deformable beam with $r = 0.05$, $\Omega = 115.0$, $a = 1.0$.

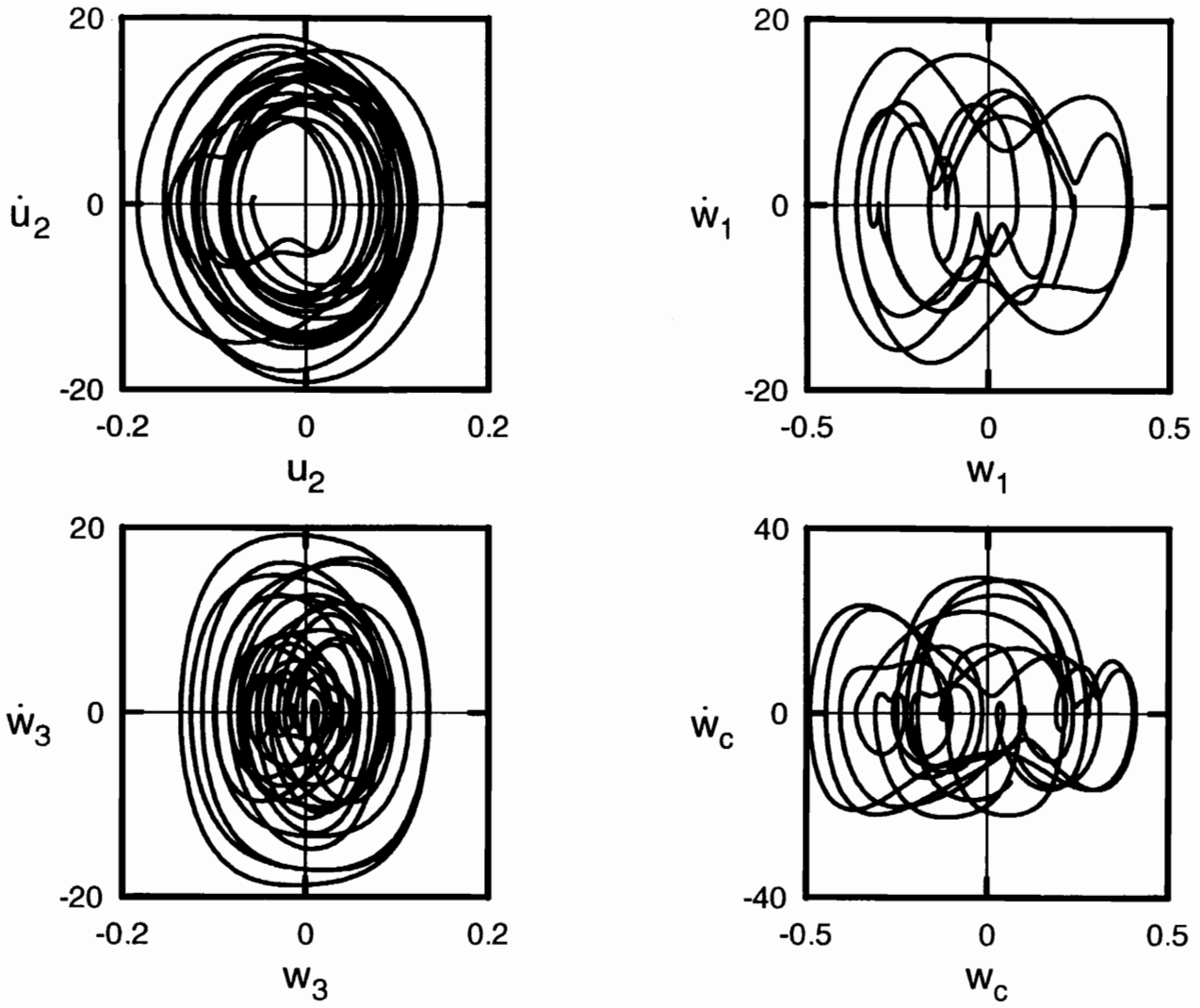

Figure A.182: Phase portraits for non shear deformable beam with $r = 0.05$, $\Omega = 120.0$, $a = 1.0$.

VITA

Christopher Hagmann was born on November 3, 1966 to Eleanor and William Hagmann in Glen Ridge, New Jersey. He had his pre-college education in Bridgewater, New Jersey. After graduating from high school he enrolled at Virginia Polytechnic Institute and State University in September of 1985. He received a Bachelor of Science degree Engineering Science and Mechanics in May of 1990.